Ultimate Strength of Composite Beams

by
Nadia Julia Molenstra

A dissertation submitted to the
University of Warwick
in partial fulfillment for the degree of
Doctor in Philosophy

August 1990

Declaration

I hereby declare that the work embodied in this thesis is the result of my own investigations except where reference has been made to published literature.

This work has not been submitted in candidature for any other degree.

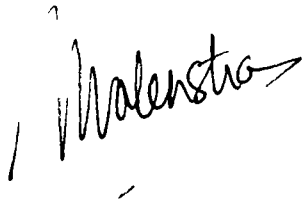

N.J. Molenstra

Acknowledgements

I would like to express my sincere thanks to Prof. R.P. Johnson for his support and criticism throughout the course of my research. My appreciation is also extended to Dr. W. Lewis for her advice on the numerical side of the work.

I am indebted to the University of Warwick, the Building Research Establishment and 'het Nationaal Fonds voor Wetenschappelijk Onderzoek' in Belgium for their financial support which made this research possible.

I would like to convey my gratitude to my colleagues Roger Fan and Zoubir Benterkia for their encouragement and the many useful discussions.

Finally, I would like to communicate my thanks to Mr. C. Banks for his devoted support in the laboratory, to Mr. J. Liddermore for the computer drawings and to Mr. C. Handley for the compilation of this written document.

Synopsis

The study of composite beams is characterised by the connection between the two components: the concrete slab and the steel girder. In this thesis, two different problems, related to this connection were studied: the problem of partial interaction in composite beams of long spans with low degrees of shear connection, and the problem of transverse flexibility of the stud connection 'joint' between the concrete slab and the steel beam as part of a discrete inverted U-frame. This thesis is therefore divided into two separate parts.

The study of beams with partial shear connection and solid slabs or slabs with metal decking is considered in the first part. Such beams, with a uniform stud spacing over each shear span, with spans longer than 10 m — generally propped during construction, and with low degrees of shear connection, could fail prematurely and suddenly in shear rather than gradually in bending, due to the limited slip deformation capacity of the studs in shear. In order to investigate the behaviour of simply supported and continuous composite beams with different degrees of shear connection, different geometry and different shear spans under design ultimate loading conditions, a numerical computer simulation program was written. The program takes account of the relative displacement between the slab and the beam and the non-linear behaviour of steel, concrete and stud connectors. A data bank of maximum slip results for different beams is obtained for ultimate beam loads designed to the interpolation method in Eurocode 4. The computer simulation gives a conservative but safe assessment of the suitability of the degree of interaction for a specific design ultimate load . The results were used to formulate a tentative design method for composite beams with solid slabs and partial shear connection.

Discrete inverted U-frame action exists between composite bridge beams with intermittent vertical web stiffeners which provide lateral restraint to the bottom flange in the hogging bending region near the internal supports. The design method in BS 5400:Part 3 for discrete U-frame action gives values for the transverse flexibility of a number of standard structural steel connections which are used in the calculation of the effective buckling length and the lateral deflection of the compression flange. To obtain similar values for steel-concrete joints, tests were done to scale 1:1 on six flange-slab connections with different stud configurations, but constant conservative dimensions for the steel flange and the concrete slab. Their crack patterns can be predicted by using a truss analogy. All test specimens either failed in shear or by pulling out of the studs, and shear cracking and shear failure criteria for concrete beams can be used to predict the cracking and failure loads. The transverse elastic flexibilities of the joints in these tests only represent the behaviour of the same joints in a complete structure up to the point where the shear cracks propagated over the full width of the specimens. Based on these few test results, a limited tentative design equation is proposed for the transverse flexibility of these type of stud connections, although further research is required into the influence of the increased flexibility on the buckling mode and the variation of the flexibility with variables other than the stud configurations.

Contents

List of Figures

List of Tables

List of Notations

A cross-sectional area
A_a cross-sectional area of the steel profile
A_c cross-sectional area of the concrete slab
A_f sum of cross-sectional areas of top and bottom flange of steel profile
A_{fc} cross-sectional area of compression flange of steel profile
A_i cross-sectional area of the top flange of the steel member when $i = 1$, of the web when $i = 2$ and of the bottom flange when $i = 3$
A_r total area of top and bottom layer of reinforcement in the slab
A_{rb} area of bottom layer of reinforcement
A_{rt} area of top layer of reinforcement
A_s cross-sectional area of tension reinforcement
A_{sh} cross-sectional area of shank of stud
A_w cross-sectional area of the web
a shear span in concrete beams
a_c shear span of high shear between the studs in tension (F_{st}) and the reaction (RF_{st}) in Fig. 8.4, due to a transverse moment applied to the connection.
a_l shortest distance between fitted vertical web stiffener and studs in the longitudinal direction
a_s distance between resultant tensile and compressive forces in vertical effective web stiffener under transverse elastic bending
a_t shortest distance between stud and web in transverse direction

b breadth
b_c breadth of slab
b_e effective breadth of slab
b_f breadth of steel flange
b_{fc} breadth of compression flange
b_h breadth of haunch
b_i breadth of top flange when $i = 1$, of web when $i = 2$ and of bottom flange when $i = 3$
b_0 width over which initial internal crack forms under transverse force $F_{t.c0}$

d effective depth of beam or slab
d_h diameter of stud head
d_{sh} diameter of shank of welded stud connector

E elastic modulus
E_a elastic modulus of structural steel
E_c elastic modulus of concrete
E_p strain-hardening modulus of structural steel
E_{sh} elastic modulus of shank of studs

F longitudinal force
F_a longitudinal force in steel profile
F_c longitudinal force in concrete slab
F_{cu} pull-out strength of studs when determined by the shear strength of the conical failure surface of concrete
F_p longitudinal interface shear force at critical cross-section where the moment reaches M_p
F_{pp} longitudinal interface shear force at critical cross-section where the moment reaches M_{pp}
F_r longitudinal force in the reinforcement at the internal support
F_{sh} axial tensile force in the shank of the stud
F_{st} axial tensile force in the stud
F_t transverse force applied at the centroid of the compression flange *or* transverse tensile force applied by the jack to the test specimen
$F_{t,cr}$ transverse load at which diagonal cracking first became visible at both sides of the tested specimen
$F_{t,u}$ maximum transverse force the tested specimen is able to resist
$F_{t,c0}$ transverse force at which initial internal cracking starts, before this crack has spread over the whole width of the test specimen
$F_{t,c1}$ transverse force at which the initial diagonal cracking has spread over the whole width of the test specimen
$F_{t,c2}$ transverse force at which a second diagonal crack will form parallel with the first one
f transverse flexibility of a bolted connection in a U-frame or inverted U-frame
f_{ay} yield stress of structural steel
f_{ad} design value of the yield stress of structural steel $= f_{ay}/\gamma_a$
f_c cylinder strength of concrete
f_{cb} strength of concrete obtained from the modulus of rupture test
f_{cd} design value of the cylinder strength of concrete $= f_{ck}/\gamma_c$
f_{ck} characteristic value of the cylinder strength of concrete
f_{cr} strength of concrete at which the concrete cracks
f_{ct} tensile splitting strength of concrete
f_{cu} cube strength of concrete
f_r transverse flexibility of embedded stud connection as part of an inverted U-frame
f_{ry} yield stress of reinforcement
f_t' tensile strength of concrete
f_u ultimate tensile strength of shank steel of studs

h depth or height
h_a depth of steel beam
h_t overall depth of beam
h_{sh} height of the shank of the stud
h_{st} overall height of studs after welding
h_w depth of web of steel beam

I second moment of area
I_a second moment of area of steel beam
I_c second moment of area of uncracked composite section
I_u second moment of area of uncracked concrete slab
i $= 1, ..., n$ numbering of nodes

k_c elastic spring constant of concrte slab as elastic support to steel flange
k_s elastic spring constant of the embedded studs

l span of beam
l_e effective length of unrestrained compression flange
l_h length of lever arm between point where the transverse load, F_t, is applied and the top of the top flange
l_u longitudinal spacing between U-frames

M bending moment in equilibrium with external loads
M_a bending moment in steel beam
M_c bending moment in concrete slab
M_D design value of moment of resistance at support in notation of BS 5400:Pt.3
M_{max} maximum bending moment reached in a test *or* a beam
M_p plastic moment of resistance of a composite section with full shear connection
M_{pa} plastic moment of resistance of steel profile alone
M_{pp}^{i} plastic moment of resistance of composite beam with partial shear connection, according to eq. (2.1)
M_{pp}^{e} plastic moment of resistance in of composite beam in sagging bending with partial shear connection, according to equations (I.2) *or* (I.3)
$M_{pp}^{e\prime}$ plastic moment of resistance of composite beam in hogging bending with partial shear connection, according to equations (I.4) *or* (I.5)
M_s computed hogging moment at internal support
M_t transverse moment at the interface of the steel girder with the concrete slab $= F_t\, l_h$
$M_{t,cr}$ transverse moment at steel – concrete interface at which diagonal cracking first became visible at both sides of the tested specimen

$M_{t,u}$ maximum transverse moment the tested specimen is able to resist

$M_{t,c0}$ transverse moment at which initial internal cracking starts, before this crack has spread over the whole width of the test specimen

$M_{t,c1}$ transverse moment at which the initial diagonal cracking has spread over the whole width of the test specimen

$M_{t,c2}$ transverse moment at which a second diagonal crack will form parallel with the first one

m modular ratio for concrete

m_s strain-hardening factor for structural steel

N_i number of shear connectors between two adjacent critical cross-sections

N_f value of N for full shear connection in accordance with either the draft Eurocode 4 or the draft BS 5950:Pt.3.

P vertical point load on a beam

P_{di} dead load component of the ultimate value for the point load on span i

P_{ui} ultimate value for the point load on span i

Q longitudinal shear force on one connector

Q_d design shear strength per stud $= Q_k/\gamma_m$

Q_k characteristic shear strength per stud

Q_u ultimate value of the shear strength Q, obtained from Push-Out tests

q longitudinal shear per unit length at steel-concrete interface

R reaction force *or* resultant force

RF_{st} resultant compressive force applied by the concrete slab to the top flange under a transverse moment M_t

RF_{cu} resultant compressive force applied by the concrete slab onto the top flange under a transverse moment M_t

t depth or thickness

t_c depth of concrete slab

t_{fc} thickness of the compression flange

t_h depth of metal decking within the slab

t_i depth of the top flange when $i = 1$, depth of the web when $i = 2$, and depth of the bottom flange when $i = 3$

t_w thickness of web of steel member

V vertical shear force

V_a vertical shear force in steel beam

V_c vertical shear force in concrete slab

V_{cr} shear cracking resistance of a beam

V_D design ultimate shear force in the notation of BS5400:Pt.3
V_u shear failure of a beam
v vertical deflection of a beam
v_{max} maximum computed deflection of a beam
v_s computed deflection at the position of the central support

w uniform distributed load
w_d dead uniform distributed load
w_{di} dead uniform distributed load on span i
w_u ultimate uniform distributed load
w_{ui} ultimate uniform distributed load on span i
w_p theoretical plastic collapse load of a composite beam with full shear connection
w_{pa} theoretical plastic collapse load of a steel beam
w_{pp}^{i} theoretical plastic collapse load of a composite beam with partial shear connection, using the interpolation method
w_{pp}^{e} theoretical plastic collapse load of a composite beam with partial shear connection, using the equilibrium method

x distance along the X–axis
x_i position of point load i along th X–axis
x_m distance between the external support and the position of maximum moment under ultimate loading conditions
x_s longitudinal spacing between studs
x_{si} longitudinal spacing between studs in shear span i along the beam

y distance along the Y–axis
y_a distance between the neutral axis of the steel profile and the top fibre of the top flange
y_c distance between the neutral axis of the concrete slab and the top fibre of the slab
y_e depth of the elastic neutral axis of the composite beam below the top of the slab
y_p depth of the plastic neutral axis of the composite beam below the top of the slab
y_r distance between the steel top flange and the neutral axis of the cracked concretre slab

Z lever arm between F_a and F_c
Z_a distance between mid-height of steel profile and the top fibre of the top flange
Z_c distance between mid-height of concrete slab and the top fibre of the slab
z distance along the Z–axis

α

α_{cr} angle betweeen the horizontal center-line through the slab and the diagonal shear crack due to F_t and M_t

β coefficient of the exponential function which models the load – slip behaviour of a stud connector embedded in a concrete slab

β_i consecutive diminishing slopes of the qualitative $M_t - \theta_r$ curve, which represents the behaviour of the steel – concrete joint of an inverted U-frame

δ transverse deflection of the centroid of the compression flange of a steel girder as part of a U-frame or inverted U-frame.

δ_i different components of the transverse deflection δ due to the transverse flexibility of the web (i=1), the transverse stiffness of the slab or the cross-member (i=2) and the transverse flexibility of the connection (i=3) between girder and slab or cross-member

ε strain

ε_a^b the strain in the bottom fibre of the steel profile

ε_{am} the strain limit in Fig. 3.10 on the strain in the steel profile in the forward integration routine of EPPIB

ε_a^t the strain in the top fibre of the steel profile

ε_{ay} the yield strain of the structural steel profile

ε_{ap} the strain of the structural steel profile at the end of the yield plateau

ε_c^b the strain in the bottom fibre of the concrete slab

ε_{cm} the strain limit in Fig. 3.10 on the strain in the concrete slab in the forward integration routine of EPPIB

ε_c^t the strain in the top fibre of the concrete slab

ε_{sh} the tensile strain measured in the shank of the stud connector, 50mm above the base

ε_u the strain in the concrete slab corresponding with σ_u, generally -0.002 or -0.0025

γ slip

γ_a partial safety factor on the yield strength of steel

γ_c partial safety factor on the characteristic strength of concrete

γ_e maximum elastic slip along a beam

γ_m partial safety factor on the limiting buckling stress *or* partial safety factor on the characteristic shear strength of the studs

$\gamma_{m(ax)}$ maximum value of slip along a beam, either elastic or plastic

$\gamma_m(x)$ maximum value of slip along a beam with x % shear connection

$\gamma_{max,b}$ maximum slip reached along a beam
$\gamma_{max,p}$ maximum slip reached in a Push-Out test
γ_p maximum plastic slip along a beam
γ_r partial safety factor on the yield strength of reinforcement

λ load factor ratio w_u/w_{pp}

ν poisson coefficient of steel

ϕ curvature

ρ density of concrete
ρ_r percentage of reinforcement in the concrete slab $(100\,A_r/(b\,d))$

θ rotation
θ_c rotation of the concrete slab at the position of the connection
θ_r relative rotation of the steel flange – concrete slab connection
θ_r^i relative rotation of the stud connection, calculated from the inclinometer readings
θ_r^d relative rotation of the stud connection, calculated from the vertical displacements on the dial gauges D_4 and D_5
θ_s rotation of the top flange near the vertical stiffener of the composite inverted U-frame connection

σ stress
σ_a the stress in the structural steel profile
σ_c the stress in the concrete slab
σ_{cr} the elastic critical buckling stress of the composite beam
σ_{fc} the design stress in the compression flange
σ_{li} the limiting buckling stress
σ_u the maximum compressive stress in the concrete slab
σ_{yc} the yield stress of the compression flange

ζ coefficient of the exponential function which models the load – slip behaviour of a stud connector embedded in a concrete slab

Chapter 1

General Introduction

Under pressure of economy, engineers in building and bridge design aim at making structures simpler in order to reduce the material, fabrication and construction costs and hence to reduce the total cost of the structure. The use of composite and steel beams becomes more material economical than the use of concrete beams for spans of more than about 10 m, although composite and steel construction always shortens the construction time compared to *in situ* concrete construction. For deflection purposes of composite beams in buildings, these longer spans might need propping. By using continuous composite construction the need for props will often disappear and the erection time of the frame is reduced, thus leading to even larger savings. In a building structure, the total time of construction is mainly determined by the time to construct one floor. Since time equals money, metal decking as permanent formwork and precast concrete slabs were introduced to enhance composite floor construction. Both flooring systems, especially the former one, lead to partial shear connection design. The number of shear connectors provided in such floors depends on the shape and direction of the metal decking and the shape of the precast slab units. In the past fifteen years a lot of experimental and theoretical research has been done on partial interaction design. Since this work focussed mainly on beams with relatively short spans, and it is composite beams with larger spans that tend to be more economical, more information is required on their behaviour.

The design of bridge structures with parallel main composite girders with inverted U-frame action could be simplified by eliminating the bracing in hogging bending regions. These types of structures span typically 10 to 50 m. Some engineers believe that this bracing leads to premature fatigue problems. Although the bracing is added to give stability to the bottom flange against lateral distortional buckling, recent research into this subject has shown that under certain

slenderness restrictions permanent bracing could be eliminated altogether, except at the supports. The elimination of bracing and the introduction of vertical web stiffeners to obtain discrete inverted U-frame action assumes transverse strength and stiffness of the stud connection between the top steel flange and the concrete deck. Although similar values for stiffness are available for typical bolted connections, so far no values have been produced for stud connections.

Both these problems on partial interaction and on transverse stiffness are related to the behaviour of the shear connectors between the concrete slab and the steel girder under ultimate loading conditions. Similarly, both of them arise from the need for simplification in the design of composite beams.

Since these two problems are so different from each other it was decided to research them separately and to discuss them in separate parts of this thesis.

In the first part the behaviour of composite beams with partial shear connection is studied. An attempt is made to give limitations on the beam characteristics with partial shear connection in order to prevent premature brittle shear stud failure before ductile flexural failure of the beam occurs under an increasing load. This part consists of four chapters:

In Chapter 2, a study is presented of previous experimental and theoretical research on partial interaction and of relevant design methods. Based on experimental evidence, the danger of sudden stud shear failure for long spans is highlighted and a numerical simulation is proposed.

In Chapter 3, a known physical model for the simulation of composite beam behaviour is implemented as a numerical programme, which uses a forward integration technique to simulate the stresses and displacements of a real composite beam. The problems encountered with this numerical approach are discussed briefly and the assumptions made in the model are checked. Finally, the programme is validated using experimental evidence from different sources.

In Chapter 4, the programme was used to perform a detailed parametric study of the relative slip between the top steel flange and the concrete slab. Having established the main parameters influencing the slip, these are discussed and studied separately, after which a number of simply supported and continuous beams are analysed. Results are obtained for over 150 simply supported beams: with and without metal decking, for hot rolled sections and plate girders. Finally a multiple regression analysis is performed on approximately 45 cases of hot rolled sections with solid concrete slab in order to predict the slip from simple beam characteristics.

In the concluding Chapter 5 of this part, a simple design rule for Eurocode 4 is proposed and further work on this subject is proposed.

The second part of this thesis describes and analyses a number of tests on the transverse flexibility of the embedded stud connector 'joint' between a plate girder with vertical web stiffeners and the concrete slab. Although the stud connectors are provided along the top flange for longitudinal shear transfer between the concrete deck and the steel girder, those placed in the vicinity of vertical stiffeners, which form part of the inverted U-frame, are also subject to transverse shear and tensile forces, due to the inverted U-frame action. It is these stud connectors which form as it were a 'joint' of the inverted U-frame. Just as for bolted steel U-frame joints, values for the transverse rotational flexibility are needed, which are produced by the experiments. This part consists also of four chapters:

Chapter 6 reviews the background to inverted U-frame action design, as given in BS 5400:Pt. 3 [7]. It also provides criticism of the conservatism of these design methods. Finally it traces back the influence of the flexibility of the joint on the design.

Chapter 7 describes the test rig and the testing procedure and discusses the measurements taken on six different test specimens. It also gives the test results and a discussion of the errors in these results.

In Chapter 8, the failure modes of the test specimens are analysed using different shear cracking models, and curves of moment against transverse rotation of the 'joints' of the test specimens are drawn up. A parallel is drawn between the moment-rotation characteristic for this joint and for the flush end plate beam-to-column connection, which leads to sketchy predictions about the behaviour of joints with different geometry.

Chapter 9 concludes this subject by proposing a limited design rule for the value of the rotational stiffness of 'joints' of this type.

Part I

Partial interaction of composite beams

Chapter 2

The problems of Partial Interaction

2.1 Origin of partial interaction

The development of shear connectors in the early 1950's made it possible to connect a concrete slab to a steel girder to obtain a composite beam with full T-beam action. In the design of such beams with *in situ* concrete slabs it is usual practice to provide sufficient shear connectors for the effects of longitudinal slip and uplift to be negligible. However, tests have shown that even when "full-interaction" behaviour is achieved, relative longitudinal movement between the slab and the flange does exist at very small loads.

For multi-storey buildings the construction time is much influenced by the time needed to construct a typical floor. Since speeding up the construction time indirectly saves the developer money, structural steel has an advantage over *in situ* concrete as long as the *in situ* slabs are replaced either by composite slabs, where corrugated metal decking acts as permanent formwork, or by precast floor slabs. The former type of slabs were originally widely used in North America, while the latter type of floor slabs were for the most part used on the Continent [9][10]. For both these types of slabs welded studs are the most commonly used type of connector. They are classified as "ductile" in draft Eurocode 4 [3]. In Fig. 2.1 it is made clear that the number of stud connectors that can be placed along one girder becomes dependent upon either the direction and trough width of the metal decking or the geometry of the precast slab. For most of these slabs "full-interaction" is no longer achieved, and the effects of longitudinal slip are no longer negligible, which leads to increased deflection, increased stresses and a

lower ultimate strength of the composite beam.

In any "partial-interaction" design method a relationship between the number of connectors and the ultimate strength of the beam is aimed for, so that the reduction in stiffness which affects the deflections and stresses under working loads can be ignored, and this for all levels of interaction permitted in the design rule.

2.2 Review of research background to present Codes of Practice

2.2.1 Background to present Partial Interaction design methods

Experimental research done in the 1960's by Chapman and Balakrishnan [11] led to those clauses in CP 117:Pt.1:1965 [1] which contain the ultimate strength full interaction design method, the calculation of the corresponding number of connectors N_f , and the spacing of connectors, following the shear flow diagram. Since it was economically impossible to incorporate a systematic variation of different composite beam parameters in these test series, a theoretical study was needed.

Yam and Chapman [12][13] developed therefore a numerical programme which simulates the behaviour of a composite beam and which made it possible to study composite beam behaviour, both in strength and deflection, under the full range of geometric and material parameters.

Since the use of metal decking and precast concrete slabs became more widespread, there grew a need to place fewer shear connectors than the number required by CP 117:Pt 1:1965. However, English [12], American [14] and Dutch [15] research had shown that the use of fewer connectors would reduce the ultimate strength of the beam below the value obtained by the ultimate strength full interaction method and that deflections under service loads could become excessive.

By the mid 1970's, BS 449:Pt 3:1976 [2] was drafted, which allowed partial shear connection for simply supported beams, by using a reduced design ultimate strength M_{pp}^{i}, which was a function of the connector ratio N/N_f, the design ultimate strength of the composite section with full shear connection M_p, and

the design ultimate strength of the steel section M_{pa} as shown in eq. (2.1):

$$M_{pp}^{i} = M_{pa} + \frac{N}{N_f}(M_p - M_{pa}) \qquad (2.1)$$

$$\text{and } 1.0 \geq N \geq 0.5$$

This simple linear design rule is called the **interpolation method**. It was first obtained by Johnson and May [16] and is based on different theoretical and experimental results [12] [14] [15]. The connector ratio limit of 0.5 was a conservative estimate mainly based on test results originating from TNO Delft [15] and the University of Missouri [17] [18].

In Europe, Frodin, *et al.* [19] came to the conclusion that the same span to depth ratios as for the full interaction design method could be kept for partial interaction design as long as eq. (2.1) is used and the connector ratio limit of 0.5 is respected.

When the Eurocode 4 [3] was drafted in the early 1980's, the method of calculation adopted for the ultimate strength of beams with partial shear connection, was mainly based on the above described research done in the 1960's and '70's, and the stud spacing became uniform between *critical sections of maximum or* zero moment. The final design method was formulated by Stark from the Netherlands. As he assumed in his own research that flexible stud connectors are able to produce an infinite slip [20] under ultimate shear load, he incorporated the **equilibrium method** as an alternative to the **interpolation method** for flexible connectors on purely theoretical grounds and extended the validity of eq. (2.1) to continuous composite beams of class 2. Both methods are compared in Appendix I. Except for limiting the connector ratio to 0.5 and the span to 20 m, no other limitations were given to eq. (2.1), which in Eurocode 4 became valid for both simply supported and continuous composite beams with flexible connectors of class 1 or 2. This limit on the span stems from the span limitation for plastic analysis of continuous composite beams, as studied by Johnson and Hope-Gill [21], to prevent buckling.

At present, BS 5950:Pt.3:Section 3.1 [4] is being drafted. Although this Code has not yet abandoned the **interpolation method** in favour of the **equilibrium method**, it places more emphasis on this method (Appendix B of the Code), since it allows the ultimate moment to be calculated from simple stress blocks. This method would give a correct and safe estimate of the ultimate load if the studs had an ideal plastic behaviour and if the shear flow remained constant, so that all uniformly distributed studs would carry equal loads in the ultimate condition,

which excludes the possibility of stud shear failure. In order to eliminate the possibility of this type of brittle failure, a relationship was introduced between the span and the connector ratio, in clause 4.5.2 of BS 5950:Pt.3. This relationship was largely based on a report [80], which contains parts of chapters 4 and 5 of this thesis.

In Table 2.1 a comparison is made between the earlier CP 117 [1] and the two more recent Codes [3] and [4]. In this table the design values of the plastic moment capacity M_p, of the longitudinal interface shear force F_p, and of the corresponding number of studs N, are calculated for eight beams from Chapman's and Balakrishnan's experiments [11], using the above mentioned Codes.

The values of M_p and F_p are identical for all three Codes, but the number of connectors required for full interaction (N_{CP}, N_{EC} and N_{BS}) is always smaller in CP 117 than in the more recent ones. Note that the cylinder strength is the average of the converted cube strength and the cylinder strength measured for these tests, using the same conversion as given in section 2.2.2. This table also shows that for beams with solid slabs, full interaction in CP 117 corresponds with approximately 80% interaction in both Eurocode 4 and BS 5950:Pt.3.

In comparing the lower limits on the shear connector ratio in Eurocode 4 against the limits in BS 5950:Pt.3, it has to be remarked that, together with lowering the ratio from 0.5 to 0.4, the effective breadth of the slab has decreased from $L/4$ to $L/5$ for continuous beams and the design shear strength of the most commonly used 19 mm diameter stud connectors has reduced by 10%. Only for continuous beams with the neutral axes in the steel girder these changes in effective breadth and ultimate concrete design stress will increase the reduction in connector ratio, as demonstrated below:

$$\begin{aligned} \text{BS 5950:Pt.3} : N_{BS}^{min} &= 0.4N_f = 0.4\frac{0.45f_{cu}bL}{P_d 5} \\ \text{Eurocode 4} : N_{EC}^{min} &= 0.5N_f = 0.5\frac{0.45f_{cu}bL}{1.1P_d 4} \\ \text{so that } N_{EC}^{min} &= 1.4N_{BS}^{min} \end{aligned}$$

However, for most composite beams, the neutral axes lies in the concrete slab so that the ratio $N_{BS}^{min}/_{EC}^{min}$ is 0.88 for both simply supported and continuous beams. This means that the **equilibrium method** in BS 5950:Pt.3. allows for a reduction of the minimum number of connectors together with an increase of ultimate load as compared to the **interpolation method** in Eurocode 4.

2.2.2 Experimental evidence

A study was made of the experimental supporting evidence of the current design methods, in order to locate possible areas where these methods, as they stand today, might become unsafe.

To the knowledge of the author, none of the experiments on simply supported and continuous beams with welded stud connectors, published up to now, include beams of spans exceeding 10 m, and the majority of connectors used in these experiments fulfill the requirements for ductile connectors of clause 6.1.4.1 of Eurocode 4.

The maximum span of beams tested by Slutter and Driscoll [22] was 4.572 m, by McGarraugh and Baldwin [14][18] was 6.705 m, by Chapman and Balakrishnan [11] was 5.9 m and by Daniels and Fisher [23] 7.62 m. Even in more recent tests on composite beams with solid slabs [24] and slabs with metal decking [25][26], the span stayed beneath 9.75 m, except for a series of three tests done at the University of Warwick [27] where the shear span was 9.05 m, simulating a beam of length 18 m.

Details of these beams are given in Table 2.2: the material properties of both structural steel (f_{ay}) and of concrete (f_c), the span (l), the type of loading: either pointload(s) (P) or uniform distributed load (UDL), the number of studs per shear span (N) and the failure mode of the beams. This table also provides calculated values of the ultimate longitudinal interface shear force F_p, the connector ratio (N/N_f), the ultimate strength M_p, and the reduced ultimate strength according to eq. (2.1) and of the reserve of strength (M_{max}/M^i_{pp}), by assuming all partial safety factors on material properties equal to 1.0. Thus, the design ultimate values become equal to the theoretical ultimate values.

Other notes on Table 2.2 are as follows:

(1) The concrete cylinder strength f_c, is the mean reported value for the concrete at the age of the beam when tested. If asterisked (*) it has been converted from reported results, including cube strengths, assuming $f_c = 0.85 f_{cu}$ when $f_{cu} \leq 35\text{N/mm}^2$ and $f_c = 0.9 f_{cu}$ when $f_{cu} > 35\text{N/mm}^2$.

(2) The ultimate shear strength Q_u, of the studs, are obtained from corresponding Push-Out tests. In the absence of such tests, the values of Q_u are asterisked (*) and are either supplied by the stud manufacturer or derived from Eurocode 4.

(3) Maximum measured longitudinal slips are given, both from the test on the

beam, $\gamma_{max,b}$, and from the associated Push-Out test(s), $\gamma_{max,p}$.

(4) The measured values M_{max}, are the maximum moments reached during tests. The values of M_{pp} between brackets are calculated for stiff connectors, according to equation (6.2) of clause 6.2.3.2 of Eurocode 4.

(5) The columns headed B3-B and B4-B are not separate test results. They are revised calculations for beams B3 and B4, respectively, with only one difference: the shear span is assumed to extend from each end support to the adjacent point load, rather than to midspan.

From Table 2.2 it can be seen that for beams with a uniform spacing of studs (beams B10 to ABR2) and nearly the same span, the reserve of strength gets smaller (compare beams B6 and ABR2) when the strength of concrete decreases.

However, a much bigger effect comes from the spacing of the studs near the supports which can significantly increase the reserve of strength. Although beams B10, B12, B11 and U5 have similar load distributions (multi-point or distributed) and similar strengths of steel and concrete, beam U5 has a certain reserve against stud failure because some studs are placed beyond the support. This gives the beam more strength against shear where it needs it most. The same can be said for beams B6 and ARB2 which have a similar point loads and shear spans, but the strength reserve of Aribert's beam is higher partly because the studs are placed beyond the support. When comparing Figs. 2.2(a) and 2.2(b) it is obvious that in case (b) a bigger redistribution of forces is needed between the connectors in order to transfer the shear. For beam B6, as for beams B10 and B11, the redistribution is not enough and the studs shear off before the theoretical ultimate value is reached. In case of a distributed load the studs shear off for a higher partial interaction percentage than for a point load, which is clear from beams B6, B10 and B11.

All three of the beams tested by McGarraugh and Baldwin [14] failed at loads lower than their theoretical design ultimate value M^i_{pp}, calculated for a shear span equal to half the span of the beam. When the shear span is reduced to the distance from the support to the point load (in accordance with Eurocode 4), then the beams still fail at loads lower than the corresponding design ultimate value, but the value of N/N_f has dropped below 0.5.

The most significant information from this table is the reduction of strength with the increasing span, shown by comparison of beams B11 and B6 with T2 and T3 respectively. The loading conditions and spacing and detailing are similar, but the span increases by a factor of nearly 4. The lack of strength increases for beams

B11 and T2 from −0.37% to −31.1% and for beams B6 and T3 from −1.3% to −5.5%. In both cases the beams fail suddenly by shearing of studs. This increase can partly be due to the fact that for beams T2 and T3 $N/N_f = 0.5$, while for the others this ratio is higher.

According to the draft Eurocode 4, the studs in beams ARB2, U3, B2, B3, B4, SC-1S, T1, T2 and T3 would not be ductile, as the cylinder strength of concrete is greater than 30N/mm^2. Therefore, their ultimate bending strength, M^i_{pp} ought to be calculated according to equation (6.2) of clause 6.2.3.2. This rule is nowhere to be found in current published research and leads to a rather conservative approach for diminishing values of N/N_f. The reserve of strength for these beams becomes much bigger (from −31% to 14% for T2 and from −6% to 48% for B4-B) which means that for beams with a concrete strength close to, but just above, 30N/mm^2 (like B4-B) either this method for stiff connectors is too conservative or the studs are not behaving as stiff connectors in concrete of a higher strength. The value of 30N/mm^2 was apparently chosen in order to assure ductility of the connectors, but in research [28][29] no loss of ductility is noticed for the behaviour of studs in higher grade concrete, which means that stud connectors of size 19 × 95 or 22 × 120 could always be regarded as ductile.

Although beam 1C-2A has a ratio N/N_f of 0.273, the studs are not evenly spaced over the shear span, as more studs are placed near the supports.

From the discussion of Table 2.2 it can be concluded that the chance of stud failure for the same N/N_f ratio increases with span. The same conclusion was drawn by Burkhardt [27], who claims that the stiffness of the studs decreases along beams with large spans. This decrease of stiffness is demonstrated by Fig. 2.3, in the comparison of the load-slip curves for different connectors along the beam, with the curve obtained from a Push-Out test. The same principle was used at the University of Missouri by Baldwin [14] and his research students Vogel [18], Skinner [30] and Woolsey [17] for beams of shorter span. While in Burkhardt's work the stiffness of some of the connectors was smaller than that obtained from the Push-Out test, in Baldwin's work the stiffness of the studs was nearly the same, the load carrying capacity was slightly smaller. Due to this reduction, sudden stud shear failure can occur, before the full flexural strength of the beam is reached.

2.2.3 Theoretical evidence

Since Newmark published a simple physical model to represent the incomplete interaction of composite beams together with an elastic closed form analytical solution [31], several other more precise numerical mathematical solutions have been found. Most of them allow for an inelastic load – slip relationship of the shear connectors, some allow for elasto-plastic material behaviour and others also incorporate uplift.

Each researcher who has developed such a simulation programme, aimed at studying a particular aspect of the behaviour of composite beams.

Newmark, *et al.* [31] studied the increase of deflections due to the slip between steel girder and concrete slab for beams with full shear connection, as opposed to the theoretical deflection of a beam with perfect interaction.

Dai and Siess [32] examined primarily the effect of shear connector parameters on the degree of interaction of the composite beam.

Yam and Chapman [12][13] explored the effects of cross-sectional properties, span, connector distribution, strength and stiffness, type of loading and strain hardening on the beam-slab interaction and the ultimate load behaviour in order to provide theoretical background to CP 117:Pt1. Although they used three different types of shear connectors, the most flexible one had an assumed ultimate slip capacity of only 2.5 mm.

McGarraugh and Baldwin [14] investigated different aspects of the behaviour of composite beams with lightweight concrete ($1350\text{kg/m}^3 \leq \rho \leq 1800\text{kg/m}^3$) with the objective of establishing design criteria. In particular, they studied the effects of modular ratio, creep and shrinkage and partial interaction on both the deflection and the ultimate load capacity of beams.

Horne and Plum [33] aimed at examining the validity of approximate methods of analysis to predict the deflection of continuous composite beams with partial shear connection. They came to the conclusion that the behaviour is extremely sensitive to the connector modulus, defined as the elastic stiffness of the connector divided by the longitudinal spacing between connectors.

Burkhardt [33] was also mainly concerned with the deflections of composite beams under serviceability limit state.

Arizumi, *et al.* [35] and Ansourian and Roderick [36] aimed only at obtaining and validating their developed methods to perform an elasto-plastic analysis of composite beams with incomplete shear interaction. The same can be said of Roberts [37].

Křístek and Studnička [38] investigated only the stresses and deflections for different connector moduli under serviceability conditions. In a later paper by Křístek [39] allowance is made for the non-linear connector behaviour in examining the same variables.

Aribert [40] sought to improve the method for partial interaction design in the Eurocode 4 by looking at three types of connectors. Although he used a powerful numerical method to do so [41][42], he did not make a parametric study of the beam behaviour but used only 3 different beams for 3 different spans to validate his proposal.

Of all this work, that of Aribert [40][41][42][43] comes closest to providing theoretical evidence for the method in Eurocode 4; but he did not make a systematic study for ductile connectors. Instead he used only one load-slip curve obtained from one type of Nelson stud connector with a high value for the ultimate slip and he ran his programme only for one 5 m, one 15 m and one 30 m span beam.

2.2.4 Missing link between Codes and Research

From the previous section it becomes clear that several numerical programmes have been developed in the past 25 years to study the behaviour of composite beams with partial shear connection. Unfortunately few of them contained load-slip curves which simulate as well the stiffness, as the ultimate strength and the slip capacity of the connectors accurately. Only some of the researchers [33][38] recognised the sensitivity of their results to the choice of the experimental load-slip characteristic used in their theoretical model.

Nearly all researchers used experiments on beams with solid slabs and small spans to validate the results of their programmes together with relatively stiff load-slip curves with low slip capacity as the characteristic for ductile connectors. Since it has been argued in section 2.2.2 that the stiffness and the slip capacity of the stud connectors in short beams with solid slabs inaccurately simulated by Push-Out tests, the stiff curves obtained from Push-Out tests with solid slabs give good simulations for the experiments on the short span beams. Unfortunately the same curves cannot be used to make predictions for beams with larger spans ($l > 10$ m) and low connector ratio under ultimate loading conditions, since these beams develop large end slips and the studs therefore require a larger slip capacity to sustain the load. Neither can the stiff load-slip curves with low slip capacity be used for beams with metal decking, where the load-slip characteristic is found to be more flexible than in beams with solid slabs [76] depending on the type of

deck.

Therefore, the behaviour of simply supported and continuous composite beams with ductile connectors in solid slabs as well as composite slabs , with spans larger than 10 m, require further examination under ultimate load conditions.

2.3 Literature survey on the Physical Partial Interaction models and their mathematical solutions

2.3.1 Elastic Partial Interaction Model

Partial Interaction in composite beams was simulated numerically for the first time by Newmark in 1951 [31] for simply supported beams. This analysis was based on the following assumptions:

1. The shear connection between slab and I-beam is assumed to be continuous along the length of the beam.
2. The strain distribution throughout the depth of the slab and the I-beam is linear.
3. The deflections of the slab and the I-beam are equal at all points along the beam.
4. Both structural materials (steel and concrete) are linear elastic.
5. The load-slip characteristic of the shear connectors is linear elastic.

By expressing both equilibrium and compatibility of the interface deformations of one beam element, Newmark derives a second-order differential equation with the longitudinal shear force F, as dependent variable, given by eq. (2.2):

$$F'' + A_1 F' + A_2 = 0 \tag{2.2}$$

Because of assumptions 4 and 5 this equation has constant coefficients A_1 and A_2 and therefore a closed form analytical solution for F exists.

2.3.2 Elasto-Plastic Partial Interaction model without uplift

To study the effects of inelasticity on the behaviour of simply supported beams, Dai and Siess [32] developed a matrix method in which assumptions 1, 4 and 5 of section 2.3.1 were replaced by the assumptions given below:

1. The studs are placed at discrete points along the beam.

4. Both structural materials have non-linear elasto-plastic stress strain relationships.

5. The load-slip characteristic for the shear connectors is a tri-linear curve.

A typical cross-section with strain distribution and resultant internal forces and moments, represented by this model, is shown in Fig. 2.4.

As a result of these changes, a set of simultaneous equations with non-linear coefficients is obtained, which was solved by a slowly converging matrix method.

Yam and Chapman [12][13] only altered Newmark's last two assumptions by introducing non-linear elasto-plastic stress-strain relationships for structural material and an exponential load-slip characteristic for the studs. Like Newmark they obtain the second-order differential eq. (2.2). Because of the non-elasticity, the coefficients A_1 and A_2 become now implicit functions of the moment and the longitudinal force in the inelastic domain. Equation (2.2) has no longer a closed form solution, but was solved with a forward integration technique. Although they extended their programme to continuous beams, symmetry was required in both geometry and loading and the load had to be incremented stepwise to ensure convergence.

In the 1970's and even the '80's, this same model was used by McGarraugh and Baldwin [14] [18], Horne and Plum [33], Burkhardt [34], Arizumi and Hamada [35], Aribert and Labib [43] and Lebet [44]. All these researchers produced different analytical and numerical approaches to obtain the slip and stress distributions along composite beams, but all their approaches have assumptions 2 and 3 of section 2.3.1 in common. McGarraugh and Baldwin's programme [18] analyses only simply supported beams, but with elasto-plastic slip characteristics and material characteristics. Horne and Plum [33] derived a closed form analytical solution for continuous composite beams with elastic material characteristics. Burkhardt [34] developed a matrix method similar to the one of Dai and Siess in which he took account of plasticity by reducing the area of steel that had yielded in a separate

iterative loop. Arizumi and Hamada [35] developed a finite element programme, treating both the slab and the steel girder as beam elements and the studs as bilinear springs, inter-connecting these two types of beam elements. Aribert and Labib [43] used a forward integration technique which needs stepwise incrementation of the load level to secure convergence. They took account of plasticity by varying the Young's modulus for both materials, which requires also a separate iterative loop. Lebet [44] used a similar approach to Burkhardt.

2.3.3 Elasto-plastic Partial Interaction model with uplift

Since the mid-1980's, a number of researchers [37], [41], [45] have used a more complete physical model for a composite beam, which takes account of the uplift between the concrete slab and the steel girder, as well as of the interface slip. A typical cross-section with strain distribution and resultant internal forces and moments, represented by this model, is shown in Fig. 2.5.

All three approaches, summarised below, have only assumption 2 of section 2.3.1 in common, and they all omit assumption 3, as uplift is taken into account. In addition to the expressions of equilibrium and compatibility of the longitudinal interface deformations of one beam element, compatibility of the vertical interface deformations needs to be expressed for this model.

In [37], Roberts obtained a general formulation for the analysis of composite beams, which expressed the basic equilibrium and compatibility equations in terms of displacements. He worked out a numerical solution only for simply supported beams with linear elastic material properties and linear load-slip characteristics of the studs. Assuming a continuous shear connection along the length of the beam, Robinson and Naraine [45] derived a system of two sixth order differential equations. Similar to eq. (2.2), the coefficients become constant when the material stress strain relationships are linear elastic and the axial force distribution and subsequently the uplift force distribution can be determined for simply supported beams.

Aribert and Aziz solved the equilibrium and compatibility conditions for both simply supported [41] and continuous beams [42] by assembling a transfer matrix for every beam element and for the total beam. They took account of the elasto-plastic material and stud connector behaviour and extended their matrix method to continuous beams of several spans. They used this method to study the effect of uplift in beams with groups of studs at large intervals and the effects of point loads hanging from the steel girder.

Both Robinson and Naraine [45] and Aribert and Aziz [41], [42], demonstrated that in beams with uniform or stepwise uniform spacing of studs, uplift has no effect on the slip distribution along the beam.

2.4 Aim and scope of research

In view of the limited experimental evidence on the behaviour on beams with long shear spans and low connector ratios, and in view of the possibility of sudden premature stud shear failure of such beams, the present limitations on the methods for partial interaction design of composite beams with ductile connectors, will be re-examined.

In order to investigate these limitations, the main parameters, both geometrical and material, which affect most the longitudinal shear, are studied first. To that effect, an elasto-plastic partial interaction programme has been developed which is more useful than a number of experiments, especially if this programme is able to simulate the beam behaviour fairly accurately.

In order to predict the failure mode of the beams correctly in the simulation, the different failure criteria are formulated within the programme. Therefore a survey was done to update the knowledge of the behaviour of stud connectors in concrete with different densities and strengths in both solid slabs and slabs with metal decking. This survey provides information on the stiffness, the shear strength and the slip capacity of the connectors.

Finally a range of practical beam sections was checked and conclusions are drawn on either replacing or adapting the present design methods in references [3] and [4].

Table 2.1: Comparisons of design values for M_p, F_p and N from three different Codes of Practice, of a number of beams from Ref. [11].

		Beam Samples taken from Ref. [11]							
		$A4$	$A5$	$A6$	$B1$	$D1$	$U1$	$U3$	$U5$
f_{ay}	(N/mm^2)	274.9	256.4	250.2	234.8	264.1	268.7	234.8	281.1
f_{cu}	(N/mm^2)	31.4	40.7	40.9	39.0	33.1	38.6	43.9	33.9
f_c	(N/mm^2)	23.4	30.7	30.3	33.0	23.8	30.5	34.6	28.8
F_p	(kN)	2295	2140	2089	1960	2205	2239	1960	2346
M_p	(kNm)	537	544	533	506	533	564	517	577
$CP117 : Pt1 :' 65$									
Q_d	(kN)	90.2	100.8	101.1	85.3	43.0	98.4	104.9	93.0
N_{CP}	$(-)$	26	21	21	23	52	23	19	26
Eurocode 4									
Q_d	(kN)	72.4	85.8	85.3	88.0	33.4	85.7	88.0	83.2
N_{EC}	$(-)$	32	25	25	23	66	27	23	29
$BS5950 : Pt.3$									
Q_d	(kN)	74.7	80.5	80.2	71.5	34.6	80.3	82.9	79.1
N_{BS}	$(-)$	31	27	26	28	64	28	24	30
N_{CP}/N_{EC}		0.81	0.84	0.84	1.0	0.79	0.85	0.83	0.89
N_{CP}/N_{BS}		0.84	0.77	0.81	0.82	0.81	0.82	0.79	0.86

Table 2.2(a): Results of tests on simply-supported composite beams.

Reference $N°$	[22]	[22]	[22]	[22]	[24]	[24]	[11]	[11]	[11]	[11]	[11]
Beam $N°$	$B10$	$B12$	$B11$	$B6$	$ARB1$	$ARB2$	A_4	A_5	A_6	U_1	U_3
Load type	$4 \times P$	$4 \times P$	$4 \times P$	$2 \times P$	P	P	P	P	P	UDL	UDL
f_{ay} (N/mm^2)	280.32	280.32	280.32	286.87	240	240	274.91	256.38	250.19	268.73	234.75
f_c (N/mm^2)	24.82	24.82	24.82	24.82	33.00	37.50	23.39*	30.68*	30.26*	30.51*	34.59*
Failure mode	stud	stud	stud	stud	concrete	stud	concrete	concrete	stud	concrete	concrete
N	20	20	20	11	12	9	28	22	16	28	28
Q_u (kN)	58.73	60.50	59.946	79.19	130*	130*	121	121	121	121	121
F_p (kN)	1393.70	1393.70	1393.70	1443.10	1733	2028	2295	2140	2089	2243	1960
$(N/N_f)_u$	0.833	0.833	0.80	0.579	0.86	0.562	1.47	1.22	0.88	1.47	1.64
l (m)	4.572	4.572	4.572	4.572	5.00	5.00	5.486	5.486	5.486	5.486	5.486
M_{max} (kNm)	293.36	296.75	288.80	273	422.50	496.25	710.61	642.29	580.79	710.80	690.10
M_{pa} (kNm)	201.831	201.831	201.831	209.111	228.20	314.30	271.56	253.2	287.25	302.40	275.10
M_p (kNm)	311.89	311.89	311.89	325.45	431.50	527.80	536.50	544.3	532.30	564.60	516.9
M^i_{pp} (kNm)	293.55	293.55	289.88	276.47	403.04	434.28	536.50	544.3	502.80	564.60	516.9
					(371.10)	(296.60)					
M_{max}/M^i_{pp}	0.999	1.011	0.996	0.987	1.05	1.14	1.32	1.18	1.15	1.26	1.34
$\gamma_{max,p}$ (mm)	4.953	4.953	4.953	4.953	2.73	2.73	2.54	2.54	2.54	2.54	2.54
$\gamma_{max,b}$ (mm)	5.029	4.318	5.054	3.048	1.23	2.48	0.958	1.579	2.35	1.341	1.765

Table 2.2(b): continued ...

Reference $N°$	[11]	[14]	[14]	[14]			[23]	[22]	[25]	[27]	[27]	[27]
Beam $N°$	$U5$	$B2$	$B3$	$B4$	$B3-B$	$B4-B$	$SC-1S$	$BR1$	$1C-2A$	$T1$	$T2$	$T3$
Load type	UDL	$2\times P$	$2\times P$	$2\times P$	$2\times P$	$2\times P$	P	P	$4\times P$	UDL	UDL	P
f_{ay} (N/mm^2)	281.1	252.4	246.2	244.2	246.2	244.2	225.2	267.22	468.5	262.5	262.5	262.5
f_c (N/mm^2)	28.83	38.34	38.76	33.82	38.76	33.82	41.4*	22.62	30.0*	45.0*	45.0*	45.0*
Failure mode	stud	stud	stud	stud	stud	stud	concrete	concrete	stud	stud	stud	stud
N	16	10	10	10	6	6	27	38	9	15	15	15
Q_u (kN)	121	95.98	95.98	88.98	95.98	88.98	110*	59.6	109	65	65	65
F_p (kN)	2346	1437.8	1402.4	1390.9	1402.4	139.9	2682	2533	3559	2013	2013	2013
$(N/N_f)_u$	0.80	0.666	0.666	0.625	0.40	0.375	1.08	0.88	0.273	0.5	0.5	0.65
l (m)	5.8928	6.7056	6.7056	6.7056	6.7056	6.7056	7.62	9.14	9.75	18.00	18.0	18.00
M_{max} (kNm)	594.5	308.501	301.721	282.5	298.72	280.95	115.0	879.77	720.4	354.6	345.6	429.6
M_{pa} (kNm)	314.9	253.09	246.86	244.83	246.86	244.83	534.9	441.8	560.4	313.3	313.3	313.3
M_p (kNm)	576.9	382.74	390.80	385.41	390.80	385.41	1044	864.79	1118	593	593	593
M^i_{pp} (kNm)	524.5	339.52	342.84	332.69	304.44	297.55	1044	814.03	712.63	453.15	453.15	453.15
					(156.32)	(144.53)				(296.5)	(296.5)	(296.5)
M_{max}/M^i_{pp}	1.13	0.908	0.880	0.849	0.981	0.944	1.107	1.08	1.01	0.782	0.763	0.948
					(1.91)	(1.94)				(1.19)	(1.17)	(1.21)
$\gamma_{max,p}$ (mm)	2.54	6.35	6.35	7.027	6.35	7.027	–	7.97	–	3.43	3.03	3.03
										(2.63)	(1.72)	(1.72)
$\gamma_{max,b}$ (mm)	2.499	4.267	3.378	4.775	3.378	4.775	–	0.711	16.0	0.91	2.20	2.40

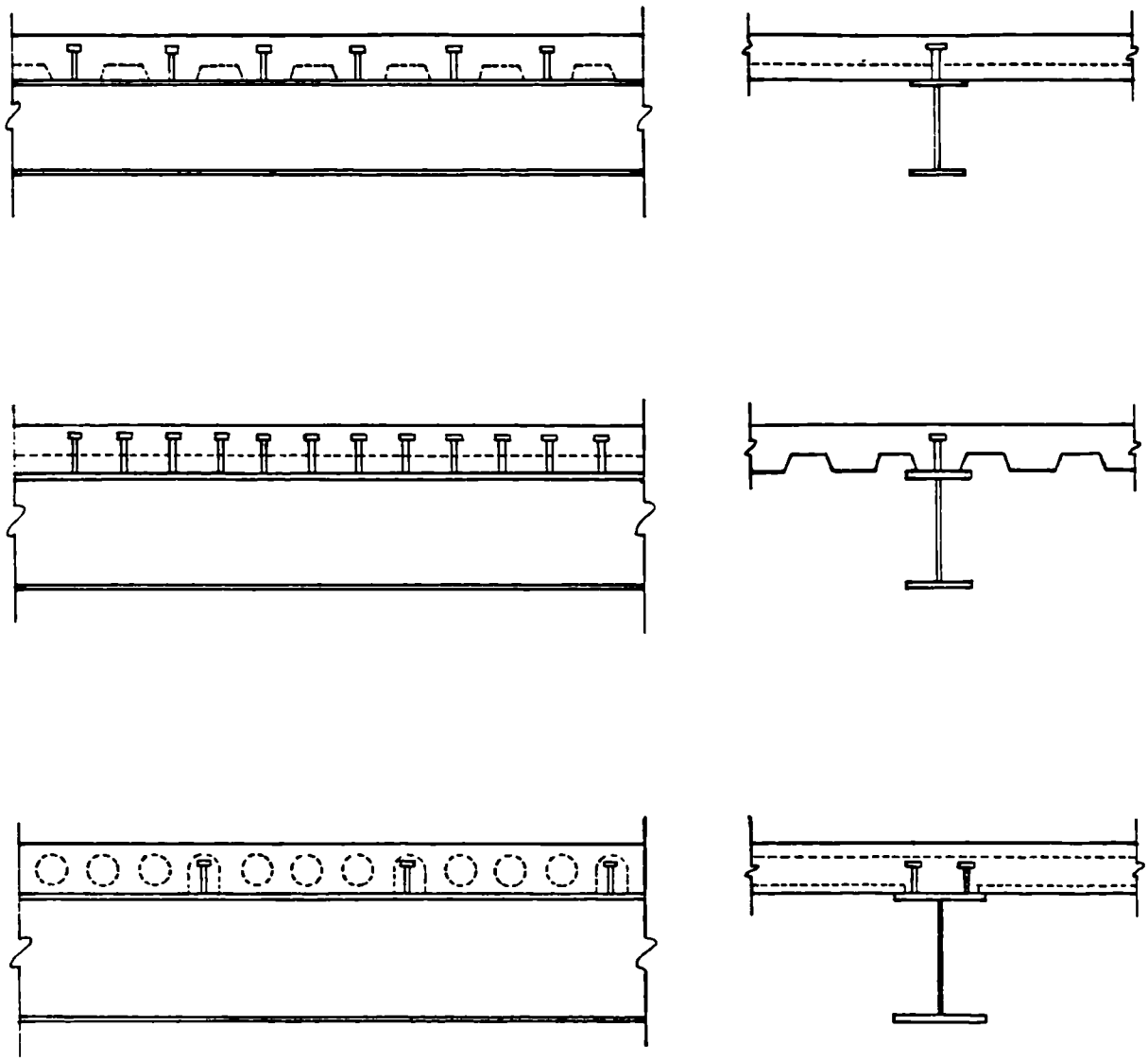

Figure 2.1: Degree of interaction determined by the direction of the decking and the type of prefabicated slabs.

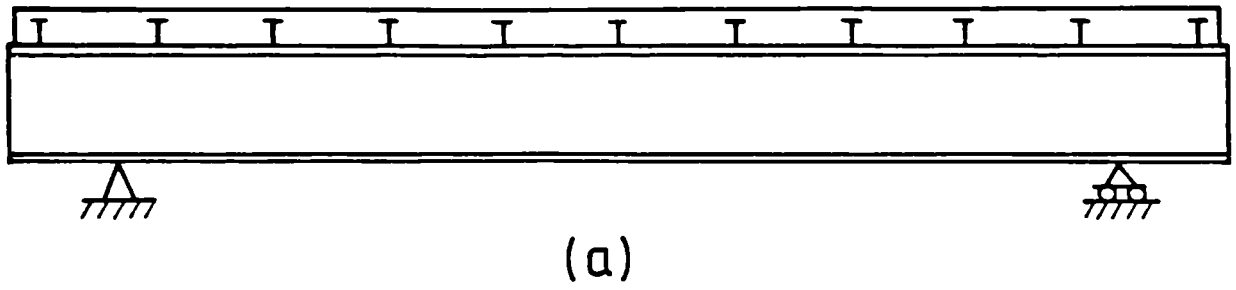

Figure 2.2(a): Uniform spacing of stud connectors with end studs close to the ends of the beams.

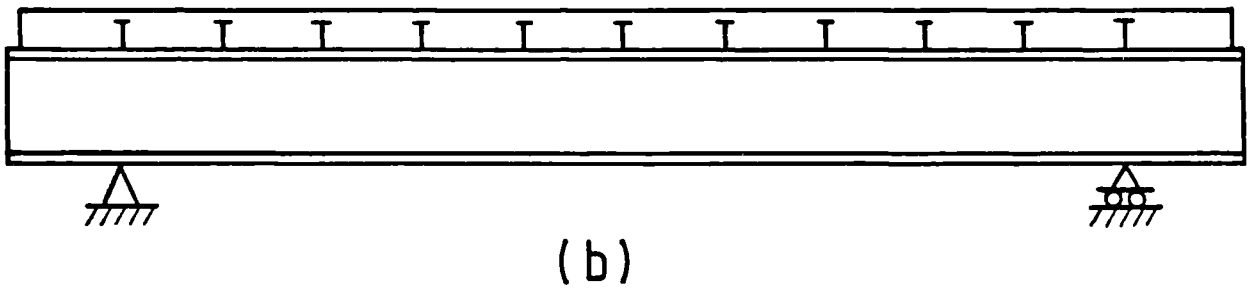

Figure 2.2(b): Uniform spacing of stud connectors with end studs further from the ends of the beam.

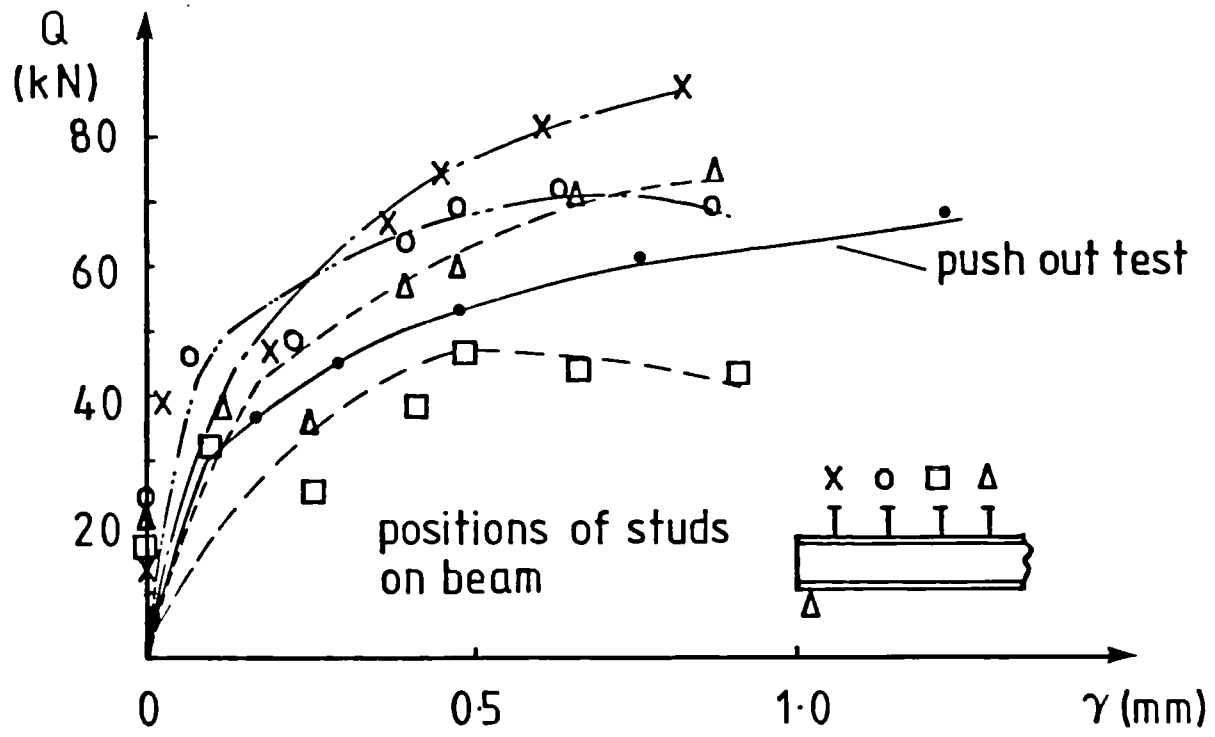

Figure 2.3(a): Reconstructed load-slip curves from strain and displacement measurements along beam T_1 in Ref. [27].

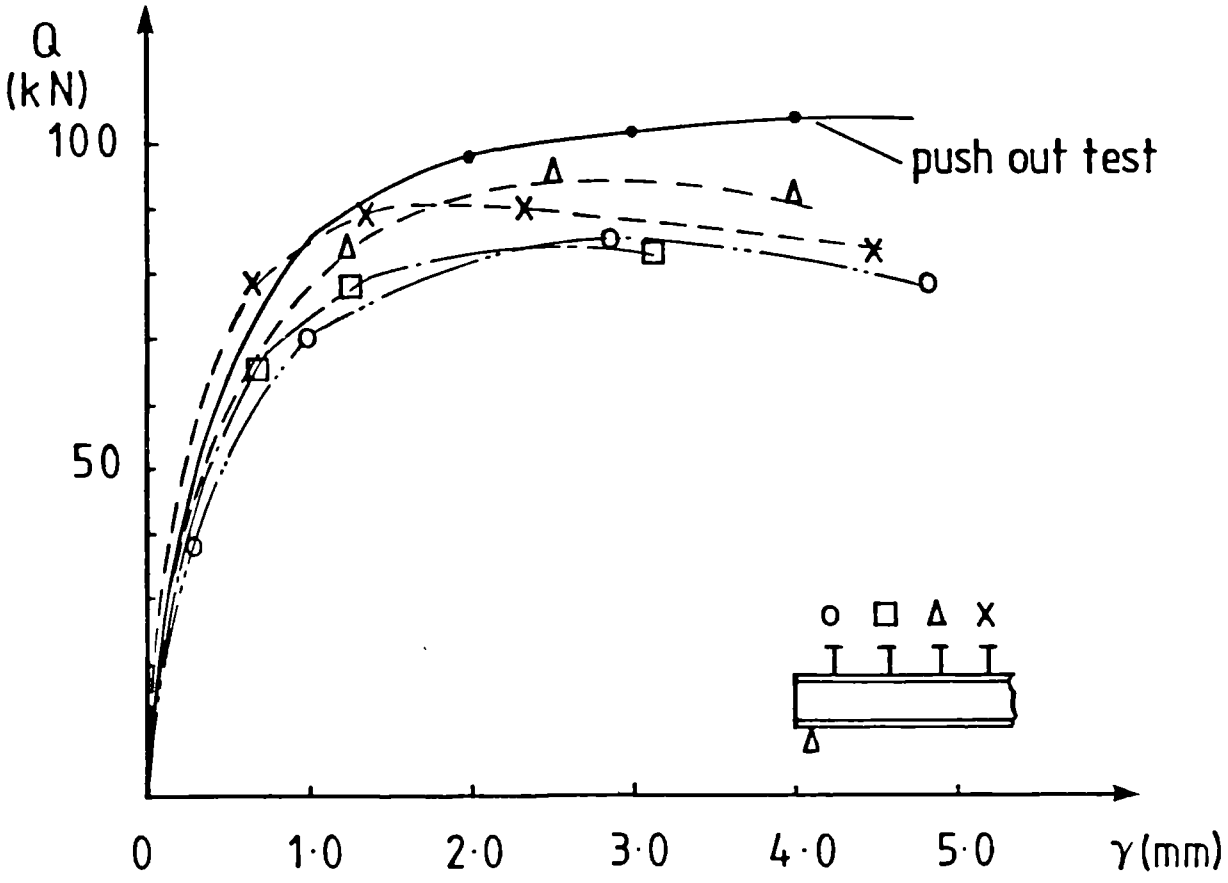

Figure 2.3(b): Reconstructed load-slip curves from strain and displacement measurements along beam PN-1 with 3.35 m shear span and 554 mm stud spacing in Ref. [18].

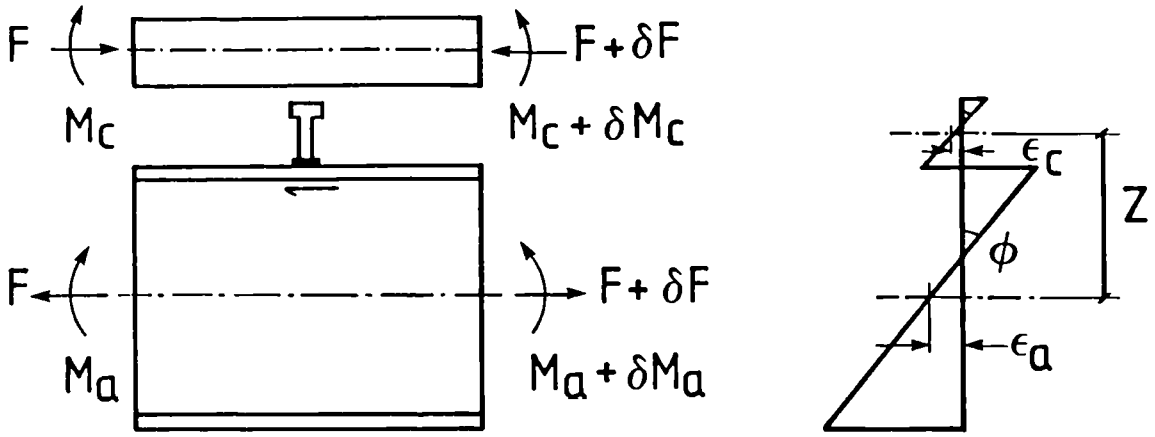

Figure 2.4: Cross-section of a composite beam with a solid slab and with strain distribution, resultant internal forces and moments for a model without uplift.

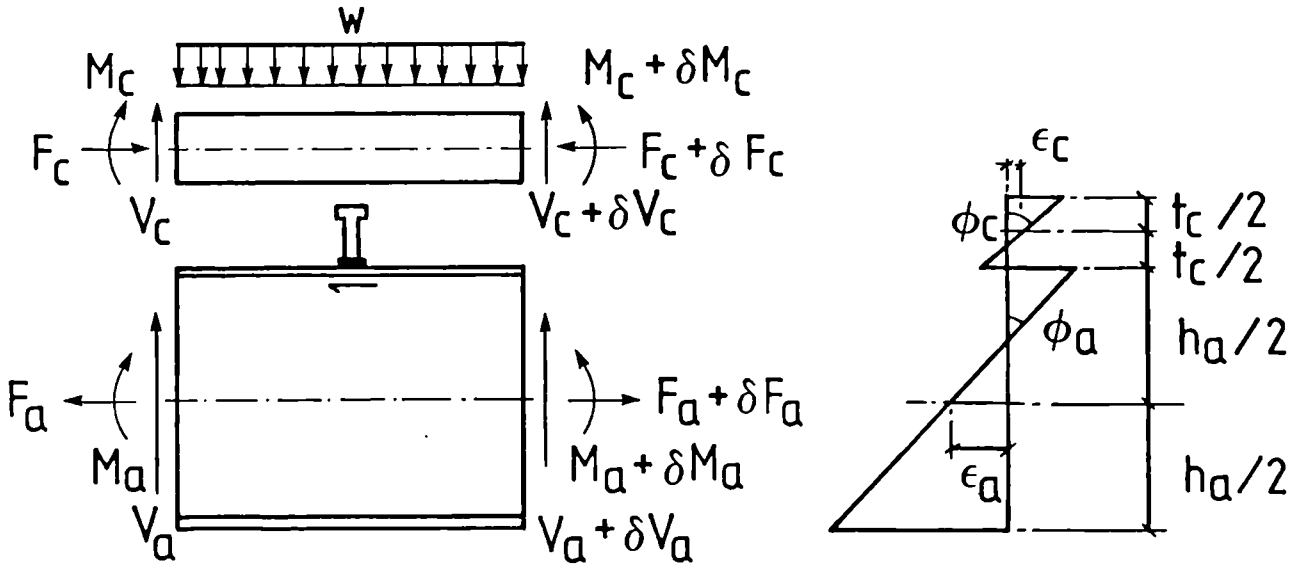

Figure 2.5: Cross-section of a composite beam with a solid slab and with strain distribution, resultant internal forces and moments for a model with uplift.

Chapter 3

Physical simulation, numerical solution and validation of the solution

In this chapter a brief description is given of the physical model used to simulate the real composite beam behaviour, of the assumptions which support this model and of the mathematical formulation of this physical model.

This description is followed by a more detailed analysis of the numerical techniques used to solve the mathematical expressions of the model and of the convergence problems encountered with the chosen approach.

Finally, the model and the numerical solution are validated by comparing their calculated stresses, deflections and slip distributions along the beam against experimentally measured values of ten different beams from four different independent investigators.

3.1 The physical model

3.1.1 Scope of the model

For the present work a programme is needed which will allow falling branches for the stress-strain curve of concrete and strain hardening for the structural steel, and which will calculate the moment, longitudinal interface force, slip and strain distributions along the beam for any given load case within the elasto-plastic region. The programme needs to determine whether a beam will fail under a specific load and which type of failure it will fail under: stud shearing, concrete

crushing or excessive structural steel yielding. All loads will be vertically applied to the top of the beam, therefore stud pull-out failure will not be a possible failure mode.

If it can be demonstrated that, under vertical loading on top of the slab, the global behaviour of the beam is not affected by uplift on beams with uniform or stepwise uniform stud spacing and the shear connector strength is not reduced by the normal forces in the studs, causing the uplift, then the elasto-plastic physical model with uplift, described in section 2.3.3, could be replaced by the simpler model without uplift for the purpose of this research.

Measured values for the uplift in beams with a uniform stud distribution stay below 20% of the measured value for maximum slip along that same beam under the same loading [11] [41]. Uplift is mainly due to vertical shear, which creates normal forces in the studs, and is only slightly increased by bending, which creates shear forces in the studs. These shear forces cause the studs to bend locally, which results in an uplift between the concrete slab and the steel girder.

Both Aribert and Aziz [41] [42] and Robinson and Naraine [45] find that the uplift associated with the change in vertical shear along the beam does not influence the global beam behaviour. Aribert's Figs. 36 and 37 in Reference [41] show that uplift increases the slip at failure by no more than 3%. The calculated value of maximum uplift near failure for beam P_1 in Table 3.5 is only 0.038mm and corresponds with an axial tension in the shank of about 22kN, or 25% of the ultimate axial resistance. This force would reduce the shear resistance by about 3% or 6%, according to References [46] and [47], respectively. Although such positive evidence is anecdotal rather than conclusive, it indicates that the shear strength reduction for studs due to the tensile forces in these studs is negligible in beams.

Neglecting the shear strains in the analyses of beams will mainly affect the deflections. For beams subject to point loads Reference [11] suggests that the calculated deflections of the beams tested by Chapman and Balakrishnan under estimate the measured deflections by about 12% to 15% . Similar differences are found in Appendix III for a number of beams of Table 3.5. In this Appendix a comparison is made between the total calculated deflections of these beams, which ignores the shear stiffness of the slab but not the shear deflection of the steel beam, with the calculated deflection due to bending only. Any effect that uplift may have on the beam deflections is far less than this.

From the above investigation into the effects of uplift on the global beam behaviour it is clear that the simplified elasto-plastic physical model without

uplift will give equally accurate results for slip and strain distributions in beams subject to vertical loads.

The programme developed for the purpose of this research, is therefore based on the original model used by Newmark, as shown in Fig. 2.4. This model has only been altered slightly to take account of beams with metal decking spanning perpendicular to the beam, as shown in Fig. 3.1.

3.1.2 Assumptions for the model

The analysis of the chosen physical model is based on the following assumptions:

(1) Bernouilli's hypothesis is valid for the bending of both materials; it allows a linear strain distribution throughout the depth of both slab and steel section.

(2) The concrete or composite slab and the steel beam deflect equally at all points along the beam. This results in equal curvatures of the slab and the steel section and no uplift, which is only possible when vertical shear strains along the beam are neglected.

(3) The stress-strain relationship for steel is the same in tension as in compression.

(4) The stress-strain relationship for concrete is a fourth order polynomial [48], and concrete can be given a tensile strength which is one tenth of its compressive strength.

(5) The studs behave similarly in shear under hogging or sagging bending.

(6) The shear connectors act as a continuous medium along the beam.

3.1.2.1 The stress-strain relationship for concrete

For composite or solid concrete slabs, the assumed stress-strain relationship is shown in Fig.3.2. The concrete stress-strain curve is a polynomial of the form

$$\frac{\sigma}{\sigma_u} = \sum_{i=1}^{n} C_i \left(\frac{\varepsilon}{\varepsilon_u}\right)^i \tag{3.1}$$

where σ_u and ε_u are the maximum values of the stress σ and the corresponding strain ε.

The polynomial is of the fourth degree and the coefficients C_i were obtained by Basu and Somerville [48] from tests done by Barnard and Johnson [49]. These values for C_i are given in Table 3.1.

These values show a close agreement with the ones obtained by Kabaila [50] from tests done by Smith and Young [51] also reported in Table 3.1.

The value of ε_u is taken as -0.0020 or -0.0025, depending on the strength of the concrete, and the crushing strain of concrete is generally taken as -0.0035. The stress-strain relationships represented by both polynomials are compared in Fig. 3.2(b) for strains up to the crushing strain. Although a difference exists between stress-strain curves of normal and lightweight concrete [53] no distinction has been made here. Other relationships by Saenz [54] and Desayi and Krishnan [55] which also give good agreement with experimental results were initially used but later abandoned as they require a numerical integration to obtain compressive forces F_c, and moments M_c, in the slab, as explained later in section 3.2.2.5.

3.1.2.2 The stress-strain relationship for structural steel and reinforcement

For the structural steel profile, the two assumed stress-strain relationships are shown in Figs. 3.3(a) and 3.3(b) respectively. The length of the yield plateau in Fig. 3.3(a) ranges between 7 ε_{ay} and 10 ε_{ay} and the strain hardening factor, $m_s = E_a/E_p$ is about 25. Since the yield plateau in this relationship leads sometimes to numerical instabilities, the stress-strain curve in Fig. 3.3(b) was introduced. This relationship is bilinear both in tension and compression, with a yield stress f_{ay}, and a corresponding yield strain ε_{ay}, and a strain hardening factor $m_s = E_a/E_p$, which varies between 70 and 210. The former factor for the strain hardening is a linear approximation to the bilinear graph ABC in Fig. 3.3(a), which overestimates the stresses produced by that relationship by not more than 10% within the strain limits -0.020 and 0.020 for Grade 43 and -0.025 and 0.025 for Grade 50 steel, for $\varepsilon_{ap} = 8\ \varepsilon_{ay}$. The latter factor for the strain hardening is also a linear approximation, but overestimates the stresses produced by that curve by less than 5% within the strain limits -0.015 and 0.015 for Grade 43 steel and -0.020 and 0.020 for Grade 50 steel.

For hot rolled high yield reinforcing bars the shape of the assumed stress-strain curve is identical to the one for structural steel, but with the yield stress equal to f_{ry} and the corresponding yield strain equal to ε_{ry}. Since these bars have a higher carbon content than structural steel, their yield plateau will be

shorter, but the strain hardening will be larger, therefore the chosen stress-strain relationship will underestimate the stress slightly outside the strain limits.

Failure of the structural steel and the reinforcement is assumed to occur when ε_a reaches either -0.04 or 0.04.

3.1.2.3 The load-slip relationship for studs

The choice and nature of this relationship will be discussed in detail in section 4.2 both for studs in solid slabs and studs in composite slabs.

3.1.2.4 Continuous shear transfer along the beam

When shear connectors are closely spaced along a beam, it is sufficiently accurate to model the transfer of shear across the steel-concrete interface as being continuous along the beam, thus assuming that the stud connectors redistribute the shear force when they are spaced fairly close in a similar manner as the studs were found to redistribute the load in Push-Out tests with several studs in each slab of the specimen. This approach was used by Yam and Chapman [12] and in most of the present work. Obviously this approach becomes less accurate when the studs are placed in pairs and spaced at a larger spacing along the beam, especially near simply supported beam ends.

Most other researchers [14] [24] [37] assume therefore a discontinuous transfer of interface shear only at the positions of the connectors, thus modeling the interface shear correctly as a step function, with the step at the longitudinal positions of the studs and the value of the step as being a function of the number of studs in the transverse direction at that position.

3.1.3 Mathematical formulation of the physical model

3.1.3.1 Equilibrium of a beam segment

Both Figs. 2.4 and 3.1 give the forces and moments which act on a composite beam segment of length dx, with solid slab and composite slab respectively, where the shear transfer along the interface is modelled as being continuous.

Equilibrium of this segment is expressed by equations (3.2) to (3.4), where eq.(3.2) only defines the longitudinal interface shear force, F. The sign convention for the variable x, is defined by Fig. 3.1.

In eq. (3.3), x_s defines the longitudinal spacing between transverse rows

of stud connectors, $Q(\gamma)$ characterises the load-slip behaviour of each row of connectors along the beam in function of the relative movement γ, between the steel profile and the concrete slab at that cross section, and $q(\gamma)$ gives the shear flow onto the steel beam. In eq. (3.4), dM represents the increment or decrement of the externally applied moment over the segment dx at each particular cross-section x, along the beam.

$$F = F_a = -F_c \tag{3.2}$$

$$\frac{dF}{dx} = q(\gamma) = \frac{Q(\gamma)}{x_s} \tag{3.3}$$

$$dM = dM_a + dM_c + Z dF \tag{3.4}$$

3.1.3.2 Compatibility of the deformations

Such a beam segment dx, between two parallel sections will become deformed after loading the beam, as a relative displacement will take place between the slab and the steel profile along the steel-concrete interface. Fig. 3.4 shows that the length of the communal fibre $R'S$ can be written as a function of the concrete strain ε_c, the rotation θ, and the relative movement γ, as well as a function of the steel strain ε_a, θ and γ. Equations (3.5) and (3.6) express therefore the same length but in function of different variables.

$$R'S = (1+\varepsilon_c)\,dx + Z_c\frac{d\theta}{dx}dx + \gamma + d\gamma \tag{3.5}$$

$$R'S = (1+\varepsilon_a)\,dx - Z_a\frac{d\theta}{dx}dx + \gamma \tag{3.6}$$

A compatibility equation of the deformations along the interface of the segment dx, is obtained by equating both expressions (3.5) and (3.6) and by expressing the result in the eq. (3.7) which defines the slip strain $d\gamma/dx$, as a function of the strains in both the concrete slab and the steel profile and the curvature ϕ.

$$\frac{d\gamma}{dx} = \varepsilon_a - \varepsilon_c - Z\phi \tag{3.7}$$

$$\text{with } Z = Z_a + Z_c$$

$$\text{and } \phi = \frac{d\theta}{dx}$$

3.1.3.3 Second order differential equation

Equilibrium in each cross-section as shown in Fig. 3.1 can be expressed by a set of three independent equations (3.8(a)) to (3.8(c)), provided that the moment M, and the longitudinal interface shear force F, are known in each cross-section.

$$M(x) = M_a(x, \varepsilon_a, \phi) + M_c(x, \varepsilon_c, \phi) + ZF(x) \tag{3.8a}$$

$$F(x) = F_a(x, \varepsilon_a, \phi) \tag{3.8b}$$

$$F_a(x, \varepsilon_a, \phi) = -F_c(x, \varepsilon_c, \phi) \tag{3.8c}$$

These equations define ε_a, ε_c and ϕ in each section uniquely as a function of M and F via non-linear elasto-plastic material characteristics, thus obtaining another set of 3 independent functions (3.9(a)) to (3.9(c)).

$$\varepsilon_a = f_a(F, M) \tag{3.9a}$$

$$\varepsilon_c = f_c(F, M) \tag{3.9b}$$

$$\phi = f_\phi(F, M) \tag{3.9c}$$

By replacing the independent variables ε_a, ε_c and ϕ in eq. (3.7) by their functions in (3.9), the compatibility equation can be rewritten as a function of M and F as shown in eq. (3.10).

$$\frac{d\gamma}{dx} = g(F, M) \tag{3.10}$$

Thus, equations (3.3) and (3.10) represent a set of two first order simultaneous differential equations in two independent variables, γ and F, with as boundary conditions that $F = 0$ at both ends of the beam. For an exponential characterisation of the load-slip behaviour, as given by eq. (4.9), these two equations can be written as one second order differential equation (3.11) in F with variable coefficients.

$$\frac{d^2F}{dx^2} + \frac{dF}{dx}\frac{1}{x_s}\frac{dx_s}{dx} - \frac{1}{x_s}\frac{dQ(\gamma)}{d\gamma}g(F, M) = 0 \tag{3.11}$$

3.2 The programme: the structure and the numerical solution

3.2.1 The structure of the programme

The programme is built up of two parts. A flow chart of both these parts is given in Fig. 3.5. The programme, called EPPIB, is written in standard Fortran-77. A

manual for the use of the programme is given in Appendix II.

The first part, named Block I in the flow chart, designs the shear connection and calculates the ultimate load to the two different design methods in draft Eurocode 4 [3] or to the design methods in BS 5950:Pt.3 [4] . This part also checks the stresses and deflections at the serviceability limit state and is described more in detail in section 4.4.2. Block I works as a pre-processor to the raw data on geometry and material properties which are fed into the programme.

The second part, called Block II in the flow chart, simulates the actual beam behaviour by means of a physical model and provides a discrete numerical solution to the mathematical formulation of the model. In this section the second part of the programme will be described.

3.2.2 The numerical solution to the mathematical formulation

Block II in Fig. 3.5 contains two iterative loops for simply supported beams and three loops for continuous beams. The actual solution of the mathematical formulation of the model only happens in the innermost loop.

The *outer loop* either increases the connector ratio N/N_f, or decreases the load factor, $\lambda = w^i_{pp}/w_p$, until no failure is encountered.

For continuous beams, the *middle loop* is needed to redistribute the support moment as a result of the combined effects of concrete cracking, plastic deformations and partial shear interaction, until compatibility of the moment diagram with the deflection shape is satisfied. For a continuous two span composite beam compatibility is obtained by the condition in eq. (3.12),

$$v_s = 0 \tag{3.12}$$

where v_s represents the deflection at the internal support.

3.2.2.1 The forward integration technique or 'shooting' method

The *innermost* iterative *loop* within the programme solves the second order differential eq. (3.11) with boundary conditions $F = 0$ at both ends $x = 0$ and $x = l_1$ for simply supported beams or $x = l_1 + l_2$ for continuous beams

Only when this equation is solved can deflections be obtained and can the middle loop be entered for continuous beams, thus modifying the bending moment

until a compatible solution is found.

In order to solve this inner loop, a 'shooting' method is used in combination with the Euler integration [125] for the first six integrations and the Milne's Predictor-Corrector method [125] for the consecutive integrations on F and γ given in equations (3.3) and (3.10).

First of all, the beam is divided into $n-1$ elements. Each two consecutive nodes define one element, thus specifying n nodes along the beam, as illustrated in Fig. 3.6. The following steps attempt to explain more clearly the sequence in the numerical integration of the above defined equations.

- At node $i = 1$
  - γ_1, the initial value for the slip, is guessed.
  - M_1, the external moment is known from equilibrium,
    x_s, the longitudinal spacing between studs, is known from Block I, and
    F_1, the longitudinal force is known from the first boundary condition.
  - therefore, starting values for $d\gamma/dx$ and dF/dx can be calculated in node 1, with equations (3.7) to (3.10) and eq. (3.3) respectively.

$$\left.\frac{dF}{dx}\right|_1 = \frac{Q(\gamma_1)}{x_s}$$
$$\left.\frac{d\gamma}{dx}\right|_1 = \varepsilon_{a,1} - \varepsilon_{c,1} - Z\phi_1$$

- At node $i = r$
  - Numerical integration of the above equations will give both the slip γ, and the longitudinal force F, in the second node along the beam.
  - This process of *numerical forward integration*, after expressing equilibrium and compatibility is repeated until $r = 6$, for continuous shear transfer, and until $r = n$ for discrete shear transfer.

$$\gamma_r = \gamma_{r-1} + (\varepsilon_{a,r-1} - \varepsilon_{c,r-1} - Z\phi_{r-1})(x_r - x_{r-1})$$

The knowledge of γ_r and x_s enables the calculation of

$$\left.\frac{dF}{dx}\right|_r = \frac{Q(\gamma_r)}{x_s}$$
$$F_r = F_{r-1} + \frac{Q(\gamma_r)}{x_s}(x_r - x_{r-1})$$

The knowledge of F_r together with M_r from equilibrium, enables the calculation of

$$\left.\frac{d\gamma}{dx}\right|_r = \varepsilon_{a,r} - \varepsilon_{c,r} - Z\phi_r$$

- At node $i = r > 6$ for continuous shear transfer
  - Numerical forward integration with Milne's Predictor-Corrector method, requires the knowledge of F and its first derivatives in the first four nodes along the beam, and the knowledge of γ and its first derivatives in the first six nodes along the beam. Therefore the Euler integration is always performed on the first six nodes.
  - the *Predictor* formulation gives

$$\gamma_r = \gamma_{r-6} + \frac{3}{10}(x_r - x_{r-1})\left(11\left.\frac{d\gamma}{dx}\right|_{r-1} - 14\left.\frac{d\gamma}{dx}\right|_{r-2} + 26\left.\frac{d\gamma}{dx}\right|_{r-3} - 14\left.\frac{d\gamma}{dx}\right|_{r-4} + 11\left.\frac{d\gamma}{dx}\right|_{r-5}\right)$$

    the knowledge of γ_r and x_s enables the calculation of

$$\left.\frac{dF}{dx}\right|_r = \frac{Q(\gamma_r)}{x_s}$$

    therefore also being able to predict

$$F_r = F_{r-4} + \frac{2}{45}(x_r - x_{r-1})\left(7\left.\frac{dF}{dx}\right|_r + 32\left.\frac{dF}{dx}\right|_{r-1} + 12\left.\frac{dF}{dx}\right|_{r-2} + 32\left.\frac{dF}{dx}\right|_{r-3} + 7\left.\frac{dF}{dx}\right|_{r-4}\right)$$

    the knowledge of F_r together with M_r from equilibrium enables the calculation of

$$\left.\frac{d\gamma}{dx}\right|_r = \varepsilon_{a,r} - \varepsilon_{c,r} - Z\phi_r$$

  - this enables the use of the *Corrector* formulation for F_r

$$\gamma_r = \gamma_{r-4} + \frac{2}{45}(x_r - x_{r-1})\left(7\left.\frac{d\gamma}{dx}\right|_r + 32\left.\frac{d\gamma}{dx}\right|_{r-1} + 12\left.\frac{d\gamma}{dx}\right|_{r-2} + 32\left.\frac{d\gamma}{dx}\right|_{r-3} + 7\left.\frac{d\gamma}{dx}\right|_{r-4}\right)$$

    therefore

$$\left.\frac{dF}{dx}\right|_r = \frac{Q(\gamma_r)}{x_s}$$

    and

$$F_r = F_{r-4} + \frac{2}{45}(x_r - x_{r-1})\left(7\left.\frac{dF}{dx}\right|_r + 32\left.\frac{dF}{dx}\right|_{r-1} + 12\left.\frac{dF}{dx}\right|_{r-2} + 32\left.\frac{dF}{dx}\right|_{r-3} + 7\left.\frac{dF}{dx}\right|_{r-4}\right)$$

  - This process of numerical forward integration is repeated until the

other end of the beam is reached.

- At the other end of the beam the second boundary condition will only be fulfilled when the guessed value for γ_1 was correct.

Obviously, the initial guess for γ_1 will propagate a value of F_n which is either larger or smaller than zero. A constant increment is given to γ_1 in correcting this initial choice and consecutive choices of γ_1, until the corresponding value of F_n changes sign, which indicates that the chosen value for γ_1 changed from an upper bound to a lower bound or *vice versa* for the last increment. To improve the following choices of γ_1 the false-position method [126] is applied to successive pairs of γ_1 and F_n values until the correct value for γ_1 is found which satisfies the second boundary condition, $-\xi \leq F_n \leq \xi$, where ξ is a fraction of F_{max}, which gives sufficiently accurate results. Unfortunately, the nature of the relationship between γ_1 and F_n, illustrated qualitatively in Fig. 3.7, does not allow the use of any faster converging methods, like the secant or the Newton Raphson method.

The Predictor-Corrector method assumes that both F and γ are polynomial functions which are continuous in their first derivative. Therefore this method can only be used when the shear is transferred continuously by the studs and the method is no longer applicable when the shear is transferred discretely by the studs.

The Predictor-Corrector method has the advantage of providing a much faster convergence for larger and therefore fewer elements as compared to the simple Euler integration over the whole beam. Unfortunately, the slower Euler integration has to be used for the simulation of beams where a discrete shear transfer is assumed at stud positions.

3.2.2.2 Convergence problems

Although the 'shooting' method seems to be able to provide a good tool to solve the mathematical formulations of the physical model, a number of convergency problems were encountered in finding a solution for the *innermost loop* for either simply supported or continuous beams.

It was found fairly early on into the development of the programme that this forward integration technique would only converge to the solution, if the initial guess for γ_1 was chosen close enough to this value. For certain beams divergence would even occur when γ_1 was within 50% of the solution.

Fig. 3.8 gives a qualitative picture of two types of longitudinal interface

shear force distributions which lead to divergence. In both figures F varies sign several times along the simply supported beam, so that the sign of F_n is no longer indicative of a lower or upper limit for γ_1. Fig. 3.9 presents two consistent qualitative distributions of F along a beam, which both lead to convergence when using the false-position method as mentioned in section 3.2.2.1: either F changes sign only once, producing a value of $F_n < 0$ or F does not change sign at all, remaining always larger than zero.

Since the nature of the $F_n - \gamma_1$ relationship, as shown earlier in Fig. 3.7, makes it impossible to choose for each beam an initial value of γ_1 which will secure the production of consistent longitudinal force distribution as in Fig. 3.9, a method had to be found to move steadily closer to the solution, regardless of the initial choice for γ_1. This method resulted in the definition of upper and lower limits to the strains in top and bottom steel and concrete fibres. These limits correspond with upper and lower bounds for γ_1, depending on the sign combinations of $M - FZ$ and F in the nodes where the limits are violated. The flow chart diagram in Fig. 3.10 summarizes the different combinations of $M_i - F_i Z$ and F_i at each node i, and the corresponding strain limits (ε_a^m, ε_c^m and ε_r^m) to the strain in the top and bottom outer fibres of the steel profile in each node ($\varepsilon_{a,i}^t$ and $\varepsilon_{a,i}^b$), the strain in the top concrete fibre in each node ($\varepsilon_{c,i}^t$) and the strain in the reinforcement in each node ($\varepsilon_{r,i}$). If one of these strain limits is violated in a node along the beam, then the forward integration is stopped at that node, the value of γ_1 is corrected and a new forward integration is started. This process is repeated until the value of γ_1 moves close enough to the solution and the longitudinal shear force distribution along the beam becomes as described in Fig. 3.9. At this point in the innermost iterative loop, a correlation exists between the sign of F_n at one end of the beam and the sign of $(\gamma_1 - \gamma_1^*)$ at the other end of the beam, where γ_1^* represents the solution.

The introduction of early corrections to γ_1 enables the programme to converge to the value γ_1^* which fits eq. (3.11), when starting with any initial choice for γ_1 smaller than γ_1^*.

In order to solve the *middle* iterative *loop* for continuous composite beams, a similar method is used on both the deflection v_s, and the moment M_s, at the internal support, as was applied previously to γ_1 and F_n. In the first iteration, 15 to 20% of the elastic support moment is redistributed and in subsequent iterations this value is increased by 5% as long as the deflection v_s, has the same sign. Once v_s changes sign, a combination of the bisection and the false-position method is applied to v_s and M_s to bring v_s theoretically to zero. Practically, the iteration is

stopped when $v_s < |v_{max}|/30$, which corresponds with an error smaller than 5% on the theoretical support moment.

3.2.2.3 The numerical solution for compatibility

Although it seems mathematically fairly straight forward to obtain the strains and curvatures from equations (3.8(a)) to (3.8(c)), the programme uses three separate subroutines to do so. In the first two routines, F_a and M_a and F_c and M_c are calculated for any combination of ε_a and ϕ and ε_c and ϕ respectively. In the third routine, the set of equations (3.8(a))to (3.8(c)) is solved by a 3-dimensional secant method. For this purpose equations (3.8(a)) to (3.8(c)) have been re-written as equations (3.13(a)) to (3.13(c)).

$$G_1(\varepsilon_a, \varepsilon_c, \phi) = M - M_a(\varepsilon_a, \phi) - M_c(\varepsilon_c, \phi) - FZ \tag{3.13a}$$

$$G_2(\varepsilon_a, \phi) = F - F_a(\varepsilon_a, \phi) \tag{3.13b}$$

$$G_3(\varepsilon_a, \varepsilon_c, \phi) = F_a(\varepsilon_a, \phi) + F_c(\varepsilon_c, \phi) \tag{3.13c}$$

$$\begin{pmatrix} \frac{\partial G_1}{\partial \varepsilon a} & \frac{\partial G_1}{\partial \varepsilon c} & \frac{\partial G_1}{\partial \phi} \\ \frac{\partial G_2}{\partial \varepsilon a} & \frac{\partial G_2}{\partial \varepsilon c} & \frac{\partial G_2}{\partial \phi} \\ \frac{\partial G_3}{\partial \varepsilon a} & \frac{\partial G_3}{\partial \varepsilon c} & \frac{\partial G_3}{\partial \phi} \end{pmatrix} \begin{pmatrix} \delta\varepsilon_a \\ \delta\varepsilon_c \\ \delta\phi \end{pmatrix} = \begin{pmatrix} \delta G_1 \\ \delta G_2 \\ \delta G_3 \end{pmatrix} \tag{3.14}$$

$$\varepsilon_a^* = \varepsilon_a + \delta\varepsilon_a \tag{3.15a}$$

$$\varepsilon_c^* = \varepsilon_c + \delta\varepsilon_c \tag{3.15b}$$

$$\phi^* = \phi + \delta\phi \tag{3.15c}$$

The error made in the assessment of the values ε_a^*, ε_c^* and ϕ^* which make G_1, G_2 and G_3 smaller than given infinitesimal values, $\xi_{i=1,2,3}$, depends on the degree of accuracy reached in the numerical differentiations, presented by eq. (3.14), which in turn depend on numerical integrations to obtain F_a and M_a. It was found that equations (3.13(a)) to (3.13(c)) would not converge to values of ξ_i smaller than $2 \times 10^{-8}\%$ of F_p and sometimes eq. (3.13) would not converge at all since the functions G_1, G_2 and G_3 are only in parts continuous in their first derivatives but not over their whole range, a requirement essential for a smooth performance of the secant method. In cases of divergence the values of ε_a, ε_c and ϕ from the previous two nodes along the beam are extrapolated and a warning is printed in the final integration. Yet, these sporadic extrapolations will hardly change the accuracy of the slip strain, given in eq. (3.7), as a function of ε_a, ε_c

and ϕ, as the number of nodes along a beam is between 10 and 20 times larger than the number of studs. Although eq. (3.14) does not guarantee convergence over the whole practical range of values for G_1, G_2 and G_3, this secant method is by far the fastest method of solution compared to more stable but much slower methods as the one used by Yam in Reference [56].

3.2.2.4 Calculation of F_a and M_a

To calculate the normal force F_a, and the moment M_a, in each steel section for any combination of strains and curvatures, a set of closed form analytical expressions can be used when the shape of the stress-strain relationship is fixed. Such expressions are tedious as provision has to made (in principle) for the 12 different types of stress distributions that can occur in the steel and are presented in Fig. 3.11. Moreover, analytical solutions have no built-in flexibility for any changes in material characteristic curves. Therefore a partly numerical, partly analytical method was used, which allows different types of bilinear stress-strain relationships for the structural steel.

With this method the slopes of the stress function across the section at top flange and bottom flange positions and at the fibre with zero strain are calculated, using six points as chosen in Fig. 3.12. The different stress functions are treated as inter-secting lines, defining a surface of which the area defines the force, F_a, as given by eq. (3.16) and of which the first moment of area defines the moment, M_a, as given by eq. (3.17), for the axes as defined in Fig. 3.12.

$$F_a(\varepsilon_a, \phi) = \int_{A_a} \sigma(z) dA_a \tag{3.16}$$

$$F_a = b_1 \int_{z_1}^{z_1 - t_1} \sigma_1(z) dz + b_2 \int_{z_1 - t_1}^{z_6 + t_3} \sigma_2(z) dz + b_3 \int_{z_6 + t_3}^{z_6} \sigma_3(z) dz$$

$$M_a(\varepsilon_a, \phi) = \int_{A_a} z\sigma(z) dA_a \tag{3.17}$$

$$M_a = b_1 \int_{z_1}^{z_1 - t_1} z\sigma_1(z) dz + b_2 \int_{z_1 - t_1}^{z_6 + t_3} z\sigma_2(z) dz + b_3 \int_{z_6 + t_3}^{z_6} z\sigma_3(z) dz$$

This is an exact method for all strain conditions within bilinear stress-strain relationships, except for these stress situations where the steel yields over a distance smaller than $h_a/4000$ away from the top or bottom fibre, as shown in Fig. 3.13. In those cases an error smaller than $10^{-4}\%$ is made on the value of F_a and M_a as calculated by equations (3.16) and (3.17) respectively. The method can lead to instability for tri-linear stress-strain relationships, where the strain

becomes larger than ε_{ap}.

3.2.2.5 Calculation of F_c and M_c

Initially, a numerical integration technique was used to calculate the normal forces F_c, and the moments M_c, at each cross-section in the concrete slab, for any combination of strains and curvatures, regardless of the mathematical model chosen for the stress-strain relationship.

After the choice of stress-strain relationship became fixed in a later stage of the research, analytical expressions were chosen for both F_c and M_c to reduce the CPU time needed to run through this central part of the programme.

For the initial numerical integration techniques a choice was made between a Newton Coates formula and a Gaussian formula (pages 886 and 887 in Ref. [125]), to produce both F_c and M_c as given by equations (3.18) and (3.19) respectively.

$$F_c(\varepsilon_c, \phi) = b_e \int_{-t_c/2}^{t_c/2} \sigma(z) dz \tag{3.18}$$

$$M_c(\varepsilon_c, \phi) = b_e \int_{-t_c/2}^{t_c/2} z\sigma(z) dz \tag{3.19}$$

The Newton Coates formulae create large truncation errors which are a function of a power of the step and higher derivatives of the stress function and which therefore can only be reduced by reducing the step and thus increasing the time for this procedure.

The Gaussian formulae have an error which is only proportional to the $2n^{th}$ or $2(n-1)^{th}$ derivative of the function, where n is the number of integration points. Since the chosen stress function, $\sigma(z)$, given by eq. (3.20),

$$\sigma(z) = \sigma_u(C_1(\frac{\varepsilon_c + Z\phi}{\varepsilon_u}) + C_2(\frac{\varepsilon_c + Z\phi}{\varepsilon_u})^2 + C_3(\frac{\varepsilon_c + Z\phi}{\varepsilon_u})^3 + C_4(\frac{\varepsilon_c + Z\phi}{\varepsilon_u})^4) \tag{3.20}$$

is a fourth order polynomial, these methods give exact solutions when $n \geq 3$.

Table 3.2 assesses the order of magnitude of the error made by using a Newton Coates formula with 6 integration points as given in eq. (3.21) as compared to the exact Gauss Lobbato integration of eq. (3.22) with less integration points.

$$\int_a^b \sigma(z) dz = \sum_{i=1}^{6} \sigma(z_i) \frac{b-a}{6} \tag{3.21}$$

$$\int_a^b \sigma(z) dz = \frac{b-a}{2} \sum_{i=1}^{5} \sigma(z_i) w_i \tag{3.22}$$

with w_i = weight factors tabulated in p.888 of Reference [125]

The stress function (3.19) is only used within the strain range -0.008 to 0.00015, where negative strains indicate compression. For compressive strains larger than -0.008 the stress decreases in a straight line between the corresponding stress and zero stress at the strain -0.013, as shown in Fig. 3.2.

3.2.3 Reasons for instability

Sometimes the programme refuses to converge to a unique solution, no matter how many elements are taken along the beam and no matter how much further the truncation error in the forward integration method is reduced.

There are several reasons, when added together, that can lead to overall instability of the forward integration technique for the kind of problem this programme deals with. Although it is not within the scope of this thesis to discuss the mathematical and numerical background of divergence, some of its causes are briefly discussed below:

(i) Since neither F, F_a, M_a, F_c, M_c or M are expressed as analytical functions of ε_a, ε_c and ϕ, every partial derivative in the matrix of eq. (3.14) is actually calculated in two steps, using a secant method. The partial derivatives of the functions G_i to ε_a, for example, are calculated as:

$$\frac{G_i(\varepsilon_a, \varepsilon_c, \phi) - G_i(\varepsilon_a + \Delta\varepsilon_a, \varepsilon_c, \phi)}{\Delta\varepsilon_a}$$

If, in this expression, $\Delta\varepsilon_a$, becomes too large or too small, then the error on this derivative grows. The optimum increment will depend on the functions G_i, at that point. Since these functions are numerical and not even continuous in their first derivative over the whole of their domain, this error cannot be controlled. Therefore the programme cannot allow a very small tolerance on the convergence of equations (3.13(a)) to (3.13(c)) with the 3D secant method, which would shrink the errors made on ε_a, ε_c and ϕ.

(ii) The choice of an exponential curve for the load-slip behaviour of the studs, will give large slip variations for small shear load increments to studs which are loaded up to more than 95% of their ultimate shear capacity. This same curve will produce small slip variations to studs for large shear load increments when the shear load is low. The exponential nature of this

curve seems to create a very steep slope in the F_n, γ_1-relationship near the solution of which the steepness increases with decreasing stud spacing, since this corresponds with larger shear force increments in between nodes (discretisation of integration of eq. (3.3)) and therefore a larger error in the integration.

(iii) Although the truncation error reduces with the number of nodes or elements along the beam, the round-off error increases when the element size reduces. Only the sum of both truncation and round-off error, represents the total error of the solution. Fig. 3.14 gives a qualitative variation of both errors with the step h, of the forward integration, which in the continuous approach is equal to the length, Δx_l, of one element. The total error becomes minimal for a specific step which in turn is a function of the second derivative of the shear function. Although this value could be assessed for an analytical function with continuous second derivatives, it cannot be calculated for the shear function which is not even continuous in its first derivative. This explains why an increase in elements does not always improve convergence.

Since the last reason for instability is inherent to the method of forward integration, the choice of another method altogether could become more favourable. Yet, in more than 90% of the beam analyses, the forward integration technique led to convergence of the problem. The added advantage of its simplicity and flexibility, makes this method suitable for the solution of this problem, despite the inherent instability.

3.3 Validation of numerical results

3.3.1 Validation of the assumption of continuous shear transfer

Using continuous shear transfer along the beam allows the application of the Predictor-Corrector method for the numerical forward integration rather than the Euler integration, thus leading to quicker convergence. This approach has the added advantage of producing continuous functions for the longitudinal interface shear F, and its first derivative F', which do not require that the nodes and elements are related to the location of the studs. Replacing the function $Q(\gamma)$ in eq. (3.3) by an exponential expression as in eq. (4.9), valid as well for positive as

negative value $Q(\gamma)$ with Q_{as}, the maximum shear resistance of all the studs in any one row, gives eq. (3.23). Numerical integration of this expression produces the discrete expression (3.24).

$$\frac{dF}{dx} = Q_{as}\frac{\gamma}{|\gamma|}\frac{\left(1-e^{-\beta|\gamma|}\right)^{\zeta}}{x_s} \tag{3.23}$$

$$\Delta F_i = Q_{as}\frac{\gamma_i}{|\gamma_i|}\frac{\left(1-e^{-\beta|\gamma_i|}\right)^{\zeta}}{x_{s,i}}\Delta x_i \tag{3.24}$$

where $x_{s,i}$ = stud spacing at node i

Δx_i = length of element over which F_i increases by ΔF_i

Q_{as} = maximum value of shear that can be transferred over Δx_i

Thus, the same layout of elements can be used for all connector ratios N/N_f, as only the denominator x_s, will change in eq. (3.23) and the solution is independent of the stud spacing in as far as the ratio Q_{as}/x_s remains constant.

Although it is more accurate to allow for discrete shear transfer only at stud locations, especially when the studs are widely spaced, such an approach requires positioning the nodes at stud locations, thus different element layouts are needed for different N/N_f-ratios. Moreover, the simple Euler integration has to be used which has a larger truncation error for identical element lengths and also leads to slower convergence.

Yet, the above stated disadvantages of discrete shear transfer might not outweigh the increased accuracy of the simulation, especially for widely spaced connectors. The difference between the proposed continuous transfer and the more accurate discrete transfer has been studied by creating a second version of the present programme and analysing the differences in main characteristics with reference to three different beams for which details are given in Table 3.3.

In this second version, the shear is transferred discretely at certain node positions which coincide with stud locations, which results in a constant slip strain as well as a constant shear between studs. In order to increase the accuracy of the integration of the slip strain, Aribert [43] introduced non-effective studs, with zero stiffness in shear, placed midway between effective studs, where the slip strain changes, but the shear remains constant, thus also reducing the length of the elements.

In Fig. 3.15, six different stud layouts near the supports are given for the

same number of uniformly spaced studs between both ends of the beam, but with different stud layouts, and with the transverse stud spacing being either single or in pairs and the shear transfer being either discrete or continuous.

If the studs are placed longitudinally in one row then the present version of the programme with continuous shear transfer will always give the same answer, regardless of the location of the studs on the beam, since it assumes a stud spacing as in Fig. 3.15(1).

When the second version of the programme is used, the location of the studs on the beam becomes more important: either the first effective stud is placed at the edge of the beam as in Fig. 3.15(2) or it is located some distance away from that edge as in Fig. 3.15(3). Both locations will give different computed results for the variables along the composite beams described in Table 3.3.

If the studs are placed transversally in pairs, then the first programme version assumes a stud spacing as in Fig. 3.15(4) while, in the second programme version, the first effective stud along the beam can be found in either of the two locations, as given in Figs. 3.15(5) and 3.15(6) respectively.

Since the number of nodes might also have an influence on the computed results, the node numbering has been changed in both programme versions and where appropriate, two sets of element layouts are given in two separate rows underneath certain figures of Figs. 3.15(1) to (6).

In Table 3.4 the percentage differences in computed results of main beam characteristics are given for different stud layouts and different programme versions for beams described in Table 3.3. Only for stud layouts (4) and (5) different element layouts were chosen, indicated as *A* and *B* underneath both Figs. 3.15(4) and 3.15(5). The main beam characteristics are defined as the slip at the end of the beam and at quarter span, the interface shear force at quarter span, the concrete compressive strain in the top fibre of the slab at midspan and the steel tensile strain in the bottom fibre of the steel profile at midspan. These particular characteristics were chosen since different values for γ, ε_c^t and ε_a^b define failure of the beam.

Comparisons between different stud layouts, stud spacings and element layouts as defined in Figs. 3.15(1) to (6) for the three different beams in Table 3.3 show that:

- For both continuous and discrete shear transfer, the number of elements along the beam has hardly any influence on the main beam characteristics which control failure: γ, ε_c^t and ε_a^t. The difference between (4)A and 4(B) is

less than 0.01% for all main characteristics and the difference between (1) and (4) is zero, which were to be expected from the nature of dF/dx in eq. (3.23), where $Q = Q_{as}$ for a single stud corresponds with $x_s = l/N_p$, while $Q = 2Q_{as}$ for a pair of studs corresponds with $x_s = 2l/N_p$, so that Q_{as}/x_s remains constant. The difference between (5)A, with one non-effective stud between two effective ones and (5)B, with no non-effective studs, remains less than 0.4% for all recorded characteristics.

- For conventional stud spacings, the difference between the continuous (1) and the discrete (3) shear transfer is very small for identical locations of studs on the beam, the percentage difference in main characteristics remaining always smaller than 0.6%. Yet, the difference between the characteristics for stud layouts (1) and (2) is no longer negligible and becomes as much as 10% for the slip in BM2. This difference is attributed to the detailing of the studs at the ends of the beam as shown in Figs. 3.15(1) and 3.15(2). A similar percentage difference is found between the characteristics corresponding with layouts (2) and (3), which are both found with the second programme version with discrete shear transfer.

- For the same number of studs placed in pairs, and therefore spaced twice as far apart longitudinally, the percentage difference in slip between stud layouts (5) and (1) is about twice as much as between layouts (2) and (1) for all three beams. In extreme cases where $x_s \approx 600$ mm, this difference for beams BM2 and BM3 becomes as large as 19%. The strains at the bottom steel fibre and at the top concrete fibre for these beams are underestimated by less than 5% by assuming continuous shear transfer. Again, hardly any percentage difference exists between the characteristic values for the identical stud layouts of Figs. 3.15(4) and 3.15(6) obtained by continuous and discrete shear transfer respectively.

In conclusion, the present programme with continuous shear transfer along the beam will simulate the physical model correctly for stud layouts (3) and (6), since there exists hardly any difference in analytical results whether this layout is analysed discretely or continuously. However, the present programme will produce values for the slip which are approximately 10% higher than the values for layout (2) when the stud spacing is about 300 mm and which are approximately 20% higher than the values for layout (5) where the stud spacing has increased to twice this value or 600 mm. The other beam characteristics like ε_a^b and ε_c^t are on average 5% lower than for layouts (2) and (5).

3.3.2 Experimental validation of the analyses produced by the programme

Although most assumptions made in the characterisation of the physical simulation model have been validated separately either by experimental evidence — assumption 2 in section 3.1.1 and assumptions 3 and 4 in sections 3.1.2.2 and 3.1.2.1 — or by theoretical comparison against other models — assumption 6 in section 3.3.1, the accuracy of the theoretical solution of this model has no bearing on the experimental validity of the model as a whole.

Therefore, results of experiments from four different sources were studied: a total of ten different beams, nine simply supported ones and one continuous one, collected from experiments by Aribert [24], Balakrishnan [11], McGarraugh and Baldwin [14] and Burkhardt [27]. The measured slip distributions, deflections and strains are compared with their corresponding computed values. Full details on the geometry and the material properties of all structural materials are given in Table 3.5 and elevations of the beams together with details of the stud spacing and the loading conditions are shown in Figs. 3.16 and 3.17. In this table A_{rt} and A_{rb} define the areas of reinforcement at distances y_{rt} and y_{rb} below the top of the concrete slab, and b_i and t_i define the width and the height of the top flange when $i = 1$, and of the web when $i = 2$, as shown in Fig. 4.1, while A_a and I_a characterise the total cross sectional area of the steel profile and its second moment of area around the major axis. In this table N represents the number of studs placed per shear span.
Other notes on Table 3.5 are given below:

- the values for the cylinder strength f_c, are either measured ones or converted in the same way as for Table 2.2

- if asterisked * the values of E_a or ε_{ay} were not obtained from measurements on parent metal of the steel profile.

The two simply supported beams and the one continuous beam tested by Aribert [24] are analysed and simulated first.

In Tables 3.6 to 3.8 the maximum measured deflection and the measured slip distributions are compared with their calculated values for different load levels for all three beams individually. In this table, m_s refers to the strain hardening factor and β, ζ and Q_u define the coefficients and the asymptotic value in the exponential function given by eq. (3.23), chosen by Aribert as

giving the best fit for the corresponding push-out tests. The polynomial stress-strain curve for concrete (P) is replaced by the parabolic rectangular curve ($P - R$) proposed by the C.E.B. [57].

For the simply supported beam P_1, there are four columns of calculated values for the maximum deflection and the slip along the beam in Table 3.6 for two different experimental load levels. The first column for each load level corresponds with the calculated values produced by Aribert's programme [24] [43]. The second column, indicated P_{11}, gives the values as produced by the second version of the programme with a stud layout identical to the one as in the experiment. The third column, indicated P_{12}, gives the values as produced by the present programme version with continuous shear transfer. For the fourth column, indicated P_{13}, identical assumptions are made as in the second column, except for less strain hardening.

For the simply supported beam P_3, five columns of calculated values for the maximum deflection and the slip along the beam are given in Table 3.7 for a lower experimental load level and four columns of values are given for the higher experimental load level. The calculated values in the first column corresponds with Aribert's computer results while the values in the second column P_{31}, correspond with the results from the second programme version for the experimental stud layout as in Fig. 3.16. The values in the third and fourth columns, P'_{32} and P_{32} of the lower load level, are both produced by the present programme with continuous shear transfer, but assume polynomial and respectively parabolic-rectangular stress-strain relationships for concrete. A comparison of the slip distributions shows that the use of the polynomial stress-strain function will increase the maximum slip. This could be expected since the slope of this function is steeper near the origin.

For the continuous beam P_2, only two columns of calculated values for each experimental load level are given in Table 3.8. The first column provides the values obtained by Aribert's computer analysis while the second one gives the values from the second version of the developed programme, with discrete shear transfer at exact stud locations.

Comparison of continuous and discrete shear transfer for beams P_1 and P_3 proves that the programme version with discrete shear transfer represents the real slip distribution better, although the differences are smaller than 10% for pairs of studs placed at approximately 600 mm spacing.

Overall, the slip distributions are over-estimated by the present analysis of continuous shear transfer which could either be due to the choice of a relatively flexible load-slip curve or to too much strain hardening of the structural steel. An over-estimation of the amount of strain hardening would definitely explain the consistent under-estimation of the maximum deflection v_{max}, by both programme versions. In Fig. 3.18, three distributions of longitudinal slip are given for each of the two load levels on beam P_2: as computed and as measured from Reference [24]; and as computed by the present programme, using the same load-slip curve as Aribert, assuming continuous shear transfer and a strain-hardening factor $m_s = 1000$. The slip distribution thus obtained in Fig. 3.18 proves to provide a better fit than P_{21} in Table 3.8.

A similar comparison is made for the strain distribution in one cross-section of each beam, and the results are presented in Fig. 3.19. For beams P_1 and P_3, the differences in strain between the continuous and the discrete shear transfer assumption remains below 2%, which is in accordance with the findings in section 3.3.1.

A series of three simply supported beams, tested by McGarraugh and Baldwin [14], are analysed and simulated next.

To obtain a better fit of the measured slip distribution by the calculated slip values, the element layout is adopted to suit the stud spacing and thus make the shear transfer discrete at the stud locations.

In Table 3.9 the maximum measured midspan deflection and the measured slip distributions are compared with their calculated values for two different load levels.

Since the beams are symmetrical, both in geometry and in loading, McGarraugh and Baldwin only reported the slip distribution over half the beam, therefore the above mentioned table only reports the slip over half the span. The comparison of slip distributions gives good results for all three beams: the slip remains fairly constant over the shear span AB in Fig. 3.17 which is well simulated by the programme. For beams B_2 and B_4 the values of the maximum slip are under-estimated by about 25%, which is probably due to the use of fairly high values for the ultimate shear strength. The chosen load-slip curves are based on the ultimate load Q_u, per stud, and the corresponding ultimate slip γ_u, measured on one push-out test corresponding to each beam. These values for Q_u and γ_u are also given in Table 3.9.

The experimental values of slip tend to reduce over a distance of 0.5m adjacent to each support. This is probably due to shrinkage of the concrete, a feature of the behaviour of composite beams that has not been simulated by the programme for several reasons. Firstly, because partial interaction normally occurs when slabs are precast or composite with metal decking spanning perpendicular to the beam, and both these types of slabs will reduce the effects of shrinkage. Secondly, because shrinkage will only reduce the slip at the beam ends and for design purposes only an upper bound for the slip is required, relevant when shrinkage is minimal.

The calculated deflections in the elasto-plastic range are systematically smaller than the measured deflections as a result of more strain hardening of the structural steel, negligence of the shear deflection and negligence of shrinkage effects in the solid slabs.

As only limited measured data are available along the beams tested by Chapman and Balakrishnan [11], only one of his simply supported specimens is analysed and simulated.

The element mesh is again adapted to suit the stud spacing and the shear is transferred discretely.

The available recorded measurements of the slip at several points along the beam, the deflection and curvature at midspan and the strains in the top concrete fibre and in the bottom steel fibre at midspan, are compared with their calculated values in Table 3.10.

The chosen load-slip curve is produced from the mean values of a set of data from five push-out tests, done by Balakrishnan. This curve is much stiffer than the one obtained by Buttry or Oehlers in Fig. 4.21 which undoubtedly explains partially why the calculated slip is smaller than the measured one. Shrinkage in the solid slab explains the reduction in slip at the beam ends.

The most relevant experiments which validate the present model for long span beams, are a set of three tests done by Burkhardt [27] at Warwick University, using a single beam. The shear span studied was ABCD in Fig. 3.17, in which the slab was cast with polystyrene prisms around two out of every three stud connectors.

The maximum measured midspan deflection and the measured slip distribution along the beam, are compared with their calculated values in Table

3.11. In Table 3.12, comparisons are also made between the measured and calculated values of the longitudinal strains at the bottom of the steel beam (ε_a^b) and at the top of the concrete slab (ε_c^t) at midspan. For the computer simulation, a continuous shear transfer was assumed and the load-slip curves used for each test, were based on results of Q_u and γ_u from Push-Out tests with slabs cast from the same concrete used to cast the beam and to fill the holes.

In test T_1, the effective studs near the supports failed while the beam was still in the elastic range. At the last recorded load level for beam T_1, mentioned in Table 3.11, the studs had not yet failed, but a load increment of less than 5% caused a sudden stud shear failure before any measurements were recorded. For the next test, T_2, half of the remaining studs, next to the studs which had failed, were made effective by filling holes with concrete, and similarly for test T_3. In test T_2 the load was applied in smaller increments and the first stud failed under only a slightly larger load than in test T_1, but failure of consecutive studs only happened gradually under an increasing load. Whereas in tests T_1 and T_2 the positions and the proportions of the applied point loads attempt to simulate bending and shear conditions in half the span of an 18 m long simply supported beam under uniform distributed loading, in test T_3 only one single point load was applied. In this test a sudden stud shear failure occurred of a total of thirteen studs at an ultimate moment which was approximately 18% higher than in test T_2. This demonstrates the influence of the stud distribution on the ultimate strength, especially for beams with solid slabs and a low degree of shear connection. By re-using the slab and only making studs effective by filling up alternate holes with concrete, shrinkage forces on the end studs were much less in tests T_2 and T_3 than in test T_1 and the programme reflects this by producing a fairly close simulation of the slip for these last two tests, showing differences of less than 10% in both γ_{max} and v_{max}.

In conclusion, this experimental validation of the programme shows that for discrete shear transfer, the predicted values of the maximum slip along the simply supported beams, will under-estimate the experimental values by a maximum of 25% (for beam B_2 [14]), and will over-estimate the experimental values by a maximum of 11% (for beam P_1 [24]). For continuous shear transfer, these predicted values of the maximum slip along the same beams will under-estimate the experimental values by only 10% (beam P_3 [24]) and they will over-estimate the experimental values by a maximum of 20% (beam P_1 [24]).

3.3.3 Conclusion on the Validation

The difference between γ_{max}'s produced by the programme, assuming discrete shear transfer and continuous shear transfer, is never larger than 20% for a double row of studs with a maximum stud spacing limited to 600 mm. This percentage reduces to about half this value for short span beams ($l \approx 5$ m).

Regardless of the assumed value for strain-hardening of the steel, the choice of experimental load-slip characteristics for the studs and the assumption on the type of shear transfer — either discrete or continuous, the difference between the experimental values and the predicted values for the maximum slip, is never larger than 25%.

Assuming continuous shear transfer along a beam, the value for γ_{max} generated by the programme will generally over-estimate the experimentally measured value. Therefore the present version of the programme produces a safe upper-bound solution for the maximum slip under ultimate loading conditions, with a maximum error of 20%.

Table 3.1: Coefficients for polynomial stress-strain curves of concrete.

$$\sigma = \sigma_u \left(C_1 \left(\frac{\varepsilon}{\varepsilon_u} \right) + C_2 \left(\frac{\varepsilon}{\varepsilon_u} \right)^2 + C_3 \left(\frac{\varepsilon}{\varepsilon_u} \right)^3 + C_4 \left(\frac{\varepsilon}{\varepsilon_u} \right)^4 \right)$$

References	C_1	C_2	C_3	C_4
[50]	2.00	−1.189	0.1763	0.0027
[48]	2.41	−1.865	0.5000	−0.045

Table 3.2: Error made with Newton-Coates integration for different ε_c and ϕ combinations.

	ε_c	ϕ	Newton integration Eq. (3.21)	Lobbato integration Eq. (3.22)	Percent Error
			$F_c(N)$	$F_c(N)$	$F_c(\%)$
	(10^{-4})	(mm^{-1})	$M_c(Nm)$	$M_c(Nm)$	$M_c(\%)$
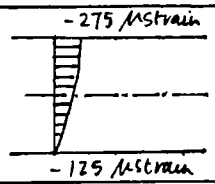	−.200	1.0	−2780284.02	−2779889.44	0.01
			23516.51	24459.67	−3.8
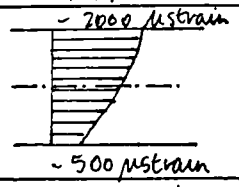	−1.25	10.0	−10746997.73	−10722989.12	−0.2
			79520.70	82858.86	−4.0
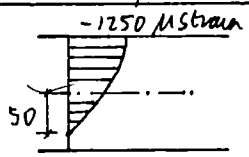	−.500	10.0	−5686407.64	−5667384.48	0.3
			165684.73	169353.78	−2.2
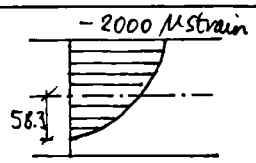	−.875	15.0	−7936242.35	−7892528.14	−0.5
			184804.30	189747.79	−2.6
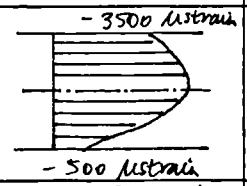	−.200	20.0	−11289027.36	−11226165.75	−0.5
			29292.23	32507.12	−9.8
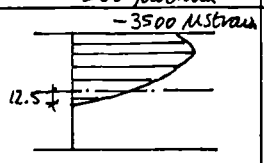	−.500	40.0	−5840910.90	−5780642.35	−1.0
			227203.28	227814.20	−0.3
	−5.00	−10.0	−5891161.83	−5895415.57	−0.07
			−35371.51	−36928.01	−4.2

Table 3.3: Geometry of three beams used in the study of the differences between continuous and discrete shear transfer.

		Beam specimen			
		$BM1$	$BM2$		$BM3$
l	(m)	17.5	10.0		10.0
b_c	(m)	4.00	4.00		3.00
t_c	(m)	0.120	0.125		0.110
t_h	(m)	0.040	0.040		0.030
		610 x 229	356 x 171		305 x 127
		$UB125$	$UB51$		$UB48$
f_{ck}	(N/mm^2)	25.0	40.0		35.0
N	$(-)$	41	14	19	17
w^i_{pp}	(kN/m)	48.75	42.65	49.47	38.90

Table 3.4: Results of study of shear transfer, given as differences between results (R) for first and second layout, percent; i.e. as $100(R_1 - R_2)/R_1$

Beam specimen	Stud layout,and spacing (mm) as in Fig. 3.15		Slip at		F at	Strain at $x = l/2$	
	First	Second	$x = 0$	$x = l/4$	$x = l/4$	ϵ^b_a	ϵ^t_c
$BM1$	(4)A, 427	(4)B, 427	0.009	0.006	−0.0003	0.009	0.004
	(1), 213	(4)A, 427	0	0	0	0	0
	(5)A, 437	(5)B, 437	0.34	0.015	−0.0005	0.43	0.25
	(1), 213	(3), 213	−0.08	−0.01	−2.42	−0.034	−0.018
	(1), 213	(2), 216	3.65	0.26	0.015	0.099	0.040
	(2), 216	(5), 437	3.42	3.13	−2.14	−0.28	−0.11
	(5), 437	(4), 427	−7.46	−3.52	2.33	0.017	0.066
	(4), 427	(6), 427	−0.23	−0.19	2.43	−0.36	−0.150
$BM2$	(1), 357	(3), 357	0.42	−0.54	−0.012	0.53	0.31
	(2), 370	(3), 357	−9.2	−3.32	−0.006	−0.24	−0.12
	(2), 270	(1), 263	−9.4	−5.3	5.9	−0.7	−0.4
	(5), 555	(1), 263	−18.3	−8.9	4.9	4.6	2.8
$BM3$	(5), 625	(1), 294	−18.8	−10.9	−6.3	4.4	2.8
	(2), 303	(1), 294	−9.6	−5.2	5.5	−0.8	−0.5

Table 3.5(a): Geometry and material properties of beam used for the experimental validation of the numerical programme.

Beam Specimen	Ref.	l_1 (m)	l_2 (m)	b_c t_c (mm)	A_{rt} A_{rb} (mm^2)	y_{rt} y_{rb} (mm)	b_1 t_1 (mm)	b_2 t_2 (mm)	A_a I_a (cm^2) (cm^4)	f_c (N/mm^2)	E_a (MPa)	ε_a $(\times 10^{-6})$	m_s $(-)$	N $(-)$	Q_u (kN)
Aribert P_1	[24]	5.00	0.	800 100	393 0.	50.0 0.	150.(120.) 10.7(8.)	7.1 300.	63.40 10593	33.00	210*	1143*	500	12	130.0
Aribert P_2	[24]	5.00	1.25	800 100	1206 0.	50.0 0.	150.(120.) 10.7(8.)	7.1 300.	63.40 10593	35.00	210*	1143*	700	12 14 6	130.0
Aribert P_3	[24]	5.00	0.	800 100	393 393	25. 75.	180 13.5	8.6 400.	84.5 23130	37.50	210*	1143*	700	9	130.0
McGarraugh B_2	[14]	6.705	0.	914.4 114.3	160 160	25. 89.3	171.02 9.928	6.858 352.04	56.96 12070.7	38.34	199.9	1262	70	10	95.65
McGarraugh B_3	[14]	6.705	0.	1828.8 114.3	320 320	25. 89.3	171.02 9.928	6.858 352.04	56.96 12070.7	38.76	199.9	1231	700	10	95.65

Table 3.5(b): continued ...

Beam Specimen	Ref.	l_1 (m)	l_2 (m)	b_c t_c (mm)	A_{rt} A_{rb} (mm^2)	y_{rt} y_{rb} (mm)	b_1 t_1 (mm)	b_2 t_2 (mm)	A_a I_a (cm^2) (cm^4)	f_c (N/mm^2)	E_a (MPa)	ε_a $(\times 10^{-6})$	m_s $(-)$	N $(-)$	Q_u (kN)
McGarraugh B_4	[14]	6.705	0.	1828.8 114.3	320 320	25. 89.3	171.02 9.928	6.858 352.04	56.96 12070.7	33.82	199.9	1221	700	10	84.53
Chapman A_6	[11]	5.468	0.	1219. 152.	222 222	25. 125.	152. 18.12	10.16 304.8	83.48 13129.6	33.53	210	1204	100	16	117.94
Burkhardt T_1	[27]	11.99	0.	1000 120	472 472	35. 85.	177.8 12.8	7.8 380.8	76.00 21508	45.00	210*	1250*	70	15	76.2
Burkhardt T_2	[27]	11.99	0.	1000 120	472 472	35. 85.	177.8 12.8	7.8 380.8	76.00 21508	45.00	210*	1250*	70	15	65.0
Burkhardt T_3	[27]	11.99	0.	1000 120	472 472	35. 85.	177.8 12.8	7.8 380.8	76.00 21508	45.00	210*	1250*	70	15	65.0

Table 3.6: Measured and calculated slip distributions and maximum deflections for beam P_1 in Table 3.5

	$w^1 = 2.34kN/m$									
	$P = 278kN$					$P = 338kN$				
	$P_{1,exp}$	$P_{1,Arib}$	P_{11}	P_{12}	P_{13}	$P_{1,exp}$	$P_{1,Arib}$	P_{11}	P_{12}	P_{13}
Layout Fig. 3.15	–	–	(5)	(4)	(5)	–	–	(5)	(4)	(5)
x_s (m)	0.454	0.454	0.454	0.416	0.454	0.454	0.454	0.454	0.416	0.454
m_s	–	∞	500	500	700	–	∞	500	500	700
Q_u (kN)	–	130	130	130	130	–	130	130	130	130
β (m^{-1})	–	700	700	700	700	–	700	700	700	700
ζ	–	0.8	0.7	0.7	0.7	–	0.8	0.7	0.7	0.7
$\sigma_c - \varepsilon_c$	–	$P-R$	$P-R$	$P-R$	$P-R$	–	$P-R$	$P-R$	$P-R$	$P-R$
x (m)	$\gamma(mm)$									
0.00	0.42	0.63	0.55	0.66	0.55	0.85	1.10	0.99	1.16	1.00
0.50	0.55	0.69	0.61	0.65	0.61	1.03	1.20	1.09	1.15	1.10
1.00	0.53	0.65	0.59	0.59	0.59	1.05	1.23	1.13	1.12	1.15
1.50	0.50	0.55	0.51	0.49	0.51	1.07	1.21	1.11	1.08	1.15
2.00	0.33	0.35	0.33	0.32	0.33	0.9	1.15	1.05	1.00	1.11
2.50	0.0	0.0	0.0	8×10^{-6}	7×10^{-7}	–	0.0	–	3×10^{-3}	–
3.00	−0.33	−0.35	−0.33	−0.33	−0.33	−0.86	−1.15	−1.06	−1.03	−1.12
3.50	−0.49	−0.55	−0.51	−0.49	−0.51	−1.07	−1.21	−1.11	−1.09	−1.15
4.00	−0.52	−0.65	−0.59	−0.60	−0.59	−1.08	−1.23	−1.11	−1.14	−1.14
4.50	−0.55	−0.69	−0.61	−0.65	−0.61	−1.02	−1.20	−1.09	−1.16	−1.09
5.00	−0.42	−0.63	−0.55	−0.67	−0.55	−0.88	−1.10	−0.99	−1.17	−1.00
v_{max} (mm)	22.5	14.5	12.88	12.91	13.62	47.5	47.5	43.9	43.5	47.3

[1] The self weight was not used in the analyses since the beams were unpropped during construction.

Table 3.7: Measured and calculated slip distributions and maximum deflections for beam P_3 in Table 3.5

	$w^1 = 2.75kN/m$										
	$P = 344kN$						$P = 397kN$				
	$P_{3,exp}$	$P_{3,Arib}$	P_{31}	P_{32}	P'_{32}	P_{33}	$P_{3,exp}$	$P_{3,Arib}$	P_{31}	P_{32}	P_{33}
Layout Fig. 3.15	–	–	(5)	(4)	(4)	(5)	–	–	(5)	(4)	(5)
x_s (m)	0.625	0.625	0.625	0.555	0.555	0.625	0.625	0.625	0.625	0.555	0.625
m_s	–	∞	700	700	700	700	–	∞	700	700	700
Q_u (kN)	–	130	130	130	130	130	–	130	130	130	130
β (m^{-1})	–	700	700	700	700	700	–	700	700	700	700
ζ	–	0.8	0.7	0.7	0.7	0.8	–	0.8	0.7	0.7	0.8
$\sigma_c - \varepsilon_c$	–	$P-R$	$P-R$	P	$P-R$	$P-R$	–	$P-R$	$P-R$	P	P
x (m)	$\gamma(mm)$										
0.00	0.85	0.96	0.80	1.08	0.94	0.88	1.81	2.24	1.59	2.03	1.72
0.50	0.94	1.06	0.86	1.05	0.91	0.93	1.91	2.39	1.69	2.00	1.82
1.00	0.96	1.03	0.83	0.95	0.83	0.89	2.02	2.48	1.71	1.92	1.84
1.50	0.92	0.92	0.70	0.77	0.68	0.76	2.12	2.48	1.66	1.77	1.79
2.00	0.60	0.66	0.48	0.51	0.45	0.52	1.80	2.38	1.53	1.55	1.65
2.50	–	0.0	10^{-3}	4×10^{-3}	4×10^{-3}	5×10^{-3}	–	0.0	2×10^{-3}	5×10^{-3}	4×10^{-3}
3.00	−0.58	−0.66	−0.48	−0.52	−0.45	−0.52	−1.76	−2.38	−1.55	−1.56	−1.65
3.50	−0.90	−0.90	−0.70	−0.78	−0.68	−0.77	−2.12	−2.48	−1.68	−1.78	−1.79
4.00	−0.96	−1.01	−0.83	−0.96	−0.83	−0.90	−2.09	−2.48	−1.73	−1.93	−1.84
4.50	−0.94	−1.06	−0.86	−1.06	−0.91	−0.94	−1.91	−2.39	−1.70	−2.01	−1.82
5.00	−0.85	−0.97	−0.80	−1.09	−0.94	−0.89	−1.84	−2.24	−1.60	−2.04	−1.72
v_{max} (mm)	22.0	22.0	14.4	14.7	14.2	15.1	67.0	84.0	49.5	48.6	51.9

[1] The self weight was not used in the analyses since the beams were unpropped during construction.

Table 3.8: Measured and calculated slip distributions and maximum deflections for beam P_2 of Table 3.5

	$w^1 = 2.34kN/m$					
	$P = 310kN$			$P = 360kN$		
	$P_{2,exp}$	$P_{2,Arib}$	P_2	$P_{2,exp}$	$P_{2,Arib}$	P_2
Layout Fig. 3.15	–	(5)	(5)	–	(5)	(5)
m_s	–	∞	700	–	∞	700
Q_u (kN)	–	130	130	–	130	130
β (m^{-1})	–	700	700	–	700	700
ζ	–	0.8	0.7	–	0.8	0.7
$\sigma_c - \varepsilon_c$	–	$P-R$	P	–	$P-R$	P
x (m)	$\gamma(mm)$					
0.00	0.38	0.54	0.46	0.52	0.70	0.55
0.50	0.46	0.60	0.50	0.66	0.79	0.59
1.00	0.50	0.60	0.47	0.74	0.80	0.56
1.50	0.45	0.50	0.37	0.75	0.77	0.44
2.00	0.29	0.33	0.17	0.60	0.65	0.21
2.50	−0.20	−0.13	−0.18	−0.48	−0.48	−0.26
3.00	−0.56	−0.56	−0.50	−1.12	−0.98	−0.64
3.50	−0.67	−0.67	−0.66	−1.20	−1.06	−0.83
4.00	−0.63	−0.65	−0.76	−1.08	−1.02	−0.92
4.50	−0.49	−0.49	−0.57	−0.95	−0.99	−0.69
5.00	−0.05	−0.12	−0.20	−0.15	−0.18	−0.24
5.50	0.28	0.22	0.10	0.50	0.50	0.15
6.00	0.20	0.29	0.20	0.40	0.57	0.26
6.25	0.09	0.25	0.16	0.09	0.46	0.21
v_{max} (mm)	19.0	12.0	9.3	35.0	28.0	21.0

[1] The self weight was not used in the analyses since the beam was unpropped during construction.

Table 3.9: Measured and calculated slip distributions and maximum deflections for beams B_2, B_3 and B_4 in Table 3.5

	$w = 4.3kN/m$				$w = 4.3kN/m$				$w = 4.3kN/m$			
	$P = 93.86kN$		$P = 147.7kN$		$P = 102.32kN$		$P = 143.25kN$		$P = 97.87kN$		$P = 137.9kN$	
	$B_{2,exp}$	B_2	$B_{2,exp}$	B_2	$B_{3,exp}$	B_3	$B_{3,exp}$	B_3	$B_{4,exp}$	B_4	$B_{4,exp}$	B_4
Q_u (kN)	–	105.8	–	105.8	–	103.5	–	103.5	–	97.87	–	97.87
γ_u (mm)	–	7.23	–	7.23	–	5.46	–	5.46	–	7.62	–	7.62
m_s $(-)$	–	70	–	70	–	700	–	700	–	700	–	700
x (m)	$\gamma(mm)$											
0	0.475	0.69	2.54	3.17	0.91	0.89	2.89	3.14	1.12	0.99	4.01	3.48
0.1524	0.711	0.68	3.175	3.15	1.06	0.88	3.05	3.12	1.27	0.97	4.77	3.46
0.7112	0.864	0.68	4.165	3.12	1.06	0.87	3.38	3.09	1.27	0.96	4.16	3.41
1.27	0.762	0.64	4.27	2.99	0.71	0.81	3.35	2.97	1.12	0.88	3.96	3.23
1.9558	0.406	0.54	2.62	2.56	0.56	0.61	2.54	2.53	0.76	0.67	2.89	2.86
2.7432	0.203	0.13	0.61	0.73	0.35	0.18	0.86	0.64	0.25	0.19	1.02	0.74
v_{max} (mm)	25.4	19.1	72.1	73.9	28.4	19.8	91.2	68.2	28.5	20.1	109.0	65.3

Table 3.10: Measured and calculated values of the slip, the maximum deflection, the curvature and the strain along beam A_6 of Table 3.5

			$A_{6,exp}$	A_6
load level	Q_u	(kN)	–	117.9
	γ_u	(mm)	–	
	m_s	$(-)$	–	100
$P = 423.5kN$	γ at $x = 0m$	(mm)	1.39	1.48
	γ at $x = 1.372m$	(mm)	2.05	1.57
	γ at $x = 5.486m$	(mm)	2.35	1.50
	ε_a^b	$(\times 10^{-6})$	17250	15611
	ε_c^t	$(\times 10^{-6})$	−4262	−4318
	ϕ	(mm^{-1})	5.77	7.1
	v_{max}	(mm)	63.6	50.2
$P = 398.6kN$	ε_a^b	$(\times 10^{-6})$	12200	23317
	ε_c^t	$(\times 10^{-6})$	−3025	−2872
	ϕ	(mm^{-1})	3.34	5.31
	v_{max}	(mm)	37.3	35.6

Table 3.11: Measured and calculated values of the slip and the deflection along beams T_1, T_2 and T_3 of Table 3.5

		$P_1 = P_2 = 17.17kN$ $P_3 = 121.1kN$ $w = 3.70kN/m$		$P_1 = P_2 = 17.94kN$ $P_3 = 123.7kN$ $w = 2.47kN/m$		$P_1 = P_2 = 0.0kN$ $P_3 = 171.4kN$ $w = 3.70kN/m$	
		$T_{1,exp}$	T_1	$T_{2,exp}$	T_2	$T_{3,exp}$	T_3
Q_u	(kN)	–	76.2	–	65.0	–	65.0
β	(m^{-1})	–	1803	–	1930	–	1930
ζ	$(-)$	–	1.148	–	1.246	–	1.246
m_s	$(-)$	–	70	–	70	–	70
x	(m)	$\gamma(mm)$					
0.30		0.82	1.70	2.20	2.02	2.40	2.16
1.50		0.91	1.58	2.06	1.89	1.95	2.07
3.30		0.76	1.17	1.56	1.43	1.91	1.74
5.22		–	0.68	0.88	0.86	1.69	1.24
6.40		0.17	0.39	0.27	0.52	1.62	0.91
8.10		–	0.06	–	–	0.73	0.36
9.40		−0.13	−0.22	−0.12	−0.24	−0.15	−0.25
11.70		−0.31	−0.35	−0.29	−0.40	−0.36	−0.52
x	(m)	$v(mm)$					
3.0		50.5	32.9	32.	32.8	53.6	34.5
6.0		59.1	47.7	48.	47.6	56.9	52.7
9.0		38.1	35.9	36.	35.8	32.8	42.4

Table 3.12: Measured and calculated values of the curvature and the strains in the extreme fibres of the concrete slab and the steel profile along beams T_1, T_2 and T_3 of Table 3.5

		$T_{1,exp}$	T_1	$T_{2,exp}$	T_2	$T_{3,exp}$	T_3
x	(m)	5.44	5.44	5.44	5.44	5.44	5.44
ε_a^b	$(\times 10^{-6})$	1647	968	782	932	688	952
ε_c^t	$(\times 10^{-6})$	−416	−329	–	−313	–	−321
ϕ	$(10^{-3}m^{-1})$	4.73	2.93	2.71	2.92	2.14	2.95
x	(m)	8.88	8.88	8.88	8.88	8.88	8.88
ε_a^b	$(\times 10^{-6})$	1060	1125	924	1107	1971	1730
ε_c^t	$(\times 10^{-6})$	−472	−387	–	−377	–	−517
ϕ	$(10^{-3}m^{-1})$	2.79	3.31	2.67	3.36	6.02	5.35
x	(m)	9.50	9.50	9.50	9.50	9.50	9.50
ε_a^b	$(\times 10^{-6})$	1415	953	806	935	1727	1174
ε_c^t	$(\times 10^{-6})$	–	−330	–	−322	–	−402
ϕ	$(10^{-3}m^{-1})$	4.08	2.71	2.32	2.72	4.98	3.54

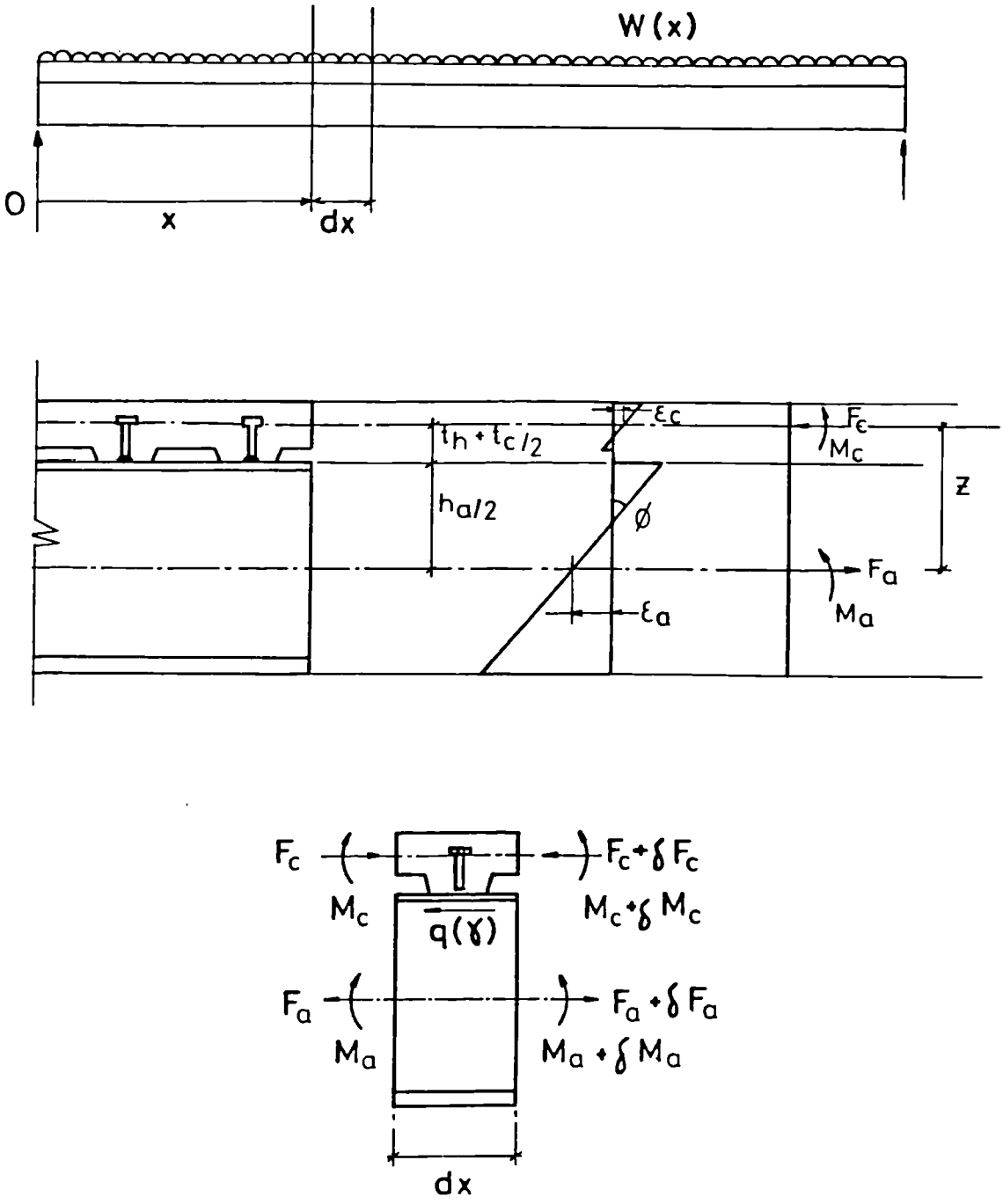

Figure 3.1: Equilibrium of an infinitesimal section of a composite beam.

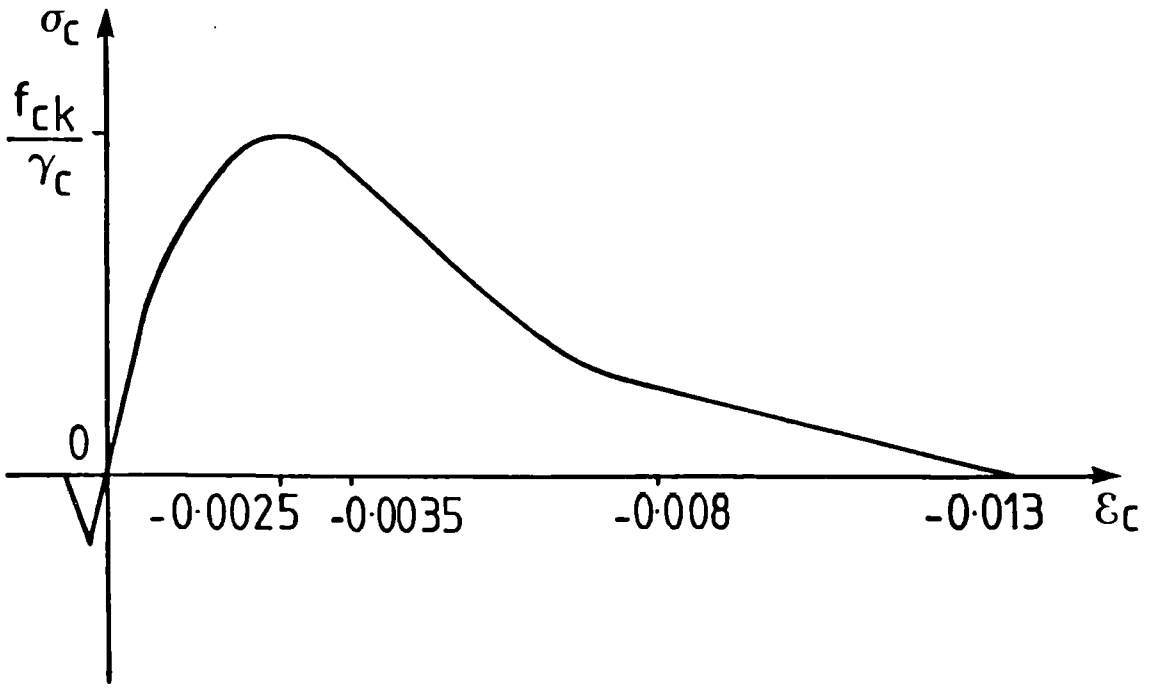

Figure 3.2(a): Range of stress-strain curve of concrete.

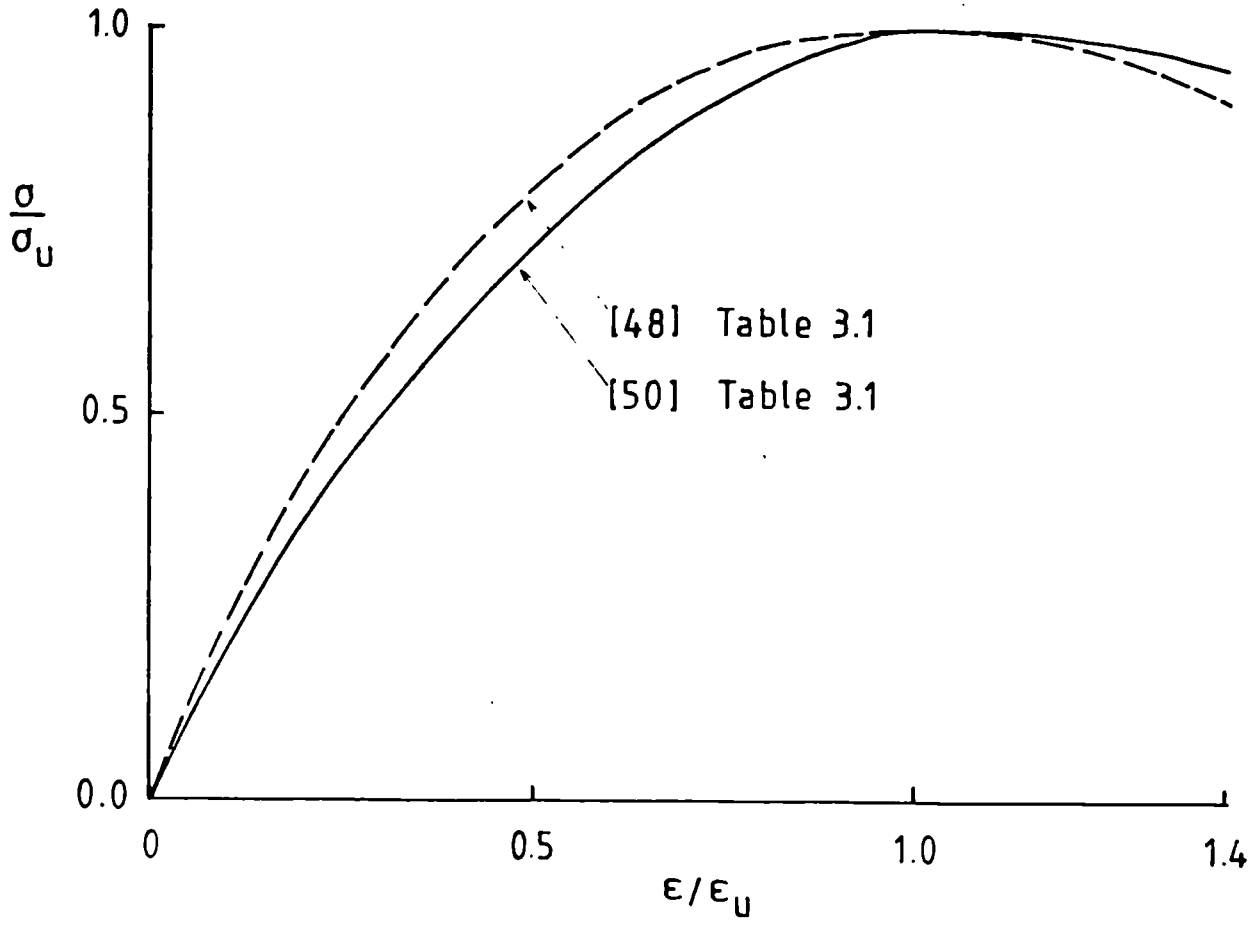

Figure 3.2(b): Comparison of stress-strain curves according to References [48] and [50] within the strain range -0.0035 to 0.

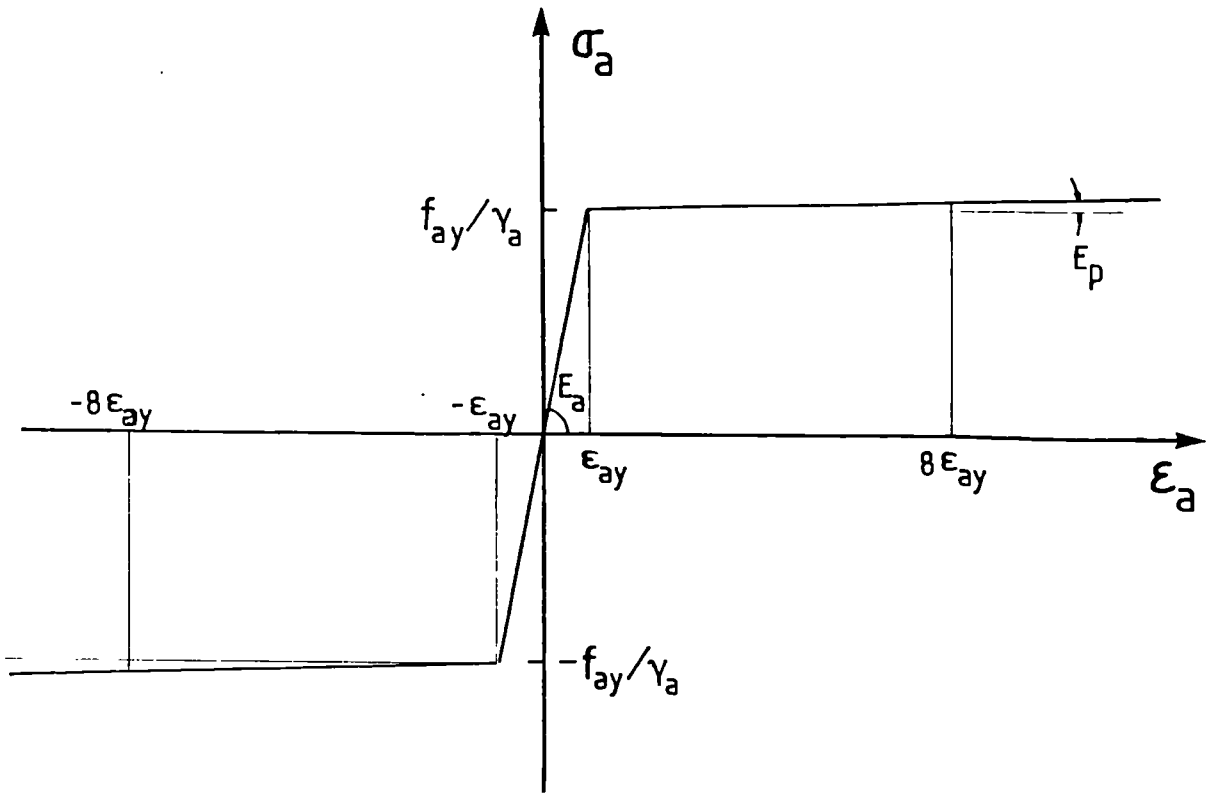

Figure 3.3(a): Bilinear stress-strain curve used for structural steel.

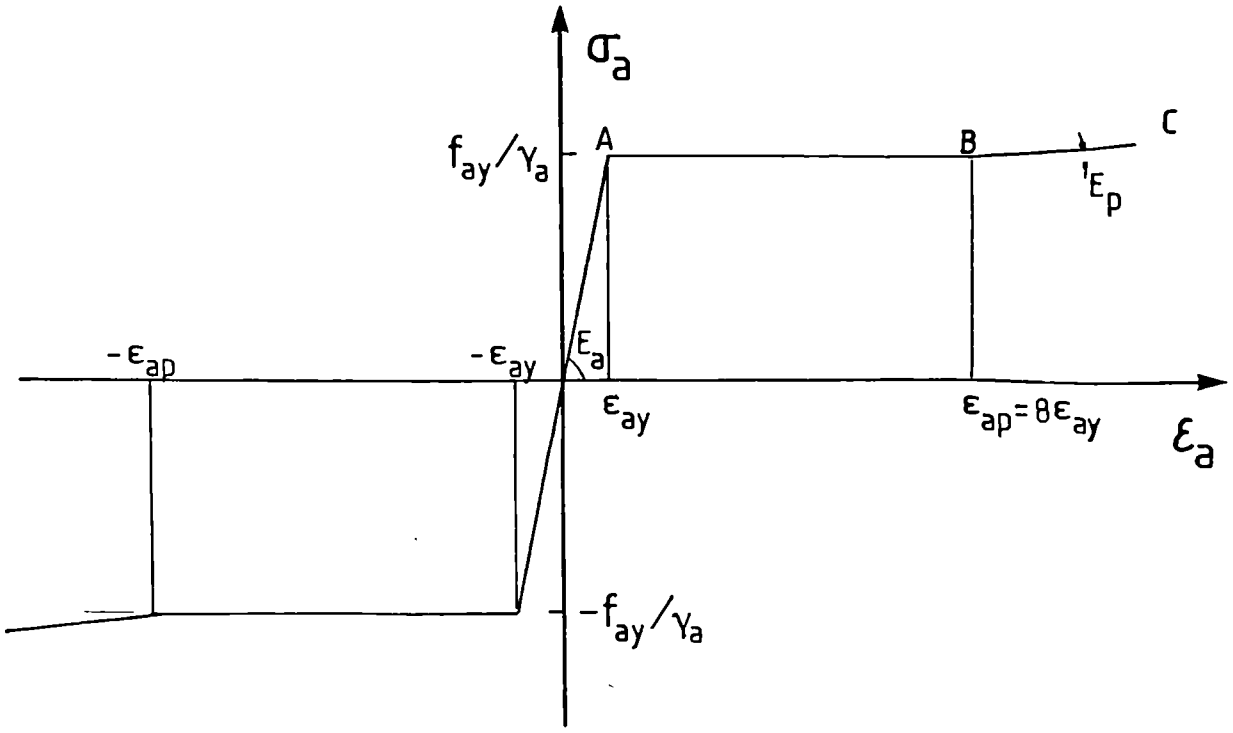

Figure 3.3(b): Average experimental tri-linear stress-strain curve for structural steel.

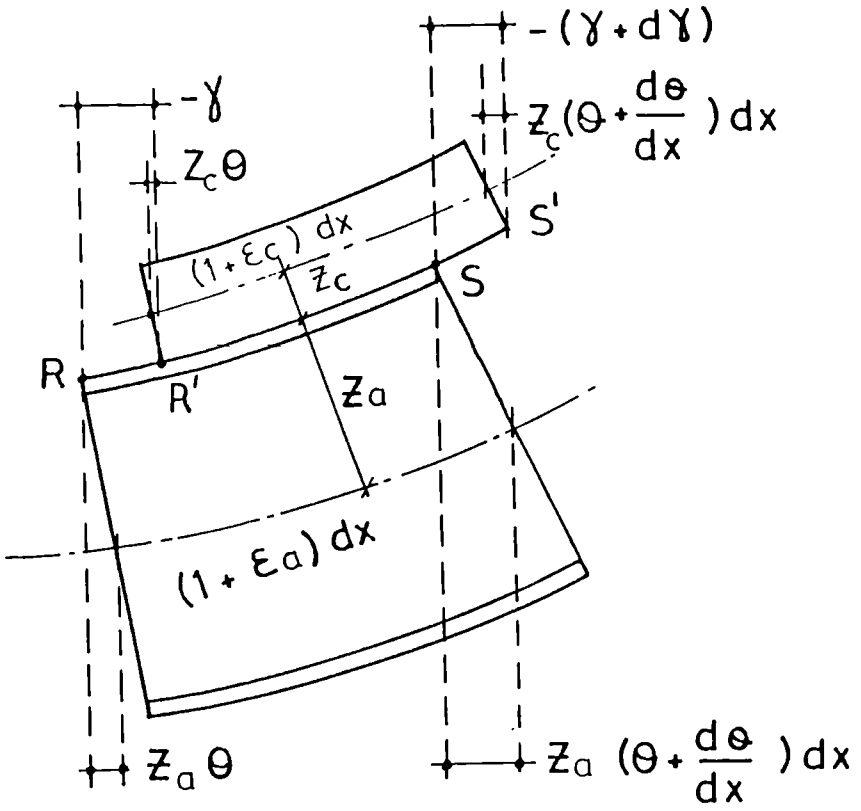

Figure 3.4: Compatibility of an infinitesimal section of a composite beam.

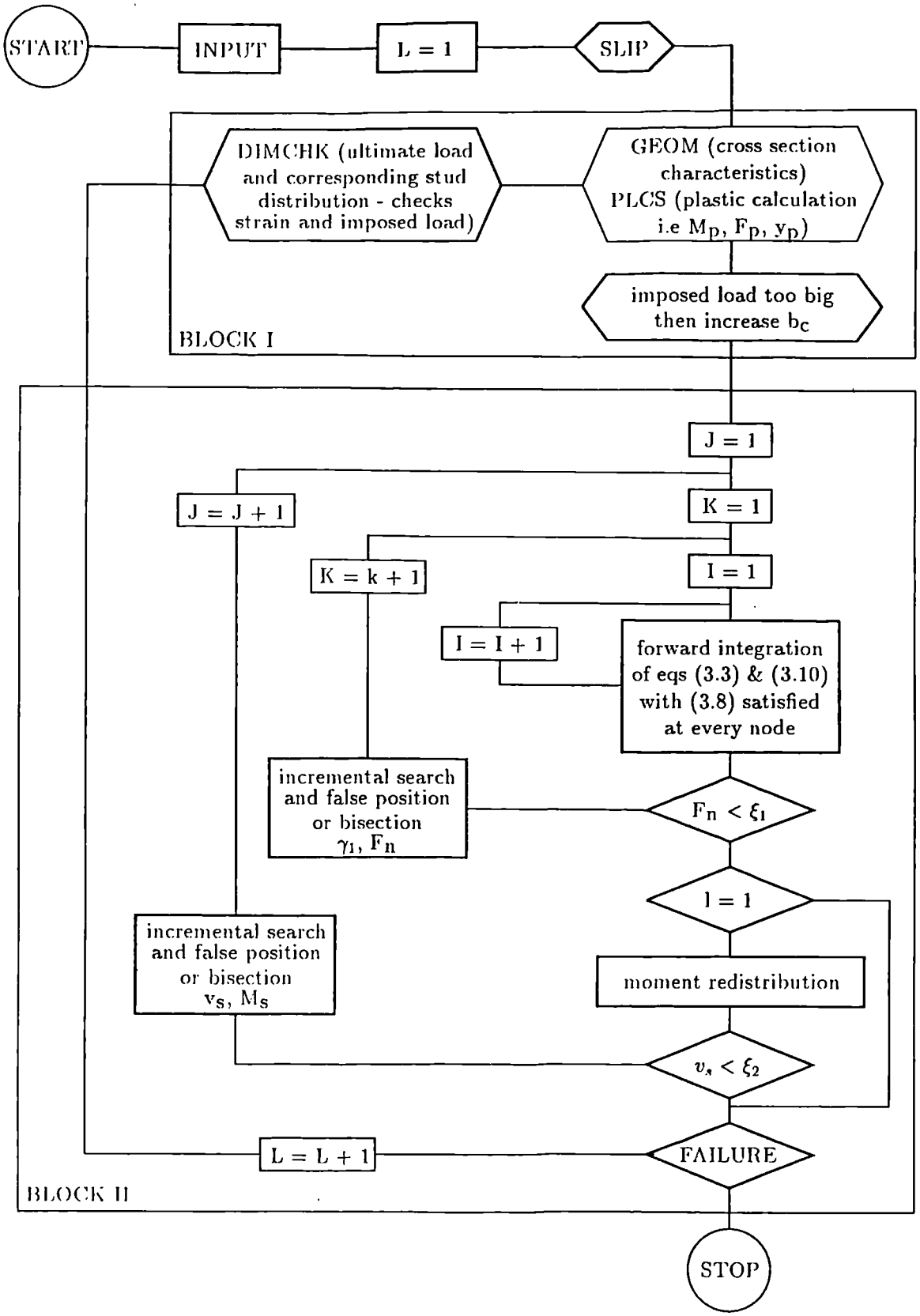

Figure 3.5: Flow chart diagram of the total computer programme.

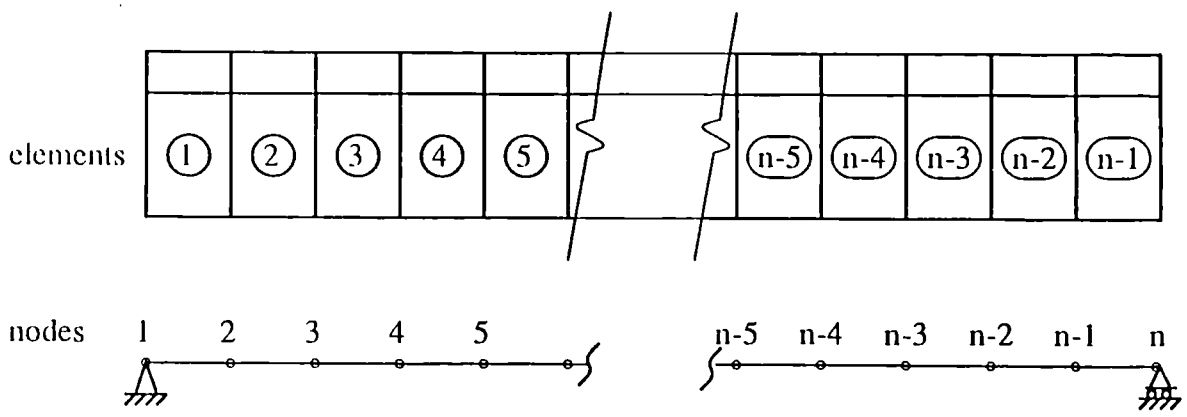

Figure 3.6: Element and node numbering of beams.

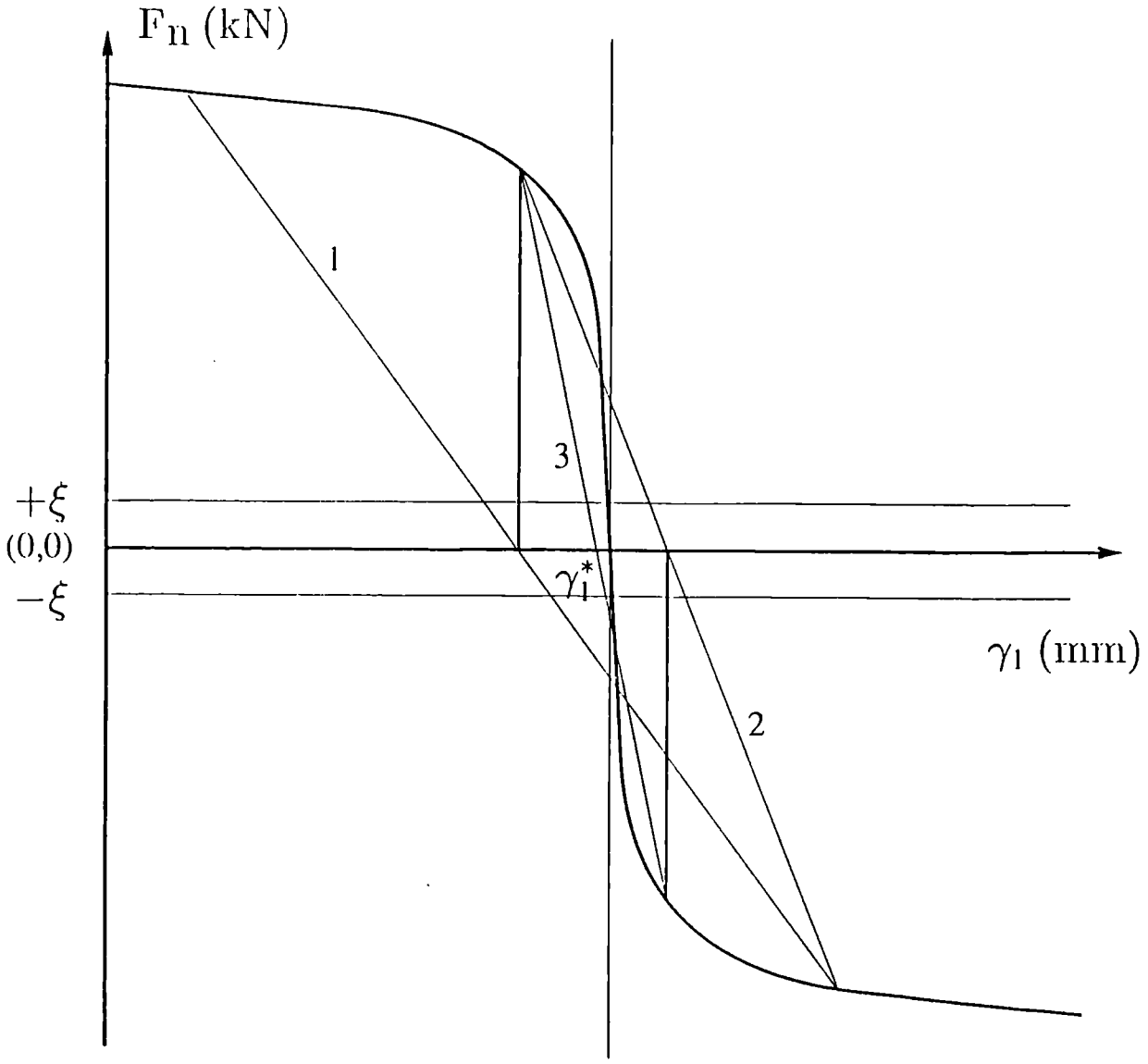

Figure 3.7: Relationship between the value of the slip γ_1, at one end of the beam, and the value of the longitudinal shear force F_n, at the other end.

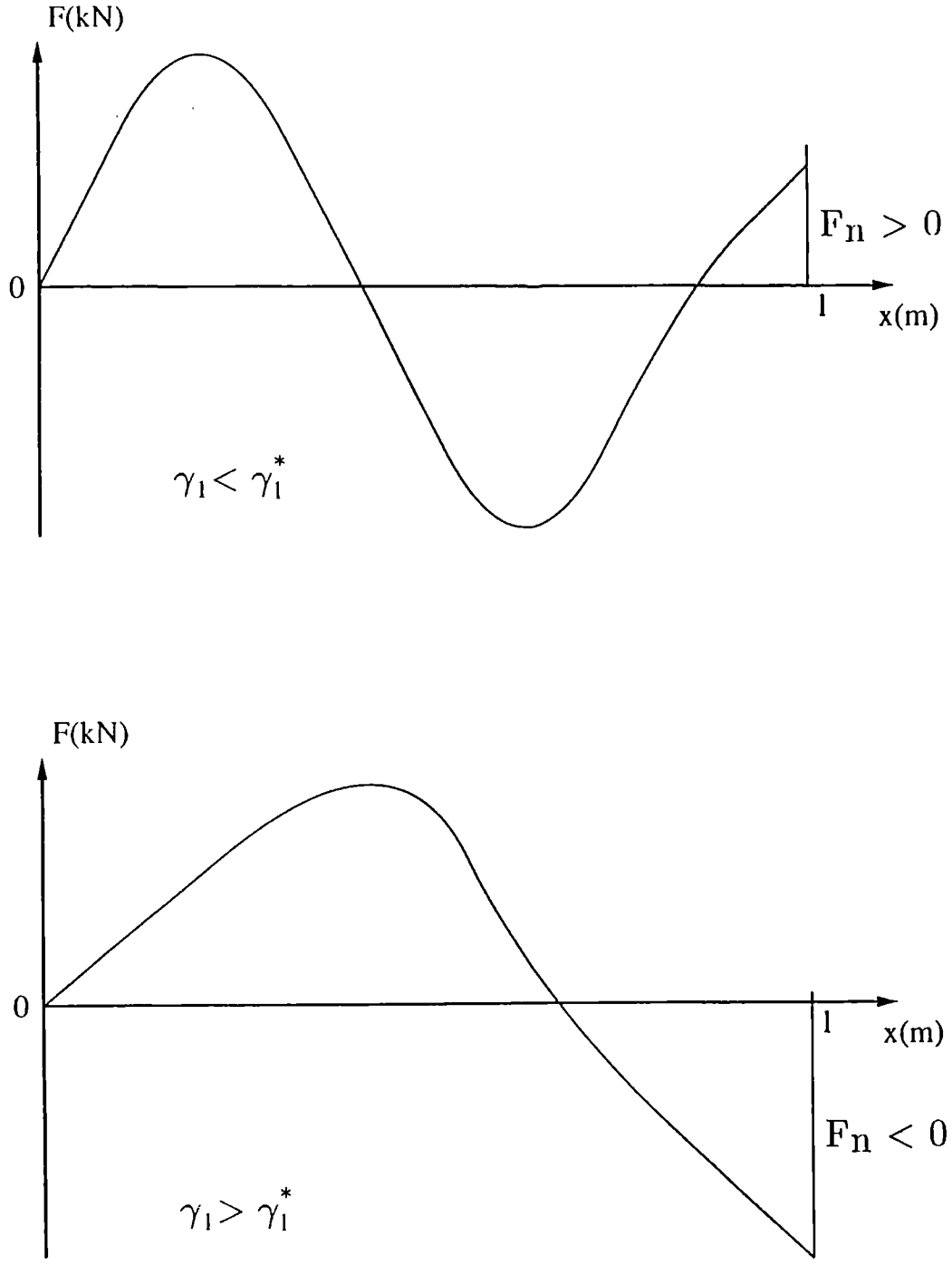

Figure 3.8: Two qualitative longitudinal interface shear distributions, without a correlation between F_n and γ_l.

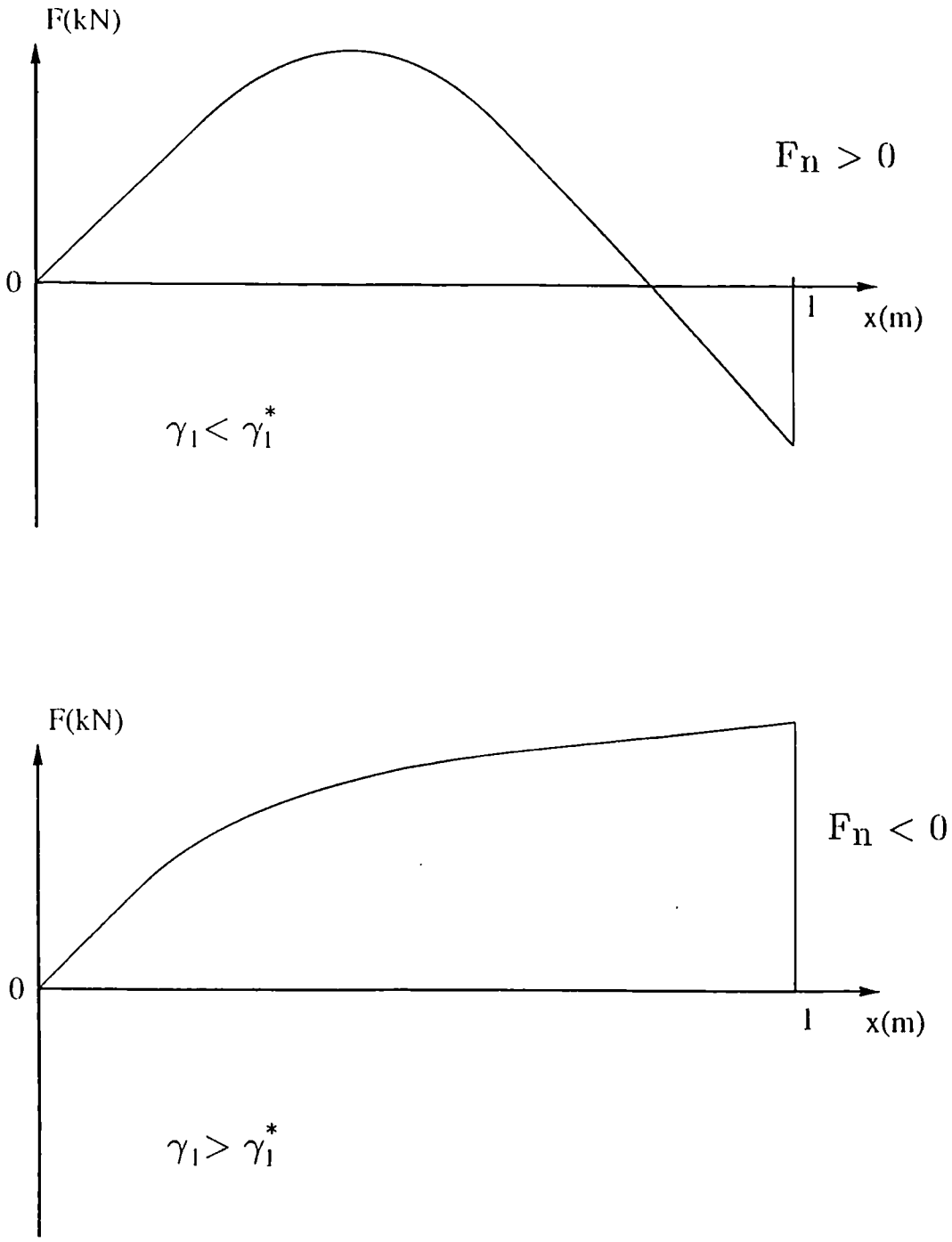

Figure 3.9: Two qualitative longitudinal interface shear distributions, with a correlation between F_n and γ_l.

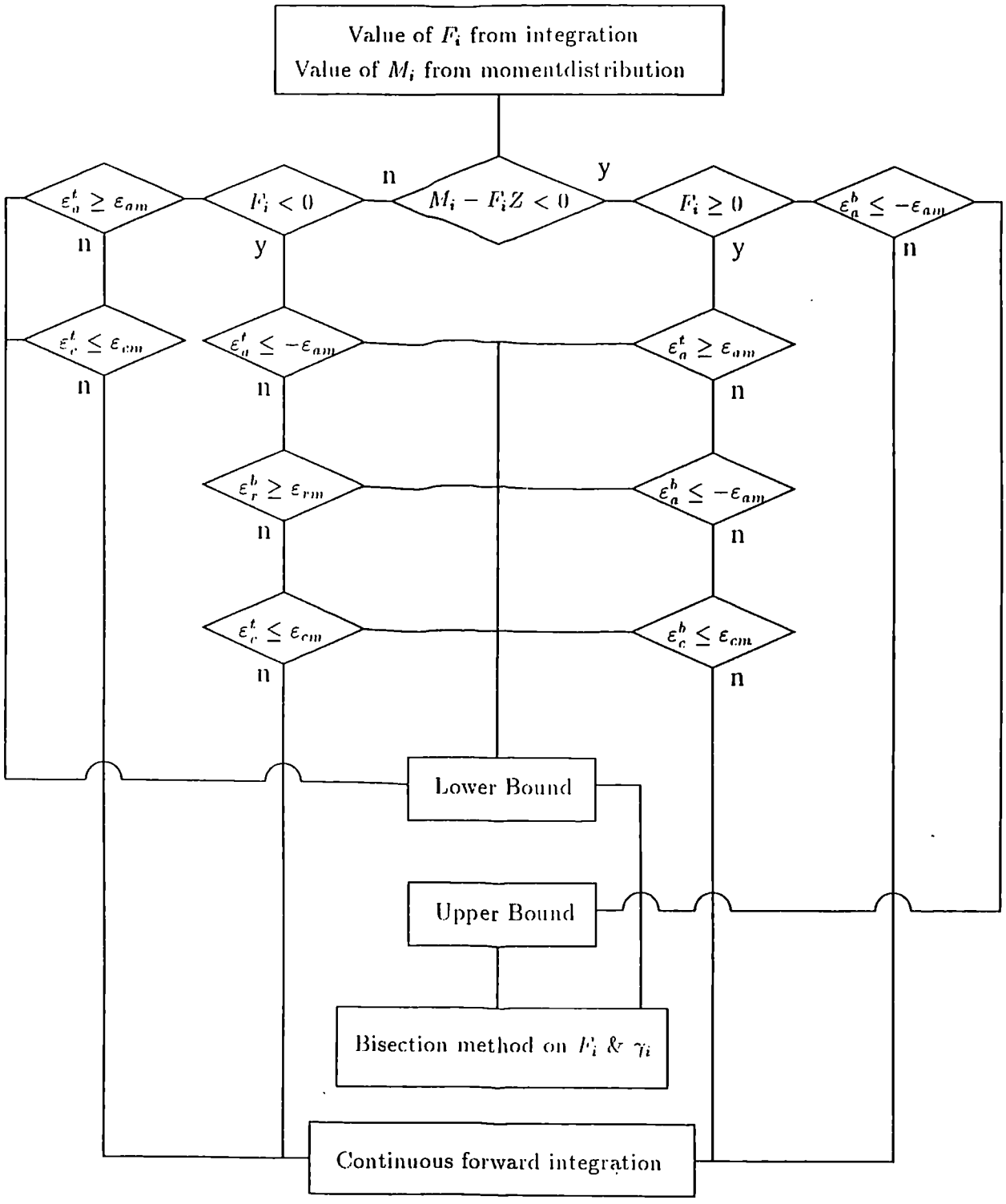

Figure 3.10: Flow chart diagram of strain limitations that cause convergence of the forward integration method.

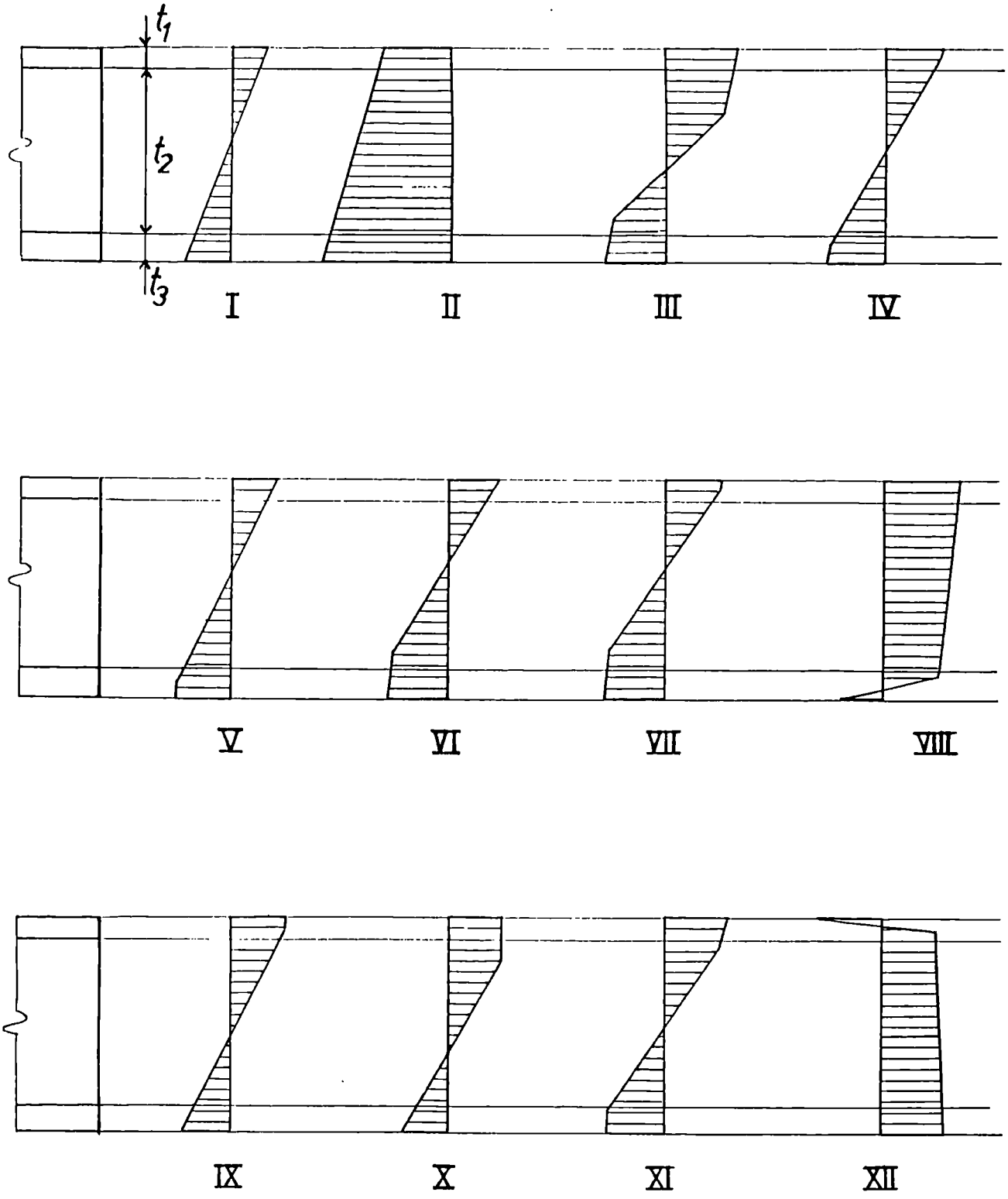

Figure 3.11: Twelve different types of stress distributions within the steelprofile.

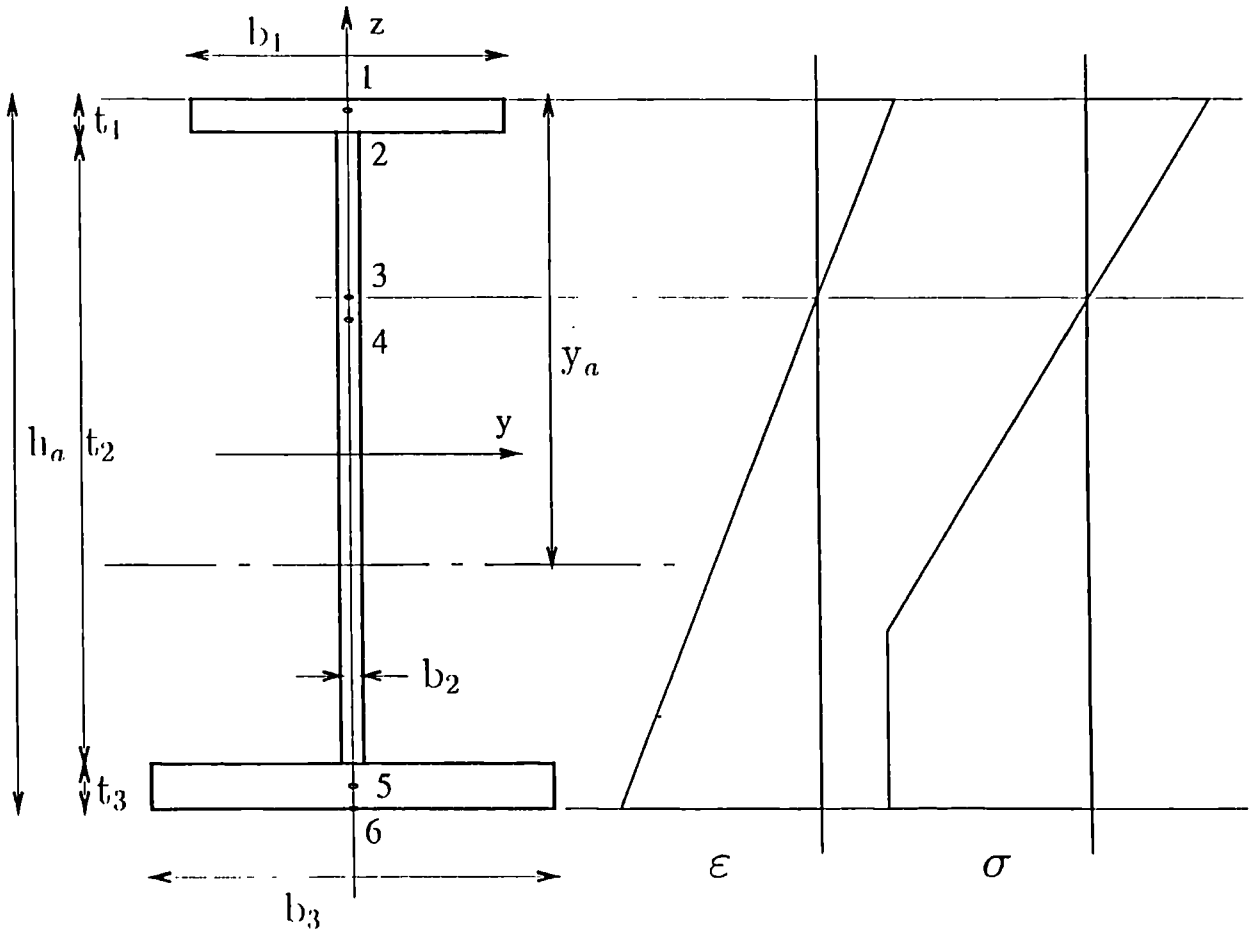

Figure 3.12: Choice of axes and nodes for the half numerical – half analytical method of calculating F_a and M_a.

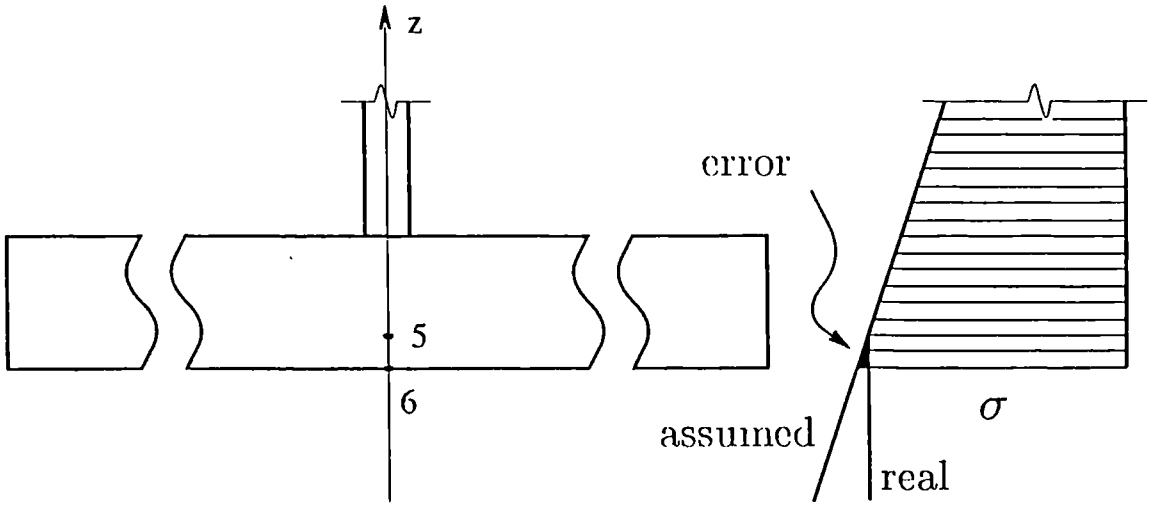

Figure 3.13: Error made with numerical – analytical method.

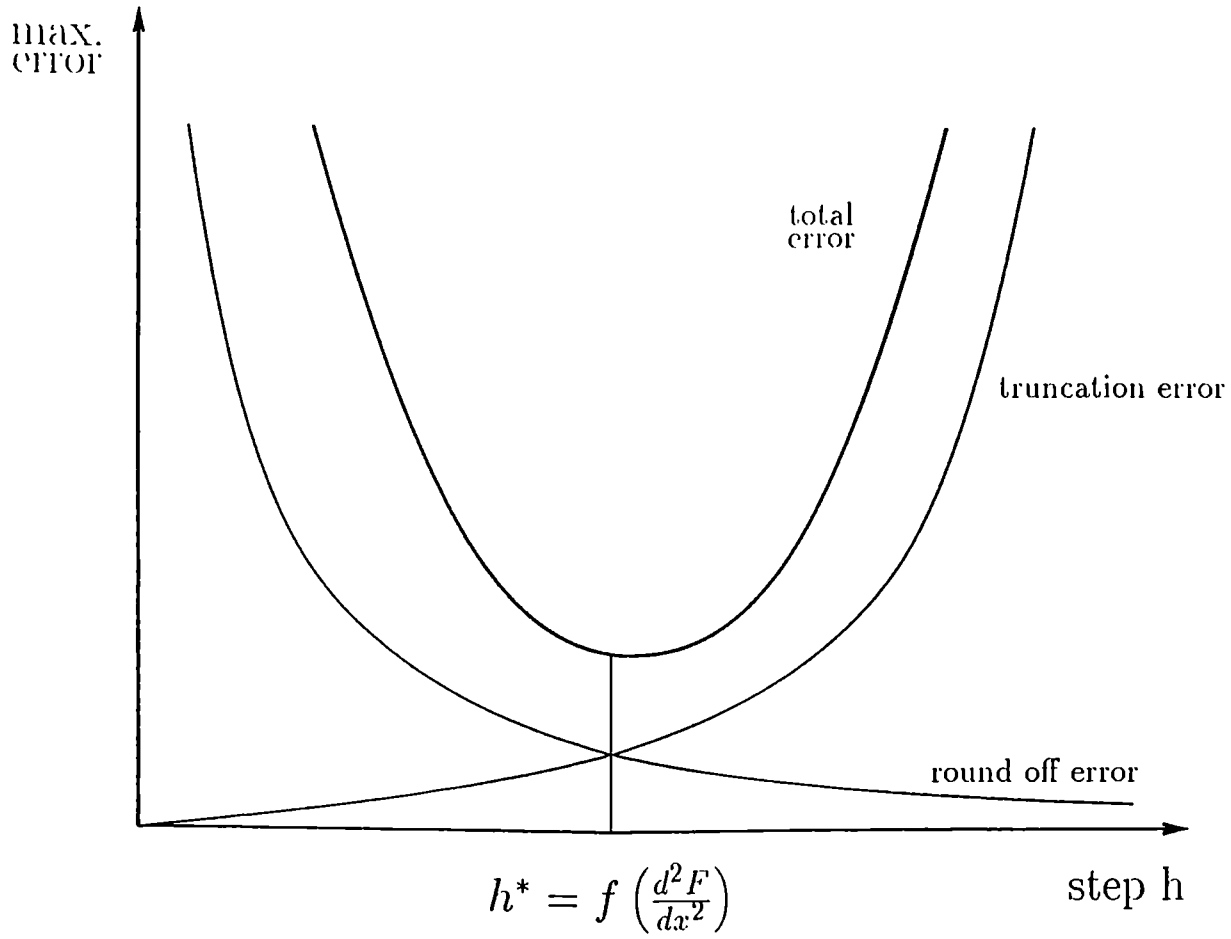

Figure 3.14: Sum of truncation error and round-off error made with the forward integration technique.

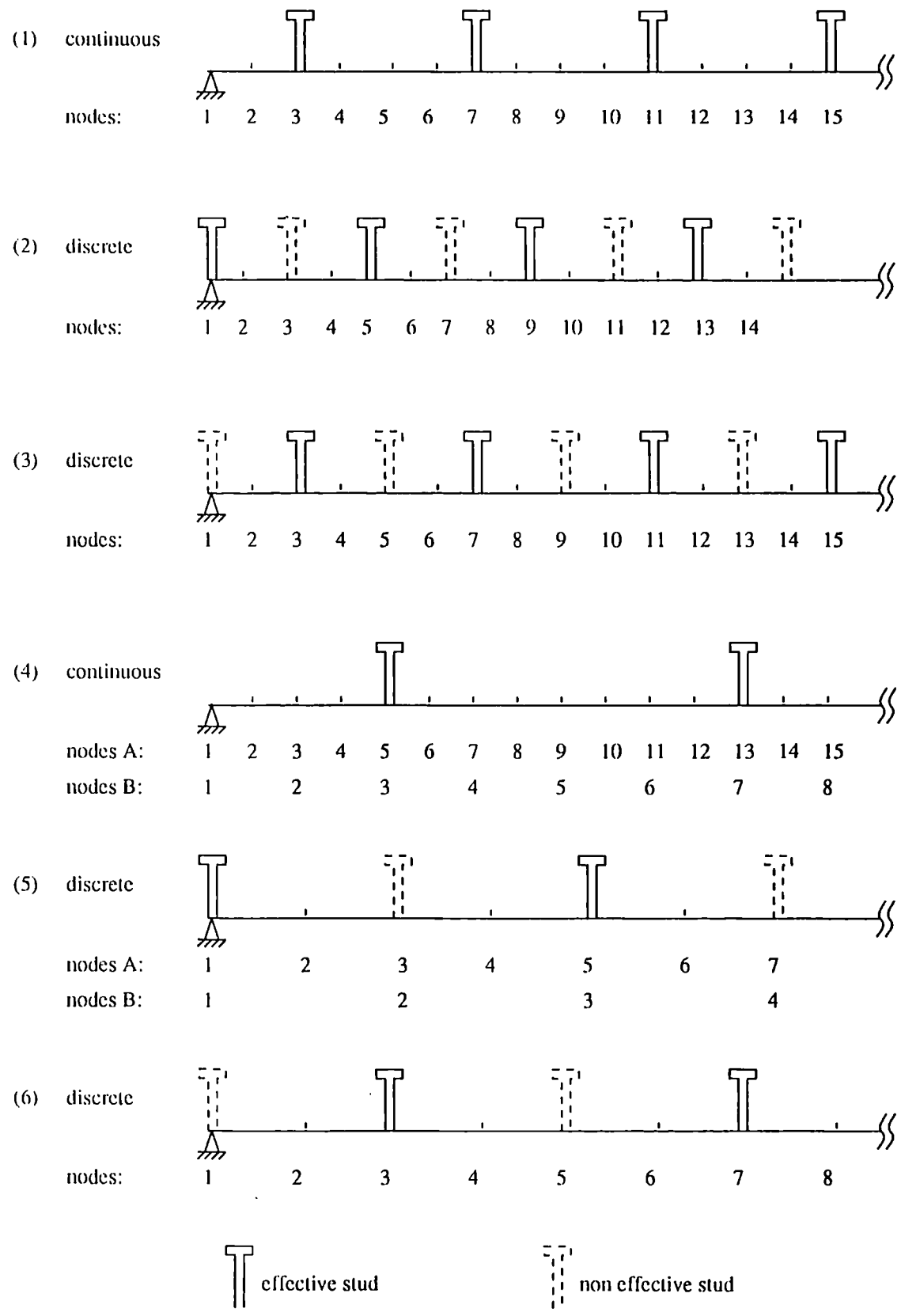

Figure 3.15: Six different stud distributions for the same number of studs along a simply supported beam.

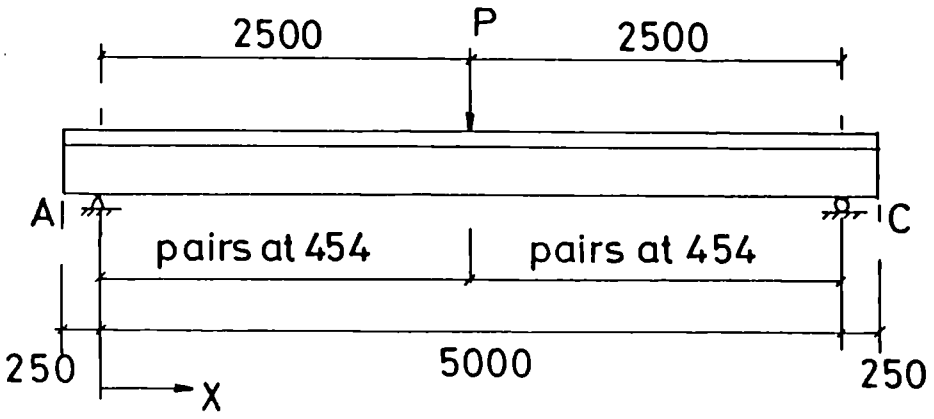

Figure 3.16(a): Stud lay-out and loading conditions on beam P_1 of Table 3.5.

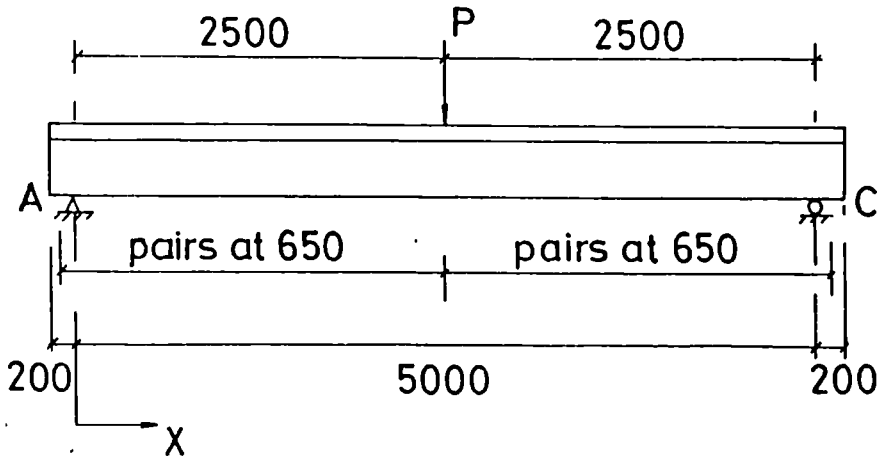

Figure 3.16(b): Stud lay-out and loading conditions on beam P_3 of Table 3.5.

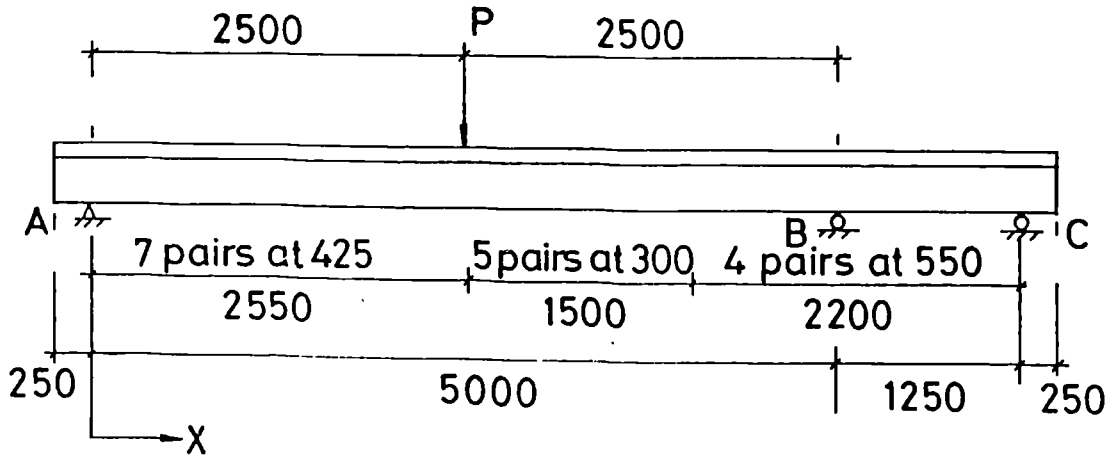

Figure 3.16(c): Stud lay-out and loading conditions on beam P_2 of Table 3.5.

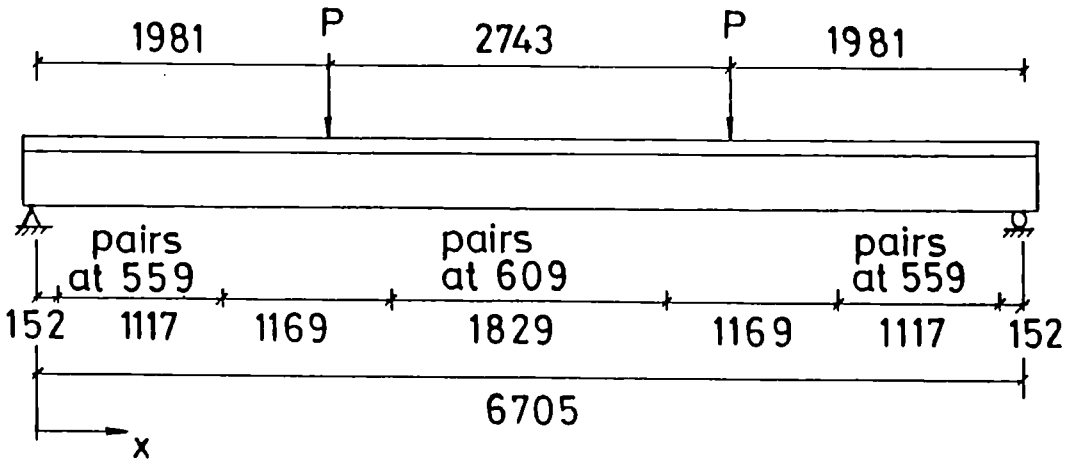

Figure 3.17(a): Stud lay-out and loading conditions on beams B_2, B_3 & B_4 of Table 3.5.

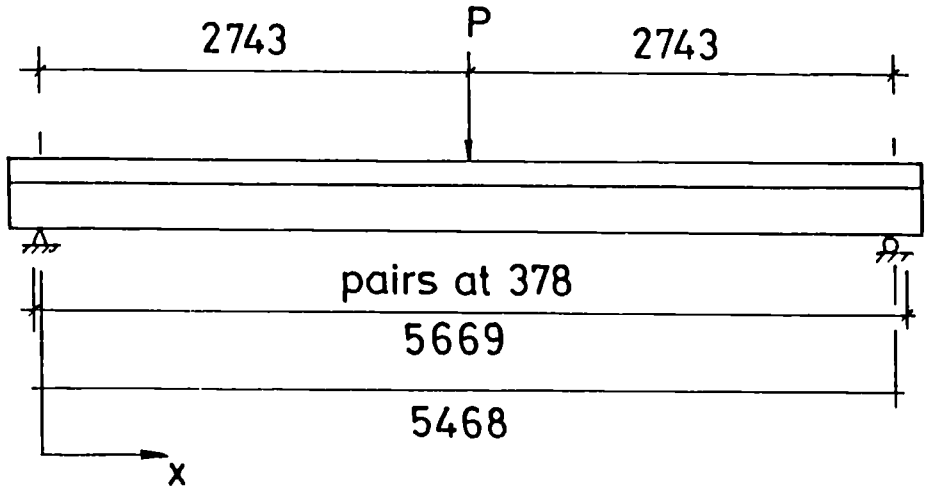

Figure 3.17(b): Stud lay-out and loading conditions on beam A_6 of Table 3.5.

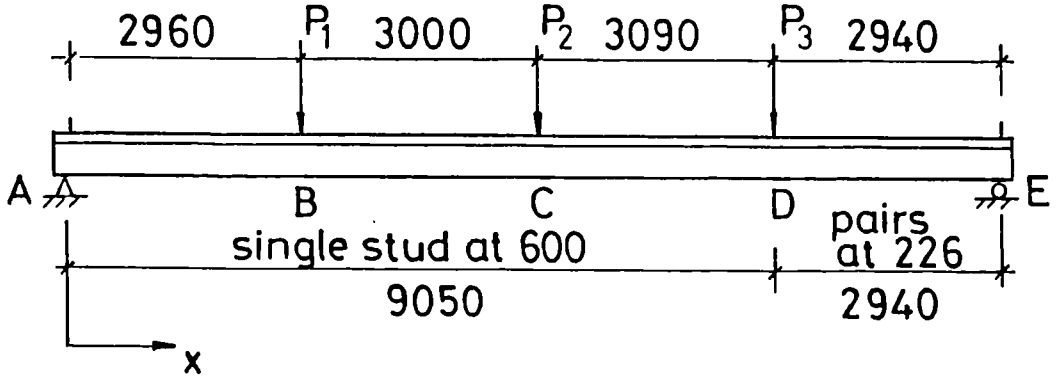

Figure 3.17(c): Stud lay-out and loading conditions on beams T_1 to T_3 of Table 3.5.

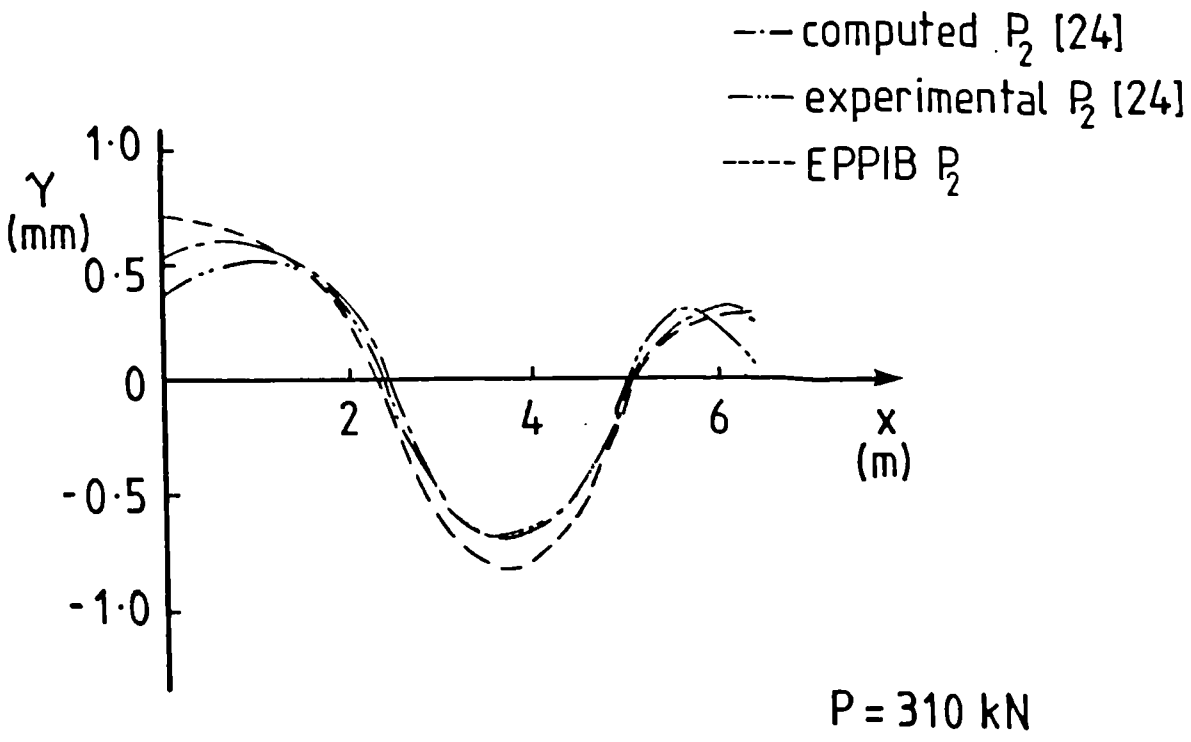

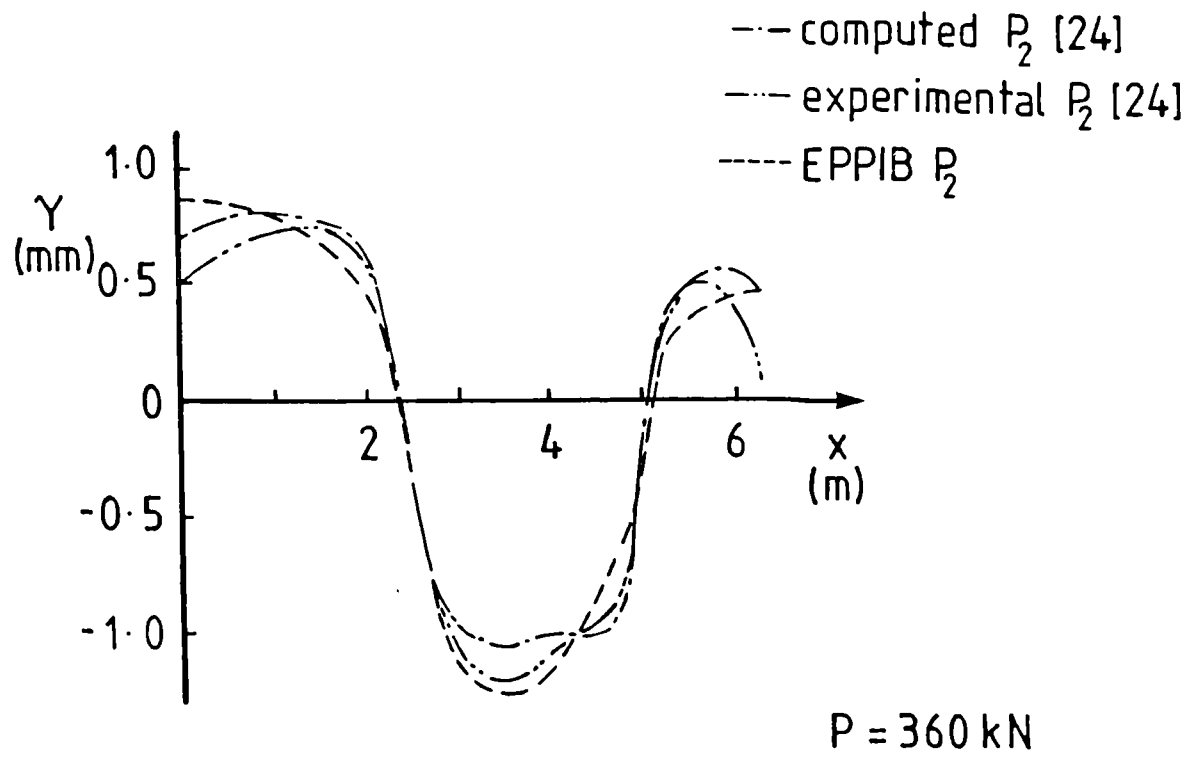

Figure 3.18: Slip distributions for beam P_2 of Table 3.5.

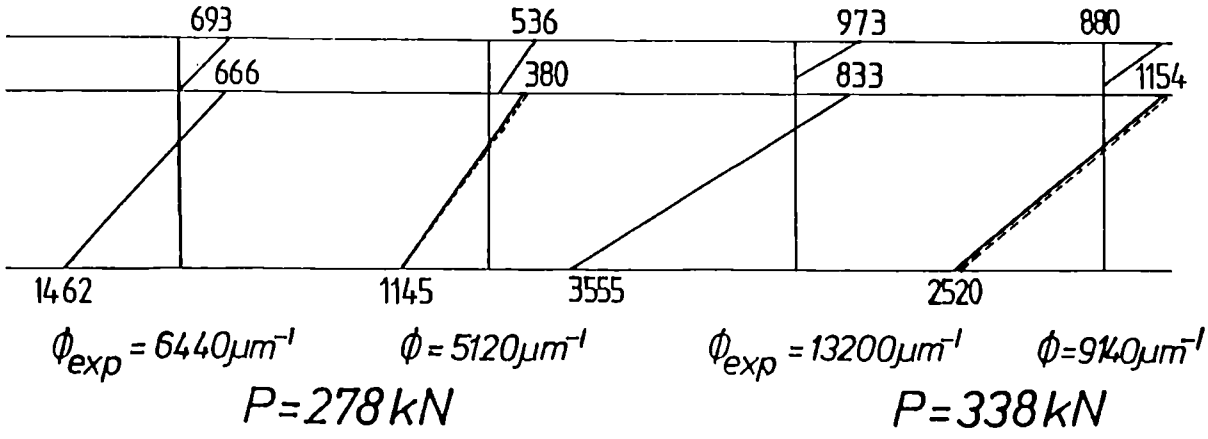

Figure 3.19(a): Comparison of experimental and calculated (—— P_{11}; ------ P_{12}) strain distributions at two different load levels at x = 2.15 m for beam P_1 of Tables 3.5 and 3.6 assuming discrete and continuous shear transfer.

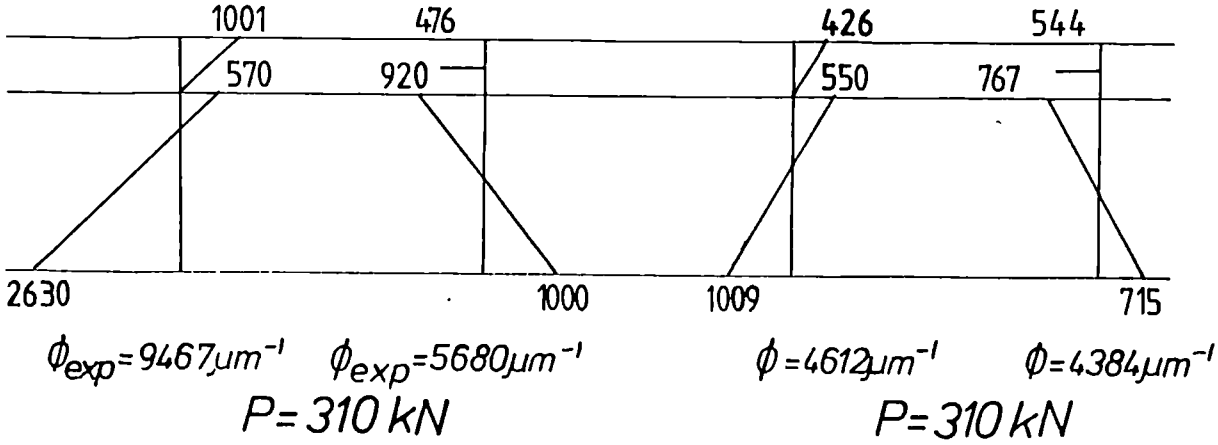

Figure 3.19(b): Comparison of experimental and calculated strain distributions at two different locations on the beam P_2 of Tables 3.5 and 3.8.

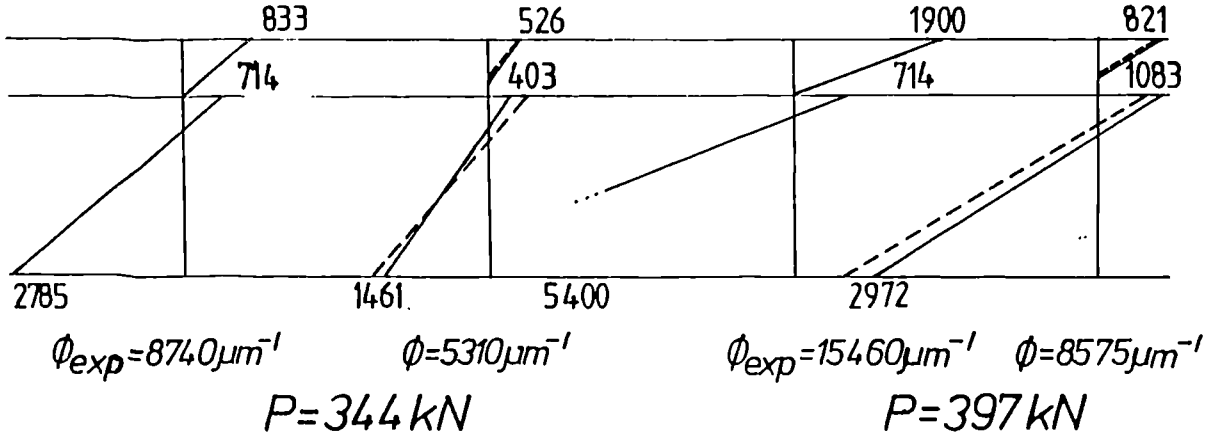

Figure 3.19(c): Comparison of experimental and calculated (——P_{31}; ----- P_{32}) strain distributions at two different load levels at x = 2.15 m for beam P_3 of Tables 3.5 and 3.7 assuming discrete and continuous shear transfer.

Chapter 4

Analyses of composite beams with Partial Interaction

4.1 Study of the slip under ultimate loading conditions

4.1.1 Elastic analytical solution for maximum slip

A linear elastic closed form analytical solution for the slip is since long available for simply supported beams, under uniform distributed service loads. It was initially reported by Newmark, *et al.* in 1951 [31] and later again by Johnson [58], [59]. The result for the maximum elastic slip, γ_e, at both ends of the beam, is given by eq. (4.1). The terms, C_1, and C_2, are functions

$$\gamma_e = C_1 w \frac{l}{2} - \left(\frac{C_1 w}{C_2}\right) \operatorname{sech}\left(C_2 \frac{l}{2}\right) \sinh\left(C_2 \frac{l}{2}\right) \tag{4.1}$$

of the geometric properties of the cross-section and of the elastic properties of the materials and the shear connection. These constants need at least 16 independent variables for their definition, even for an unhaunched beam of uniform cross-section.

Although the result of eq. (4.1) is only relevant to situations in which the loads on the connectors do not exceed about half their ultimate strength, the equation could be used to identify the main variables which influence the slip under ultimate loading conditions, if this elastic solution were representative of the elasto-plastic behaviour. To determine whether similarity exists between the elastic and plastic slip behaviour, analytical elastic slip values, γ_e, and numerical

elasto-plastic slip values, γ_p, have been compared in the next section for different geometric and material parameters.

4.1.2 Comparison between γ_e and γ_p-values

The numerical elasto-plastic solution is available from the program described and validated in chapter 3.

One could approach both elastic and elasto-plastic problems mathematically by regarding the maximum slip as a surface in a multi-dimensional space. In this space, each independent variable has its own boundaries, the practical limits to that variable as used in design. In total about 20 independent variables define γ_p. In other words, one seeks maxima of a surface in a 20-dimensional sub-space. This task is not straight forward, and is further complicated by the many relationships between the independent variables. Furthermore, some combinations are more likely to occur than others; for example, because designers prefer to use rolled steel sections rather than welded ones.

In design of a beam one starts off by knowing the span (l), the transverse spacing between beams (b_c) and the ultimate load to be carried (w_u). In his choice of the materials and the composite cross-section, the designer will consider mainly the following parameters, for reasons of cost and deflection:

- area of steel section (A_a) and its yield strength (f_{ay}),
- thickness of concrete slab (t_c) and its strength (f_c or f_{cu}),
- ratio of area of steel web to total area of flanges (A_w/A_f),
- slenderness of steel web (h_w/t_w), and
- ratio of span to overall depth of beam (l/h_t).

In order to determine the influence of these main parameters on the value of maximum slip, two beams were studied: B1 with $l = 17.5$ m and B2 with $l = 12.5$ m. Two values of maximum slip were found: γ_e using elastic theory, eq. (4.1), and γ_p using our elasto-plastic program.

In Table 4.1 and Fig. 4.1 the geometry and the material properties of both beams are given. In this table the load-slip relationship for the studs is exponential and is characterised by its asymptotic shear strength Q_d, the slip γ_1 at half the asymptotic strength, and the slip γ_2 at 99% of the asymptotic strength.

For different values of the main parameters listed above, the corresponding plastic collapse loads w^i_{pp}, and the number of connectors N, for the different beams, are calculated according to the **interpolation method** of Eurocode 4 as given in Appendix I, assuming a degree of partial interaction of 50% for each beam. In Tables 4.2 and 4.3, the values for γ_e and γ_p under the corresponding w^i_{pp} and for the corresponding stud spacing are compared for different parameters for both beams B1 and B2 respectively.

For beam B2 the following conclusions are drawn from Table 4.3:

The maximum values of γ_e and γ_p, at given slab width, are not reached for the same slab thickness for beams B2-1 to B2-9; and the relative increase in the maximum plastic slip γ_p, with t_c is much larger than the relative increase of the elastic slip, for all widths of slab (e.g. for a 3.0 m width, γ_p increases by 33% while γ_e increased by only 2.6%, for t_c increasing from 120 mm to 180 mm).

A similar lack of correlation between γ_e and γ_p is visible for B2-3 and B2-16, B2-17, where the maximum elastic slip, γ_e, tends to increase with increasing web slenderness, while γ_p decreases by nearly 18% between the extreme h_w/t_w ratios.

A reduction in web over flange area also moves γ_e and γ_p in opposite directions (compare B2-3 with B2-18, B2-5 with B2-19, and B2-7 with B2-20).

Likewise, γ_e behaves opposite to γ_p for an increase in bottom flange to top flange ratio (compare B2-2, B2-21 and B2-22).

The above comparisons for beam B2 demonstrate that the elastic analytical expression does not represent the real behaviour under ultimate loading conditions very well.

Similar conclusions can be drawn for beam B1 in Table 4.1.

Since no correlations have been established, the many different analyses in this table are mainly used in a further discussion on the influence of the different parameters on the maximum elasto-plastic slip value, γ_p.

4.1.3 Parameters affecting the maximum slip, γ_m

The different parameters listed in section 4.1.2 are both geometrical and material ones. The way in which they will affect the maximum slip has been closely

studied by systematic variations of only one parameter at a time within practical boundaries.

4.1.3.1 Geometric parameters affecting γ_p

In this section five different parameters will be studied. These parameters are numbered G(i) to G(v) to make cross-references to Tables 4.2 and 4.3 easier.

G(i): cross-sectional area of concrete slab, A_c For both beams B1 and B2, the cross-sectional area of the concrete slab has a large effect on the maximum slip as can be seen from Fig. 4.2 for both beams. In both cases the maximum slip increases with the slab thickness by between 15 and 35 percent; the increment being higher for broader slabs. This increment is nearly solely due to the increase of load w^i_{pp}, as a result of the increase of lever arm in the calculation of the moment of resistance for wider slabs, as the number of studs over the beams remains constant, due to a constant value of F_p. This influence can be demonstrated by applying the ultimate load, w^i_{pp}, calculated for beam B1-2 on an identical beam B1-5. The result is given as B1-26 and shows that the value of γ_p, for this beam with slab dimensions 3000 mm ×150 mm, is nearly equal to the value of elasto-plastic slip obtained for B1-2 with slab dimensions 4000 mm ×180 mm.

This increase of γ_p with A_c is not always correct, as shown on Fig. 4.3 which represents beams with increasing cross-sectional slab area for different concrete strength. For the beams B1-4 and B1-7 in this figure, the plastic neutral axes does not fall within the concrete slab, thus limiting the longitudinal interface shear force to $A_c f_{cd}$, and the number of studs in one shear span to $A_c f_{cd}/Q_d$. Fig. 4.4 shows the stress distribution and the resultant forces for these beams. Although the longitudinal interface shear is limited, the overall compressive and tensile forces in the cross-section of Fig. 4.4 are not. Therefore, the ultimate moment of resistance will be barely affected and the ratio F_p/w^i_{pp} will reduce.

Comparisons of the behaviour of γ_p with F_p/w^i_{pp} in Tables 4.2 and 4.3 indicate that these two variables are inversely proportional.

G(ii): ratio l/h_t and h_w/t_w The ratio h_w/t_w has a large effect on the maximum slip as shown in Fig. 4.5. This figure demonstrates that for both beams B1 and B2 the slip increases with diminishing values of h_w/t_w, while the corresponding values in Tables 4.2 and 4.3 show that this slip increase is not due to an increase in ultimate load, on the contrary, w^i_{pp} is the lowest for the beam with the highest slip.

Since the increase of h_w/t_w under a constant A_w/A_f ratio coincides with a reduction of the span over depth ratio, l/h_t, it is difficult to tell whether the slip changes are mainly due to h_w/t_w or l/h_t variations. Comparisons of beams B1-3, 10 and 11 illustrate this problem by showing a 10% increase of γ_p to coincide with a 17% increase of l/h_t and a 33% decrease of h_w/t_w. Similar comparisons for beams B2-3, 16, 17 show a 20% increase of γ_p to coincide with a 22% increase of l/h_t and a 45% decrease of h_w/t_w.

In order to determine which parameter weighs more in determining γ_p, two comparisons are made: one between B1-11 and 28 and a second one between B1-11 and 27.

The first group of beams have the same span over depth ratio and carry the same load as the one carried by B1-11. For an increase in h_w/t_w of 30% the slip drops by 13%. The second group of beams have the same web slenderness ratio and both beams also carry the same load as B1-11. A reduction in l/h_t of 9% brings about a slip increase of 15%. Although both parameters, l/h_t and h_w/t_w, are obviously interrelated, this comparison indicates that the slip is more sensitive to l/h_t. A comparison of B1-11 with different rolled European sections B1-12 and 13 confirms this close relationship between h_w/t_w, l/h_t and the maximum slip, γ_p.

G(iii): ratio A_3/A_1 The influence of the ratio A_3/A_1, of the bottom flange area over the top flange area of the steel beam, on the maximum slip is shown in Fig. 4.6 for both beams. This figure demonstrates that the increase of γ_p with A_3/A_1, is entirely due to the increase of the ultimate load, w^i_{pp}, which coincides with the increase of A_3/A_1. Since this parameter has only an indirect effect on the slip it can be regarded as a secondary parameter.

G(iv): ratio A_w/A_f For steel beams with a constant cross-sectional area of steel, the stiffness of the steel girder is inversely proportional with the ratio A_w/A_f, an important beam parameter. Yet, comparisons between B1-11, 12 and 13 show that large changes in the A_w/A_f ratio have little influence on γ_p, except through changes in l/h_t. Similar comparisons between B1-18 and 19 and B1-20 and 21 show that a more than 100% increase in A_w/A_f hardly influences γ_p systematically: for the first group, γ_p increases for the second group it reduces. Any changes in γ_p can be explained by a simultaneous increase of w^i_{pp} and a reduction of l/h_t which coincides with the change in A_w/A_f.

Therefore, this parameter can also be regarded as a secondary parameter in

the determination of γ_p.

G(v): use of metal decking For beams with relatively narrow composite slabs, with profiled metal decking running perpendicular to the span direction, the longitudinal interface shear often is determined by the thickness of the slab above the trough, especially when the steel girder is rather large, depending on the position of the plastic neutral axis.

When the plastic neutral axis falls within the steel section these beams will exhibit a much larger value of the maximum slip, γ_p, than a similar beam with a solid concrete slab would produce, where the plastic neutral axis lies within the slab.

When the plastic neutral axis falls within the composite slab, then the maximum slip produced by these beams is nearly the same as the maximum slip in a beam with identical material properties and steel profile but where the slab is solid.

For both positions of plastic neutral axis the ultimate moment of resistance is nearly the same. Fig. 4.8 shows the relationship between the slip and the slab area, $b_e \times t_c$, for different beams B1 and B2.

The amount and the position of the reinforcement has less than 3% effect on the value of the maximum slip, when it ranges from 0.2 to 1.0 % of the slab area.

The slip is therefore related to the position of the plastic neutral axis y_p, or the ratio $y_p/(t_c + t_h)$ otherwise written as F_p/F_a.

4.1.3.2 Material characteristics affecting γ_p

In this section three different parameters will be studied. These parameters are numbered M(i) to M(iii) to make the cross-references to Tables 4.2 and 4.3 easier.

M(i): the concrete strength, f_{ck} As long as the plastic neutral axis is located within the concrete slab, the maximum slip is an increasing function of the concrete strength. Changes in concrete strength will affect beams with larger slabs in the same manner as they affect beams with smaller slabs. This behaviour has been demonstrated in Fig. 4.8 for beam B2. This figure shows the relationship between the maximum slip and the concrete strength. Once the plastic neutral axis lies within the slab, the reduction of F_p/w_{pp}^i will influence this relationship as shown in Fig. 4.8 for beam B1.

Although the ultimate load is also an increasing function of the concrete

strength, the percentage rate of increase of w_{pp}^i is much smaller than the percentage rate of increase of γ_p with f_{ck}. For beams B1-1 to B1-3, a 5% increase in w_{pp}^i corresponds with a 25% increase in γ_p for a 100% increase in f_{ck}.

The only compound parameter that changes consistently for increasing values of f_{ck} is the ratio F_c/F_a for the cross-section, where F_c represents the crushing strength of the slab and F_a the full yield capacity of the steel girder.

Taking account of a tensile strength of concrete of not more than 10% of the compressive strength, will reduce the maximum slip by not more than 10%, as shown from comparisons of beams B1-3 with 30, and B1-9 with 31.

M(ii): **the yield strength, f_{ay}** For both beams B1 and B2, the maximum slip is an increasing function of the yield strength of the structural steel, as shown in Fig. 4.9. Unlike the concrete strength, this increase cannot entirely be attributed to the increase in ultimate load, as the ratio F_p/w_{pp}^i stays practically the same for these beams (compare B1-3, 4 and 9, with B1-24, 25 and 23 respectively).

M(iii): **the load-slip curve of the studs** Although the design value for the shear strength is a function of the material properties of the slab and of the dimensions and the material properties of the stud connection, the exponential load-slip curve used in the program is a product of experimental Push-Out tests. This curve therefore is not completely arbitrary and its variation has to be within realistic boundaries. This parameter will be the subject of section 4.2 and has not been varied for the purpose of these comparisons.

4.1.3.3 Conclusion on main parameters

From the above-detailed parametric study, the main parameters which affect the maximum slip in a simply supported beam, can be identified as:

the ratio l/h_t

the ratio F_p/w_{pp}^i

the ratio $y_p/(t_c + t_h)$ or F_p/F_a

the ratio F_c/F_a

In order to make the second parameter dimensionless, F_p/w_{pp}^i and F_p/F_a could be replaced by w_{pp}^i/F_a, where F_a already appears in the ratio F_c/F_a.

Therefore only w_{pp}^{i} is left and is easiest made dimensionless by expressing it as $(w_p - w_{pa})/w_{pa}$, thus reducing the dimensionless parameters to:

$$\frac{l}{h_t}, \frac{w_p - w_{pa}}{w_{pa}}, \frac{y_p}{t_c + t_h}, \frac{F_c}{F_a}$$

4.2 The experimental load-slip curve

In a composite beam, the axial force in the steel beam is transferred to the concrete slab via shear connectors. The behaviour of one connector is characterised by its load-slip relationship, which in turn is characterised by its **initial stiffness**, its **ultimate shear strength** and corresponding **ultimate slip** and its **slip capacity**. This load-slip relationship has traditionally been obtained from a standard Push-Out test.

This Push-Out test was first standardised in Britain in 1965 in CP 117:Pt. 1, and the specifications for this test have not been changed since, neither in the draft Eurocode 4 [3] nor in the more recent BS 5950:Pt.3:Section 3.1 [4]. The standard test specifies solid concrete slabs with uniform thickness although provision is made for metal decking, which is presently more currently used. Research, both in Britain and abroad [60], [29] has proven the results of this standard test to be conservative, due to the narrow concrete flanges and the lack of anchorage of the transverse reinforcement. The values [4] or formulae [3] given in the above-mentioned Codes for the characteristic or nominal shear strength of stud connectors are mainly based on standard Push-Out test results and are therefore only valid for studs in solid slabs.

Since no standard Push-Out test has been defined for studs in slabs with metal decking, the more recent Codes define different reduction factors for the ultimate shear strength of these studs, depending on the orientation of the sheeting. For profiled sheeting running perpendicular to the span of the beam, which is the most frequent orientation in design, the reduction factor described in clause 6.3.2.4 of Eurocode 4 or clause 4.4.7 of BS 5950:Pt.3 was derived in the late 1970's from experimental results of composite beams, obtained at Lehigh University by Grant, *et al.* [61]. Since these tests were done, non-standard Push-Out tests have been performed, using different profiles, which have shown this reduction factor to be unsafe [62], while standard Push-Out tests were found to be unsuitable for use with metal decking.

The load-slip behaviour of studs in solid slabs and slabs with metal decking running perpendicular to the span, were studied therefore independently and

separately.

4.2.1 Load-slip behaviour of studs in solid slabs

For years it has been assumed that the load-slip behaviour of a connector in a Push-Out test represents fairly well the behaviour of that same connector in a beam, as long as the same failure mode of the connector could occur in the beam.

The shear capacity It is known that the standard Push-Out test can give reduced values of the connector strength due to splitting of the slab. Oehlers [63] explained this phenomenon of slab-splitting - which does not appear in beams under static loading - as a failure mode due to (i) a small width of the slab, (ii) a small amount of transverse reinforcement, (iii) a lack of anchorage of this reinforcement.

In more recent research [64] he developed a new Push-Out test in order to eliminate the compressive forces working on the connectors in the standard Push-Out test, as shown in Fig. 4.11. By eliminating these forces - which are again not present in beams - the ultimate shear strength of the stud connector was found to reduce by about 7% as compared to the ultimate shear strength of the same connector in a standard Push-Out test of similar geometry and stud spacing, where such compressive forces are induced on the studs [65].

Research in the U.S.A. and in Germany [67], [29] shows that the strength per connector on specimens with more connectors (on both flanges, different spacing), wider slabs and more transverse reinforcement, is larger than the strength per stud connector in the standard Push-Out tests. This increase is due to a better shear redistribution between the two slabs and between the connectors, which prevents failure until the mean shear in both slabs has reached a certain value. One could argue that the same amount of redistribution as found in Roik's specimens with 16 stud connectors, is not necessarily present in a beam with partial shear connection, where only a few studs appear at relatively large longitudinal spacing and where the shear is not uniform. Therefore, Oehlers and Johnson [65] derived eq. (4.2), an expression for the characteristic static strength of studs in a beam, which depends on the number of shear connectors in one shear span.

$$Q_k = K A_{sh} \left(\frac{E_c}{E_a}\right)^{0.4} f_{cu}^{0.35} f_u^{0.65} \tag{4.2}$$

with $K = 4.1 - N^{-0.5}$

and N = number of shear connectors in one shear span

Fig. 4.10 compares the characteristic shear strength of 19 mm diameter studs calculated according to eq. (4.2), for $N = 9$ and ∞, with the characteristic shear strength Q_k, of the same stud according to clause 6.3.2.1 in Eurocode 4 and with the nominal shear strength of that stud according to clause 4.4.6 in BS 5950:Pt.3. In this figure the shear strength is compared for different cylinder strength of concrete, ranging from 20 N/mm^2 to 40 N/mm^2, with the conversion of cube strength into cylinder strength as in section 2.2.2.

For $f_c = 20$ N/mm^2 the percentage difference between the nominal shear strength obtained from Table 5 in BS 5950:Pt.3 and the average characteristic shear strength according to eq. (4.2) is about 18% and reduces to about 8% for $f_{ck} = 40$ N/mm^2. For Eurocode 4 these percentage differences between characteristic strength reach a maximum of 25% for the lower Grade concrete, since the values of Q_k in Eurocode 4 were derived from non-standard Push-Out tests by Roik and Hanswille [29].

This comparison agrees therefore with Oehlers' and Johnson's findings that eq. (4.2) forms a lower bound to the experimental research used in American, European and British Codes, because it allows for variations between the restraints on the connectors in Push-Out tests and in composite beams.

In much earlier research by Johnson, *et al.* [67] the ultimate strength of studs in hogging bending regions was reduced on average by 20% as compared to the strength obtained from standard Push-Out tests. This reduction was introduced to allow for an increase in slip at the ultimate shear load. However, in continuous beams the longitudinal shear in hogging regions ($A_r f_{ry}$), which isbeing transmitted by the studs to the cracked concrete is much smaller than the longitudinal force in the shear span. Neglecting this reduction in shear strength in Eurocode 4 has a very small effect on the beam.

Both these findings on the reduction in stud shear strength in beams as compared to Push-Out tests and in hogging regions as compared to sagging regions prove that the recent Codes of Practice are not conservative in their evaluation of the ultimate shear strength of studs in beams with solid slabs.

The application of partial safety factors on these characteristic or nominal ultimate shear strength, will produce design values for the strength which are still lower than the values obtained by eq. (4.2), as is shown in Fig. 4.10. In future analyses, the load-slip curves, which are used to model the behaviour of

the shear connectors in the beam, will have as maximum shear load, the design ultimate load as either given by Eurocode 4 or BS 5950:Pt.3. That way, the values obtained from the numerical analyses are directly comparable with the design values for material strength, stresses and deformations.

The elastic stiffness The other main characteristic of the load-slip behaviour is the elastic stiffness of the connector embedded in the solid slab of the composite beam.

The stiffness obtained by Push-Out tests is on average fairly similar to the stiffness in a beam in sagging bending. This conclusion is drawn from the analyses of experimental research by Skinner [30] and McGarraugh and Baldwin [14] where load-slip curves were reconstructed from slip and strain measurements along the beam. Some results of these experiments were already shown in Fig. 2.3. The same research team came also to the conclusion that there is no difference in stiffness whether the stud is embedded in normal density or lightweight concrete, when $\rho > 1350 kg/m^3$.

Although Dallam [68] claims that studs are less stiff when embedded in light weight concrete, Menzies obtains in Fig. 9 of Reference [69] a half-dimensionless load-slip curve from over 34 Push-Out tests. For this curve the load is given as a proportion of the maximum load and the curve is only valid for studs in slabs with concrete densities of $1400 kg/m^3$ and above.

Buttry [70] constructed a similar complete dimensionless load-slip curve from a series of 57 Push-Out tests, with the load as a proportion of the maximum load on the Y-axis and a dimensionless expression of slip, stud diameter, secant modulus of concrete and maximum load on the X-axis.

In more recent research, Oehlers and Coughlan [28] produced another dimensionless load-slip curve with the load as a proportion of the maximum load on the Y-axis and the slip as a proportion of the diameter of the stud on the X-axis. The stiffness becomes a function of the characteristic cube strength of the concrete. The dimensionless curve thus obtained is the result of a series of 53 Push-Out tests, of which only 42 specimens were used to determine the ultimate slip, since some of the specimens had split slabs, which values were omitted. A linear regression analysis on these 42 results shows that the studs are stiffer in stronger concrete but that their ultimate slip becomes smaller.

Fig. 4.12 compares Menzies, Buttry's and Oehlers' curves for 19 mm diameter stud connectors embedded in 35 N/mm^2 strong concrete slabs. To dimension the X axis on Buttry's curve, average values of ultimate shear and secant modulus

were taken from his test results on 19 mm studs. This figure demonstrates that Menzies and Buttry's curves are much stiffer than Oehlers' curve. This difference is partly caused by the higher strength of concrete used in Menzies and Buttry's tests and is partly due to the differences between the Push-Out tests used in the United States and in the United Kingdom. Yet the main reason for this difference is undoubtedly the fact that both Menzies and Buttry incorporated the load-slip curves from Push-Out specimens which had failed by slab splitting in their calculation of an average dimensionless or semi-dimensionless load-slip curve. Both Oehlers and Buttry found a large scatter in Push-Out test results. The shaded area in Fig. 4.12 represents the area where one has 95% chance of finding a load-slip result from a Push-Out test on 19 mm diameter studs embedded in 35 N/mm^2 strong concrete, as given by Oehlers' analysis. A similar scatter of results was found by Buttry from his results and is given in Fig. 19 of Reference [70].

The ultimate slip and slip capacity Presently, both in Britain and the United States, the minimal degree of shear connection in Codes of Practice tends to reduce from 50% to 40% and even lower.

By using longer spans with such low degrees of shear connection the required slip before loss of strength occurs will increase, as was demonstrated in the parametric study in section 4.1. This increase is needed to enable the beam to develop enough slip to load its connectors to their design ultimate shear strength so that the beam can sustain its design ultimate load.

Since stud connectors are ductile, Push-Out tests show them to have a much larger **slip capacity** than **ultimate slip**. Under **ultimate slip** is understood the slip corresponding to the ultimate load, under **slip capacity** is understood the slip reached after the ultimate load has reduced by 5% after reaching its peak value.

Although a lot of different types of Push-Out tests on different studs embedded in slabs of different strength and different concrete density have been done in the past, very few recordings were made of the ultimate slip and even fewer recordings were made of the slip capacity of the connectors. The aim of most investigators in the past was to establish the ultimate shear capacity of the embedded connectors, not the corresponding slip.

There is clearly a need to obtain a minimum ultimate shear requirement for the stud connectors as well as a minimum slip capacity requirement to ensure that bending failure of a composite beam will not be preceded by stud shear

failure before the design ultimate load of the beam is reached. For every beam, the available slip capacity needs to be larger than the slip required to develop its design ultimate load, in the same way as the shear capacity is larger than the shear required to develop the ultimate moment of resistance. Therefore, the slip capacity needs to be studied as a function of the geometry and the material properties of the slab.

Oehlers' and Coughlan's [28] linear regression analysis which was used to find the stiffness of the load-slip curves can also be employed to give both the ultimate slip and the slip capacity as a function of the stud diameter, d_{sh}, and the concrete cube strength, f_{cu}.

The **characteristic ultimate slip** for 13 mm, 19 mm and 22 mm diameter studs is obtained from eq. (4.3), while the **mean ultimate slip** is obtained from eq. (4.4) for concrete cube strength ranging from 20 N/mm^2 to 70 N/mm^2.

$$\gamma_{u,k} = (0.340 - 0.0023 f_{cu})\, d_{sh} \tag{4.3}$$

$$\gamma_{u,m} = (0.389 - 0.0023 f_{cu})\, d_{sh} \tag{4.4}$$

This point was reached by one quarter of the 42 specimens, since in the other specimens, either one or both sides had split. These values for ultimate slip are therefore conservative for beams in which splitting does not occur, unless transverse reinforcement is deficient.

In the same paper, failure is defined as the point where the shear force has fallen to 95% of its peak value, therefore corresponding with our definition of slip capacity.

The **characteristic slip capacity** and the **mean slip capacity** are given by equations (4.5) and (4.6) respectively.

$$\gamma_{f,k} = (0.374 - 0.00178 f_{cu})\, d_{sh} \tag{4.5}$$

$$\gamma_{f,m} = (0.453 - 0.00178 f_{cu})\, d_{sh} \tag{4.6}$$

This point was reached by half of the specimens which did not split, whereas the other half had failed by stud shank fracture just above the weld collar.

Roik and Hanswille [29] find mean values of the ultimate slip in their Push-Out tests on 19 mm studs which are on average 10% higher than the ones obtained by eq. (4.4), while they find mean ultimate slip values of 22 mm studs which are on average 11% lower. Yet their values of the slip capacity seem to correspond with the values obtained from eq. (4.6).

Dallam [68] registered only average values of the slip for his 25 Push-Out tests, which were on average 13% lower than the values obtained by eq. (4.4) for 19 mm diameter studs, and 16% lower than the values obtained by this equation for 22 mm diameter studs.

The reconstructed load-slip curves from beam measurements obtained by Baldwin's team [14] [30] show ultimate slip values which are comparable to the values given by eq. (4.4).

It is concluded that the values produced by Oehlers' and Coughlan's eq. (4.4) can be used as average values for the ultimate slip of studs in Push-Out tests as well as in beams. Possible three **average** limiting **ultimate slip levels** could be considered:

for studs with a diameter smaller than 13 mm: 3.0 mm

for studs with a diameter equal to 16 mm: 5.0 mm

for studs with a diameter equal to 22 mm: 7.0 mm

Although the values for the slip capacity given by eq. (4.6) can only be used as a guideline for the limiting slip capacity, due to a lack of experimental evidence, similar three **average** limiting **slip capacity levels** could be defined:

for studs with a diameter smaller than 13 mm: 4.0 mm

for studs with a diameter larger than 16 mm: 6.0 mm

for studs with a diameter larger than 22 mm: 8.5 mm

4.2.2 Load-slip behaviour of studs in slabs with metal decking

Both draft Codes [3] [4] give the same design approach for stud connectors in slabs with profiled metal decking spanning perpendicular to the beam. For the design ultimate shear strength of these connectors they specify both the same reduction factor, given by eq. (4.7), to be applied to the design ultimate shear strength of the same stud, embedded in a solid slab of the same concrete.

$$k = \left(\frac{0.85}{\sqrt{N}}\right)\left(\frac{b_{md}}{h_{md}}\right)\left[\left(\frac{h_{st}}{h_{md}}\right) - 1\right] \tag{4.7}$$

with N = number of studs per trough

b_{md} = average width of trough for open profiles

= minimal width of trough for re-entrant profiles

h_{md} = height of trough

h_{st} = height of stud after welding

This equation was derived more than 10 years ago by Grant, *et al.* [61] from test results on beams with certain shapes and types of metal decking. In their research, they made no attempt to study the interaction between deck and studs nor did they study the failure mechanism of the studs in these slabs. Grant, *et al.* [61] aimed only at deriving a reduction factor for the existing empirical shear strength formulae for studs in solid slabs as derived by two of the authors, Fisher and Slutter, in an earlier publication [66].

Today, profiled metal decking is commonly used in the construction of building floors and more and different shape profiles have come onto the market. In general terms, two main types of deck can be distinguished: open profiles and re-entrant trough profiles. Both are shown in Fig. 4.13. Some of the profiles have a central stiffening rib, therefore forcing the stud to be welded off-centre within the trough of the sheeting. In later research, it was found that off-centre welding can have a weakening effect on the shear resistance of the stud connectors depending on the direction of the shear flow, as shown in Fig. 4.14. Similarly, the position of more than one stud per trough, either longitudinal, transverse or diagonal, was also found to have an effect on the shear resistance of the studs, as shown in Fig. 4.15.

Although both Codes have managed to make minor adaptions to eq. (4.7) to take account of the weakening effect on the shear strength for stud configurations as in Fig. 4.14, they completely ignore the influence of stud configurations as in Fig. 4.15.

Several recent publications on tests and analyses of Push-Out tests of studs in slabs with metal decking, describe a completely different failure mode for these studs. The use of a reduction to the strength of studs in solid slabs does therefore no longer represent reality in slabs with metal decking since the failure modes in both types of slabs are completely different. Instead, a new expression ought to be derived for the shear strength of stud connectors in slabs with metal decking; an expression which depicts the failure mode of these studs. Although the study of studs in metal decking is not within the scope of this thesis, some attention was paid to recent research on this subject in order to characterise realistic load-slip

curves for studs embedded in composite slabs with the metal decking spanning perpendicular to the span of the beam.

Hawkins and Mitchell [71] observed in their 13 Push-Out tests on slabs with open metal decking with different height over width ratios, four different failure modes: stud shearing, stud pull out, rib shearing and rib punching. Rib shearing had also been reported in previous experiments by Robinson [72] and Fisher [73] on composite beams with composite slabs. Their tests showed that rib shearing failure was more critical for connections with large rib heights, but they did not develop any model to predict the geometric combinations that must be used to avoid rib failure.

Jayas and Hosain [74] investigated the influence of longitudinal spacing of the studs and of the rib geometry on the shear strength in beams as well as in Push-Out tests. Unlike Hawkins and Mitchell, they observed only pull-out failure in all their Push-Out specimens as well as in three of their four beam tests. The failure was characterised by the separation of the concrete slab from the studs, which remained attached to the beam flanges together with a series of concrete wedges, surrounding a row of studs in a rib. They proposed a failure model for their tests based on the pull-out strength of studs in concrete, given by equations [5] and [6] in Reference [74].

A recent test at the University of Warwick [75] of a beam with open Ribdeck 60 decking confirmed the rib shearing failure found by Robinson [72] and Fisher [73]. Although slips up to 18 mm were measured at one of the beam ends, the studs in the corresponding push-out tests had far less deformation capacity. This lack of correlation between beam and push-out specimens could be attributed to the narrow slab widths used in the push-out specimens [62].

Lungerhausen [76] measured both shear strength and deformation capacity of studs in a number of full-scale composite beam tests, with open metal decking where studs were welded through holes in the deck, unlike the through-deck welding technique as applied in the U.K. His results for strength and deformation capacity correlated very well with the results of a collection of 46 push-out tests from different sources, but with slab widths ranging from 1300 to 1500 mm, and with more favourable boundary conditions at the base of these slabs.

The stud deformations found in these push-out tests were similar to the ones found in Johnson's beam test [75]: an S-shaped deformation of the

stud as shown in Fig. 4.16. Lungerhausen obtains a load-slip curve which is quite different from the ones found from other push-out tests or from some direct measurements on composite beam tests. He explains the origin of the two peak values, Q_1 and Q_2 in Fig. 4.17 copied from Fig. 1.4 of Reference [76] and obtained from Push-Out tests. The first peak value, Q_1, is characterised by failure of a concrete wedge between the stud and the rib and the formation of two plastic hinges in the shank. The second peak value, Q_2, is reached when either a conical concrete failure under the stud head takes place or when the studs pull out in tension just above the weld collar. The shear strength of these studs is therefore defined as being the first peak, Q_1, which is calculated by eq. (4.8).

$$Q = \frac{\beta}{\sqrt{N}} \frac{2M_{sh}}{x_{md} d_{sh}} \tag{4.8}$$

with β = 1 for open profiles
= 1.1 for re-entrant profiles;
N = number of studs per trough;
$M_{sh} = \frac{f_u d_{sh}^3}{6}$;
and $x_{md} = 0.8 \left(\frac{h_{md}}{b}\right)^2 + 0.6$
with b as indicated on Fig. 4.13

The results of these different investigators show clearly that more than one stud-rib failure mode can occur in beams, depending on the geometry of the deck, the size of the studs and the detailing of the welding of studs to top flange. It is therefore imperative to characterise and model these different failure modes, just like for studs in solid slabs, and to find a push-out test that will give results which reflect the behaviour in a real beam.

Just as for studs in solid slabs, the load-slip curves will be characterised by their **elastic stiffness**, their **ultimate shear strength** and corresponding **ultimate slip** and their maximum slip or **slip capacity**.

The ultimate shear strength The current draft Codes [3] [4] give values for the ultimate shear strength which are unsafe in comparison with the maximum shear values as measured by Mottram and Johnson [62] and Jayas and Hosain [74] or in comparison with the first peak values Q_1,as measured by Lungerhausen [76], for decking with high b_{md}/h_{md} ratios (> 2). This is demonstrated in Table 4.4

where the ratios of the measured ultimate shear to the calculated ultimate shear are smaller than 1. This same table also indicates over-conservative design rules for decking with low b_{md}/h_{md} ratios (< 1), as the shear ratios for such decking is always much larger than 1.

From the above description of observations by different investigators, it becomes obvious that the ultimate shear strength will be a function of the failure mode, which in turn will be a function of the decking geometry, the stud positions and the material strength of concrete, studs and deck.

With a multitude of different deck geometries presently on the market and new ones being launched, many more tests need to be done in order to establish not only the main parameters which determine the different failure mechanisms, but also to model these mechanisms.

The elastic stiffness For the limited number of different profiles studied, the elastic stiffness of the studs is fairly similar to the stiffness of the same studs in solid slabs. Fig. 4.18 compares the half-dimensionless load-slip curves from Mottram and Johnson's [62] and Jayas and Hosain's [74] push-out tests of studs in composite slabs with the ones obtained by Menzies, Buttry and Oehlers of studs in solid slabs.

For all these curves the slip ranges between 0.3 and 0.5 mm for a working shear load $Q/Q_u = 0.5$, with the exception of Oehlers' load-slip curve.

The ultimate slip and slip capacity Since the importance of the slip capacity of studs was only recently recognised only the more recent experiments record the slip behaviour after peak load of the studs in push-out tests.

The type of decking, as well as the stud configuration within the profiled deck, seem to have an influence on both the ultimate slip, γ_u, and the slip capacity of the studs, γ_f. For re-entrant profiles as Holorib and open profiles as Ribdeck 60 and 38 mm T-15 Hi bond deck in normal and inverted position, the average test values for γ_u and γ_f are recorded in Table 4.4 from push-out tests by Mottram and Johnson [62] and Jayas and Hosain [74]. Lungerhausen's beam results show much larger slip capacities up to 25 mm per stud for his open profiles with large h_{md}/b_{md} ratios, although no slip measurements were registered for the push-out tests recorded in his thesis.

From this limited study it seems therefore prudent to accept for design purposes the same limiting ultimate slip and slip capacity values as were accepted for studs in solid slabs, although for 19 mm or 22 mm diameter studs in open

profiles with high h_{md}/b_{md} ratios (> 2) or in the favourable side of Ribdeck 60, the slip capacity will increase to 15 mm or more.

4.2.3 Choice of load-slip curves for numerical 'experiments'

For the numerical simulation program an exponential curve, of the type given by eq. (4.9), was used to represent the load-slip relationship of the stud connector in both solid slabs and slabs with metal decking.

$$Q = Q_{as}\left(1 - e^{-\beta\gamma}\right)^{\zeta} \tag{4.9}$$

This curve is defined by two points and an asymptotic value Q_{as}, equal in this case to the design ultimate shear strength of stud connectors either in solid slabs or in composite slabs. The two points correspond with the load-slip values at half the ultimate strength and at 99% of the ultimate strength, as is shown in Fig. 4.19.

For studs embedded in solid slabs a total of five different exponential curves were used for the numerical 'experiments' in sections 4.3 and 4.4, although all curves had following characteristics in common:

- the asymptotic value equals the design ultimate shear load, Q_d, according to either Eurocode 4 or BS 5950:Pt.3.
- at $Q/Q_d = 0.50$, the slip measures between 0.3 and 0.5 mm
- at $Q/Q_d = 0.99$, the slip measures between 3 and 6 mm

For most 'experiments', two sets of exponents, β and ζ, were chosen, equal to 1000 m^{-1} and 0.558 and 1535 m^{-1} and 0.989 respectively. These exponents produce two curves both with elastic stiffness and ultimate slip within the shaded area of Fig. 4.12, but as close as possible to Menzies and Buttry's curves, so that they are also located within the band width around Buttry's average curve, which is much stiffer. In Fig. 4.20 the two exponential curves are compared with Menzies, Buttry's and Oehlers' load-slip curves.

For studs embedded in slabs with metal decking spanning perpendicular to the span, no reductions were made on the design ultimate strength of the stud connectors as it was judged not to be within the scope of this thesis to make an analysis of composite beams with different composite slabs. It was therefore

generally assumed that the reduction factor k, in eq. (4.7) would be larger than 1. For most profiled deck geometries with one stud per rib, this assumption will be right, but for transversely spaced studs in Holorib decking, the unreduced design strength would be closer to the ultimate shear strength, as measured by Mottram and Johnson [62].

Due to the limited data on experimental load slip curves of studs in composite slabs and the large variations between the data, the chosen exponential curves are given the same characteristics as the ones for studs in solid slabs, although these might be conservative sometimes.

4.2.4 Influence of load-slip curves on numerical results

The load-slip curve could also be regarded as a parameter in the study of parameters affecting the maximum slip in simply supported beams. Since the load-slip curve has realistic experimental limitations, it would have been premature to have added the curve as yet another parameter to the parametric study in section 4.1. Therefore this section provides a comparative study of the variation of the maximum slip reached in the numerical 'experiments' with the choice of experimental load-slip curves.

In Fig. 4.21 six different load-slip curves are drawn: some have the same elastic stiffness, but different values of the slip at 99% of their ultimate load, others have different elastic stiffness, but the same slip value at 99% of their ultimate load. All curves lie within the shaded area of Fig. 4.12.

Table 4.5 gives the geometry, the material properties and the design ultimate loading of two different beam specimens with only 50% shear interaction together with the different calculated values of the maximum slip $\gamma_m(50)$, in those beams for the six different load-slip curves presented in Fig. 4.21. The differences in maximum slip along each beam are either caused by the variation of the elastic stiffness in the load-slip curves, or by the variation of the slip at 99% of the ultimate load, since the shear strength of the studs remained unchanged throughout. Decreasing the elastic stiffness by a factor of two only resulted in a less than 5% increase of $\gamma_m(50)$ for both beams. Similarly, an increase in slip at 99% of the ultimate strength by a factor of two only resulted in a 10% increase of $\gamma_m(50)$. Both these increments are of the same order of magnitude as the slip increment due to the elimination of one stud along the shear span. This means that neither the change in elastic stiffness nor the changes in slip near the ultimate load have a significant influence on the numerical results of $\gamma_m(50)$, when chosen within the

experimental range.

A change in the value of the asymptotic ultimate shear strength will obviously have a much larger effect on $\gamma_m(50)$. The last row of values in Table 4.5 shows that increasing this asymptotic value from the design strength Q_d, to the characteristic strength Q_k, will reduce the maximum slip by more than 30%, for both beam specimens.

The decision to use design values of the ultimate shear for all the studs along the beams in the numerical 'experiments' in sections 4.3 and 4.4, could be regarded as being over-conservative on the grounds that not all connectors along the same shear span would have an inferior strength. The counter arguments are that some sources of weakness can be systematic in a given beam: weak concrete mix or bad through-deck welding. Together with a low degree of shear connection, such weaknesses require that a partial safety factor is used for the shear strength of all stud connectors.

4.3 Analyses of continuous composite beams

4.3.1 Interpretation of draft Eurocode 4

By following the method of clause 6.2.3.2 of Eurocode 4 (see Appendix I) to calculate the design ultimate load for continuous composite beams with partial shear connection, an apparent inconsistency is discovered in the analyses of Class 2 beams. Given a Class 2 continuous beam with 99% shear interaction, its design ultimate load would be $0.99w_p$, where w_p is the load found by plastic hinge theory. If that same beam were to have 100% interaction, it would have to be analysed elastically, having a design ultimate load far less than $0.99w_p$. This anomaly is due to an incorrect interpretation of Eurocode 4, which leads to errors and confusion.

It is therefore useful to give first a correct and consistent interpretation of the clauses of Eurocode 4 which influence the design of continuous composite beams.

For each composite beam, the Classes of the critical cross-sections and the corresponding design ultimate load for full shear connection ($N = N_f$) on each span are determined first. For simply-supported beams this load will always be calculated by plastic hinge analysis in accordance with clause 4.4.7, whether the critical cross-section is in Class 1 or 2. For continuous beams however, the load is calculated by plastic hinge analysis only when all critical cross-sections are

in Class 1. If one critical cross-section is in Class 2 then the ultimate load is calculated in accordance with clause 4.4.3.2 (1). The design ultimate load for the beam has to be in accordance with clause 4.4 and is therefore not related to the design ultimate loads, W_f and W_a (in the notation of Eurocode 4) mentioned in clause 6.2.3.2, which are always calculated by plastic hinge theory in order to determine the shear connection ratio N/N_f, needed to resist the longitudinal shear force. This means that for a continuous beam of Class 2, two sets of calculations are needed. The first is to find the design ultimate load for a beam with full shear connection, w_u, using elastic global analysis with redistribution, as in clause 4.4.3.2, and plastic moments of resistance for the cross-sections. The second is to find the plastic collapse load, w_p, for that beam with full shear connection, which is the corresponding value for Class 1 beams, using global plastic analysis. Obviously, w_u will be less than w_p. For the interpolation eq. (I.1) in Appendix I also the plastic collapse load w_{pa}, for the steel girder alone is required.

In practice, the designer replaces w_{pp}^i in eq. (I.1) by the known load, w_d, for which the beam was being designed and calculates N/N_f from eq. (4.10).

$$\frac{N}{N_f} = \frac{w_d - w_{pa}}{w_p - w_{pa}} \tag{4.10}$$

Even when $w_d = w_u$, this equation gives $N/N_f < 1$, because $w_u < w_p$. This seems reasonable, because N_f connectors in the shear span are only needed to resist the higher load, w_p, obtained by plastic hinge analysis.

Table 4.6 shows that these methods can give strange results for continuous composite beams made up with certain Universal Beam sections, where a small increase in reinforcement ratio ρ_r, at the internal support can move a beam from Class 1 into Class 2. This table give data for beams in Fe 510 steel, with cross-section geometry given on p. 198 of Reference [77], but with different ratios of l_1/l_2 and w_{u1}/w_{u2}, where w_{u2} is the uniform distributed load on the second span l_2, and also with different values of ρ_r. In this table, w_{us} represents the load for which the plastic moment of resistance M_p, is reached at midspan, M_{max} defines the maximum sagging moment along the beam and M'_{max} defines the maximum hogging moment.

The first column gives data for a Class 1 beam with two equal spans of 17.5 m each, both subject to the same uniform distributed load w_p. The full interaction design ultimate load is 57.4 kN/m on both spans.

Increasing the reinforcement ratio ρ_r, from 0.22% to 0.23% moves the beam

into Class 2 (column (2)) and reduces its design ultimate load to $w_{u1} = 41.5$ kN/m. The design load is governed by the moment of resistance at the internal support. At midspan, the ratio M_{max}/M_p is only 0.64, therefore the ratio F_{max}/F_p will be smaller than 0.70, thus giving a reserve in strength to the beam - both in shear and bending - of over 30%. For this beam w_{u1} exceeds only slightly $w_{pa} = 38.1$ kN/m. For $w_d = w_{u1}$, eq. (4.10) gives a connector ratio equal to only 0.175, yet in a design in accordance with Eurocode 4 a minimal connector ratio of 0.5 would be provided to resist the design load.

The other columns in Table 4.6 produce results for other l_1/l_2 and w_{u1}/w_{u2} ratios and a higher value of ρ_r (column (8)). For all beams with $w_{u1}/w_{u2} \leq 2$, the design load is governed by the moment of resistance at the internal support and leads to higher reductions in N/N_f. Only columns (4) and (6) give beams with $w_{u1}/w_{u2} = 4$, which in comparison with the results of the beam in column (1), show reductions in w_{u1} of 3% and 4% and reductions in N/N_f of 8% and 11% respectively.

The beam examples in Table 4.6 show that the results from the design methods in Eurocode 4 are sensitive to the Class of the web, which cannot be determined with precision because of uncertainty over the effective area of slab reinforcement at the internal support.

These examples also demonstrate that for Class 2 beams these methods lead to low degrees of interaction for continuous, Class 2, two span beams with near to equal spans both subject to the same uniform distributed load. For these beams, partial interaction will occur even when the beam is used to its full flexural capacity, as determined by the global elastic analysis.

In order to avoid the double calculation of w_p, w_{pa} and w_u for Class 2 continuous composite beams, the connector ratio could be calculated using w_u and w_{ua} according to clause 4.4.3.2 (1) of Eurocode 4 instead of w_p and w_{pa}. Eq. (4.10) is then being replaced by eq. (4.11).

$$\frac{N}{N_f} = \frac{w_d - w_{ua}}{w_u - w_{ua}} \tag{4.11}$$

This is consistent with what one would expect: for $w_d = w_u$, $N = N_f$.

This method does not only reduce the number of calculations for Class 2

beams, but does also increase the connector ratio for these beams and thus over-designs the shear connection unless the longitudinal interface shear at the critical sections would also be calculated elastically, when the section remains elastic.

For simply-supported beams or continuous Class 1 beams, partial interaction design is often applicable when either metal decking or pre-fabricated slabs are used, so that there is only limited space on the top flange to weld the stud connectors. According to Reference [19], it is sometimes even more economical to save on connectors and take larger Universal Beam Sections than to place the full number of connectors.

4.3.2 Numerical 'experiments' on 15 continuous beams

In the analysis of two span continuous beams, two different moment envelope types can be distinguished due to different span ratios and different loading conditions on these spans. The first type, given in Fig. 4.22 is the most common one, since it exists for all continuous composite two span beams with constant cross-section, which carry equal loads on both spans and which have a span ratio not exceeding 8:1.

The second type of moment envelope, represented in Fig. 4.23, could only exist when the continuous composite beams have unequal spans and the shorter span carries a smaller live load so that the second span remains constantly in hogging bending. In these beams the shortest span has only one shear span. This means that a beam with only 0.5% reinforcement in say a 3.0 m $\times$0.130 m composite slab with PMF46, theoretically only needs eight 19 mm diameter shear studs in the shorter span to resist the longitudinal shear, regardless of the length of this span. This number of studs will be increased to fulfill a minimum requirement on the longitudinal spacing between studs, a requirement needed to prevent uplift of the composite slab.

From an economic perspective, it is very unlikely to have span ratios l_1/l_2 larger than 4, without reducing the cross-section of the beam over the shorter span, unless this span is very short ($l < 3$ m say) and it would become more economical to run the same beam through without splicing a smaller beam on to it.

A comparison of theoretical shear flow diagrams with their corresponding stud distributions according to the draft Eurocode 4, as shown in Fig. 4.24 for continuous composite beams, indicates that uniform distributed loads are more onerous for the slip distribution, since the outer studs will tend to carry a higher

shear load and thus undergo more deformation. Since the shear flow diagrams in Fig. 4.24 are only theoretically correct for beams with full interaction, a number of the beams numerically analysed will carry point loads as well as distributed loads to verify the conclusions drawn from the theoretical shear flow diagrams. It would be quite pointless to examine the behaviour of beams under point loads only, since such a loading condition would never occur in practice.

In Table 4.7 the numerical values of the maximum slip at 50% shear interaction $\gamma_m(50)$, are recorded for a number of two span continuous beams, together with the geometry and the material properties of these beam. These beams are named CB and are numbered according to span. The notation used for the dimensions of the cross-section is in accordance with the notation in Fig. 4.1. The stud diameter and length after welding are given as $d_{sh} \times h_{st}$ and the notation for the loads, the load positions and the stud spacing is in accordance with the notation used in Figs. 4.22 and 4.23. The ultimate sagging and hogging moment before and after redistribution are given as M_u and M_r and M'_u and M'_r respectively. A comparison is made of the maximum slip along beams with different equal and unequal spans, different moment envelopes and different loading conditions. In this table the longer of the two spans never falls below 10 m. This limitation was introduced as Class 1 or 2 beams with spans less than 10 m will generally be unpropped during construction, therefore reducing the interface shear at ultimate load and consequently decreasing the maximum slip. Another reason for this limitation originates from the parametric study in section 4.1 where the maximum slip was found to be proportional to l/h_t, therefore reducing the chances of stud failure in shorter beams.

From this Table 4.7, the following conclusions were drawn:

The maximum slip is far less in beams with a moment envelope type 1, as given by Fig. 4.22, than it is in beams with a moment envelope type 2, where only the minimal number of studs are placed in the second span, mainly to prevent separation between slab and steel beam (compare CB3 and CB4).

The maximum slip reached along a continuous beam with a constant uniform distributed load is always larger than the maximum slip along a beam with a combination of uniform distributed load and point load, regardless of the position of the point load on the first span (compare CB11, CB12 and CB13). Figs. 4.25(a) to (d) compare moment, deflection, longitudinal shear force and slip distributions along beams CB11 and CB12 and Figs. 4.26(a)

to (d) compare moment, deflection, longitudinal shear and slip distributions along beams CB11 and CB13.

The maximum slip is an increasing function of the span (compare CB2 and CB6) and of the yield strength of the structural steel (compare CB6 and CB7) for continuous beams, as was predicted by the parametric study on simply supported beams.

Before studying the slip in continuous composite beams any further, the values of maximum slip reached in these beams are compared with the slip values registered in corresponding simply supported beams with the same cross-section and with a span equal to the longer of the two spans. This comparison is made to determine which type of beam (continuous or simply supported) will give more onerous slip distributions. Only that type will be studied further to provide data for a possible design rule to limit the slip.

4.3.3 Comparison of maximum slip in continuous and simply supported beams

In Table 4.8, the design ultimate loads and the corresponding maximum slip results at 50% shear interaction are given for simply supported beams with identical spans, cross-sections and material properties as for the largest span of the corresponding continuous beams in Table 4.7. In Table 4.8, x_{m1} defines the length of each shear span, $x_{s1} = x_{s2}$ represents the spacing in between the studs along the beam and y_p defines the position of the plastic neutral axes beneath the top of the slab. These beams are named SB.CB and are numbered the same way as in Table 4.7.

A comparison of matching pairs leads to the following conclusions:

For moment envelope type 1, the maximum slip is larger along the corresponding simply supported beams than it is along the continuous beams, regardless of the the loading type applied to the beams. Figs. 4.27(a) to (e) show a comparison of moment, deflection, longitudinal shear force, slip and compressive strain distributions in the slab for both CB1 and CB-SB1.

For moment envelope type 2, the maximum slip in the corresponding simply supported beam is smaller than the slip in the continuous beam. Figs. 4.28(a) to (d) show a comparison of M, δ, F and γ-distribution for both CB10 and CB-SB10. Although it would seem logical that a designer would

continue the calculated stud spacing for the longer span, also over the shorter one, technically speaking, the stud spacing can be reduced over this short span to a maximum limit, thus causing excessive slip in the longer shear span next to the internal support.

Since moment envelopes of type 2 are very unlikely to occur in practice and since for moment envelopes of type 1, the slip developed in the matched simply supported beams is larger than the slip developed in the continuous beams for all other loading conditions, only simply supported beams will be studied further.

This choice has the additional advantage of simplifying the numerical analyses, since continuous beams take between five times and ten times as much CPU time to analyse.

4.4 Analyses of simply supported beams

4.4.1 Existing design approaches

For simply supported composite beams both the **equilibrium** and the **interpolation** methods, as given in Appendix I, will be used to produce the design values which are fed into the simulation part of the program.

The draft Eurocode 4 [3] allows both methods, therefore the **interpolation method**, defined by eq. (I.1), will be used to determine the design ultimate load, w^i_{pp}, for different connector ratios, N/N_f. Since the **equilibrium** method has not yet replaced the **interpolation** method in the more recent BS 5950:Pt. 3.1 [4], the simplicity of the latter method, its long time use and the fact that it was based on experimental findings, rather than on certain theoretical assumptions, makes it a safer starting point than the **equilibrium** method.

It is obvious that the difference in design ultimate loads w^i_{pp} and w^e_{pp}, produced by these different methods, will vary for different beams and for different degrees of shear connection of that beam, a subject which will be discussed more in depth in section 4.6.

Presently, having established the failure criterion for both structural materials in section 3.1 and for the stud connectors in section 4.2.3, further limitations should be placed on the design method in clause 6.2.3.2 of Eurocode 4 to prevent premature stud shear failure, a failure mode which was not fully explored for the derivation of this clause, as demonstrated in Chapter 2. Either the design ultimate load could be reduced for certain beams, which would otherwise develop

too much slip, or the number of stud connectors could be increased for these beams.

In order to retain as much of the existing design rule as possible, the latter approach has been chosen. This is unlike the approach adopted in a preliminary report where three continuous beams were numerically analysed for increasing load factor, $\lambda = w^i_{pp}/w_p$, under a constant 50% degree of shear connection in the longest and more heavily loaded span, assuming a slip capacity of 5 mm. This approach requires several load factors for each degree of shear connection, depending on the different slip capacity limits, which results in several analyses for each degree of shear connection for each beam. The chosen approach however, only requires several slip limits for each degree of shear connection, which results only in one analysis for each beam.

A comparison of the theoretical shear flow diagrams for uniform distributed (u.d.) loading and point loading, with a uniform stud spacing between critical sections, shows that under u.d. loading the outer studs will be more heavily loaded and therefore undergo most deformation.

A similar conclusion is drawn from a comparison of the global ultimate load carried by identical beams: under u.d. loading this global load equals $8M_p/l$ and under a point load this load equal $4M_p/l$; one is twice as much as the other. Moreover, u.d. loading is a more common form of loading in design practice, therefore all analyses on simply supported beams were performed under u.d. loading only.

4.4.2 Numerical 'experiments' on 110 beams

In total about 110 simply supported beams were analysed in as much as the partial interaction ratio N/N_f, was increased for each beam in steps of 0.1 or more, from 0.5 to 1.0 or some lesser number, depending on the slip distribution for that ratio.

In a pre-processing part of the program, called Block I in Fig. 3.5 , all beams were realistically designed before entering Block II, which contains the number crunching physical simulation, explained in section 3.2.

In Block I, the **design ultimate load** is calculated for each N/N_f ratio, according to eq. (I.1) and the corresponding **stresses** and **maximum deflections** under service loads are checked, using a reduced stiffness for the composite beam, which takes account of the amount of partial interaction. The formulae for the stiffness was taken from p. 62 in Reference [79]. Although this approach differs

from the ones proposed in the Codes of Practice, the deflection results are similar.

In this same block the design imposed load was checked to be less than a given value — normally 5 + 1 kN/m^2 or 7.5 kN/m^2 — and the dead load to live load ratio was checked to be less than 1.0 and preferably less than 0.5. Neither of these routines will stop the analysis, they will only flash a warning if live load or dead to live load ratios become excessive.

The load-slip curves used in these analyses were chosen in accordance with the type of slab, as described in section 4.2.3 of this chapter.

In order to obtain realistic beams, the main geometric and material parameters were chosen within the following ranges:

f_{ck} – from 20 N/mm^2 to 40 N/mm^2

f_y – 252, 275, or 355 N/mm^2
(though all the results given in this section are for 355 N/mm^2 as the slip is then greater)

l/h_t – from 18 to 26

$t_c + t_h$ – from 120 mm to 180 mm

The parametric study in section 4.1.3.3 has identified about four dimensionless groups, which seem to influence the maximum slip in simply supported beams most, plus one dimensionless geometric property group, which indirectly influences γ_m:

$$\frac{l}{h_t}, \frac{w_p - w_{pa}}{w_{pa}}, \frac{F_c}{F_a}, \frac{y_p}{t_c + t_h}, and \frac{A_w}{A_f}$$

It is possible to divide all beams into one of the following categories:

(i) hot rolled sections with solid slabs

(ii) hot rolled sections with metal decking spanning perpendicular to the beam

(iii) welded I-girders with solid slabs

(iv) welded I-girders with metal decking spanning perpendicular to the beam

By dividing all the analysed beams into one of these four categories, the fifth dimensionless group can be eliminated (A_3/A_1), and two others give similar information (F_c/F_a and $y_p/t_c + t_h$), thus leaving only three parameters:

$$\frac{l}{h_t}, \frac{w_p - w_{pa}}{w_{pa}}, \text{ and } \frac{F_c}{F_a}$$

For all simply supported beams with uniform distributed loads, the diameter and consequently the spacing of the stud connectors has hardly any influence on the results produced by the numerical simulation for a certain load level and connector ratio. The only influence is due to the introduction of truncation errors in the calculation of the integer number of connectors. Although the use of continuous shear transfer along the beam is one of the basic assumptions in the solution of the mathematical model, this transfer happens only after the calculation of an integer number of studs N, and the spacing of the studs, x_s. With $N = F_p/Q_d$, $x_s = l/2N$, and $Q = Q_d\left(1 - e^{-\beta\gamma}\right)^{\zeta}$ the shear increment between elements along the beam is given by:

$$\Delta F = \frac{Q}{x_s} = \frac{2F_p}{l}\left(1 - e^{-\beta\gamma}\right)^{\zeta} \tag{4.12}$$

The results obtained by this simulation are therefore valid for any type of ductile connector. This gives a more general interpretation to the results although the truncation error might become quite large for beams with short shear spans and large diameter studs.

4.4.2.1 Hot rolled sections with solid concrete slab

Partial shear connection **might** occur in beams with precast concrete slab elements, as omnia deck shown in Fig. 4.29, where *in situ* concrete is cast only to provide the shear connection with the steel beam and to make the different slab panels work as one continuous slab.

In total, 45 such simply supported beams were analysed. Geometric and material details for these beams are given in Table IV.1 of Appendix IV, together with the design values for the ultimate interface shear F_p, the position of the plastic neutral axes beneath the top of the slab y_p, the plastic collapse load of the composite beam w_p, and the plastic collapse load for the steel girder,w_{pa}. This table also produces for each beam computed values of the maximum slip for different degrees of partial shear connection.

The beams are numbered according to the span length.

Since the parametric study indicated that the span is definitely the major parameter in determining the maximum slip along a beam, the most onerous results from Table IV.1 are shown in Fig. 4.30. This figure gives different relationships between the connector ratio and the span for different values of mean slip capacity as defined in section 4.2.3: with each slip capacity limit and each span corresponds a minimal connector ratio, N/N_f, below which premature shear stud

failure might occur before w_{pp}^{i} is reached.

4.4.2.2 Hot rolled sections with slabs with metal decking perpendicular to the span

Partial shear interaction will mostly occur in beams with composite slabs, where the metal decking runs perpendicular to the span, as the number of studs that can be placed along such a beam is limited by the shape of the profile and the width of the top flange, as shown in Fig. 4.31.

In total, 28 such beams were analysed by the physical simulation program. Geometric and material details for these beams are given in Table IV.2 of Appendix IV, together with the design values F_p, y_p, w_p, w_{pa} and with the computed values of the maximum slip for different degrees of partial shear connection.

The beams are numbered according to the span length.

Fig. 4.32 gives different relationships between the connector ratio and the span for different values of the mean slip capacity as defined in section 4.2.3, for any type of decking based on the most onerous beam specimens from Table IV.2.

For beams where the plastic neutral axis falls within the slab or just within the steel flange, the maximum slip reached along the beam is hardly any different from the maximum slip in an identical beam with a solid slab, with slab thickness t_c, equal to the total thickness $t_c + t_h$, of the composite slab. This is demonstrated in Fig. 4.33 by comparing the slip distributions along beams SRM-25 and SRM-30 from Table IV.2 with the slip distributions along nearly identical beams, with solid slabs with overall slab thickness equal to $t_c + t_h$ instead of the composite slabs. For both beams SRM-25 the plastic neutral axis remains in the concrete slab ($F_p^{met.deck}/F_p^{solidslab} = 1$) and the ratio of $\gamma_m^{met.deck}$ to $\gamma_m^{solidslab}$ is about 1 for both 50% and 75% interaction, while for both beams SRM-30 where the neutral axis reaches the steel top flange for the beam with the composite slab ($F_p^{met.deck}/F_p^{solidslab} = 0.87$) this ratio becomes around 1.2 for both 50% and 75% interaction. Only for beams where the plastic neutral axes lie within the web of the steel profile, as is the case for the beam with composite slab SRM-29 ($F_p^{met.deck}/F_p^{solidslab} = 0.55$) the difference in γ_m between solid slab and composite slab becomes considerable as demonstrated in Fig. 4.34: the ratio $\gamma_m^{met.deck}$ to $\gamma_m^{solidslab}$ reaches 1.9 for 50% interaction and 3.0 for 75% interaction.

It could be argued that since most beams studied have a plastic neutral axis within the top steel flange, the difference in γ_m-values between composite and solid slabs is really not large enough to make a distinction in the formulation

of a design rule. However, both categories could not be made into one categoty for rolled sections if future work on load-slip behaviour of studs in metal decking confirms Lungerhausen's [76] and Johnson's [75] experimental findings of much larger slip capacities of studs in different types of decking as compared to studs in solid slabs and enables to categorize the decking.

4.4.2.3 Beams with welded steel profiles and solid concrete slabs

In total, 30 beams with unequal flanges ($A_3 > A_1$) were analysed using the physical simulation model. Geometric and material details for these beams are given in Table IV.3 of Appendix IV, together with the design values F_p, y_p, w_p and w_{pa} and with the computed values of γ_m for different degrees of partial shear connection.

The beams are numbered according to the span length.

Fig. 4.35 gives different relationships between the connector ratio and the span for different values of the mean slip capacity as defined in section 4.2.3, based on the most onerous beam specimens from Table IV.3.

The minimal connector ratio limits obtained for welded beams are more onerous for the same span and slip capacity than for rolled sections, with either solid or composite slabs. The welded sections with $A_3 \geq 1.5A_1$, form another separate category of beam section.

4.5 Prediction equation for the maximum slip

Knowing the main dimensionless parameters which determine the maximum slip along a simply supported beam from section 4.1.3.3, it becomes possible to produce enough computer results for a certain connector ratio, to obtain a general formula for γ_m as a function of these parameters, as indicated by eq. (4.13):

$$\gamma_m(x) = f\left(\frac{l}{h_t}, \frac{w_p - w_{pa}}{w_{pa}}, \frac{F_c}{F_a}\right) \tag{4.13}$$

$$50 \leq x = 100 \times \frac{N}{N_f} \leq 100$$

In order to make this expression completely dimensionless, the value of maximum slip at a certain degree of shear connection x, has to be divided by $\gamma_m(0)$, the value of maximum slip along the beam at zero percent interaction which is

analytically calculated by eq. (4.14):

$$\gamma_m(0) = \frac{M_{pa} h_a l}{6 E_a I_a} \tag{4.14}$$

Dividing eq. (4.13) by eq. (4.14) gives eq. (4.15):

$$\frac{\gamma_m(x)}{\gamma_m(0)} = g\left(\frac{l}{h_t}, \frac{w_p - w_{pa}}{w_{pa}}, \frac{F_c}{F_a}\right) \tag{4.15}$$

Mathematically, this problem can either by solved by an exponential or by a polynomial regression analysis. In the latter case, polynomials of different degrees could be produced to fit the data. Since in the earlier parametric study no indication of higher order functions were visible, the polynomials were limited to the second degree only.

As the principle behind the analysis is the same for all beam categories, the regression was limited to the data from the first category only: hot rolled sections with solid concrete slabs. In Table 4.9, the values of l/h_t, $(w_p - w_{pa})/w_{pa}$, etc... which are used for the basis of both regression analyses are given for 45 beams. Some of the results for very short beams ($l \leq 7.5$ m) were eliminated as they gave rather large errors on γ_m due to rounding off the number of connectors to an integer number. For some of these short beams where the number of connectors in a shear span can be as small as 8, this value can be obtained by rounding off say $F_p/Q_d = 7.1$ to 8, therefore introducing an error of $\frac{0.9 \times 100}{7.1} = 13\%$.

4.5.1 Exponential curve-fitting for γ_m along hot rolled sections with solid concrete slab

The general exponential expression used to fit the data, is given by eq. (4.16):

$$\frac{\gamma_m(x)}{\gamma_m(0)} = \left(\frac{l}{h_t}\right)^{\alpha} \left(\frac{w_p - w_{pa}}{w_{pa}}\right)^{\beta} \left(\frac{F_c}{F_a}\right)^{\zeta} \tag{4.16}$$

A multiple linear regression analysis was performed by taking the logarithm of both sides, thus transforming eq. (4.16) into eq. (4.17) and this for all 45 data points:

$$\log\left(\frac{\gamma_m(x)}{\gamma_m(0)}\right)_i = \alpha \log\left(\frac{l}{h_t}\right)_i + \beta \log\left(\frac{w_p - w_{pa}}{w_{pa}}\right)_i + \zeta \log\left(\frac{F_c}{F_a}\right)_i \tag{4.17}$$

$\forall i$, $i = 1$ to 45

$$
\begin{aligned}
y_i &= \log\left(\frac{\gamma_m(x)}{\gamma_m(0)}\right)_i \\
x_{1i} &= \log\left(\frac{l}{h_t}\right)_i \\
x_{2i} &= \log\left(\frac{w_p - w_{pa}}{w_{pa}}\right)_i \\
x_{3i} &= \log\left(\frac{F_c}{F_a}\right)_i
\end{aligned}
$$

After solving this system, the coefficients were substituted back into eq. (4.16).

Alternatively, two other exponential expressions, given by eqs. (4.18) and (4.19) were also used to fit the data, using the same linear multiple regression analysis method.

$$\frac{\gamma_m(x)}{\gamma_m(0)} = \left(\frac{l}{h_t}\right)^{\alpha}\left(\frac{w_p - w_{pa}}{w_{pa}}\right)^{\beta}\left(\frac{y_p}{t_c}\right)^{\zeta} \tag{4.18}$$

$$\frac{\gamma_m(x)}{\gamma_m(0)} = \left(\frac{l}{h_t}\right)^{\alpha}\left(\frac{w_p - w_{pa}}{w_{pa}}\right)^{\beta}\left(\frac{F_c}{F_a}\right)^{\zeta}\left(\frac{y_p}{t_c}\right)^{\eta} \tag{4.19}$$

In order to assess the influence of the three different dimensionless parameters on the accuracy of the prediction, three or four separate regression analyses were performed for each equation, with successively only one, two and eventually three and/or four parameters. For each regression, the coefficient of multiple determination, r^2, and the coefficient of variation, CV, were calculated so that an assessment could be made of the quality of the curve-fitting and of the size of the error.[1]

The results of these different regressions are given in Table 4.10 for a degree

[1]The sample coefficient of multiple determination r^2, gives an indication about the strength of the relationship between the y_i and x_i values.
r^2 is defined by

$$r^2 = 1 - \frac{SSD \times nt}{SST \times (nt - ni)}$$

with SSD = the Sum of Squares of the Deviations about the regression

$$= \sum_{i=1}^{nt}\left(y_i - x_{1i}^{\alpha}x_{2i}^{\beta}x_{3i}^{\zeta}\right)^2$$

SST = the Sum of Squares of the Deviations from the mean for the dependent variable

$$= \sum_{i=1}^{nt}(y_i - \overline{y})^2$$

of shear connection of 50% and in Table 4.11 for a degree of shear connection of 75%.

Comparison between results of the different exponential equations shows that the parameters F_c/F_a and y_p/t_c are inter-changeable, with hardly any changes in r^2 or CV. A two-parameter expression for $\gamma_m(x)/\gamma_m(0)$, as a function of l/h_t and $w_p - w_{pa}/w_{pa}$, is still very good with a standard error of estimate only marginally larger than for the three parameter exponential expression and a maximum percent relative error still smaller than 10% for both degrees of shear connection. Yet, a one-parameter expression has a coefficient of variation larger than 24% and a maximum percent relative error larger than 50%. This explains the scatter of γ_m-values for a constant span in Figs. 4.30, 4.32 and 4.35, where minimal connector ratios are given for different span lengths as a function of different slip capacity limits.

4.5.2 Polynomial curve-fitting for γ_m along hot rolled section with solid concrete slabs

Although in most cases a polynomial fit is more accurate than any other function, for this set of data the polynomial fit has the same r^2 and CV characteristics as the exponential fit.

Two types of polynomials were fitted: one without a constant term and one with a constant term. Both polynomials were restricted to the second order terms only.

---

and $\overline{y} = \frac{1}{nt}\sum_{i=1}^{nt} y_i$

nt = number of sample points

ni = number of independent variables

The Coefficient of Variation CV, measures the amount of variability relative to the size of the variable being measured.

CV is defined by:

$$CV = \frac{S_{yx}}{\overline{y}}$$

with S_{yx} = the standard error of estimate or standard deviation
= of the y_i values around the line of estimate

$$= \sqrt{\frac{\sum_{i=1}^{nt}\left(y_i - x_{1i}^{\alpha} x_{2i}^{\beta} x_{3i}^{\zeta}\right)^2}{(nt - ni)}}$$

4.5.2.1 Second order polynomial without constant

The general second order polynomial expression, which fits the 45 data points of the maximum slip at 50 and 75 percent shear connection, is given by eq. (4.20):

$$y(x) = a_1x_1 + a_2x_1^2 + a_3x_2 + a_4x_2^2 + a_5x_1x_2 + a_6x_3 + a_7x_3^2 + a_8x_1x_3 + a_9x_2x_3 \quad (4.20)$$

$$\begin{aligned} \text{with } y(x) &= \frac{\gamma_m(x)}{\gamma_m(0)} \\ x_1 &= \frac{l}{h_t} \\ x_2 &= \frac{w_p - w_{pa}}{w_{pa}} \\ x_3 &= \frac{F_c}{F_a} \\ \text{and with } x &\quad \text{either} \quad 50\% \text{ or } 75\% \end{aligned}$$

A linear multiple regression analysis was performed by rewriting eq. (4.20) as a linear system of 45 equations where the 9 unknowns and 10 variables are given by eq. (4.21).
$\forall i$, $i = 1$ to 45

$$\begin{aligned} x_{1i} &= x_1 \\ x_{2i} &= x_i^2 \\ x_{3i} &= x_2 \\ x_{4i} &= x_2^2 \\ x_{5i} &= x_1x_2 \\ x_{6i} &= x_3 \\ x_{7i} &= x_3^2 \\ x_{8i} &= x_1x_3 \\ x_{9i} &= x_2x_3 \\ y_i &= y(x) \end{aligned} \quad (4.21)$$

In order to assess the influence of the three different dimensionless parameters on the regression characteristics, three separate polynomial regressions were performed with successively the first two, the first five and all nine terms of eq. (4.20). For 50% and 75% shear connection the results are shown in Tables 4.12 to 4.13 respectively. They show that most coefficients change remarkably when more terms are added, although the accuracy of the regression does not increase sharply when the number of terms increases from five to nine.

4.5.2.2 Second order Polynomial with constant term

The second order polynomial expression with a constant term, which fits the 45 data points of maximum slip at 50 and 75 percent shear connection, is given by eq. (4.22).

$$\begin{aligned} y(x) &= a_1 + a_2x_1 + a_3x_1^2 + a_4x_2 + a_5x_2^2 + a_6x_1x_2 \\ &\quad + a_7x_3 + a_8x_3^2 + a_9x_1x_3 + a_{10}x_2x_3 \end{aligned} \tag{4.22}$$

$$\begin{aligned} \text{with } y(x) &= \frac{\gamma_m(x)}{\gamma_m(0)} \\ x_1 &= \frac{l}{h_t} \\ x_2 &= \frac{w_p - w_{pa}}{w_{pa}} \\ x_3 &= \frac{F_c}{F_a} \end{aligned}$$

Similarly, a linear multiple regression analysis was performed by rewriting eq. (4.22) as a linear system of 45 equations in 10 unknowns.

In order to assess the influence of the three dimensionless parameters on the dimensionless polynomial expression, three separate regression analyses were performed with successively the first three, the first six and finally all ten terms of eq. (4.22). The coefficients of these separate regressions are again given in Tables 4.14 to 4.15 for 50% and 75% interaction respectively. Just as for the polynomial regression without a constant term, most coefficients change remarkably when terms are added to the polynomial.

By replacing x_3 in eq. (4.22) by y_p/t_c, all regression coefficients change, but the overall fit characterised by r^2 and CV remains the same, which indicates that these parameters are inter-changeable.

4.5.3 Proposal of expression for γ_m for beams with 50% and 75% shear connection

Since the exponential expression has the same coefficient of multiple determination, the same coefficient of variation and is a much simpler expression to use, the exponential expression is preferred above the polynomial one.

Since there is hardly any improvement in either of the regression characteristics nor in the percent relative error by adding F_c/F_a or y_p/t_c as a third parameter

to the expression for γ_m, the maximum slip will be written only as a function of l/h_t, $(w_p - w_{pa})/w_{pa}$ and $\gamma_m(0)$.

For hot rolled steel girders with solid concrete slabs and a 50% degree of shear connection, the following prediction equation for the maximum slip is suggested:

$$\gamma_m(50) = \gamma_m(0)\left(\frac{l}{h_t}\right)^{-0.13}\left(\frac{w_p - w_{pa}}{w_{pa}}\right)^{1.03} \tag{4.23}$$

$$\text{with } \gamma_m(0) = \frac{M_{pa} l h_a}{6 E_a I_a}$$
$$\text{and } w_{pa} = \frac{8 M_{pa}}{l^2}$$

For hot rolled steel girders with full concrete slabs and a 75% degree of shear connection, the following expression for maximum slip is suggested:

$$\gamma_m(75) = \gamma_m(0)\left(\frac{l}{h_t}\right)^{-0.24}\left(\frac{w_p - w_{pa}}{w_{pa}}\right)^{1.70} \tag{4.24}$$

with $\gamma_m(0)$ and w_{pa} as defined above.

4.6 Systematic influence of steel Grade and connector strength on the maximum slip along simply supported beams

In all previous analyses, steel of Grade 50 has been used, since high Grade steel gives worse results for the slip distribution along a beam and a designer is only interested in a lower bound for the connector ratio for a certain span. As in practice more Grade 43 than Grade 50 steel is used, it would be interesting to establish whether there is any relationship between the maximum slip results along beams with Grade 50 and Grade 43 steel profiles.

Similarly, design values for the shear strength were used in all previous analyses, thus assuming that all stud connectors in a beam will either have some defect or will be badly embedded within the concrete. Although these situations may occur in practice, in most cases the workmanship is good and studs could sustain their full characteristic shear load.

Again, it would be interesting to establish whether there is any relationship

between the slip results of identical beams where only the shear strength of the studs differ in value and the tangential stiffnesses at the origin are nearly the same as those shown in Fig. 4.36.

If such relationships exist for either or both parameters, then the question arises whether the previously drawn conclusive graphs could not be scaled down for different values of the above-mentioned parameters.

4.6.1 Influence of structural steel Grade on γ_m

In Table 4.16 a number of beams with the same geometry and the same material properties (except for the yield strength) as certain beams of Table 4.18 have been analysed, using the two different design methods from the draft Eurocode 4 and the **equilibrium** design approach of the draft BS 5950:Pt.3. The design ultimate loads produced by the **interpolation method** (ECI) and the **equilibrium method** (ECE) of Eurocode 4 and their corresponding values of maximum slip, are compared for different connector ratios and for the last two beams in this table the comparison is extended to the **equilibrium** method (BSE) of BS 5950:Pt.3.

The ratio of the maximum slip for Grade 50 steel to the maximum slip for Grade 43 steel increases nearly linearly with the connector ratio.

In Figs. 4.37 and 4.38, the relationship between the design ultimate load (w_{pp}), the connector ratio (N/N_f) and the maximum slip (γ_m) for steel Grades 50 and 43 has been compared for beams SEBC 8 and SEBC 17 of Table 4.16 respectively. For both beams, the $N/N_f - \gamma_m$ relationship has undergone nearly a pure translation by reducing the steel Grade from 50 to 43: the slip reduces by a nearly constant value for all N/N_f ratios, yet different for the two beams. Having only analysed four different beams, this reduction seems close to $355\Delta\gamma_m(0)/275$ when the yield strength drops from 355 N/mm^2 to 275 N/mm^2, regardless of the method of analysis.

In the absence of a proper analysis for the different beam categories for Grade 43 steel, a tentative reduction of $355\Delta\gamma_m(0)/275$ would give some estimate for the maximum slip for composite beams with Grade 43 steel sections and different degrees of shear connection.

4.6.2 Influence of the stud shear strength on the slip distribution

Table 4.17 gives the maximum slip at different connector ratios for different beams using the characteristic shear strength for all shear connectors instead of the design shear strength. All the beams used in this table are identical to the corresponding beams in Table 4.19, apart from the stud shear strength. Since the difference between design strength and characteristic strength is larger in Eurocode 4 for the most commonly used 19 and 22 mm diameter studs than it is in BS 5950:Pt.3, two sets of maximum slip values are given for each beam: one for design according to the equilibrium method in Eurocode 4 (ECE) and one for design according to the equilibrium method in BS 5950:Pt.3 (BSE).

Comparisons of the γ_m-values in both tables show that for each connector ratio, the slip difference is nearly constant. This means graphically that the $N/N_f - \gamma_m$ relationships become two parallel curves as is shown for beams EBC 2 and EBC 8 in Figs. 4.39 and 4.40 respectively. The distance between these lines is obviously a function of the different shear strengths.

Although the shear strength increases by different amounts for the different Code approaches, the values for γ_m hardly differ for different connector ratios.

From the few examples it seems that for a connector ratio of 0.5, $\Delta\gamma_m$ could be written as $(Q_k - Q_d)\gamma_m(50)/Q_d$, with $\gamma_m(50)$, the maximum slip corresponding with the design shear strength.

To obtain a better expression for $\Delta\gamma_m$, independent of the connector ratio, more results are needed. Yet, these few analyses already indicate very clearly that under good conditions, where every stud along the beam can reach its ultimate value, excessive slips no longer occur. Only for larger span beams ($l > 15$ m), with low connector ratios, where the longitudinal interface shear force F_p, is limited by the force in the slab due to the orientation of the metal decking, slips will still become excessive.

4.7 Comparison between interpolation and equilibrium methods

Thusfar, in the analyses of continuous and simply supported composite beams in sections 4.3 to 4.5, the **interpolation** method has been used to determine the relationship between the number of shear connectors N, and the reduced design

ultimate load, w^i_{pp}.

The draft Eurocode 4 also allows the designer to use the **equilibrium** method, which is less conservative and which allows the same beam to carry a higher load for the same connector ratio, as shown in Fig. I.2 of Appendix I.

Also in the draft BS 5950:Pt.3 both methods of analyses can be applied to all beams of uniform cross section in their sagging region and with spans less than 16 m. The ultimate load produced by the equilibrium method is on average 10 to 15 percent higher than the load produced by the interpolation method for beams with connector ratios of 0.5 and less. Although the interface slip along the beam is an increasing function of the load onto the beam, the nature of this function at ultimate load levels is not exactly known. The question could be posed whether the beam will be able to sustain the increase of slip which coincides with the increase of load or whether premature stud shear failure might occur.

One has to look not only at the difference between the two methods in the Eurocode 4, but also at the difference between the results obtained with the equilibrium method in both Eurocode 4 and BS 5950:Pt.3. In the latter Code, different changes have been made to the design values for material strength and geometry, which affect not only w^e_{pp}, but also M_p and F_p and in addition the minimum connector ratio has been reduced from 0.5 to 0.4.

4.7.1 Comparison of the two methods in Eurocode 4

In Table 4.18 the design ultimate loads and the maximum interface slip values for identical beams are compared for different connector ratios, using the two design methods for partial interaction described in clause 6.2.3.2 of Eurocode 4.

From this table an average ratio for $(\gamma^e_m/\gamma^i_m)/(w^e_{pp}/w^i_{pp})$ of about 1.5 is obtained, with an average error of about 10%. Similarly, Fig. 4.41 shows that the relationship of the proportional increase of slip, $(\gamma^e_m - \gamma^i_m)/\gamma^i_m$, against the proportional increase of load, $(w^e_{pp} - w^i_{pp})/w^i_{pp}$, for varying connnector moduli, is more or less a straight line. Although the samples in Fig. 4.41 were randomly chosen from Table 4.18, they all have a slope at the origin which varies between 5.0 and 10.0 with an average of 7.0.

The same table provides the data for Figs 4.37, 4.42 and 4.38 where the relationships between w_{pp} and N/N_f and N/N_f and γ_m are presented for beams SEBC 8, 13 and 17 respectively. These figures show an almost exponential increase in γ_m for a linearly decreasing number of connectors with their corresponding decreasing design ultimate load, w_{pp}, calculated either according to the interpolation

method or to the equilibrium method.

A comparison between the two methods is made for the moment, the longitudinal force and the slip distributions along beams SEBC 6 and SEBC 16 in Figs. 4.43 and 4.44 respectively.

Using the **interpolation** method, the slip along the 10 m long beam SEBC 6 will not exceed the 7.5 mm mean slip capacity limit of the most commonly used 19 mm diameter stud connectors.

Using the **equilibrium** method, this same beam will fail in shear over a length of 2.0 m on either end of the beam under 50% shear connection, thus shearing off seven 19 mm diameter stud connectors on either side. Even at 62.5% shear connection the 7.5 mm slip limit is just reached at either end.

Using the **interpolation** method, the slip along the 20 m long beam SEBC 16 will reach the 8.5 mm slip capacity limit of the 22 mm diameter studs only for 50% shear connection. This same beam will need a degree of shear connection of at least 75% or more to sustain the increased loads, produced by the **equilibrium** method for partial interaction design . For 50% shear connection the slip will exceed the 8.5 mm slip capacity over a length of 6 m on either end of the beam, thus shearing off sixteen 22 mm diameter studs at these locations.

This stark difference in *minimum interaction limits* for the two methods needs to be emphasized to the designer in the formulation of any design method.

4.7.2 Comparison of equilibrium method in Eurocode 4 and BS 5950:Pt.3.

Although the span-interaction limitations in the method in clause 4.5.2 of draft BS 5950:Pt.3:Section 3.1 were partly based on the conclusions of an earlier report [80], in this report the **interpolation method** was used to determine the design ultimate loads w^i_{pp}, of the beams. Since the draft BS 5950:Pt.3 allows the use of the **equilibrium method** with these limitations, the current clause might become unsafe under certain conditions. The design values in BS 5950:Pt.3 which affect the plastic moment of resistance and the number of stud connectors per shear span differ in a number of places from the design values in Eurocode 4: the slab has a reduced effective width when the beam is continuous; the design ultimate strength of 19 and 22 mm diameter studs are smaller in solid slabs and the minimum shear connector ratio is reduced from 0.5 to 0.4.

In order to estimate the influence of these differences on the slip behaviour

along the beam, Table 4.19 shows a comparison between the results obtained by using both methods for ten different beams of spans 10, 15 and 20 m.

For some beams, the maximum slip γ_m, is marginally larger, when using the design values of BS 5950:Pt.3., for others, γ_m becomes larger when using the design values in Eurocode 4.

Figs. 4.45 to 4.46 give the moment distribution, shear force distribution and slip distribution for two sets of beams from Table 4.19 using the design values of BS 5950:Pt.3. Fig. 4.45 represents beam EBC 3 = SEBC 6 and the results can be compared to the corresponding distributions in Fig. 4.43 for the equilibrium design method in Eurocode 4. Such a comparison shows that the moment and the shear force are lower for the same connector ratio although the maximum slip is higher than with design values from to BS 5950:Pt.3.

Fig. 4.46 represents beam EBC 10 = SEBC 16. A similar comparison with the distributions produced for the design to Eurocode 4 in Fig. 4.44 demonstrates that the differences between the equilibrium methods in both Codes are only marginal.

More important than these marginal differences between the results is their similarity: for beam EBC 10 the maximum slip is excessive at 50% shear interaction and could cause the outer studs to shear off, regardless of the set of design values used. The slip distributions along both beams show that for 37.5% interaction the slip becomes even more excessive over more than half of the total span, therefore overloading more than half of the shear connectors. For the studied beams with 40% shear connection, designed in accordance with BS 5950:Pt.3, the slip at the beam ends ranges from 12 mm to 20 mm for spans ranging from 10 m to 20 m respectively. Although BS 5950:Pt.3 increases the minimum connector ratio for beams with spans larger than 10 m, stud shear failure could still occur along beams of span 10 m and slightly above, when designed in accordance with this Code. For the same beams with 50% shear connection, designed in accordance with Eurocode 4, the slip at the beam ends ranges from 10 mm to 18 mm for spans ranging from 7.5 m to 20 m respectively, which will certainly cause stud shear failure in beams with solid slabs.

4.7.3 Conclusions on the use of the equilibrium method

Undoubtedly the **equilibrium** method has a sounder mathematical basis than the empirical **interpolation** method and will in time replace this method altogether. Yet, for beams with solid concrete slabs, where the slip capacity limits

are fairly accurately known, severe limitations will be needed on the connector ratio to prevent premature stud shear failure.

In the absence of a more rigorous analysis which produces a regression curve predicting the maximum slip, the equations (4.23) and (4.24) can be adapted for the **equilibrium** method, by multiplying the right hand side of the equation by 1.6. Thus, for hot rolled sections with solid concrete slab, an average value for γ_m at 50% and 75% interaction can be given by equations (4.25) and (4.26):

$$\gamma_m(50) = 1.6\,\gamma_m(0)\left(\frac{l}{h_t}\right)^{-0.13}\left(\frac{w_p - w_{pa}}{w_{pa}}\right)^{1.03} \tag{4.25}$$

$$\gamma_m(75) = 1.6\,\gamma_m(0)\left(\frac{l}{h_t}\right)^{-0.24}\left(\frac{w_p - w_{pa}}{w_{pa}}\right)^{1.70} \tag{4.26}$$

These expressions give only crude averages and do not have the same accurate regression characteristics as the original equations (4.23) and (4.24), since 1.6 is only an average multiplication factor.

In the absence of similar expressions for the other beam categories, only lower connector ratio limits can be given for different spans and different stud diameters. From Tables IV.1, IV.2 and IV.3, the values of γ_m for different connector ratios are scaled up and superimposed onto the Figs. 4.30, 4.32 and 4.35 for the different beam categories. Lines of equal slip, equal to mean different slip capacity limits for different diameter studs, define minimal connector ratio limits as functions of the span, to prevent premature stud shear failure, when using the **equilibrium** method.

Since there exists only a marginal difference between the slip results obtained by the Eurocode 4 or the BS 5950:Pt.3 **equilibrium** methods, no distinction

Table 4.1: Geometry and material properties of beams B1 and B2, used in the parameter study of γ_e and γ_p.

		Beam specimen	
		$B1$	$B2$
l	(m)	17.5	12.5
f_{ay}	(N/mm^2)	355.	355.
ρ_r	(%)	0.32	0.20
Q_d	(kN)	as in EC 4	as in EC 4
γ_1 at $Q/Q_d = 0.50$		1.9	1.9
γ_2 at $Q/Q_d = 0.99$		6.2	6.2
$d_{sh} \times h_{st}$	(mm)	19 × 95	19 × 95
$b_1 - t_1$	(mm)	686 × 254	150 – 12.5
$b_2 - t_2$	(mm)	UB140	8.8 – 429.8
$b_3 - t_3$	(mm)		150 – 12.5
A_a	(mm^2)	17860	7500

Table 4.2(a): Results of maximum elastic and plastic slip along Beam 1 in Table 4.1 for varying geometric and material parameters.

	f_{ck}	b_c	t_c	t_h	$\frac{A_2}{A_1}$	$\frac{A_w}{A_f}$	$\frac{h_w}{t_w}$	$\frac{l}{h_t}$	w^i_{pp}	γ_e	γ_p	Comparison type as in main test							$\frac{y_p}{t_c+t_h}$	$\frac{F_p}{w^i_{pp}}$
												G					M			
	(N/mm^2)	(m)	(m)	(m)	$(-)$	$(-)$	$(-)$	$(-)$	(kN/m)	(mm)	(mm)	i	ii	iii	iv	v	i	ii		(m^{-1})
$B1-1$	20	4.00	0.180	–	1.0	0.81	51.9	20.3	57.99	2.939	6.569	•					•		0.78	109.5
$B1-2$	30	"	"	"	"	"	"	"	58.89	3.625	7.303	•					•		0.52	107.7
$B1-3$	40	"	"	"	"	"	"	"	60.85	3.978	8.153	•	•	•			•	•	0.39	104.2
$B1-4$	20	3.00	0.150	–	1.0	0.81	51.9	21.0	53.88	3.330	6.949	•						•	1.05	94.7
$B1-5$	30	"	"	"	"	"	"	"	56.18	3.572	6.198	•							0.83	112.9
$B1-6$	40	"	"	"	"	"	"	"	57.43	3.757	6.717	•							0.62	110.4
$B1-7$	20	2.00	0.120	–	1.0	0.81	51.9	21.8	50.59	4.830	10.050	•							1.35	53.8
$B1-8$	30	"	"	"	"	"	"	"	51.95	4.493	7.742	•							1.10	78.5
$B1-9$	40	"	"	"	"	"	"	"	53.17	3.854	6.305	•					•	•	1.04	102.3
$B1-10$	"	4.00	0.180	–	"	"	60.0	19.2	64.32	3.951	7.868		•						0.39	98.6
$B1-11$	"	"	"	"	"	"	40.0	22.4	55.08	4.023	8.726		•		•				0.39	115.1
$B1-12^1$	"	"	"	"	"	0.72	43.6	21.9	56.18	3.998	8.516		•		•					
$B1-13^2$	"	"	"	"	"	0.34	34.4	28.2	44.62	4.006	9.387		•		•					
$B1-14$	"	"	"	"	1.5	0.81	51.9	20.3	63.25	4.178	8.941			•					0.39	100.3
$B1-15$	"	"	"	"	2.0	"	"	"	64.82	4.313	9.699			•					0.39	97.8
$B1-16$	"	"	"	"	1.0	"	"	"	"	–	10.530			•					–	–

Table 4.2(b): continued ...

	f_{ck} (N/mm^2)	b_c (m)	t_c (m)	t_h (m)	$\frac{A_3}{A_1}$ $(-)$	$\frac{A_w}{A_f}$ $(-)$	$\frac{h_w}{t_w}$ $(-)$	$\frac{l}{h_t}$ $(-)$	w^i_{pp} (kN/m)	γ_e (mm)	γ_p (mm)	Comparison type as in main test							$\frac{y_p}{t_c+t_h}$	$\frac{F_p}{w^i_{pp}}$ (m^{-1})
												G					M			
												i	ii	iii	iv	v	i	ii		
$B1-17$	"	"	"	"	1.5	"	"	"	"	–	9.687			•					–	–
$B1-18$	40	4.00	0.180	–	1.0	0.51	51.9	22.4	56.27	3.946	8.308				•				0.39	112.6
$B1-19$	"	"	"	"	"	1.11	"	19.2	63.47	4.017	8.508				•				0.39	99.9
$B1-20$	"	2.00	0.120	–	1.0	0.51	"	24.2	48.61	3.225	6.455				•				1.04	111.9
$B1-21$	"	"	"	"	"	1.11	"	20.5	55.80	3.322	5.929				•				1.04	97.5
$B1-22$	40	4.00	0.180	–	"	1.45	40	20.3	58.89	–	9.134				•					
$B1-23$[3]	"	"	"	"	"	0.81	"	21.8	38.94	3.103	4.545							•	0.82	114.7
$B1-24$[3]	"	4.00	0.180	–	1.0	"	"	20.3	43.88	3.682	6.556							•	0.27	101.8
$B1-25$[3]	20	3.00	0.150	–	"	"	"	21.0	40.04	2.725	4.540							•	0.88	111.5
$B1-26$	30	"	"	"	"	"	"	"	58.89	3.745	7.157	•							0.83	107.7
$B1-27$	40	4.00	0.180	–	"	"	"	"	55.08	–	7.341		•		•					
$B1-28$	40	4.00	0.180	–	"	0.51	51.9	22.4	55.08	–	7.551		•		•					
$B1-29$	40	4.00	0.180	–	"	1.11	"	19.2	56.27	–	5.922				•					
$B1-30$[4]	40	4.00	0.180	–	"	"	"	20.3	60.85	–	7.581						•		0.39	104.2
$B1-31$[4]	"	2.00	0.120	–	"	"	"	21.8	53.17	–	5.689						•		1.04	102.3
$B1-32$	20	"	0.084	0.036	"	"	"	"	49.59	–	12.130					•			2.12	38.4
$B1-33$	"	3.00	0.120	0.030	"	"	"	21.0	53.55	–	9.170					•			1.08	76.2
$B1-34$	"	4.00	0.140	0.040	"	"	"	20.3	57.99	–	6.612					•			0.78	109.5

[1] section 610x229 UB140 with $A_a = 178.4\ cm^2$
[2] section HEA 450 with $A_a = 178.0\ cm^2$
[3] $f_{ay} = 250\ N/mm^2$
[4] $f_{ay} = 3.3\ N/mm^2$

Table 4.3(a): Results of maximum elastic and plastic slip along Beam 2 in Table 4.1 for varying geometric and material parameters.

	f_{ck} (N/mm^2)	b_c (m)	t_c (m)	$\frac{A_3}{A_1}$	$\frac{A_w}{A_f}$	$\frac{h_w}{t_w}$	$\frac{l}{h_t}$	w^i_{pp} (kN/m)	γ_e (mm)	γ_p (mm)	Comparison type as in main test							$\frac{y_p}{t_c+t_h}$	$\frac{F_p}{w^i_{pp}}$ (m^{-1})
											G					M			
											i	ii	iii	iv	v	i	ii		
$B2-1$	40	4.00	0.120		1.0	48.57	23	33.10	3.687	6.335	•							0.32	80.4
$B2-2$	"	"	0.150		"	"	22	35.10	3.615	7.327	•		•					0.25	75.9
$B2-3$	"	"	0.180		"	"	20	37.16	3.441	8.415	•	•	•	•		•	•	0.21	71.6
$B2-4$	"	3.00	0.120		"	"	23	33.05	3.705	6.296	•						•	0.33	80.6
$B2-5$	"	"	0.150		"	"	22	35.07	3.709	7.287	•			•		•		0.26	75.9
$B2-6$	"	"	0.180		"	"	20	37.10	3.614	8.374	•							0.22	71.8
$B2-7$	"	2.00	0.120		"	"	23	32.38	3.649	5.841	•			•		•		0.49	82.2
$B2-8$	"	"	0.150		"	"	22	34.41	3.748	6.767	•							0.39	77.4
$B2-9$	"	"	0.180		"	"	20	36.43	3.756	7.793	•					•	•	0.33	73.1
$B2-10$	30	"	0.120		"	"	23	31.71	3.395	5.423		•			•	•		0.65	83.9
$B2-11$	20	"	"		"	"	"	30.42	2.710	4.854		•		•	•	•		0.98	87.9
$B2-12$	30	3.00	0.150		"	"	22	34.62	3.282	6.976		•		•		•		0.35	76.9
$B2-13$	20	"	"		"	"	"	33.75	2.712	6.429		•		•		•		0.52	78.9
$B2-14$	30	4.00	0.180		"	"	20	36.71	2.813	8.198			•			•		0.22	72.5
$B2-15$	20	"	"		"	"	"	35.88	2.385	7.505			•			•		0.33	74.2
$B2-16$	40	"	"	1.0	"	30.00	23.1	31.74	3.290	9.662		•	•					0.21	83.0

Table 4.3(b): continued ...

	f_{ck} (N/mm^2)	b_c (m)	t_c (m)	$\frac{A_3}{A_1}$	$\frac{A_w}{A_f}$	$\frac{h_w}{t_w}$	$\frac{l}{h_t}$	w^i_{pp} (kN/m)	γ_e (mm)	γ_p (mm)	Comparison type as in main test							$\frac{y_p}{t_c+t_h}$	$\frac{F_p}{w^i_{pp}}$ (m^{-1})
											G					M			
											i	ii	iii	iv	v	i	ii		
$B2-17$	40	4.00	0.180	1.0	1.0	55.00	18.9	38.73	3.470	7.965		•	•	•				0.21	68.00
$B2-18$	"	"	"	"	0.5	48.57	22.4	33.67	3.278	8.435				•				0.21	79.00
$B2-19$	"	3.00	0.150	"	"	"	23.7	31.60	3.613	7.343				•				0.26	84.00
$B2-20$	"	2.00	0.120	"	"	"	25.1	28.91	3.594	6.294				•				0.49	92.00
$B2-21$	"	4.00	0.180	2.0	1.0	"	19.7	40.01	3.156	9.218			•					0.21	66.00
$B2-22$	"	"	"	1.5	"	"	"	39.18	3.092	8.695			•					0.21	68.00
$B2-23$	20	2.00	0.084	1.0	"	"	21.7	30.46	–	7.242					•		•	1.14	62.00
$B2-24$	30	"	"	"	"	"	"	31.89	–	5.635					•		•	0.65	82.00
$B2-25$	40	4.00	0.180	2.0	0.5	"	22.6	36.10	–	9.609			•	•			•	0.21	73.00
$B2-26$	"	"	"	"	"	30.00	26.1	30.99	–	11.830	•							0.21	85.00
$B2-27$	"	"	"	1.0	"	"	"	29.41	–	11.120		•							
$B2-28$	"	"	"	"	"	72.90	19.7	37.16	–	6.531		•							

Table 4.4: Measured and calculated ultimate shear strength of studs in composite slabs with different deck geometry.

Ref.	Test specimen	f_c or f^*_{cu}	Q_u^{test}	b_{md}	h_{md}	Q_u^{EC}	Q_u^{BS}	$\frac{Q_u^{test}}{Q_u^{EC}}$	$\frac{Q_u^{test}}{Q_u^{BS}}$	γ_u	γ_f
		(N/mm^2)	(kN)	(mm)	(mm)	(kN)	(kN)	$(-)$	$(-)$	(mm)	(mm)
Table 4.1 [76]	1 to 9	27.4	55.5	127	60	99.2	101.8	0.56	0.55	–	–
	10 to 19	36.5	107.0	114	51	133.0	139.0	0.80	0.77	–	–
	21	31.1	78.5	175	106	57.8	61.2	1.35	1.28	–	–
	22 to 25	22.6	96.0	175	106	122.0	111.0	0.79	0.87	–	–
	26	19.6	67.5	175	106	84.8	75.1	0.80	0.90	–	–
	29 to 32	25.1	85.0	155.5	125	42.0	42.1	2.03	2.02	–	–
	35	26.8	37.0	75	106	24.8	25.2	1.49	1.47	–	–
	42 to 46	28.8	35.0	80	125	21.6	22.4	1.62	1.56	–	–
[62]	$H25-1$	24.1*	92.9	115.5	51	96.4	94.1	0.96	0.98	3.38	5.85
	$H30-1$	34.5*	100.9	115.5	51	96.4	103.6	1.05	0.97	3.00	4.85
	$H30L-1$	35.1*	96.4	115.5	51	96.4	93.7	1.00	1.03	3.83	5.85
	$H40-1$	41.5*	107.1	115.5	51	96.4	110.5	1.11	0.97	2.05	5.25
	$H30-2-50$	32.4*	71.4	115.5	51	107.6	101.9	0.66	0.70	3.57	4.85
	$H30-2-76$	35.0*	77.7	115.5	51	107.6	104.0	0.72	0.75	4.35	5.88
	$R30-1-F$	32.6*	113.4	86	60	73.9	70.2	1.53	1.61	2.18	7.52
	$R30-1-U$	31.6*	73.2	76	60	65.6	61.8	1.12	1.18	4.4	8.16
	$R30-2-S$	35.6*	75.0	86	60	76.4	73.8	0.98	1.02	2.6	6.13
[74]	$JDT-1$	26.6	41.1	60.7	38	60.8	72.0	0.68	0.57	2.2	4.0
	$JDT-3$	26.6	37.4	60.7	38	60.8	72.0	0.62	0.52	2.4	4.0
	$JDT-5$	34.5	44.8	60.7	38	60.8	79.2	0.74	0.57	2.1	3.5
	$JDT-2$	34.5	44.8	60.7	38	60.8	79.2	0.74	0.57	2.1	3.5
	$JDT-2$	26.6	58.6	91.8	38	63.3	75.0	0.93	0.78	2.5	5.0
	$JDT-4$	26.6	54.8	91.8	38	63.3	75.0	0.87	0.73	3.0	4.8
	$JDT-6$	34.5	62.95	91.8	38	63.3	82.5	0.99	0.76	3.4	4.5

Table 4.5: Geometry, material properties and design values for beams B1 and B2 used in the study of the influence of the load-slip curve on the maximum slip.

		Beam specimen	
		$B1$	$B2$
l	(m)	10.0	20.0
b_c	(m)	3.00	3.00
t_c	(m)	0.075	0.085
t_h	(m)	0.065	0.060
		356 x 171UB51	762 x 267UB147
f_{ck}	(N/mm^2)	25.0	40.0
f_{ay}	(N/mm^2)	355.0	355.0
w_{pp}^i	(kN/m)	39.39	49.42
Q_d	(kN)	77.5	88.0
Curve type as in Fig. 4.21		$\gamma_m(50)(mm)$	
1		5.15	7.56
2		5.37	7.63
3		5.54	7.75
4		5.64	7.83
5		5.77	7.94
6		6.02	8.12
Q_u	(kN)	116.2	110
Curve type as in Fig. 4.21		$\gamma_m(50)(mm)$	
2		3.72	5.79

Table 4.6: Examples of design calculations to draft Eurocode 4

		Beam geometry as on p.198 of Ref. [77]							
		(1)	(2)	(3)	(4)	(5)	(6)	(7)	(8)
l_1	(m)	17.50	17.50	17.50	17.50	17.50	17.50	17.50	17.50
l_1/l_2	$(-)$	1.00	1.00	1.00	1.50	1.50	1.15	1.15	1.00
Class		1	2	2	2	2	2	2	2
w_{u1}/w_{u2}	$(-)$	1.00*	1.00	2.00	4.00	1.00	4.00	1.00	1.00
w_u	(kN/m)	57.41*	41.51	54.98	55.75	52.96	55.28	46.51	47.11
m	$(-)$	15.00	15.00	15.00	15.00	15.00	15.00	15.00	15.00
ρ_r	$(\%)$	0.22	0.23	0.23	0.23	0.23	0.23	0.23	0.70
w_{us}	(kN/m)	57.41	64.47	58.14	55.75	58.80	55.28	61.48	64.44
M_{max}/M_p		1.00	0.639	0.945	1.00	0.901	1.00	0.756	0.731
M'_{max}/M'_p		1.00	1.00	1.00	0.871	1.00	0.835	1.00	1.00
$(N/N_f)_{w_d=w_{u1}}$		1.00	0.175	0.874	0.914	0.769	0.889	0.435	0.426

* $w_{u1} = w_p$ for this beam

Table 4.7(a): Values of $\gamma_m(50)$ obtained with EPPIB for different two-span continuous composite beams.

		$CB1$	$CB2$	$CB3$	$CB4$	$CB5$	$CB6$	$CB7$
l_1	(m)	10.0	15.0	15.0	15.0	18.0	20.0	20.0
l_2	(m)	10.0	15.0	15.0	15.0	18.0	20.0	20.0
BM-envelope as in Figs. 4.22 and 4.23		type 1	type 1	type 2	type 1	type 1	type 1	type 1
f_{ck}	(N/mm^2)	30.0	30.0	30.0	30.0	30.0	30.0	30.0
f_{ay}	(N/mm^2)	275.	252.	252.	252.	252.	252.	355.
b_e	(mm)	2500	2500	2500	2500	2500	2500	2500
$t_c(t_h)$	(mm)	84(46)	150	120	150	150	150	150
$b_1 - t_1$	(mm)	$150-12$	$200-15$	$250-15$	$250-15$	$250-15$	$250-15$	$250-15$
$b_2 - t_2$	(mm)	$10-280$	$11-575$	$11-675$	$11-675$	$11-675$	$11-675$	$11-675$
$b_3 - t_3$	(mm)	$175-15$	$250-20$	$300-20$	$300-20$	$300-20$	$300-20$	$300-20$
$d_{sh} \times h_{st}$	(mm)	19×95	19×95	19×95	19×95	19×95	19×95	19×95
w_{u1}	(kN/m)	40.90	59.19	63.25	80.16	29.18	45.18	61.87
P_{u1}	(kN)	–	–	237.2	–	262.6	–	–
x_1	(m)	–	–	10.0	–	8.0	–	–
w_{u2}	(kN/m)	40.90	59.19	9.48	80.16	29.18	45.18	61.87
x_{m1}	(m)	4.462	6.54	10.0	5.92	8.00	8.69	8.71
x_{m2}	(m)	4.462	6.54	0.0	5.92	6.02	8.69	8.71
x_{s1}	(mm)	372	297	417	237	333	335	242
x_{s2}	(mm)	396	326	192	336	357	377	275
x_{s3}	(mm)	396	326	480	336	357	377	275
x_{s4}	(mm)	372	297	480	237	333	335	242
$\gamma_m(50)$	(mm)	4.02	3.41	10.62	3.34	3.29	4.79	5.68
$(M_r' - M_u') \times 100/M_u'$	(%)	−38	−33	−12	−19	−21	−33	−32
$(M_r - M_u) \times 100/M_u$	(%)	29	25	3	11	9	24	24
ρ_r	(%)	0.29	0.48	0.33	0.48	0.43	0.48	0.48

Table 4.7(b): (continued ...)

		$CB8$	$CB9$	$CB10$	$CB11$	$CB12$	$CB13$	$CB14$	$CB15$
l_1	(m)	12.5	15.0	15.0	20.0	20.0	20.0	20.0	20.0
l_2	(m)	10.0	12.5	5.0	10.0	10.0	10.0	13.3	13.3
BM-envelope as in Figs. 4.22 and 4.23		type 1	type 1	type 2	type 1	type 1	type 1	type 2	type2
f_{ck}	(N/mm^2)	30.0	30.0	35.0	30.0	30.0	30.0	30.0	30.0
f_{ay}	(N/mm^2)	355.	355.	275.	252.	252.	252.	252.	252.
b_e	(mm)	3250	3250	3000	2500	2500	2500	2500	2500
$t_c(t_h)$	(mm)	115(35)	115(35)	145	150	150	150	150	150
$b_1 - t_1$	(mm)	140 – 13	135 – 13.5	150 – 12	200 – 14	200 – 14	250 – 14	250 – 15	250 – 15
$b_2 - t_2$	(mm)	8 – 310	12 – 375	10 – 325	11 – 600	11 – 600	11 – 600	11 – 675	11 – 675
$b_3 - t_3$	(mm)	230 – 18	220 – 18	225 – 15	250 – 18	250 – 18	250 – 18	300 – 20	300 – 20
$d_{sh} \times h_{st}$	(mm)	19 × 95	19 × 95	19 × 95	19 × 95	19 × 95	19 × 95	19 × 95	19 × 95
w_{u1}	(kN/m)	47.31	43.66	16.49	16.96	33.02	16.55	22.07	44.38
P_{u1}	(kN)	–	–	61.83	169.6	–	165.5	220.7	–
x_1	(m)	–	–	7.0	7.0	–	9.0	8.5	–
w_{u2}	(kN/m)	47.48	44.15	8.45	44.91	44.91	44.91	6.62	13.31
x_{m1}	(m)	5.51	6.61	7.00	7.0	8.71	9.0	8.50	8.75
x_{m2}	(m)	4.26	5.11	0.0	4.35	4.35	4.35	0.0	0.0
x_{s1}	(mm)	306	301	500	333	415	429	340	350
x_{s2}	(mm)	291	299	533	520	452	440	383	417
x_{s3}	(mm)	249	246	580	226	226	226	600	600
x_{s4}	(mm)	237	232	580	207	207	207	600	600
$\gamma_m(50)$	(mm)	6.77	7.61	6.24	2.86	5.13	3.67	6.31	7.23
$(M_r' - M_u') \times 100/M_u'$	(%)	−26	−26	−40	−25	−25	−23	−14	−13
$(M_r - M_u) \times 100/M_u$	(%)	15	15	19	8	13	10	5	4
ρ_r	(%)	0.65	0.65	0.16	0.48	0.48	0.48	0.43	0.22

Table 4.8: Values of $\gamma_m(50)$ obtained with EPPIB for simply supported beams with identical spans, cross-sections and material properties as for the largest span of the corresponding continuous beams in Table 4.7.

		CB-SB1	*CB-SB2*	*CB-SB3*	*CB-SB4*	*CB-SB5*	*CB-SB6* *CB-SB14* *CB-SB15*	*CB-SB7*	*CB-SB8*	*CB-SB9*	*CB-SB10*	*CB-SB11* *CB-SB12* *CB-SB13*
l_1	(m)	10.0	15.0	15.0	15.0	18.0	20.0	20.0	12.5	15.0	15.0	20.0
w_{u1}	(kN/m)	31.10	43.42	55.41	58.67	40.75	33.00	45.23	32.09	32.69	19.15	24.18
x_{m1}	(m)	5.0	7.5	7.5	7.5	9.0	10.0	10.0	6.25	7.5	7.5	10.0
$x_{s1} = x_{s2}$	(mm)	417	341	300	300	346	385	278	368	341	536	476
$\gamma_m(50)$	(mm)	5.07	4.30	3.15	3.55	4.44	5.95	6.23	8.19	9.06	7.40	5.72
y_p	(mm)	46.75	84.94	121.9	101.8	101.8	101.8	143.5	51.79	66.07	39.12	82.42

Table 4.9(a): Parametric values of 45 rolled sections with solid slabs used for the exponential and polynomial regression analyses.

Sample No.	$\frac{\gamma_m(50)}{\gamma_m(0)}$	$\frac{l}{h_t}$	$\frac{w_p - w_{pa}}{w_{pa}}$	$\frac{F_c}{F_a}$	$\frac{y_p}{t_c}$	$\frac{\gamma_m(75)}{\gamma_m(0)}$
1	0.6646	19.00	1.078	1.632	0.6216	0.4868
2	0.8162	19.00	1.171	1.599	0.4971	0.6737
3	0.7777	19.00	1.223	2.445	0.4146	0.6161
4	0.7818	19.00	1.256	2.852	0.3554	0.6232
5	0.8080	19.00	1.282	3.260	0.3109	0.6545
6	0.9548	14.50	1.349	1.867	0.5418	0.8735
7	0.9954	14.50	1.414	2.240	0.4152	0.9849
8	1.0873	14.50	1.465	2.614	0.3870	1.0690
9	0.5996	16.20	0.8573	1.436	0.6961	0.3973
10	0.6847	18.30	0.9950	2.287	0.4433	0.4827
11	0.7294	19.80	1.052	2.289	0.4428	0.5406
12	0.9324	19.90	1.335	4.241	0.2333	0.8635
13	0.7710	20.50	1.163	2.726	0.3628	0.6411
14	0.8066	20.50	1.202	3.272	0.3024	0.6894
15	0.6209	22.70	0.9254	1.489	0.4439	0.4439
16	0.8205	20.38	1.107	2.502	0.3333	0.5953
17	0.6074	17.60	0.8816	1.583	0.6382	0.3802
18	0.5533	17.90	0.8074	1.439	0.7020	0.3377
19	0.6289	20.79	0.9770	2.117	0.4724	0.4829
20	0.8904	21.69	1.218	3.347	0.2966	0.7430

Table 4.9(b): (continued ...)

Sample No.	$\frac{\gamma_m(50)}{\gamma_m(0)}$	$\frac{l}{h_t}$	$\frac{w_p - w_{pa}}{w_{pa}}$	$\frac{F_c}{F_a}$	$\frac{y_p}{t_c}$	$\frac{\gamma_m(75)}{\gamma_m(0)}$
21	0.6829	22.47	0.9982	1.890	0.5233	0.4827
22	0.7914	24.72	1.232	3.415	0.2569	0.7305
23	0.6872	25.05	1.026	2.271	0.4404	0.5058
24	0.4349	17.49	0.6684	1.062	0.8873	0.2699
25	0.5180	20.00	0.7524	1.381	0.7333	0.3115
26	0.5542	20.00	0.8261	1.842	0.4404	0.3813
27	0.7319	20.85	1.021	2.326	0.4242	0.5054
28	0.6919	21.14	0.9718	2.196	0.4491	0.4711
29	0.5519	22.60	0.8494	1.709	0.5704	0.3555
30	0.6370	25.10	0.9504	2.470	0.4047	0.4638
31	0.5725	25.30	0.8907	1.985	0.5036	0.4083
32	0.4464	19.69	0.6940	1.504	0.6615	0.2789
33	0.5311	20.89	0.7806	2.160	0.4689	0.3072
34	0.5138	20.89	0.7600	1.889	0.5359	0.2945
35	0.4857	20.76	0.7386	1.689	0.5990	0.2731
36	0.4691	20.99	0.6960	1.580	0.6329	0.2832
37	0.5494	22.24	0.8833	2.134	0.4762	0.3463
38	0.5979	22.24	0.8997	2.444	0.4079	0.4265
39	0.5438	26.38	0.7900	1.709	0.5704	0.3389
40	0.3905	19.04	0.6022	1.176	0.8502	0.2038
41	0.4457	20.19	0.6721	1.454	0.6979	0.2368
42	0.5192	22.13	0.7910	2.228	0.4551	0.2949
43	0.4482	23.99	0.7131	1.437	0.7101	0.2607
44	0.6397	25.25	0.9082	2.197	0.4586	0.4017
45	0.4918	26.25	0.7696	1.613	0.6348	0.2965

Table 4.10: Exponential curve fitting for the maximum slip at 50% interaction.

$$\frac{\gamma_m(50)}{\gamma_m(0)} = \left(\frac{l}{h_t}\right)^a \left(\frac{w_p - w_{pa}}{w_{pa}}\right)^b \left(\frac{F_c}{F_a}\right)^c$$

a (−)	b (−)	c (−)	N (−)	CV (%)	r^2 (−)
−0.151	–	–	45	24	0.05
−0.131	1.033	–	45	4.9	0.96
−0.139	1.001	0.031	45	5.0	0.96

$$\frac{\gamma_m(50)}{\gamma_m(0)} = \left(\frac{l}{h_t}\right)^a \left(\frac{w_p - w_{pa}}{w_{pa}}\right)^b \left(\frac{y_p}{t_c}\right)^c$$

a (−)	b (−)	c (−)	N (−)	CV (%)	r^2 (−)
−0.145	0.974	−0.054	45	4.95	0.96

$$\frac{\gamma_m(50)}{\gamma_m(0)} = \left(\frac{l}{h_t}\right)^a \left(\frac{w_p - w_{pa}}{w_{pa}}\right)^b \left(\frac{F_c}{F_a}\right)^c \left(\frac{y_p}{t_c}\right)^d$$

a (−)	b (−)	c (−)	d (−)	N (−)	CV (%)	r^2 (−)
−0.145	0.976	−0.077	−0.126	45	4.9	0.96

Table 4.11: Exponential curve fitting for the maximum slip at 75% interaction.

$$\frac{\gamma_m(75)}{\gamma_m(0)} = \left(\frac{l}{h_t}\right)^a \left(\frac{w_p - w_{pa}}{w_{pa}}\right)^b \left(\frac{F_c}{F_a}\right)^c$$

a (−)	b (−)	c (−)	N (−)	CV (%)	r^2 (−)
−0.270	–	–	45	42	0.03
−0.237	1.697	–	45	8.0	0.96
−0.242	1.675	0.021	45	8.1	0.97

$$\frac{\gamma_m(75)}{\gamma_m(0)} = \left(\frac{l}{h_t}\right)^a \left(\frac{w_p - w_{pa}}{w_{pa}}\right)^b \left(\frac{y_p}{t_c}\right)^c$$

a (−)	b (−)	c (−)	N (−)	CV (%)	r^2 (−)
−0.260	1.598	−0.090	45	7.9	0.97

$$\frac{\gamma_m(75)}{\gamma_m(0)} = \left(\frac{l}{h_t}\right)^a \left(\frac{w_p - w_{pa}}{w_{pa}}\right)^b \left(\frac{F_c}{F_a}\right)^c \left(\frac{y_p}{t_c}\right)^d$$

a (−)	b (−)	c (−)	d (−)	N (−)	CV (%)	r^2 (−)
−0.258	1.607	−0.271	−0.343	45	7.6	0.97

Table 4.12(a): Second order polynomial prediction equation for $\gamma_m(50)$, without constant term in function of l/h_t,$(w_p - w_{pa})/w_{pa}$ and F_c/F_a.

$$\frac{\gamma(50)}{\gamma(0)} = a_1 + a_2\left(\frac{l}{h_t}\right) + a_3\left(\frac{l}{h_t}\right)^2 + a_4\left(\frac{w_p - w_{pa}}{w_{pa}}\right) + a_5\left(\frac{w_p - w_{pa}}{w_{pa}}\right)^2 + a_6\left(\frac{w_p - w_{pa}}{w_{pa}}\right)\left(\frac{l}{h_t}\right) + a_7\left(\frac{F_c}{F_a}\right) + a_8\left(\frac{F_c}{F_a}\right)^2 + a_9\left(\frac{l}{h_t}\right)\left(\frac{F_c}{F_a}\right) + a_{10}\left(\frac{w_p - w_{pa}}{w_{pa}}\right)\left(\frac{F_c}{F_a}\right)$$

NT	a_1	a_2	a_3	a_4	a_5	a_6	a_7	a_8	a_9	a_{10}	CV (%)	r^2	$100 \times \frac{N}{N_f}$
45	2.8110	−0.1906	0.00409	–	–	–	–	–	–	–	22.4	0.239	
45	0.0976	−0.0197	0.00054	0.9408	−0.06274	−0.0061	–	–	–	–	5.11	0.963	50
45	0.2662	−0.0390	0.00095	0.8549	0.03210	−0.0022	0.0960	0.0173	−0.00156	−0.1181	5.3	0.965	

Table 4.12(b): Second order polynomial prediction equation for $\gamma_m(50)$, without constant term in function of l/h_t,$(w_p - w_{pa})/w_{pa}$ and y_p/t_c.

$$\frac{\gamma(50)}{\gamma(0)} = a_1 + a_2\left(\frac{l}{h_t}\right) + a_3\left(\frac{l}{h_t}\right)^2 + a_4\left(\frac{w_p - w_{pa}}{w_{pa}}\right) + a_5\left(\frac{w_p - w_{pa}}{w_{pa}}\right)^2 + a_6\left(\frac{w_p - w_{pa}}{w_{pa}}\right)\left(\frac{l}{h_t}\right) + a_7\left(\frac{y_p}{t_c}\right) + a_8\left(\frac{y_p}{t_c}\right)^2 + a_9\left(\frac{l}{h_t}\right)\left(\frac{y_p}{t_c}\right) + a_{10}\left(\frac{w_p - w_{pa}}{w_{pa}}\right)\left(\frac{y_p}{t_c}\right)$$

NT	a_1	a_2	a_3	a_4	a_5	a_6	a_7	a_8	a_9	a_{10}	CV (%)	r^2	$100 \times \frac{N}{N_f}$
45	−2.246	0.05546	0.0003329	3.273	−0.5684	−0.05253	2.307	−0.4488	−0.05026	−1.032	5.05	0.968	50

Table 4.13(a): Second order polynomial prediction equation for $\gamma_m(75)$, without constant term in function of l/h_t,$(w_p - w_{pa})/w_{pa}$ and F_c/F_a.

$$\frac{\gamma_m(75)}{\gamma_m(0)} = a_1 + a_2\left(\frac{l}{h_t}\right) + a_3\left(\frac{l}{h_t}\right)^2 + a_4\left(\frac{w_p - w_{pa}}{w_{pa}}\right) + a_5\left(\frac{w_p - w_{pa}}{w_{pa}}\right)^2 + a_6\left(\frac{w_p - w_{pa}}{w_{pa}}\right)\left(\frac{l}{h_t}\right)$$
$$+ a_7\left(\frac{F_c}{F_a}\right) + a_8\left(\frac{F_c}{F_a}\right)^2 + a_9\left(\frac{l}{h_t}\right)\left(\frac{F_c}{F_a}\right) + a_{10}\left(\frac{w_p - w_{pa}}{w_{pa}}\right)\left(\frac{F_c}{F_a}\right)$$

NT	a_1	a_2	a_3	a_4	a_5	a_6	a_7	a_8	a_9	a_{10}	$CV(\%)$	r^2	$100 \times \frac{N}{N_t}$
45	3.597	−0.2783	0.00605	–	–	–	–	–	–	–	36.7	0.290	
45	0.9255	−0.0666	0.00139	−0.3695	0.5340	0.0079	–	–	–	–	7.7	0.97	75
45	0.4255	−0.0344	0.00083	0.3503	0.5335	−0.0174	−0.1582	0.0309	0.00756	−0.1228	7.65	0.974	

Table 4.13(b): Second order polynomial prediction equation for $\gamma_m(75)$, without constant term in function of l/h_t,$(w_p - w_{pa})/w_{pa}$ and y_p/t_c.

$$\frac{\gamma_m(75)}{\gamma_m(0)} = a_1 + a_2\left(\frac{l}{h_t}\right) + a_3\left(\frac{l}{h_t}\right)^2 + a_4\left(\frac{w_p - w_{pa}}{w_{pa}}\right) + a_5\left(\frac{w_p - w_{pa}}{w_{pa}}\right)^2 + a_6\left(\frac{w_p - w_{pa}}{w_{pa}}\right)\left(\frac{l}{h_t}\right)$$
$$+ a_7\left(\frac{y_p}{t_c}\right) + a_8\left(\frac{y_p}{t_c}\right)^2 + a_9\left(\frac{l}{h_t}\right)\left(\frac{y_p}{t_c}\right) + a_{10}\left(\frac{w_p - w_{pa}}{w_{pa}}\right)\left(\frac{y_p}{t_c}\right)$$

NT	a_1	a_2	a_3	a_4	a_5	a_6	a_7	a_8	a_9	a_{10}	$CV(\%)$	r^2	$100 \times \frac{N}{N_t}$
45	−0.7583	0.006376	0.001080	1.074	0.2706	−0.03147	1.434	−0.1378	−0.04883	−0.4877	7.65	0.974	75

Table 4.14(a): Second order polynomial prediction equation for $\gamma_m(50)$, with constant term, in function of l/h_t,$(w_p - w_{pa})/w_{pa}$ and F_c/F_a.

$$\frac{\gamma_m(50)}{\gamma_m(0)} = a_1\left(\frac{l}{h_t}\right) + a_2\left(\frac{l}{h_t}\right)^2 + a_3\left(\frac{w_p - w_{pa}}{w_{pa}}\right) + a_4\left(\frac{w_p - w_{pa}}{w_{pa}}\right)^2 + a_5\left(\frac{w_p - w_{pa}}{w_{pa}}\right)\left(\frac{l}{h_t}\right) + a_6\left(\frac{F_c}{F_a}\right) + a_7\left(\frac{F_c}{F_a}\right)^2 + a_8\left(\frac{l}{h_t}\right)\left(\frac{F_c}{F_a}\right) + a_9\left(\frac{w_p - w_{pa}}{w_{pa}}\right)\left(\frac{F_c}{F_a}\right)$$

NT	a_1	a_2	a_3	a_4	a_5	a_6	a_7	a_8	a_9	$CV(\%)$	r^2	$100 \times \frac{N}{N_f}$
45	0.08239	−0.002411	–	–	–	–	–	–	–	25.16	0.01717	
45	−0.01305	0.000431	1.000	−0.07174	−0.008198	–	–	–	–	5.05	0.963	50
45	−0.02042	0.0006362	1.199	−0.06868	−0.01381	0.007496	0.01388	0.001221	−0.07378	5.19	0.965	

Table 4.14(b): Second order polynomial prediction equation for $\gamma_m(50)$, with constant term, in function of l/h_t,$(w_p - w_{pa})/w_{pa}$ and y_p/t_c.

$$\frac{\gamma_m(50)}{\gamma_m(0)} = a_1\left(\frac{l}{h_t}\right) + a_2\left(\frac{l}{h_t}\right)^2 + a_3\left(\frac{w_p - w_{pa}}{w_{pa}}\right) + a_4\left(\frac{w_p - w_{pa}}{w_{pa}}\right)^2 + a_5\left(\frac{w_p - w_{pa}}{w_{pa}}\right)\left(\frac{l}{h_t}\right) + a_6\left(\frac{y_p}{t_c}\right) + a_7\left(\frac{y_p}{t_c}\right)^2 + a_8\left(\frac{l}{h_t}\right)\left(\frac{y_p}{t_c}\right) + a_9\left(\frac{w_p - w_{pa}}{w_{pa}}\right)\left(\frac{y_p}{t_c}\right)$$

NT	a_1	a_2	a_3	a_4	a_5	a_6	a_7	a_8	a_9	$CV(\%)$	r^2	$100 \times \frac{N}{N_f}$
45	−0.03216	0.001121	1.558	−0.2456	−0.01763	0.2585	0.02383	−0.009149	−0.2798	5.03	0.967	50

Table 4.15(a): Second order polynomial prediction equation for $\gamma_m(75)$, with constant term, in function of l/h_t,$(w_p - w_{pa})/w_{pa}$ and F_c/F_a.

$$\frac{\gamma_m(75)}{\gamma_m(0)} = a_1\left(\frac{l}{h_t}\right) + a_2\left(\frac{l}{h_t}\right)^2 + a_3\left(\frac{w_p - w_{pa}}{w_{pa}}\right) + a_4\left(\frac{w_p - w_{pa}}{w_{pa}}\right)^2 + a_5\left(\frac{w_p - w_{pa}}{w_{pa}}\right)\left(\frac{l}{h_t}\right) + a_6\left(\frac{F_c}{F_a}\right) + a_7\left(\frac{F_c}{F_a}\right)^2 + a_8\left(\frac{l}{h_t}\right)\left(\frac{F_c}{F_a}\right) + a_9\left(\frac{w_p - w_{pa}}{w_{pa}}\right)\left(\frac{F_c}{F_a}\right)$$

NT	a_1	a_2	a_3	a_4	a_5	a_6	a_7	a_8	a_9	CV (%)	r^2	$100 \times \frac{N}{N_f}$
45	0.07108	−0.002271	–	–	–	–	–	–	–	41.8	0.0571	
45	−0.003107	0.0003324	0.1951	0.4486	−0.01167	–	–	–	–	7.94	0.968	75
45	−0.004662	0.0003332	0.9003	0.3725	−0.03597	−0.2997	0.02542	0.01201	−0.05208	7.56	0.974	

Table 4.15(b): Second order polynomial prediction equation for $\gamma_m(75)$, with constant term, in function of l/h_t,$(w_p - w_{pa})/w_{pa}$ and y_p/t_c.

$$\frac{\gamma_m(75)}{\gamma_m(0)} = a_1\left(\frac{l}{h_t}\right) + a_2\left(\frac{l}{h_t}\right)^2 + a_3\left(\frac{w_p - w_{pa}}{w_{pa}}\right) + a_4\left(\frac{w_p - w_{pa}}{w_{pa}}\right)^2 + a_5\left(\frac{w_p - w_{pa}}{w_{pa}}\right)\left(\frac{l}{h_t}\right) + a_6\left(\frac{y_p}{t_c}\right) + a_7\left(\frac{y_p}{t_c}\right)^2 + a_8\left(\frac{l}{h_t}\right)\left(\frac{y_p}{t_c}\right) + a_9\left(\frac{w_p - w_{pa}}{w_{pa}}\right)\left(\frac{y_p}{t_c}\right)$$

NT	a_1	a_2	a_3	a_4	a_5	a_6	a_7	a_8	a_9	CV (%)	r^2	$100 \times \frac{N}{N_f}$
45	−0.02310	0.001346	0.4955	0.3795	−0.01969	0.7430	0.02168	−0.03496	−0.2340	7.54	0.974	75

Table 4.16: Values of γ_m for Grade 43 steel profiles,analysed according to the interpolation method (ECI) and the equilibrium method (ECE) in Eurocode 4, and according to the equilibrium method in BS5950:Pt.3 (BSE)

		$SEBC8$		$SEBC20$		$SEBC19 = EBC8$			$SEBC17 = EBC9$		
		ECI	ECE	ECI	ECE	ECI	ECE	BSE	ECI	ECE	BSE
l	(m)	10.00		20.00		20.00			20.00		
f_{ay}	(N/mm^2)	275.0		275.0		275.0			275.0		
$w_{pp}(50.0)$	(kN/m)	30.30	33.62	47.12	53.84	37.35	41.96	41.33	33.77	38.39	37.94
$w_{pp}(62.5)$	(kN/m)	32.96	35.75	50.40	55.79	39.57	43.65	43.07	35.93	39.64	39.16
$w_{pp}(75.0)$	(kN/m)	35.61	37.76	53.68	57.50	41.79	44.71	44.22	38.10	40.73	40.19
$w_{pp}(87.5)$	(kN/m)	38.26	–	56.95	58.96	44.01	45.54	45.00	40.27	41.66	41.08
$\gamma_m(50.0)$	(mm)	4.09	7.01	4.98	9.68	7.05	11.58	12.07	5.46	10.82	11.02
$\gamma_m(62.5)$	(mm)	3.71	5.56	3.92	7.23	5.94	10.37	10.93	4.45	8.45	8.91
$\gamma_m(75.0)$	(mm)	3.57	5.41	3.03	4.59	5.04	8.17	8.83	3.29	5.52	6.72
$\gamma_m(87.5)$	(mm)	3.22	–	2.50	2.91	4.03	5.33	6.97	2.65	3.68	4.37
$\gamma_m(100.0)$	(mm)	–	–	–	2.10	3.63	3.63	–	1.97	–	–
y_p	(mm)	41.80		87.15		154.5		156.1	147.9		149.9
F_p	(kN)	1776		6050		3612		3374	4335		4051
w_p	(kN/m)	40.92		60.23		46.24		46.08	42.82		42.22
N_f	$(-)$	32		85		51		43	61		49

Table 4.17: Influence of the stud shear strength on the maximum slip along beams with same geometry and material properties as certain beams in Table 4.19

		*EBC*1		*EBC*2		*EBC*3		*EBC*8	
		ECE	*BSE*	*ECE*	*BSE*	*ECE*	*BSE*	*ECE*	*BSE*
l	(m)	10.00		10.00		10.00		20.00	
Q_u	(kN)	89.3	109	89.3	104	89.3	99	89.3	99
N_f	$(-)$	36	30	33	28	32	29	51	43
y_p	(mm)	51.69	56.56	53.96	57.75	62.75	67.42	160.3	161.6
$\gamma_m(50.0)$	(mm)	5.16	4.98	4.93	5.06	5.13	4.50	12.16	11.41
$\gamma_m(62.5)$	(mm)	3.34	3.35	3.38	3.20	3.62	3.58	9.84	9.03
$\gamma_m(75.0)$	(mm)	2.37	2.37	2.57	2.55	2.67	2.46	7.38	7.04
$\gamma_m(87.5)$	(mm)	1.88	2.02	2.03	1.83	2.05	2.06	4.98	5.22
$\gamma_m(100.0)$	(mm)	1.08	1.55	1.65	1.54	1.63	–	–	–

Table 4.18(a): Comparison of γ_m values produced by EPPIB for loads generated by both the interpolation (ECI) and the equilibrium (ECE) method of Eurocode 4 onto the same beams.

		SEBC1		*SEBC2*		*SEBC3*		*SEBC4*	
		ECI	*ECE*	*ECI*	*ECE*	*ECI*	*ECE*	*ECI*	*ECE*
l	(m)	5.00		5.00		7.50		7.50	
t_c	(m)	0.090		0.090		0.125		0.135	
t_h	(m)	0.050		0.050		–		–	
b_e	(m)	1.250		1.250		1.875		1.875	
$b_1 - t_1$	(mm)	100 – 5.5		203 × 133		254 × 102		125 – 8.5	
$b_2 - t_2$	(mm)	4.0 – 200		UB25		UB22		5.5 – 300	
$b_3 - t_3$	(mm)	130 – 6.5						125 – 9.0	
f_{ck}	(N/mm^2)	35.00		40.00		40.00		30.00	
f_{ay}	(N/mm^2)	355.		355.		355.		355.	
$d_{sh} \times h_{st}$	(mm)	13 × 65		13 × 65		13 × 65		13 × 65	
$w_{pp}(50.0)$	(kN/m)	41.73	46.42	57.67	61.93	24.04	26.60	38.30	43.46
$w_{pp}(62.5)$	(kN/m)	46.90	50.66	64.70	67.87	26.75	28.77	42.05	46.60
$w_{pp}(75.0)$	(kN/m)	53.35	55.16	71.73	74.35	29.45	30.87	45.80	49.62
$w_{pp}(87.5)$	(kN/m)	57.47	58.82	78.77	79.83	32.16	32.90	49.55	52.52
$\gamma_m(50.0)$	(mm)	5.28	10.64	5.27	9.40	4.84	8.57	4.31	7.60
$\gamma_m(62.5)$	(mm)	5.09	10.13	5.03	10.38	4.03	7.81	3.88	6.90
$\gamma_m(75.0)$	(mm)	5.54	9.96	5.62	11.54	4.73	6.56	3.63	6.23
$\gamma_m(87.5)$	(mm)	–	9.86	–	–	–	5.61	–	5.58
y_p	(mm)	31.43		40.48		23.72		42.74	
F_p	(kN)	779.2		1147		1008		1362	
w_p	(kN/m)	60.79		85.80		34.86		54.54	
N_f	$(-)$	24		35		31		41	

Table 4.18(b): (continued ...)

		$SEBC5$		$SEBC6$		$SEBC7$		$SEBC8$	
		ECI	ECE	ECI	ECE	ECI	ECE	ECI	ECE
l	(m)	10.00		10.00		10.00		10.00	
t_c	(m)	0.140		0.084		0.135		0.084	
t_h	(m)	–		0.046		–		0.046	
b_e	(m)	2.500		2.500		2.500		2.500	
$b_1 - t_1$	(mm)	$220 - 13$		IPE		356×127		356×171	
$b_2 - t_2$	(mm)	$8 - 300$		330		UB39		UB51	
$b_3 - t_3$	(mm)	$250 - 15$							
f_{ck}	(N/mm^2)	35.00		25.00		30.00		30.00	
f_{ay}	(N/mm^2)	355.		355.		355.		355.	
$d_{sh} \times h_{st}$	(mm)	19×95		19×95		19×95		19×95	
$w_{pp}(50.0)$	(kN/m)	53.80	61.39	34.87	39.29	30.15	33.43	39.12	42.42
$w_{pp}(62.5)$	(kN/m)	58.69	65.20	37.87	41.72	33.03	35.67	42.55	44.92
$w_{pp}(75.0)$	(kN/m)	63.58	68.72	40.87	43.95	35.92	37.81	45.98	47.25
$w_{pp}(87.5)$	(kN/m)	68.46	71.93	43.87	45.97	38.81	39.83	49.40	49.43
$\gamma_m(50.0)$	(mm)	5.07	8.94	4.68	10.35	5.69	8.90	6.17	9.39
$\gamma_m(62.5)$	(mm)	4.59	8.09	4.35	8.72	4.79	7.22	5.78	8.20
$\gamma_m(75.0)$	(mm)	3.90	6.36	3.63	7.05	4.17	5.72	5.67	7.01
$\gamma_m(87.5)$	(mm)	–	5.50	3.18	5.47	4.57	5.49	5.53	5.86
y_p	(mm)	64.86		62.75		41.27		53.95	
F_p	(kN)	3216		2222		1754		2293	
w_p	(kN/m)	73.35		46.87		41.70		52.83	
N_f	$(-)$	37		32		21		32	

Table 4.18(c): (continued ...)

		$SEBC9$		$SEBC10$		$SEBC11$		$SEBC12$	
		ECI	ECE	ECI	ECE	ECI	ECE	ECI	ECE
l	(m)	10.00		15.00		15.00		15.00	
t_c	(m)	0.080		0.080		0.085		0.080	
t_h	(m)	0.055		0.055		0.051		0.055	
b_e	(m)	2.500		3.500		3.000		3.500	
$b_1 - t_1$	(mm)	406 × 140		457 × 152		533 × 210		533 × 210	
$b_2 - t_2$	(mm)	UB39		UB74		UB82		UB92	
$b_3 - t_3$	(mm)								
f_{ck}	(N/mm^2)	35.00		35.00		35.00		40.00	
f_{ay}	(N/mm^2)	355.		355.		355.		355.	
$d_{sh} \times h_{st}$	(mm)	22 × 95		22 × 95		22 × 95		22 × 95	
$w_{pp}(50.0)$	(kN/m)	32.79	36.66	30.70	34.59	37.19	42.33	42.81	48.20
$w_{pp}(62.5)$	(kN/m)	35.86	38.93	33.26	36.41	40.05	44.17	46.05	50.39
$w_{pp}(75.0)$	(kN/m)	38.93	41.10	35.81	38.09	42.90	45.84	49.29	52.40
$w_{pp}(87.5)$	(kN/m)	42.00	43.18	38.37	39.61	45.76	47.32	52.54	54.21
$\gamma_m(50.0)$	(mm)	5.64	9.26	7.14	12.56	7.06	10.54	6.73	11.45
$\gamma_m(62.5)$	(mm)	5.69	8.85	6.04	10.02	5.86	8.23	5.68	9.06
$\gamma_m(75.0)$	(mm)	5.03	6.89	5.83	8.67	4.98	6.09	4.96	6.95
$\gamma_m(87.5)$	(mm)	5.43	6.55	5.29	6.54	4.39	4.33	4.47	5.31
y_p	(mm)	35.36		48.59		62.05		52.80	
F_p	(kN)	1754		3373		3692		4189	
w_p	(kN/m)	45.08		40.93		48.61		55.78	
N_f	$(-)$	19		36		39		44	

Table 4.18(d): (continued ...)

		$SEBC13$		$SEBC14$		$SEBC15$		$SEBC16$	
		ECI	ECE	ECI	ECE	ECI	ECE	ECI	ECE
l	(m)	15.00		17.50		17.50		20.00	
t_c	(m)	0.085		0.100		0.100		0.110	
t_h	(m)	0.065		0.050		0.050		0.065	
b_e	(m)	3.000		3.500		3.000		3.500	
$b_1 - t_1$	(mm)	533 × 210		533 × 210		533 × 210		610 × 229	
$b_2 - t_2$	(mm)	UB92		UB109		UB92		UB113	
$b_3 - t_3$	(mm)								
f_{ck}	(N/mm^2)	30.00		35.00		40.00		35.00	
f_{ay}	(N/mm^2)	355.		355.		355.		355.	
$d_{sh} \times h_{st}$	(mm)	22 × 95		22 × 95		22 × 95		22 × 120	
$w_{pp}(50.0)$	(kN/m)	43.06	48.44	37.78	42.66	32.03	36.11	34.32	38.65
$w_{pp}(62.5)$	(kN/m)	46.34	50.56	40.68	44.66	34.56	37.85	37.09	40.53
$w_{pp}(75.0)$	(kN/m)	49.63	52.44	43.58	46.46	37.09	39.44	39.82	42.25
$w_{pp}(87.5)$	(kN/m)	52.91	54.09	46.48	48.04	39.61	40.88	42.56	43.79
$\gamma_m(50.0)$	(mm)	6.57	11.65	6.80	12.62	7.63	13.97	8.36	16.22
$\gamma_m(62.5)$	(mm)	5.26	8.95	5.35	9.66	6.08	10.89	6.79	12.61
$\gamma_m(75.0)$	(mm)	4.32	6.44	4.34	6.89	4.97	7.97	5.67	9.09
$\gamma_m(87.5)$	(mm)	3.70	4.37	3.66	4.66	4.22	5.48	4.49	6.09
y_p	(mm)	78.81		71.09		61.50		73.64	
F_p	(kN)	4019		4935		4192		5112	
w_p	(kN/m)	56.20		49.38		42.14		45.31	
N_f	$(-)$	42		52		44		54	

Table 4.18(e): (continued ...)

		$SEBC17$		$SEBC18$		$SEBC19$		$SEBC20$	
		ECI	ECE	ECI	ECE	ECI	ECE	ECI	ECE
l	(m)	20.00		20.00		20.00		20.00	
t_c	(m)	0.085		0.085		0.085		0.100	
t_h	(m)	0.060		0.060		0.060		0.060	
b_e	(m)	3.000		3.000		3.000		3.500	
$b_1 - t_1$	(mm)	686 × 254		762 × 267		762 × 267		762 × 267	
$b_2 - t_2$	(mm)	UB140		UB147		UB147		UB173	
$b_3 - t_3$	(mm)								
f_{ck}	(N/mm^2)	30.00		40.00		25.00		35.00	
f_{ay}	(N/mm^2)	355.		355.		355.		355	
$d_{sh} \times h_{st}$	(mm)	19 × 95		22 × 95		19 × 95		19 × 95	
$w_{pp}(50.0)$	(kN/m)	42.41	47.25	49.61	56.54	47.19	51.25	60.27	67.86
$w_{pp}(62.5)$	(kN/m)	44.91	49.00	52.84	58.37	49.80	53.56	64.36	70.05
$w_{pp}(75.0)$	(kN/m)	47.41	50.16	56.06	59.83	52.42	55.26	68.45	71.91
$w_{pp}(87.5)$	(kN/m)	49.91	51.15	59.28	61.08	55.04	56.46	72.54	73.48
$\gamma_m(50.0)$	(mm)	10.42	15.48	8.25	14.43	12.50	17.56	7.45	13.64
$\gamma_m(62.5)$	(mm)	9.15	13.66	6.09	10.78	11.47	15.64	5.75	10.62
$\gamma_m(75.0)$	(mm)	7.47	10.45	4.81	7.56	10.51	13.39	4.26	7.25
$\gamma_m(87.5)$	(mm)	6.56	7.84	3.92	4.86	9.67	10.77	3.49	4.53
y_p	(mm)	155.2		148.9		160.3		162.8	
F_p	(kN)	4335		5780		3612		6942	
w_p	(kN/m)	52.41		62.50		57.65		75.46	
N_f	$(-)$	61		61		51		98	

Table 4.19(a): Comparison of γ_m -values for simply supported beams produced by EPPIB for data generated by the equilibrium methods of Eurocode 4 (ECE) and BS 5950:Pt.3 (BSE).

		*EBC*1		*EBC*2		*EBC*3		*EBC*4		*EBC*5	
		ECE	*BSE*	*ECE*	*BSE*	*ECE*	*BSE*	*ECE*	*BSE*	*ECE*	*BSE*
l	(m)	10.00		10.00		10.00		15.00		15.00	
rolled		356 × 171		356 × 171		IPE330		533 × 210		533 × 210	
sections		UB57		UB51				UB92		UB82	
$d_{sh} \times h_{st}$	(mm)	19 × 95		19 × 95		19 × 95		19 × 95		19 × 95	
$t_c - t_h$	(mm)	65 – 60		84 – 46		84 – 46		85 – 65		85 – 51	
b_e	(m)	2.50	2.50	2.50	2.50	2.50	2.50	3.00	3.00	3.00	3.00
Q_d	(kN)	71.5	87.2	71.5	83.2	71.5	79.2	71.5	83.2	71.5	87.2
$f_{ck} - f_{cu}$	(N/mm^2)	35.0	40.0	30.0	35.3	25.0	29.3	30.0	35.3	35.0	41.2
w_p	(kN/m)	57.98	57.53	52.35	52.60	46.87	46.50	56.20	56.75	48.63	49.24
$w_{pp}(50.0)$	(kN/m)	47.94	47.83	43.08	43.01	39.29	39.21	48.44	48.63	42.33	42.82
$w_{pp}(62.5)$	(kN/m)	50.76	50.58	45.67	45.56	41.72	41.58	50.56	50.73	44.17	44.61
$w_{pp}(75.0)$	(kN/m)	53.37	53.12	48.08	47.92	43.95	43.75	52.44	52.56	45.84	46.17
$w_{pp}(87.5)$	(kN/m)	55.78	55.43	50.30	50.08	45.97	45.71	54.09	54.12	47.32	47.90
$\gamma_m(37.5)$	(mm)	*n.a.*	9.90	*n.a.*	10.77	*n.a*	11.50	*n.a.*	14.7	*n.a.*	13.92
$\gamma_m(50.0)$	(mm)	10.16	9.57	9.19	10.17	10.35	9.09	11.6	12.4	10.54	10.78
$\gamma_m(62.5)$	(mm)	8.11	7.59	7.88	8.21	8.72	8.46	8.95	9.6	8.23	8.41
$\gamma_m(75.0)$	(mm)	7.32	5.77	6.58	6.95	7.05	6.11	6.44	7.07	6.09	6.21
$\gamma_m(87.5)$	(mm)	5.39	5.17	5.33	4.87	5.47	5.29	4.37	4.78	4.33	4.41
$\gamma_m(100.0)$	(mm)	–	–	4.23	–	4.14	–	3.01	–	2.81	–
y_p	(mm)	51.69	56.96	53.96	57.75	62.75	67.42	78.81	84.34	62.05	66.38
N_f	$(-)$	36	30	33	28	32	29	57	49	52	43
F_p	(kN)	2563		2293		2222		4019		3692	

Table 4.19(b): (continued...)

		*EBC*6		*EBC*7		*EBC*8		*EBC*9		*EBC*10	
		ECE	*BSE*	*ECE*	*BSE*	*ECE*	*BSE*	*ECE*	*BSE*	*ECE*	*BSE*
l	(m)	20.00		20.00		20.00		20.00		20.00	
rolled		762 × 267		762 × 267		762 × 267		686 × 254		610 × 229	
sections		UB173		UB147		UB147		UB140		UB113	
$d_{sh} \times h_{st}$	(mm)	19 × 95		19 × 95		19 × 95		19 × 95		19 × 95	
$t_c - t_h$	(mm)	100 − 60		85 − 60		85 − 60		85 − 60		110 − 65	
b_e	(m)	3.50	3.50	3.00	3.00	3.00	3.00	3.00	3.00	3.50	3.50
Q_d	(kN)	71.5	87.2	71.5	87.2	71.5	79.20	71.5	83.2	71.5	87.2
$f_{ck} - f_{cu}$	(N/mm^2)	35.0	40.0	40.0	47.0	25.0	29.4	30.0	35.3	35.0	40.0
w_p	(kN/m)	75.46	73.25	62.50	61.68	57.65	57.08	52.00	51.35	45.32	44.63
$w_{pp}(50.0)$	(kN/m)	67.86	66.64	56.54	55.79	51.25	50.51	47.25	46.60	38.78	38.57
$w_{pp}(62.5)$	(kN/m)	70.05	68.86	58.37	57.72	53.56	52.76	49.00	48.43	40.67	40.38
$w_{pp}(75.0)$	(kN/m)	71.91	70.59	59.83	59.10	55.26	54.53	50.16	49.60	42.38	42.03
$w_{pp}(87.5)$	(kN/m)	73.48	72.05	61.08	60.29	56.46	55.83	51.15	50.54	43.94	43.50
$\gamma_m(37.5)$	(mm)	*n.a.*	17.14	*n.a.*	17.48	*n.a.*	–	*n.a.*	–	*n.a.*	21.09
$\gamma_m(50.0)$	(mm)	13.64	14.93	14.43	15.29	17.56	16.55	15.48	15.98	18.13	17.15
$\gamma_m(62.5)$	(mm)	10.62	12.05	10.78	12.38	15.64	15.38	13.66	14.42	14.44	13.77
$\gamma_m(75.0)$	(mm)	7.25	9.00	7.56	9.09	13.39	14.07	10.45	12.19	10.76	10.36
$\gamma_m(87.5)$	(mm)	4.53	6.15	4.86	6.05	10.77	12.62	7.84	9.16	7.35	7.24
$\gamma_m(100.0)$	(mm)	–	4.04	–	–	8.59	10.37	5.06	6.80	4.71	–
y_p	(mm)	162.8	166.2	148.9	150.9	160.3	161.6	155.2	156.8	73.64	81.14
N_f	$(-)$	798	73	81	62	51	43	61	49	72	59
F_p	(kN)	6942	6300	5780	5393	3612	3374	4335	4051	5112	

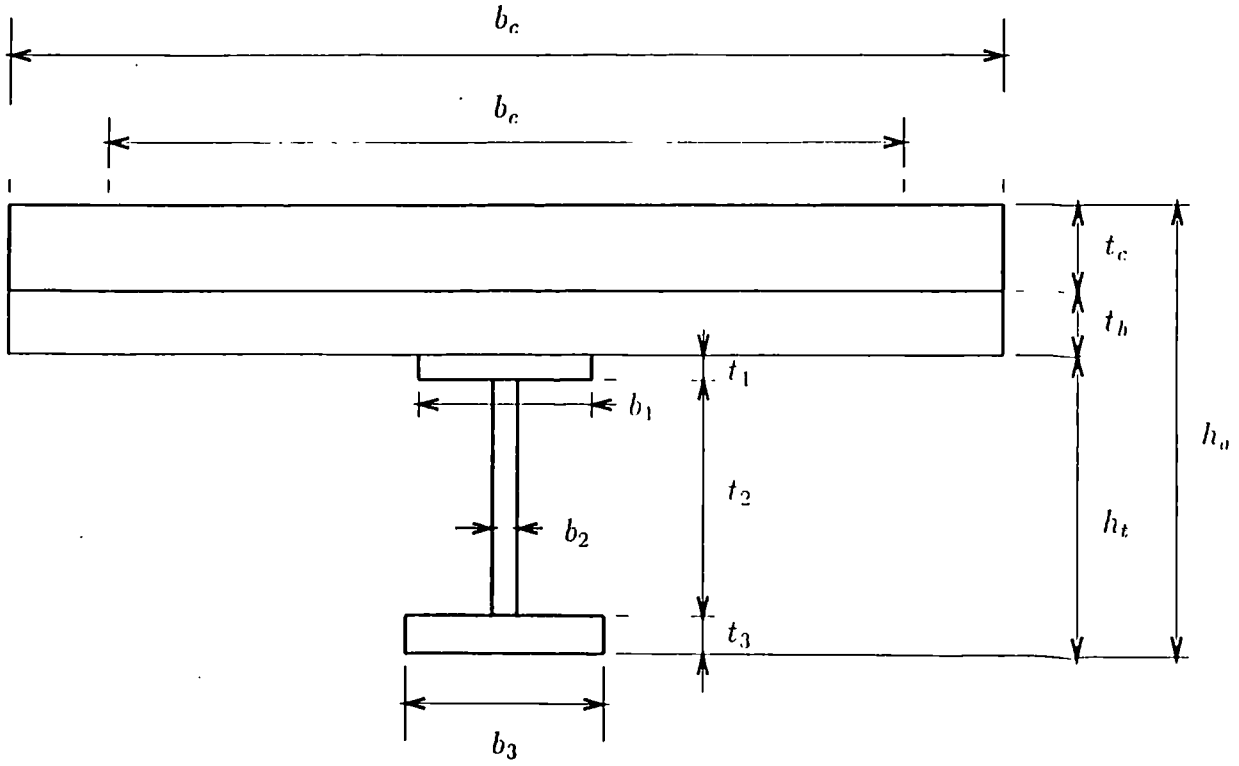

Figure 4.1(a): Geometry and dimensions of cross section of composite beam with metal decking.

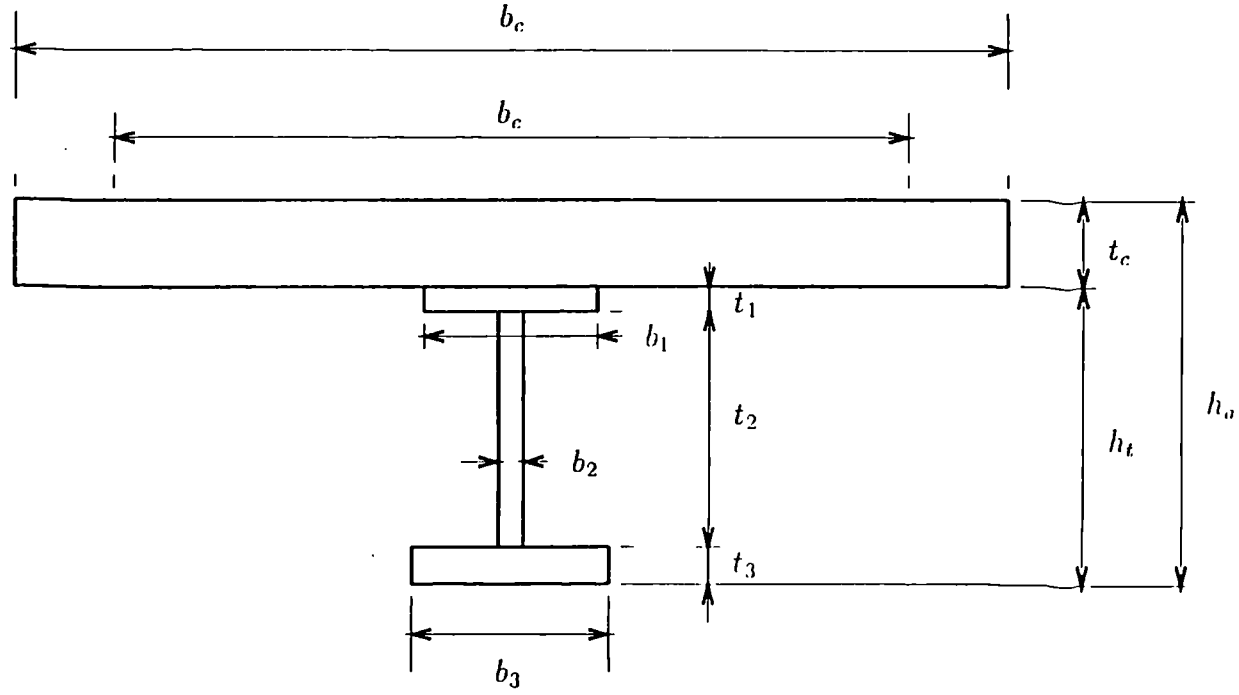

Figure 4.1(b): Geometry and dimensions of cross section of composite beam without metal decking.

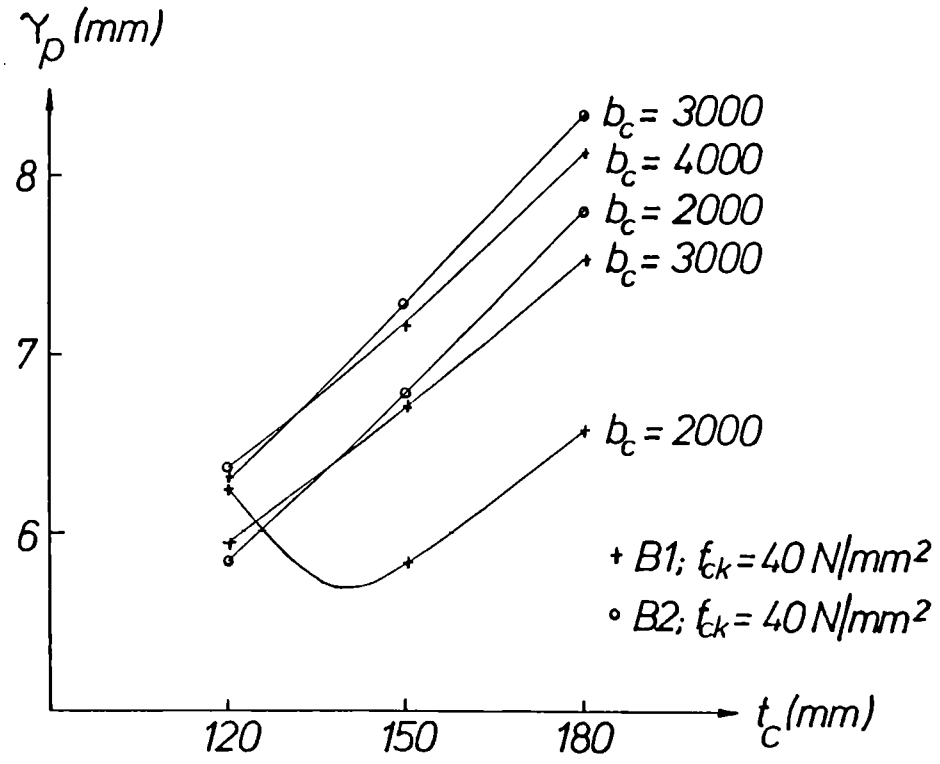

Figure 4.2: Relationship between the maximum slip and the thickness of the concrete slab for beams B1 and B2 of Table 4.1.

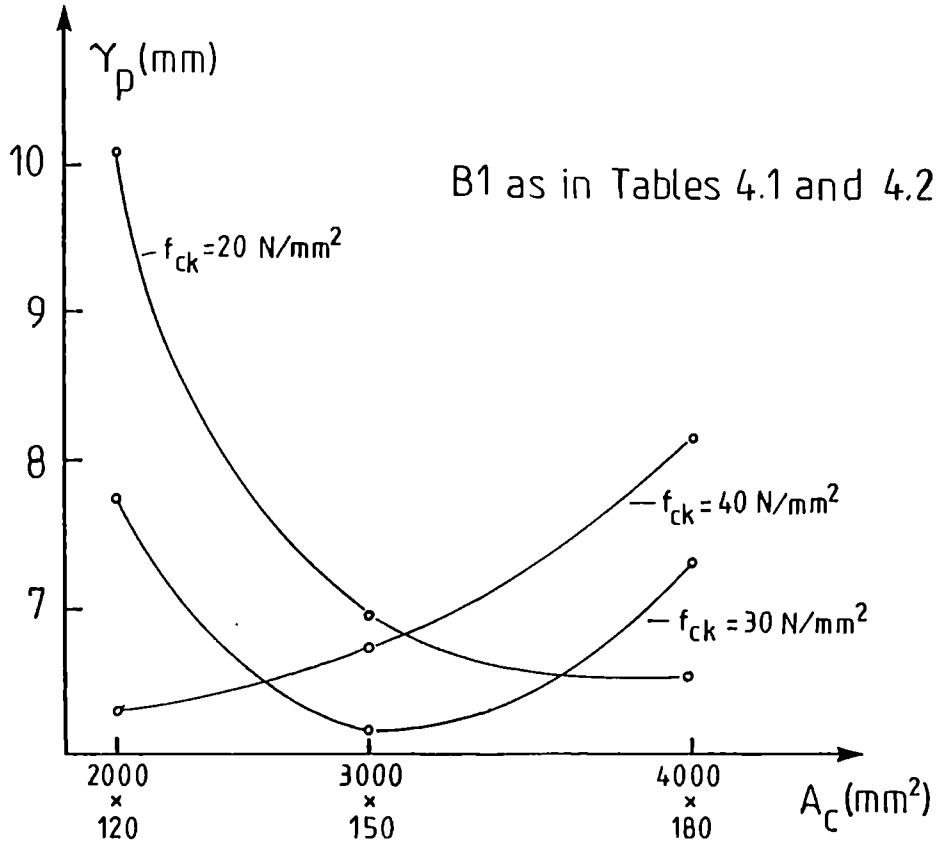

Figure 4.3: Relationship between the maximum slip along beam B1 and the cross-sectional area of concrete slab for different concrete strength.

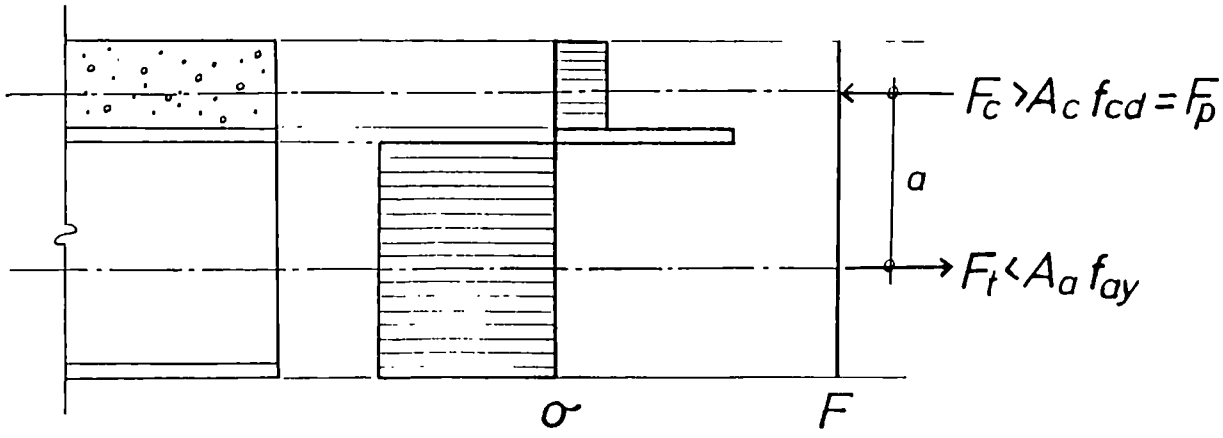

Figure 4.4: The longitudinal interface force is the lesser value of the longitudinal force in the steel profile and in the concrete slab.

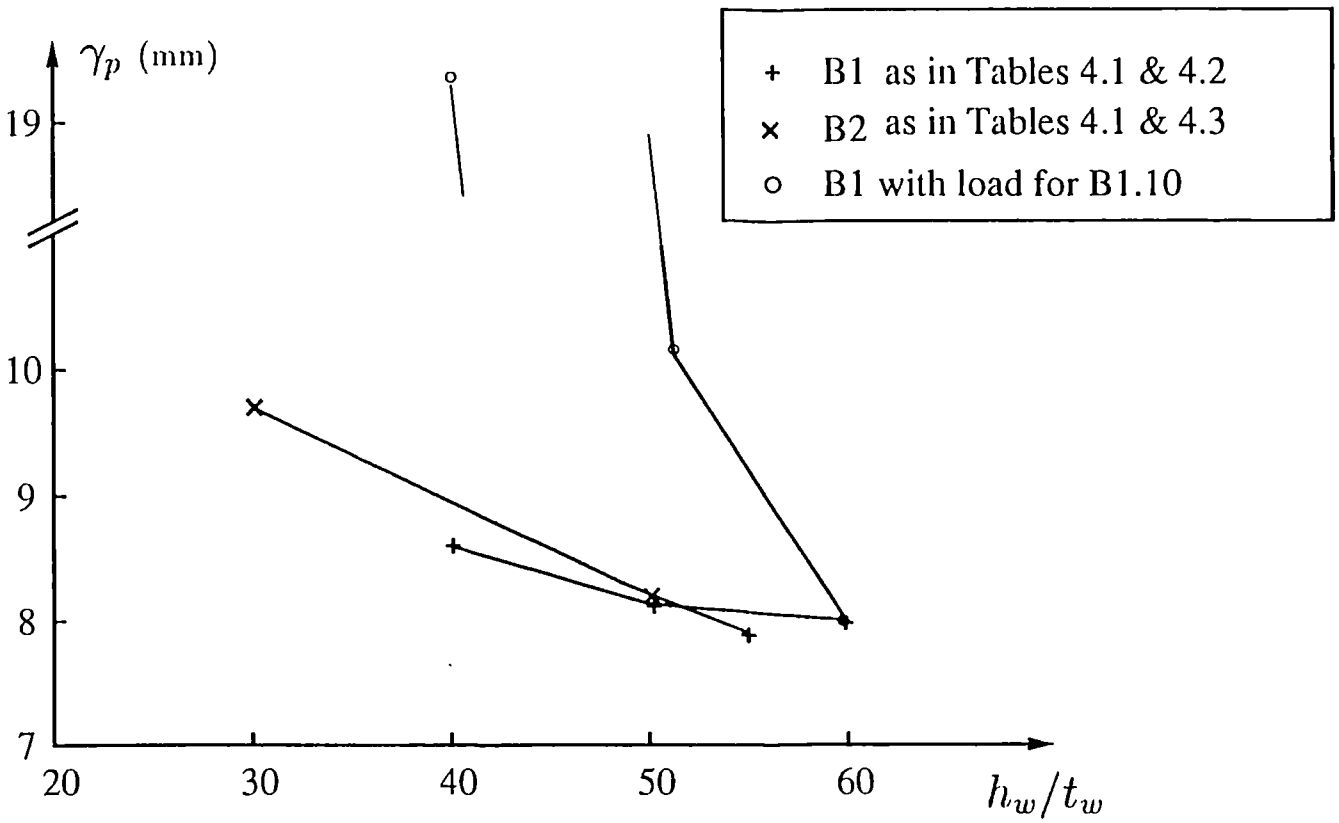

Figure 4.5: Relationship between the maximum slip along beams B1 & B2 and the web slenderness of their steel profiles.

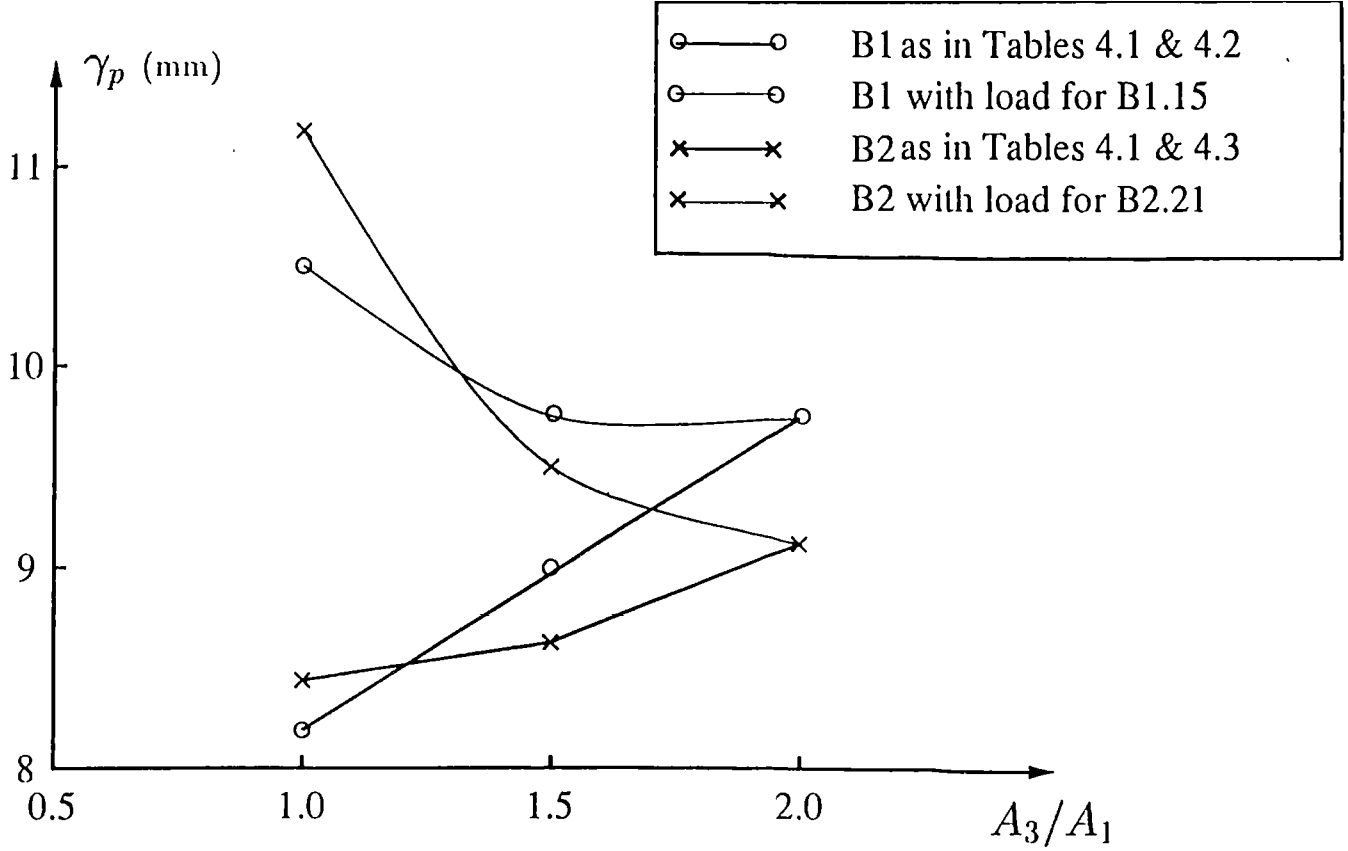

Figure 4.6: Relationship between the maximum slip along beams B1 and B2 and the ratio of the bottom flange to the top flange.

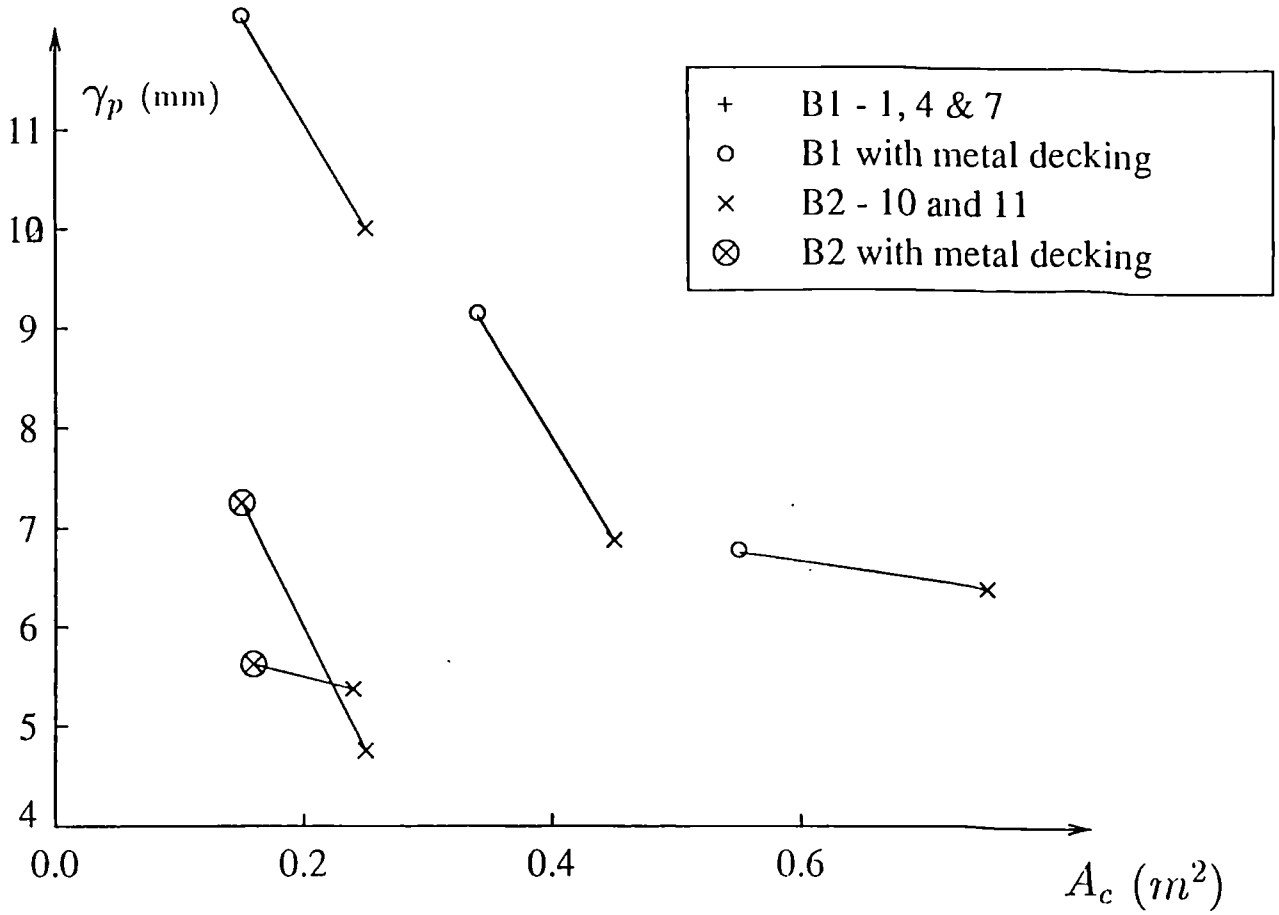

Figure 4.7: Relationship between the maximum slip along beams B1 and B2 and the area of their concrete slabs.

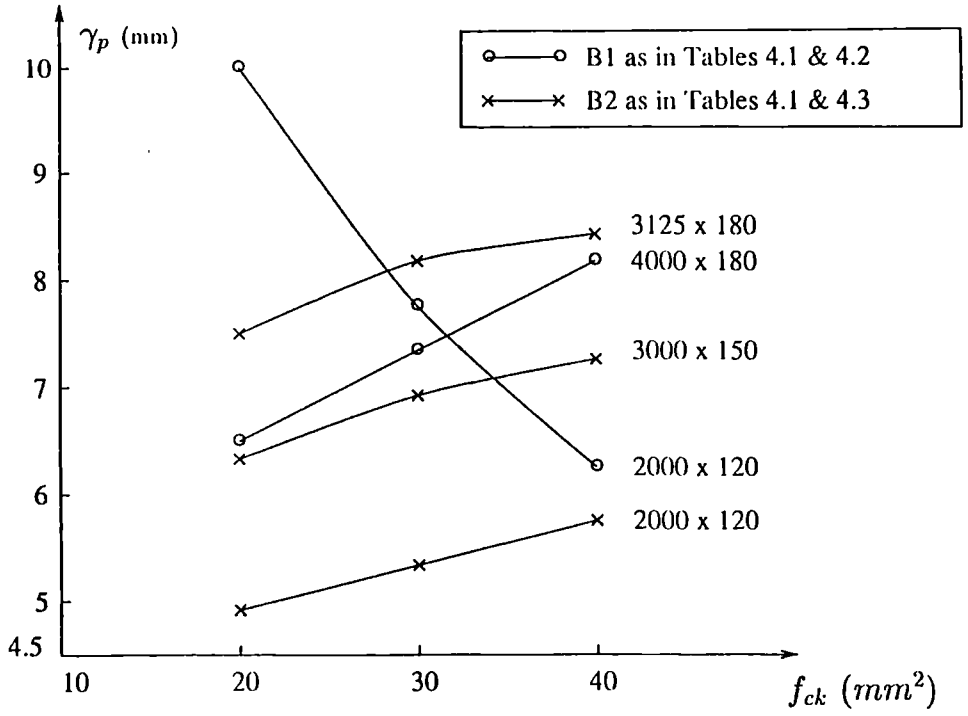

Figure 4.8: Relationship between the maximum slip along beams B1 and B2 and the concrete strength of the slab.

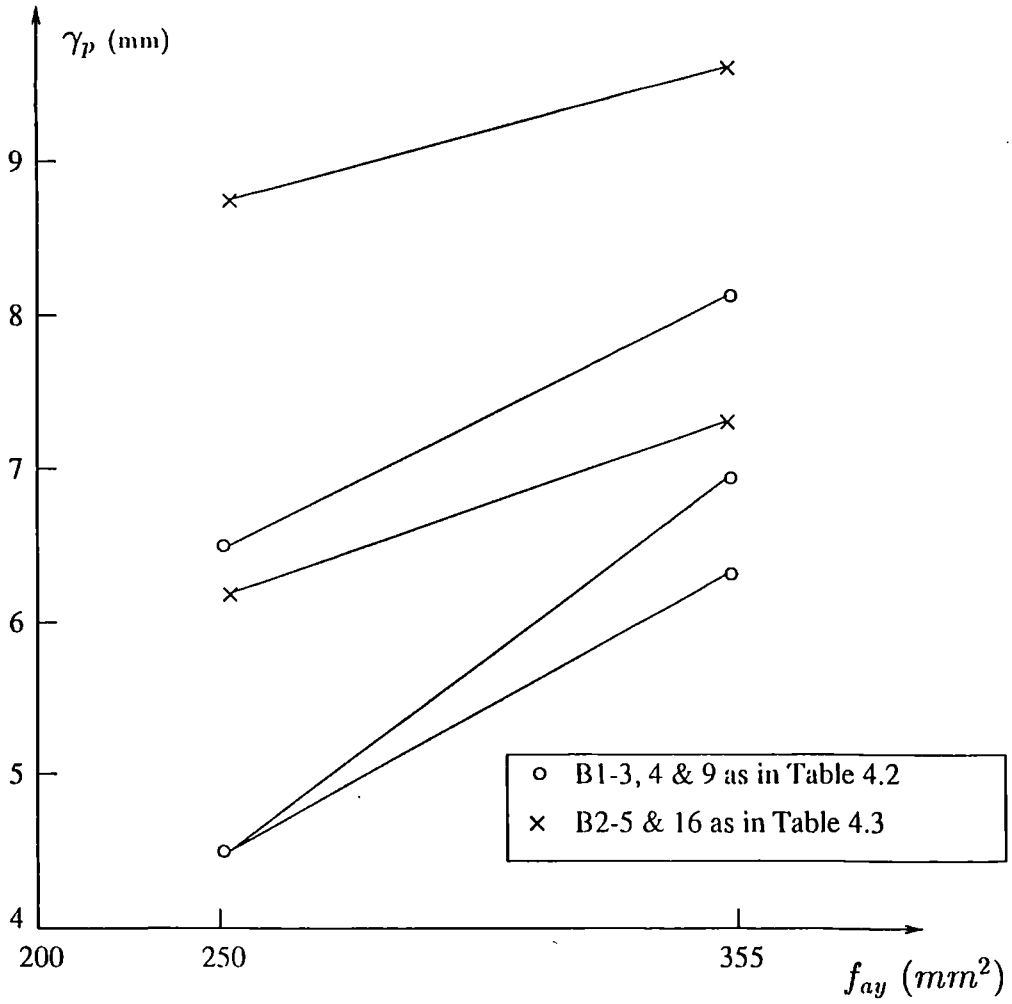

Figure 4.9: Relationship between the maximum slip along beams B1 and B2 and the Grade of structural steel.

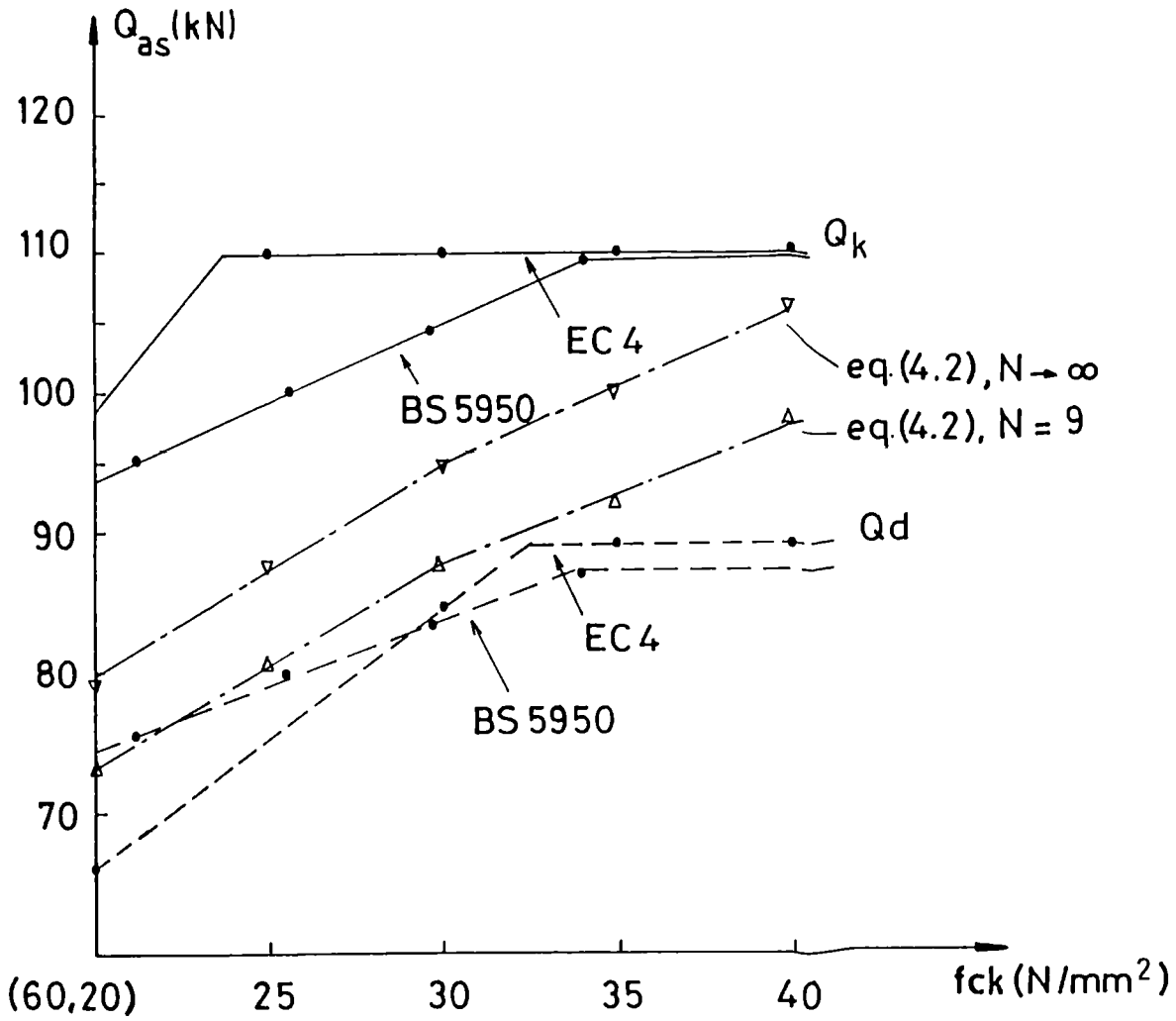

Figure 4.10: Variation of the shear strength of 19 mm diameter studs with the characteristic cylinder strength of the concrete in which they are embedded.

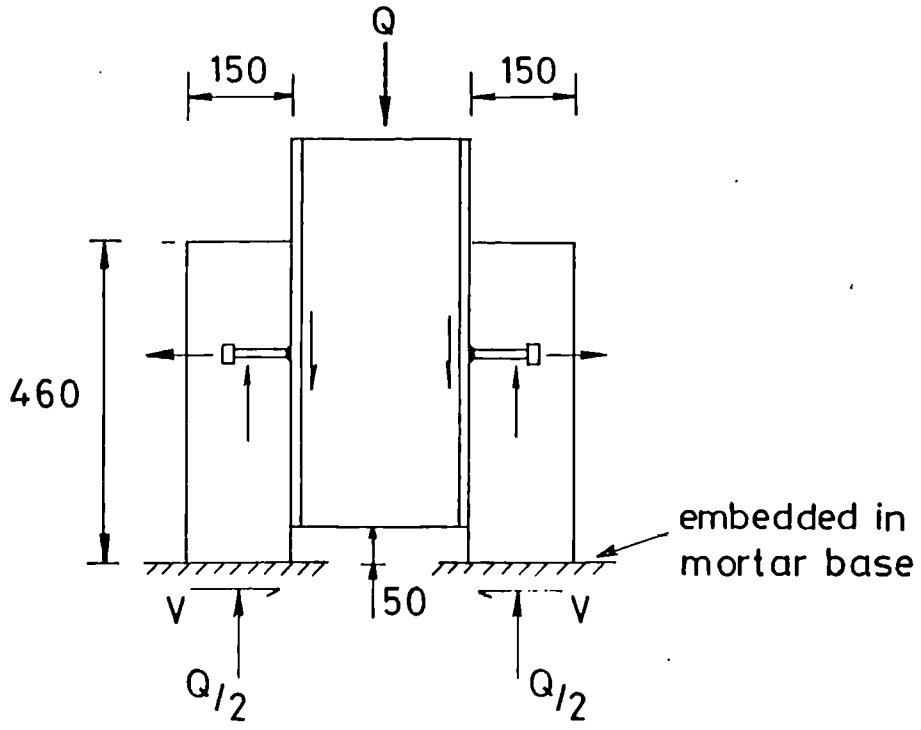

a) Standard push - out test as in ref. [3]

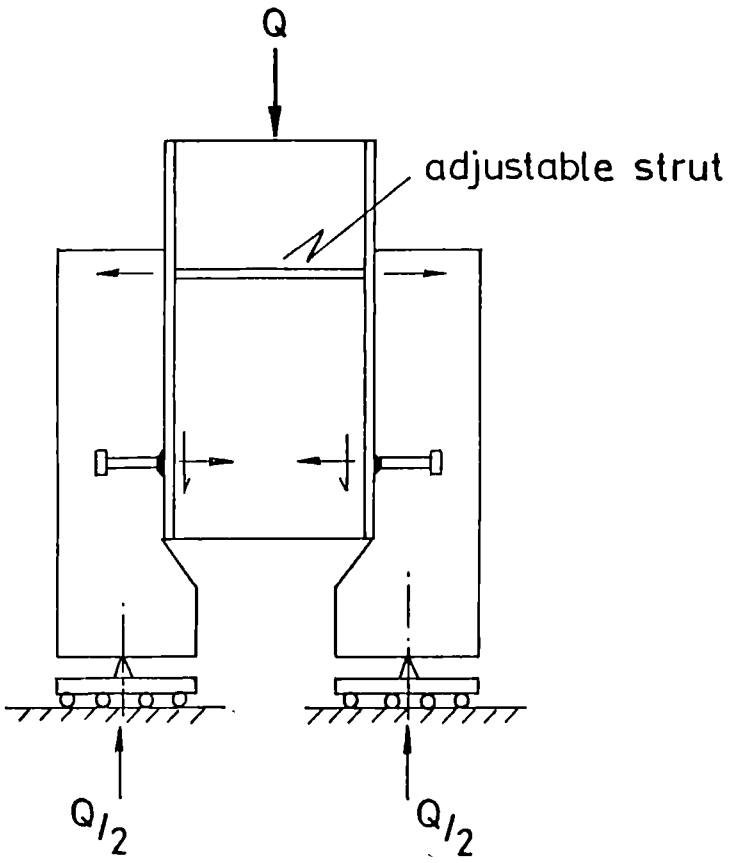

b) Oehlers' push - out test as in ref. [64]

Figure 4.11: Comparison between the Standard Push-Out test and Oehlers' push-out test.

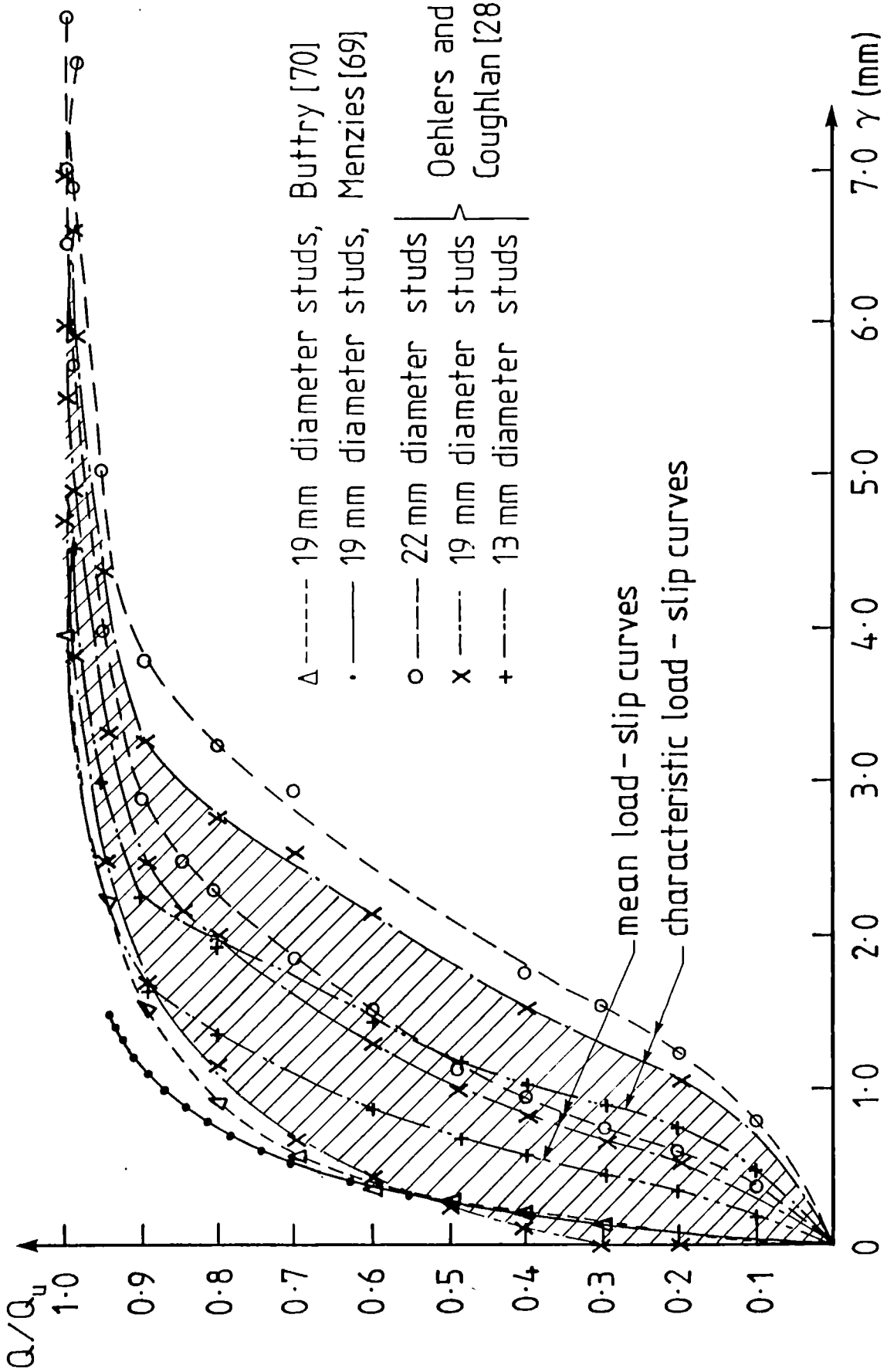

Figure 4.12: Load-slip curves of stud connectors in solid slabs.

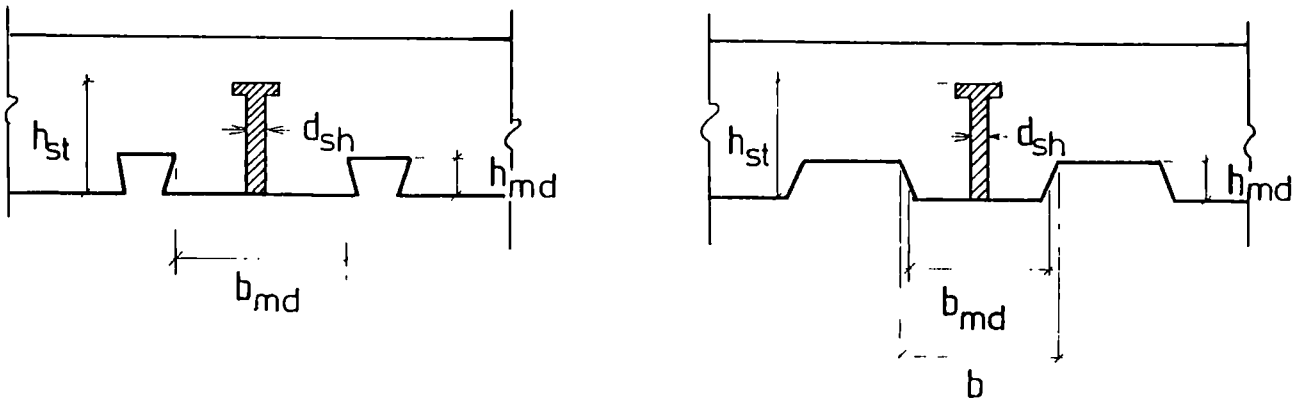

Figure 4.13: re-entrant and open trough types of metal decking profiles.

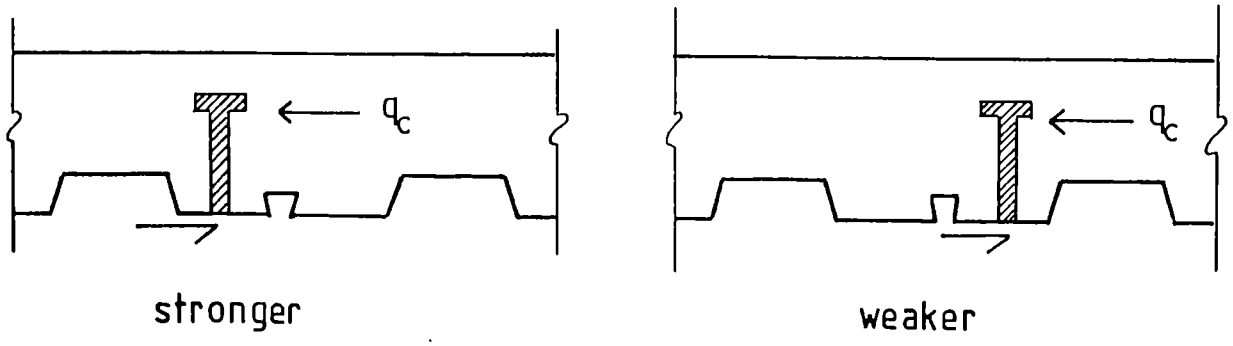

Figure 4.14: Influence of the longitudinal position of the studs from the sides of the trough on the shear strength of the studs.

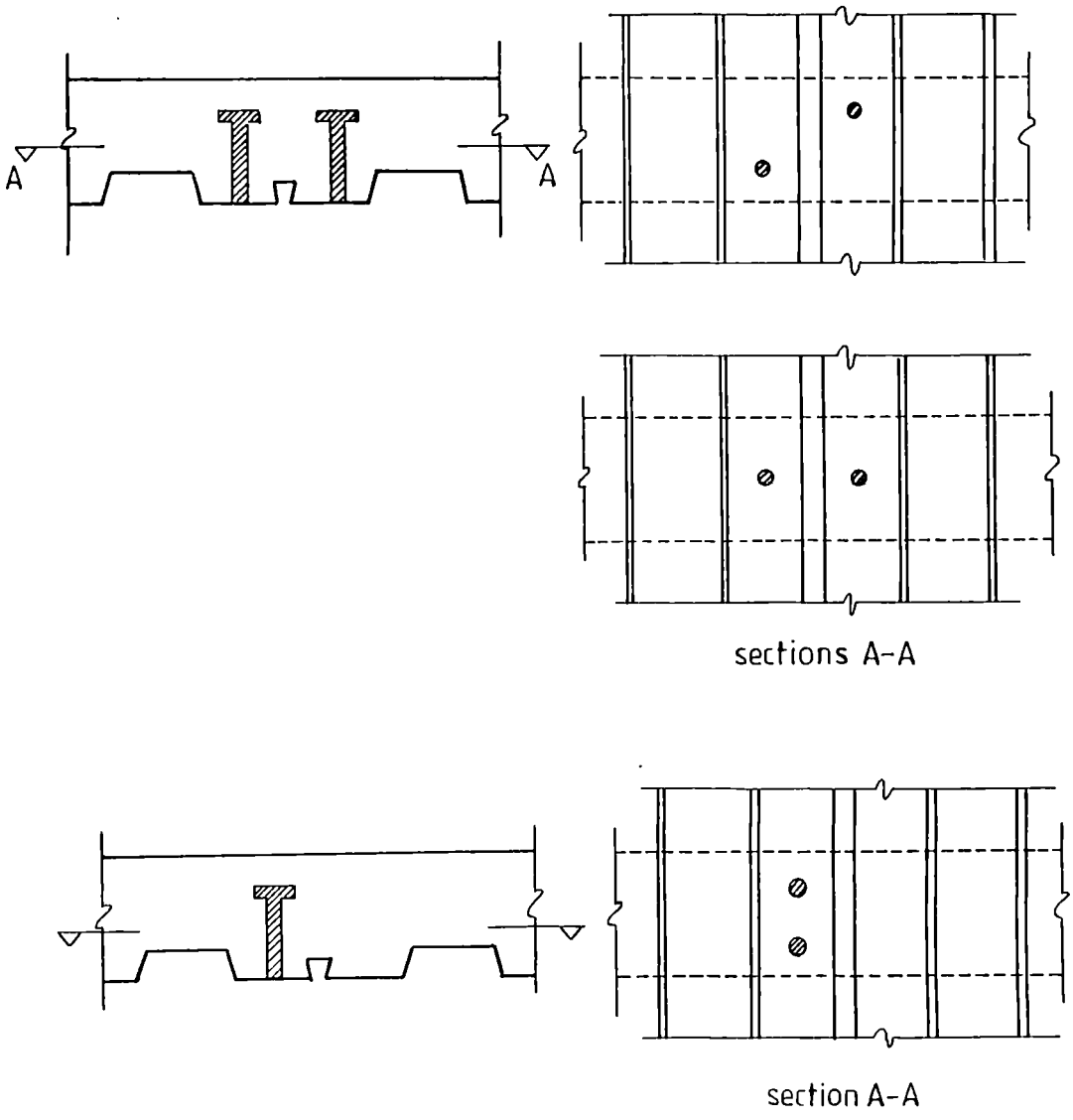

Figure 4.15: Influence of transverse position of more than one stud per trough on the shear strength of the studs.

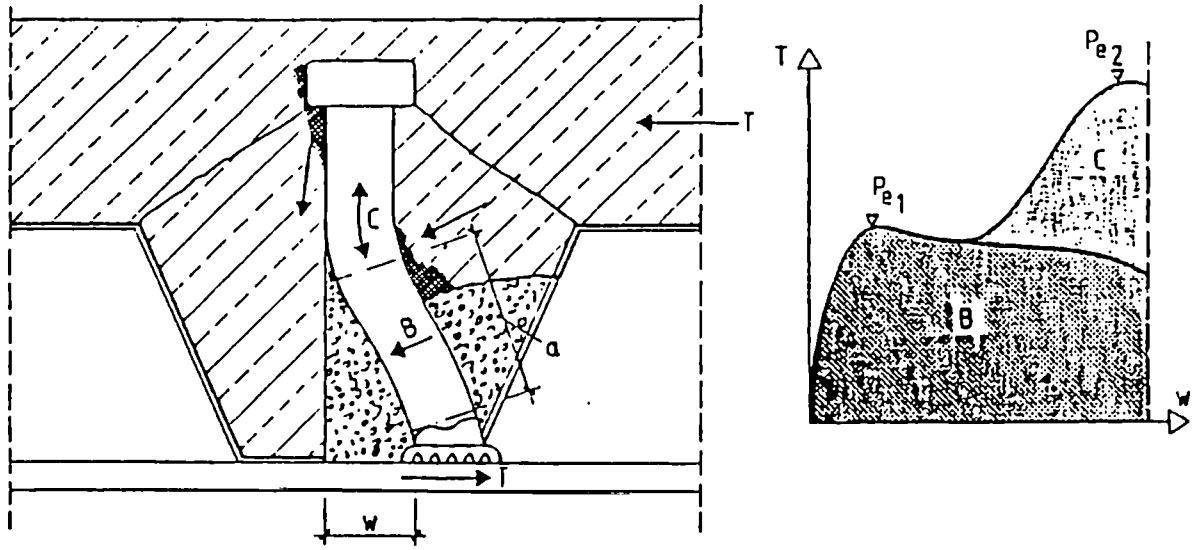

Figure 4.16: The two-hinge failure mechanism of studs in slabs with metal decking spanning perpendicular to the span of the beam, as described by Lungerhausen [76].

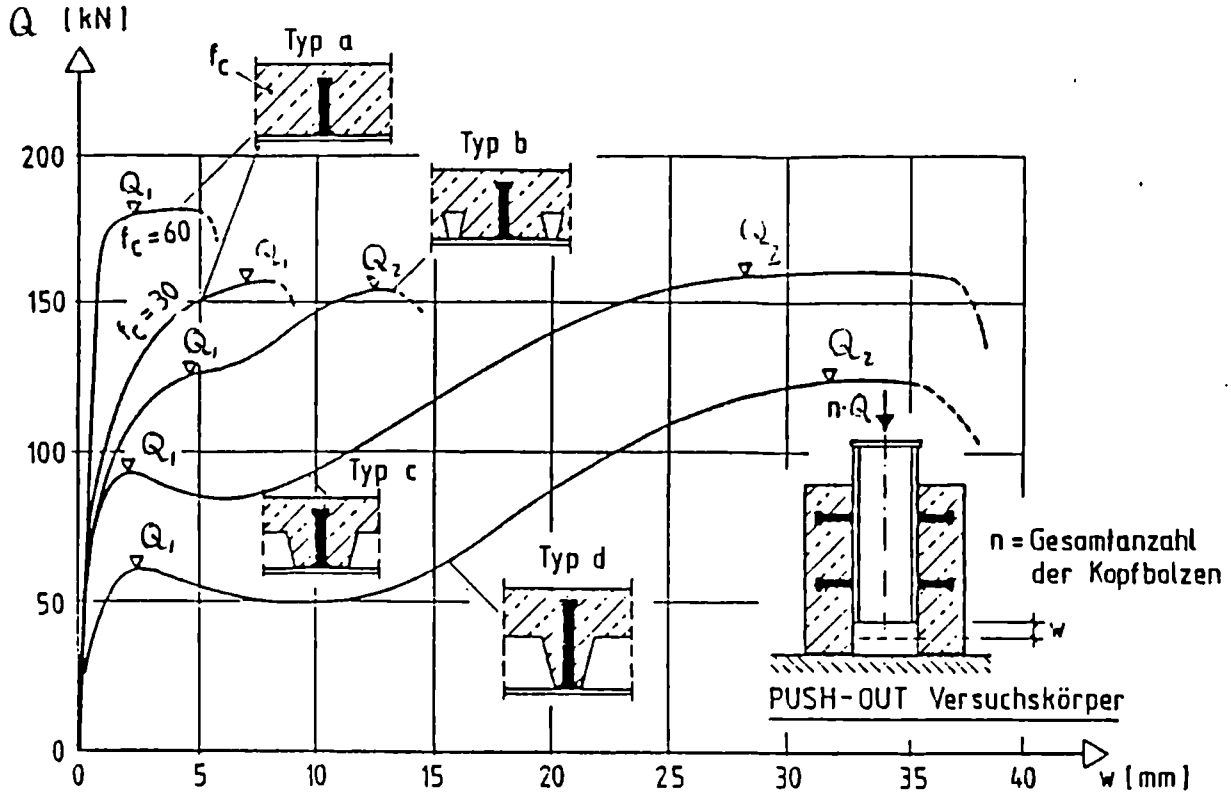

Figure 4.17: Different load-slip curves of studs embedded in different types of slabs, as found by Lungerhausen [76].

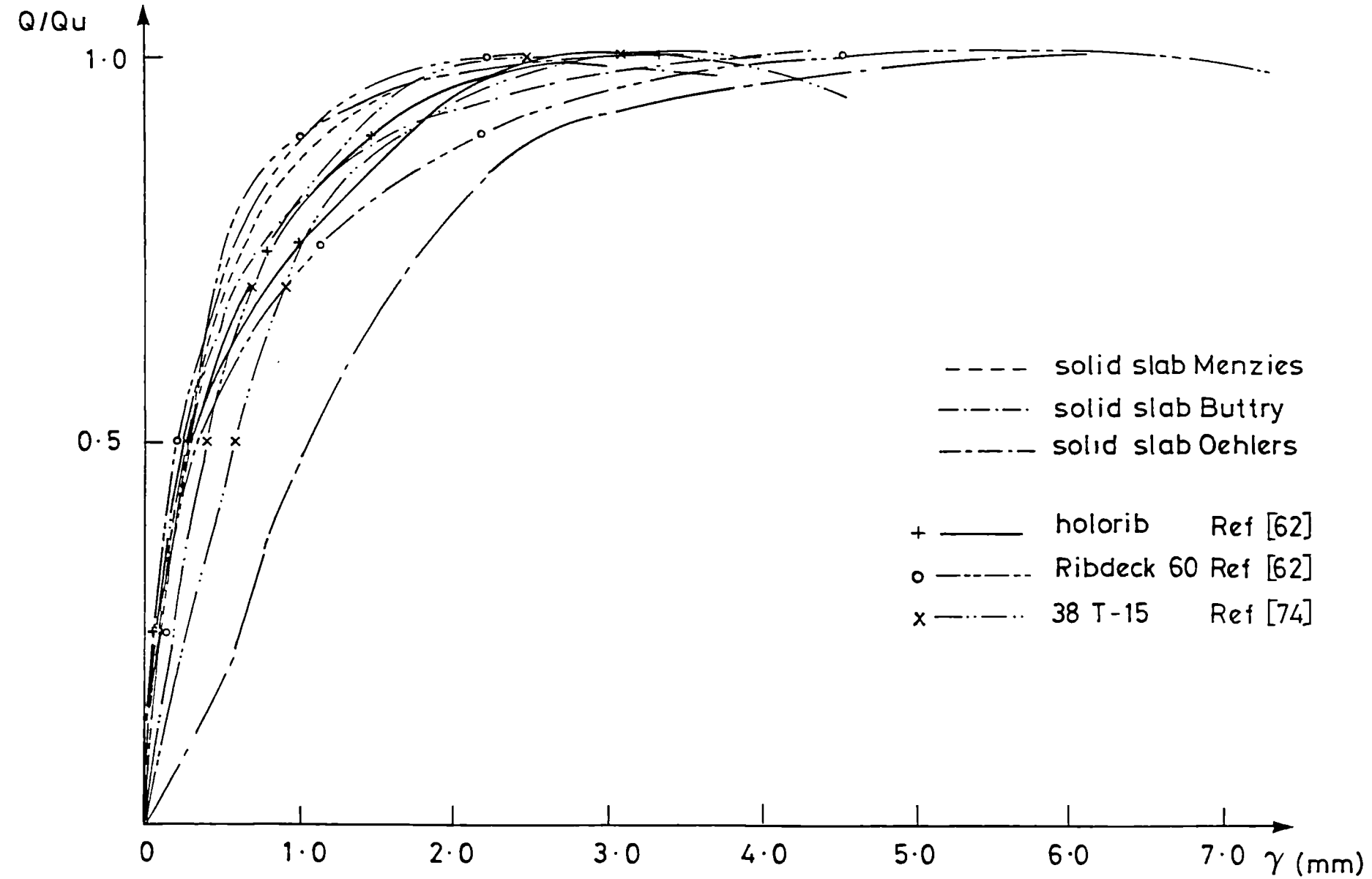

Figure 4.18: Comparison of the elastic stiffness of the load-slip curves of studs in solid slabs and slabs with metal decking running perpendicular to the span of the beam.

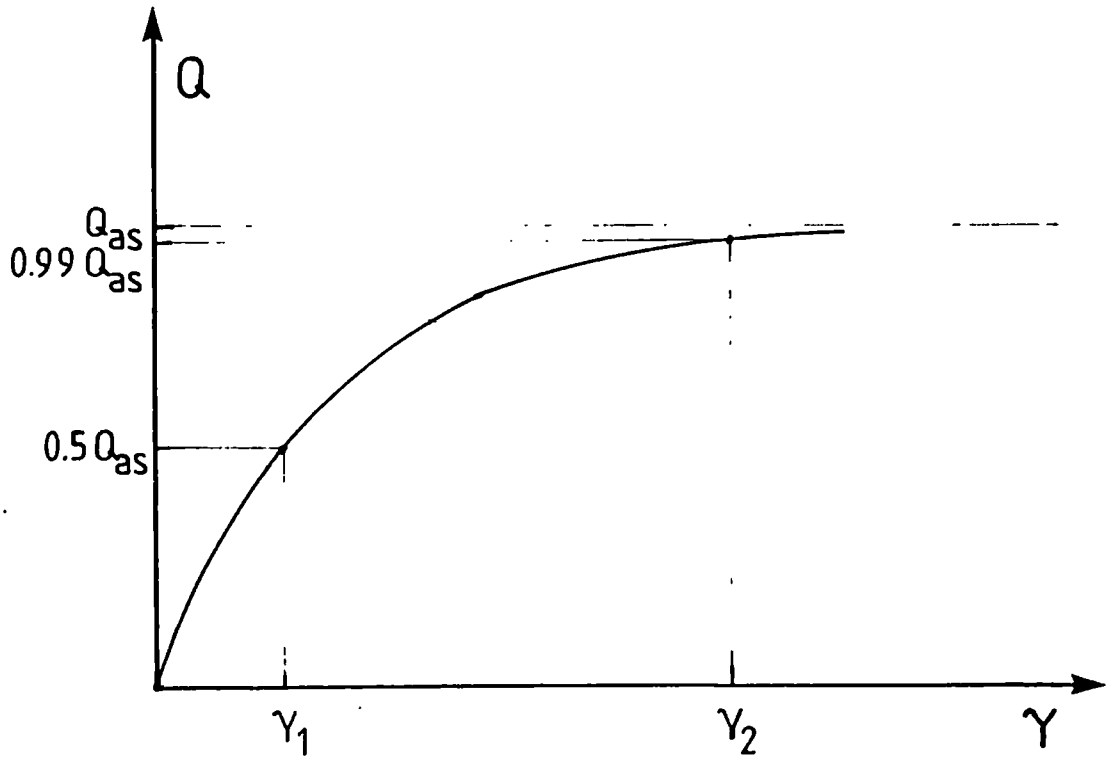

Figure 4.19: Numerical exponential model of the experimental load-slip curves of studs in solid slabs, characterised by an asymptotic value for the shear strength and by two points : one at $0.5Q_{as}$ and one at $0.99Q_{as}$.

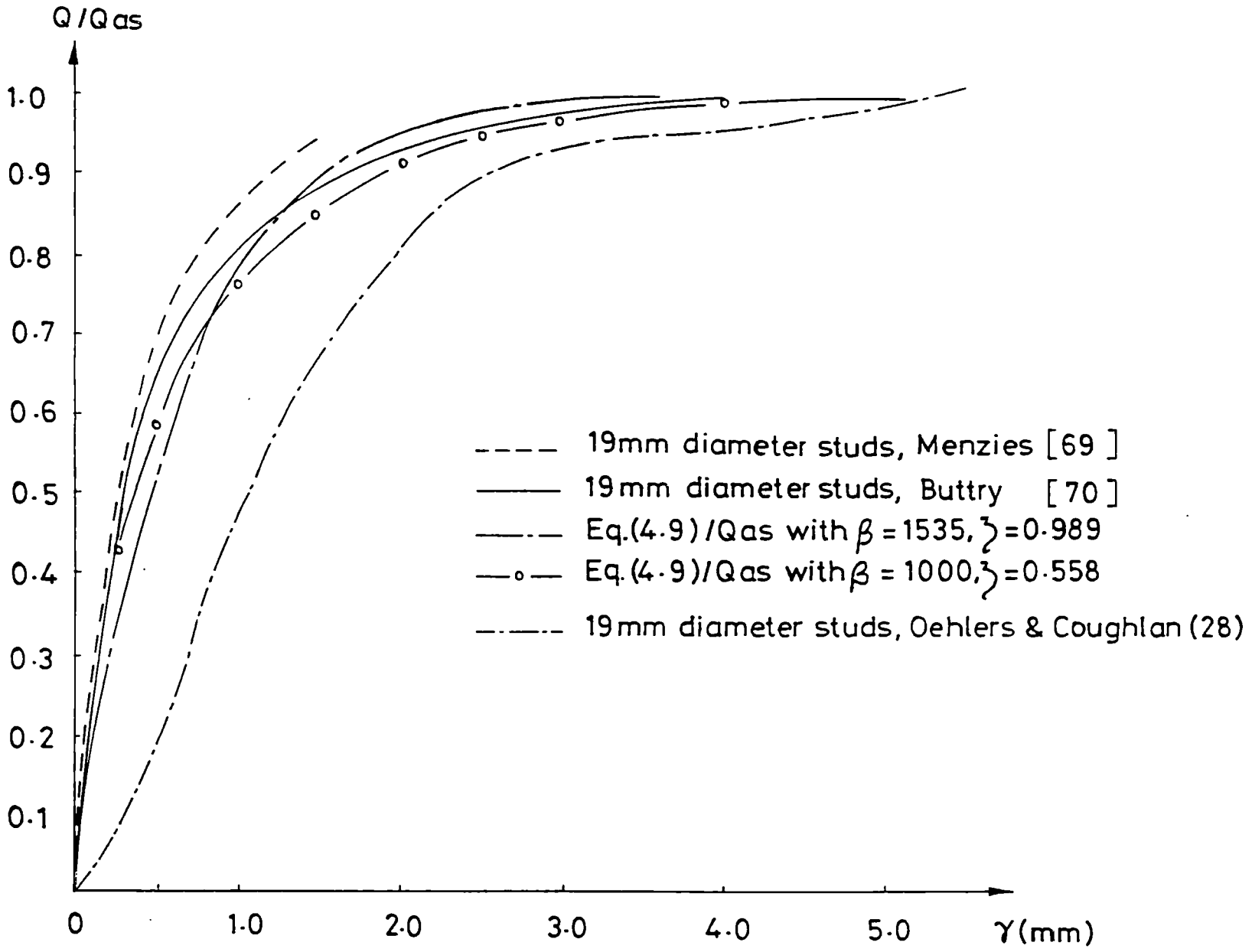

Figure 4.20: Comparison of commonly used numerical exponential load-slip curves with the average experimental curves generated from Push-Out tests.

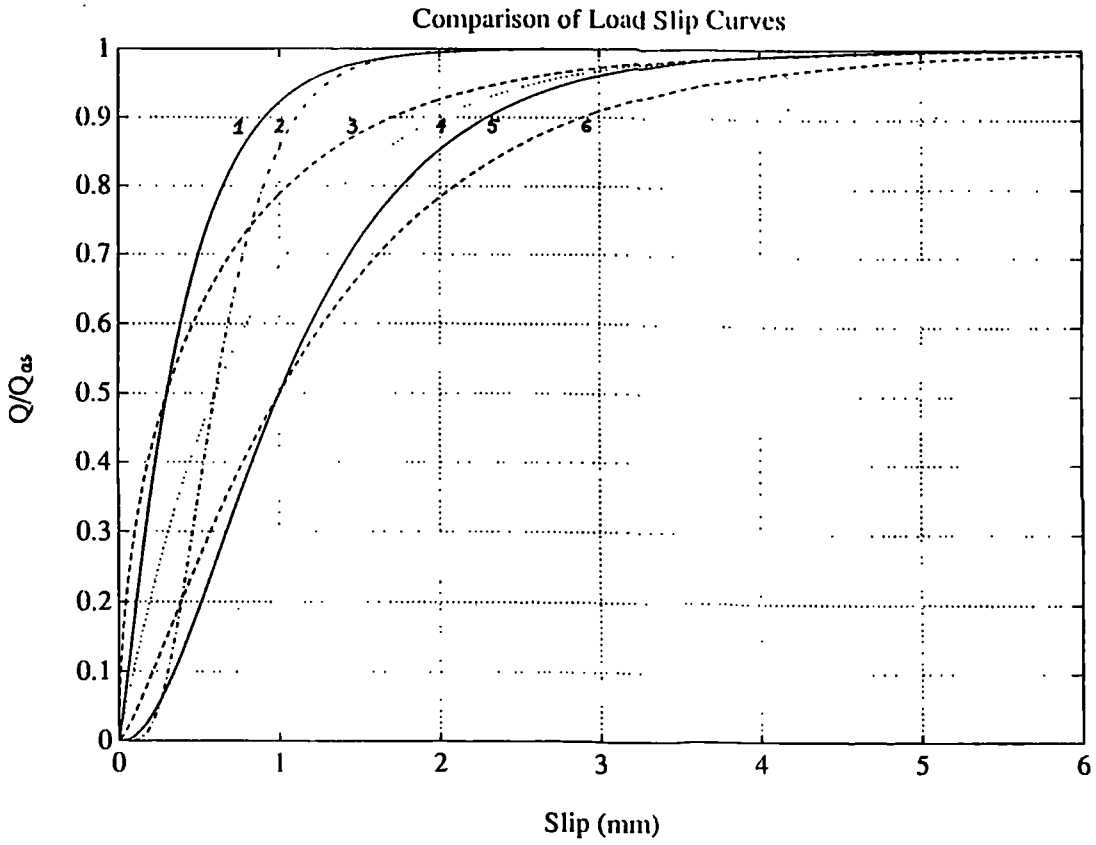

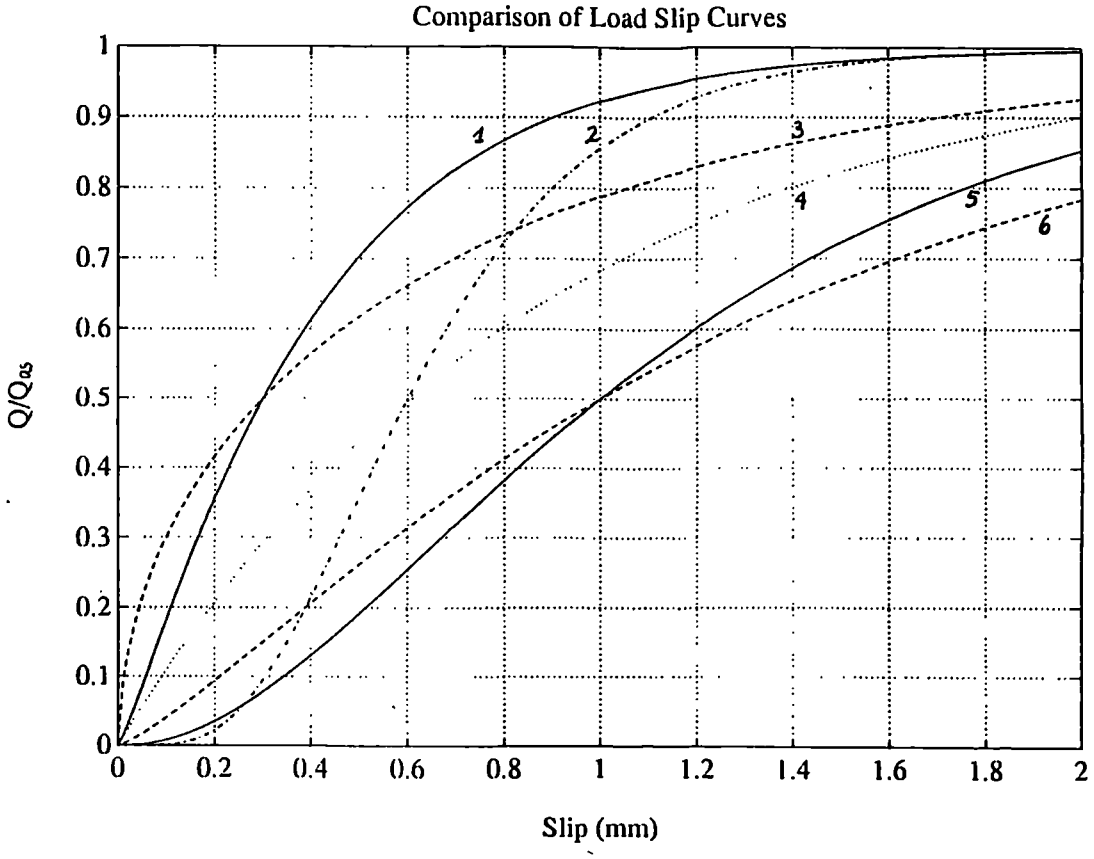

Figure 4.21: Six different exponential load-slip curves characterised by the same asymptotic shear strength, different elastic stiffnesses and different values of the slip at $0.99Q_{as}$.

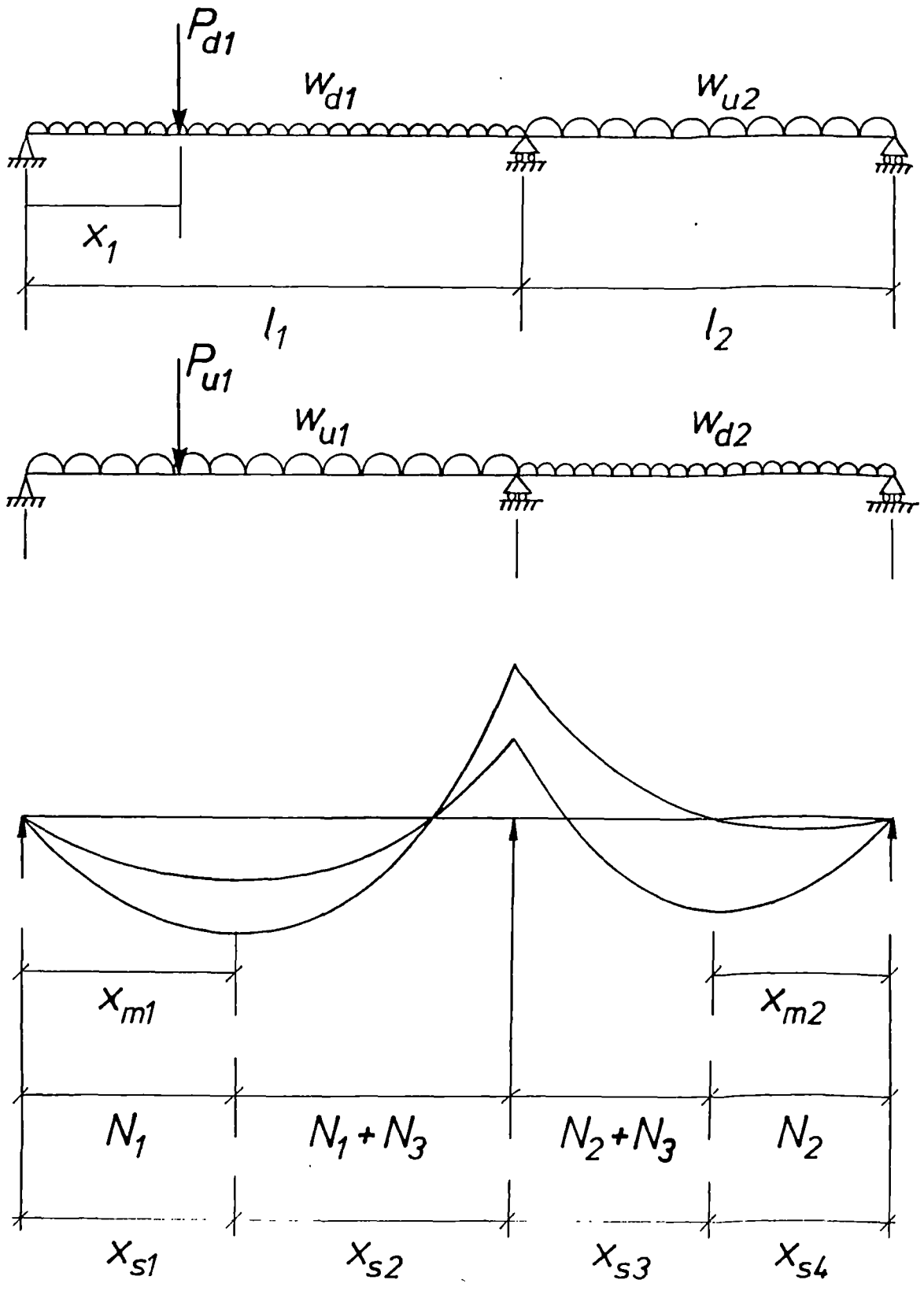

Figure 4.22: Moment envelope type 1 for two span continuous composite beams with sagging bending in both spans.

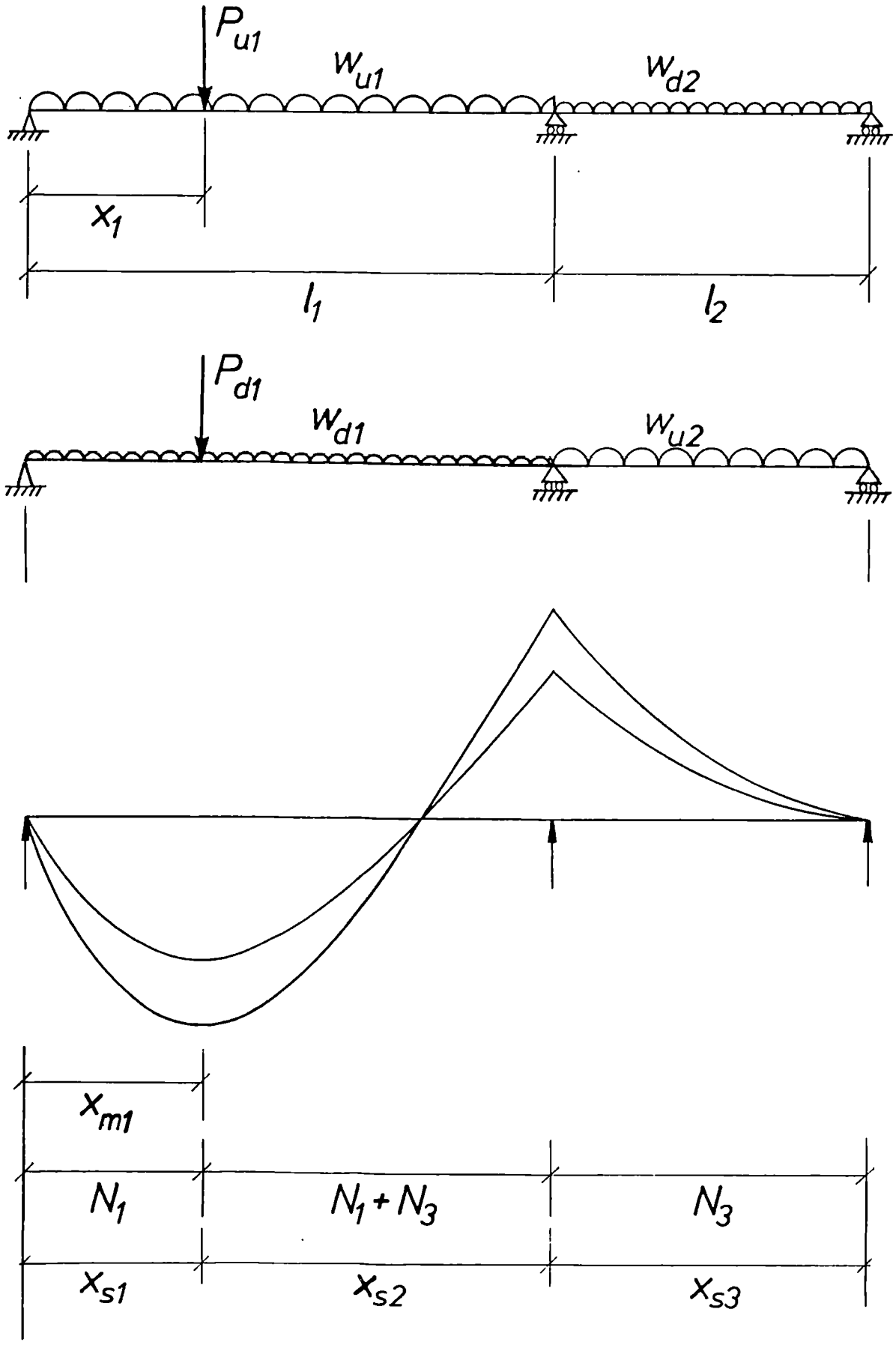

Figure 4.23: Moment envelope type 2 for two span continuous composite beams, where the second span remains permanently in hogging bending.

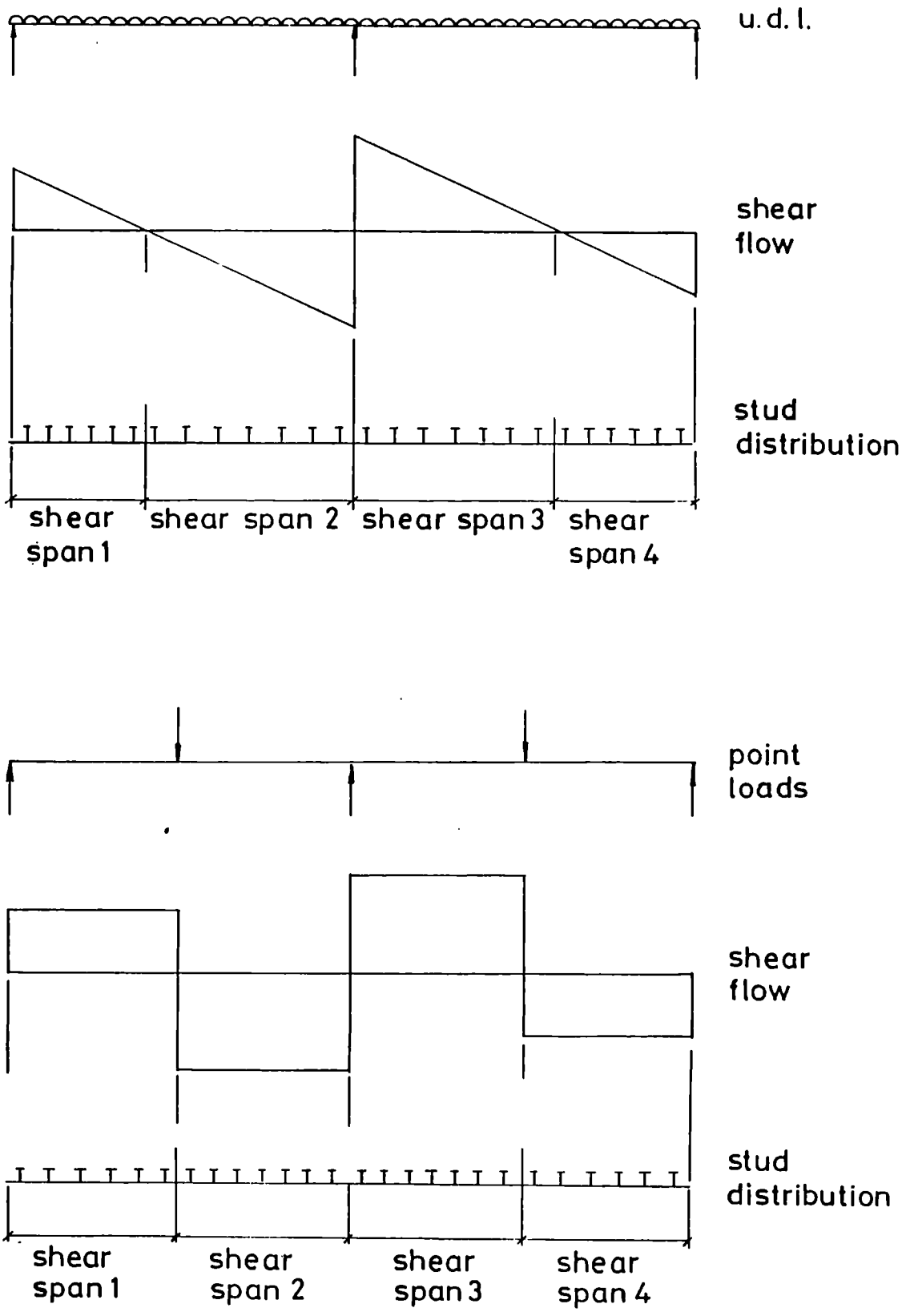

Figure 4.24: Comparison of theoretical shear flow diagrams for two span continuous composite beams subject to a uniform distributed load and a point load.

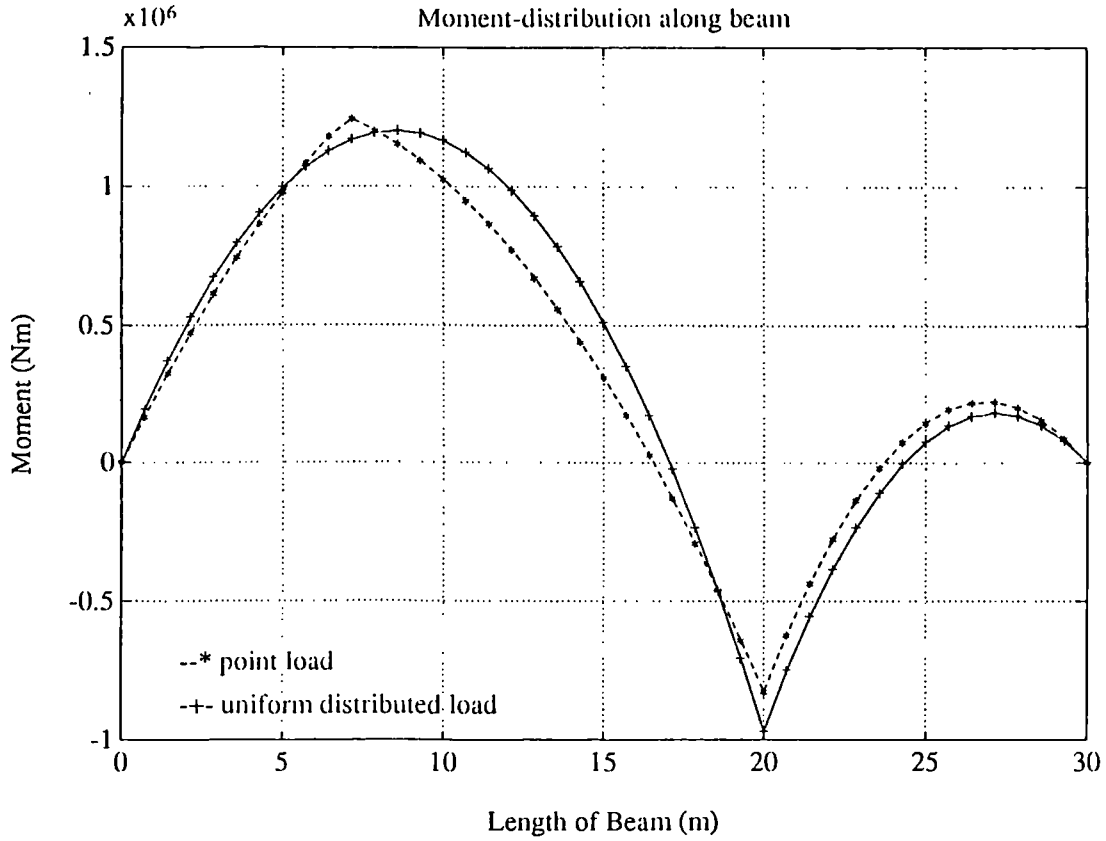

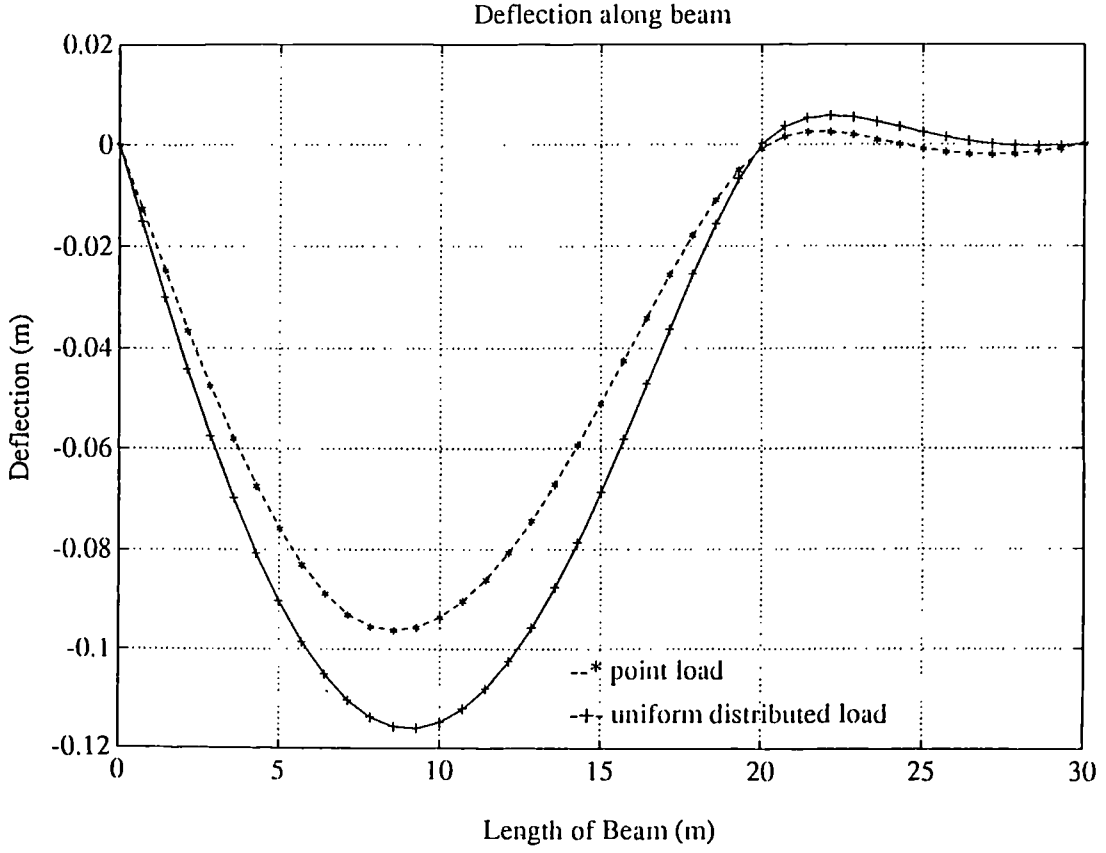

Figure 4.25(a): Comparison of moment and deflection distributions along beams CB11 and CB12 of Table 4.7.

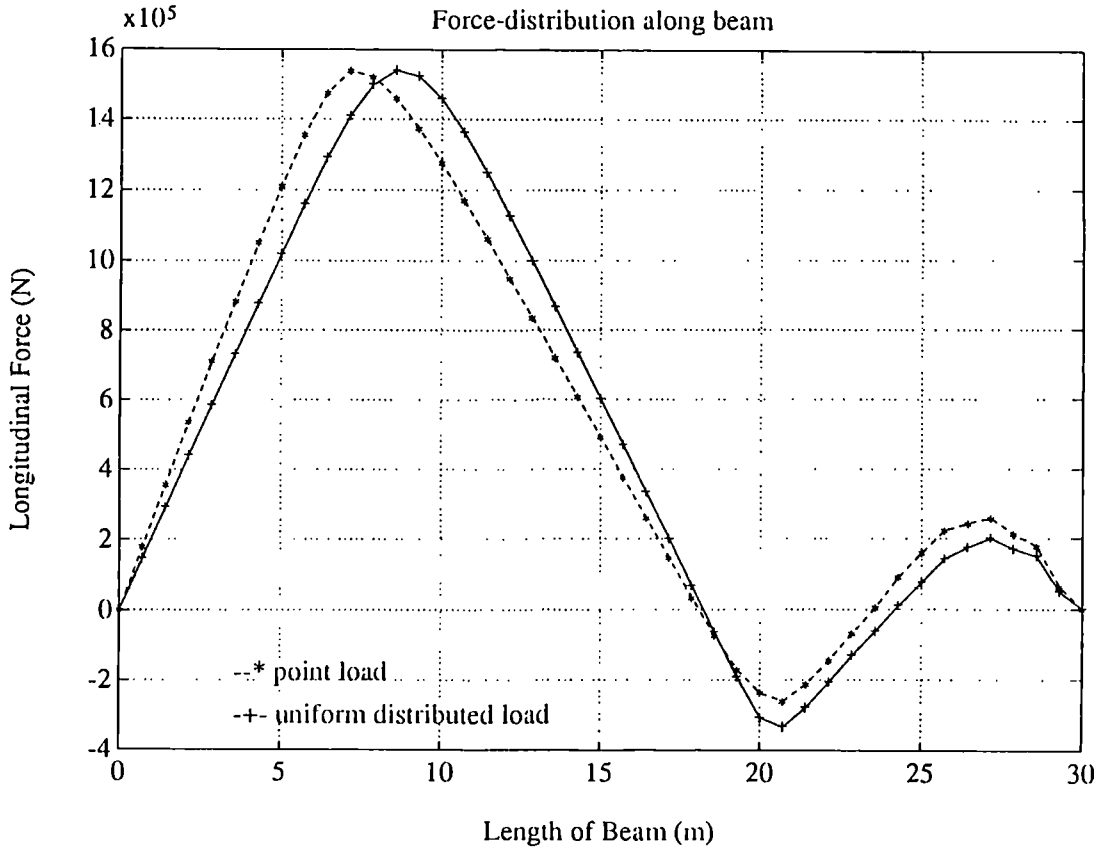

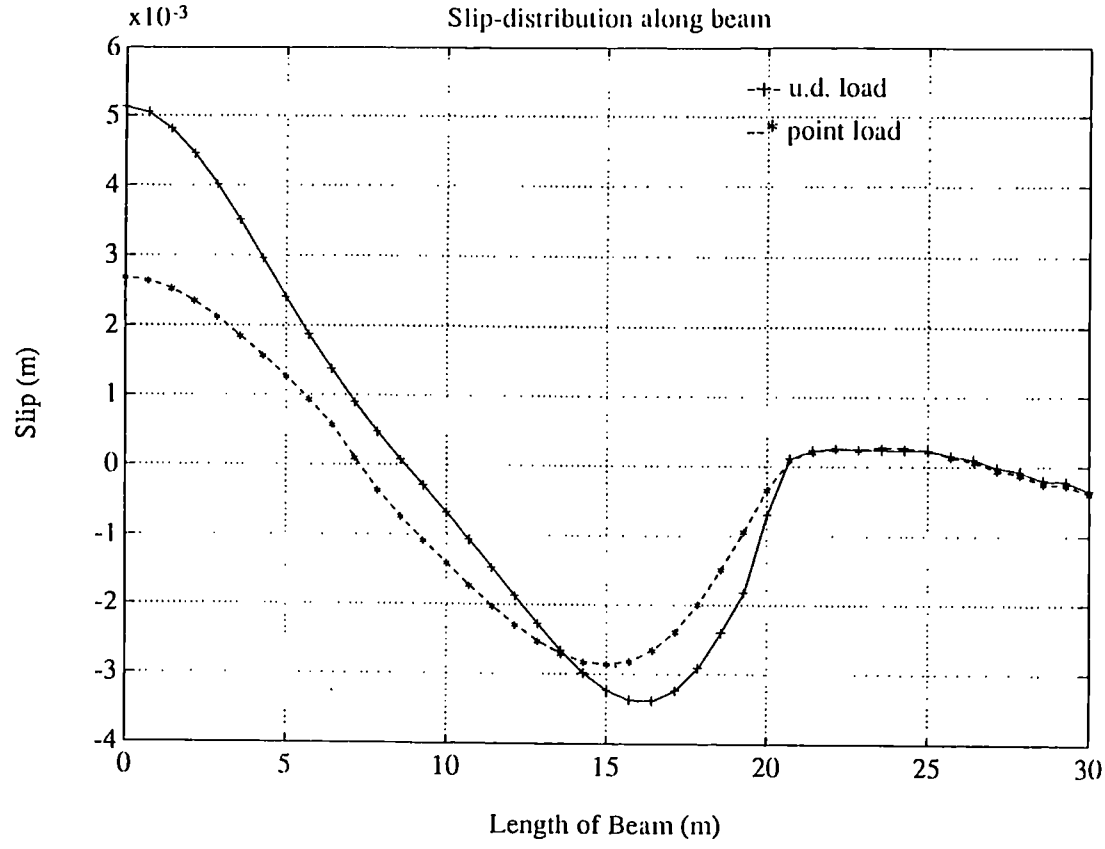

Figure 4.25(b): Comparison of shear force and slip distributions along beams CB11 and CB12 of Table 4.7.

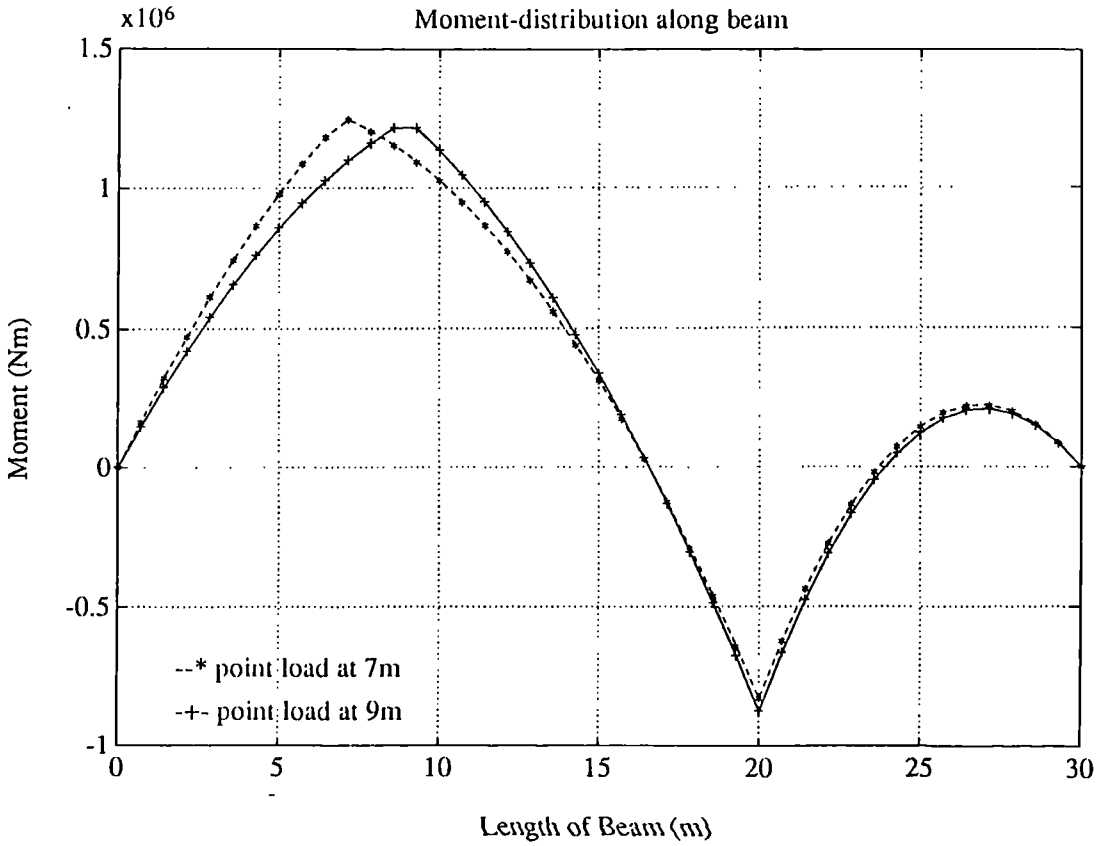

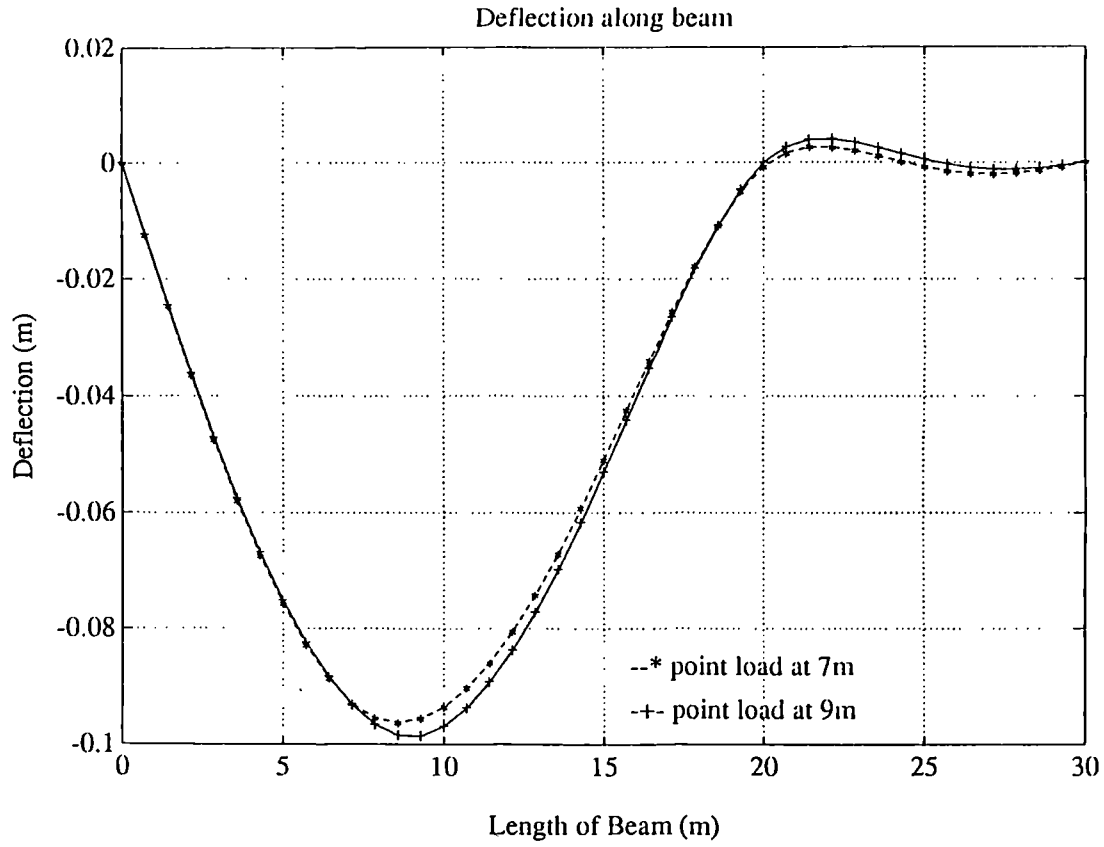

Figure 4.26(a): Comparison of moment and deflection distributions along beams CB11 and CB13 of Table 4.7.

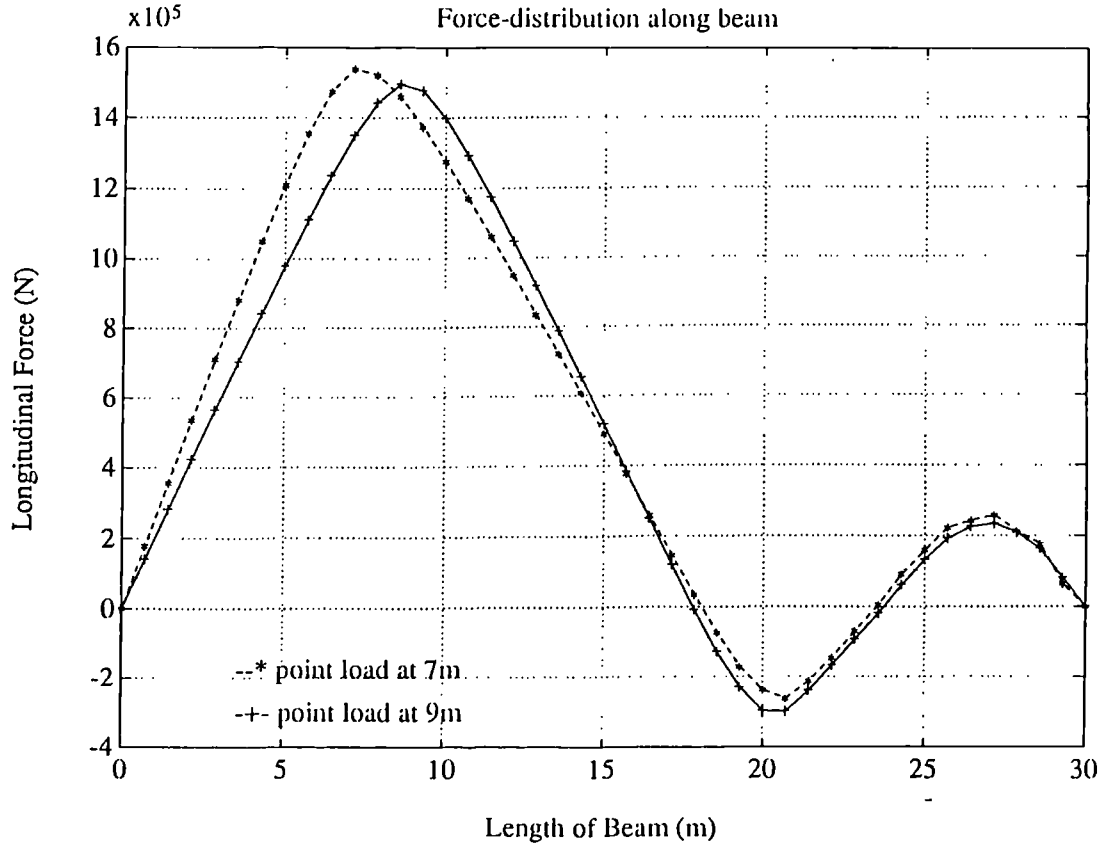

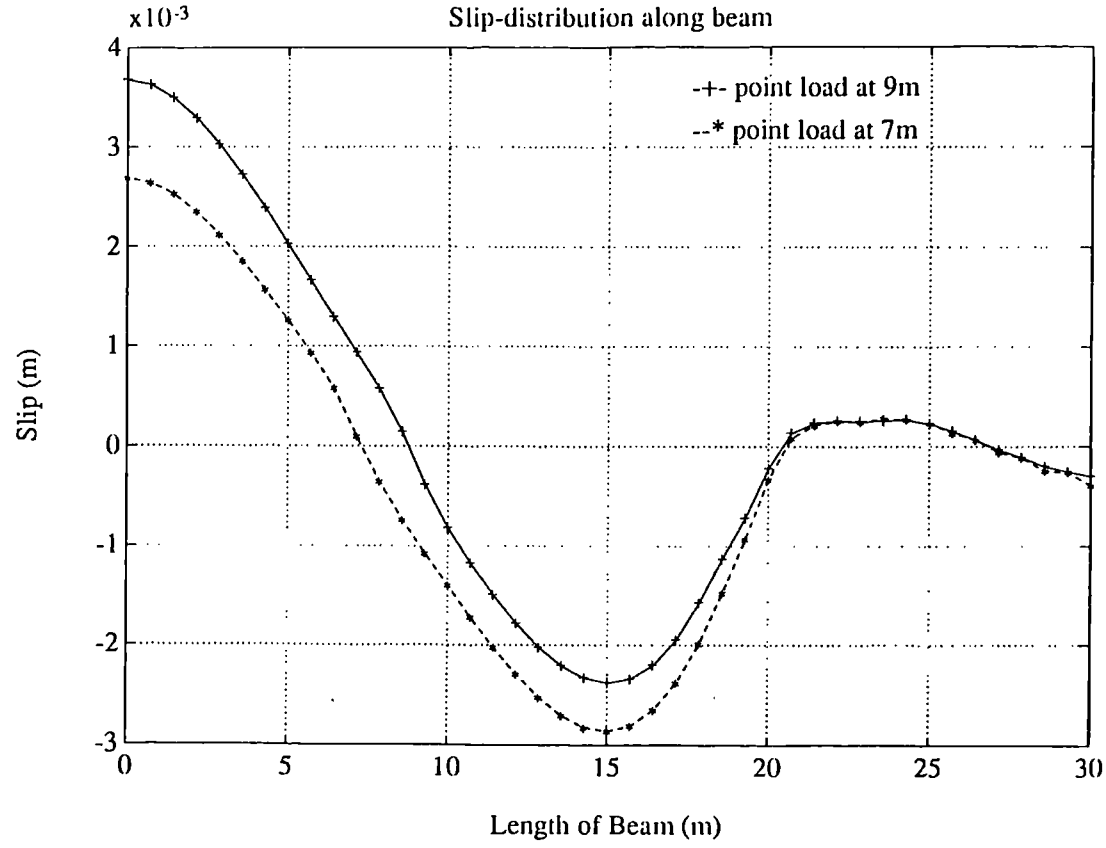

Figure 4.26(b): Comparisons of shear force and slip distributions along beams CB11 and CB13 of Table 4.7

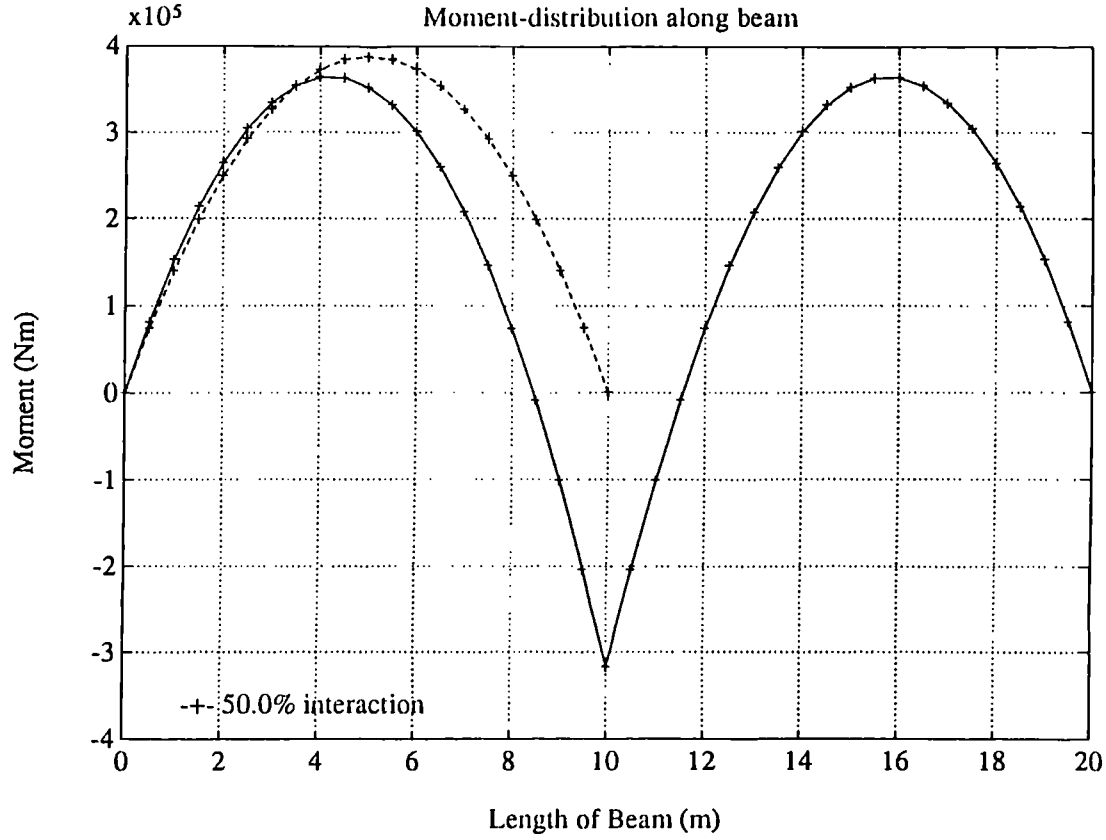

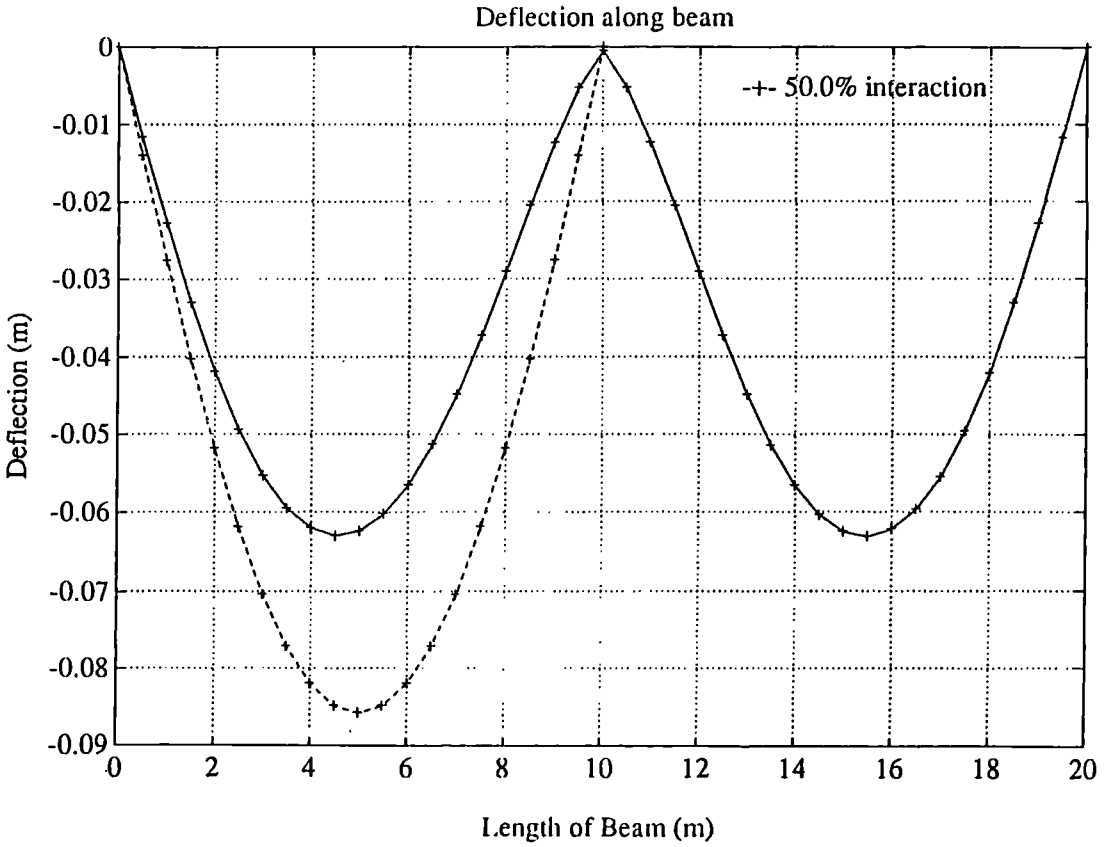

Figure 4.27: Comparisons between moment, deflection, shear force, slip and strain distributions at 50% interaction along beam $CB1$ of Table 4.7 and beam $CB - SB1$ of Table 4.8.

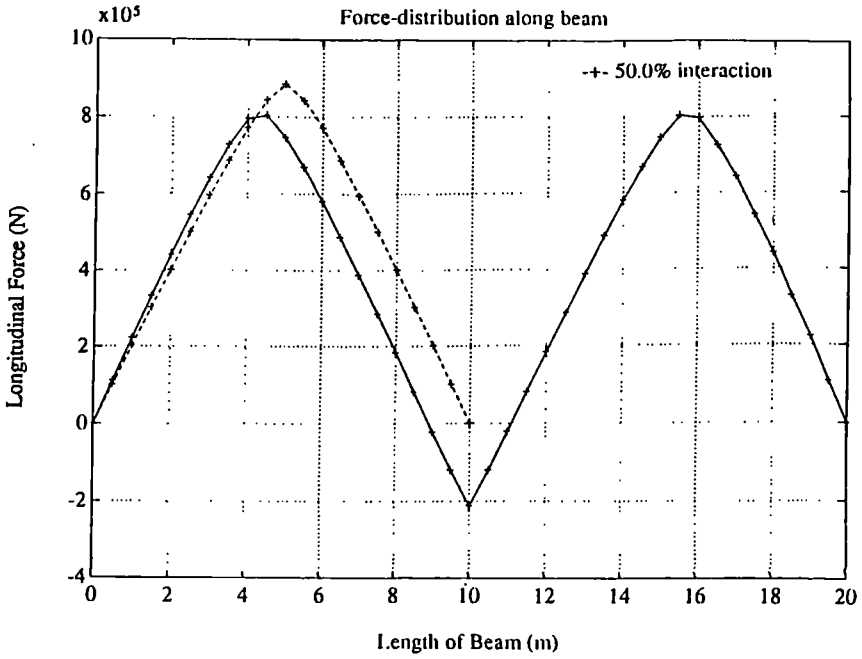
x10^5
Force-distribution along beam
-+- 50.0% interaction
Longitudinal Force (N)
Length of Beam (m)

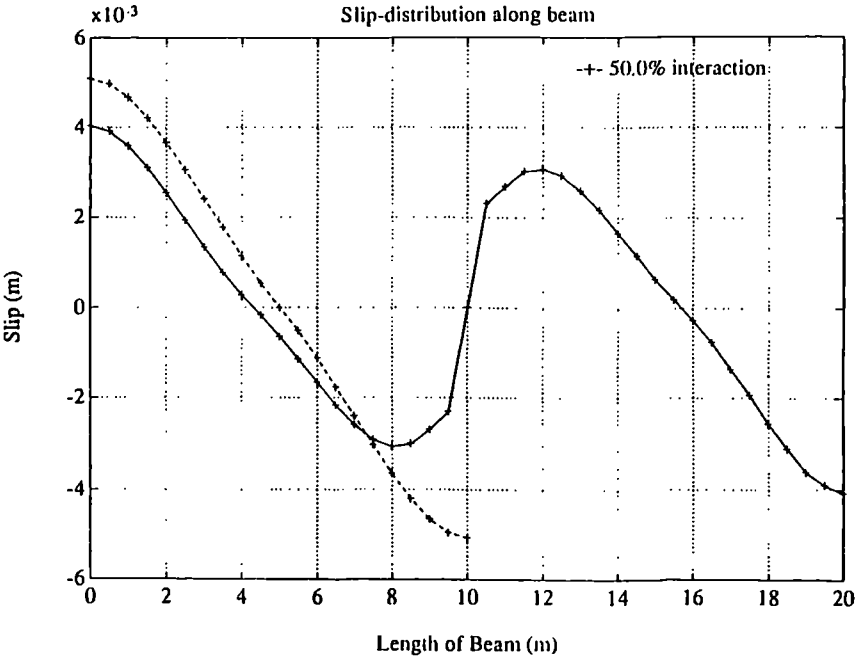
x10^-3
Slip-distribution along beam
-+- 50.0% interaction
Slip (m)
Length of Beam (m)

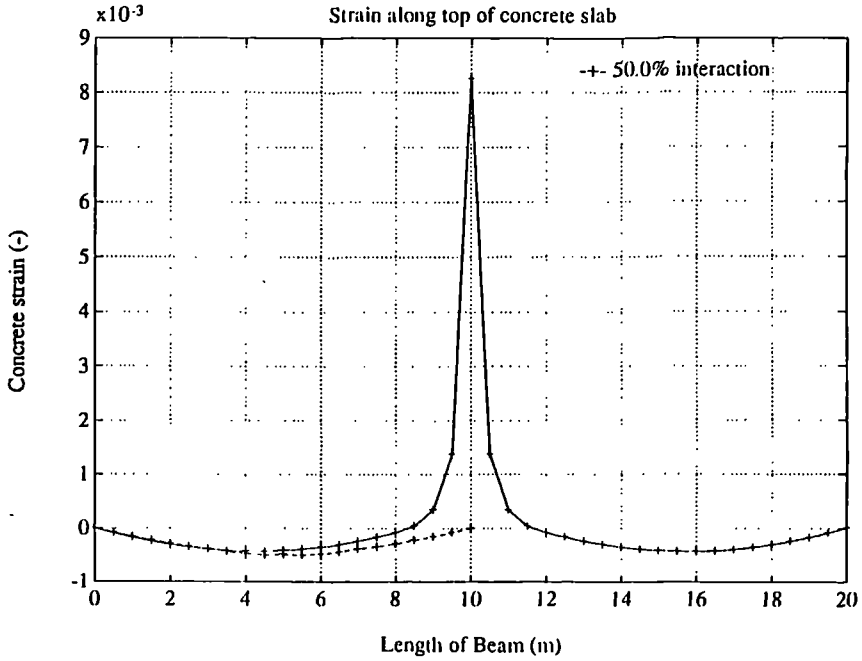
x10^-3
Strain along top of concrete slab
-+- 50.0% interaction
Concrete strain (-)
Length of Beam (m)

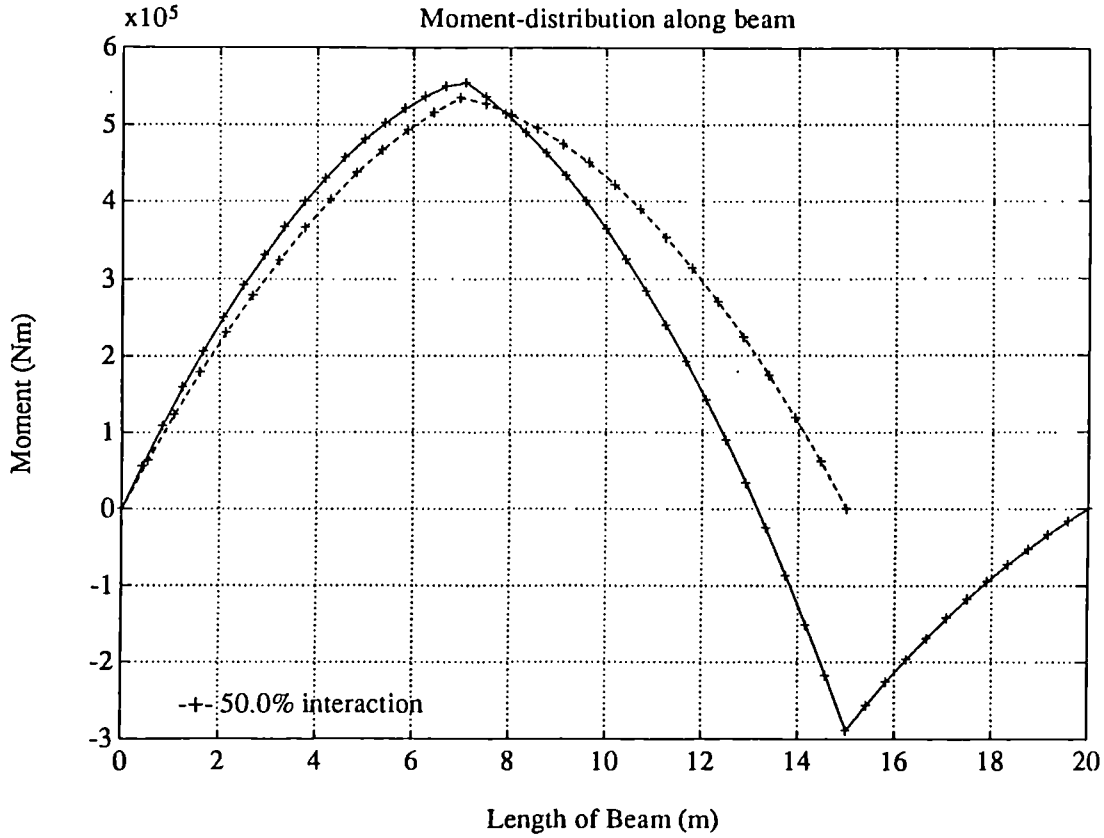

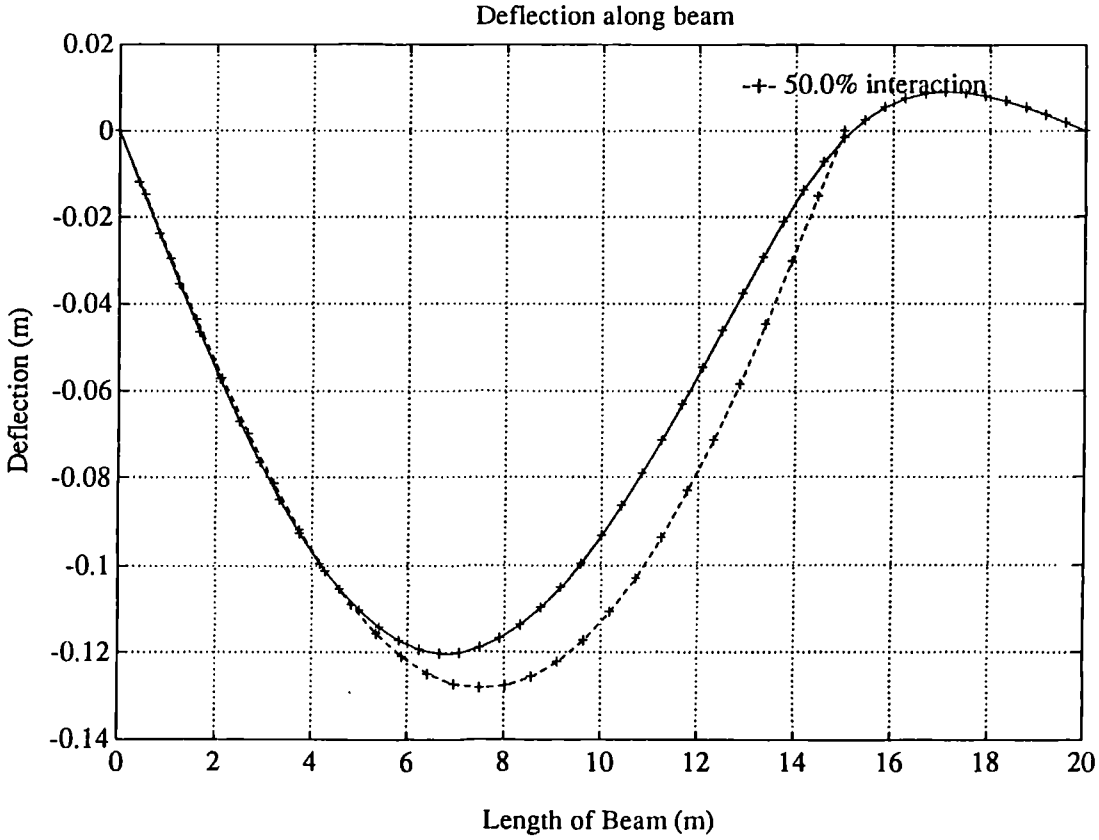

Figure 4.28: Comparisons between moment, deflection, shear force, and slip distributions at 50% interaction along beam $CB10$ of Table 4.7 and beam $CB - SB10$ of Table 4.8.

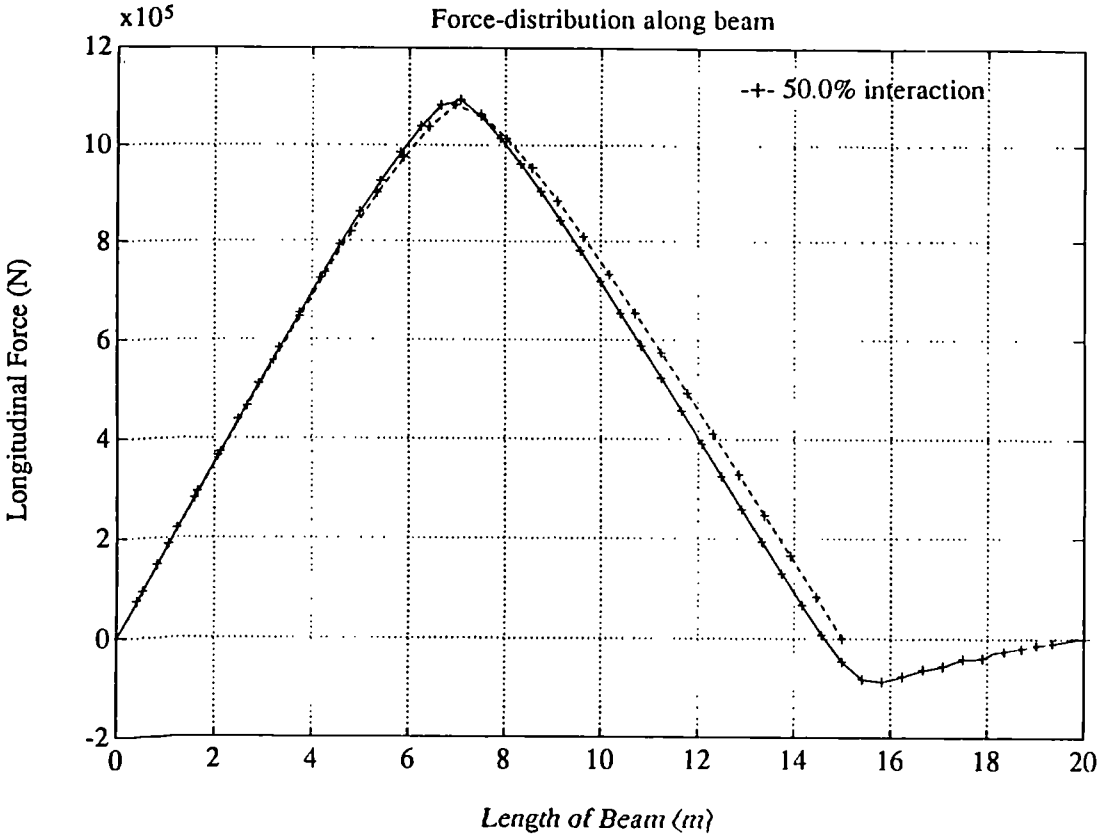
x10^5
Force-distribution along beam
-+- 50.0% interaction
Longitudinal Force (N)
Length of Beam (m)

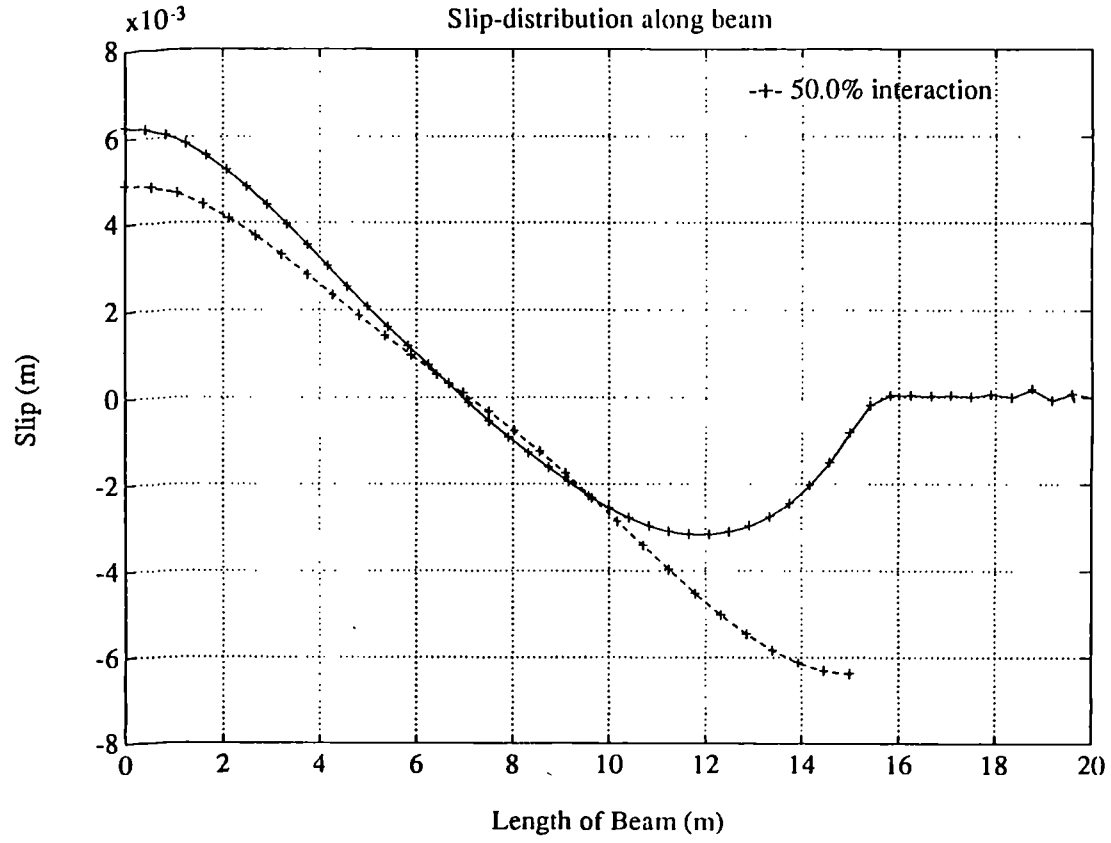
x10^-3
Slip-distribution along beam
-+- 50.0% interaction
Slip (m)
Length of Beam (m)

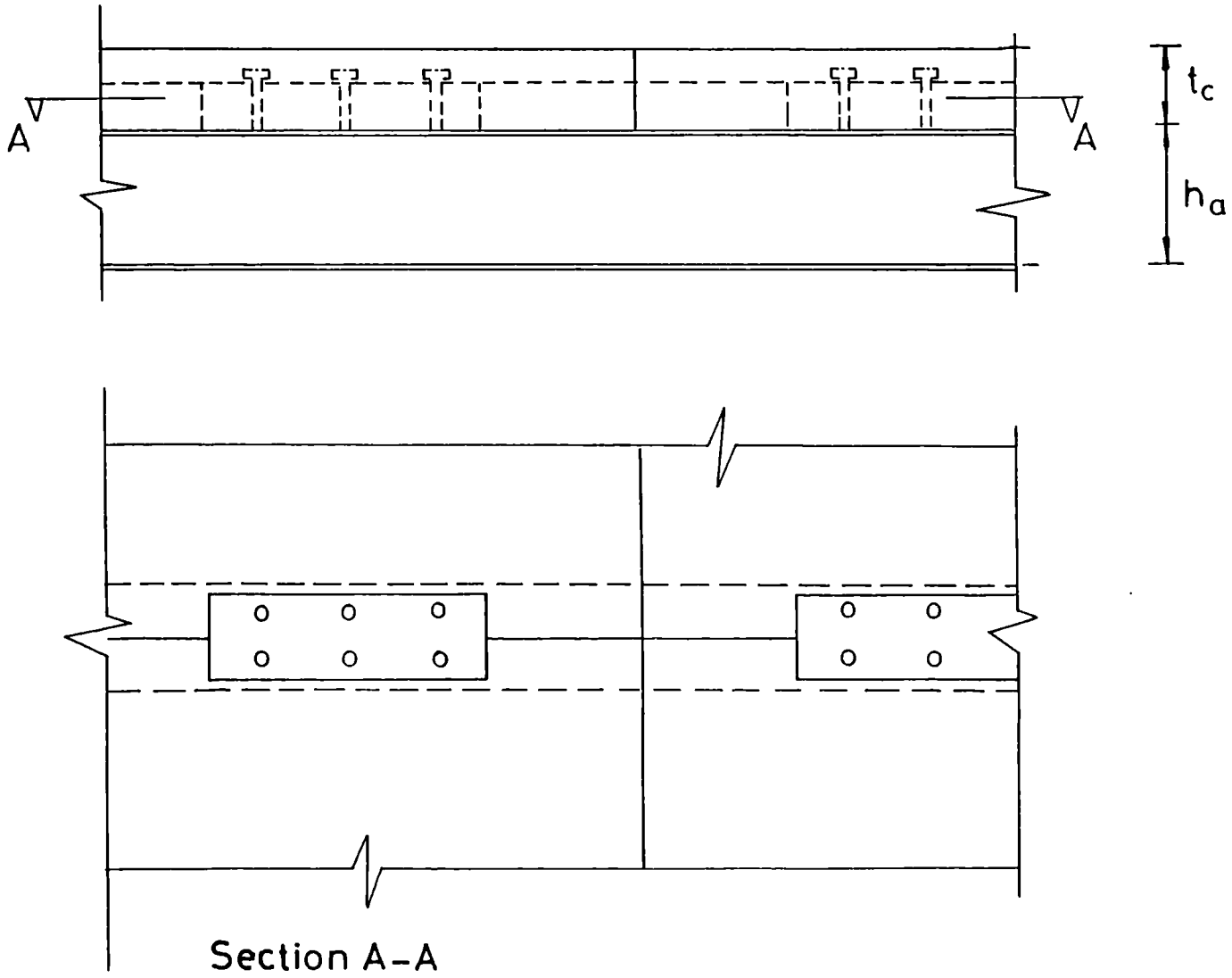

Figure 4.29: Elevation and plan view of beams with prefabricated slabs, leaving limited space for the positioning of stud connectors.

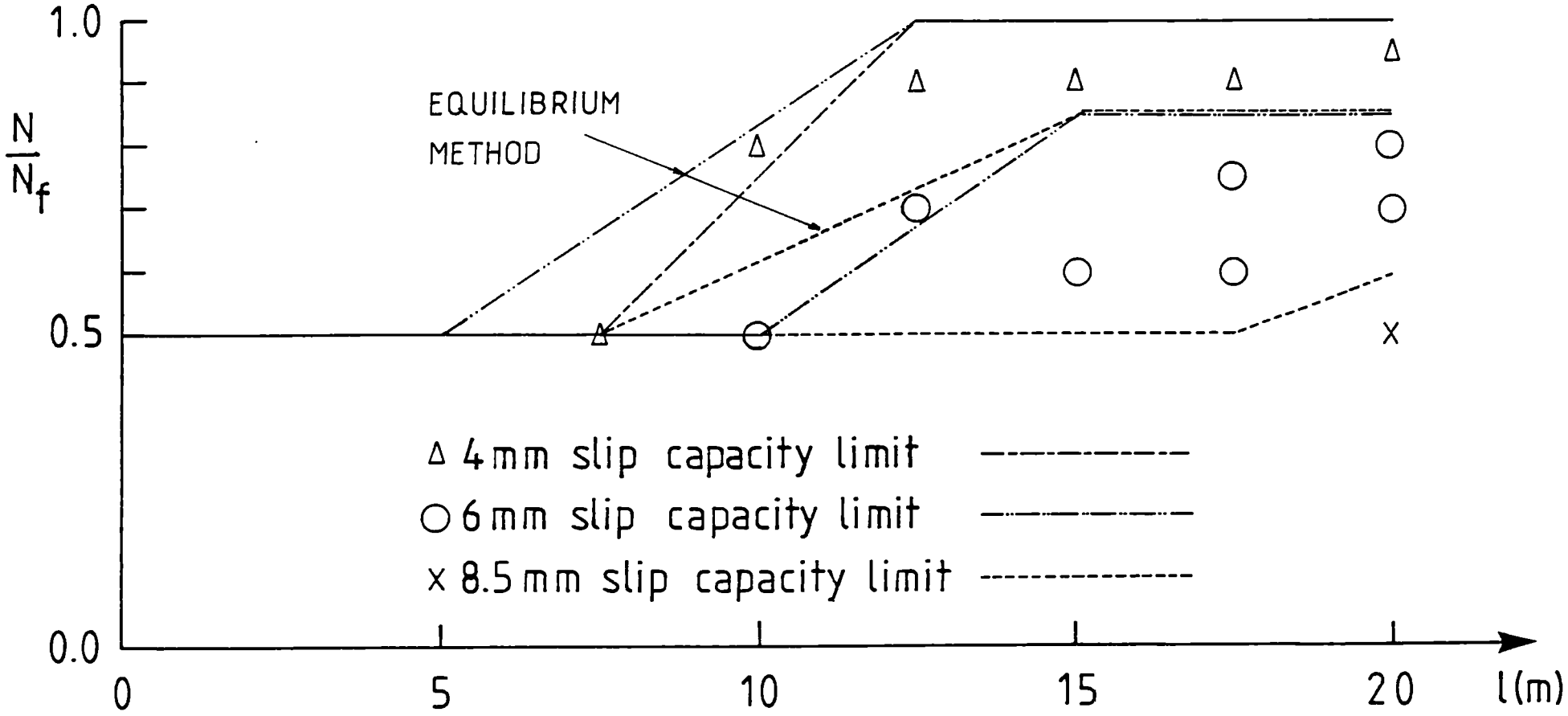

Figure 4.30: Span limitations on beams with rolled steel sections and solid concrete slabs in function of the connector ratio and of different slip capacity limits.

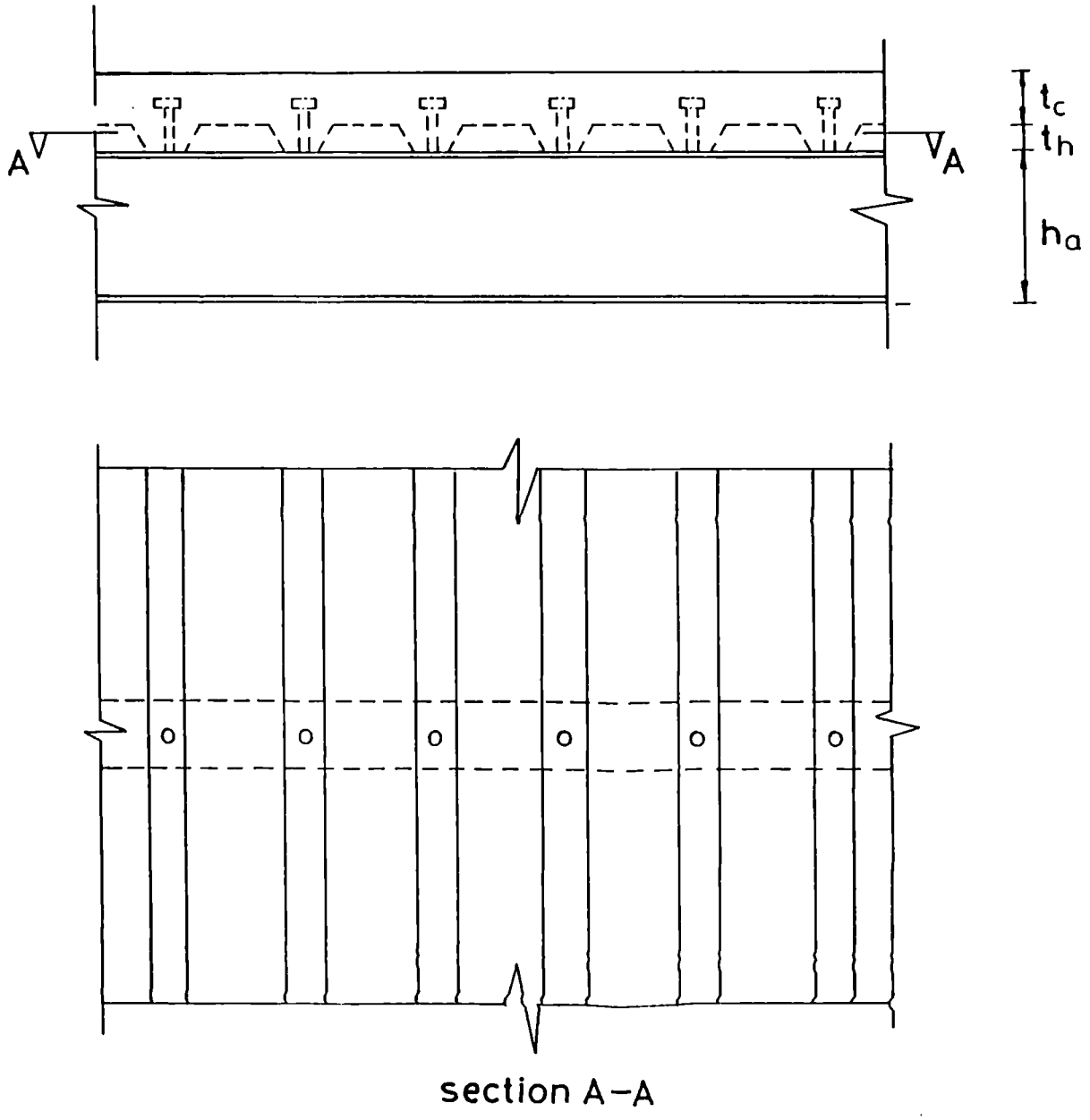

Figure 4.31: Elevation and plan view of beams with composite slabs, where the profiled steel sheeting runs perpendicular to the span of the beam.

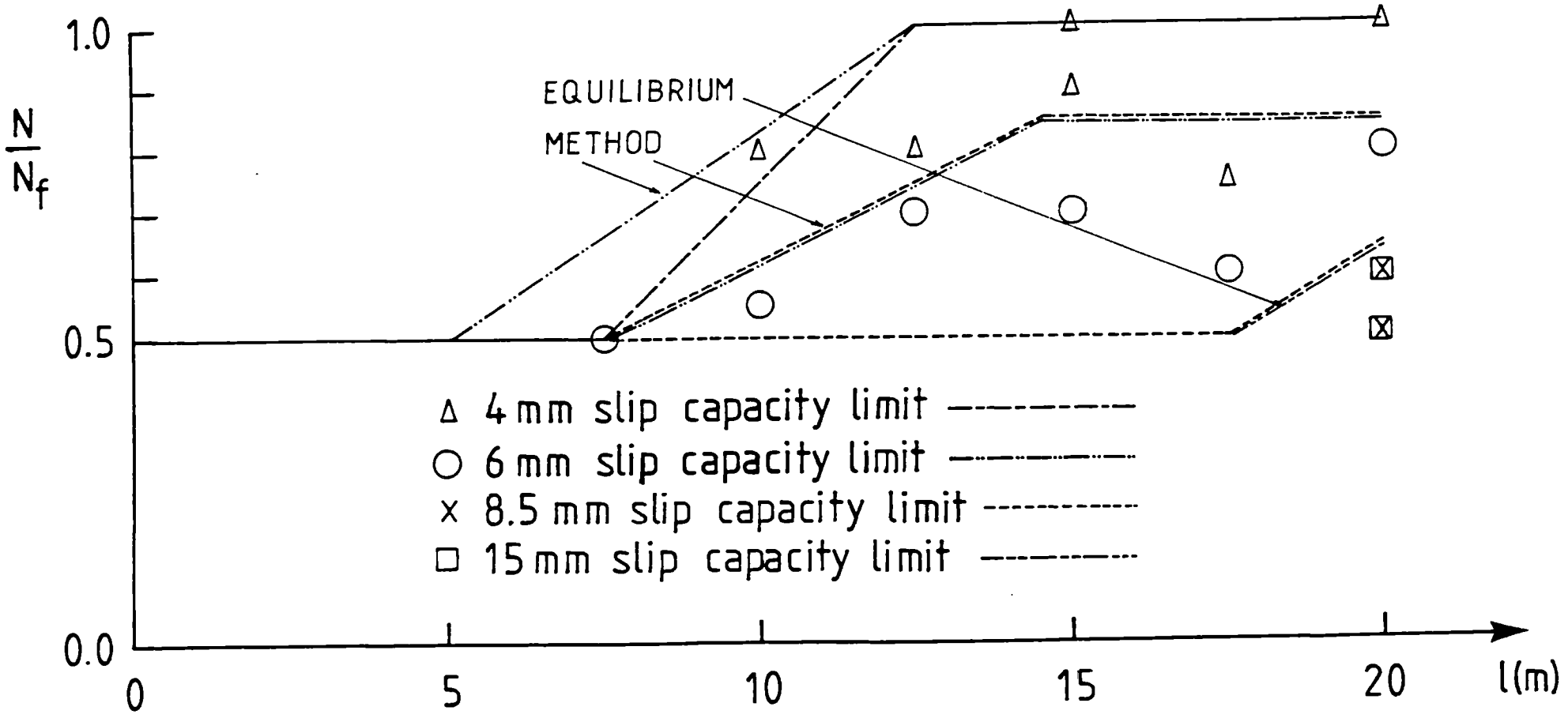

Figure 4.32: Span limitations on beams with rolled steel sections and composite slabs spanning perpendicular to the span, in function of the connector ratio and of different slip capacity limits.

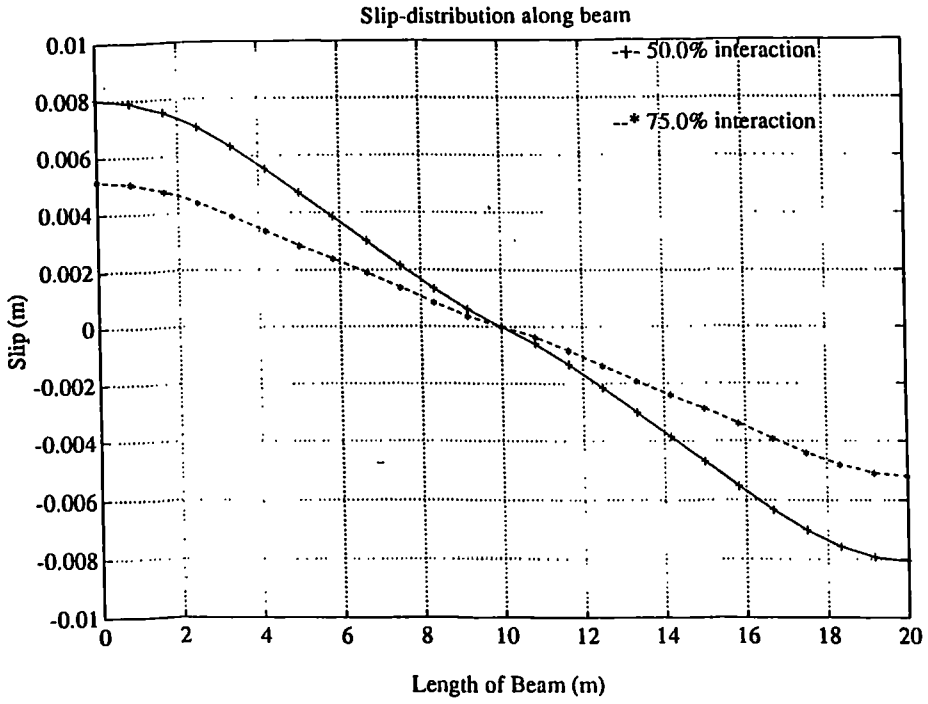

beam with solid slab

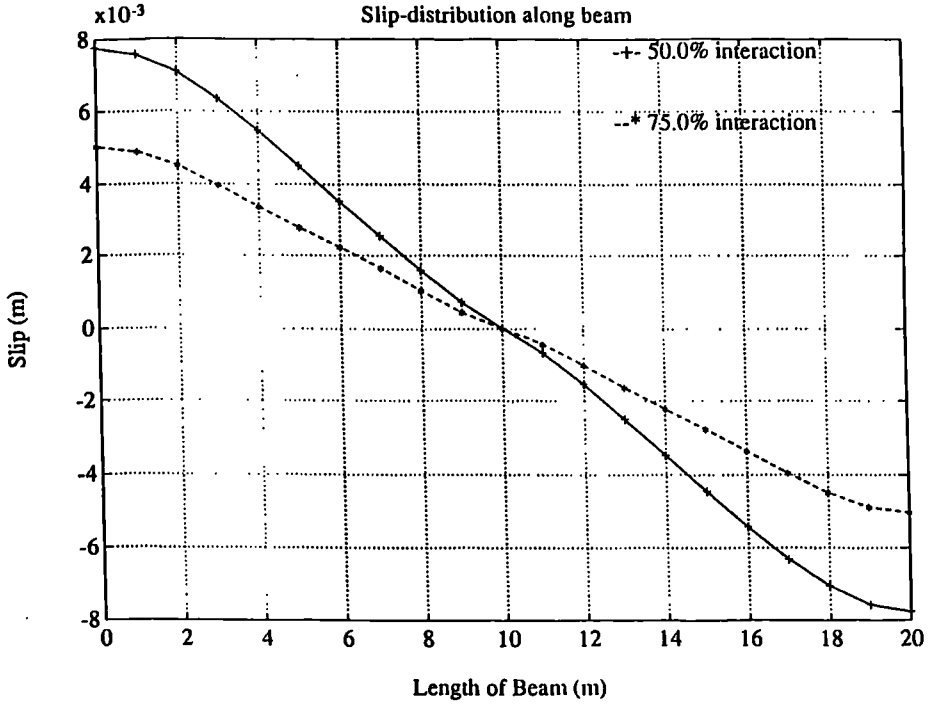

beam with metal decking perpendicular to the span

Figure 4.33(a): Influence of replacing a solid slab by a slab with metal decking of identical overall thickness, for beam SRM-25 of Table IV.2.

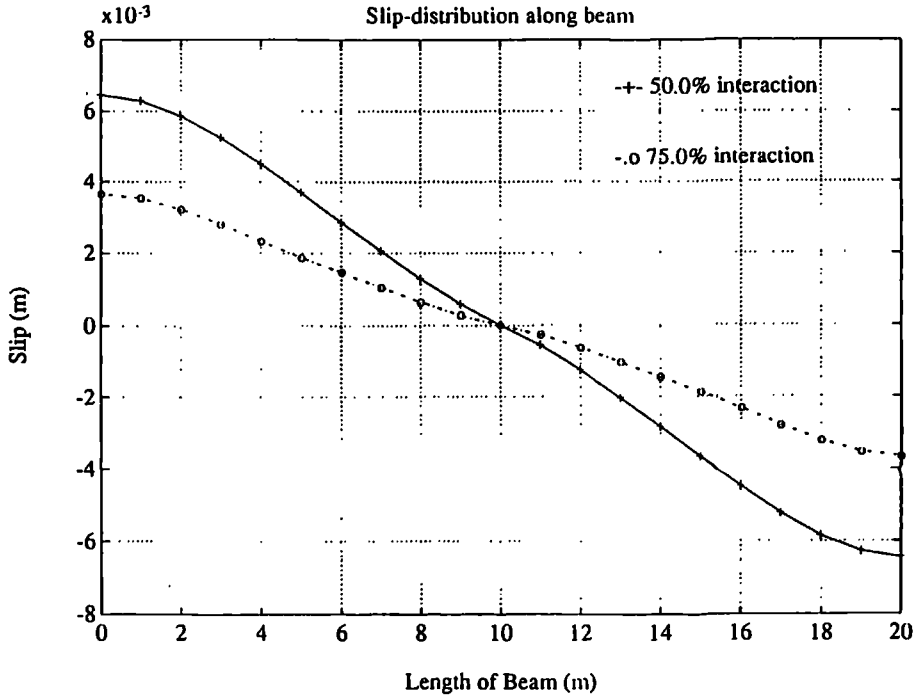

beam with solid slab

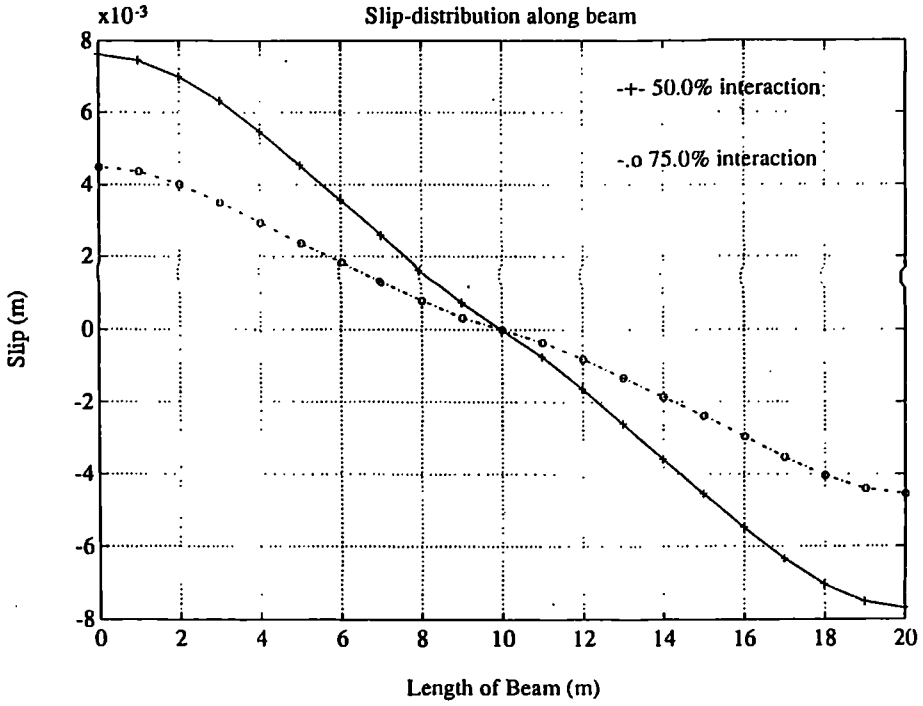

beam with metal decking perpendicular to the span

Figure 4.33(b): Influence of replacing a solid slab by a slab with metal decking of identical overall thickness, for beam SRM-30 of Table IV.2.

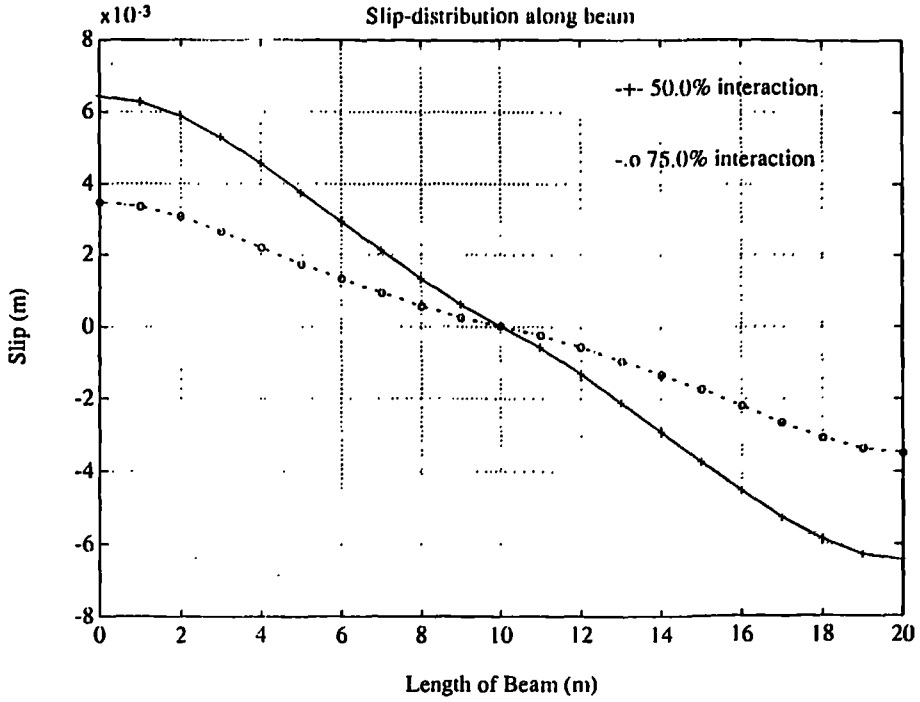

beam with solid slab

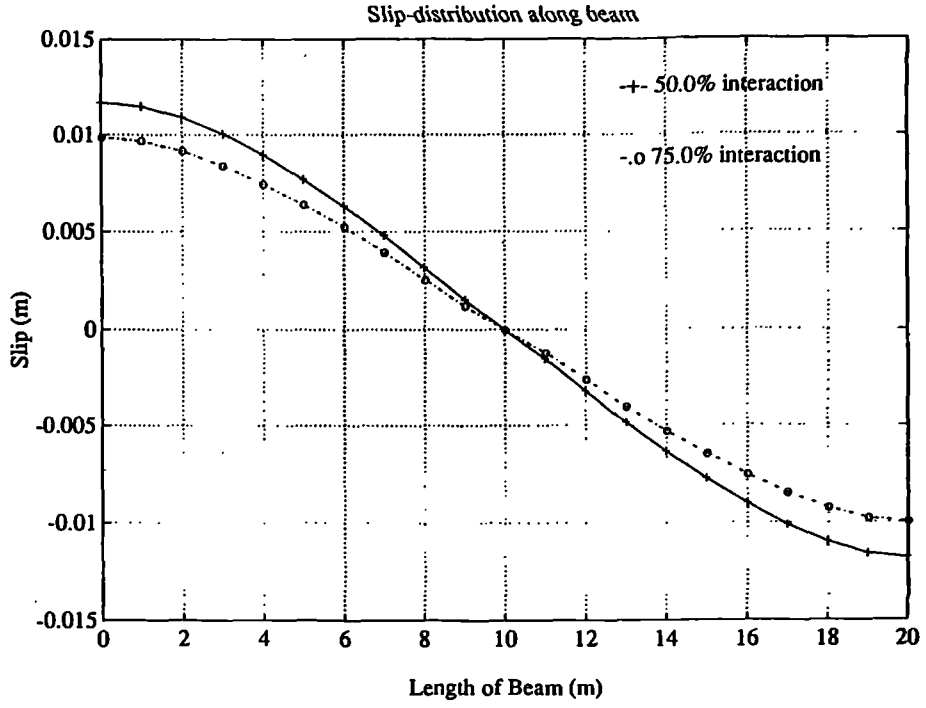

beam with metal decking perpendicular to the span

Figure 4.34: Influence of replacing a solid slab by a slab with metal decking of identical thickness for beam SRM-29 of Table IV.2.

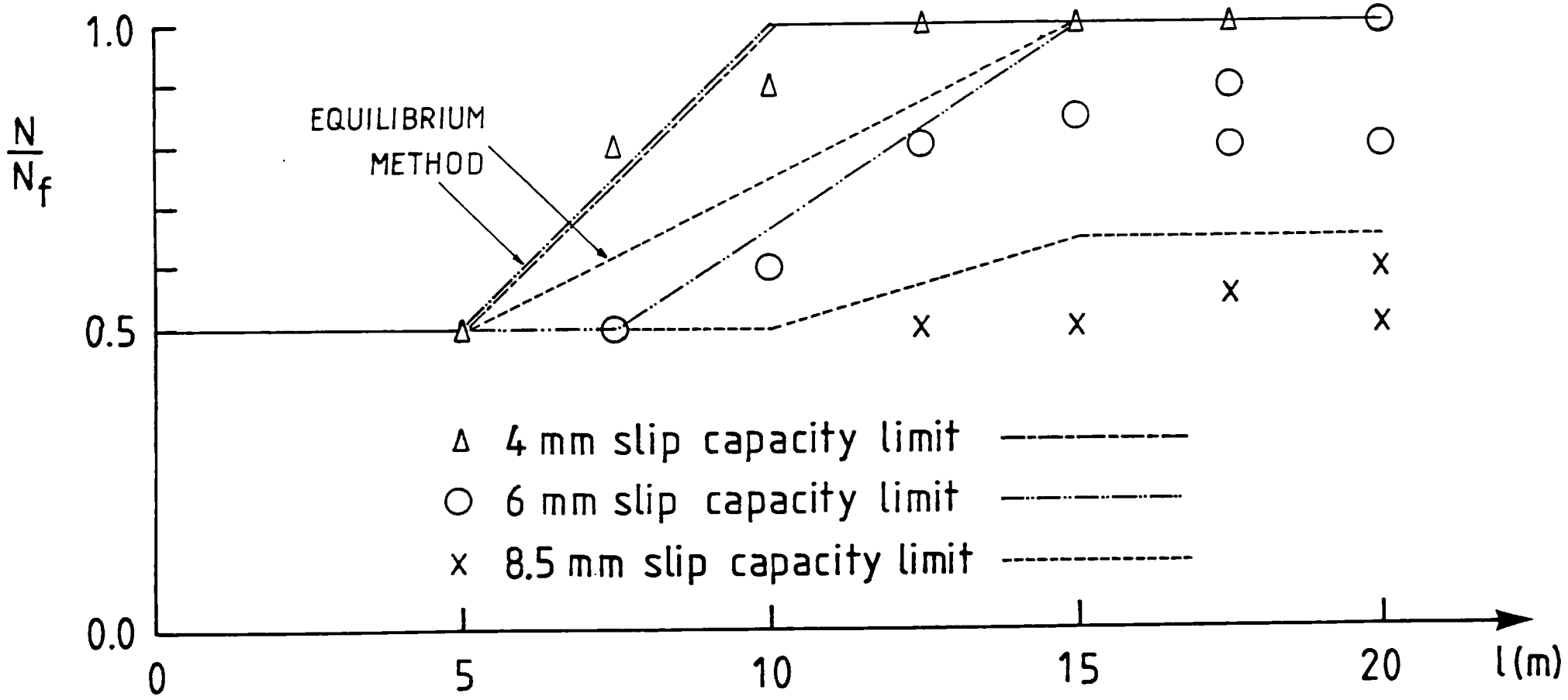

Figure 4.35: Span limitations on beams with welded sections and solid concrete slabs in function of the connector ratio and of different slip capacity limits.

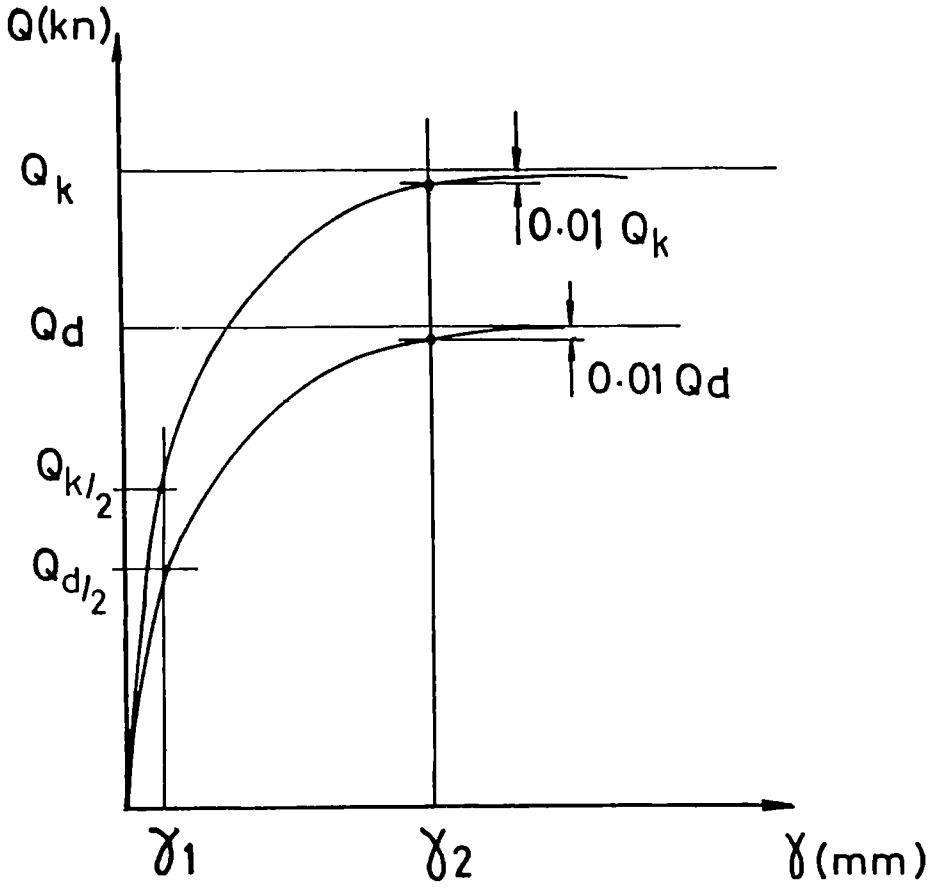

Figure 4.36: Load-slip curves of studs which vary in strength but not significantly in tangential stiffness.

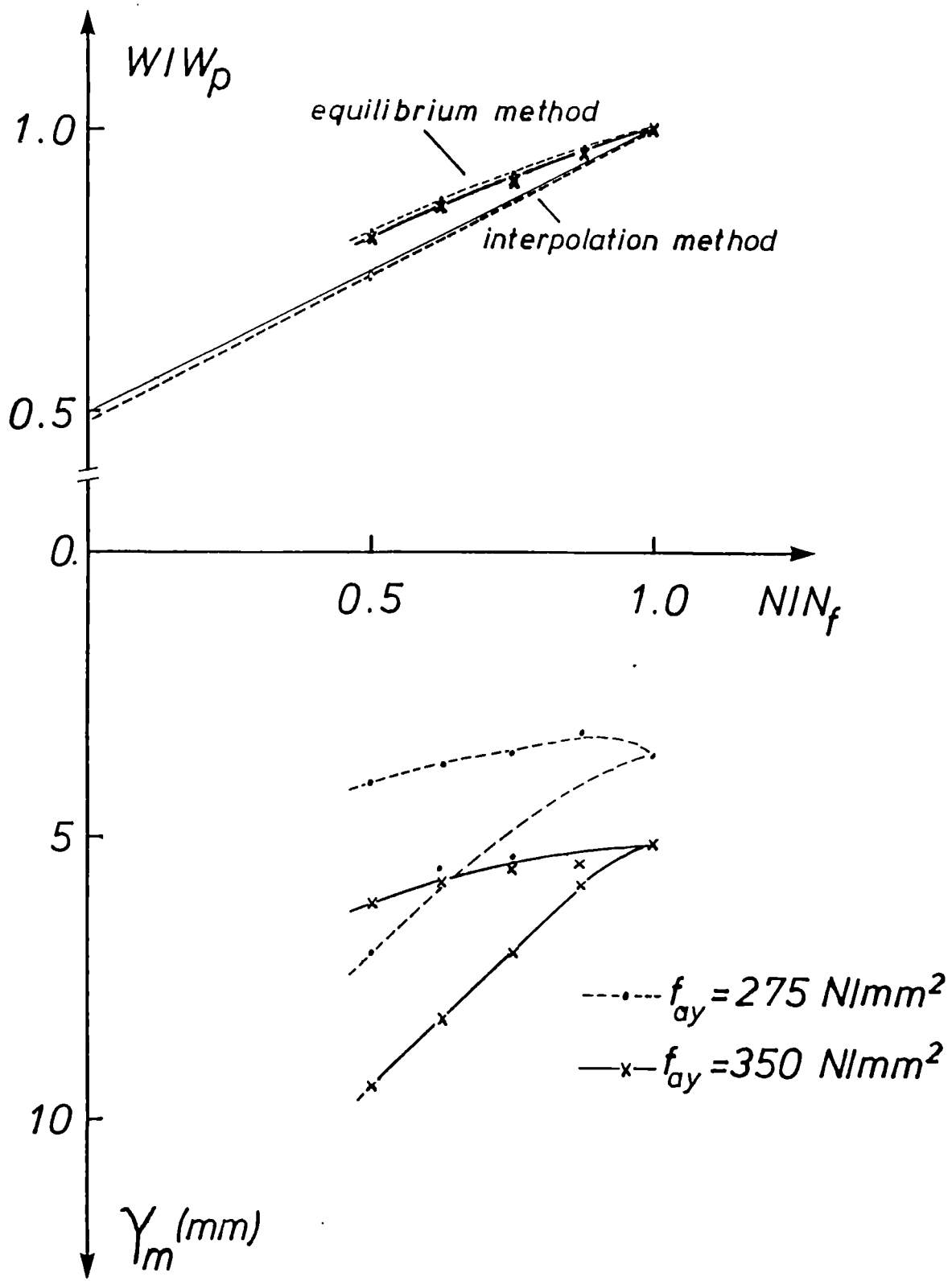

Figure 4.37: Influence of the design method, the Grade of steel, and the connector ratio on the maximum slip along beam SEBC 8 of Tables 4.16 and 4.18.

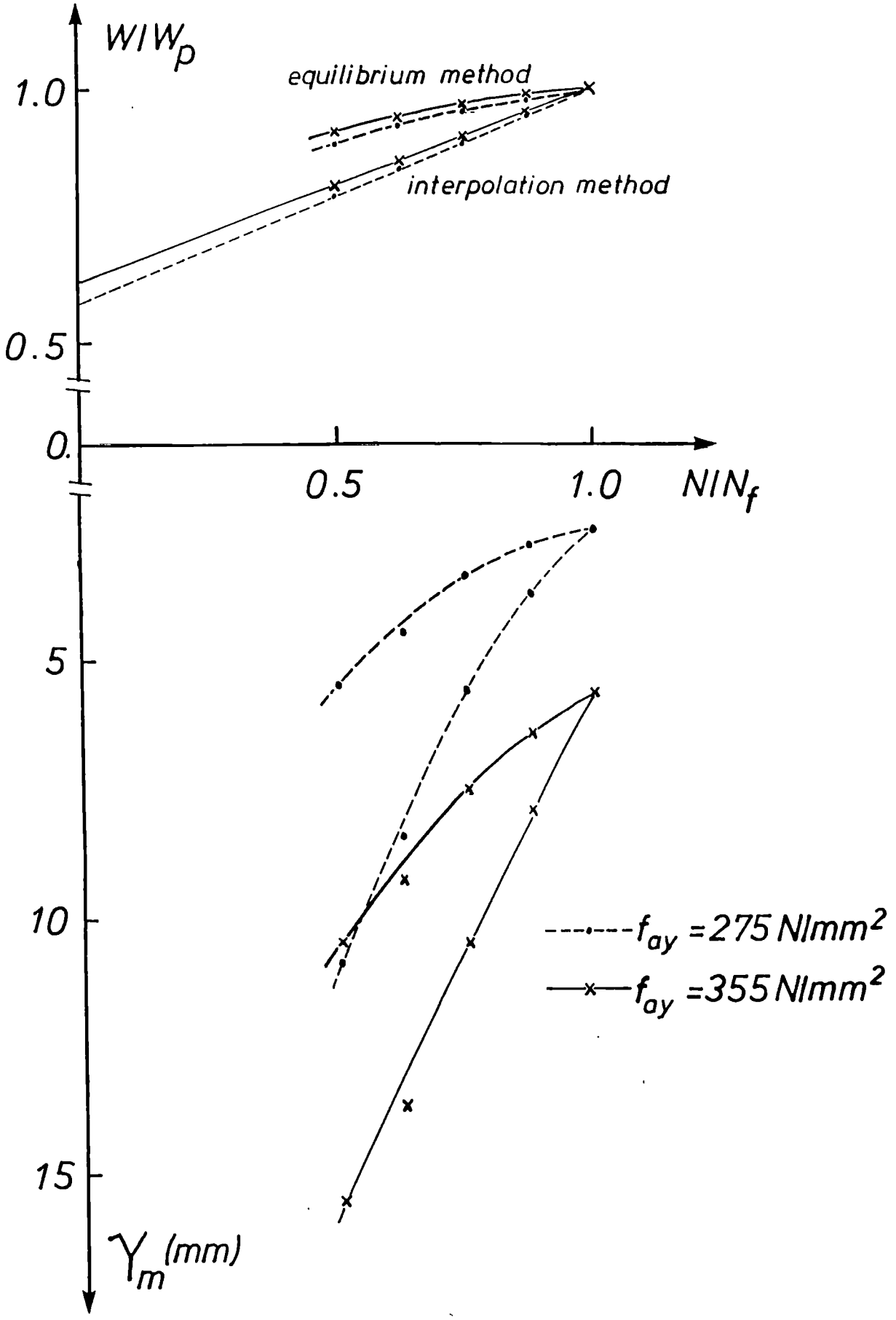

Figure 4.38: Influence of the design method, the Grade of steel, and the connector ratio on the maximum slip along beam SEBC 17 of Tables 4.16 and 4.18.

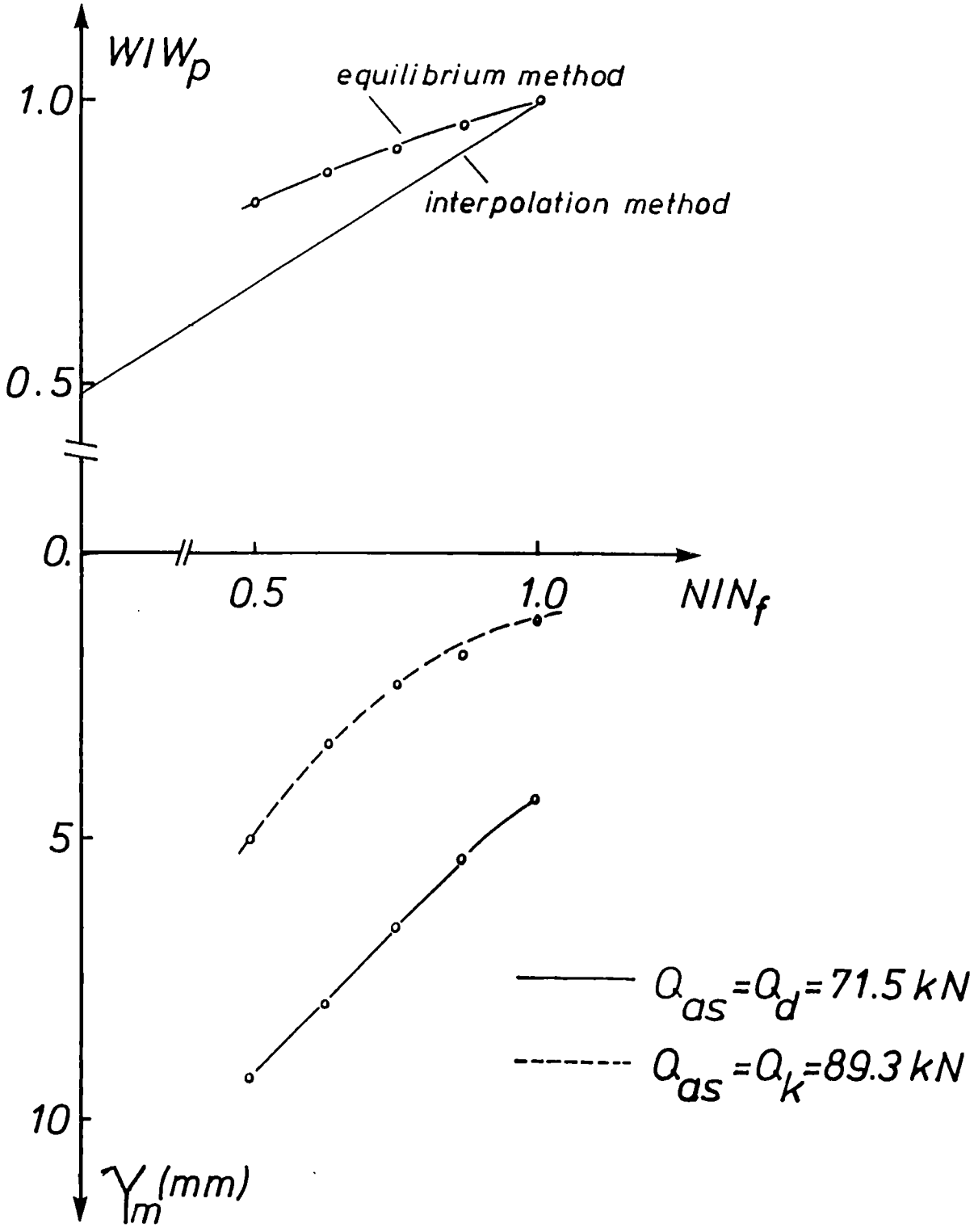

Figure 4.39: Influence of the design method, the stud shear strength, and the connector ratio on the maximum slip along beam EBC 2 of Tables 4.17 and 4.19.

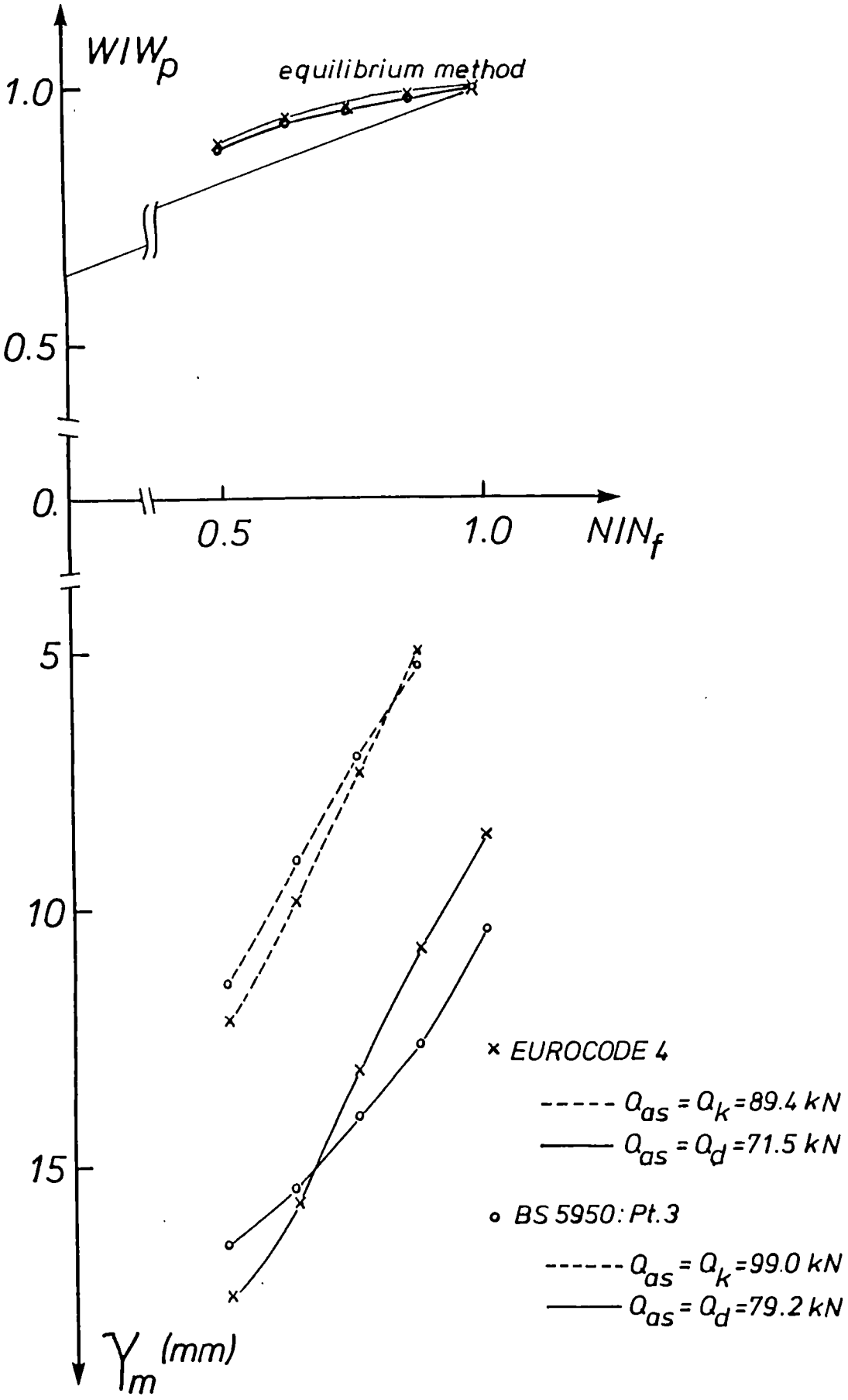

Figure 4.40: Influence of the design method, the stud shear strength, and the connector ratio on the maximum slip along beam EBC 8 of Tables 4.17 and 4.19.

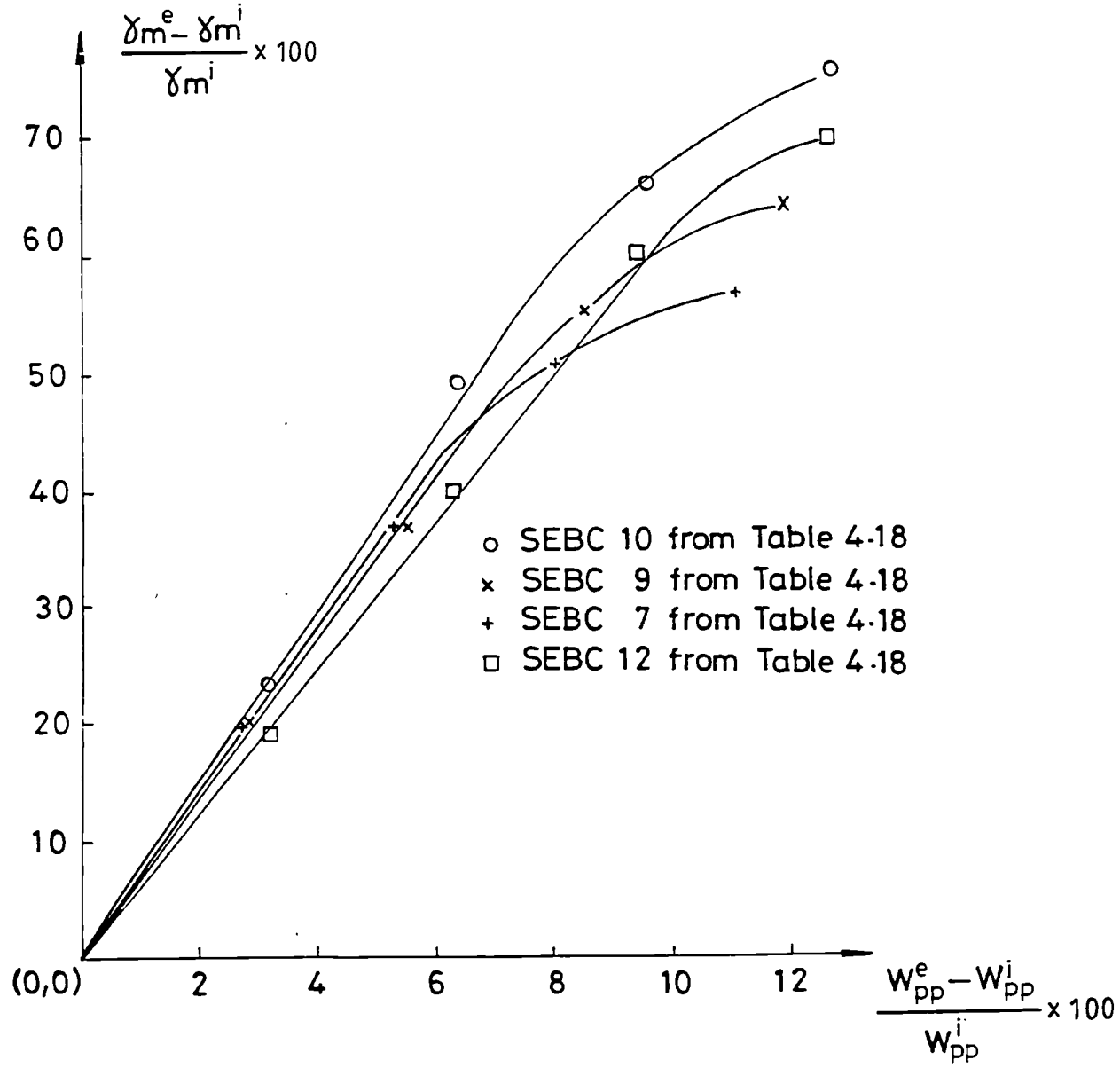

Figure 4.41: Relationship between the percent of slip increase with the percent of load increase of a number of beams from Table 4.18 for varying connector ratios.

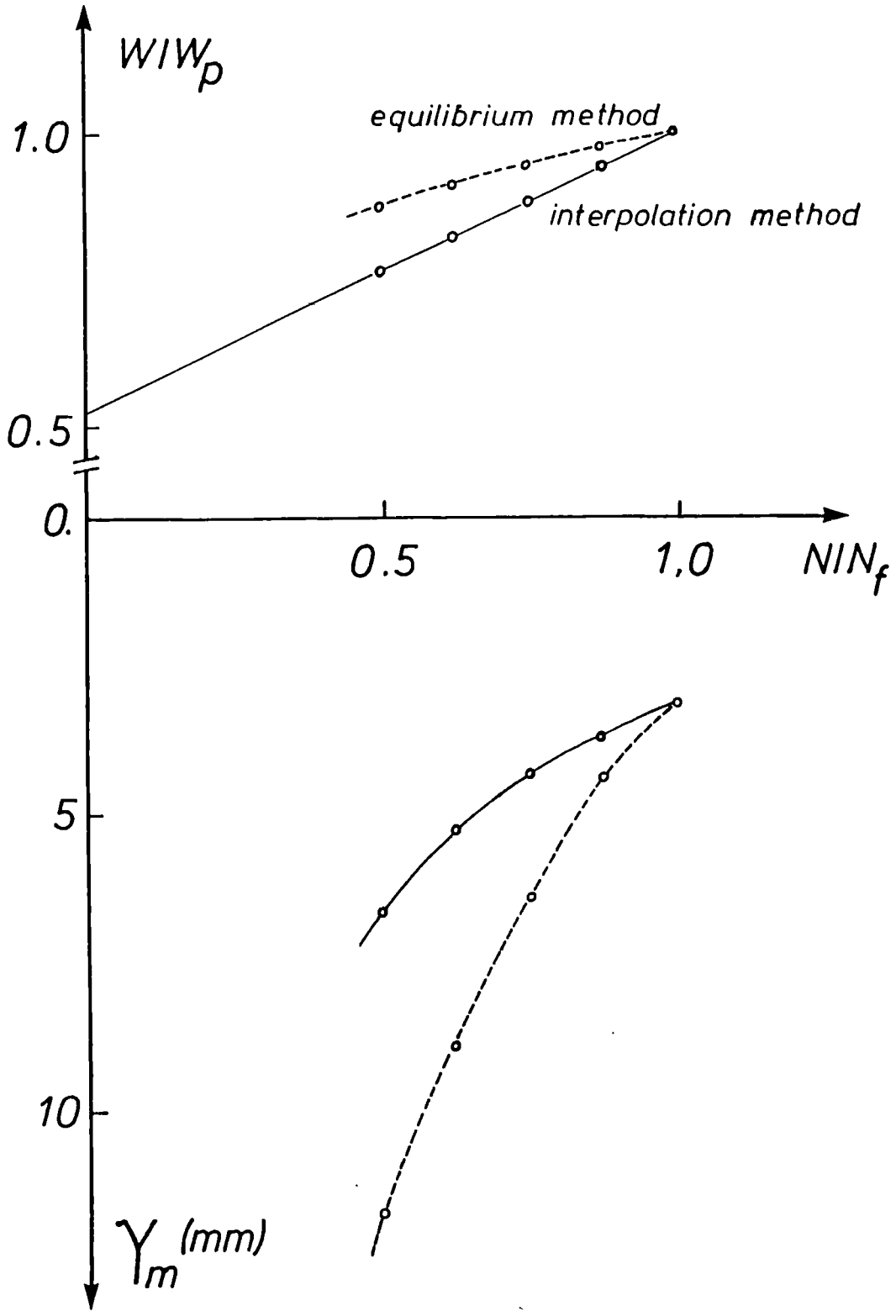

Figure 4.42: Influence of the design method and the connector ratio on the maximum slip along beam SEBC 13 of Table 4.18.

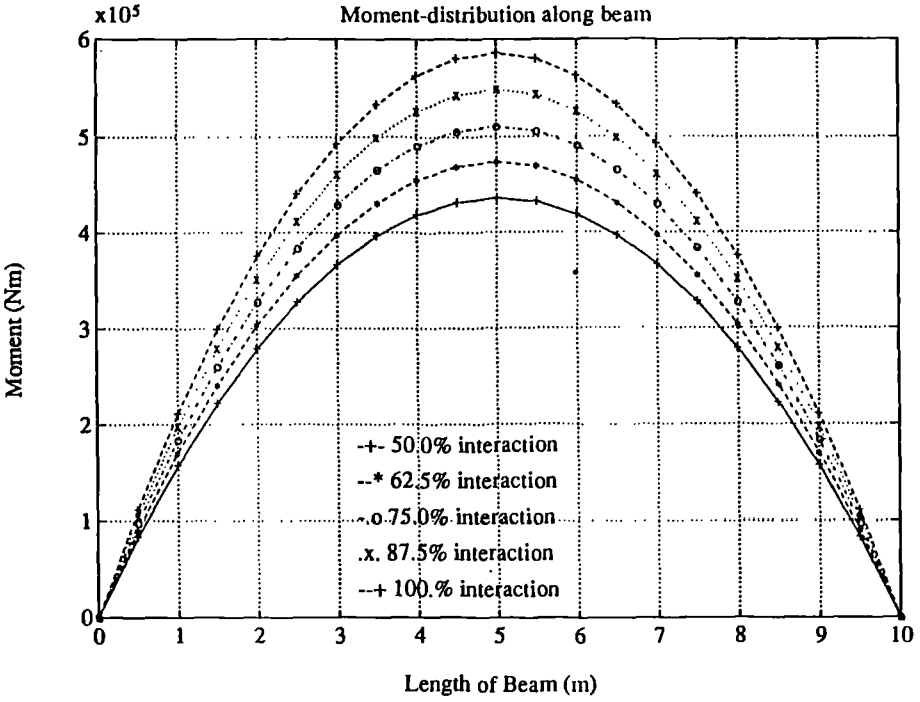

ECI

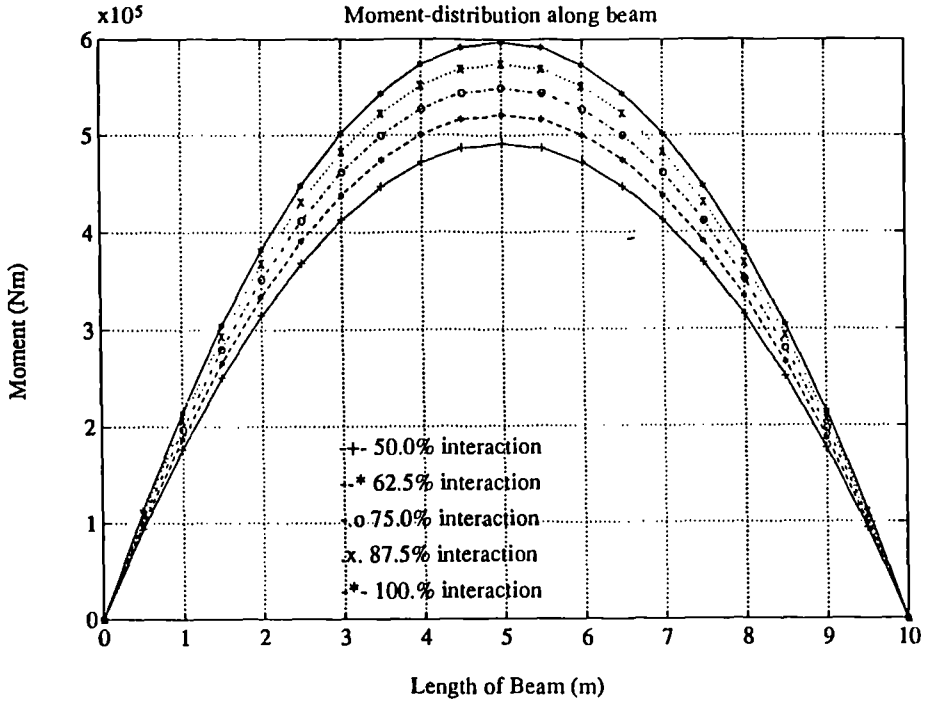

ECE

Figure 4.43: Comparison between moment, shear force and slip distributions along beam SEBC 6 at different degrees of interaction for the two design methods of Eurocode 4.

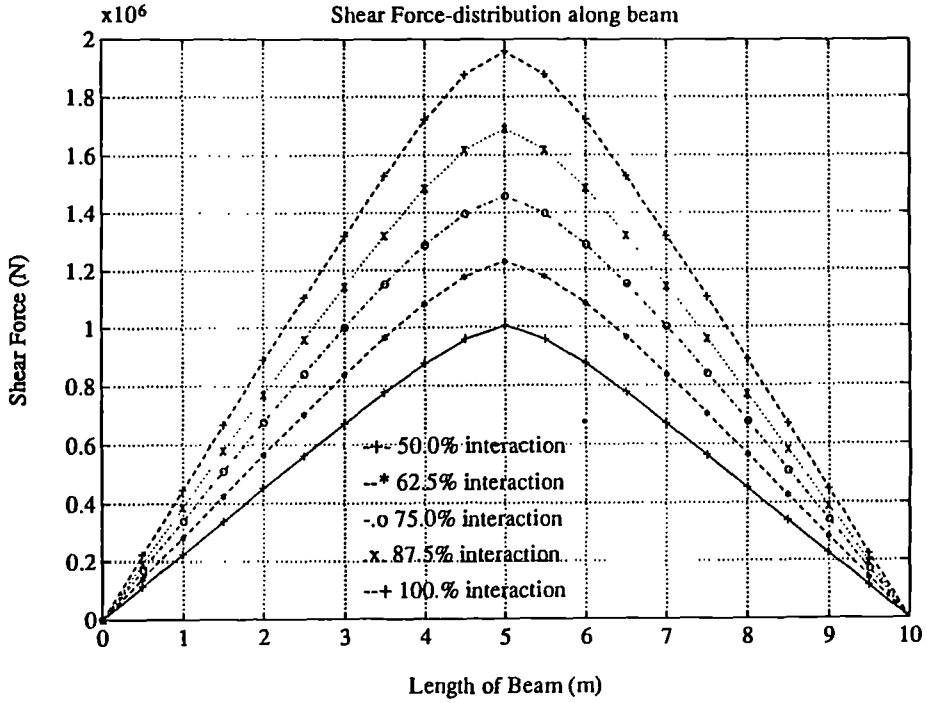
x10^6
Shear Force-distribution along beam
Shear Force (N)
Length of Beam (m)
-+- 50.0% interaction
--* 62.5% interaction
-.o 75.0% interaction
.x. 87.5% interaction
--+ 100.% interaction

ECI

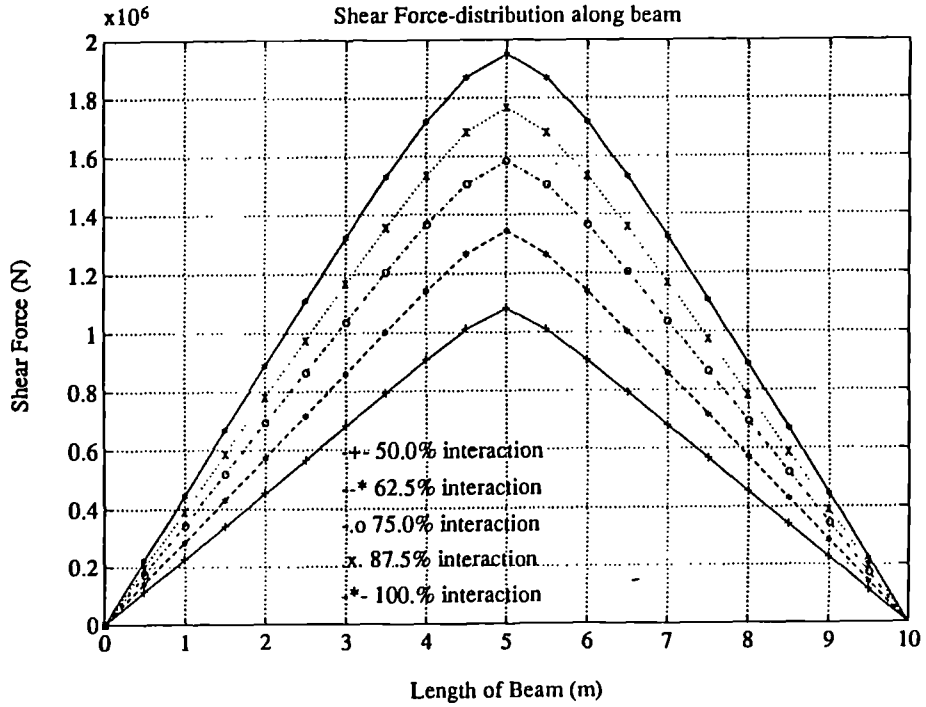
x10^6
Shear Force-distribution along beam
Shear Force (N)
Length of Beam (m)
-+- 50.0% interaction
--* 62.5% interaction
-.o 75.0% interaction
.x. 87.5% interaction
--*- 100.% interaction

ECE

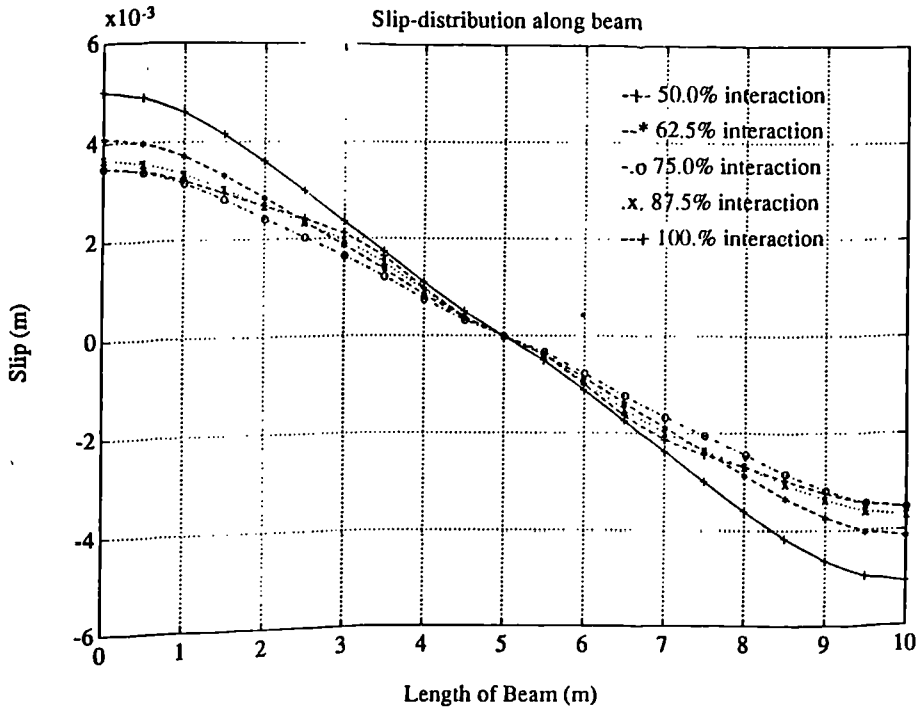
x10-3
Slip-distribution along beam
-+- 50.0% interaction
--* 62.5% interaction
-.o 75.0% interaction
.x. 87.5% interaction
--+ 100.% interaction
Slip (m)
Length of Beam (m)

ECI

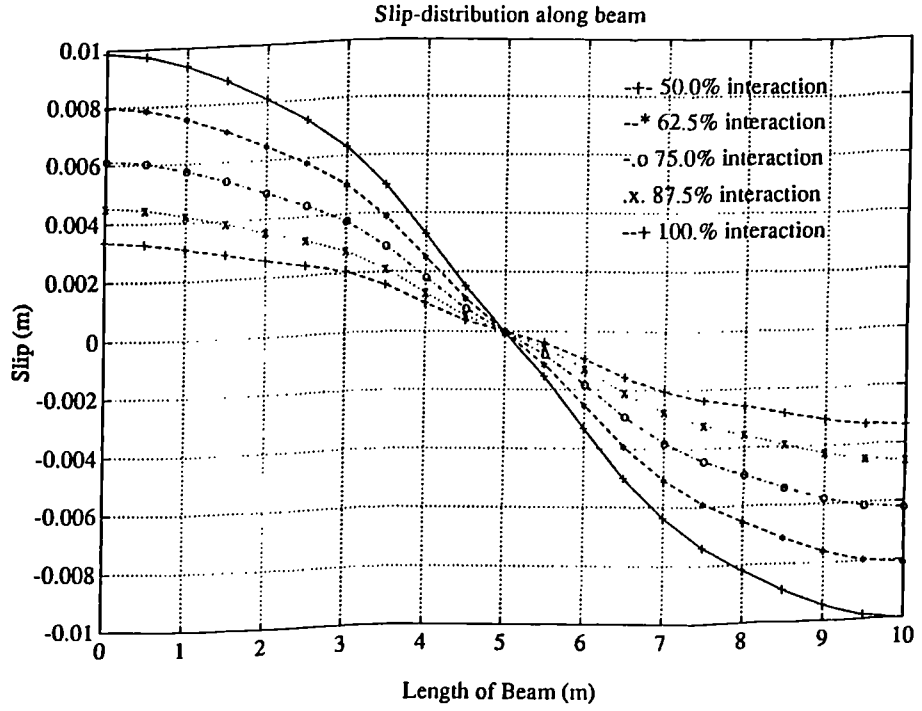
Slip-distribution along beam
-+- 50.0% interaction
--* 62.5% interaction
-.o 75.0% interaction
.x. 87.5% interaction
--+ 100.% interaction
Slip (m)
Length of Beam (m)

ECE

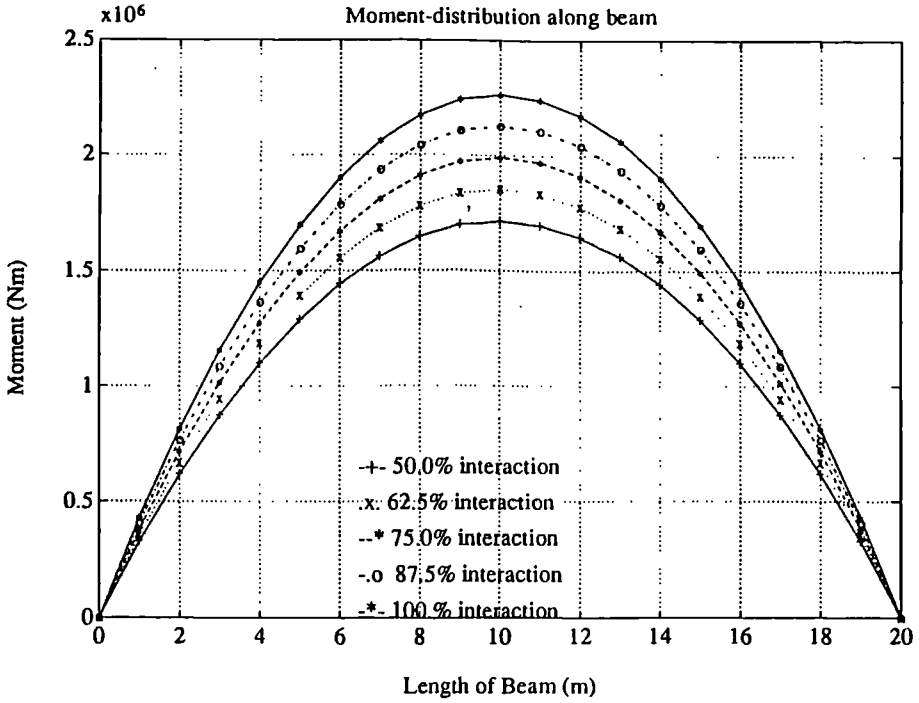

ECI

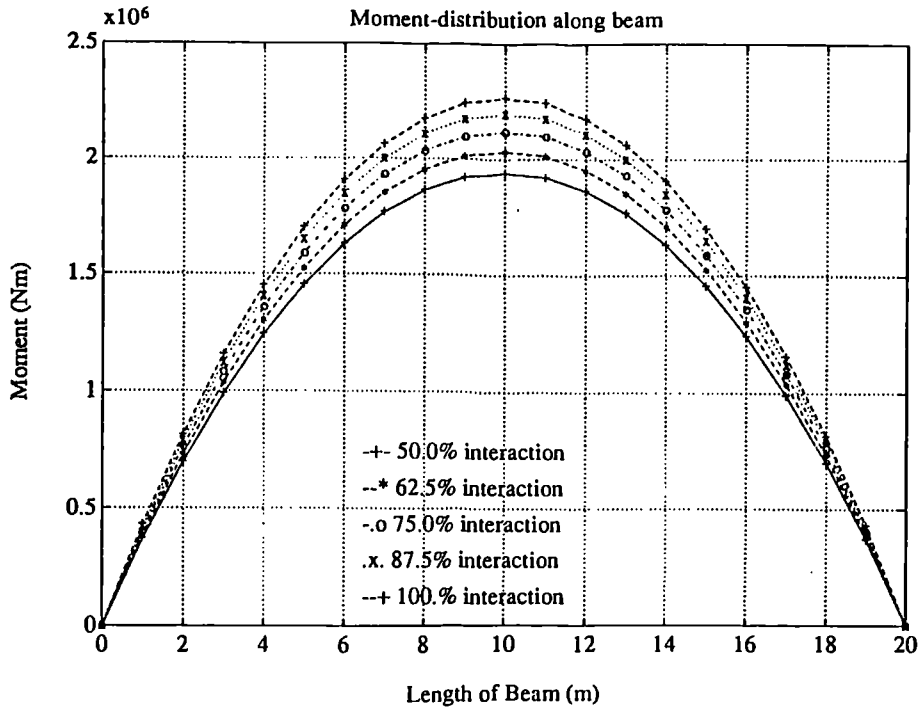

ECE

Figure 4.44: Comparison between moment, shear force and slip distributions along beam SEBC 16 at different degrees of interaction for the two design methods of Eurocode 4.

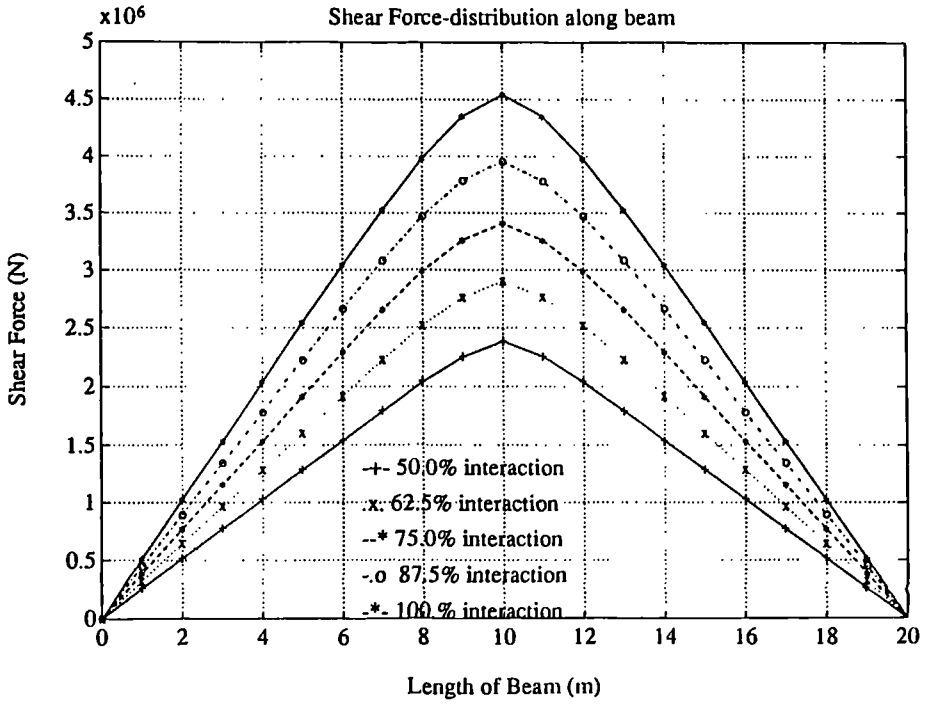
x10^6
Shear Force-distribution along beam
Shear Force (N)
Length of Beam (m)
-+- 50.0% interaction
x- 62.5% interaction
--* 75.0% interaction
-.o 87.5% interaction
-*- 100.% interaction

ECI

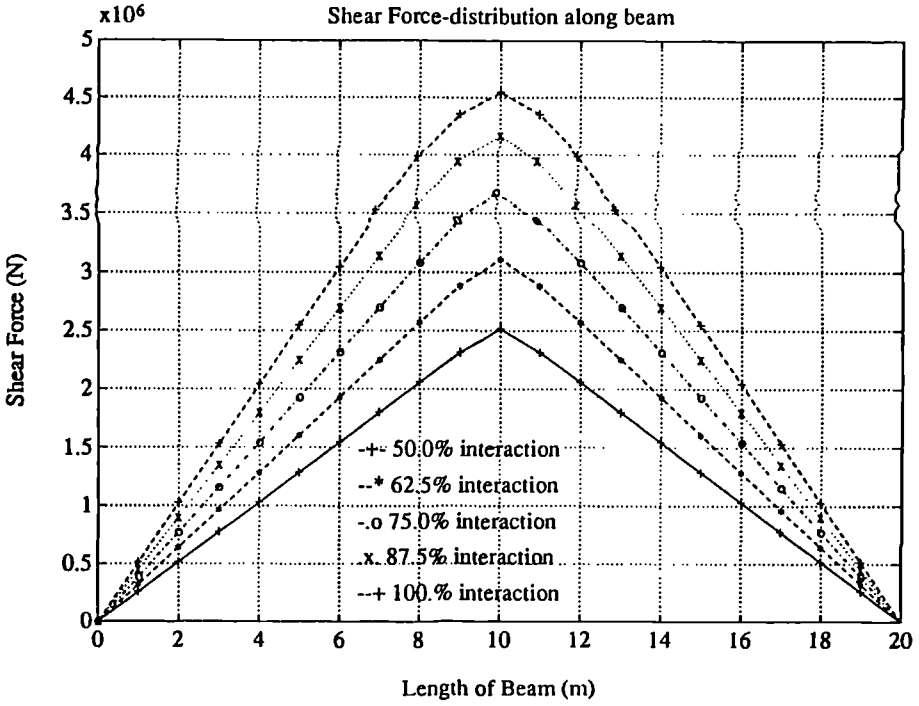
x10^6
Shear Force-distribution along beam
Shear Force (N)
Length of Beam (m)
-+- 50.0% interaction
--* 62.5% interaction
-.o 75.0% interaction
-x- 87.5% interaction
--+ 100.% interaction

ECE

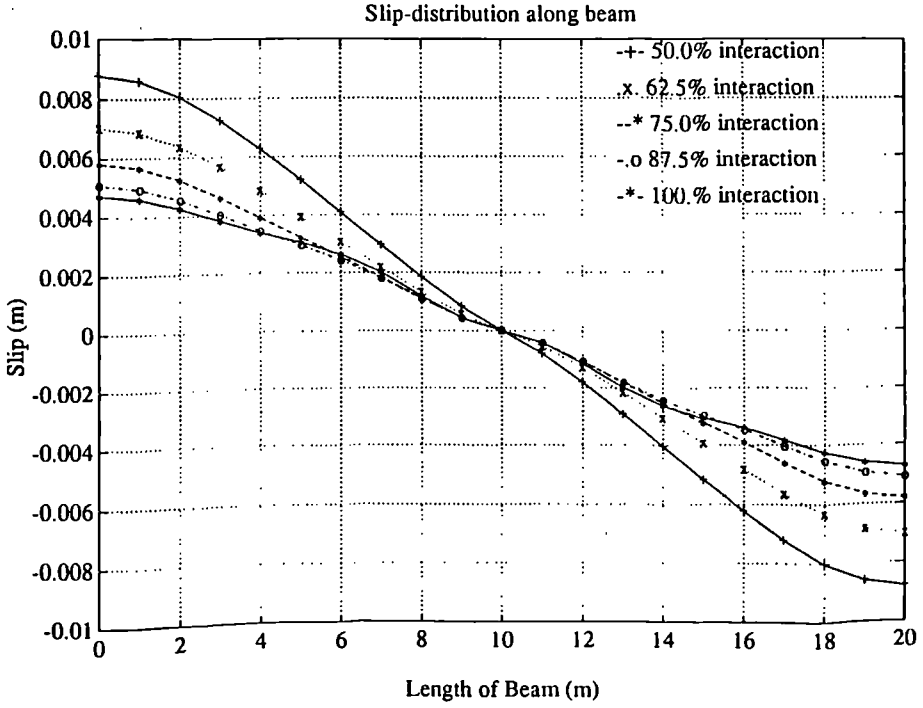
Slip-distribution along beam
-+- 50.0% interaction
.x. 62.5% interaction
--* 75.0% interaction
-.o 87.5% interaction
-*- 100.% interaction
Slip (m)
Length of Beam (m)

ECI

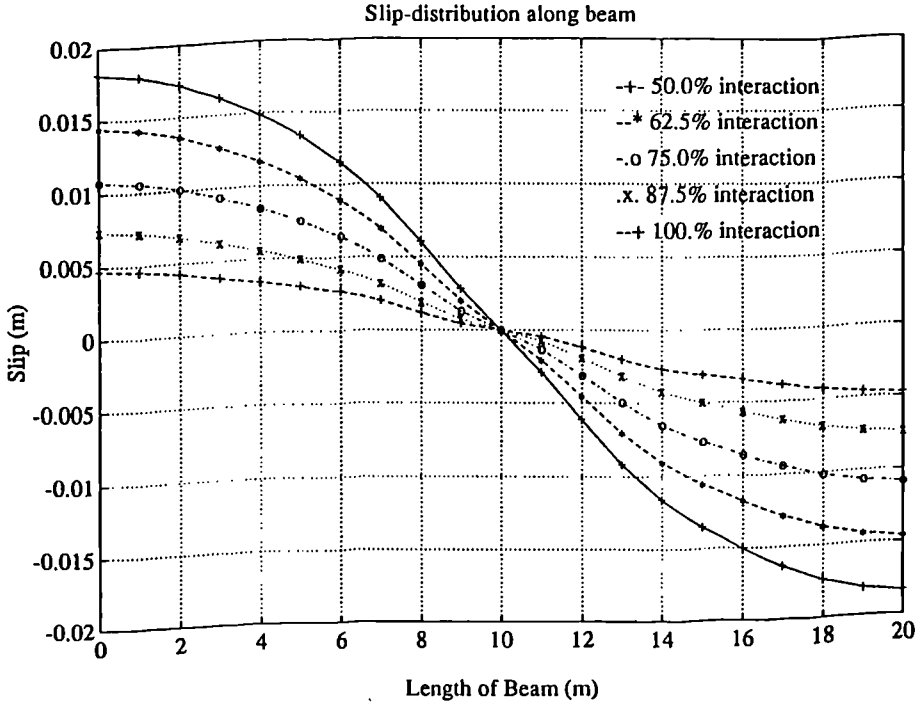
Slip-distribution along beam
-+- 50.0% interaction
--* 62.5% interaction
-.o 75.0% interaction
.x. 87.5% interaction
--+ 100.% interaction
Slip (m)
Length of Beam (m)

ECE

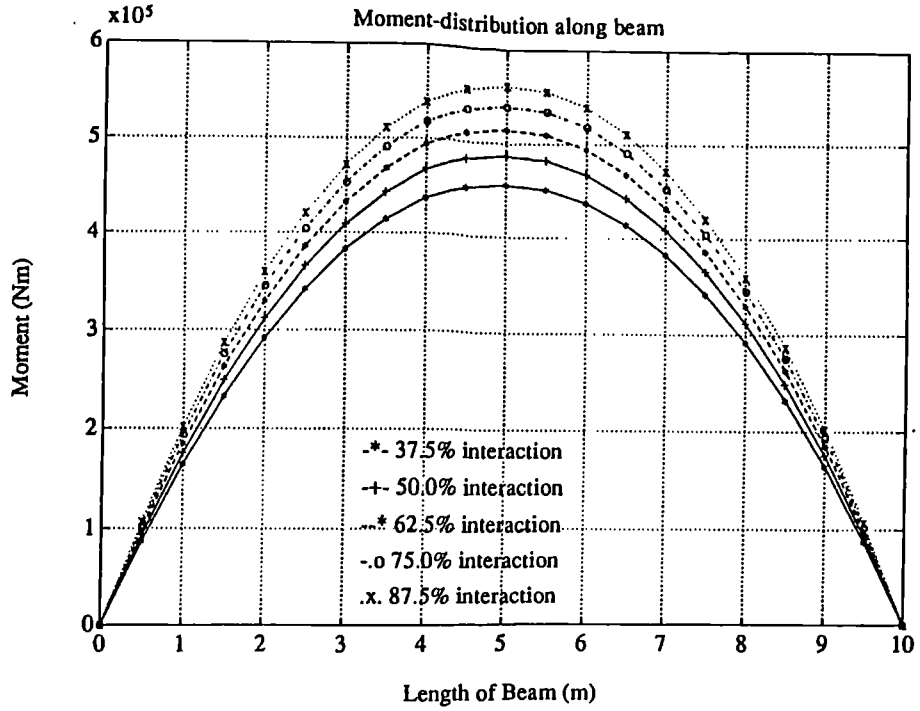

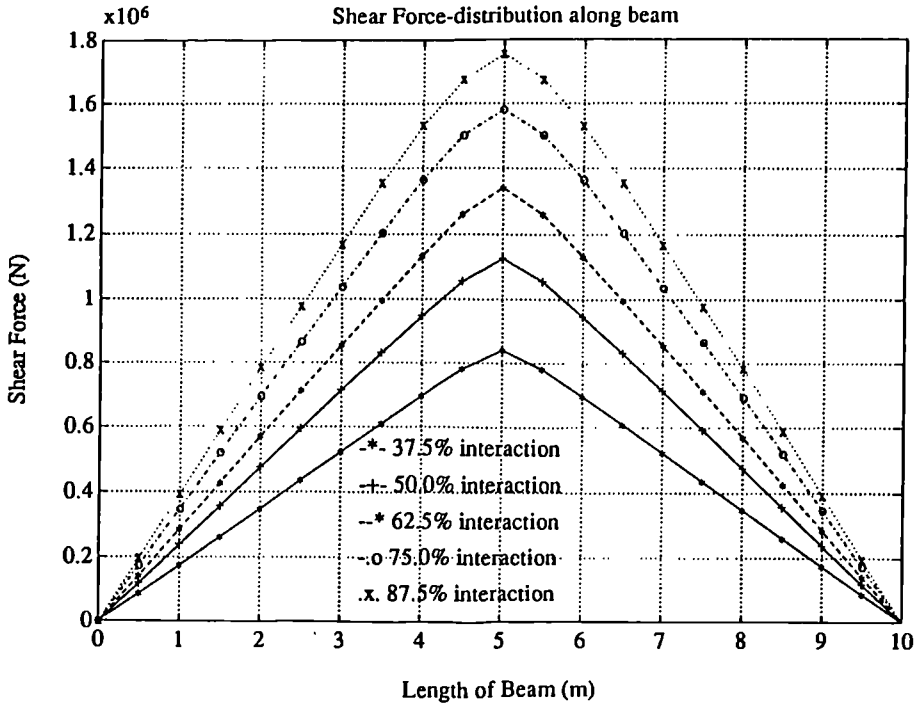

Figure 4.45: Moment, shear force and slip distributions along beam EBC 3 (= SEBC 6) at different degrees of interaction for the equilibrium method in BS5950:Pt.3.

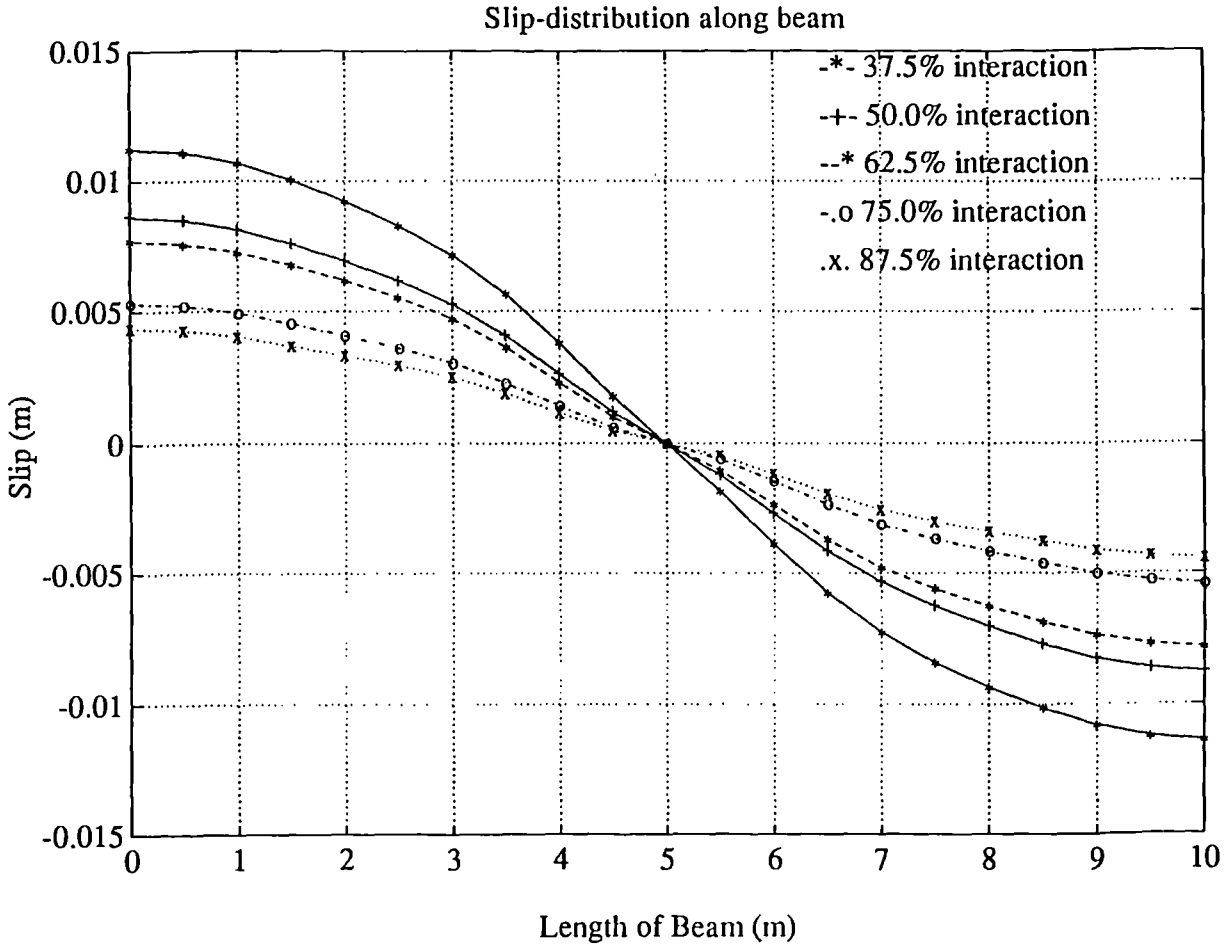
Slip-distribution along beam
-*- 37.5% interaction
-+- 50.0% interaction
--* 62.5% interaction
-.o 75.0% interaction
.x. 87.5% interaction
Slip (m)
Length of Beam (m)
0.015
0.01
0.005
0
-0.005
-0.01
-0.015
0
1
2
3
4
5
6
7
8
9
10

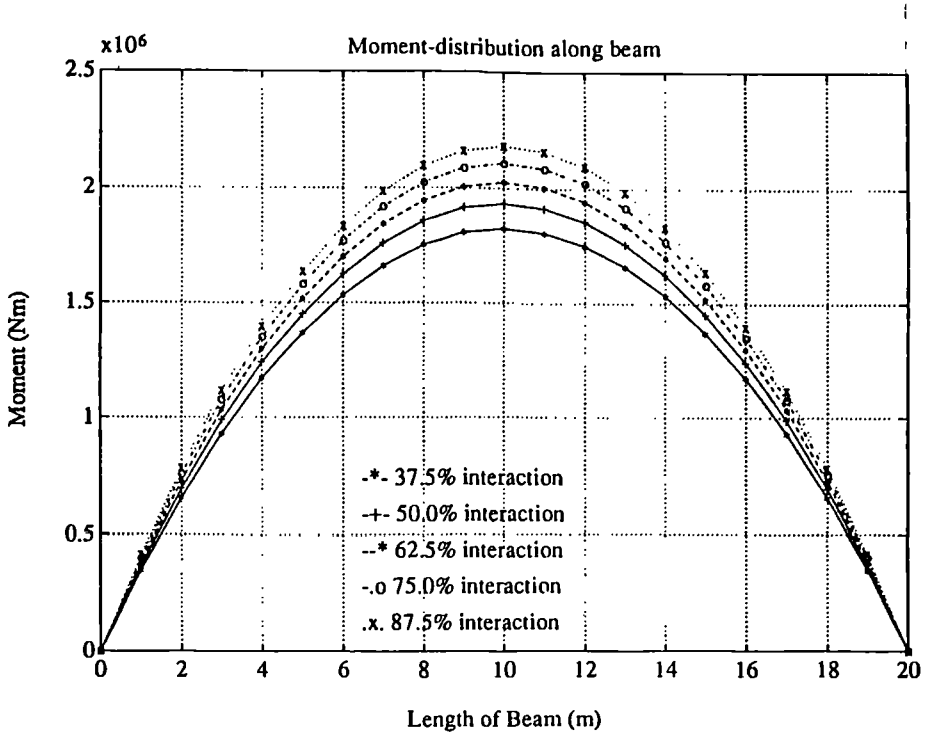

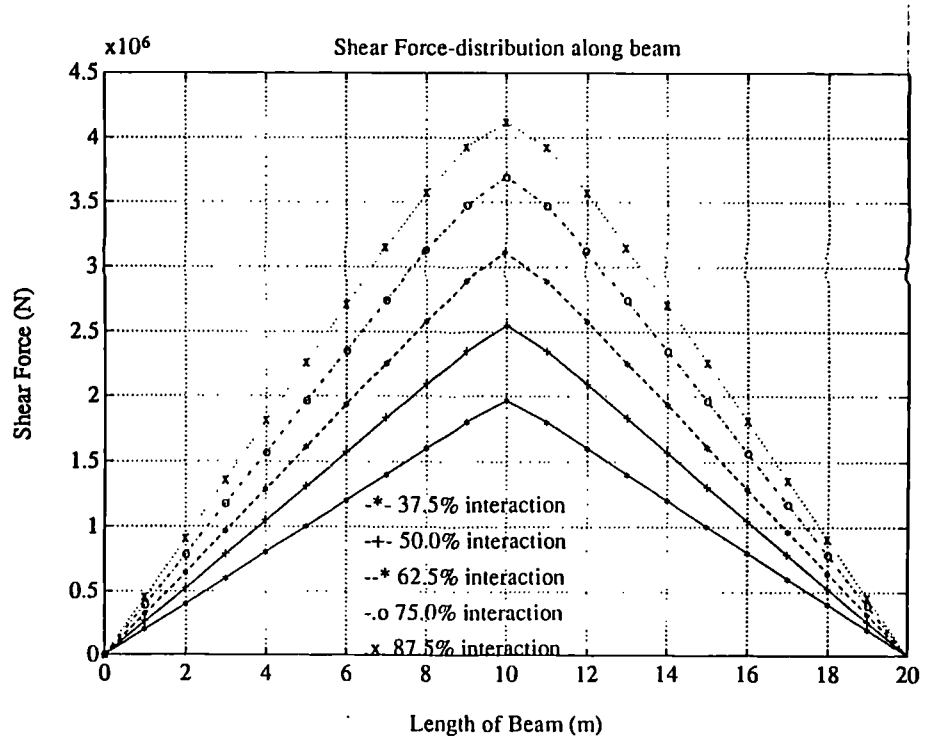

Figure 4.46: Moment, shear force and slip distributions along beam EBC 10 (= SEBC 16) at different degrees of interaction for the equilibrium method in BS5950:Pt.3.

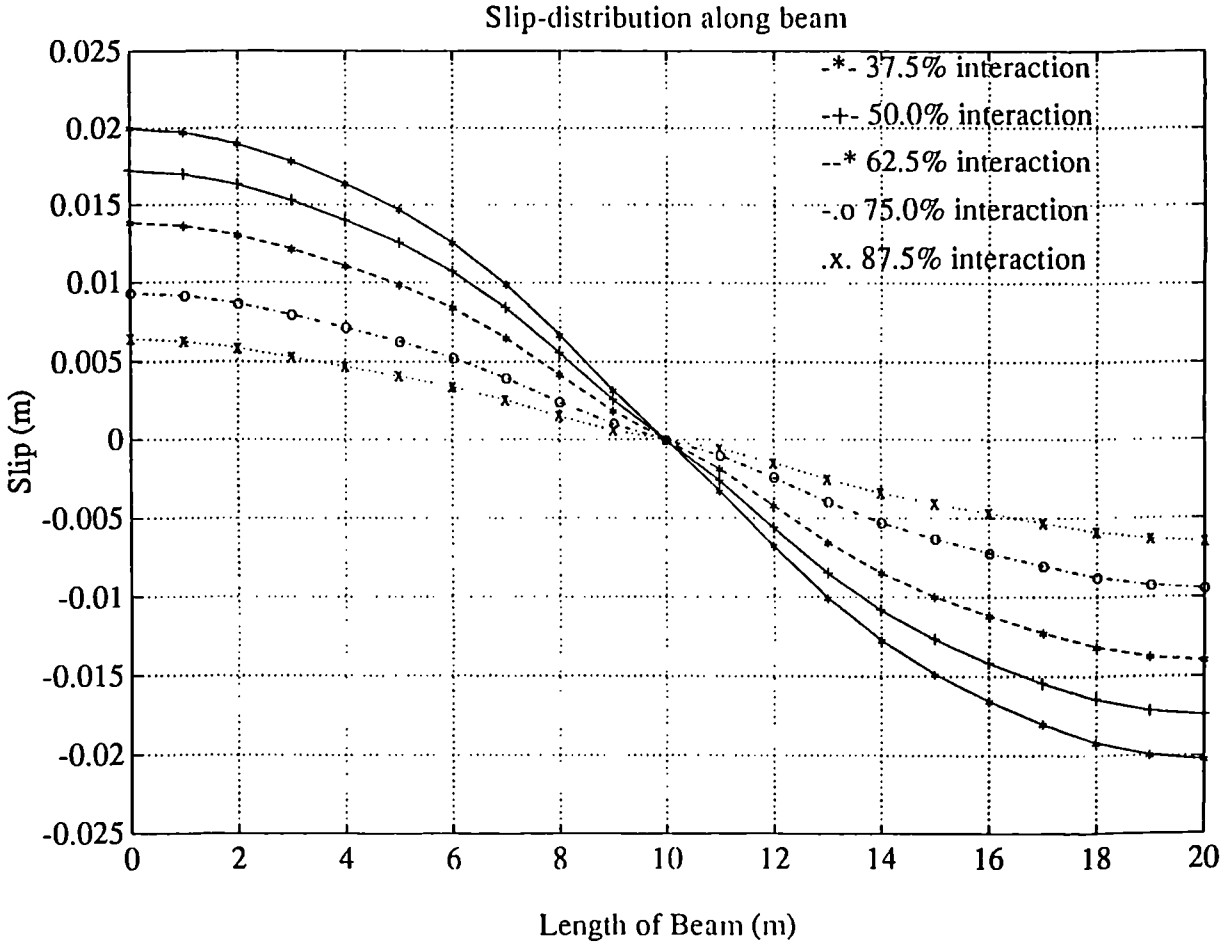
Slip-distribution along beam
-*- 37.5% interaction
-+- 50.0% interaction
--* 62.5% interaction
-.o 75.0% interaction
.x. 87.5% interaction
Slip (m)
Length of Beam (m)
0.025
0.02
0.015
0.01
0.005
0
-0.005
-0.01
-0.015
-0.02
-0.025
0
2
4
6
8
10
12
14
16
18
20

Chapter 5

Conclusions on Partial Interaction design

5.1 Summary of partial interaction design in Euro and British Codes

The design rules for composite beams with partial shear interaction in the draft Eurocode 4 [3] do not take sufficient account of the possibility of shear stud failure in beams with long spans ($l > 10$ m). The limitations of the design rules are based on experimental evidence of many beams, all with shear spans smaller than 5 m ($l < 10$ m), yet the design method in the Code is extended to beams with shear spans up to 10 m ($l = 20$ m).

Beams with larger shear spans and with small degrees of shear connection failed prematurely in shear in more recent laboratory tests, before reaching either w^i_{pp} and/or w^e_{pp}.

Granted that the draft BS 5950:Pt.3 has taken account of the danger of premature stud shear failure by introducing different minimal connector ratios for different spans, the Code does not consider sufficiently the effect of replacing the smaller w^i_{pp} by the larger w^e_{pp} on the slip distribution.

Recent experiments in Europe on composite beams with composite decks and low connector ratios, show that the studs possess large deformation capacities, probably due to the falling branch in the load-slip curve ($\gamma_f > 15mm$). These experiments would justify the application of w^e_{pp} to composite beams with composite slabs made up of corrugated metal decking, which spans perpendicular to the steel beam. Unfortunately, similar evidence of large deformation capacities is

not available for studs in solid slabs. On the contrary, several test results exist on 'shank' shear failure of studs embedded in solid slabs after the peak shear load has dropped by 5 to 10%.

Since the present programme does not model the falling branch of the load slip curve of studs embedded in composite slabs with metal decking, it could be argued that the results thus far produced by the programme for beams with composite slabs are over-conservative. The descending part of the curve allows the shear to redistribute from the most heavily loaded studs near the ends of the beam to the less heavily loaded studs along the span, without causing premature failure, but under increasing relative displacement between the composite deck and the steel beam.

This same argument cannot as easily be used for numerical results obtained for beams with solid slabs, since the load-slip curves for the studs in such slabs do not have a consistent falling branch. Therefore, the load produced by the equilibrium methods in both EC4 and BS 5950:Pt.3, when applied to beams with large spans ($l > 15$ m), solid slabs and minimal connector ratios as presently stated in BS 5950:Pt.3, might still cause premature stud shear failure along the composite beam.

The readiness to use the **equilibrium method** and to allow for smaller degrees of shear connection, stems from design practice in the United States, where this method has been in use without limitations for some years now. However, even experiments on beams with certain types of metal decking [74] have demonstrated that stud pull-out failure occurred before large slips were measured. Too little is still known about the relationship between the profile geometry and the load-slip behaviour of the stud, to allow for a large stud deformation capacity to be built into a Code design rule.

5.2 A tentative proposal for Euro and British Composite Codes

Since the slip capacity or horizontal deformation capacity of a stud is a function of the slab geometry (solid, composite or haunched) as well as of the number of studs placed in the transverse direction onto the top flange as of the diameter of the studs, stud shear failure in a beam will be a function of the above parameters as well as of the applied load and the stud spacing.

Before applying any limitations to the beam geometry to reduce the maximum

slip along this beam, different slip levels need to be defined for studs embedded in different slabs, above which studs with certain diameters will fail in shear.

Both Dallam [68] and Roik and Hanswille [29] measured values for the ultimate slip of studs in solid slabs which are scattered around the mean ultimate slip values obtained by Oehlers and Coughlan [28] in eq. (4.4). Some of these measured values differ by more than 20% for studs with the same diameter. Therefore, for design purposes, characteristic slip capacity values will be used, instead of mean slip capacities, to ensure that the slip levels thus defined are definitely lower bounds.

The characteristic slip capacity levels for studs in solid slabs are set up as follows:

- for studs with diameter < 13 mm: $\gamma_{f,k} = 3.5$ mm
- for studs with diameter $= 16$ mm: $\gamma_{f,k} = 5.0$ mm
- for studs with diameter ≥ 22 mm: $\gamma_{f,k} = 7.0$ *mm*

Since 19 mm diameter studs are by far the most commonly used, the middle level is replaced by:

- for studs with diameter $= 19$ mm: $\gamma_{f,k} = 6.0$ mm

The easiest design rule would undoubtedly be an analytical expression for the maximum plastic slip reached in the beam as a function of the major beam parameters. Ideally, one formula should be provided for all degrees of partial interaction; alternatively, different formulae could be used for different degrees of interaction. The value for γ_m obtained by this formula would have to be compared with the slip capacity level of the studs embedded in the slab of that beam. If $\gamma_m > \gamma_{f,k}$, the designer could either change the studs and thereby increase $\gamma_{f,k}$ or he/she could increase the number of studs per shear span.

For the beam category of rolled sections with solid slabs, equations (4.23) and (4.24) represent such expressions for degrees of 50% and 75% interaction respectively. A similar set of equations could be obtained for the category of plated girders with solid slabs.

Unfortunately, for the category of rolled sections with composite slabs for which such a set of equations would be most useful, insufficient information is still available on the exact shape of the load-slip curves of studs embedded in slabs with different profiled decks, and on the slip capacity of the studs in such slabs, to derive a universal expression presently.

A conservative, but safe design rule for beams with solid slabs could consist of limiting the minimum connector ratios for different spans and different slip capacity levels. As known from sections 4.1 and 4.5, the maximum slip is not only a function of the ratio l/h_t. The scatter will therefore be quite large and consequently the choice of a lower bound for N/N_f might become fairly conservative for certain beams. However, the rule has the dual advantage of simplicity and safety.

The two different categories of beams with solid slabs can be condensed in only one category: valid for beams with rolled sections and with plate girders.

In Figure 5.1 minimal connector ratios are drawn for different slip capacity limits and different design methods as functions of the span of beams which were propped during construction. Since the percent relative error in the estimation of the maximum slip in function of the span can be as large as 50%, the upper bound given by this figure will be quite onerous for certain beams.

It is suggested to add both sets of limitations on the connector ratios corresponding with the **interpolation** and the **equilibrium method** to the main methods in Eurocode 4 and the BS 5950:Pt.3.

Figure 5.2 shows three limiting slip capacity limits for the results of beam SRF 43 of Table IV.1 in Appendix IV as a function of the connector ratios for different load factors $\lambda = w_u/w_{pp}^i$. This graph demonstrates that the load factor increases linearly with the connector ratio for any given slip limit at a ratio 1:2. When beams are unpropped during construction, the dead load will always be larger than 0.1 w_u, therefore the N/N_f-ratio could be decreased by 0.2 for those beams. This would leave the present design rule in Eurocode 4 unchanged for most beams of span smaller than 10 m.

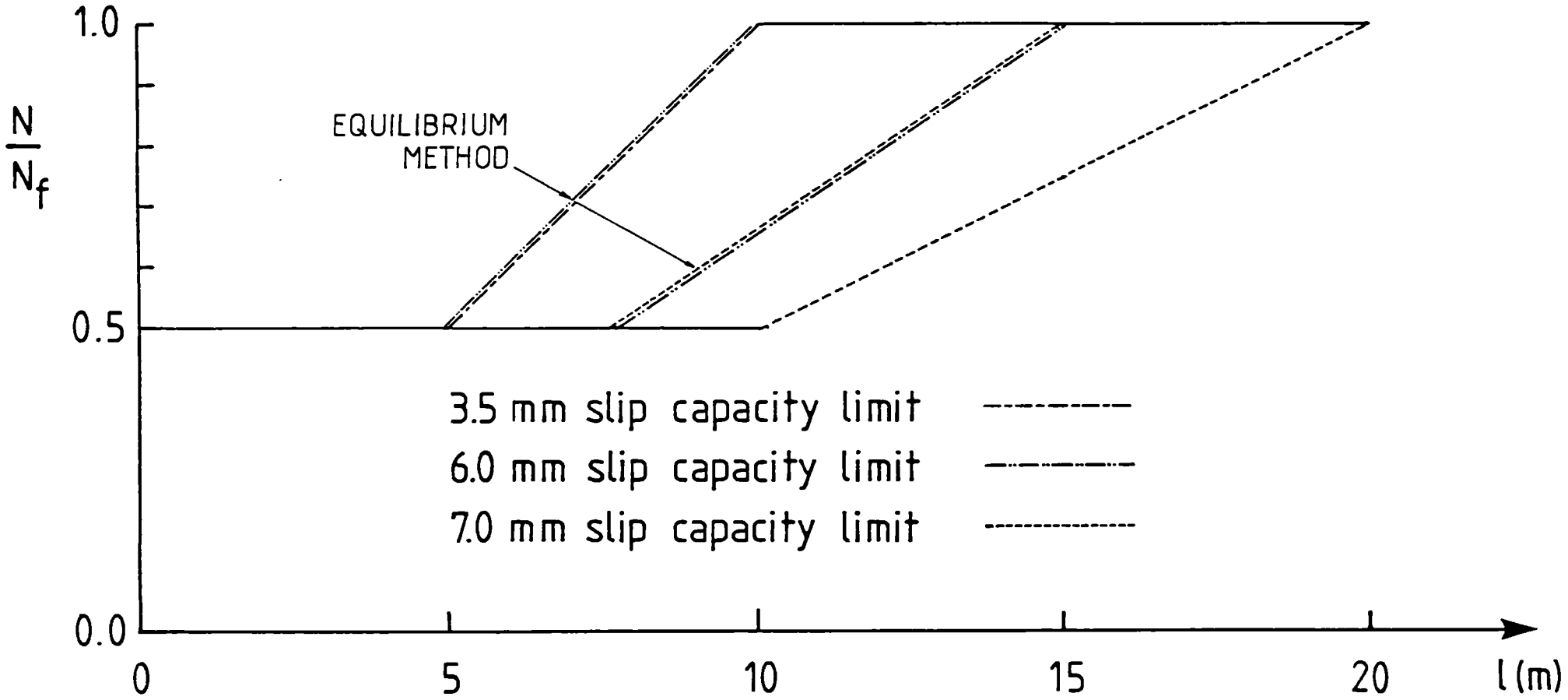

Figure 5.1: Limitations on the span of beams with solid slabs in function of the connector ratio and different characteristic slip capacity limits.

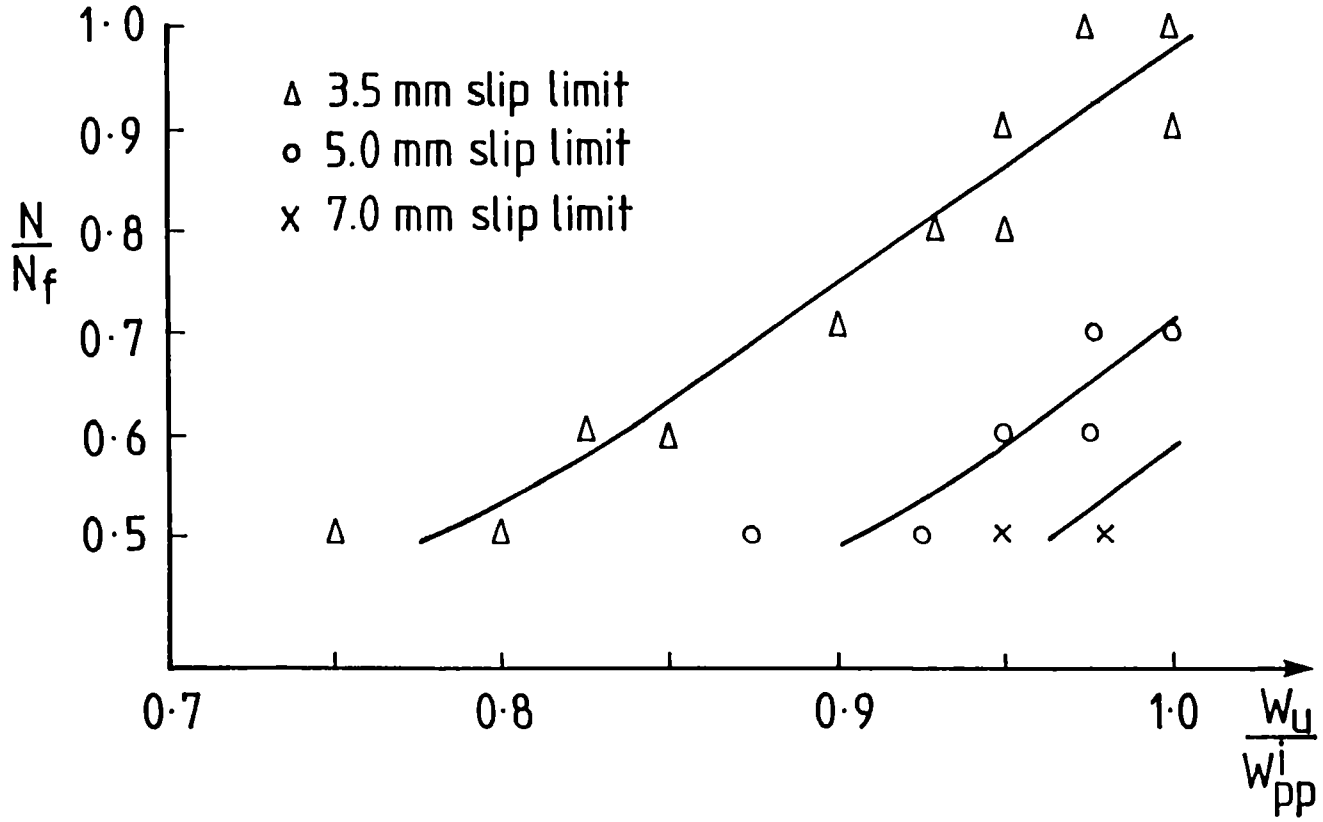

Figure 5.2: Relationships between the degree of shear connection and the load-factor at different constant maximum slips.

Part II

Transverse flexibility of *inverted* U-frame steel – conrete stud connections

Chapter 6

The problem of transverse flexibility of inverted U–frames

6.1 Review of U–frame action

6.1.1 Historical background to U–frame design

The use of 'U' frames in plate girder bridges originates from half 'through'-type riveted railway bridges (Fig. 6.1). It was not until the advent of modern welded fabrication that **U-frame action** was appreciated as a means of stabilising laterally the compression flanges of the main girders. In 1956 it was introduced in a revision of BS 153 [6], in a form which was mainly developed for half 'through'-type bridges.

The bases and formulae given in BS 153 for the **stiffness** of U-frames are still identical with those currently stated in clause 9.6.5 of Part 3 of BS 5400 [7], except that no account was taken of the connection between the main girder and the cross girder in the old Code.

The formulae for lateral torsional buckling, which determine the old permissible stress level and the new limiting stress level in the compression flange, have been changed only slightly. These formulae are still based on an extended analogy between existing theoretical solutions for the classic elastic lateral non distortional buckling of an I member and the Euler buckling of an axially loaded strut. However, formulae have been simplified and advantage can be taken of the actual moment distribution, rather than designing the beam for the maximum moment. The major changes from BS 153 are given by Nethercot in [81].

The formula for the **strength** of the U-frame however is different from BS

153. In the latter, the connections of the members of the U-frames were designed to resist a transverse horizontal force at the centroid of the compression flange of the girder which has a value equal to 1.25% of the force in the flange, in addition to the effects of wind and other applied forces. In the new Bridge Code this force is obtained by representing the compression flange as a laterally restrained Euler strut with initial bow.

6.1.2 Application of U-frame approach to composite plate girder bridges

In continuous composite plate girder bridges, where the main girders are closely spaced so that no cross girders are needed and where lateral bracing is omitted, except at the supports, both continuous and discrete **inverted U-frame action** can be applied for stabilising the bottom flanges near the intermediate supports.

Continuous restraint is provided to the compression flange by the deck slab and the web for unstiffened plate girders. Discrete restraint is provided to the compression flange by intermediate vertical stiffeners, which act as discrete inverted U-frames together with a part of the slab. Especially in the hogging bending regions near the internal supports reliance needs to be placed on the stiffness of the shear connection in the transverse plane in the vicinity of these stiffeners.

In this piece of work only the discrete inverted U-frame action will be studied and in particularly the transverse flexibility of the connection between the steel flange and the concrete slab.

6.1.3 Bases of and criticism on the current design formulae

The bases of the design formulae for stiffness and strength of U-frames and inverted U-frames according to BS 5400:Pt.3 are given below:

(i) THE STIFFNESS OF U-FRAMES: determination of l_e For half 'through-bridge' girders and continuous composite plate girders with intermediate vertical stiffeners, intermittent restraint is provided to the compression flange by attachment of vertical stiffeners connected to the main girder. The sections where they occur can be considered as discrete and stiff U-frames at spacing l_u. The lateral deflection per unit horizontal force at the level of the centroid of the

compression flange, is calculated per frame to give the maximum total deflection per frame per unit force.

This deflection δ, is the sum of the deflection of the stiffener (δ_1), the cross girder or slab deflection (δ_2) and the deflection due to the flexibility of the connection (δ_3). The breakdown of the deflection is shown in Fig. 6.4 for the half 'through'-type girder presented in Fig. 6.2 and the total deflection δ, is calculated by eq. (6.1).

$$\delta = \delta_1 + \delta_2 + \delta_3$$

$$\delta = \frac{d_1^3}{3E_aI_1} + u\frac{Bd_2^2}{E_aI_2} + fd_3^2 \qquad (6.1)$$

for half 'through'-type girders $d_3 = d_1$

d_1 and d_2 are represented in Fig. 6.2

for composite girders d_1, d_2 and d_3 are represented in Fig.6.3

In the second term of this equation, u is either 0.50 or 0.33. For a single bay $u = 0.5$ as derived in Fig. 6.5(a), while for a multi-bay $u = 0.33$ as derived either from the conservative model of Fig. 6.5(b) where the stiffening effect of the right hand span is being ignored or from Fig. 6.5(c) where it constitutes a conservative upper bound to the given layout.

In the third term of eq. (6.1), 'f' is obtained from typical bolted connections between main and cross girders in half 'through'-type bridge girders as shown in Fig. 42 of BS 5400:Pt.3. To the author's knowledge no directions are as yet available on the transverse flexibility f_r, of any type of connection between the concrete slab and the top steel flange of a composite girder with intermediate vertical stiffeners.

In deriving the expression in clause 9.6.5 of the BS 5400:Pt.3 for the elastic buckling length l_e of the girder, by treating the compression flange as an elastic pin ended strut, a number of assumptions are taken:

(a) The compression flange is assumed to be subject to a uniform increasing axial load N, until buckling occurs when N reaches a critical value N_{cr}.

(b) This strut is assumed to be restrained vertically by the web and laterally by a variable force z/δ per unit length as shown in Fig. 6.6, where z represents an infinitesimal displacement that occurs when N_{cr} is reached.

(c) The deflected shape is assumed to be sinusoidal for which Timoshenko [82]

obtains eq. (6.2)

$$l_e = \frac{\pi}{\sqrt{2}}(E_a I_c^y \delta)^{0.25} \tag{6.2}$$

with I_c^y = the second moment of area of the compression flange around the local y-axis;
δ as in eq. (6.1)

These assumptions are valid for simply supported half 'through'-type bridge girders where the axial compression force is more or less constant over the midspan region, due to a small moment gradient, and where the deflected shape can therefore be modelled as being sinusoidal over that region as shown in Fig. 6.6.

Unfortunately, for continuous composite plate girders with intermediate vertical stiffeners acting as inverted U-frames, these assumptions are no longer valid and lead to over conservative design. The axial compression force decreases very rapidly away from the internal support region due to a high moment gradient and reaches only N_{cr} at the internal support section, while the deflected shape is no longer sinusoidal. In fact, from lateral distortional analysis [83] it has been found that for unstiffened girders the maximum lateral deflection occurs approximately $0.12l$ away from the internal support.

(ii) THE STRENGTH OF U-FRAMES: determination of F_t After ensuring that the U-frame is stiff enough to provide sufficient lateral restraint to the compression flange it is also necessary to ensure that the U frame is strong enough to retain this stiffness at the ultimate limit state. According to clause 9.12.2.2 of BS 5400:Pt.3, this means that the frame has to be designed to carry a transverse force F_t per U-frame, in addition to transverse forces due to wind load.

In deriving the expression in clause 9.12.2.2 for the transverse strength of all U-frames within l_e, a number of assumptions are made.

(a) It is assumed that $l_e \gg l_u$ so that there are l_e/l_u U frames within l_e, each of stiffness l_u/δ.

(b) The compression flange is assumed to behave as a laterally restrained pin ended strut with an initial bow of $l_e/1000$ and is subject to a uniform compressive force $N_f = A_{fc}\sigma_{fc}$.

(c) The deflected shape is assumed to be sinusoidal and Allen and Bulson [84] obtain under these assumptions a transverse force given by eq. (6.3)

$$F_t = k_f v \tag{6.3}$$

with k_f = amplification factor,
function of compressive stress in the flange (σ_{fc})
and the initial elastic non distortional bucking stress (σ_{cr})
$= \sigma_{fc}/(\sigma_{cr} - \sigma_{fc})$

$$v = \frac{l_u}{\delta}\frac{l_e}{1000}\sin\frac{\pi x}{l_e}$$

According to clause 9.12.2.2 the design value for the strength of all U-frames within l_e is given by eq. (6.4)

$$F_t = \gamma_f \left[\frac{l_e}{1000\delta/l_u}\right]\left[\frac{1}{\sigma_{cr}/\sigma_{fc} - 1}\right] \tag{6.4}$$

Again, the assumptions are only valid for simply supported half 'through'-type bridge girders. Even so, eq. (6.4) becomes rather conservative for U-frames away from the mid length $l_e/2$, since the transverse force is assumed to be equal to its maximum value over the whole length l_e, whereas this maximum is only reached at $l_e/2$ where the deflection is maximal. In 1959 Chwalla developed a matrix method [85] for beams with discrete U-frame action, where account is taken of the moment distribution over the whole span in calculating the limiting buckling load on the compression flange. Along the entire span the U-frames are replaced by springs, which provide an equivalent lateral restraint to the compression flange. In order to assess the error made by assuming F_t constant over l_e, Van de Pitte [86] applied Chwalla's method to a simply supported half 'through'-type bridge girder under uniform distributed load and found that the lateral force dropped by about 50% at a distance of 0.16 l away from midspan, where $M/M_{max} = 0.88$. The value of the transverse force F_t, at the mid length $l_e/2$ is only a little conservative for these types of girders as the amplification factor remains more or less constant due to a small moment gradient and as the value of this factor depends on σ_{cr} and σ_{fc} which are both known for this type of girders. The elastic critical buckling stress σ_{cr}, is obtained from non distortional theoretical analyses and $\sigma_{fc} = \sigma_{li}/\gamma_f$ is proportional to the limiting buckling stress σ_{li}, which is derived from data of lateral torsional buckling tests on I and] sections with equal and unequal flanges

[87], [88] where very little web distortion occurred, the type of buckling behaviour which would occur in half 'through'-type girders.

Unfortunately, for continuous composite plate girders with intermediate vertical stiffeners acting as inverted U-frames, the assumptions made in deriving eq. (6.4) are no longer valid and lead to an overconservative design. The amplification factor $\sigma_{fc}/(\sigma_{cr} - \sigma_{fc})$, defined in this equation reaches its peak value at the support section but decreases very rapidly away from the support due to the high moment gradient. The value of this factor is also conservative as only distortional buckling can occur in these types of girders and the Bridge Code does not provide expressions for elastic critical distortional buckling stresses nor does it provide data of lateral distortional buckling tests.

Just like for half 'through'-type girders, the value of F_t is not constant over l_e as assumed by eq. (6.4) , and the reduction away from the support due to Chwalla's matrix method will be at least the same if not larger due to the high moment gradient.

6.2 6.2. Design of composite plate girder with inverted U-frame action

6.2.1 Alternatives for the current design methods for U-frames in BS 5400:Pt.3

It is clear from the background of both formulae on stiffness and strength of U-frames in the BS 5400:Pt.3, that the current design methods are conservative and in especially so for inverted U-frames. This is not surprising as in a real structure buckling of the compression flange can only occur when that cross section distorts, requiring much higher values of both σ_{li} and σ_{cr} and than those obtained by the non distortional buckling tests and theory.

Although the current methods in the Bridge Code lead to over conservative results for inverted U-frames, most of the present doubts relating to the use of discrete inverted U-frames, arise from the use of the appropriate joint flexibility f_r. As this value is unknown for most modern connections and as $f_r d_3^2$ in eq. (6.1) is often of the same order of magnitude as the other terms, there exists a certain degree of uncertainty in the determination of l_e.

These deck type bridge girders are therefore more commonly restrained in practice by means of cross-frames. Provided the bracings are located at reason-

ably frequent intervals, this design will be more economical as it allows a more efficient use of the compression flange by permitting the stresses in them to be σ_{yc}/γ_m rather than σ_{li}/γ_m. However, there appears to be a growing opinion that the use of this type of frame attracts localised fatigue effects arising from eccentricity of the connections and local flexure of the deck slab under moving wheel load [89].

In this light Johnson and Bradford [90] have suggested for unstiffened plate girders of spans smaller than 30 m a design method to deal with the stability of the bottom flange in hogging regions, without bracing which allows for the flexibility of the connections and still produces design moments of resistance M_D, at the support which are about 1.5 to 2.0 times the moment obtained with the present Bridge Code. The design method also produces much higher design stresses than at present, which raises the question whether inelastic local buckling of the bottom flange near the internal support could not determine the strength of these beams instead. Limited experimental evidence is present [91], [92] to show that for uniform composite bridge members with non compact cross sections local buckling of the bottom flange does indeed precede distortional buckling, but no design criterion was known. In this light Johnson and Bradford [93] studied the inelastic local buckling behaviour. From both these results a new, less conservative design method was obtained by determining one value of the slenderness function β for local buckling of the compression flange (β_L) and another value for distortional lateral buckling (β_d), and taking the higher of the two as β. This value is used in place of $\lambda_{LT}(\sigma_{yc}/355)^{0.5}$ in the method in clause 9.7.3 of Part 3 of the Bridge Code and gives resistance moments that are much bigger than the ones given by the present Code method.

In [94] Nethercot and Weston developed another less conservative design method for distortional lateral buckling of unstiffened composite plate girders. This method resulted from a Finite Element analysis on a number of unstiffened bridge girders. Although the analysis was also tried on girders with light vertical stiffeners, it gave premature failure under unrealistic loads.

Unfortunately, Johnson and Bradford and Nethercot and Weston only produced less conservative solutions for continuous inverted U-frames, build up of unstiffened composite girders, which are only provided of vertical bearing stiffeners and lateral bracings at the internal supports, where a theoretical estimate of the joint flexibility f_r, along the girder is found to be still at least an order of magnitude less than the flexibility of the slab, which is in itself at least an order of magnitude less than the web, as shown in section 6.2.2. Therefore this value

can be ignored.

Although it is clear that vertical stiffeners will provide additional lateral restraint to the bottom flange if this joint were rigid ($f_r \rightarrow 0$), so that the new design method described in above stated paragraphs could be extrapolated; it is not clear what will happen if the joints are very flexible ($f_r \gg$). A theoretical lower bound estimate for f_r can be obtained which is found to be of the same order of magnitude as the flexibilities of the effective stiffener and the slab, as shown in section 6.2.2. Therefore this value cannot be ignored and the joints regarded as being rigid.

It is obvious that for any future theoretical work, which tries to incorporate the effects of the vertical stiffeners on the distortional buckling load, realistic values for f_r are needed. Such values can only be obtained from experiments on different connections under realistic loads.

6.2.2 Design example of a vertically stiffened plate girder as part of a U-frame

In this section an inner girder of a hypothetical three span bridge with a parallel plate girder system with discrete U-frame action has been designed in accordance with Parts 2 and 3 of the Bridge Code. This bridge has equal spans of 40 m, with a span over depth ratio of 24 and a total width of 13.25 m where the girders are spaced 2.58 m apart.

Some idea is gained this way of the order of magnitude and the type of moments and forces that could occur in vertically stiffened plate girders which are part of an inverted U-frame. Especial attention is drawn to the moments and forces on the connection between the deck slab and the top flange near the internal support at the position of a vertical stiffener.

In Appendix V all relevant information and calculations concerning the dimensioning and the design of this girder are given, following the same order as stated below:

(1) The most severe load combinations of dead load, superimposed dead load and live load are selected to obtain the maximum longitudinal moment and shear force at the internal support.

(2) With these values a first estimate can be made of the dimensions of the steel girder and the amount of reinforcement.

(3) After this, the design values for shear, V_D, and bending, M_D, of the girder at the internal support can be determined. These need to fulfill the requirements of clause 9.9.3.1 of Part 3 for pure bending, pure shear and the interaction of both.

(4) Also the strength requirements for the U-frame and especially for the connection, need to be fulfilled.

When for the girder calculated in Appendix V, the lower bound value of the deflection due to the transverse flexibility of the connection (δ_3) is taken into account in the calculation of the total lateral deflection (δ), then the values of δ_1, δ_2 and δ_3 as defined in eq. (6.1) stand in following proportion to each other

$$\frac{\delta_1}{\delta_2} = 0.56; \quad \frac{\delta_3}{\delta_2} = 0.15; \quad \frac{\delta_3}{\delta_1} = 0.28$$

If the same girder were unstiffened, these proportions would become

$$\frac{\delta_1}{\delta_2} = 288; \quad \frac{\delta_3}{\delta_2} = 2.3 \times 10^{-4}; \quad \frac{\delta_3}{\delta_1} = 8.3 \times 10^{-7}$$

It is clear that by stiffening the web, the contribution of the flexibility of the connection to the lateral deflection δ, is no longer negligible. For a beam where the slab thickness would be larger, the stiffener stockier and the connectors spaced further apart along the main girder, even the theoretical lower bound value of δ_3 can become larger than δ_1. Therefore, the real value of δ_3 can easily become the largest term in eq. (6.1).

Although not presented here, two other inner girders of similar depth (1.66 m), smaller spans and smaller aspect ratio ($\phi < 1.5$) were analysed and dimensioned in the same way as the girder in Appendix V. These analyses were done mainly to obtain different values of F_t, to be used in the next chapter as a guideline for the maximum transverse strength requirement on the equivalent joint as defined by the Note in clause 9.12.2.2 of BS 5400:Pt.3. For all three girders the design value of F_t was around 20 kN, which means that the real value would probably be much smaller, due to the conservative simplifications made in the Code.

6.3 Objective of Experimental work

6.3.1 Choice of test layout

To the author's knowledge no tests have been reported thus far on the measurement of the transverse flexibility f_r of the connection between the steel flange and the concrete slab of a stiffened composite plate girder, at the position of a vertical web stiffener.

In a real structure different forces would be working on this connection, i.e. the longitudinal shear along the steel-concrete interface, the longitudinal bending moment in the entire cross section, the transverse shear and the transverse-bending moment due to live loads in the slab and transverse shear force and bending moment due to F_t and wind loads. In order to take account of all of them in a test, a layout has to be chosen similar to the one in Fig. 6.7, where the different moments and forces on a real bridge girder are simulated. For this sort of test lots of space and material is required. However, if one neglects the longitudinal forces on the girder and the transverse forces on the slab, which would cause the slab to be cracked in both directions, the test layout can be tremendously simplified to the one in Fig. 6.8. By omitting these forces in a test, the slab remains uncracked at the start and therefore the measured flexibility will be smaller than if the slab were cracked. This difference is small as the transverse cracks caused by longitudinal bending do not influence the transverse bending (Fig. 6.9(a)) and as the longitudinal cracks caused by transverse bending only appear at the top of the slab and therefore do not interfere with the relative rotation between slab and steel plate at the slab soffit (Fig 6.9(b)).

In the statically determinate layout, chosen for the tests described in Chapter 7, only the lateral horizontal force F_t, is applied to the structure at the intersection of the centroid of the compression flange and the vertical stiffener. For this layout all the forces can be found from equilibrium as shown in Fig. 6.10. The only difficulty in this layout is the practical realisation of the support at point A, taking account of the self weight of the structure and the externally applied force F_t. In Fig. 6.11 it is shown that neither the moment nor shear force do vary considerably if this support in A were fixed or simply hinged.

6.3.2 Scope of the test results

These tests will provide different values for the transverse flexibility of different stud connector joints between the concrete slab and the vertically stiffened steel

girder for different stud configurations, under an increasing transverse force F_t. The stiffener forms part of a discrete inverted U-frame of a composite plate girder bridge, where bracing is only placed at the supports.

From these results a safe estimate for the flexibility will be obtained for each of the different stud configurations, assuming an equivalent joint length in accordance with the active part of the connection. It was hoped to obtain an indication of the relationship between the spacing of the connectors and their flexibility so that one safe value of f_r can be used for all configurations.

In the absence of a better design rule, this value of f_r could be added to the current clause 9.6.5 of BS 5400:Pt.3, which thus far only provides the flexibilities for three standardised bolted connections.

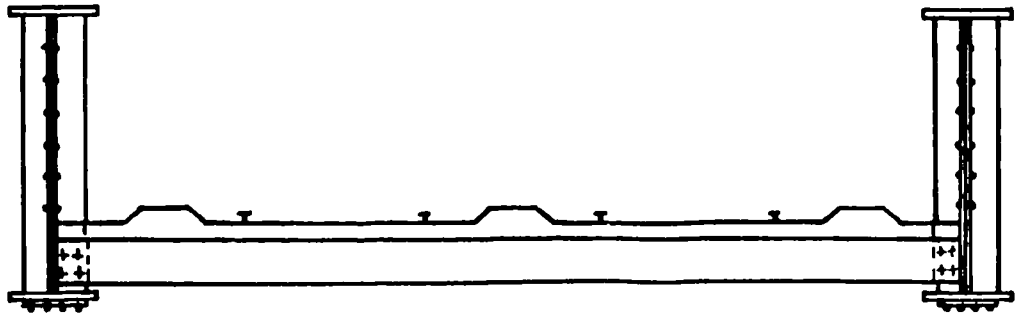

Figure 6.1: Cross-section of half 'through'-type riveted railway bridges.

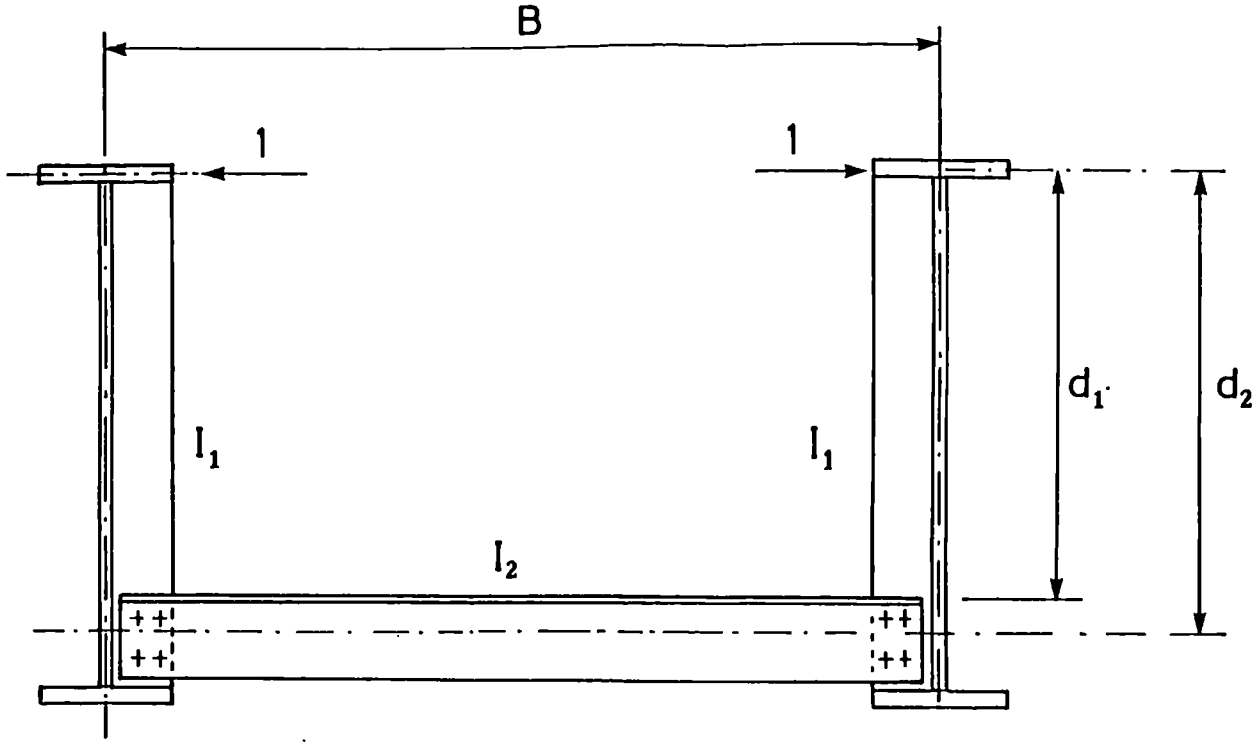

Figure 6.2: U-frame of half 'through'-type bolted bridge girders.

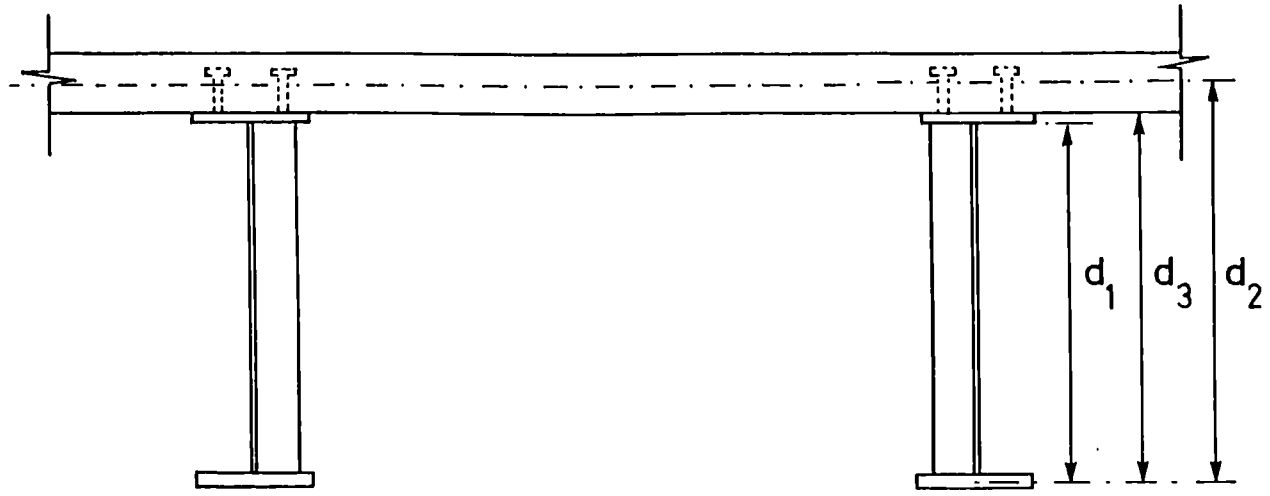

Figure 6.3: Inverted U-frame of composite bridge girders.

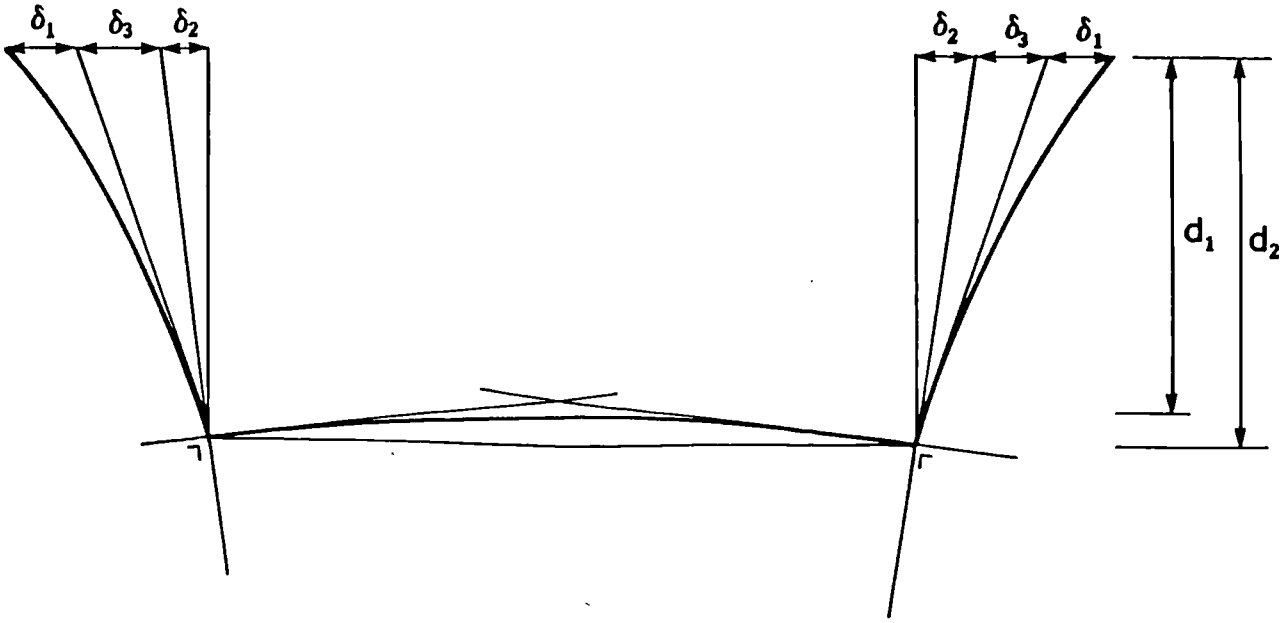

Figure 6.4: Deflection breakdown for U-frame of half 'through'-type bridge.

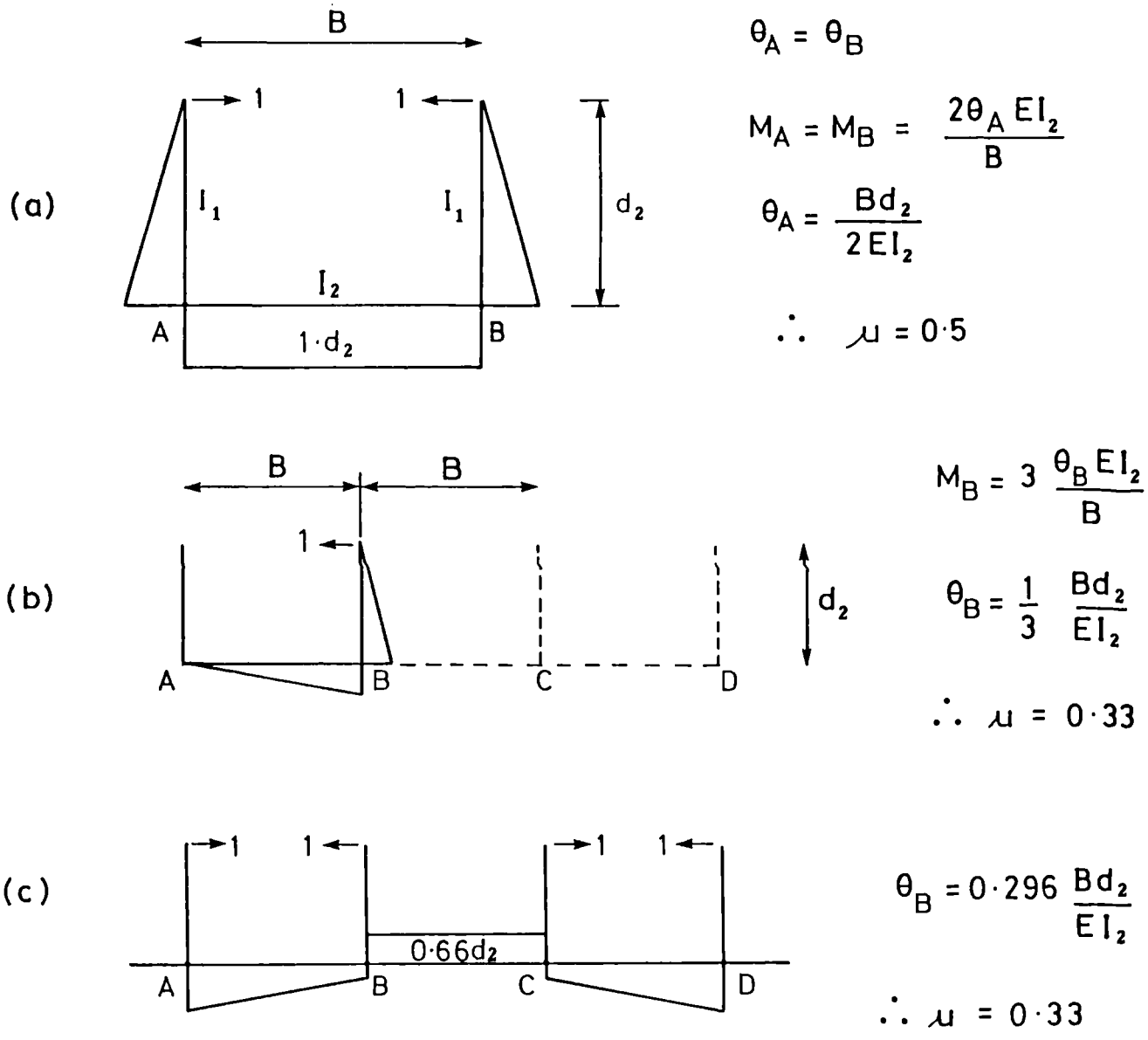

Figure 6.5: Theoretical rotations of the transverse member of the inverted U-frame or series of U-frames at the intersection with the longitudinal bridge beams.

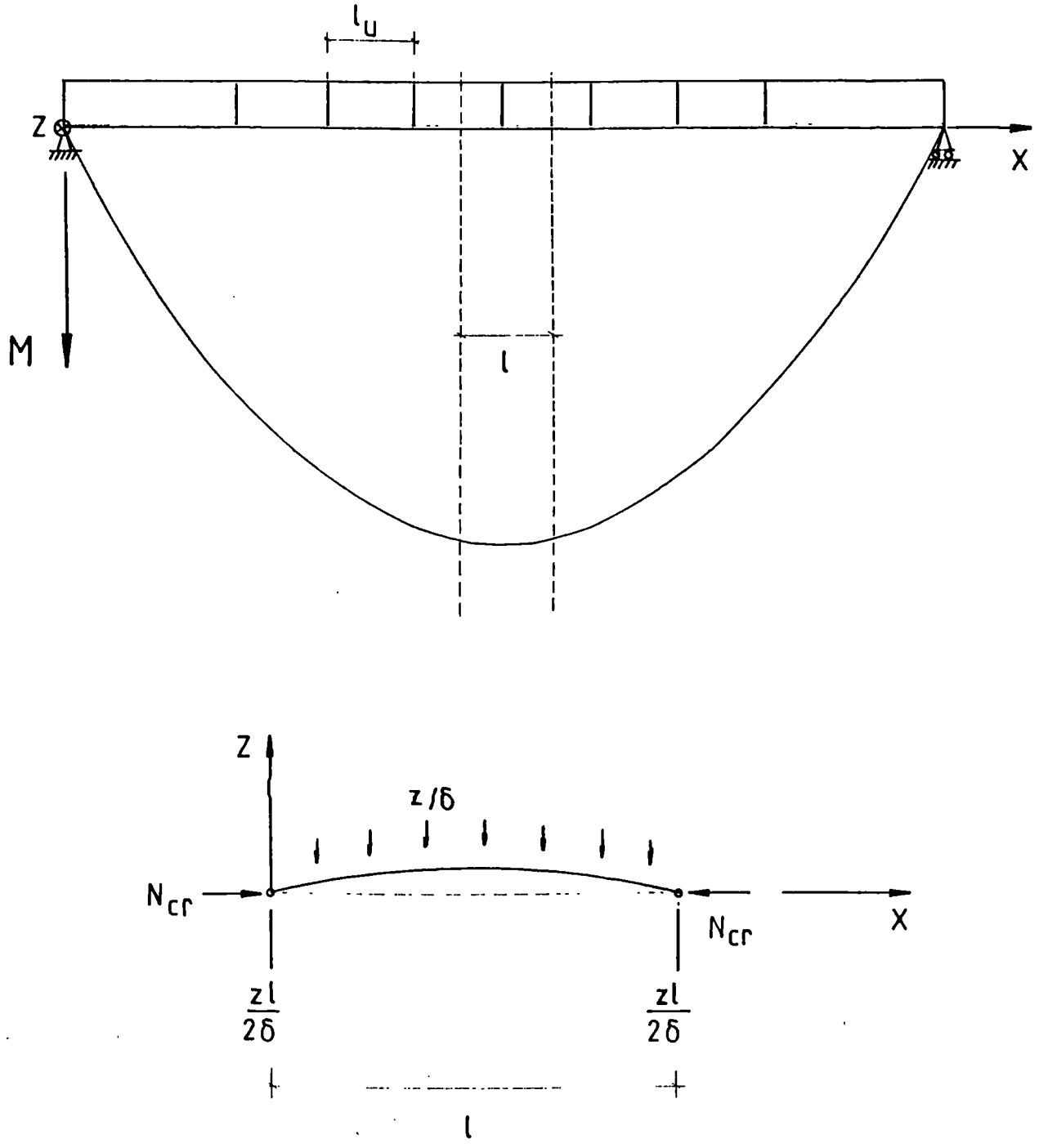

Figure 6.6: Strut analogy for the compression flange of the half 'through'-type bridge girder.

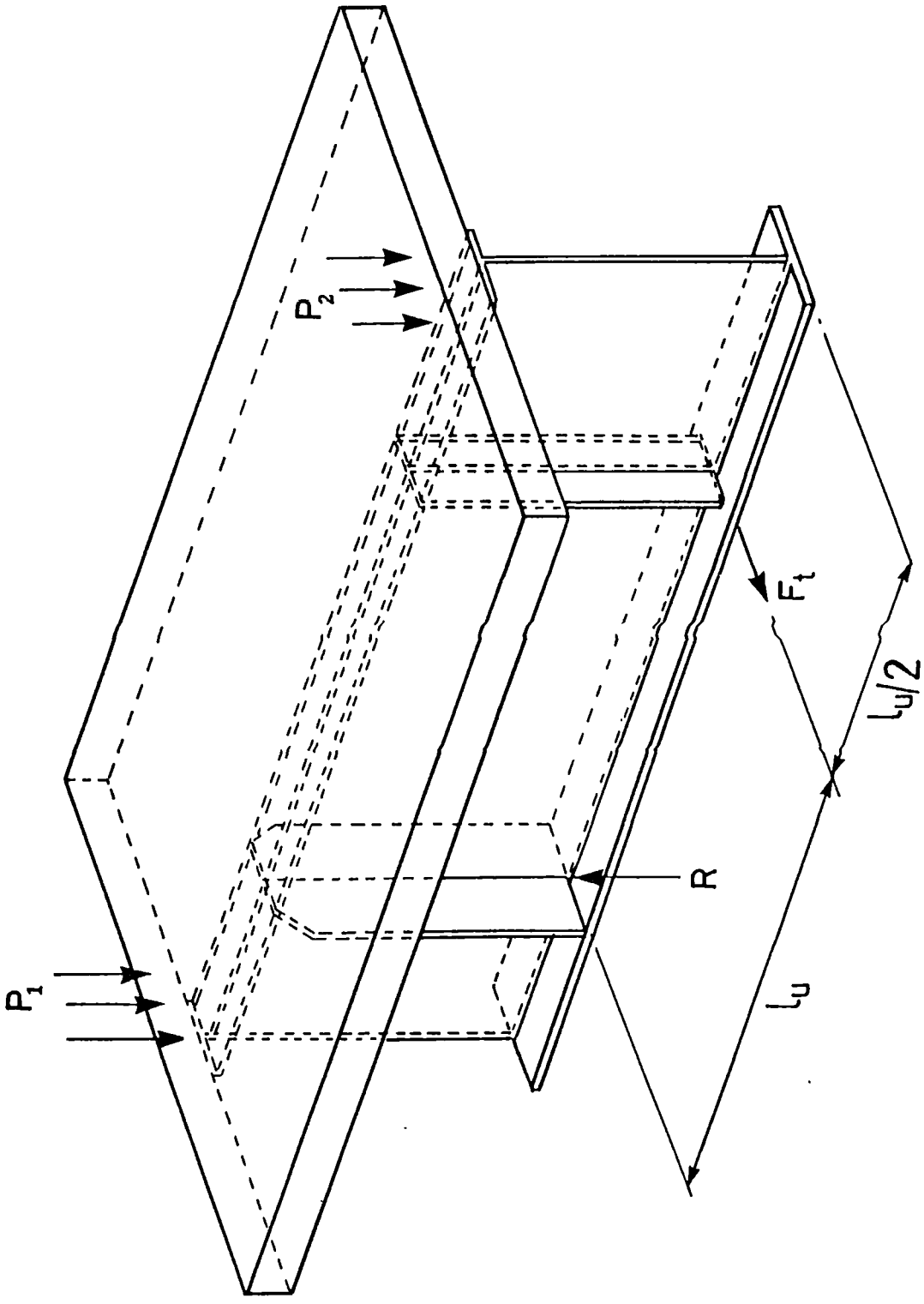

Figure 6.7: Test layout simulating all forces in the real bridge girder.

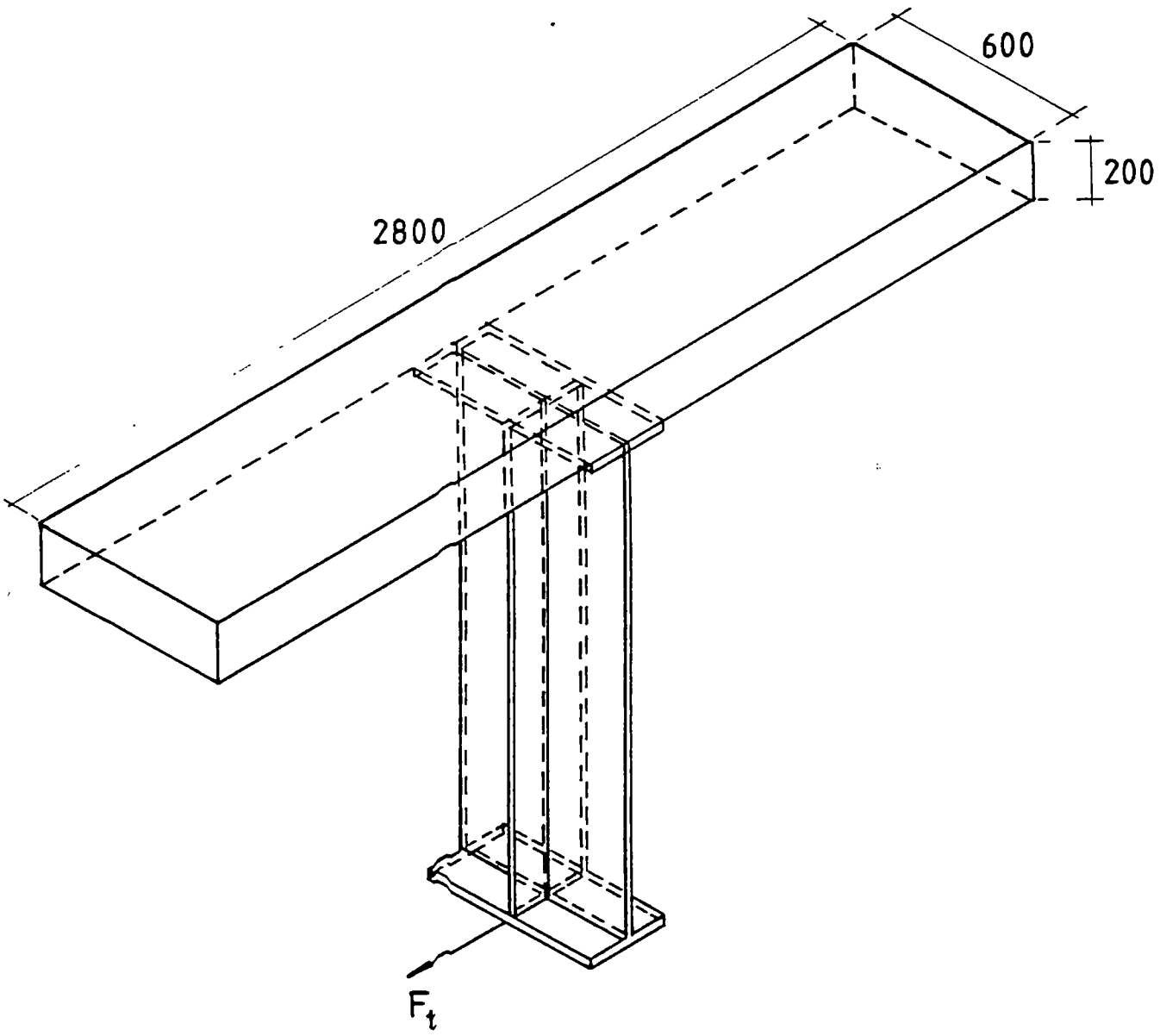

Figure 6.8: Chosen test layout, ignoring the longitudinal forces.

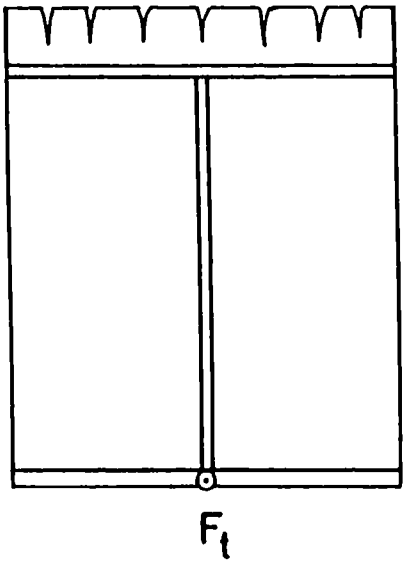

Figure 6.9(a): Transverse cracks caused by longitudinal bending.

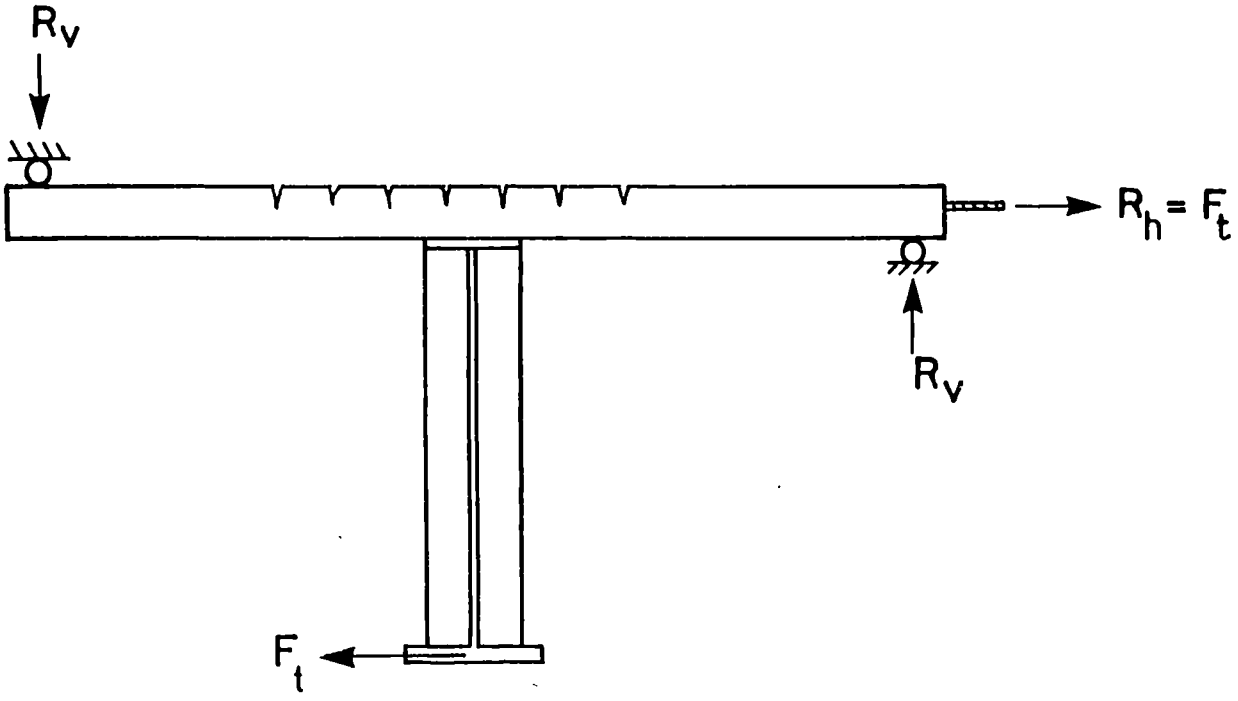

Figure 6.9(b): Longitudinal cracks caused by transverse bending.

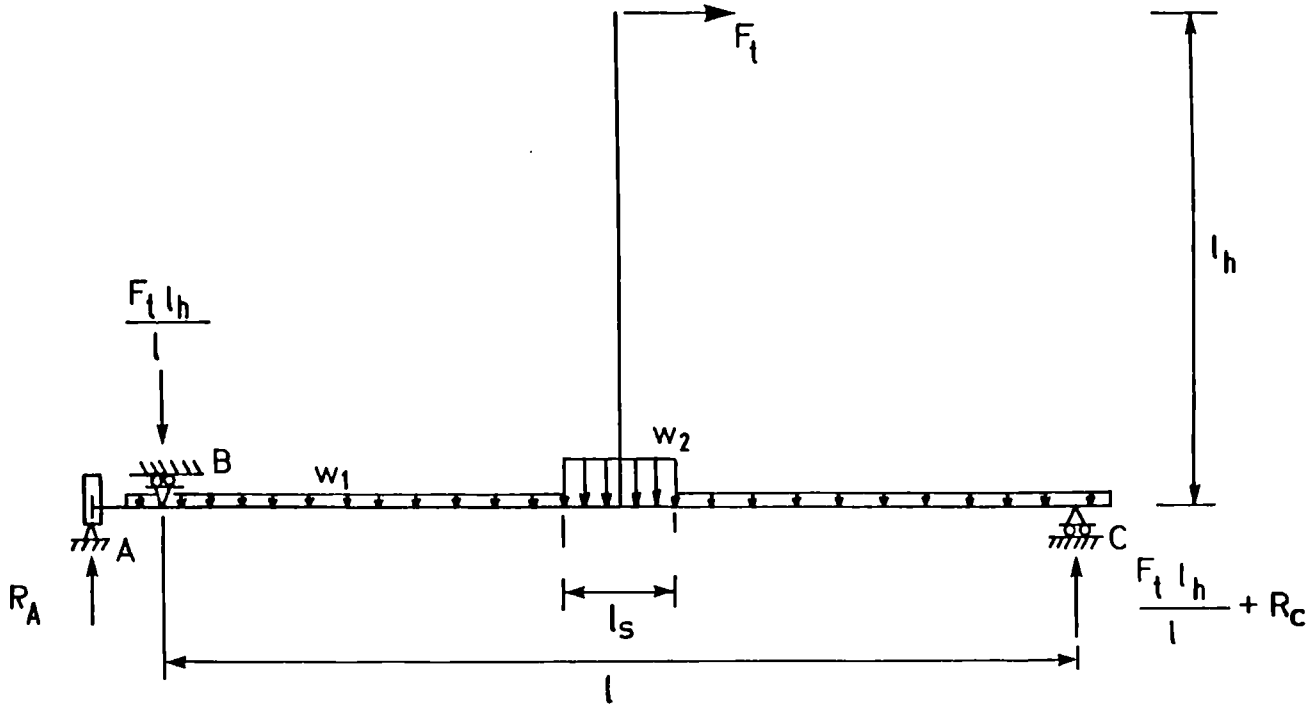

$$R_A = \frac{w_1 \left(l_1^2 + (l_1 + l)^2 - l_2\, l \right) + w_2\, l_2\, l}{2\,(l_3 - l_1 - l)}$$

$$R_C = w_1\,(l + 2l_1) + (w_2 - w_1)\, l_2 - R_A$$

Figure 6.10: Mechanical modelling of the test layout.

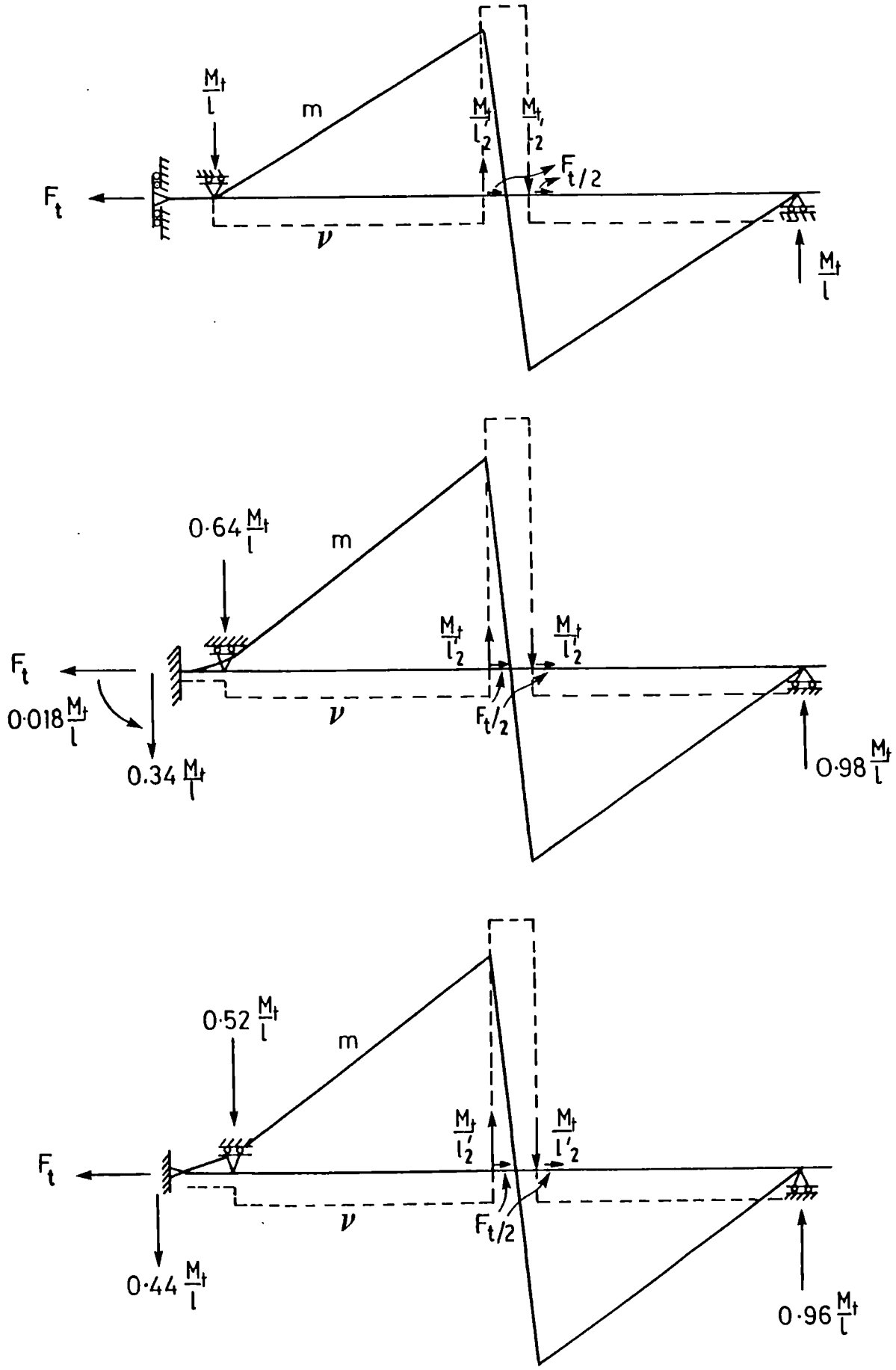

Figure 6.11: Influence of different support conditions on mechanical model.

Chapter 7

Tests on inverted U-frame connections

7.1 Introduction

A series of six composite slab-flange connections have been tested to observe their behaviour under a transverse moment. In a real structure, this moment is caused by a transverse force, applied at the intersection of the compression flange and the vertical stiffener in the hogging bending region of a main bridge girder. This force is due to initial imperfections in the bottom flange and hence tends to cause the flange to buckle laterally.

Experimental data had to be provided for a proposed transverse flexibility formula for slab-flange connections as part of an inverted U-frame.

Each tested beam was given a serial number from BM2 to BM7.

The first test specimen, with serial number BM1, was not provided with a slab, but instead, was bolted onto the strong floor to measure the flexibility of the steel girder alone.

7.2 Test Specimen

7.2.1 Choice of Specimen

It was decided that the test specimen would be chosen to be representative of a part of a longitudinal bridge plate girder near the internal support, with symmetrical vertical fitted stiffeners acting as a part of a discrete inverted U-frame.

In Fig. 7.1 the test specimen is being represented as part of the longitudinal bridge girder designed in Appendix V. The length of this specimen had to be larger than the longitudinal length spreading equally on both sides of the vertical stiffener, which represented the joint at the corner of the U-frame. The chosen length is 600 mm which is nearly as much as is required for stiffness by clause 9.6.5 of BS 5400:Pt.3 and which is more than three times as much as is suggested by clause 9.12.2.2 for strength.

All test specimens comprised a 600 × 330 × 25 top flange with a 600 × 500 × 12 web plate, two 159 × 500 × 12 stiffeners and a slab of 2800 mm wide, 600 mm long and 200 mm deep. Onto one stiffener two 152 × 76 channels were bolted back to back, as shown in Fig. 7.2, to extend the lever arm to 1437.5 mm above the slab soffit surface, where a transverse horizontal force was applied in the plane of the stiffeners. The use of the channels was introduced to reduce the amount of fabricated steelwork needed for each test specimen.

The geometric parameters changing in each test were the number and the position of the stud connectors on the top flange.

7.2.2 Detailing of the test specimen

7.2.2.1 The steel girder

Details of the top flange, the stiffeners, and the connections are given in Fig. 7.2. The channels, connected with eight HSFG Bolts to one stiffener, were used for all beams. They were cut from a single length of Grade 43 steel.

7.2.2.2 The shear connection

Headed studs, 125 mm long after welding and with a diameter of 19 mm, were used to provide shear connection and anchorage between the top flange and the concrete slab under transverse shear load and transverse moment.

Those studs, which during the test would be in tension, were slotted as shown by Fig. 7.3. These slots were made to fit strain gauges with a 25 mm × 4 mm wide base.

Details of the number, type and position of the stud connectors for each test, are given in Fig. 7.4, while Figs. 7.5 and 7.6 show the steelwork of test specimens BM3 and BM4.

7.2.2.3 The reinforced concrete slab

The arrangement of the longitudinal and transverse reinforcement in each test in the region of the connection depends on the position of the studs.

In Fig. 7.7 the arrangement of the transverse reinforcement for the different tests is given. This reinforcement consisted normally of two layers, top and bottom, of 16 mm ϕ Torbars at 150 mm spacing. In order to avoid a non-symmetric spacing as in test specimen BM4, or a spacing between bars larger than 200 mm as in test specimens BM3 and BM7, the bottom reinforcement in test specimen BM6 contained two 12 mm ϕ Torbars.

In Fig. 7.8 the only two different arrangements of longitudinal reinforcement used, are given together with a cross-section of the slabs for test specimens BM2 and BM3. Because no longitudinal forces are applied to the slab, the longitudinal reinforcement can be varied and reduced below the required minimum according to BS 5400:Pt.4, without affecting the behaviour of the tested specimens under the applied load.

7.2.3 Construction of test specimen

Stiffeners and web plate were welded in the laboratory's workshop. Studs were welded to the top flange using a semi-automatic arc-welding apparatus, provided by Crompton-Parkinson.

The concrete needed for each slab was obtained from 5 separate batches, mixed in a CUMFLOW RP 100 Rotating Pan Mixer in the laboratory. The same order of casting was used for all tests as the one shown in Fig. 7.9, where the volume of the final batch was spread equally over the total top surface area of the slab. In this way, the concrete strength is determined more accurately in different areas of the slab, especially in the important region near the shear connectors.

Rapid hardening Portland cement and 20 mm uncrushed aggregate were used throughout. A minimum 14-day cube crushing strength of 30 N/mm^2 was aimed for. However, for test BM6, sand and coarse aggregate of two different deliveries with different sieve analysis had to be mixed and the time lapse between casting the slab and testing the beam was reduced to 12 days.

The slab was cast in the same position as it would be in a bridge. The wooden formwork was supported by four horizontal steel channels spanning across the 600 mm length at four equally spaced points along its width. The formwork was removed three days after casting, but the damp hessian under which the slab had

cured, remained in place for five days.

Samples were taken from each batch of concrete mixed, to make up specimens as follows:

(1) Ten 150 mm cubes for crushing tests, two from each batch

(2) Five cylinders 100 × 200 diameter for indirect tensile test, one from each batch

(3) Two prisms 500 × 100 × 100 for modulus of rupture test, one each from batches 3 and 4.

All specimens were cured under damp hessian for 24 hours, then they were all transferred to a curing tank until they were tested in accordance with BS 1881: Parts 116, 117 and 118.

7.3 The test rig

The test rig for test specimens BM2 to BM7 is shown in Figs. 7.10 to 7.12. The origin of the axes in Fig. 7.11 is the intersection of the centre-lines through the web (X-axes) and the stiffener (Y-axes) at the steel flange concrete slab interface. The load was applied to the rod through a 5-tonne hydraulic jack, fed from a manual pump. The reaction frame at one end of the beam, the frame over the middle of the beam specimen, and the portal frame which supports the jack and load cell were built from standard laboratory 'Meccano'.

Theoretically, all test specimens are geometrically symmetrical about the Y-axis and the transverse load F_t, is applied in the YZ plane, parallel with the Y-axis, thus producing only a transverse moment M_t^x, about the X-axis. In reality, the free end of the stiffener can be slightly twisted due to welding and the channels are not perfectly straight, which brings point T, where the tensile load is applied to the specimen, out of the YZ plane. Therefore the real force applied at point T has also a component in the X direction, which causes a moment M_t^y, around the Y-axis.

Originally, cylindrical bearings were used, but the moment M_t^y which caused the slab to twist around the Y-axis, would make the bearings support the beam specimen only at points A_1 and A_2 shown on Fig. 7.12, rather than over the whole width of the bearing. The slab then spanned diagonally in the direction A_1A_2 and point T showed visible displacements in the X direction which increased proportionally with the load ($\Delta x_T \approx \Delta y_T/4$).

In order to eliminate the lateral movement of the stiffener in the X direction, the component of the applied load in the X direction has to be minimised or ideally eliminated and the corresponding moment M_t^y should not influence the measurements.

Both requirements can be fulfilled by better positioning of each beam specimen vis-à-vis the jack and rod and by replacing the cylindrical bearings by spherical bearings.

A theodolite was placed behind the jack, as close as possible to the YZ plane. The theodolite was set up in such a way that the centre of the stiffener near the flange and the centre of the slab at the bearing were within one near-to-vertical plane. Afterwards the centre of the rod was placed within the same plane (3 points determine one plane). This was possible by bolting a slotted plate onto the Meccano behind which the load cell and jack were placed (Fig. 7.10). In this way, the lateral displacement of point T and the moment M_t^y were minimised.

By placing two spherical bearings, instead of two cylindrical ones, on the same centre line, the moment M_t^y will cause a rotation around the Y-axis (Fig. 7.13) until F_t^x has disappeared.

Therefore, in all tests two spherical bearings were used, which allowed rotations in all directions, in combination with roller bearings, which allowed a translation only in one direction: parallel to the axes of loading (Fig. 7.14). Under the applied load the test specimen can still move freely in the Y direction. In order to prevent that movement, three 20 mm diameter reinforcement bars, fully anchored in the slab at one end, were bolted to two equal angles at the other end, which form part of the 'Meccano' of the reaction frame.

7.4 INSTRUMENTATION

7.4.1 Measurements taken

Figs. 7.11, 7.12 and 7.15 illustrate the positions at which angular and linear displacements were measured. In the following sections all indications of positions on the test specimen are given in relation to a real bridge girder i.e. the slab soffit of the test specimen is that side of the slab which would be the soffit in a real girder.

The rotation of the slab was measured around the axes X', parallel with the X-axis through O' (Fig. 7.11), at mid-depth of the slab and the centre of the

gauge length coincided with the plane through the center of the web plate. The angle of rotation of the top flange at the position of the stiffener, was obtained by measuring the rotation of the stiffener at approximately 2.5 cm under the top flange.

The **displacement** gauges, D_4 and D_5, measuring the relative vertical displacement between the top flange near the stiffener and the soffit of the concrete slab, were used to check the difference between the two measured rotations. The displacement gauges, D_1, D_2, D_3 and D_6, measuring the horizontal displacement of the slab and of point T can also be used as control measurements, provided the displacement due to the deformation of steelwork is known.

The **strains** were measured in the slotted stud connectors, which were placed on the tensile side of the stiffener. They were also measured in the compression side of the stiffener to check the stress level, at the positions shown in Fig. 7.2.

The applied **load** was measured at the jacking point.

7.4.2 Instruments used

The 100 kN DATA-sense compression load cell used in all tests was calibrated three times by the technician: once before the test, once after three tests and a final time after the last test was completed.

Dial gauges, where used, were of a sensitivity of 0.01 mm per division and had a maximum travel of 10 mm except the gauge D_6 at the top T (Fig. 7.11) which needed a maximum travel of 25 mm up to first cracking.

Strains in the studs and in the stiffener were always measured with electrical resistance strain gauges connected in 1/4 bridge i.e. a portable 5 channel strain-indicator type B105 with a 10 channel extension unit. This instrument was calibrated prior to testing by the technician. The strain gauges are from the polyester gauges series 'P', from TML-strain gauge manufacturers. The ones on the stiffener are type PL-10 (gauge length 10 mm and width 3 mm) and the ones in the studs are type PLS-10 (gauge length 10 mm and width 1.5 mm). Both types are temperature compensated.

Rotations of the crucifix-shaped stiffener were measured with a demountable inclinometer with a 3 in. gauge length. The instrument has a measuring range of -0.32 rad to $+0.32$ rad and is fitted with a micrometer thimble (graduated in 0.0001 in./div.) to obtain the vertical displacement and with an accurate bubble spirit level to provide a zero datum with a theoretical sensitivity of 2.9×10^{-4} rad/div..

Rotations of the concrete slab were also measured with a demountable inclinometer, but one with a 4 in. gauge length, a measuring range only from -7.069 mrad. to +7.069 mrad. and a theoretical sensitivity smaller than 1.57×10^{-6} rad/div.. This instrument, which will be referred to as clinometer throughout the text, was manufactured by Huggenberger and has a spirit level where the eyepiece presents two halves of each end of the bubble, side by side. A less sensitive spirit level was also mounted in the transverse direction to ease the setting of the initial position.

Both inclinometer and clinometer are set up on three bearing plates: one with a plane ground face, one with a groove and one with an internal conical seat. This layout and combination of setting plates enables the instruments, at any time, to be set up in exactly the same position as that used for the initial measurement, which guarantees reliability, repeatability and accuracy of the measurements.

7.5 Testing Procedure

For test BM2 the load was increased in increments of 5 kN up to 20 kN in a first load cycle and up to the maximum load carrying capacity in a second load cycle. In a third load cycle, the horizontal displacement of point T (Fig. 7.11) was increased in increments of 3 mm until failure occurred. After each load/displacement increment the load/displacement was held constant for about 30 minutes while a set of readings was taken and while the slab was examined for cracks. This test was completed in one day, but the load increment was too large, especially after initial flexural cracks had formed at the top of the slab.

For test BM3 the load was increased in increments of 2.5 kN up to a load where no visible cracking had yet occurred, at about 75% of the load where initial cracking occurred in BM2. In a second load cycle the load was increased to the point where first flexural cracks became visible and in the final load cycle the beam was brought to failure. After visible initial diagonal cracking had occurred, the load increment was reduced to 1 kN, until the cracks widened and the displacement of the jack had to be more than twice as large as just after cracking to produce this load increment of 1 kN. At this point in the test the horizontal displacement of point T (Fig. 7.11) was monitored instead of the load increment and displacement increments of 4 mm were given to point T until failure occurred. As in test BM2, readings were taken after each load/displacement increment and decrement and the load/displacement was held constant for about 30 minutes. The test was completed in two days. Due to creep there was a slight fall off of

load overnight, during the second load cycle, but the original loading curve was regained on continued loading.

For test BM4 a similar procedure was followed as in test BM3, but the load increments were reduced to 2 kN in order to obtain a closer estimate of the initial diagonal cracking load. Also, in the second load cycle, the load was increased until first diagonal cracking became visible rather than flexural cracking.

For tests BM5 and BM6 the load was increased and decreased in three cycles, primarily to study the elasticity of the connection under small loads, before any cracking occurs. In the third and final load cycle the load was increased in load increments of 2 kN until first diagonal cracking became visible and in load increments of 1 kN until the cracks widened. Again, the displacement of point T was monitored in displacement increments of 4 mm until failure occurred.

For test BM7 the load was increased in load increments of 2 kN up to a very small load in a first load cycle, in order to check elasticity. In the second load cycle the load was increased in increments of 2 kN until diagonal cracking became visible, followed by increments of 1 kN until the cracks widened and load control was replaced by displacement control of point T until failure.

7.6 Auxiliary tests

7.6.1 Material properties

Tension tests were performed on samples of the top flange, the studs and the reinforcement, using a 100 kN Monsanto extensometer machine type 'E'. For the mild steel of the top flange, with its well-defined yield point, coupons were cut and machined and the stress-strain curves were obtained from the x-y plotter. These measurements were supplemented by measuring the extension with a Baty dial gauge extensometer with a 2 in. gauge length and a sensitivity of 1/20 000 in. per division. For the high-yield studs, coupons were machined, but the grips of the Monsanto machine came too close for the extensometer to fit. Therefore the tensile tests were performed on a DARTEC fatigue machine. Again, the extension was measured with the Baty extensometer. For the high-yield reinforcing bars no accurate strain measurements were needed: the stress-strain curves from the Monsanto extensometer were sufficient. The dimensions of the coupons from the top flange and the studs are given in Fig. 7.16.

Tests on concrete specimens were carried out in accordance with BS 1881

where appropriate, using a compression Denison machine. Cube crushing tests, modulus of rupture tests and tensile splitting tests were normally conducted only a few hours before the corresponding test specimen was tested, without performing a 7-day cube test to assess the strength of the concrete and therefore the readiness of the test specimen to be tested. Only for test specimen BM6, three preliminary cube tests were performed after 10 days to assess the readiness to test after 12 days.

7.6.2 Tests on instrumentation

Before each test was started the readings on the inclinometer and the clinometer were taken several times in order to assess the repeatability of the different readings and prior to all testing their sensitivity and accuracy had been tested by adding slip gauges to the plane-bearing plate.

The dial gauges were tested at the start of the test series by positioning the measuring rod on a plane-bearing surface and adding different slip gauges. In this way the repeatability, the sensitivity and the accuracy of the measurements could be tested. This knowledge of the sensitivity and the accuracy is especially useful, although the repeatability of the reading has little use as the dial gauges remained static throughout the tests.

7.6.3 Test on specimen BM1

Test specimen BM1 was bolted on one side to the strong floor and was embedded on the other side in dental paste as shown in Fig. 7.15. This test was carried out to determine the behaviour of the steel without the concrete slab, under a transverse load.

The test procedure was much simpler than for the other test specimen. The load increased in load increments of 2 kN and in three different load cycles.

7.7 Test results

7.7.1 Introduction

The results which were relevant to the global behaviour of the test specimens BM2 to BM7 are presented in this section.

7.7.2 Formation of the crack pattern

Initial flexural cracking occurred on the top and bottom of the slab when the externally applied moment at that position corresponded within 20% to the moment at initial flexural cracking, $M_{in.cr}$, obtained by equations (7.1) to (7.4), where the second moment of inertia for the slab I_u, is calculated for an uncracked slab, with a modular ratio, as given in the Bridge Code.

$$M_{in.cr} = \frac{M_{cb} + M_{ct}}{2} = \frac{f_{cr} I_u}{Z} \tag{7.1}$$

$$\text{with } M_{cb} = \frac{f_{cb} I_u}{Z} \tag{7.2}$$

$$M_{ct} = \frac{f_{ct} I_u}{Z} \tag{7.3}$$

$$f_{cr} = \frac{f_{cb} + f_{ct}}{2} \tag{7.4}$$

$$\text{and } Z = \text{distance from top or bottom of slab to the elastic neutral axis}$$

In Table 7.1 the positions of the initial flexural cracks are given within the axis as defined in Fig. 7.11 together with the corresponding total externally applied moments $M_{e,tot}$, and the calculated moments at initial flexural cracking, using eq. (7.1).

Usually, a first flexural crack would form at the top of the slab at distances of 160 mm to 220 mm away from the centre of the slab width, where the applied moment is largest as shown in Fig. 7.17, where both shear and bending moment diagrams are represented for test specimen BM5. At higher load stages, a flexural crack would form at the soffit of the slab near the row of studs in tension. In this region a biaxial stress state exists, created by transverse bending of the slab, transverse normal forces in the slab and compressive forces applied by the stud head onto the concrete below.

At a certain point, under increasing load, an initial diagonal shear crack becomes visible on the sides of the slab. This initial crack appears only at mid-depth of the slab near the position of the heads of the row of studs in the sagging bending region of the slab as shown in Fig. 7.17. Under increasing load, the crack pattern changes in different ways for different test specimens. The main cracks in the final crack patterns are given in Figs. 7.18 to 7.23 for tests BM2 to BM7, with the indication of the load cycles (in Roman numerals) and the load levels or

displacement levels at which the cracks appeared.

A more detailed description of the behaviour of the different test specimens, after initial shear cracking, is given below.

Specimen BM2: The initial shear crack formed at an angle of 37° with the horizontal centre line at mid-depth of the slab. Under decreasing load, but increasing displacement of the applied force this crack grew towards the slab soffit, without widening, while at the same time more flexural cracks appeared on the slab soffit. Finally, after the load resisted by the specimen had dropped to 15 kN, the structure failed by pulling out of the studs. These studs, embedded in concrete pulled out a shallow section of concrete, which formed an angle of 16° with the horizontal, as shown in Fig. 7.24.

Specimen BM3: The initial shear crack formed an angle of 31° with the centre line at mid-depth of the slab. Under increasing load, a second diagonal crack appeared parallel to the first, near the position of the row of stud heads in the hogging bending region of the slab. At the same time the first crack gradually spread along the top layer of reinforcement. The load carrying capacity continued to increase while the two parallel cracks widened and finally joined up at the top layer of transverse reinforcement. At this load stage, the concrete started also to crack along the bottom layer of transverse reinforcement. The load carrying capacity had reached its peak of 33.4 kN and the load decreased under increasing displacement of the applied force. The concrete started to crush in the hogging bending region under the flange edge when the load resisted by the specimen had dropped to approximately 31 kN.

Specimen BM4: The initial diagonal shear crack formed an angle of 43° with the centre line at mid-depth of the slab. Under increasing load this crack bifurcated: one part grew at an angle of 43° and the other part at an angle of 21°, reaching the compression zone near the edge of the flange in the hogging region. The other end of the crack propagated at the same angle until it joined up with the top transverse reinforcement. At the slab soffit, in the sagging bending region of the slab, small cracks appeared near the transverse reinforcement due to pull out forces. The load carrying capacity continued to increase. The diagonal cracks widened, propagated further along the top layer of transverse reinforcement and they bifurcated more into the compression zone until the concrete started to crush under the flange edge at the hogging region of the slab, under a load of 37.5 kN.

Specimen BM5: The initial diagonal shear crack formed an angle of 26° with the centre line of the slab. This crack initially propagated in both directions. Under increasing load a parallel crack appeared, which joined up with the bottom reinforcement in the hogging bending region. The load carrying capacity still increased until the first diagonal crack bifurcated and propagated towards the bottom transverse reinforcement in the sagging region of the slab and the transverse load reached its peak value of 26.5 kN. The load carrying capacity diminished while the displacement of the force increased. Finally at a transverse load of 21 kN the concrete crushed under the flange edge in the hogging region and at 20 kN the beam failed by pulling out of the studs. The shear plane of the concrete section pulled out by the studs, formed an angle of 15° with the horizontal.

Specimen BM6: The initial diagonal shear crack grew from a flexural crack under an angle of 37° with the centre line of the slab at the position of the heads of the middle row of studs. Under increasing load, a second crack appeared at an angle of 30° with the centre line of the slab, at the position of the heads of the row of studs in the sagging region of the slab. This crack widened and propagated towards the top layer of transverse reinforcement in the sagging bending region when the load carrying capacity of the specimen reached its peak at 33 kN. Afterwards, while the load diminished, a third crack formed near the heads of the third row of studs while the second crack widened. Finally, at a load carrying capacity of 30 kN the concrete crushed under the edge of the steel flange in the hogging bending region of the slab.

Specimen BM7: Initially a diagonal shear crack formed at an angle of 33° with the centre line of the slab, at the position of the heads of the row of studs in tension. Under increasing load, this crack propagated at the same angle in both directions. The crack widened and joined up at one side with the top layer of reinforcement, while on the other side the crack bifurcated at the position of the heads of the studs. At this stage, the crack pattern was very similar to the one in test specimen BM4 and the test was terminated at a transverse load of 36 kN.

The crack patterns for test specimens BM2 to BM7 are also shown in the photographs on Figs. 7.24 to 7.29. For BM7, the photograph was taken before the test was completed, and so does not show the full crack pattern.

7.7.3 Relative transverse rotation and flexibility of the connection

The average value of the two rotations, θ^i_{s1} and θ^i_{s2}, measured on opposite sides of both stiffeners with the 3″ gauge length inclinometer, as indicated in both Figs. 7.2 and 7.11, gives the rotation of the top flange near the stiffener around the X-axis. The average value of the two rotations, θ^i_{c1} and θ^i_{c2}, measured on both sides of the concrete slab with the 4″ gauge length clinometer, as indicated in Fig. 7.12, gives the rotations of the slab around the axis X' through 0′ and parallel with X, as shown in Fig. 7.11.

The difference between the rotation of the top flange θ^i_s, and the rotation of the concrete slab θ^i_c, both measured with different inclinometers, gives the relative rotation of the connection, as expressed by eq. (7.5):

$$\theta^i_r = \theta^i_s - \theta^i_c \tag{7.5}$$

A less accurate value for this rotation can be obtained by dividing the difference in relative vertical displacements ΔZ, between flange and slab at points D_4 and D_5 of Fig. 7.11 by the distance between them, as expressed by eq. (7.6).

$$\theta^d_r = \frac{\Delta Z(D_4, D_5)}{|D_4 D_5|} \tag{7.6}$$

$$\text{with } \Delta Z(D_4, D_5) = \Delta Z(D_4) - \Delta Z(D_5)$$

The measured rotations and displacements and the calculated relative rotations from these measured values are given in Appendix VI for different load stages and different load cycles for tests BM2 to BM7.

Similar information is represented in six relationships between the transverse moment M_t, and the rotation around the X-axis, one for each of the different test specimens as shown in Figs. 7.30 to 7.35. In these figures, the vertical axis represents the externally applied transverse moment at the top flange concrete slab interface, while the horizontal axis represents the different rotations at the same position. The transverse moment M_t, is calculated by multiplying the load-cell reading F_t, by the average length of the lever arm l_h under transverse loading, between the point of applying this tensile force and the slab soffit, as indicated in Fig. 7.11.

The rotation of the transverse connection developed more or less in proportion to the applied moment until the first diagonal cracking occurred, when a sudden

increase in rotation took place under constant moment. Thereafter, the slope of the moment rotation curve is much smaller, but still positive. This slope depends on the position of the diagonal crack and the crack pattern. In this research only the initial rotation before the formation of the first diagonal shear crack is relevant. Therefore, consistent measurements of rotations were terminated after extensive cracking, but sporadic measurements were still taken up to failure.

If at any load stage after initial shear cracking, the moment was slowly reduced and then increased to its former value, as was the case for specimens BM2, BM4 and BM6, the relationship between the transverse moment and the rotation during the increase was quasi-linear.

The relevant rotation did not return to zero when the external moment was removed, not even within the elastic range. Instead it returned to some value of residual rotation, which grew larger when the maximum external moment to which the connection had been subjected was increased.

The rotations, θ^i_{s3} and θ^i_{s4}, measured at 200 mm away from the stiffener as indicated in Fig. 7.12 showed that the flange deformed in the X-direction. They also showed that the rotations are quite different in the sagging and hogging bending region of the specimen, depending on the positions of the studs. The average value of this rotation is about 1.6 times smaller than θ^i_{s1}, or θ^i_{s2} near the stiffener. This difference is probably due to the variation in torsional rotation of the flange between the stiffener and the edge of the specimen, although the rotations, θ^i_{s5} and θ^i_{s6}, shown on Fig. 7.12 and measured only on specimens BM2 and BM3, hardly showed any consistent variation under loading.

The rotations, θ^i_{c3} and θ^i_{c4}, measured on the slab soffit as indicated in Fig. 7.12 gave little information after flexural cracking of the slab in that area had occurred.

7.7.4 Strains in stud connectors

The ratio of the shear force to the tensile force in any stud in tension is smaller than 0.10 for all studs. According to Johnson and Millard [46] and to McMackin, *et al.* [47] the shear force will not influence the tensile strength and behaviour of the stud for such small proportions. Moreover, by measuring the strain in the middle of the stud, close to the weld collar (50 mm above it), it is assumed that any tensile stresses due to bending of the stud, caused by the small shear forces, will not influence the measured values. A linear strain distribution is assumed under elastic bending and tension of the shank.

For test specimens BM2 and BM5 the strains in the studs and subsequently the calculated forces in the shanks of these studs F_{sh}, increased proportionally with the applied transverse load, until first diagonal cracking visibly occurred. The work done by the applied transverse force F_t, gets partly dissipated in the formation of a shear crack. The relationship between the transverse moment M_t, and the tensile forces in the shanks of the studs show clearly when the diagonal cracks formed, for both test specimens BM2 and BM5, in Figs. 7.36 and 7.37 respectively: the slope of the $M_t - F_{sh}$ curve diminishes.

For tests BM4 and BM7, the strains in the studs in tension near the stiffener initially increased proportionally with the applied transverse load, while the strains in the outer studs hardly changed. In Figs. 7.38 and 7.39 the relationships between the transverse moment and the tensile forces in the shanks of the studs are given for specimens BM4 and BM7 respectively. The superscripts for the forces F_{sh}, in the different shanks in these figures correspond with the stud numbers in Fig. 7.4. In both figures the tensile forces in the shanks of the studs closest to the stiffener diminish suddenly under an external transverse moment M_t, of approximately 15 kNm, while the rate of change of the tensile forces in the shanks of the studs further from the stiffeners increases suddenly under this moment. Similar changes occurred when the first diagonal shear crack became visible on both sides of the test specimen. After the crack had formed, the tensile forces in the shanks of the studs increased again, under an increasing transverse moment.

For test BM6 a similar behaviour was noted for the forces in the shanks of studs S_1 and S_7, and S_4 and S_6 of Fig. 7.4. The relationship between the transverse moment and the tensile forces in the shanks of these studs is given in Fig. 7.40. Under an external moment M_t, of approximately 16 kNm the outer studs in tension started to take up load, while the first diagonal crack only became visible under an external moment of 30 kNm. At this load level, the strains in the shanks of the centrally placed studs S_4 and S_6 decreased while the strains in the shanks of the outer studs increased enormously.

The strain measurements and the corresponding calculated tensile forces in the shanks of the studs, are given numerically in Appendix IV for the highest load stages in the final load cycles for all test specimens.

7.7.5 Auxiliary tests

7.7.5.1 Material properties

The results of the tests on the steel coupons of the top flange are given in Table 7.2 and the proof stresses of the different samples of the different reinforcement bars are given in Table 7.3.

The results of the tests on the concrete specimens are given in Table 7.4. For test specimen BM7, a number of technical problems in the laboratory produced increasingly stronger batches of concrete. Therefore, only the average value of the concrete cube strength of batches 4 and 5 is given which surrounds the stud connectors as shown in Fig. 7.9.

For the stud samples, no results were needed for the yield stress nor for the tensile strength, as the studs would never be stressed to more than 75% of their yield stress. The Young's modulus was measured at different strain levels for the different specimens and the stress-strain results are shown in Fig. 7.41.

7.7.5.2 Accuracy of the instrumentation

The accuracy of the Dial gauges, measured with slip gauges, proved to be ± 0.02 mm, which is about the same as the repeatability of these instruments.

The measured sensitivity and accuracy of the 3″ gauge length inclinometer with the slip gauges, became as small as its repeatability: 0.033 mrad., since it was fairly easy to read the bubble spirit level to much less than 1 division.

The compression load cell was calibrated, using a Monsanto tensometer testing machine, type 'E', which in itself was only calibrated according to BS 1660:Pt.1 as Grade 1.0 from 8 kN upwards. This calibration took place just before the last calibration of the load cell. Therefore only the last calibration curve is used for the load cell readings.

The accuracy of the strain readings from the portable 5 channel strain indicator ranged from -1.0 to $+1.0$ microstrain as obtained from the calibration curve, using an extensometer, while the repeatability was measured to range from -0.2 to $+0.2$ microstrain.

7.7.5.3 Test on specimen BM1

Contrary to the aim of this test, rotations of the top flange still occurred due to the indentation of the dental paste in which the flange was embedded. Therefore

Table 7.1: Prediction of moment at flexural cracking

Test specimen	y (mm)	M_{dead} (kNm)	M_{live} (kNm)	$M_{e,tot}$ (kNm)	M_{cb} (kNm)	M_{ct} (kNm)	$M_{in.cr}$ (kNm)
$BM2$	170	3.37	11.68	15.05	17.78	12.89	15.33
	325	3.06	11.68	14.74	17.78	12.89	15.33
	−165	after shear cracking					
$BM3$	−95	3.51	−17.46	−13.96	−15.70	−13.38	−14.54
	190	3.34	13.11	16.45	19.42	13.49	16.46
	330	3.05	13.80	16.85	19.42	13.49	16.46
$BM4$	190	3.34	13.36	16.70	23.00	11.22	17.11
	345	3.01	14.64	17.65	23.00	11.22	17.11
	−130	3.51	−20.39	−16.88	−18.51	−11.12	−14.82
$BM5$	165	3.38	14.08	17.45	26.42	13.42	19.92
	325	3.06	12.08	15.14	26.42	13.42	19.92
	−120	3.52	−19.76	−16.24	−22.17	−13.32	−17.75
$BM6$	160	3.38	9.43	12.81	15.16	6.90	11.03
	−135	3.51	−16.41	−12.90	−11.43	−6.83	−9.13
	375	2.93	10.91	13.83	15.16	6.90	11.03
	−360	3.30	−15.02	−11.72	−11.43	−6.83	−9.13
$BM7$	240	3.25	11.26	14.51	19.96	12.30	16.13
	−165	3.38	−18.32	−14.95	−15.86	−10.93	−13.39
	−350	3.30	−16.98	−13.68	−15.86	−10.93	−13.39

Table 7.2: Material properties of top flange specimens

Sample	$N°$ measurements	E_{SF} (kN/mm^2)	f_{ay} (N/mm^2)	f_{au} (N/mm^2)
SF_1	10	215.5	243.5	445.9
SF_2	10	207.3	245.3	446.5
SF_3	10	207.6	247.7	445.1

Table 7.3: Proof stress of different reinforcement bars

Type and diameter of bar	0.2% proof stress (N/mm^2)		
	SR_1	SR_2	SR_3
$Y10$	427	433	433
$Y12$	407	423	432
$Y16$	418	424	448

Table 7.4: Tests on concrete samples according to BS.1881

		Test specimens					
		$BM2$	$BM3$	$BM4$	$BM5$	$BM6$	$BM7$
f_{cu}[1]	(N/mm^2)	42.66	37.83	44.64	50.56	16.68	–
Standard deviation	(N/mm^2)	2.29	1.19	4.17	1.53	1.23	–
$f_{cu}^{4,5}$[2]	(N/mm^2)	43.11	37.81	41.44	50.83	16.24	48.93
f_{cb}[3]	(N/mm^2)	4.15	4.94	5.86	6.26	3.43	4.68
f_{ct}[4]	(N/mm^2)	2.96	3.16	2.86	3.18	1.59	2.56
Age at testing	$(days)$	> 28	20	> 28	> 28	12	> 28

[1] Average cube crushing strength
[2] Average cube crushing strength for batches 4 & 5
[3] Modulus of rupture strength
[4] Indirect tensile strength

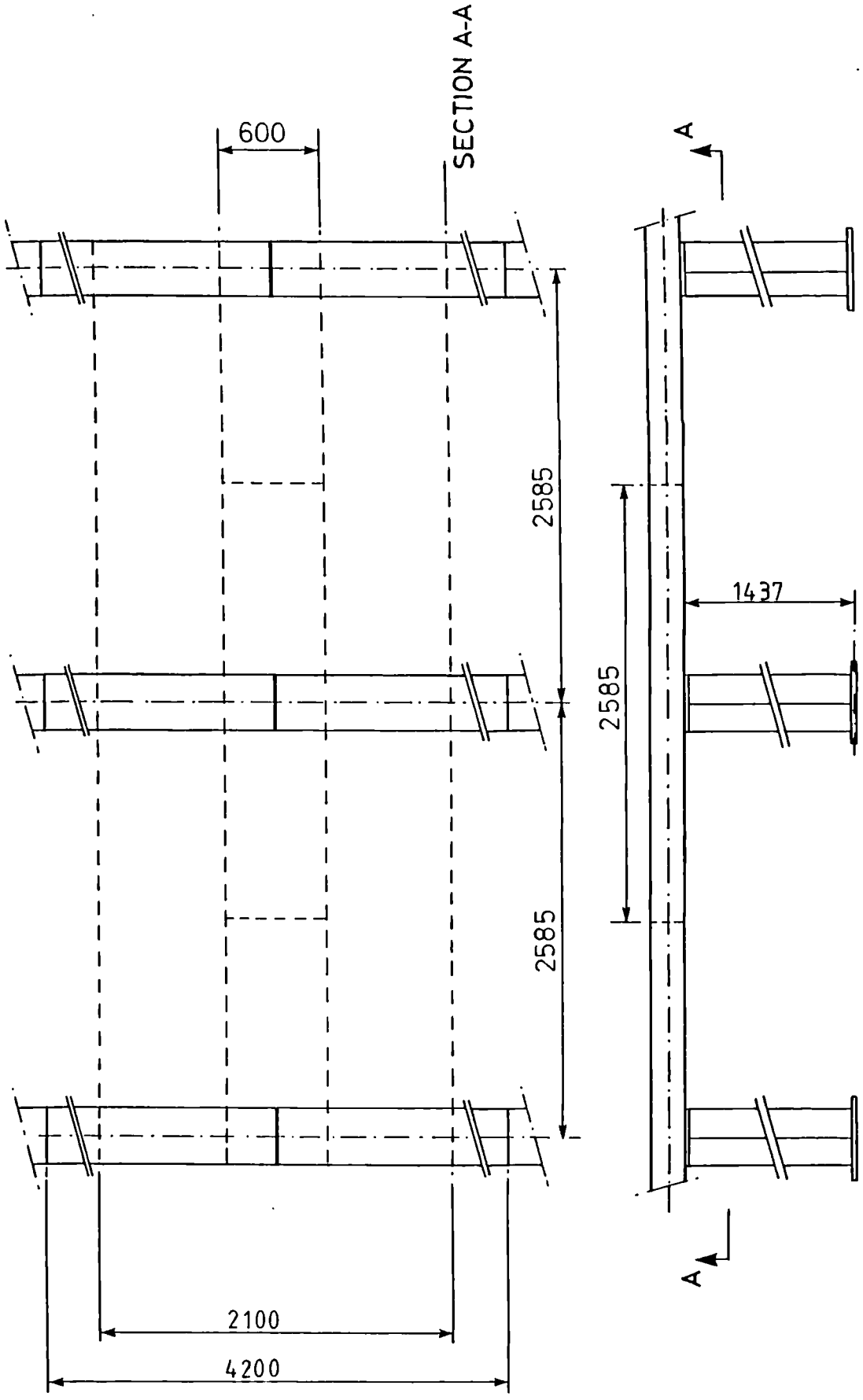

Figure 7.1: Test specimen as that part of a longitudinal bridge girder which acts as an inverted U-frame.

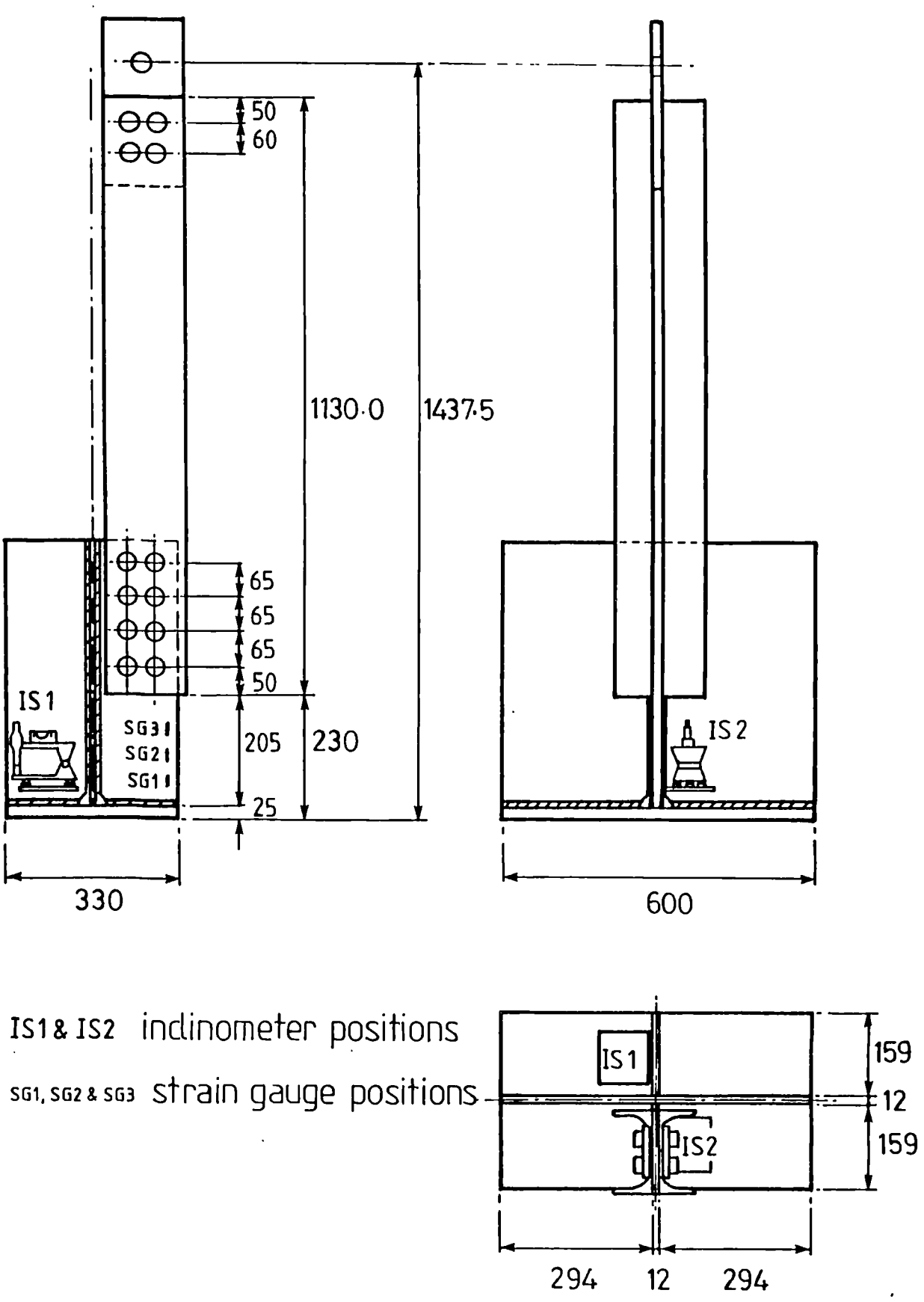

Figure 7.2: Fabricated and constructed steelwork for all seven test specimens.

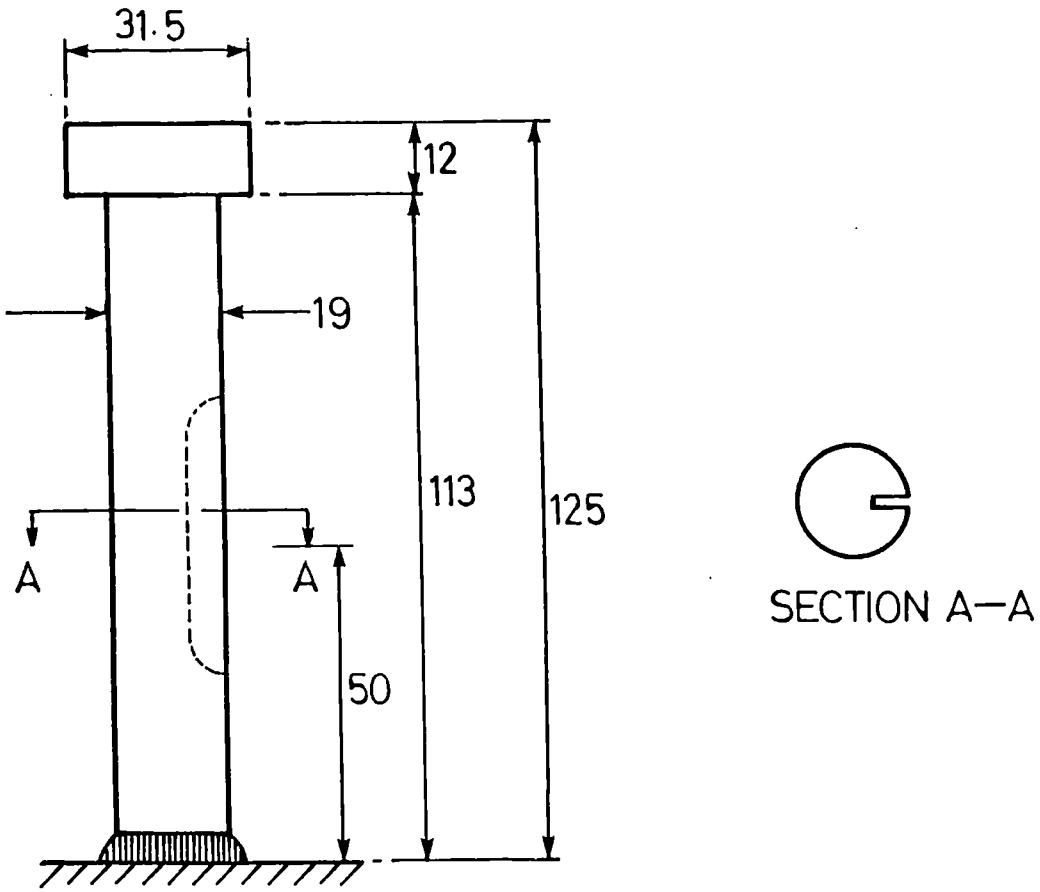

Figure 7.3: Details of the slotted studs used in the test specimens.

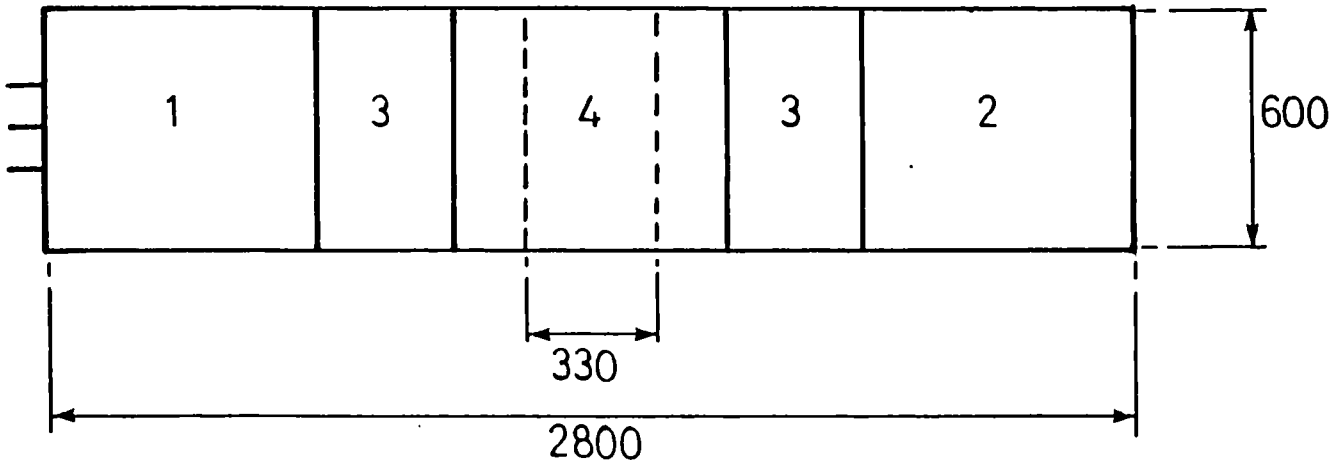

Figure 7.9: Casting sequence of the 5 different batches of concrete needed to cast the slabs of the test specimens.

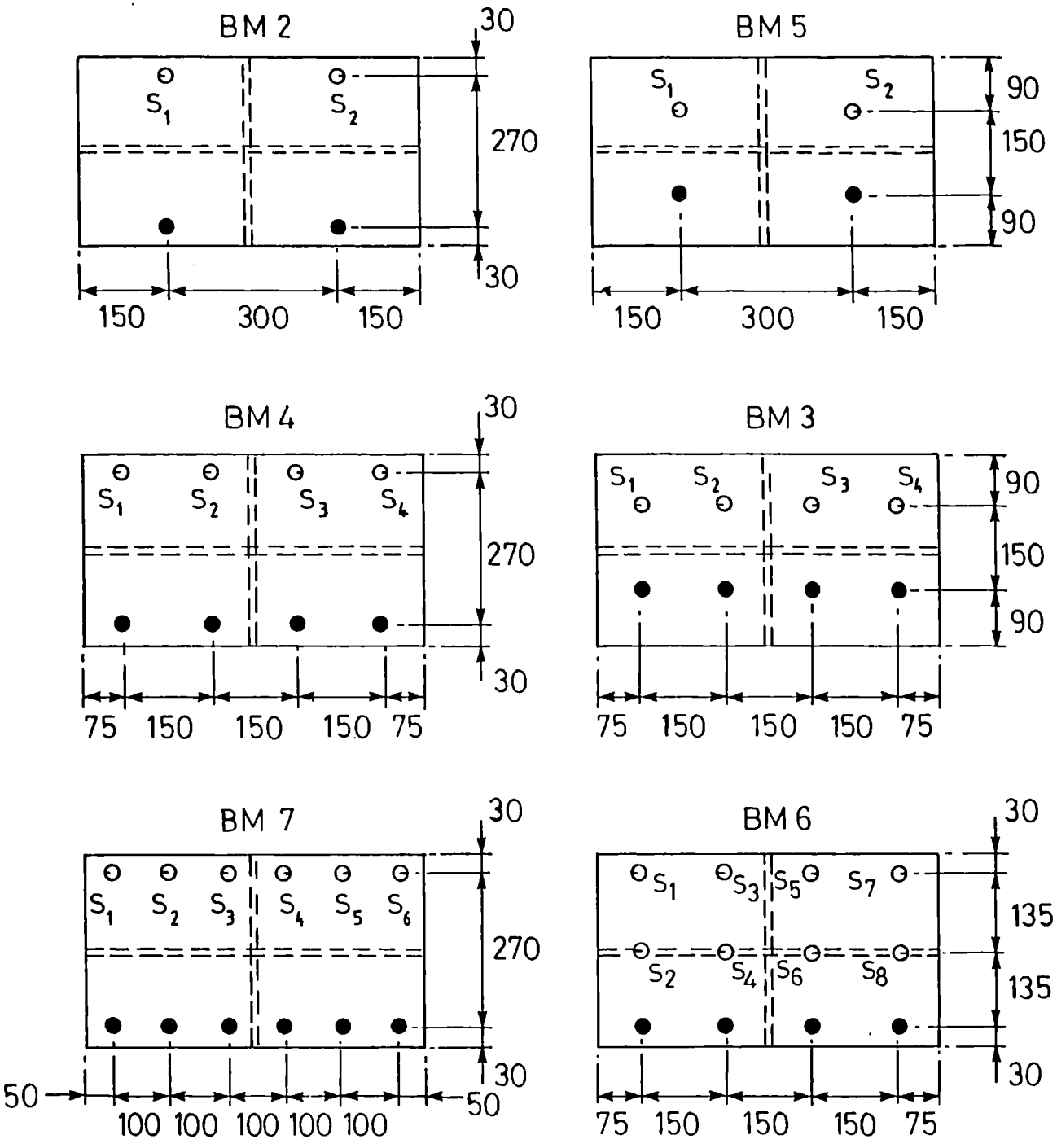

Figure 7.4: Slotted and non-slotted stud configurations for the different test specimens.

Figure 7.5: Plate of fabricated steelwork for test specimen BM3.

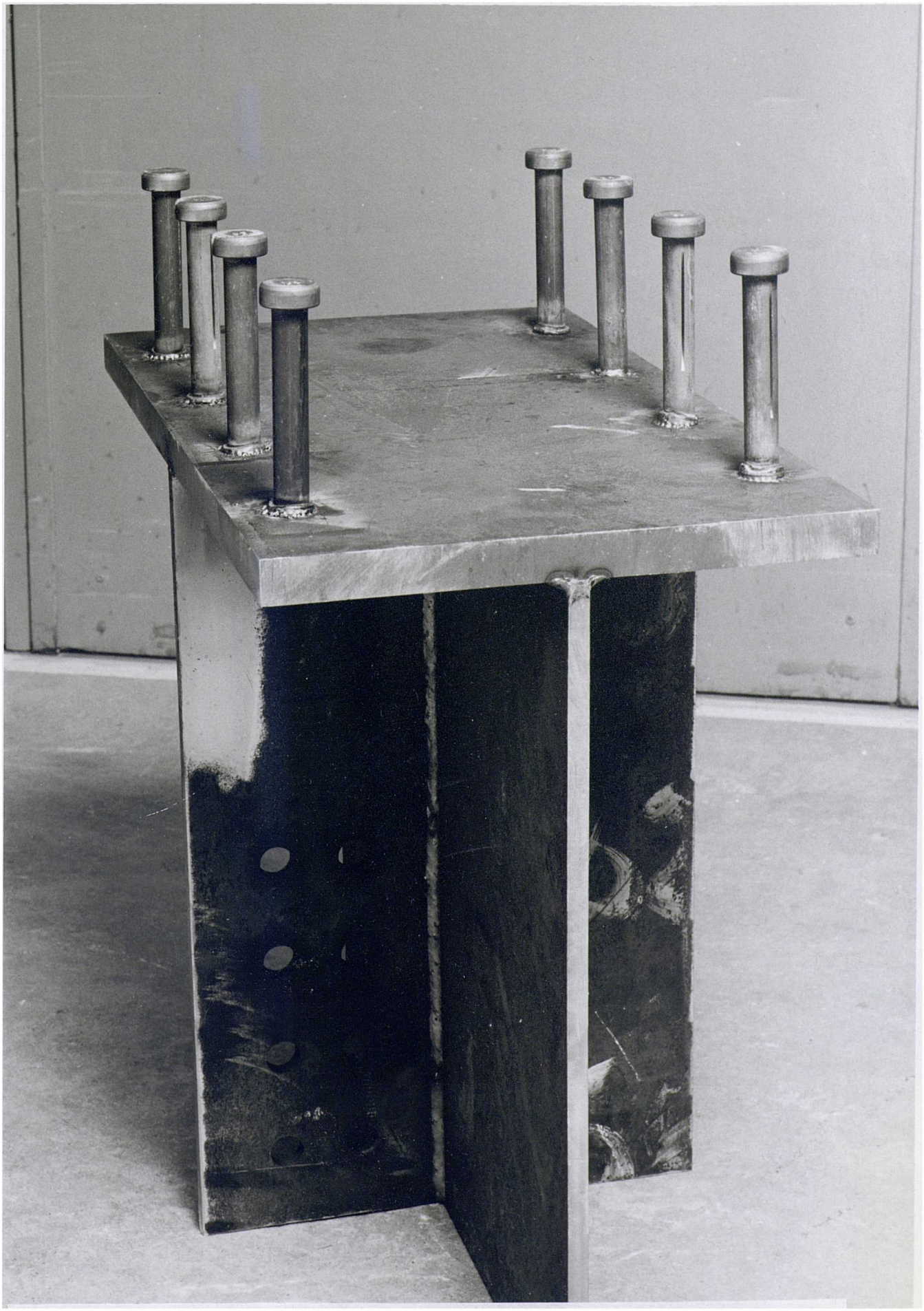

Figure 7.6: Plate of fabricated steelwork for test specimen BM4.

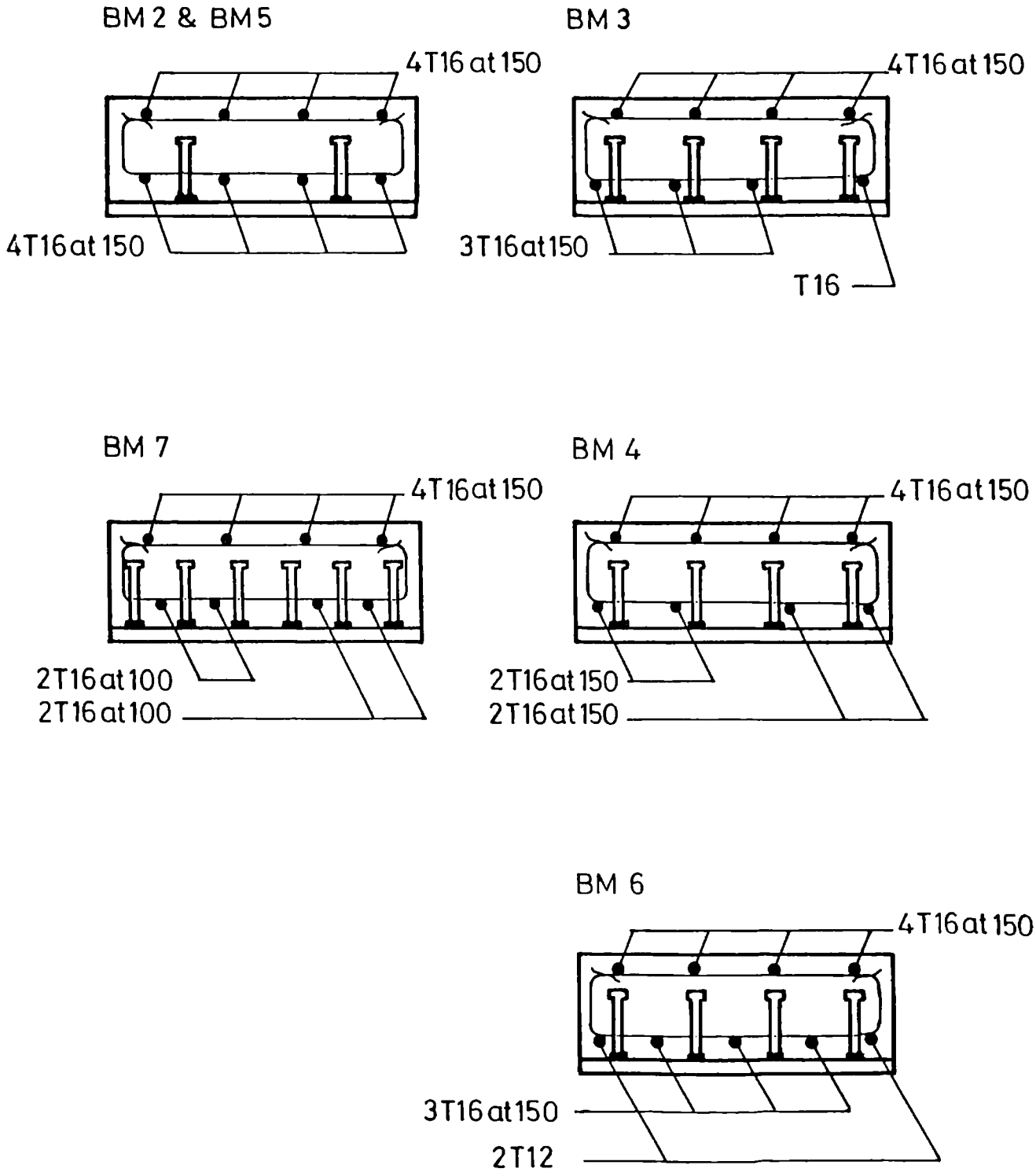

Position of transverse reinforcement for different tested specimen at scale 1:10

All have top cover 25 mm
bottom cover 35 mm
side cover 25 mm

Figure 7.7: Detailing arrangements of the transverse reinforcement in the slabs of the different test specimens.

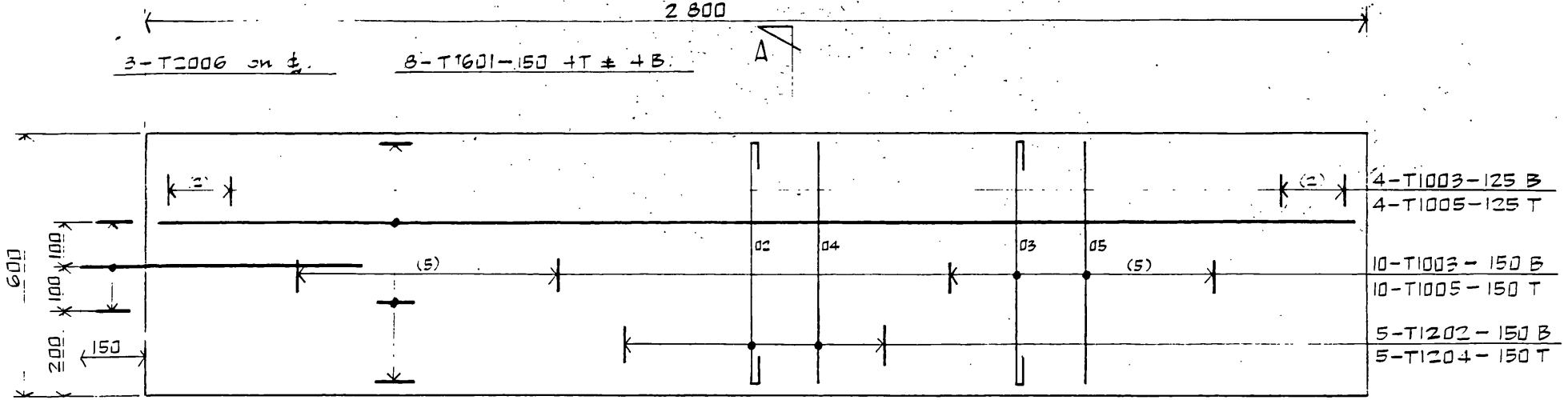

REINFORCEMENT FOR SLABS 3 & 5.

A-A

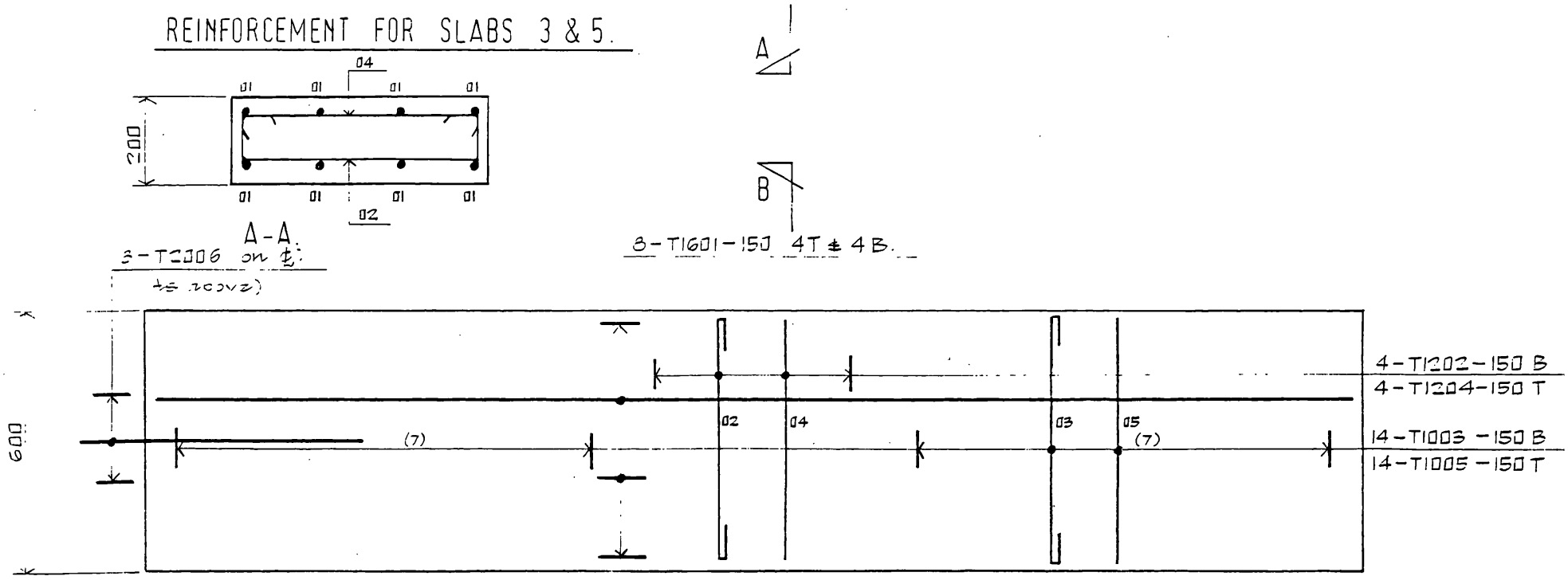

REINFORCEMENT FOR SLABS 2, 4, 6 & 7.

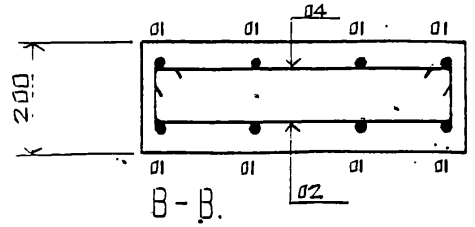

B-B.

Figure 7.8: Two different detailing arrangements of the longitudinal reinforcement in the slabs of the different test specimens.

RS.

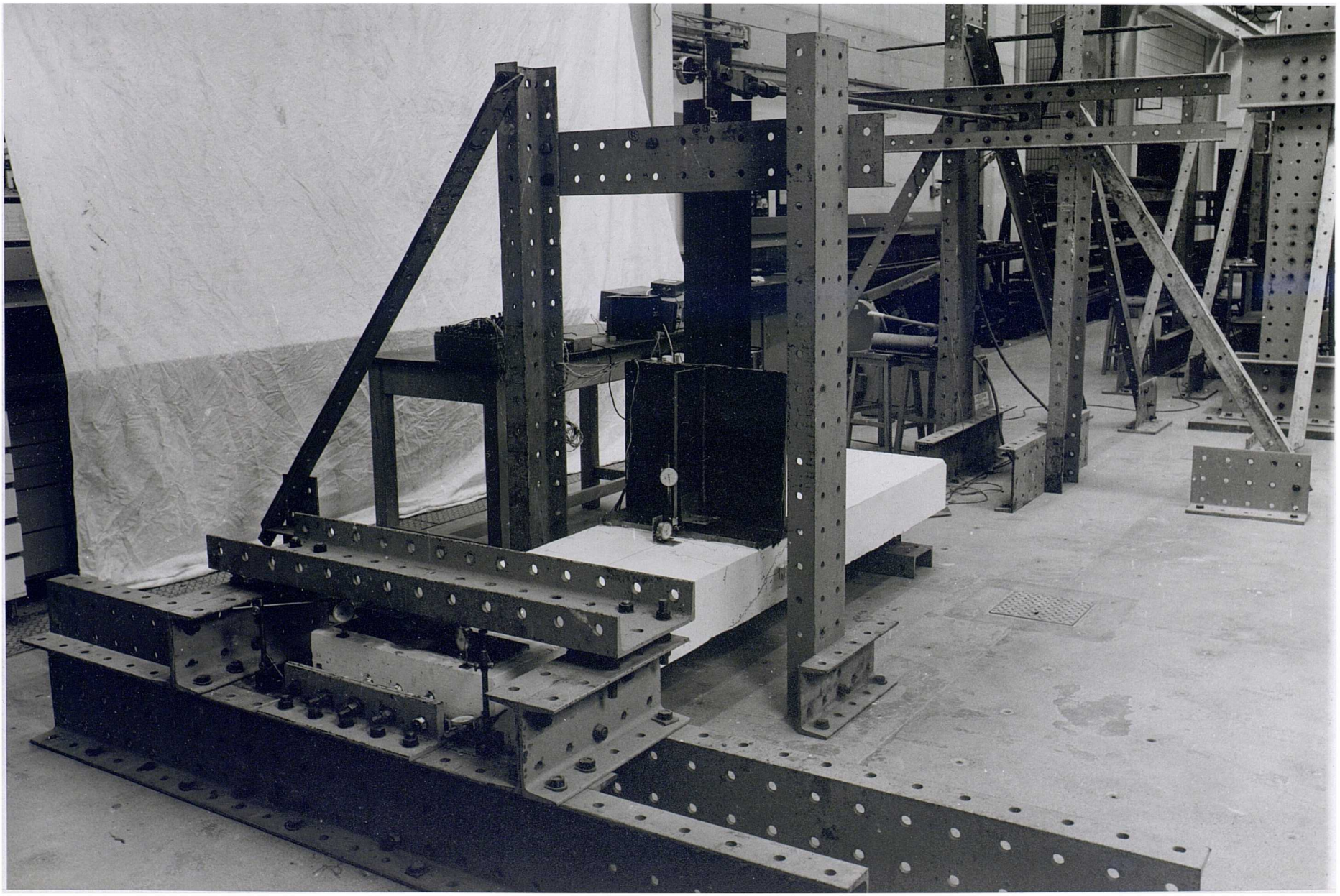

Figure 7.10: Plate of the test rig with test specimen BM7 mounted.

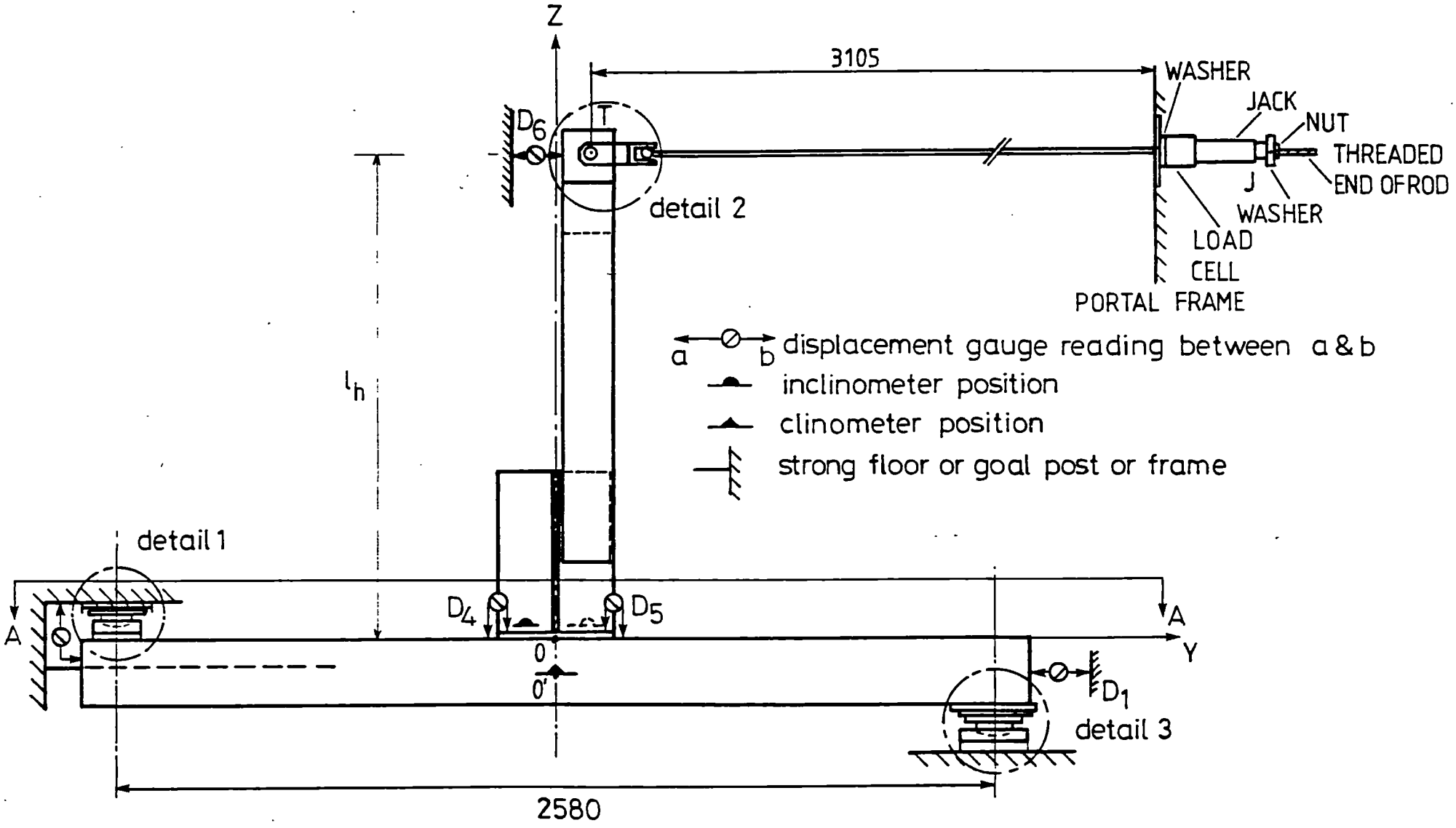

Figure 7.11: Schematic representation on elevation of test lay-out and measurements on specimens *BM2* to *BM7*.

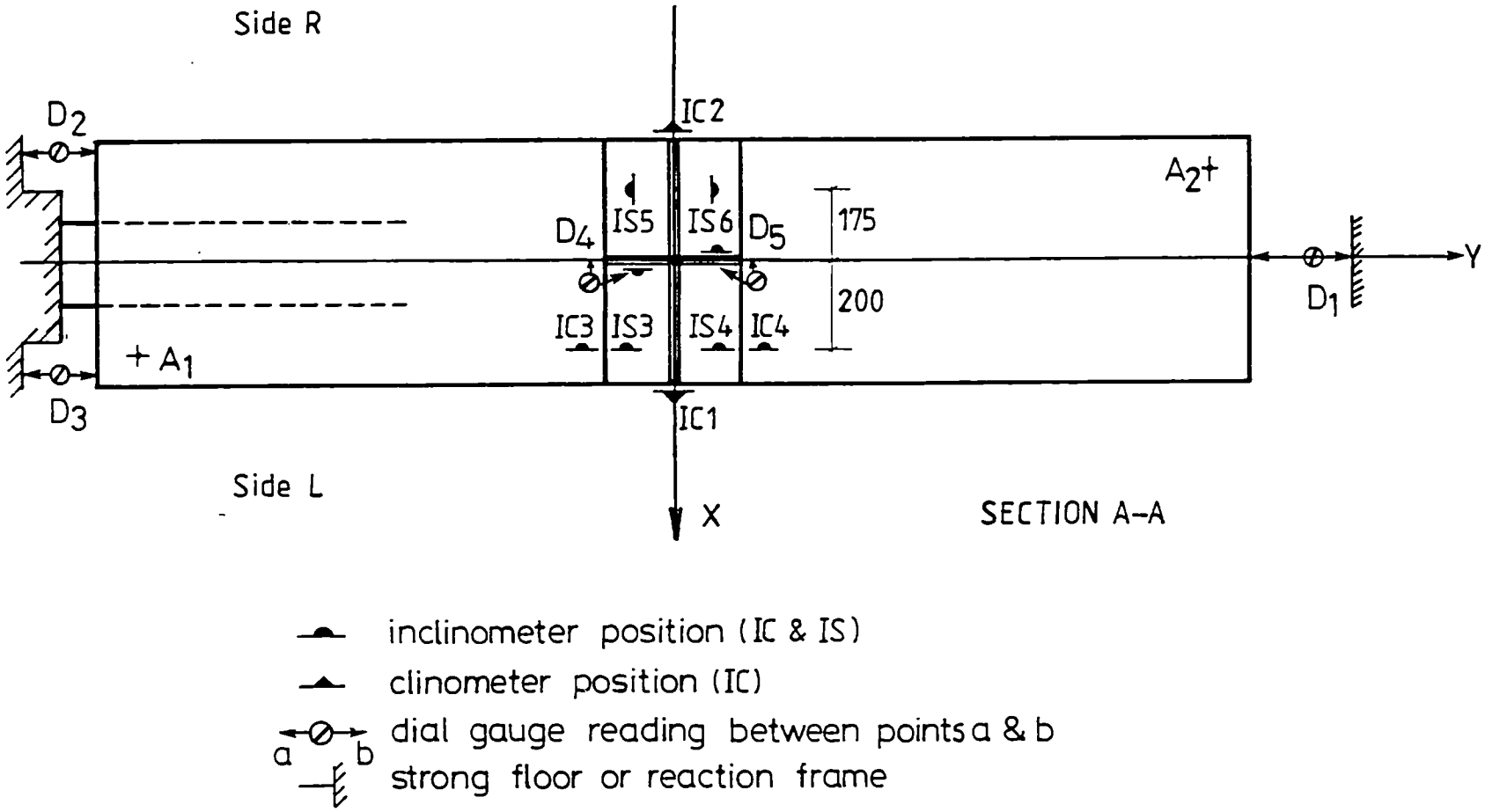

Figure 7.12: Schematic representation on plan of test lay-out and measurements on specimens BM2 to BM7.

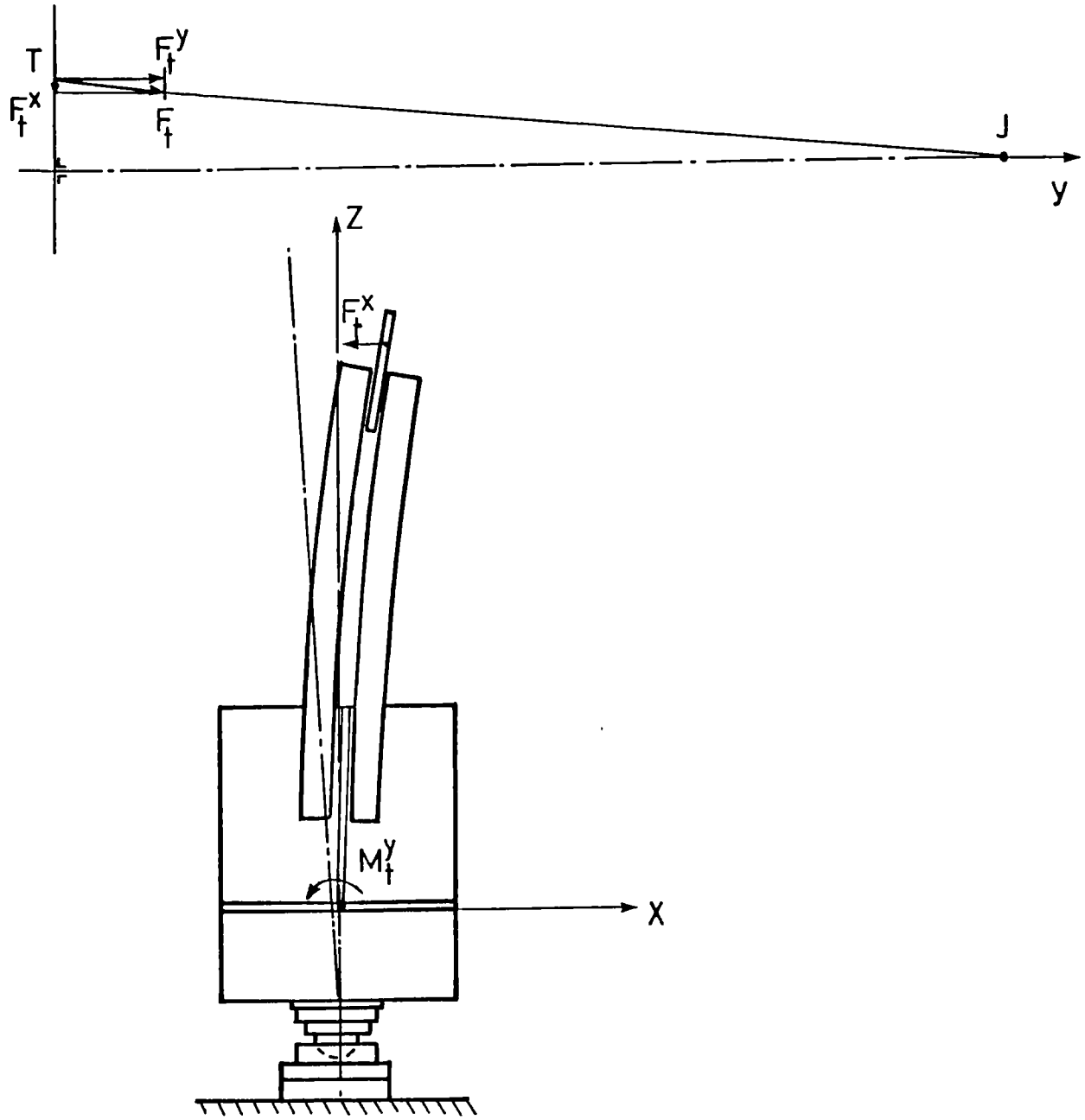

Figure 7.13: Reduction of the lateral movement at point T, due to spherical bearings.

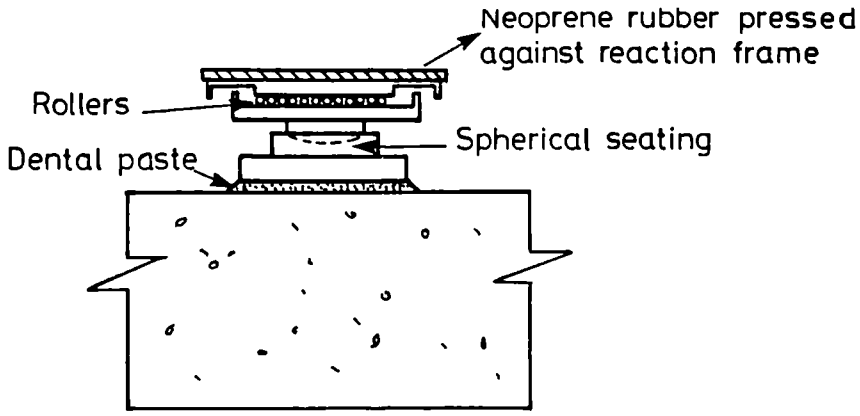

Detail 1

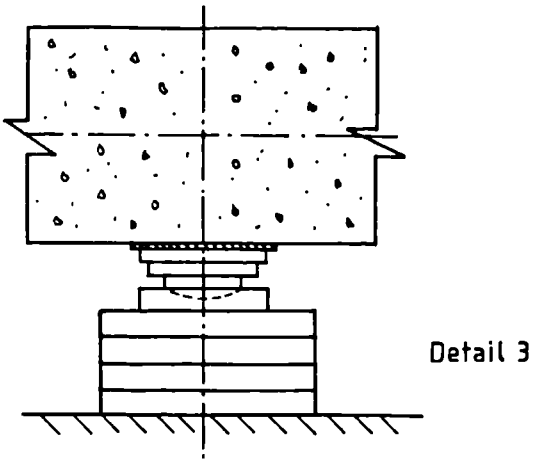

Figure 7.14(a): Details of spherical bearings at both ends of the slab.

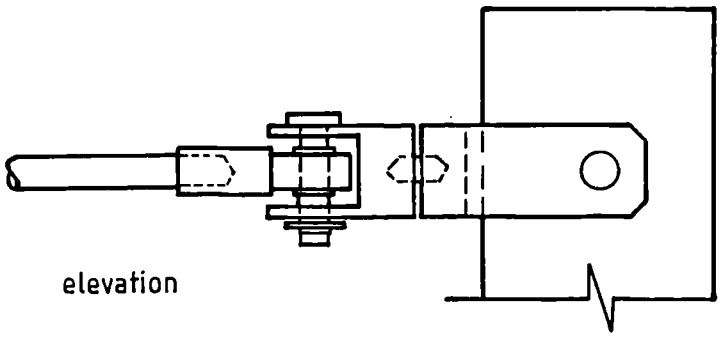

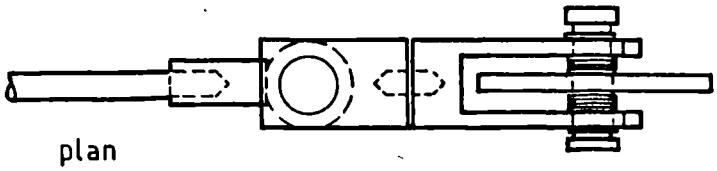

Detail 2

Figure 7.14(b): Hinge at the top of the channels

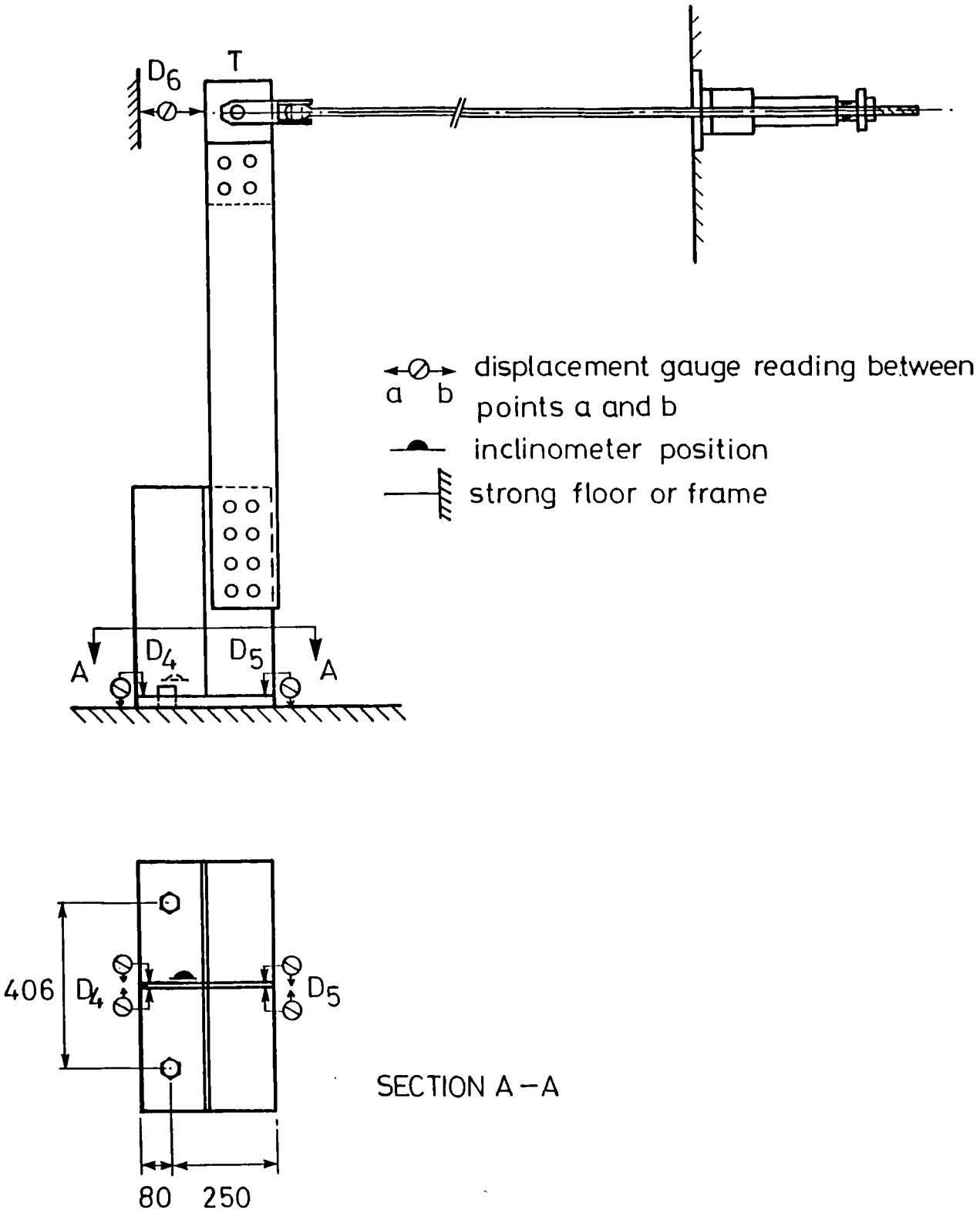

Figure 7.15: Schematic representation on plan and on elevation of test lay-out and measurements on specimen BM1.

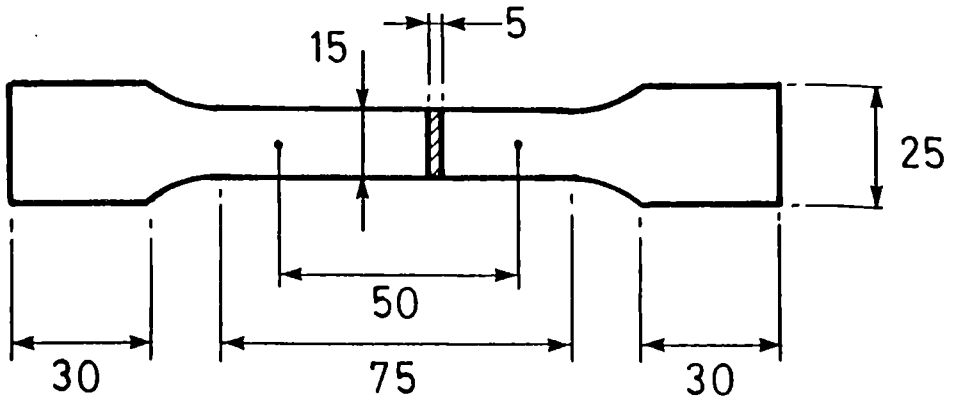

(a) sample size of top flange steel coupons (SF)

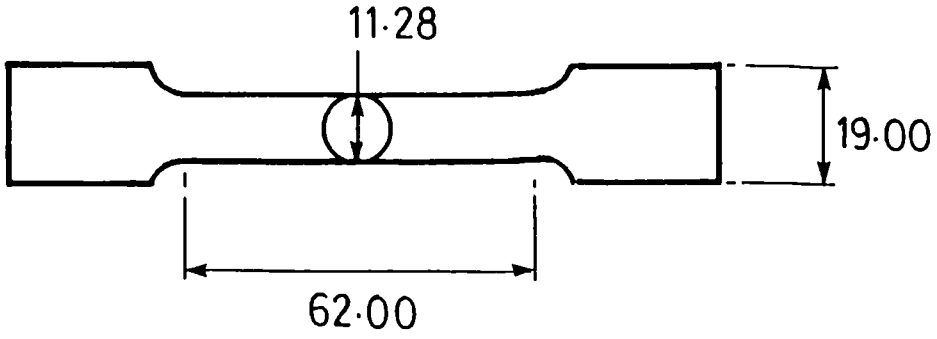

(b) sample size of stud steel coupons (SH)

Figure 7.16: Dimensions of coupons for tensile testing taken from the top flange and of the studs.

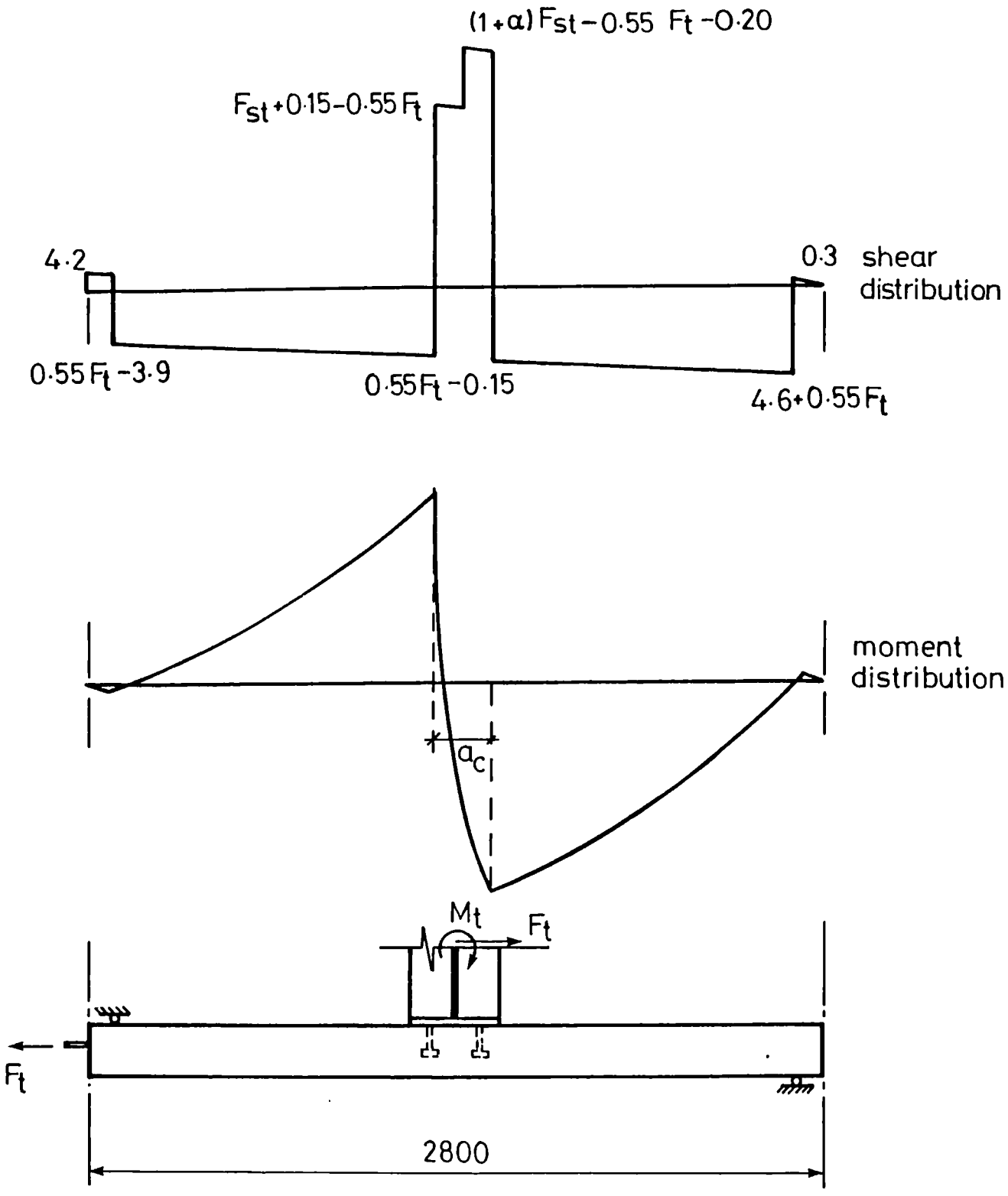

Figure 7.17: Moment and shear force diagram under total applied loads for specimen BM5.

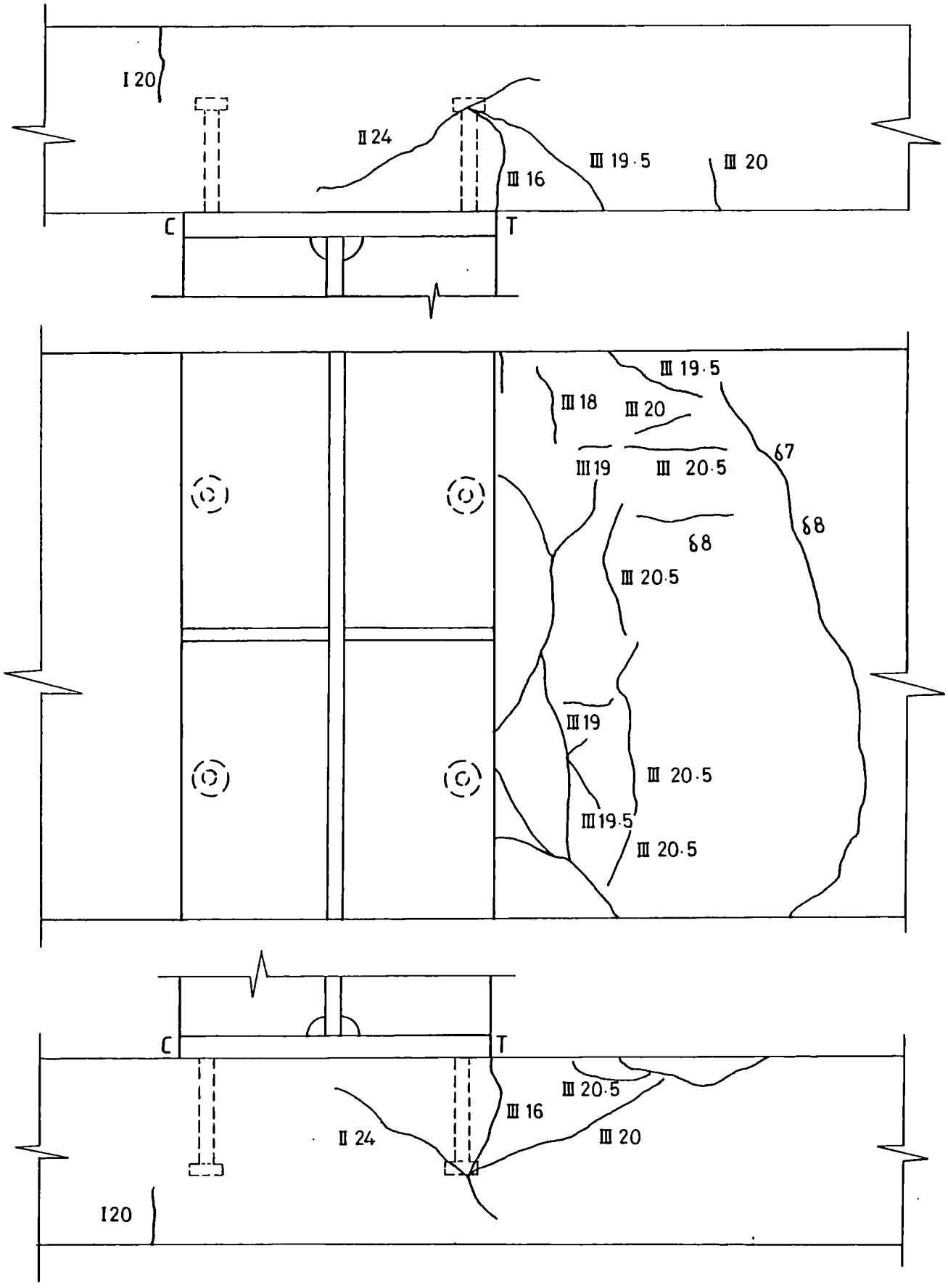

Figure 7.18: Main crack pattern in the slab of test specimen BM2, with indication of load cycle (Roman numeral) and load levels and displacement levels.

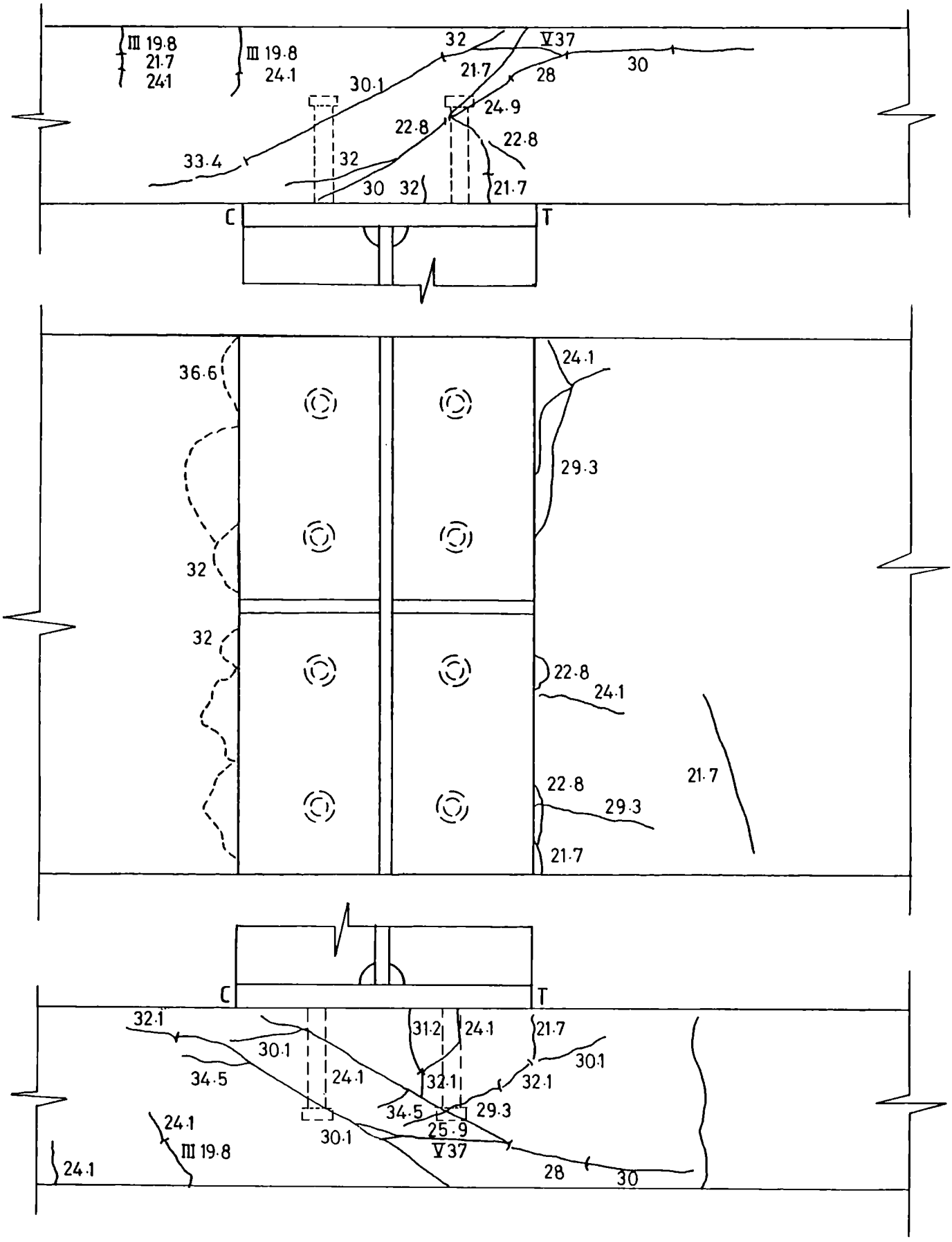

Figure 7.19: Main crack pattern in the slab of test specimen BM3, with indication of load cycle (Roman numeral) and load levels and displacement levels.

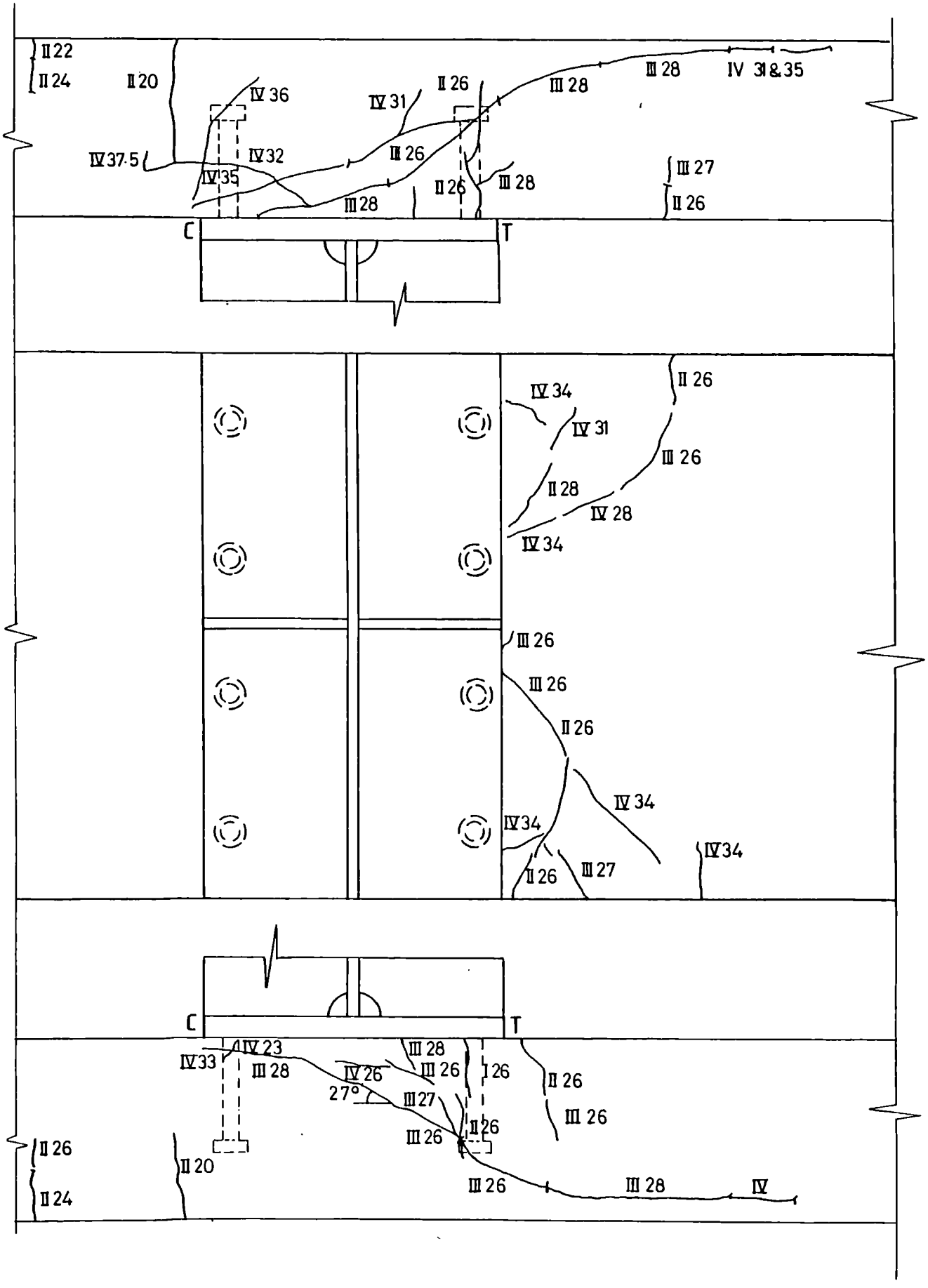

Figure 7.20: Main crack pattern in the slab of test specimen BM4, with indication of load cycle (Roman numeral) and load levels and displacement levels.

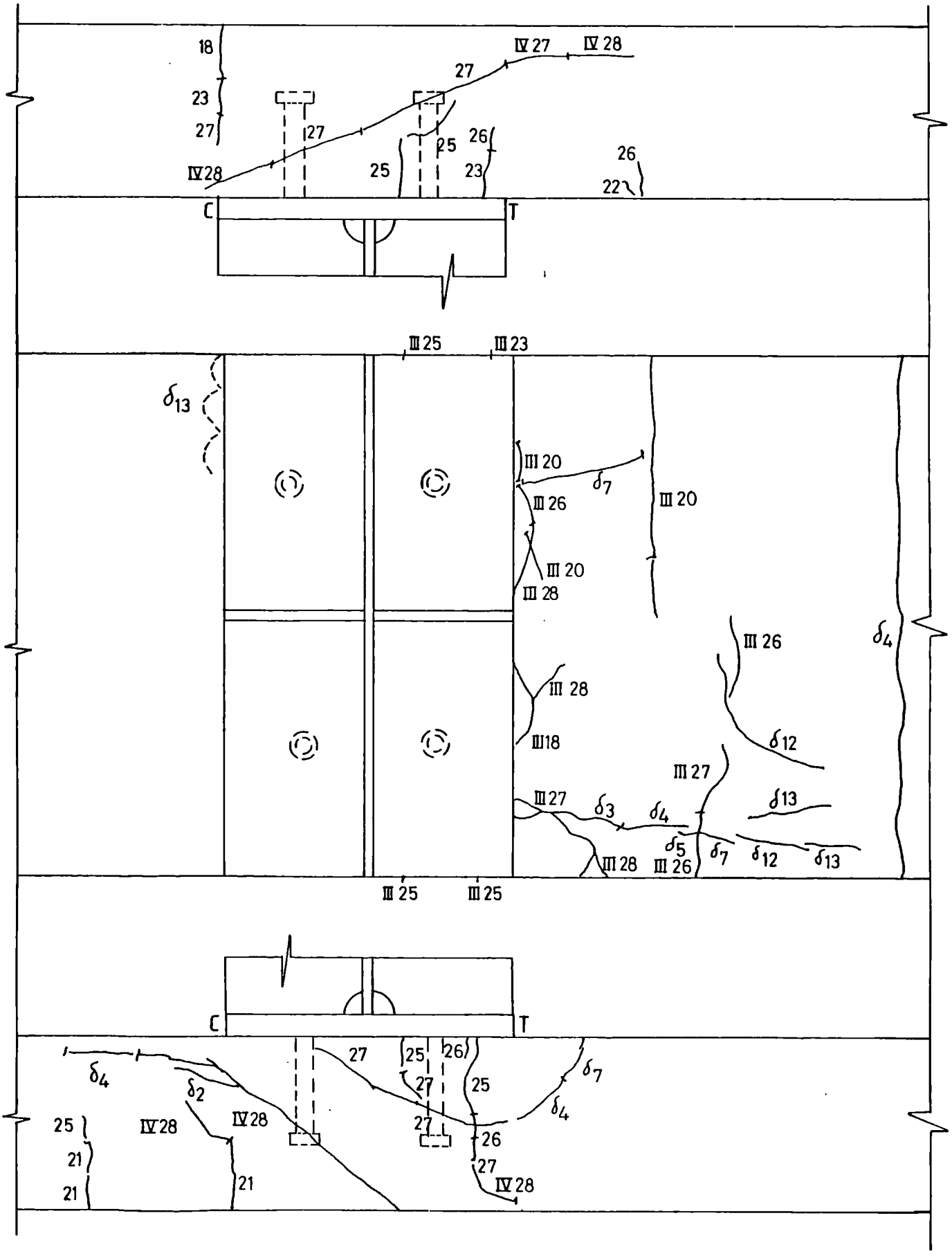

Figure 7.21: Main crack pattern in the slab of test specimen BM5, with indication of load cycle (Roman numeral) and load levels and displacement levels.

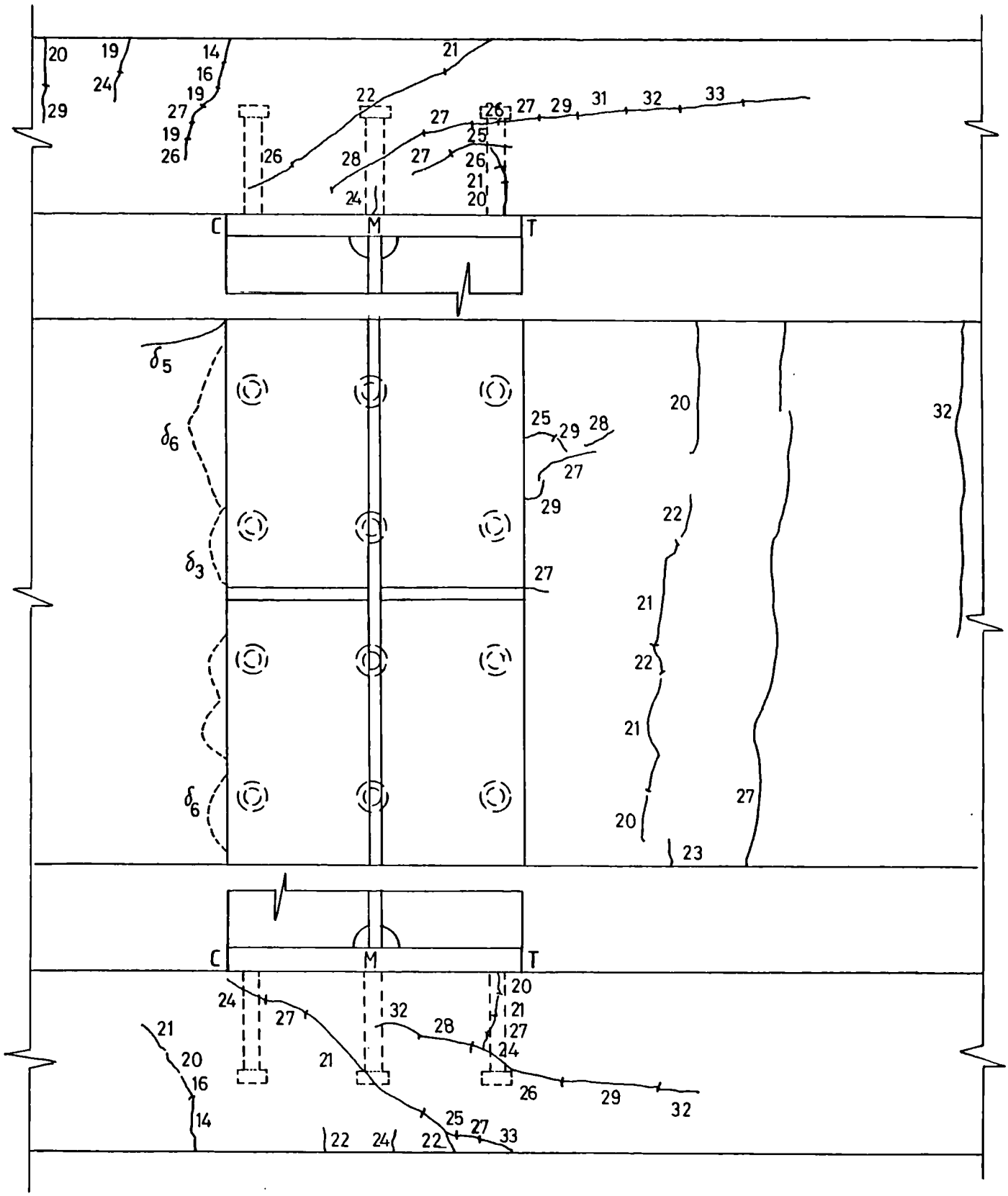

Figure 7.22: Main crack pattern in the slab of test specimen BM6, with indication of load cycle (Roman numeral) and load levels and displacement levels.

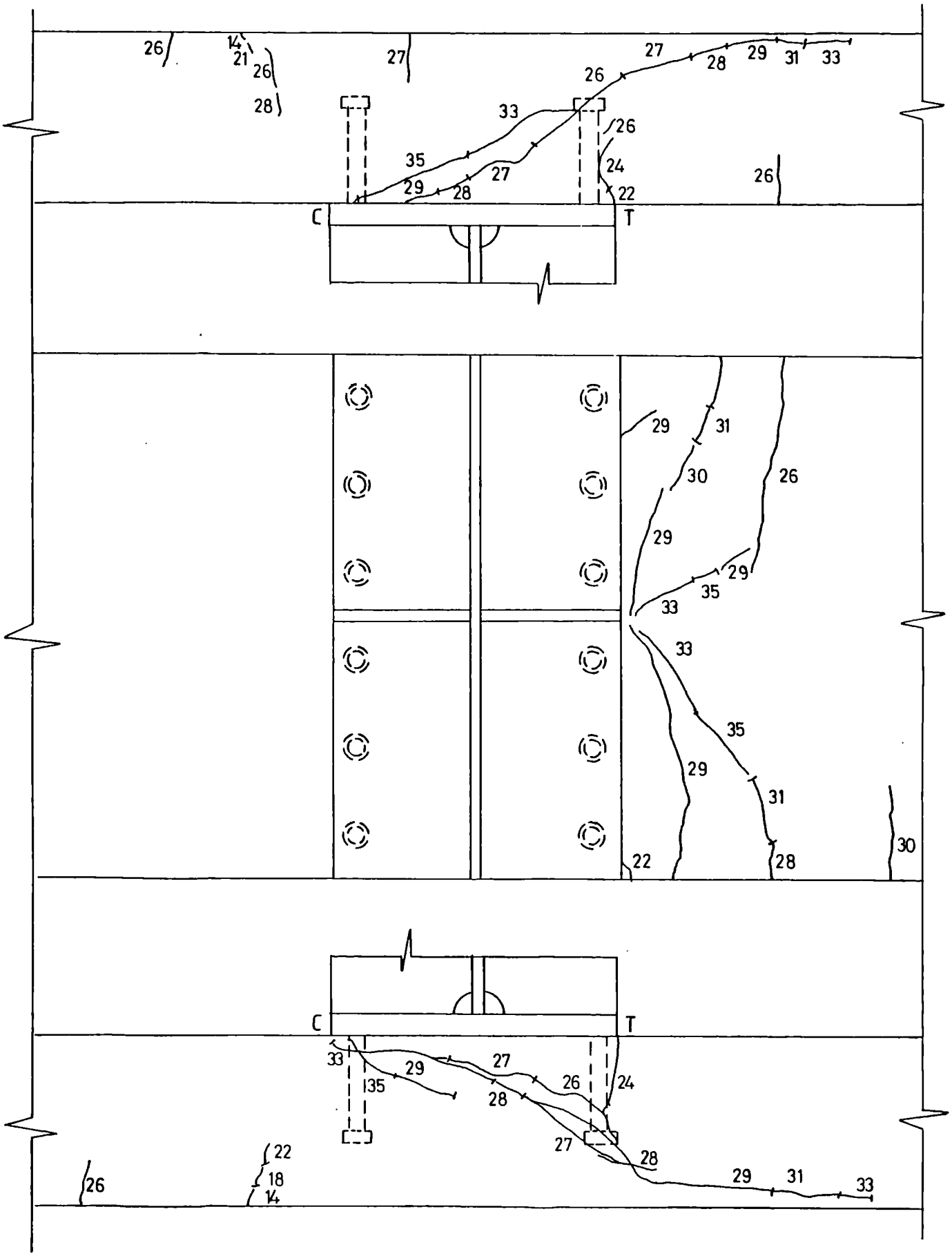

Figure 7.23: Main crack pattern in the slab of test specimen BM7, with indication of load cycle (Roman numeral) and load levels and displacement levels.

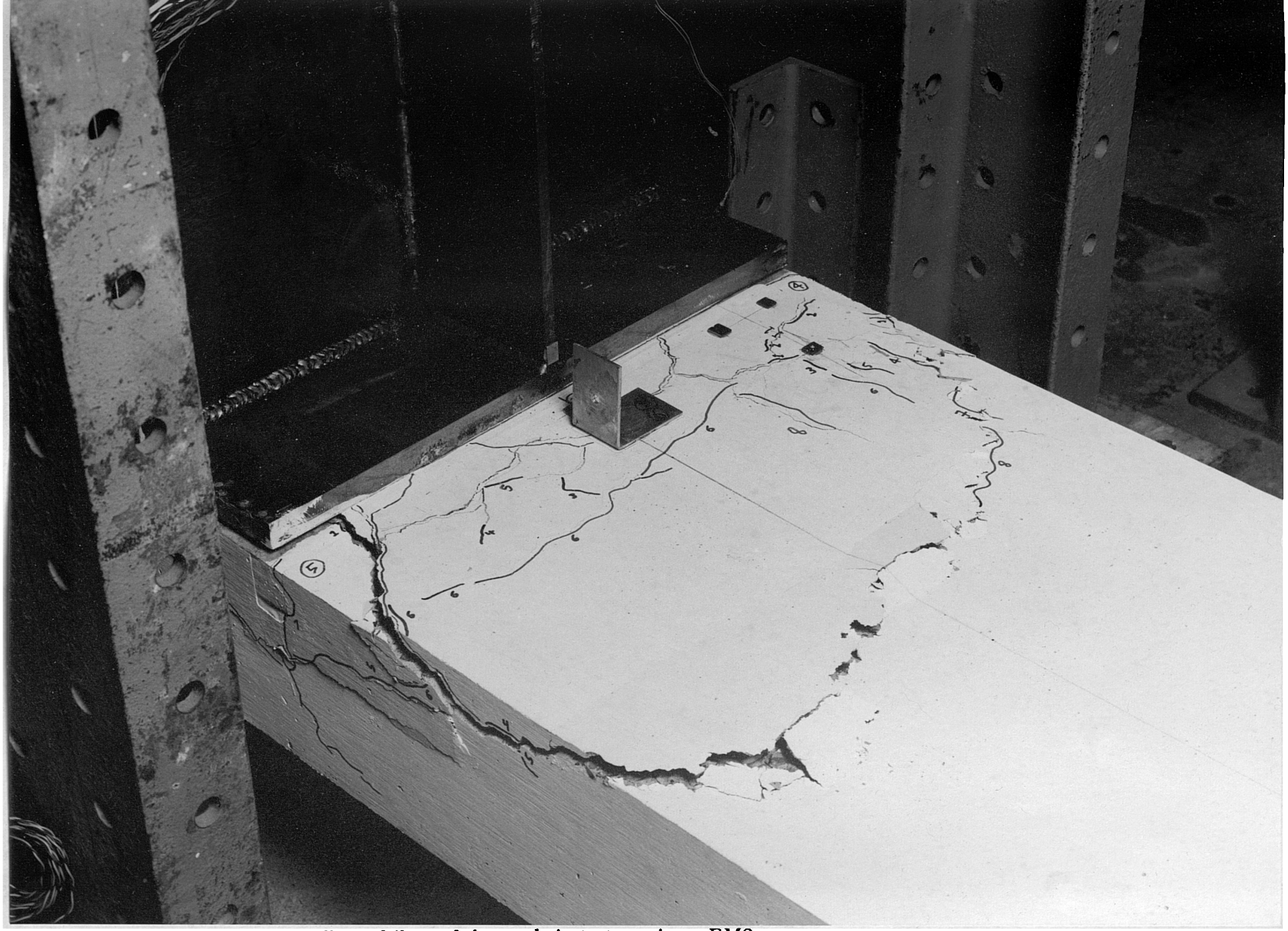

Figure 7.24: Plate of the pull-out failure of the studs in test specimen BM2.

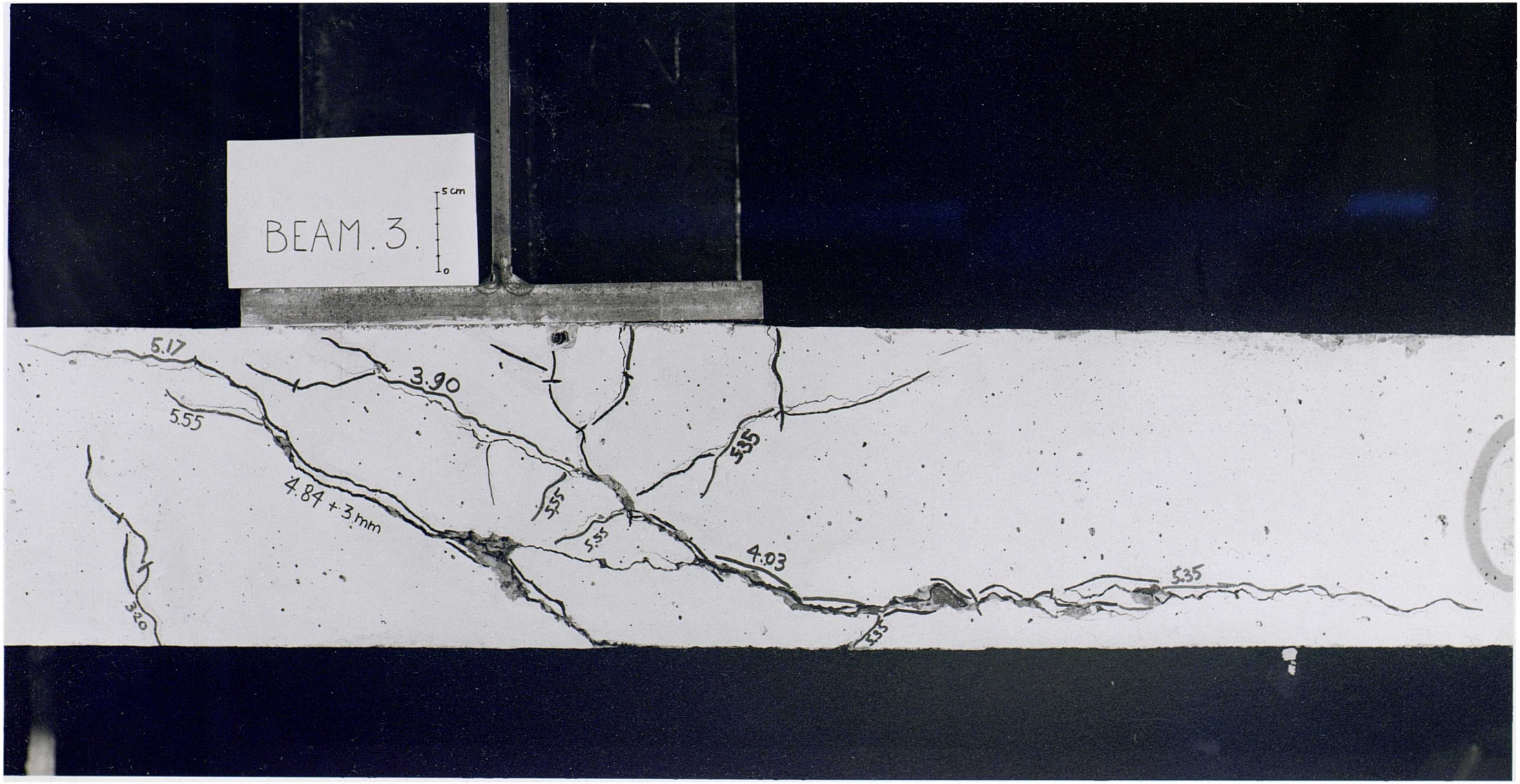

Figure 7.25(a): Plate of side-elevation R of the connection of test specimen BM3, as indicated on Fig. 7.12.

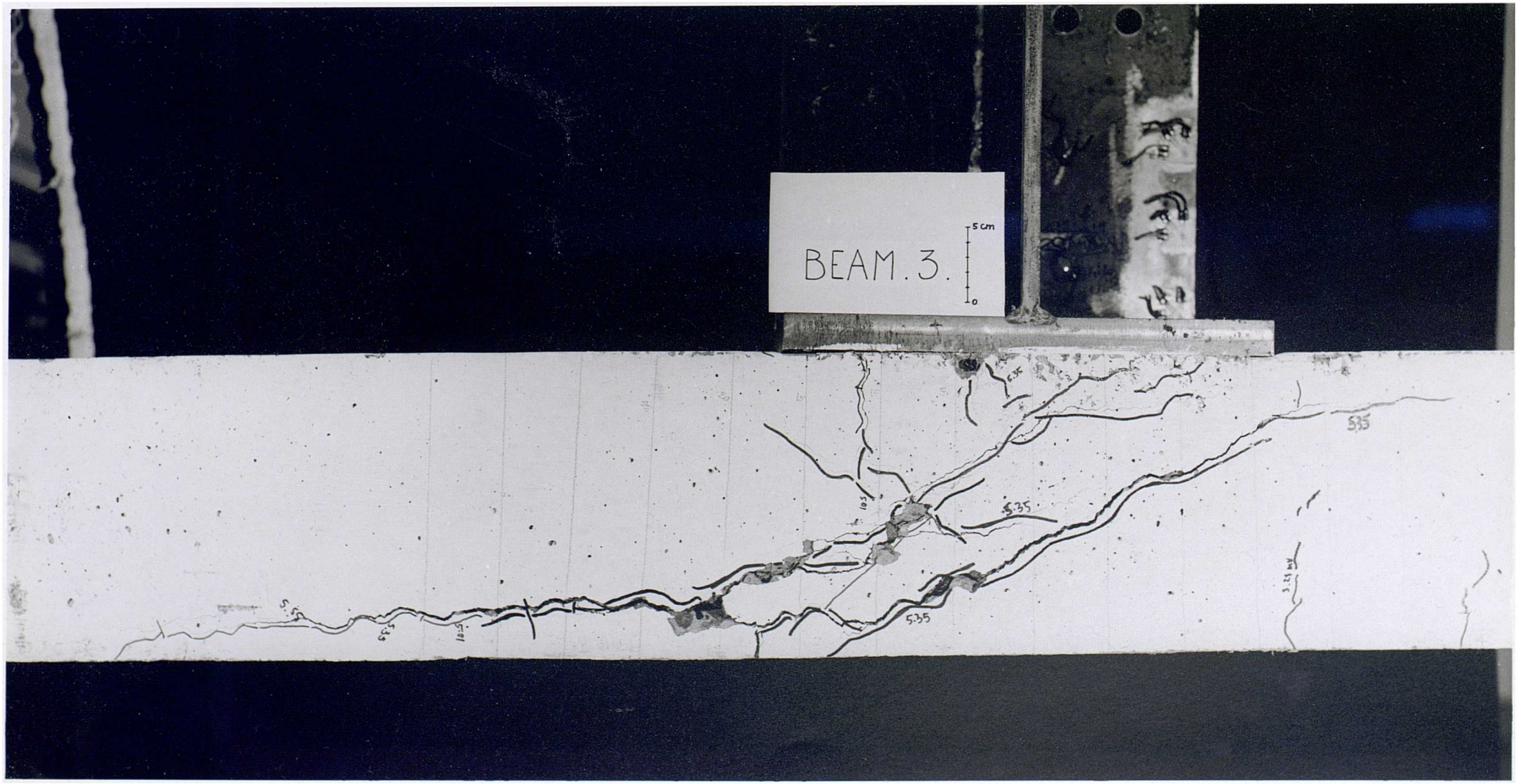

Figure 7.25(b): Plate of side-elevation L of the connection of test specimen BM3, as indicated on Fig. 7.12.

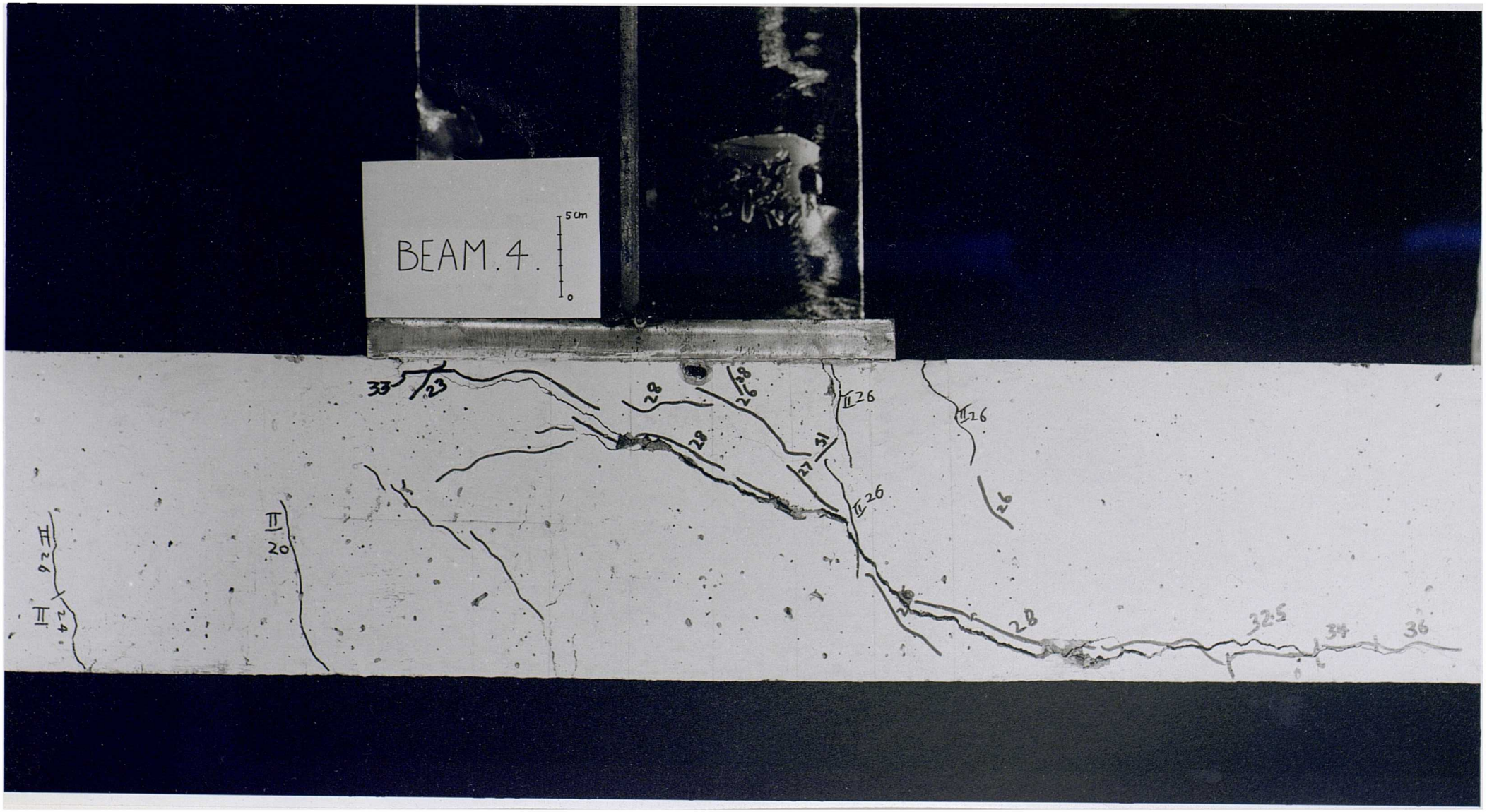

Figure 7.26(a): Plate of side-elevation R of the connection of test specimen BM4, as indicated on Fig. 7.12.

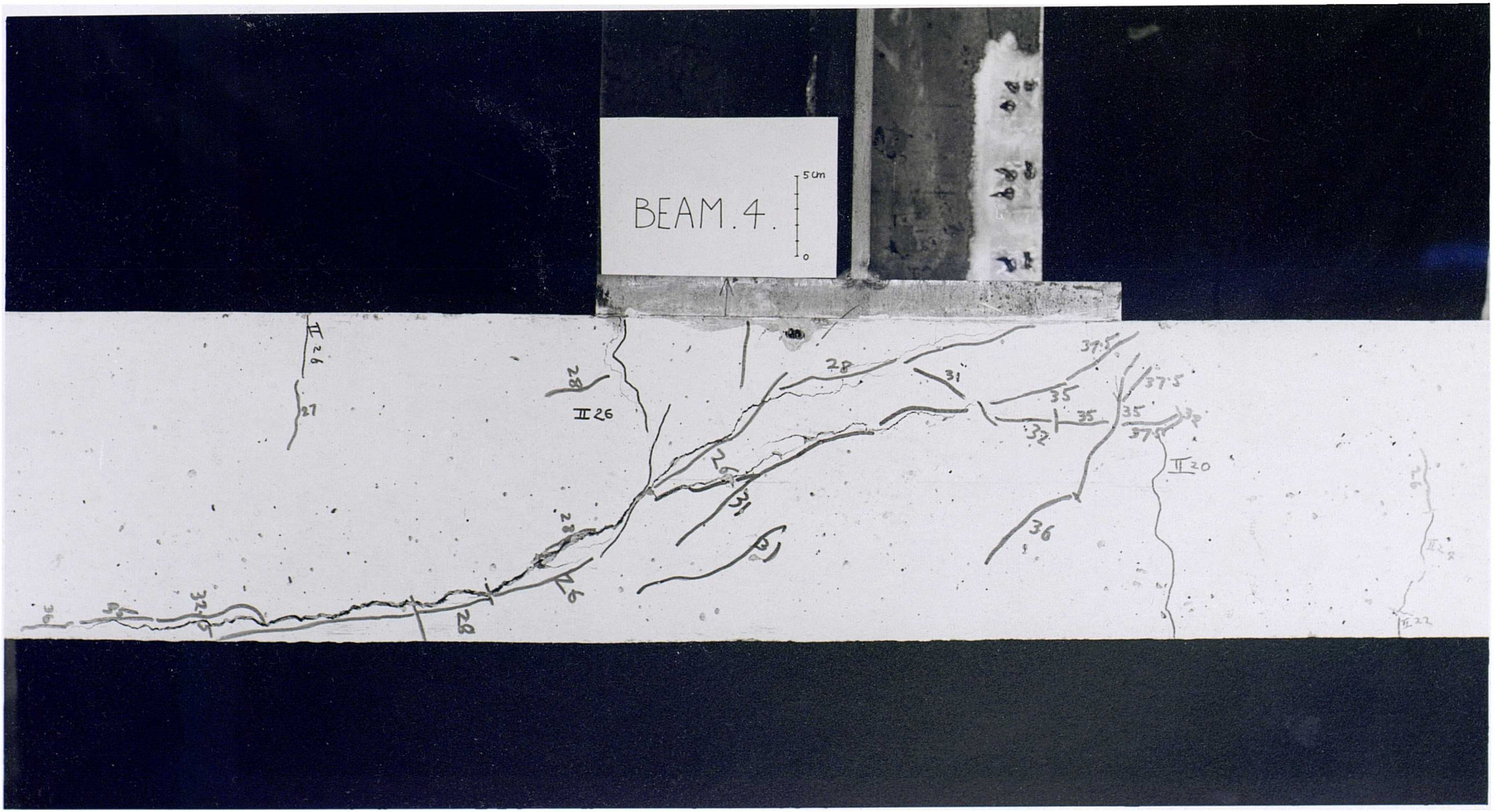

Figure 7.26(b): Plate of side-elevation L of the connection of test specimen BM4, as indicated on Fig. 7.12.

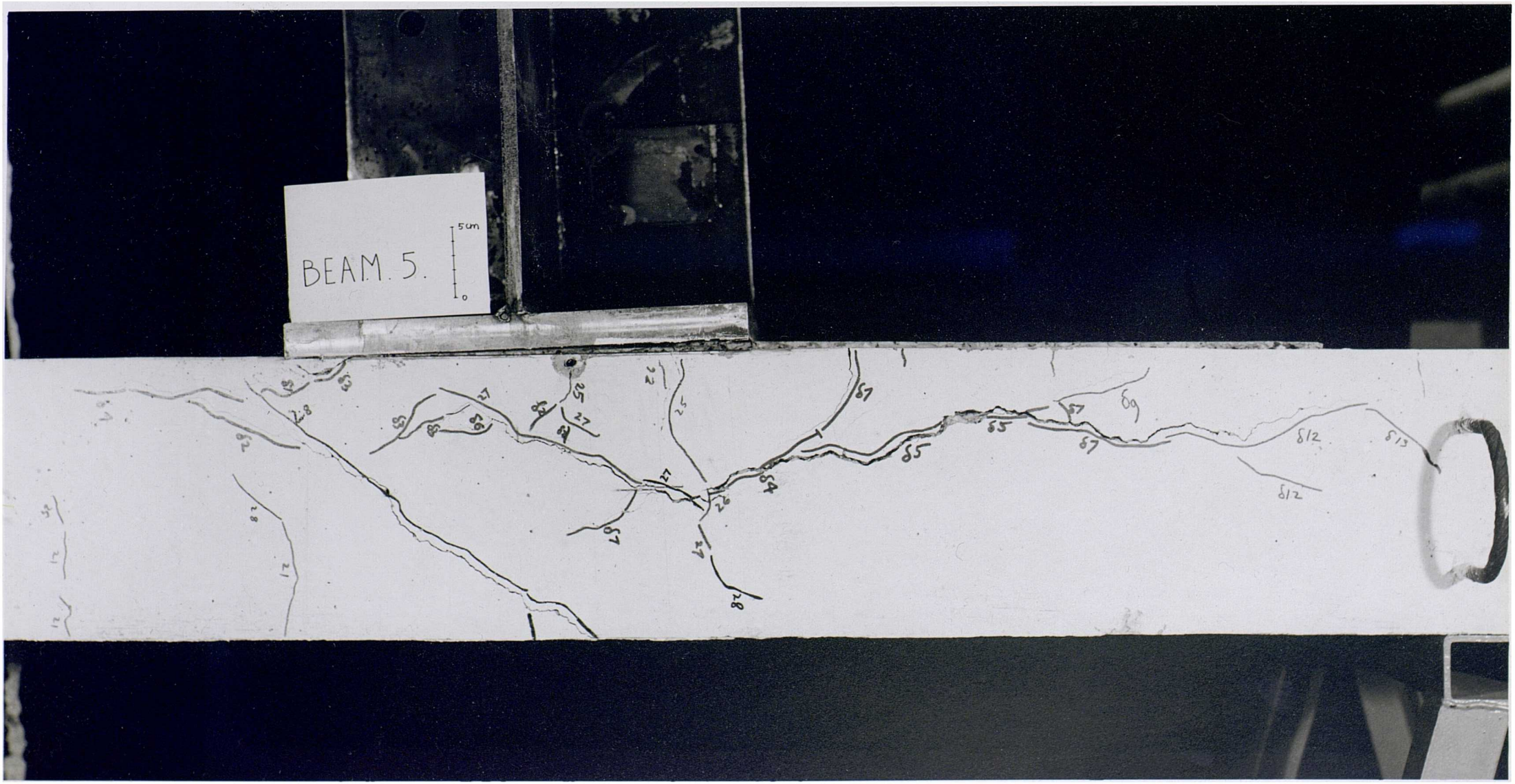

Figure 7.27(a): Plate of side-elevation R of the connection of test specimen BM5, as indicated on Fig. 7.12.

Figure 7.27(b): Plate of side-elevation L of the connection of test specimen BM5, as indicated on Fig. 7.12.

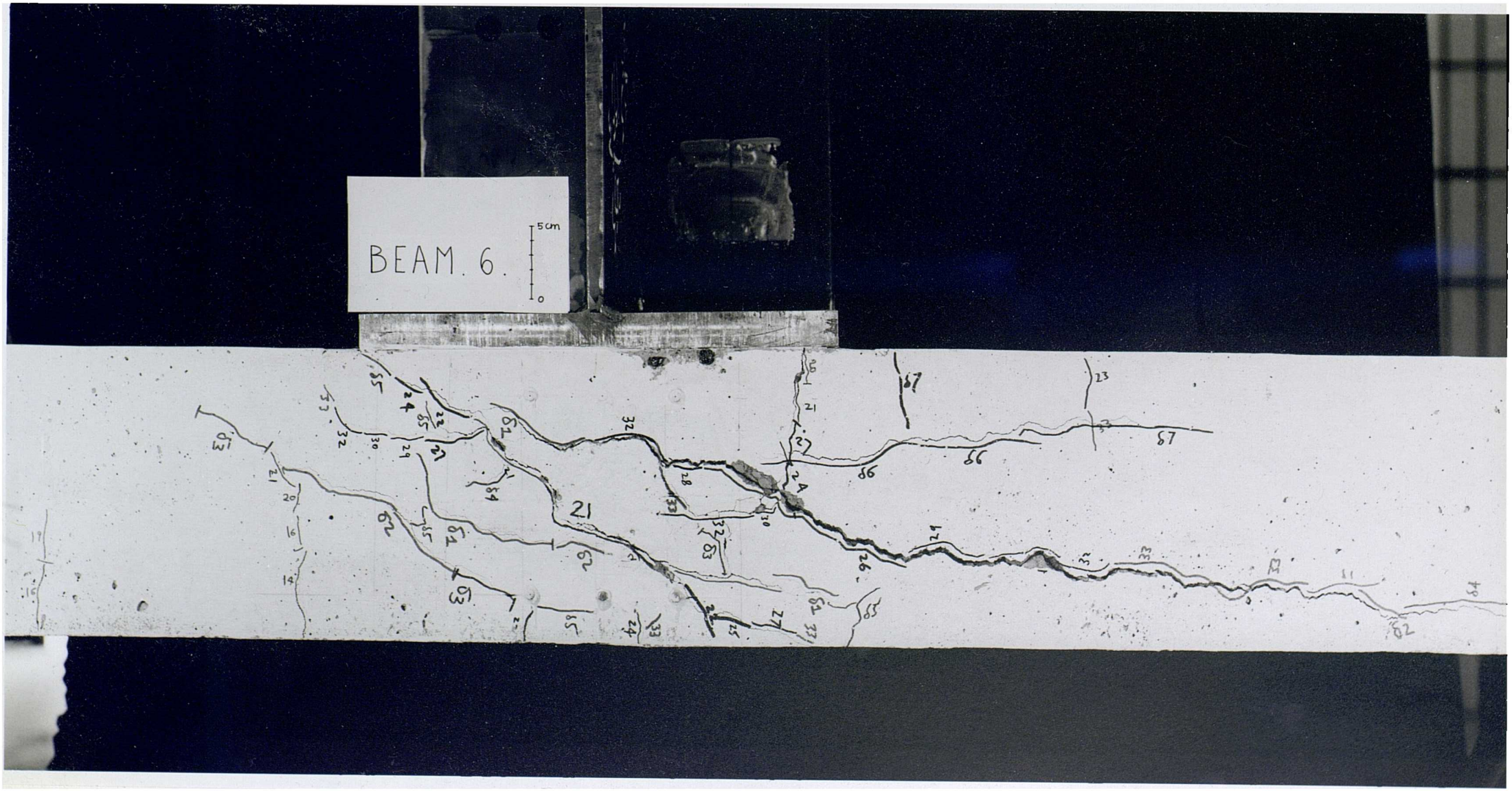

Figure 7.28(a): Plate of side-elevation R of the connection of test specimen BM6, as indicated on Fig. 7.12.

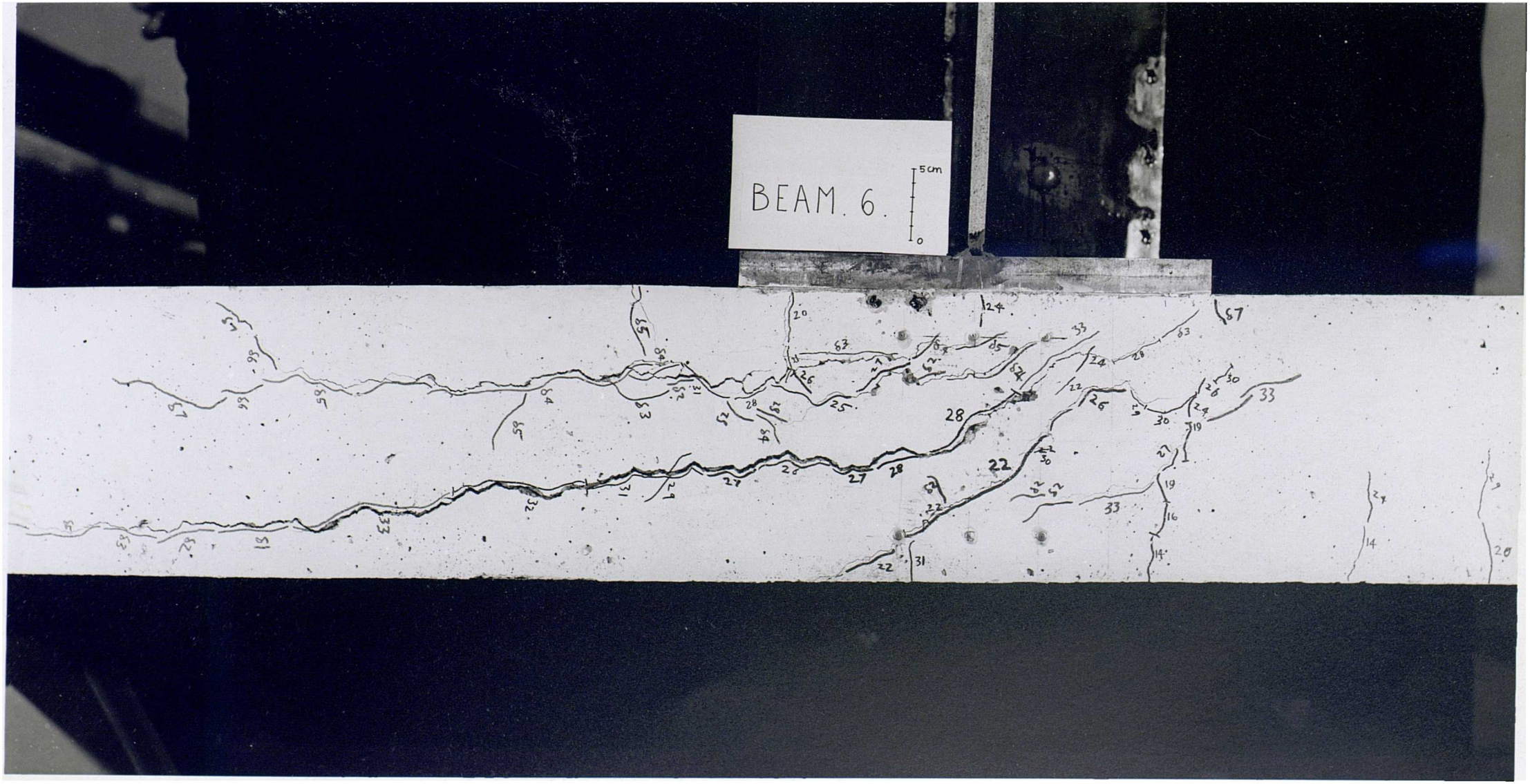

Figure 7.28(b): Plate of side-elevation L of the connection of test specimen BM6, as indicated on Fig. 7.12.

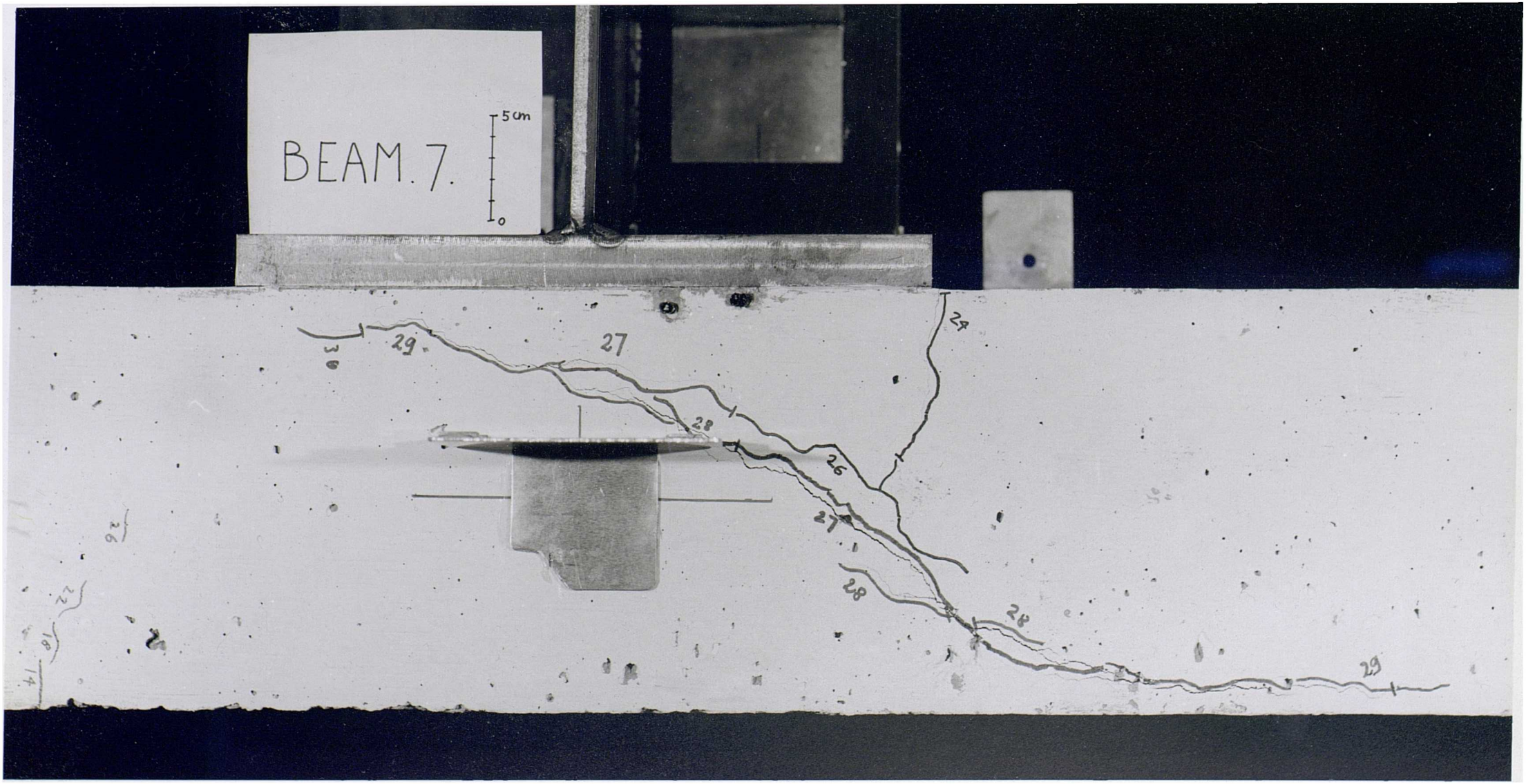

Figure 7.29(a): Plate of side-elevation R of the connection of test specimen BM7, as indicated on Fig. 7.12.

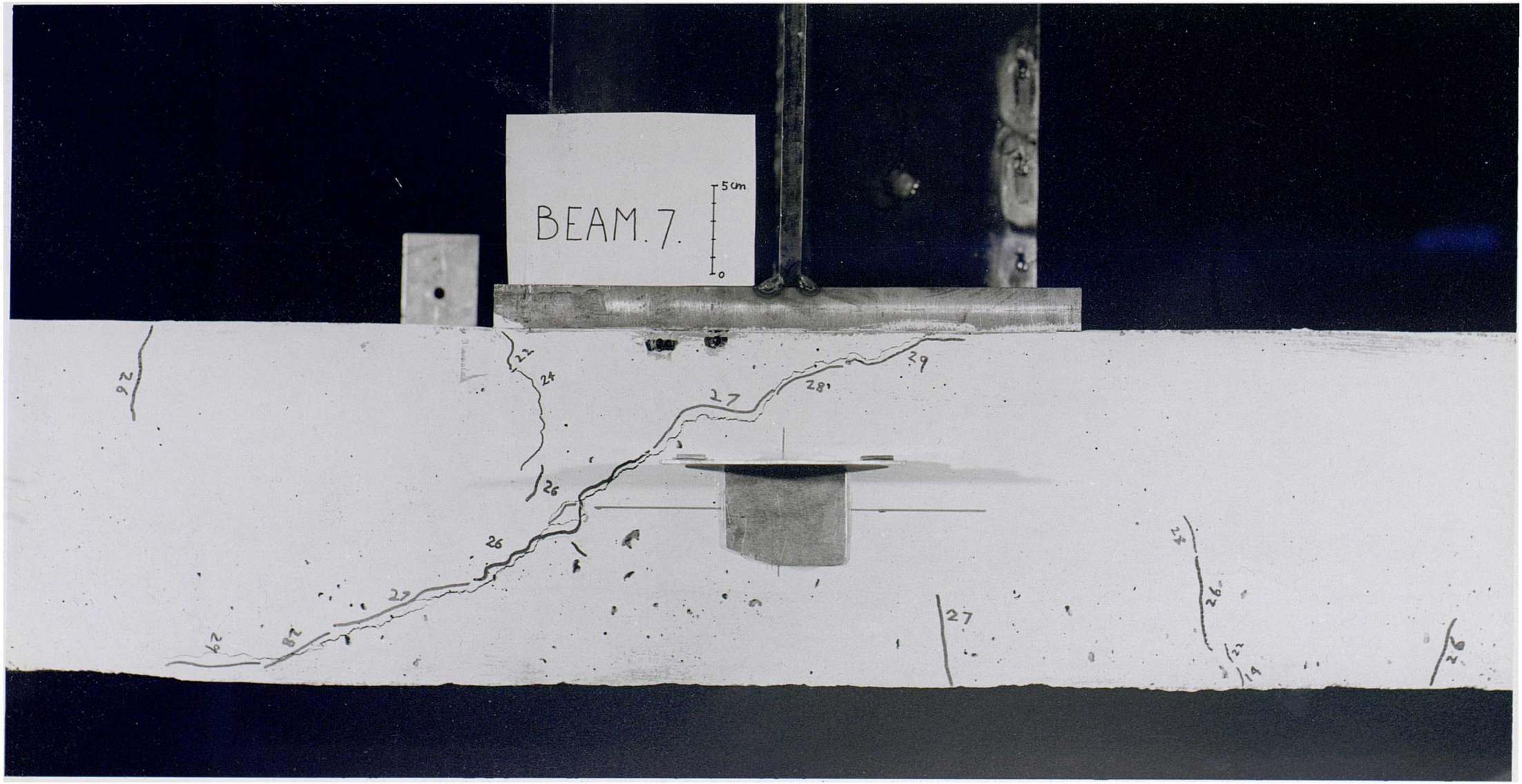

Figure 7.29(b): Plate of side-elevation L of the connection of test specimen BM7, as indicated on Fig. 7.12.

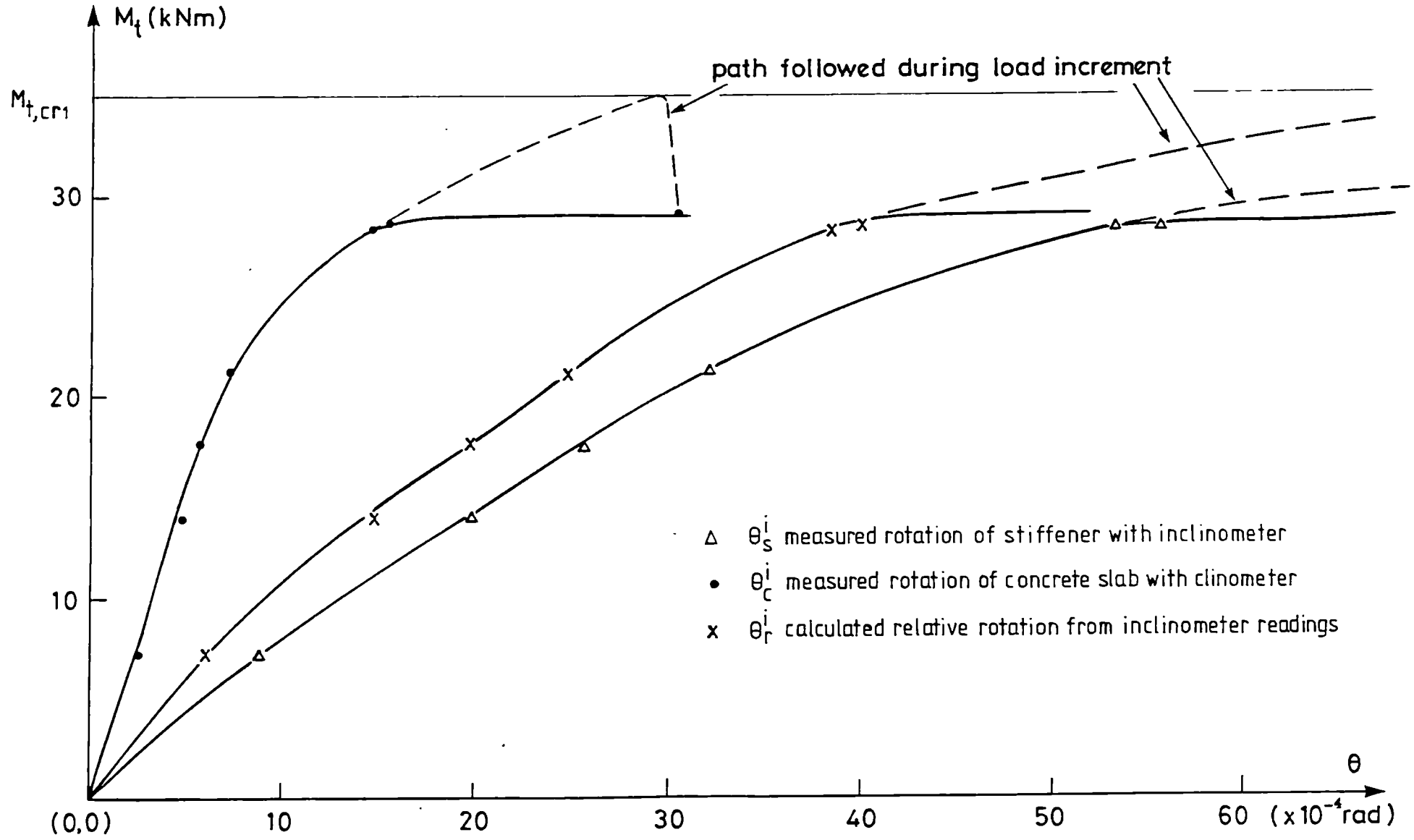

Figure 7.30: Relationship between the applied transverse moment and the rotations of the slab, the stiffener and the connection, around the X-axis for test BM2.

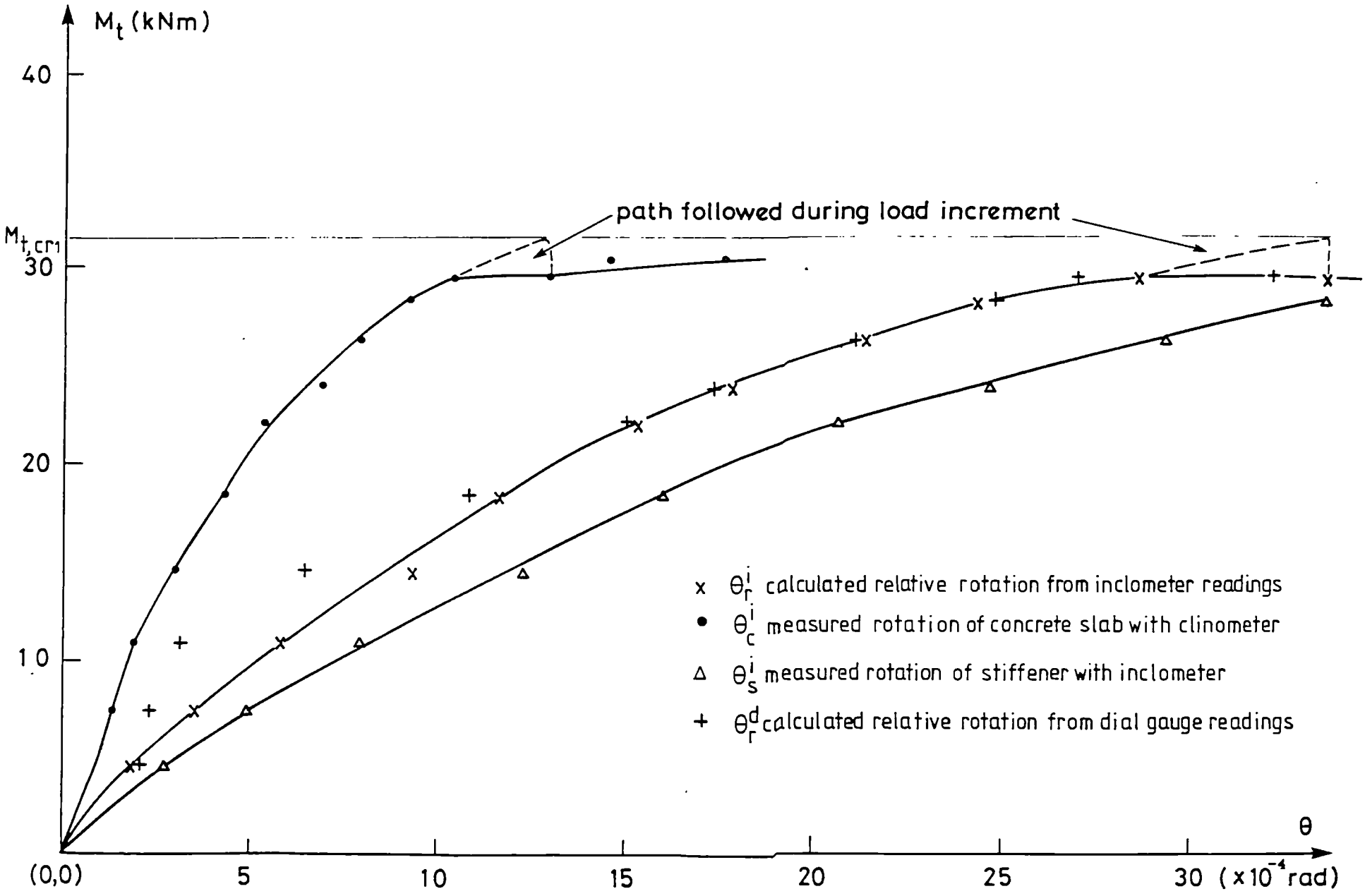

Figure 7.31. Relationship between the applied transverse moment and the rotations of the slab, the stiffener and the connection, around the X-axis for test BM3.

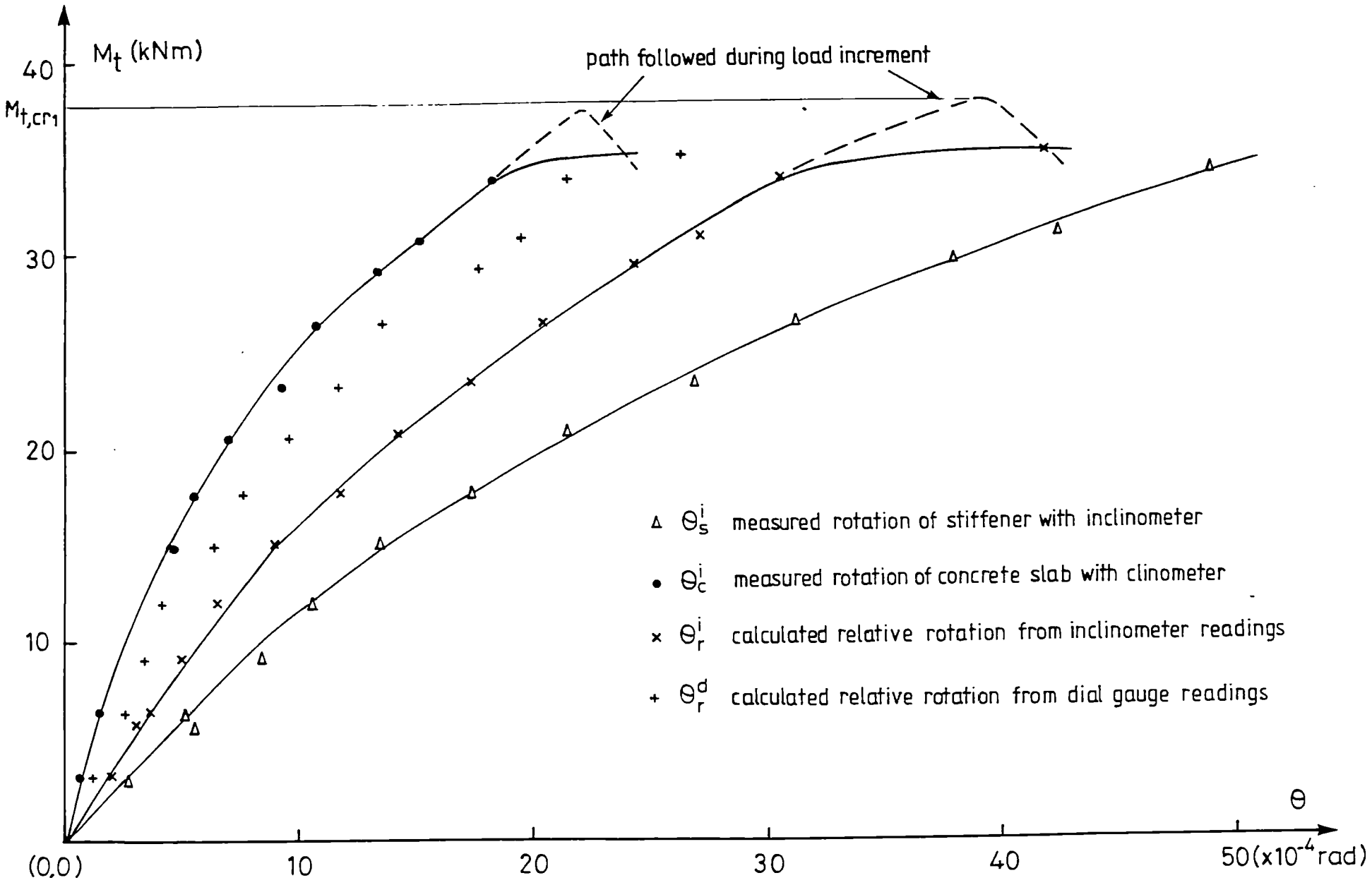

Figure 7.32: Relationship between the applied transverse moment and the rotations of the slab, the stiffener and the connection, around the X-axis for test BM4.

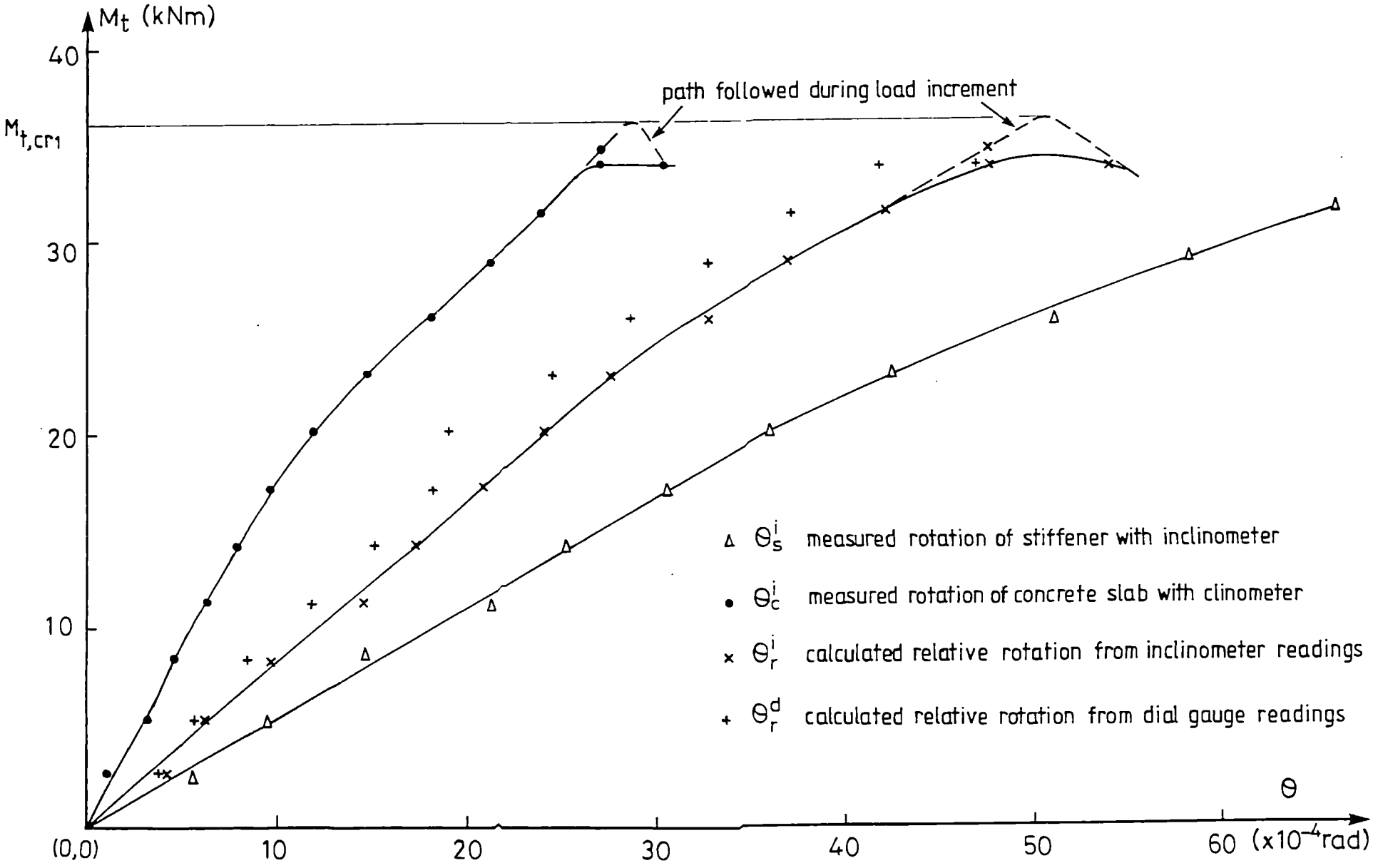

Figure 7.33: Relationship between the applied transverse moment and the rotations of the slab, the stiffener and the connection, around the X-axis for test BM5.

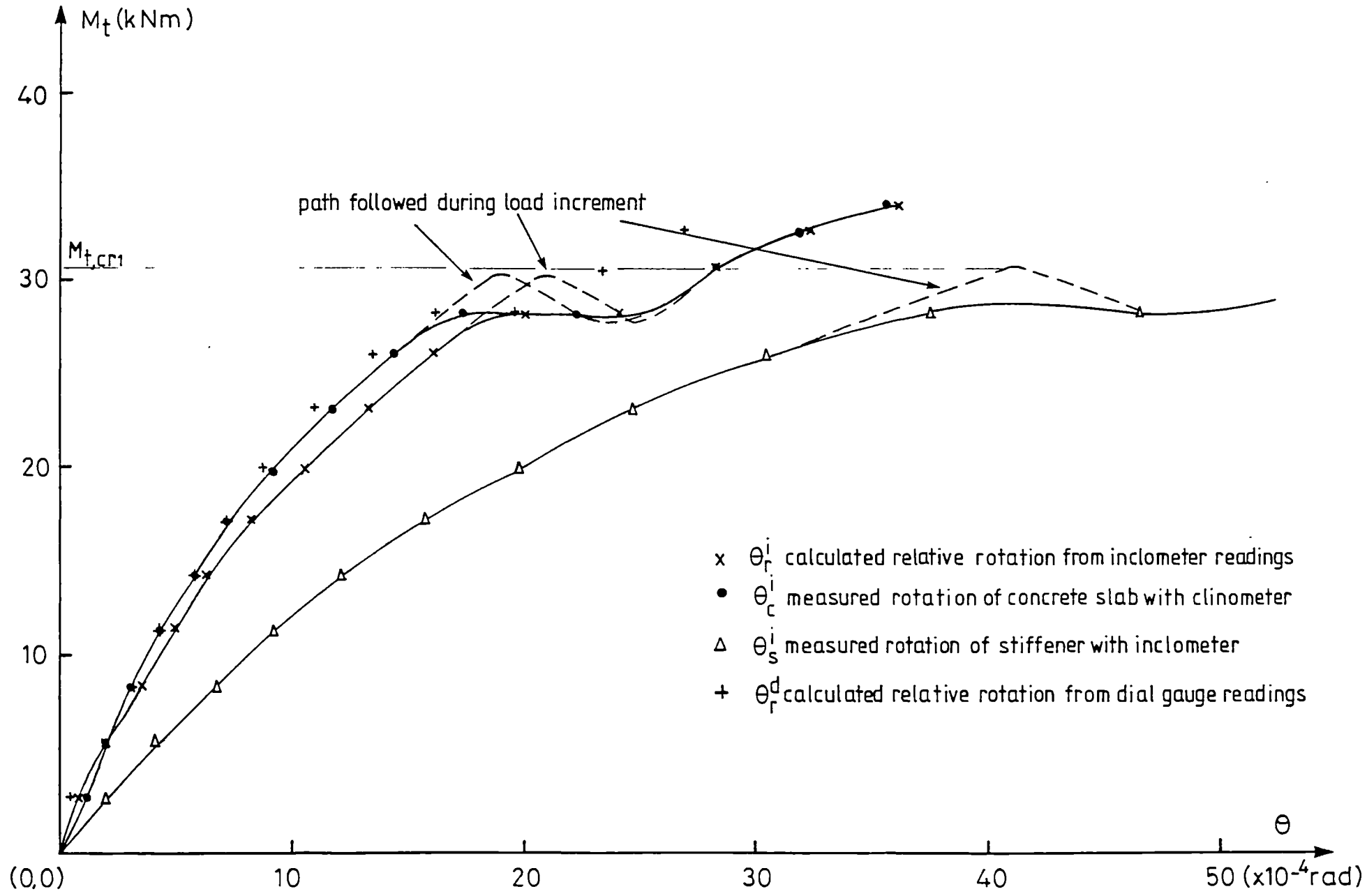

Figure 7.34: Relationship between the applied transverse moment and the rotations of the slab, the stiffener and the connection, around the X-axis for test BM6.

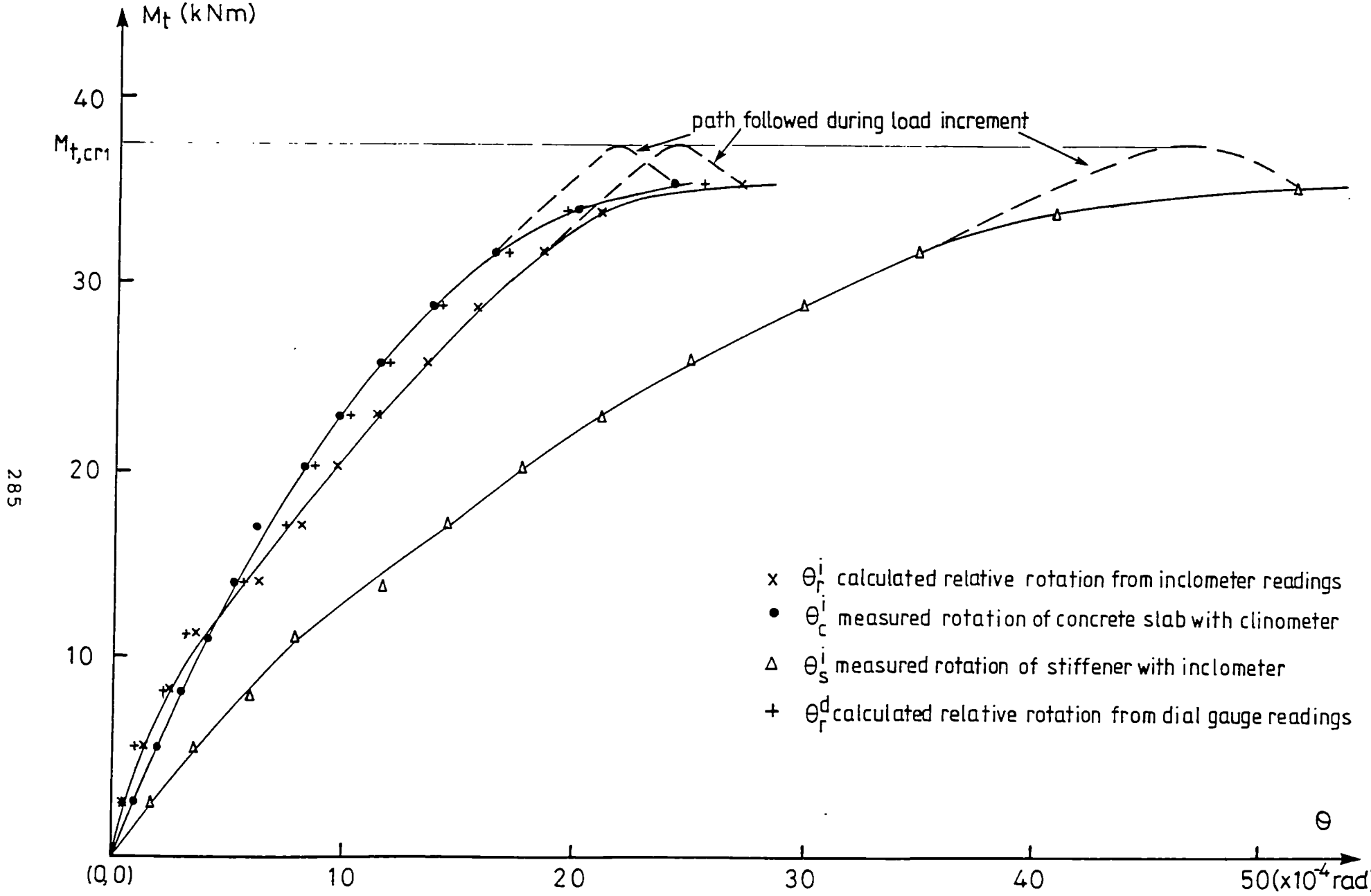

Figure 7.35: Relationship between the applied transverse moment and the rotations of the slab, the stiffener and the connection, around the X-axis for test BM7.

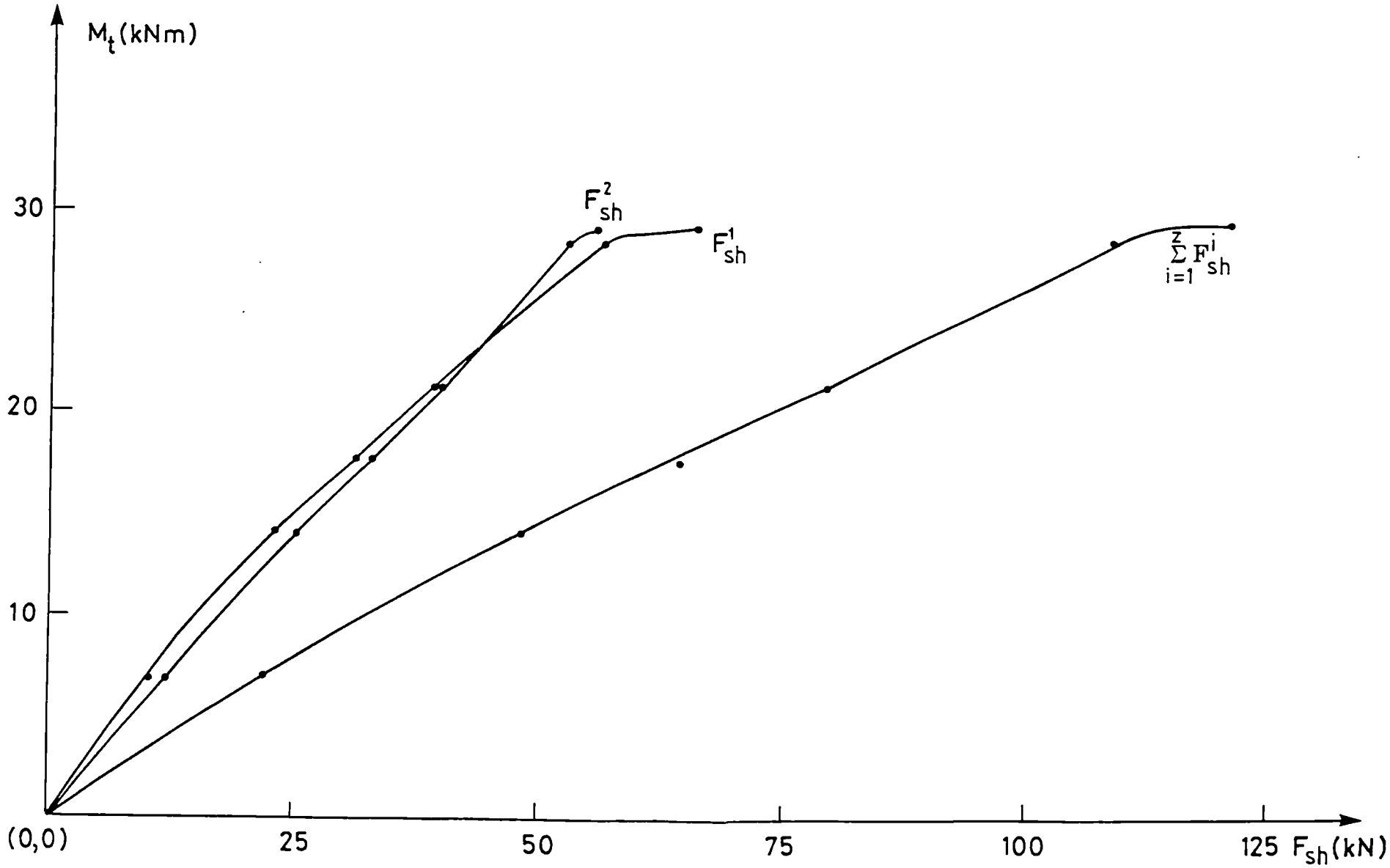

Figure 7.36: Relationship between the applied transverse moment and the tensile forces in the shanks of the studs of test specimen BM2.

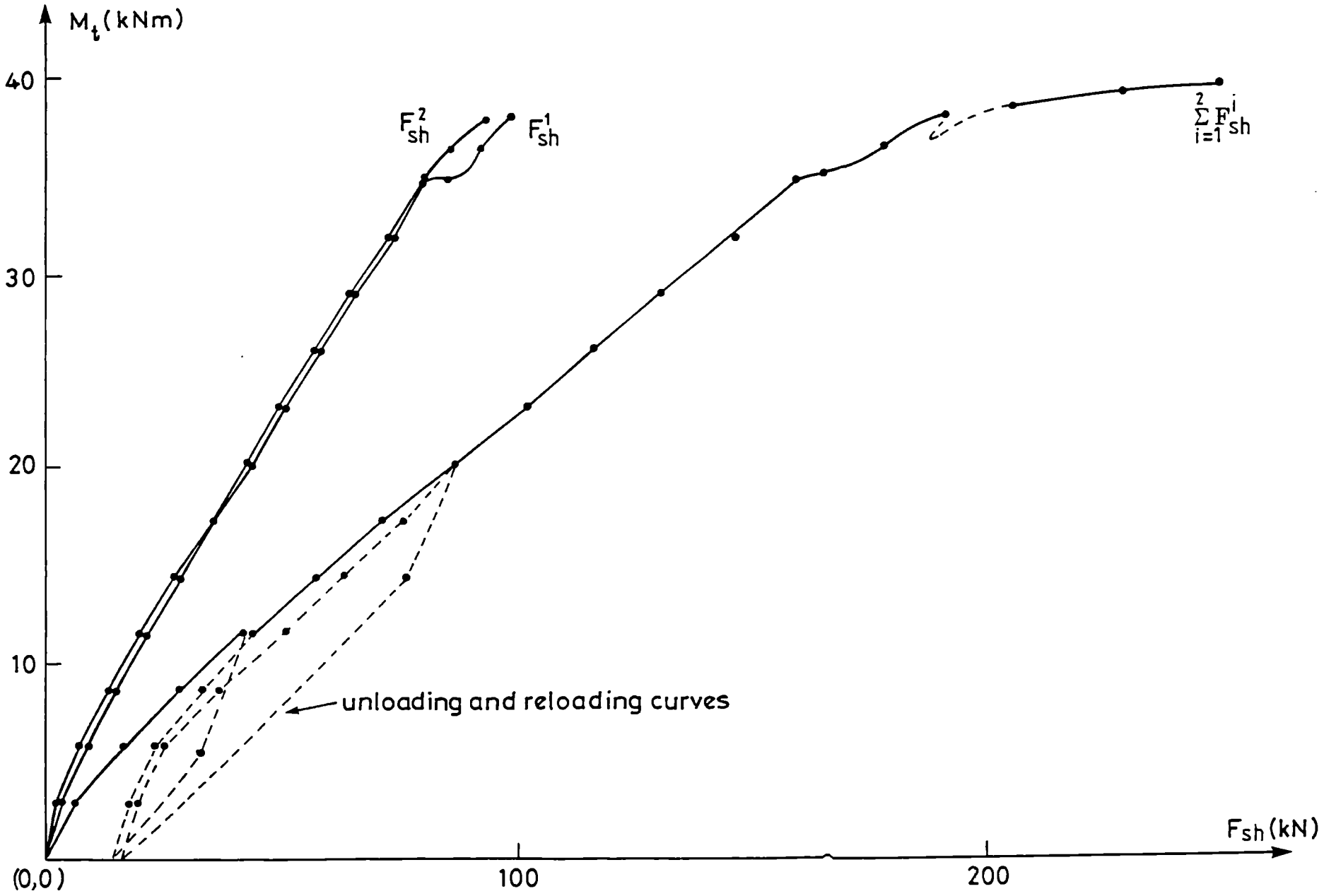

Figure 7.37: Relationship between the applied transverse moment and the tensile forces in the shanks of the studs of test specimen BM5.

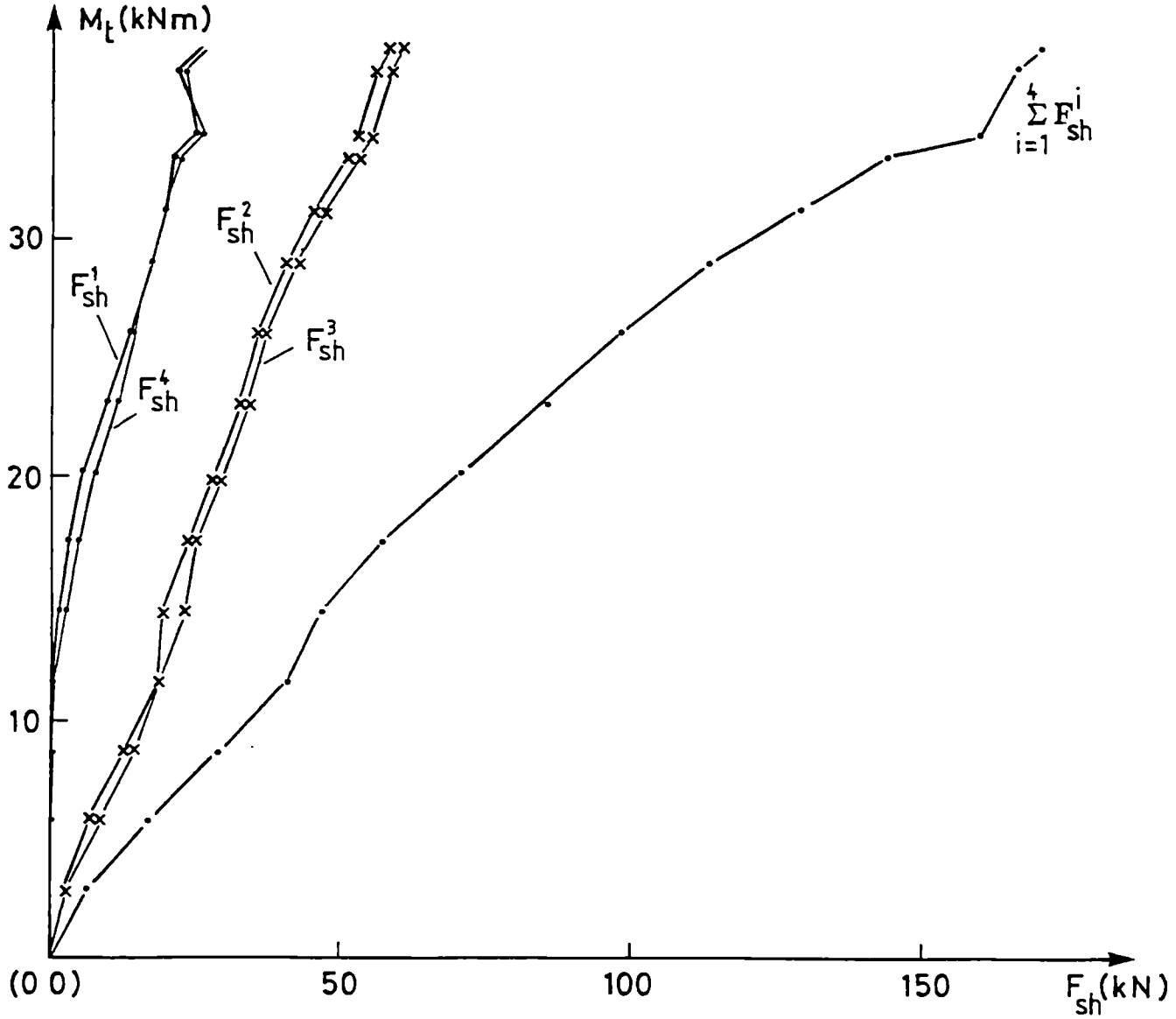

Figure 7.38: Relationship between the applied transverse moment and the tensile forces in the shanks of the studs of test specimen BM4.

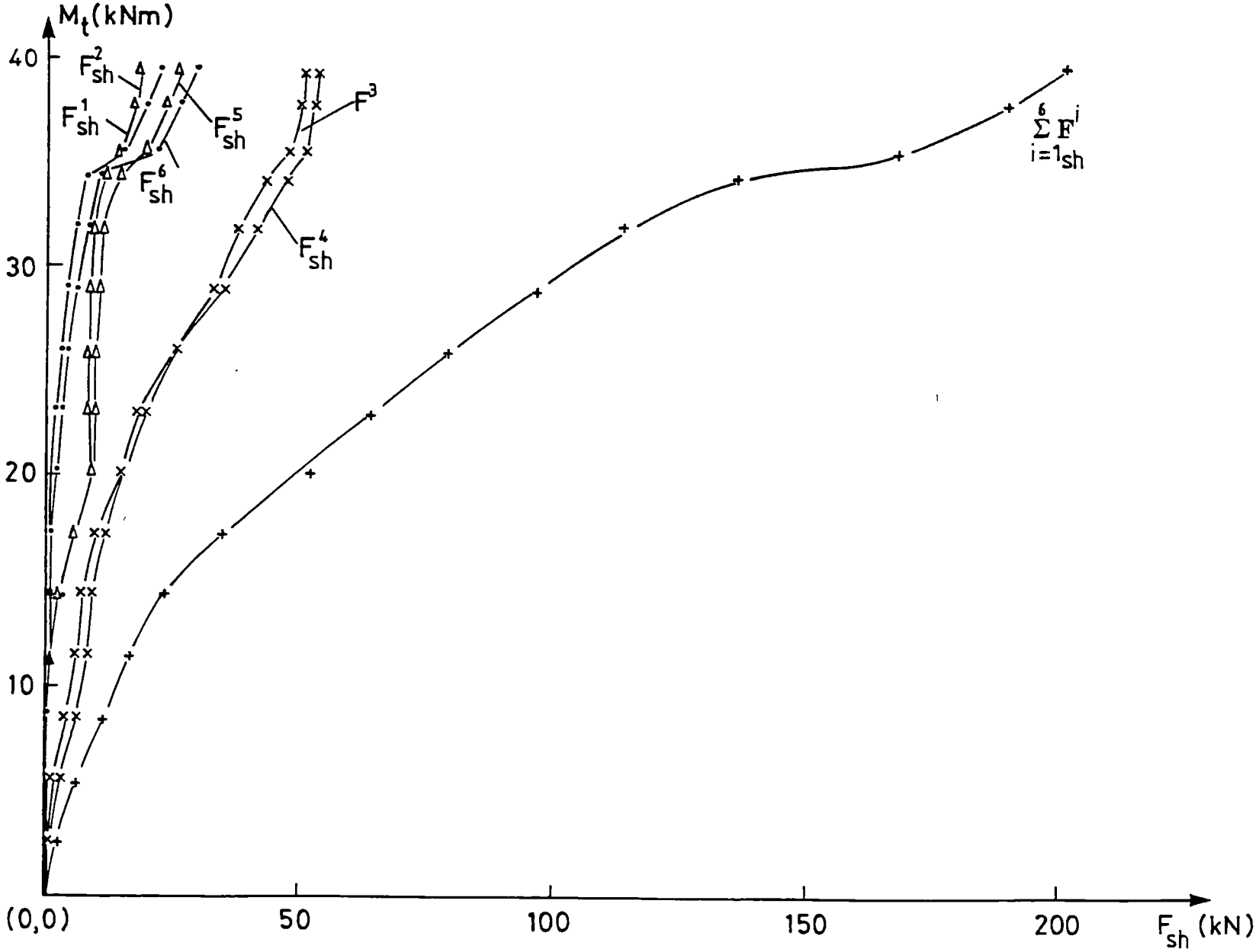

Figure 7.39: Relationship between the applied transverse moment and the tensile forces in the shanks of the studs of test specimen BM7.

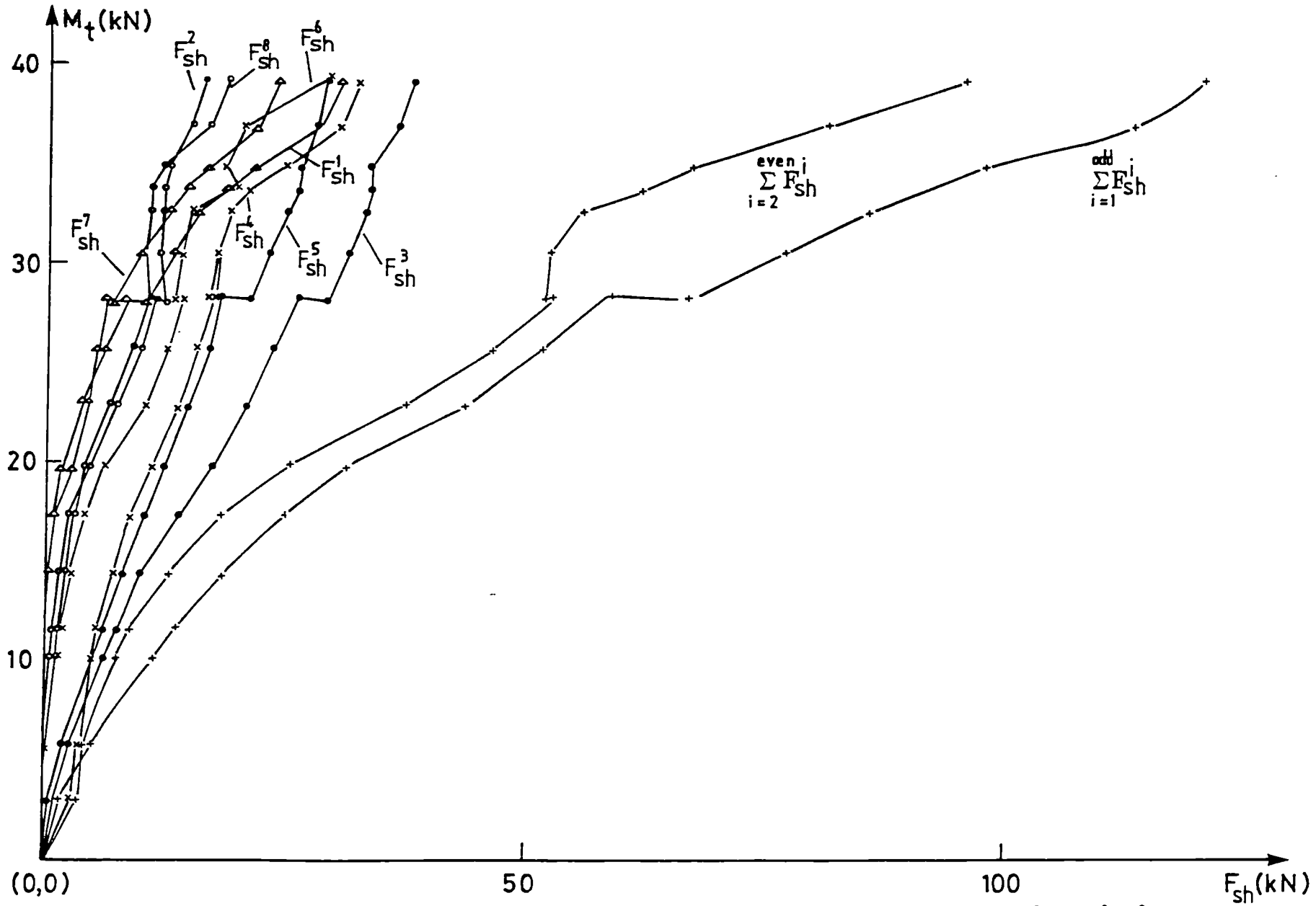

Figure 7.40: Relationship between the applied transverse moment and the tensile forces in the shanks of the studs of test specimen BM6.

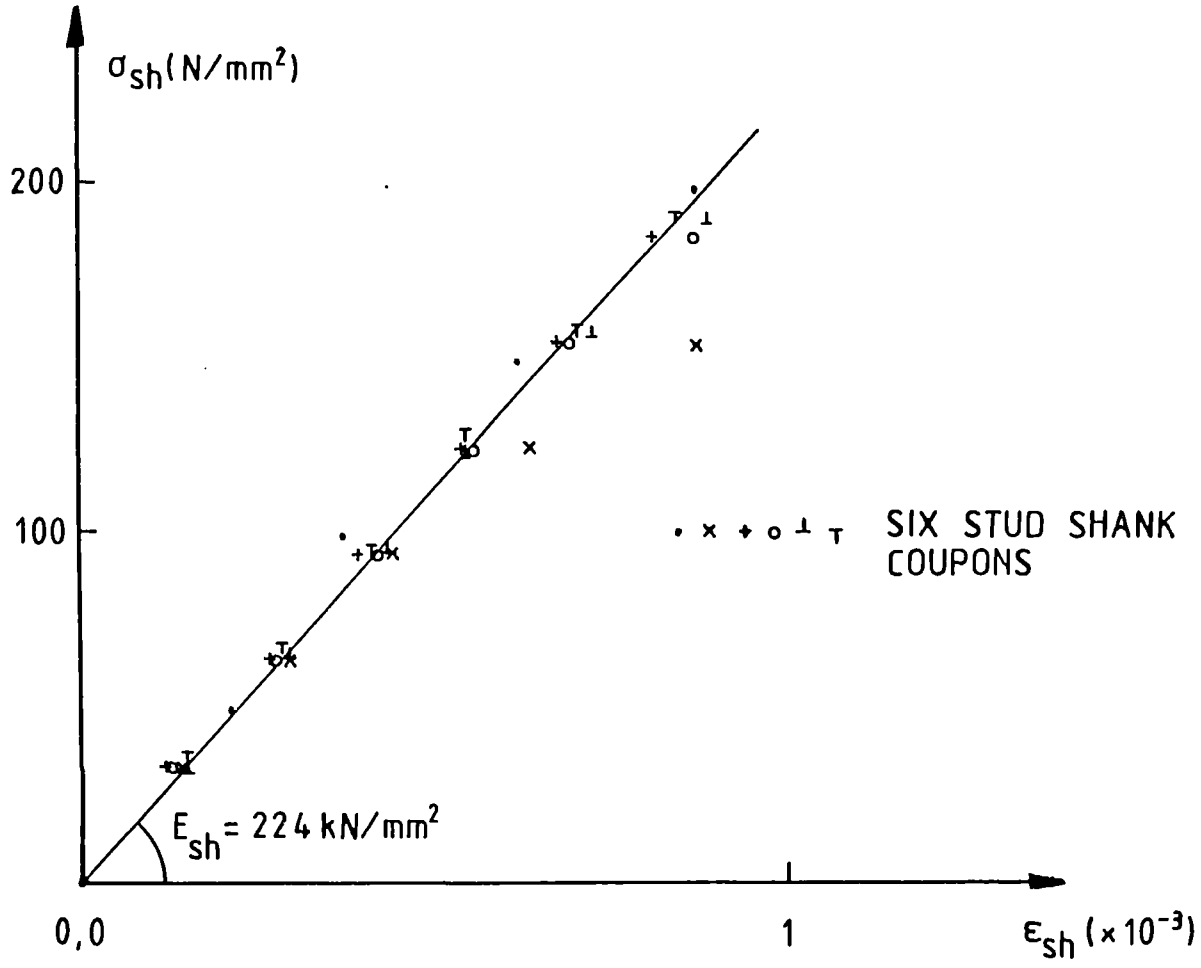

Figure 7.41: Average value of the Young's modulus of the shank steel from six coupon tests.

Chapter 8

Analysis and discussion of test results

8.1 Introduction

Before any model is being fitted to the results, it is vital to assess the accuracy of the measured variables and therefore the range of uncertainty of the experimental results.

A global behaviour of the test specimen is discussed with particular reference to the effects of cracking. A truss analogy model is being used to predict the crack pattern and a shear mechanism is used to predict the loads at initial cracking and at failure.

An analogy with semi-rigid steel beam-column connections was found to exist in determining the relative rotation of the connection under a transverse moment.

In the last section of this chapter the range of application of the different models is discussed in view of the limited available test results.

8.2 Degree of uncertainty in the experimental results

8.2.1 Degree of uncertainty in the value of the transverse force and moment

In Table 8.1 the absolute error and the percent relative error for the values of the transverse tensile forces F_t, are given for different load levels. The absolute error ΔF_t^{tot}, is made up of three values: the first one is the error of calibration of the Monsanto tensometer within the ranges $0-20$ kN and $0-40$ kN, ΔF_t^{cal}, the second one is the maximum residual between the regression analysis on the different calibration data for the load-cell and the individual data points ΔF_t^{res}, and the third one is the relative error of each measurement under repeated loading ΔF_t^{rep}. The standard error of estimate of the linear regression analysis on the different calibration data is only 0.02 kN. The value of F_t is therefore estimated within the range $F_t \pm \Delta F_t^{tot}$.

In calculating the absolute error for the values of the transverse bending moment at interface level, only two sources of error exist: the first is obviously the absolute error, ΔF_t^{tot}, for the transverse force F_t, and the second is the variation of the lever arm l_h, under increasing transverse loading. This value can be estimated for a maximum displacement of 55 mm of point T at the top in Fig. 7.11 to be less than 0.30% and therefore only half of this value when the lever arm is reduced to the average value of 1435 mm for all load levels throughout the tests.

8.2.2 Degree of uncertainty in the values of the relative rotations of the connections

The absolute error for the calculated relative rotation θ_r^i, is equal to the sum of the absolute errors for the measured rotations of the steel flange (θ_s^i) and the concrete slab (θ_c^i). For each load cycle and each load level these absolute errors are obtained by equation (8.1), whereby $\theta_j^{i1}(0)$ or $\theta_j^{i2}(0)$ indicate the zero reading of the first ($i1$) and the second ($i2$) inclinometer for both steel and concrete at the start of each new load cycle.

$$\Delta\theta_j^i = \frac{\left[\left(\theta_j^{i1}(F_t) - \theta_j^{i1}(0)\right) - \left(\theta_j^{i2}(F_t) - \theta_j^{i2}(0)\right)\right]}{2} \tag{8.1}$$

$$\begin{aligned} \text{with } j &= \text{s for steel,} \\ \text{and} &= \text{c for concrete} \end{aligned}$$

These zero readings are assumed to have a relative error equal to their measured repeatability, so that the errors are similar for different load cycles at each load level.

The absolute error for the calculated relative rotation θ_r^d is theoretically given by equation (8.2).

$$\Delta\theta_r^d = \left[\left(\frac{5mm}{|D_4D_5|}\right) + \left(\frac{0.04mm}{\Delta Z(D_4D_5)}\right)\right]\theta_r^d \tag{8.2}$$

$$\begin{aligned} \text{with} \quad |D_4D_5| &= \text{distance between measuring points } D_4 \\ &\quad \text{and } D_5 \text{ as indicated in Fig. 7.12} \\ &\quad \text{and measured with 5 mm accuracy} \\ \Delta Z(D_4, D_5) &= \text{relative vertical displacement of points } D_4 \\ &\quad \text{and } D_5 \text{ as defined in eq. (7.5)} \\ &\quad \text{and measured with 0.04 mm accuracy} \end{aligned}$$

Although this error is generally smaller than $\Delta\theta_r^i$ (less measuring points therefore no precision error) the accuracy is much less. This is due to the measuring method: the relative vertical displacement was measured between the steel flange and the slab soffit in a region where a pull out force is applied to the studs which gives rise to local deformations of the concrete surface and therefore unknown, unquantified errors.

Both values of $\Delta\theta_r^i$ and $\Delta\theta_r^d$ are given in Tables VI.1 to VI.6 of Appendix VI for test specimens BM2 to BM7. The percent relative error obtained from these values for θ_r^i and θ_r^d, will reach at initial diagonal cracking values of 8% and 6% respectively.

8.2.3 Degree of uncertainty in the values of the forces in the studs

In assuming that the tensile strain is uniform over the whole cross section of the shank, a systematic error is made in the calculation of the tensile forces in the stud shanks, which cannot be quantified theoretically.

If this systematic error is ignored, two sources of absolute errors remain on the calculated tensile shank forces, F^i_{sh}. Firstly, there exists an error on the measured strains in the shank, due to temperature variations ($\pm 1°$ C = 10 microstrain) and secondly there is a standard deviation of 15.6 kN/mm^2 on the Young's moduli of the six shank specimens. Therefore the absolute errors for the calculated values of the shank forces F^i_{sh}, which are calculated from the measured values of the strains in the stud shanks, are approximately $\pm$ 0.07 F^i_{sh}.

Unfortunately, these calculated forces are not equal to the forces F^i_{st}, applied to the studs as is made clear in Fig. 8.1. When a tensile force is applied to an embedded stud, shear forces q^+, build up along the shank and equilibrium is obtained by equation (8.3)

$$F^i_{st} = F^i_{sh} + \int_0^{50mm} q^+ dx \tag{8.3}$$

As the shank diameter reduces slightly under tensile forces, the bond stresses change. When this tensile force is removed ($F^i_{st} = 0$) frictional forces q^-, are applied to the shank and cause the shank to be in tension as is clear from equation (8.4)

$$F^i_{sh}(0) = \int_0^{50mm} q^- dx \tag{8.4}$$

The more the concrete structure which surrounds the shank breaks down, the smaller the frictional forces become and therefore the smaller the residual strains in the shanks under increasing load cycles.

Without additional pull out tests it is impossible to obtain an accurate assessment of the difference between F^i_{st} and F^i_{sh}. Yet, taking into account that the residual strain in a shank is not larger than one tenth of the maximum obtained strain in that stud, it could be assumed that the difference between F^i_{st} and F^i_{sh} values is not larger than 0.10 F^i_{sh}. Therefore the calculated forces in the shanks are only used as indicative values for the forces applied to the studs.

8.3 Global behaviour of the test specimen

In order to get a better understanding of the behaviour of the tested specimens, the derivatives of all the main measured variables with respect to the applied load, were examined for all tests. This way sudden changes showed up more clearly. It is found from Tables 8.2 to 8.5 for tests BM3, BM4, BM6 and BM7 with more than 4 studs, that all the derivatives change either slightly or dramatically at a transverse load which is around half the load at which first shear cracking became

visible at the sides of these specimens. The derivatives of the rotations increase slightly, while the derivatives of the strains in the shanks of the studs change suddenly. From the description of these changes, given in section 7.7.4, it is clear that a crack had formed inside the concrete slab, without being visible on the outside. This crack results in a slight change in slope of the moment rotation curve for each test specimen, which can therefore be modelled as a bilinear curve up to a load level just before diagonal cracking becomes visible.

For all four specimens these same tables show also dramatic changes in all the derivatives at a load level just below the load at which the diagonal cracks become visible on both sides of the slab of the specimen. This indicates that the real cracking load of the test specimen is lower than the load corresponding to the observed crack formation. These cracking loads are easily recognised on the $M_t - \theta_r$ curves, as they correspond to the point where the second linear part of the curve ends.

From the regular measurements of rotations at different load levels up to excessive shear cracking, sporadic measurements of rotations thereafter and the above mentioned tables, three different qualitative transverse moment-relative rotation curves can be constructed for the different tests. These curves are represented in Fig. 8.2. The transverse moments M_t, indicated on the Y-axis are calculated by multiplying the transverse forces F_t, measured with the load cell, by a constant average value $l_h = 1.435$ m for the lever arm. These forces initiate different stages in the cracking process as stated below:

$F_{t,c0}$ = transverse force at which invisible internal cracking near the stiffener starts, before this crack propagates over the whole width of the test specimen.

$F_{t,c1}$ = transverse force at which the initial diagonal cracking has spread over the whole width of the specimen, but is not yet visible.

$F_{t,c2}$ = transverse force at which a second diagonal crack forms parallel with the first one.

$F_{t,u}$ = maximum transverse capacity of the connection.

The values of these different forces are given in Table 8.6 for the different tests. The values of $F_{t,c1}$ and $F_{t,c2}$ are smaller than the values of $F_{t,cr1}$ and $F_{t,cr2}$ which define the values of the transverse force when the first and second diagonal crack becomes visible on both sides of the slab. The value of $F_{t,cr1}$ corresponds with $M_{t,cr1}$, which indicates the maximum values of the dotted lines in Figs. 7.30 to

7.35. By measuring the relative rotation, the transverse cracking load of the test specimen can be determined more accurately than by eye observation of cracks on the sides of the slab.

8.4 Prediction of the crack pattern using truss analogy

Apart from specimen BM2, in all other test specimens a diagonal shear crack formed which extended from the top reinforcement to the bottom reinforcement at an angle varying from 24° to 43°.

Both the shear force diagram and the internal force distributions will help to explain the formation of this crack and other major cracks in the crack patterns of the different test specimens.

It is clear from the shear force distribution in Fig. 7.17 that the diagonal shear crack can be initiated within the connector region near the vertical stiffener, and from the moment distribution that flexural cracks may appear in the top and bottom of the concrete slab on either side of the connection respectively.

A conventional truss model, based on the analogy between a chord truss and a reinforced concrete beam as postulated by Mörsch [97], was used initially to find the internal force distribution in the slab of each test specimen.

In Fig. 8.3 such a truss model is shown for the different test specimens. The top and bottom layers of transverse reinforcement on either side of the stud connection form the top and bottom chords of the analogous pin jointed truss. The arch actions in the shear spans on either side of the connection act as compression struts. In the connection area, a compression strut was parallel with the diagonal shear crack. In the truss model of Fig. 8.3(a) the row of studs in tension and part of the concrete under the heads form a tensile chord, whereas in the truss model of Fig. 8.3(b) this tensile chord stops at the position of the head of the row of studs.

In Appendix VII the force distribution is worked out as a function of the variable diagonal shear crack angle α_{cr}, for both truss models for test specimens BM3 and BM7 and their applied forces at first diagonal cracking. Assuming a compressive chord width of 30 mm produces stresses in the chords which are lower than half the cube strength and therefore are too low to correspond to cracking. Normally such an analogy provides a reliable model of behaviour as ultimate conditions are approached and gives reasonable predictions for the ultimate load

for 2 dimensional stress situations such as a corbel or beam. Unfortunately, in the slab the forces are applied locally at the positions of the studs only so that no 2 dimensional model can adequately be applied for the 3 dimensional stress distributions in the region of the connection where the diagonal shear crack is initiated. Furthermore, in these test specimens the position of the applied forces changes over the connection region after the inital diagonal shear crack has formed. Generally, the reaction force is thought to move towards the right as is shown in Fig. 8.4, and for test specimens BM3, BM5 and BM6 this reaction force RF_{stud}, reaches further than the second row of studs. For these specimens, at ultimate load, two rows are in tension and the original truss model of Fig. 8.3 is no longer valid. The only valuable information yielded by this analogy and the internal force distribution is an indication of the crack pattern. For both truss models the expected crack patterns corresponding with the internal force distribution, fit the real crack pattern of the slab quite well as can be seen from a comparison between Figs. 8.3(a) and (b) where the expected crack patterns are drawn in, with the crack patterns in Figs. 7.18 to 7.23 obtained from the experiments.

8.5 Prediction of the initial cracking load and failure load using a shear failure model

By looking at the moment and shear force distribution over the slab in the region of the connection of the test specimen BM5 given in Fig. 7.17 and at the diagonal shear crack over the width of the test specimen, an analogy can be drawn with the shear failure in beams without web reinforcement, subject to shear and flexure and with an a/d ratio smaller than 2.0.

The amount of research done on shear is vast and although progress has been achieved by the application of several different theories, i.e. theory of plasticity which governs ductile failure of concrete, all these theories are still based on the concept of strength of concrete to predict the shear failure of rectangular beams and slabs. In more recent research [98] it has been remarked that the scatter of the deviations of the test results from these formulae cannot be due to the scatter of strength, but is caused by the incorrect use of a strength criterion for shear failure of concrete.

As only the usage and not the development of a prediction equation for shear cracking and/or failure is aimed for in this thesis, attention is only given to

the theories supporting the equations of BS 5400:Pt.4 on shear and to the most reliable amongst the established equations on shear failure, in order to apply these equations to our test results. Yet, some attention is given to a paper by Bažant [99], who obtains a new prediction equation for shear failure based on an energy criterion of failure, treating concrete as a brittle heterogeneous material, subject to a non linear fracture process. In the same paper he explains why previous prediction equations are reasonably correct for small size structures, although they were based on the wrong concept.

8.5.1 Recent developments in shear failure concepts for concrete beams

The main design formula for the nominal shear stress for beams and slabs in clause 5.3.3. of BS 5400:Pt.4 is directly taken from the prediction equation obtained by Regan [100], [101]. Not knowing the exact relative importance of interlock forces, dowel forces and shear in the compressive zone on the shear cracking resistance, Regan proposed an analytical equation [102] in terms of shear and interlock only, using as a shear cracking criterion the occurrence of a critical biaxial stress condition anywhere within the uncracked concrete. He adjusted it numerically to allow for the dowel action and thus comply with test data. Regan established this way a semi-empirical expression for the shear cracking resistance V_{cr}, of a beam with normal proportions, as shown in Fig. 8.5, given by eq. (8.5) which is expressed in metric units.

$$V_{cr} = 0.27 \sqrt[3]{f_{cu} \frac{100 A_s}{bd}}\, b\, d \tag{8.5}$$

with b = width of the beam

d = distance between the compression face of the beam and the tension reinforcement

A_s = cross-sectional area of tension reinforcement

Under *normal proportions* is here understood beams with $a/d > 3.0$, and as Kennedy [103] later points out, beams where the depth ranges primarily not further than 300 mm. In beams with such proportions and without web reinforcement collapse occurs immediately after the appearance of shear cracks so that $V_u \approx V_{cr}$ of eq. (8.5).

Based on studies by Kani [104][105], Leonhardt [106] and Taylor [107] on the shear strength of large concrete beams, with larger depth, the Code modified eq. (8.5) to eq. (8.6) to take account of the variation of the strength with depth

$$V_{cr} = 0.27 \sqrt[3]{f_{cu} \frac{100 A_s}{bd}} \left(\frac{500}{d}\right)^{0.25} b\,d \tag{8.6}$$

From the same experiments it was found that short beams with $a/d < 2.0$ have a considerable reserve strength after inclined cracks form at a load level corresponding with V_{cr} of eq. (8.5) in the shear span and that they eventually fail by crushing of concrete at an ultimate load V_u, for which a lower bound is given by eq. (8.7)

$$V_u = 0.27 \sqrt[3]{f_{cu} \frac{100 A_s}{bd}} \left(\frac{500}{d}\right)^{0.25} \left(\frac{2d}{a}\right) b\,d \tag{8.7}$$

During the same period as Regan developed his eq. (8.5) in the U.K., Zsutty [108][109] developed in the U.S.A. two purely empirical relationships for the ultimate strength of simple rectangular slender beams (a/d > 2.5) and short beams (a/d < 2.5), given by equations (8.8) and (8.9) respectively, both expressed in metric units.

For $a/d > 2.5$

$$V_{cr} = 2.02 \sqrt[3]{f_{cu} \rho \frac{d}{a}}\, b\,d \tag{8.8}$$

For $a/d < 2.5$

$$V_u = 5.05 \sqrt[3]{f_{cu} \rho \frac{d}{a}}\, \frac{d}{a}\, b\,d \tag{8.9}$$

with $\rho = A_s/bd$

Zsutty applied a combined technique of dimensional analysis and regression analysis to most existing sources of test data and used the minimization of the coefficient of variation of error, CV, on the multiple linear regression as a criterion to segregate the test beam results and to find two or more prediction equations. Heeding the experience of Leonhardt [106] and Kani [105] concerning the effect of the a/d ratio, he established the value of $a/d = 2.5$ as a means of segregating the test beam results into beam action ($a/d > 2.5$) and arch action ($a/d < 2.5$).

In his prediction equation (8.8) for beam action, Zsutty did not use the shear cracking resistance V_{cr}, but the shear at sudden diagonal tension failure, which is a lower bound to the ultimate shear strength V_u, which has an unstable range of 0 to 10 – 15% above V_{cr}. The main reason for doing so was that a main part of the percentage error on the cracking shear for slender beams is due to different

laboratory testing conditions and definitions of shear cracking, whereas shear at sudden diagonal tension failure was more consistently identifiable by all observers and resulted in a smaller overall error.

Prediction eq. (8.9) for arch action provides also a lower bound to the wide scatter of very unstable and non predictable experimentally measured ultimate loads. A scatter, which according to Zsutty [109], may be due to variations in load block size, loading rate and beam section configurations.

In a paper of 1984, Bažant [99] used a nonlinear fracture mechanism for diagonal shear failure of concrete beams and applied this to predict the effect of structure size on the nominal shear stress σ_N, at failure. Due to the dispersed nature and progressive development of cracking in concrete he obtained equation (8.10) by dimensional analysis.

$$\sigma_N = f_t' \, \phi(\lambda) \tag{8.10}$$

$$\begin{aligned} f_t' &= \text{direct tensile strength of concrete} \\ \phi(\lambda) &= \frac{1}{\sqrt{1+\frac{\lambda}{\lambda_0}}} \\ \text{with } \lambda_0 &= \text{empirical constant} \\ \lambda &= \frac{d}{d_a} \\ \text{and } d &= \text{depth of tensile reinforcement} \\ d_a &= \text{max. aggregate size} \end{aligned}$$

In Fig. 8.6 the strength criterion and the non-linear fracture mechanism are represented in a graph giving nominal shear stress at failure against size. For structures of small size relative to the size of the aggregate, which is the case for most structures tested in laboratories, $\phi(\lambda) \approx 1$ and σ_N is nearly constant, so that the strength criterion is correct for these structures as shown in Fig. 8.6.

Bažant argues that the huge scatter of data, when the above stated formula is used, is due not only to the size effect but also to the manner in which f_t' and d_a are taken into account. To that effect he builds up a formulation similar to equation (11.6) of ACI 318-83 [1], but one which contains more empirical parameters found

[1] $$V_{cr} = \left(0.1475\sqrt{f_{cu}} + 17.2\rho\frac{d}{a}\right) b\,d$$

from test results. He multiplies this formula with the size function $\phi(\lambda)$ and applies a statistical multiple regression analysis on nearly 300 test data to obtain the different empirical constants. Bažant proposes for the mean ultimate shear strength equation (8.11)

$$V_u = \frac{10\rho^{0.33}}{\left(1+\left(\frac{d}{25da}\right)\right)^{0.5}}\left(0.0765\, f_{cu}^{0.5} + 20.69\,\rho^{0.5}\left(\frac{d}{a}\right)^{2.5}\right) b\,d \qquad (8.11)$$

For design he proposes equation (8.12), obtained by scaling down (8.11) so that only a few test data would lie below it.

$$V_{cr} = \frac{8}{10} V_u \text{ (eq. 8.11)} \qquad (8.12)$$

As the philosophy in present design Codes — given by equations (8.7) and (11.6) of ACI 318-83 — is to achieve a certain safety against the shear cracking load and not against the ultimate load, Bažant had to use (the much less numerous) available data of about 120 tests to find the empirical constants and thus to obtain equation (8.13) for shear cracking strength.

$$V_{cr} = \frac{10\rho^{0.33}}{\left(1+\left(\frac{d}{25da}\right)\right)^{0.5}}\left(0.0765\, f_{cu}^{0.5} + 2.758\,\rho^{0.5}\left(\frac{d}{a}\right)^{1.5}\right) b\,d \qquad (8.13)$$

For true crack initiation, the size effect should be non-existent since beams do not contain any initial stress concentrators. The fact that size effects seemed to be apparent indicates that the observed initial shear cracking stress ν_{cr}, does not correspond with the true cracking initiation which begins by gradual formations of invisible microcracks and therefore cannot be detected by strain measurements or surface crack observations.

8.5.2 Prediction of the load at initial cracking and prediction of the failure load for all test specimens

8.5.2.1 Determination of the lever arm a_c, between shear forces

In order to calculate V_{cr} or V_u for the six test specimens, d and a_c need to be determined for each one of them.

According to Fig. 8.3(a), d = 167 mm and according to Fig. 8.3(b), d = 113 mm, while a_c is amongst other variables dependent on the number and the positions of the stud connectors. Since the number and positions of the studs

were the only geometric variables which changed in these six tests, only this dependence can be studied.

For the test specimens considered, F_{st} is defined as ΣF_{st}^i, where F_{st}^i are the tensile forces in the studs in row T in Fig. 8.7, except for BM6, where F_{st}^i are all the tensile forces in rows T and M. Similarly, F_{sh} is defined as ΣF_{sh}^i, where F_{sh}^i are the tensile forces in the shank calculated from the measured strains in that shank and the average measured Young's modulus of the stud shanks.

If F_{st} is approximated by F_{sh}, which becomes a better approximation for higher load cycles, as explained in section 8.2.3, then a_c can be found by equation (8.14) for test specimens BM2, BM4 and BM7, by equation (8.15) for BM3 and BM5, and by equation (8.16) for BM6, where $l_h = 1.435$ m is the average value of the lever arm between the point where F_t is applied and the steel concrete slab interface.

$$F_t l_h = F_{st} a_c \tag{8.14}$$

$$F_t l_h = F_{st} a_c + \alpha F_{st} (a_c - s_t) \tag{8.15}$$

In these equations, s_t represents the transverse distance between longitudinal rows of studs and α is derived from equilibrium, assuming a linear stress distribution at the steel-concrete contact surface as shown in Fig. 8.7.

$$a_c = a_c^* - s_t \frac{\sum_{i=1}^{odd} F_{st}^i}{F_{st}} \tag{8.16}$$

$$F_t l_h = F_{st} a_c^* + \alpha F_{st} \left(a_c^* - s_t \left(1 + \frac{\sum_{i=1}^{odd} F_{st}^i}{F_{st}} \right) \right)$$

Equation (8.14) is applicable to test specimens BM2, BM4 and BM7, which have only two parallel rows of studs where the calculated value for a_c is smaller than the measured transverse distance s_t, between these rows, so that only one row of studs is in tension under F_t, as is shown in Fig. 8.7(a). Indeed, this linear model for the stress distribution of the concrete onto the steel flange corresponds fairly well with the initial diagonal crack patterns of these specimens, given in Figs. 7.18, 7.20 and 7.23. These patterns show that the diagonal crack reaches the slab soffit at a point between the web of the steel section and row C, as defined in Fig. 8.7. Also, under increasing load, no second diagonal crack is formed, but the existing diagonal crack widens and propagates further along the top layer of

transverse reinforcement. These two observations indicate that the studs of row C are not in tension and that the resultant reaction force of the steel flange onto the concrete slab is therefore applied between row C and the web of the steel section.

Equation (8.15) is applicable to test specimens BM3 and BM5 which also have two parallel rows of studs, but where the calculated value of a_c is larger than the transverse distance s_t, between these rows, so that the studs in both rows T and C became in tension under F_t, as shown in Fig. 8.7(b). Again, a linear model is used for the stress distribution between the steel and concrete interface, which corresponds fairly well with the diagonal crack patterns of BM3 and BM5, given in Figs. 7.19 and 7.21. These patterns show that under increasing load a second parallel diagonal crack is formed, through the heads of the studs of row R, fairly soon after the first one has developed, without visibly widening. This explains the statement that both rows of studs were already in tension when the first diagonal crack formed.

The total forces in the studs of row T were of similar magnitude for tests BM3 and BM4, but crushing of the concrete slab under the steel flange occured at a much higher load for specimen BM4 than for specimen BM3. This difference in failure load can partly be explained by the linear stress distribution model for these test specimens as is shown in Fig. 8.7(b) and partly by the difference in concrete strength.

Equation (8.16) is applicable to test specimen BM6, which had three parallel rows of studs and where all studs became in tension under F_t as shown in Fig. 8.7(c). The shear force diagram corresponds with the position of the initial diagonal crack, as shown in Figs. 7.22 and 7.28, and goes through the heads of the studs of row M, as defined in Fig. 8.7(c). There would be little difference in the shear diagram if the studs of row C were in compression. As the total forces in the studs of rows T and M are found to be of a similar magnitude, they can be replaced by their resultant as indicated in Fig. 8.7(c). The lever arm a_c^*, found by equation (8.16) is larger than $s_t \left(1 + \sum_{i=1}^{odd} F_{st}^i / F_{st}\right)$, the distance between the resultant tensile stud force and row C. Also, under increasing load, three parallel cracks were formed and failure by crushing occured at a relatively low load. It can therefore be assumed that the studs in all rows were in tension. In reality the stress distribution at the interface is not uniform over the width of the specimen, neither is it linear in any transverse direction. The linear stress distribution model is therefore merely a tool used to construct equations (8.14), (8.15) and (8.16).

Using these equations, the values of a_c and a_c/b_f are registered in Table 8.7 for all test specimens, for values of F_t before and after the initial diagonal crack became visible, while the measured value of l_h varies between 1433 mm and 1437.5 mm, but is taken as 1435 mm for the calculations. For test specimen BM6, the estimated values of F_{st} before cracking are too low, so that the estimated resultant reaction force RF_{st}, would no longer be positioned on the flange, therefore the shear span a_c, is taken as 165 mm before cracking.

As there is an estimated error between 0 and -17% on F_{st} and as there is no accurate way of predicting the position of RF_{st} (the reaction force on the slab), it is pointless to try to determine a_c by different formulae at this stage, which all will overestimate a_c, as these calculated values of F_{st} are lower bounds to their real values anyway. It would therefore be accurate enough, and much simpler, to use an average value of a_c for all test specimens. It would also be useful if this value could be related to the geometry of the connection.

By assuming the top flange fixed over its total width and by assuming an effective section of the stiffener in accordance with the Bridge Code, the positions of the resultant tensile and compressive forces in the stiffener can be calculated theoretically. In doing so for our test specimen, one obtains a distance $a_s = 220$ mm between these resultants, as shown in Fig. 8.8.

This value compares with an average distance $a_{c,m} = 243$ mm obtained for the values of a_c before cracking as taken from Table 8.7. Since a_c in Table 8.7 is an upper bound and since one would only make an average error of 9% by replacing $a_{c,m}$ by a_s, this simplification in the application of the shear model to our test specimen outweighs the loss of accuracy.

8.5.2.2 Prediction of the initial diagonal cracking load

Under **initial diagonal cracking load $\mathbf{F_{t,cr}}$**, is understood the load level at which diagonal cracking first became visible at both sides of the tested specimen. Although this value is known not to define cracking very accurately, it is consistent with the definition of cracking used in obtaining the prediction equations for shear cracking in the previous section.

Use of the four different shear cracking equations (8.6), (8.8), (11.6) and (8.13) of section 8.5.1, together with the values of a_c just before cracking, as calculated in Table 8.7, enables us to obtain four different values for the theoretical shear force V_{cr}^{th}, at which the slabs of each test specimen start cracking. By applying equation (8.17) it is possible to estimate the corresponding theoretical total tensile

force F_{st}^{th}, in the studs of row T, taking also account of the shear force V_w, due to the dead weight of the structure.

$$F_{st}^{th} = \frac{\left(V_{cr}^{th} - V_w\right)}{\left(1 - \frac{a_c'}{l}\right)} \tag{8.17}$$

$$\begin{aligned}
\text{where } a_c' &= a_c \text{ when } a_c < s_t \\
\text{and } a_c' &= a_c + \alpha\left(a_c - s_t\right) \text{ when } a_c > s_t \\
\text{and } a_c' &= a_c^* + \alpha\left(a_c^* - \left(1 + \frac{\sum_{i=1}^{odd} F_{st}^i}{F_{st}}\right) s_t\right) \text{ when 3 rows of studs}
\end{aligned}$$

Knowing a_c and l_h, the corresponding value of $F_{t,cr}^{th}$ can be calculated for each value of V_{cr}^{th}.

Comparing the experimentally measured transverse forces with the above calculated ones, it was found that Zsutty's equation gives the best prediction, producing a maximal error of 10%, whereas Regan's equation produced a maximal error of 28%. In Table 8.8 the experimentally measured forces $F_{t,cr}^{exp}$ are compared to the calculated ones, $F_{t,cr}^{th}$, obtained from Zsutty's equation (8.8), using the value of a_c before cracking from Table 8.7.

The transverse forces $F_{t,c0}$, reported in Table 8.6, give the load level at which internal diagonal cracking started. These values can only be explained theoretically by assuming that for test specimens with more than two pairs of studs, the diagonal crack will form in two stages. At a first load level $F_{t,c0}$, the shear force must reach V_{cr}, over an identifiable width, b', which is ideally related to the longitudinal stud spacing, s_l, so that the crack forms over b'. At a second load level $F_{t,c1}$, this crack spreads to the sides over the whole width b of the specimen but is just not yet visible. The load level $F_{t,c1}$ marks the end of the linear elastic part in the $M_t - \theta_r$ curves and can only be read from these experimental curves, whereas $F_{t,cr}$ marks the first visible cracking at either side of the slab. Theoretical values of $F_{t,c0}$ can be obtained by assuming a value of b' equal to $2s_l$ and replacing b in equation (8.8) by b' for all tested specimens except BM2 and BM5. In Table 8.9 these values are compared to the measured values $F_{t,c0}$, and shown to be correct within 25%, which means that our assumption $b' \approx 2s_l$ is acceptable.

8.5.2.3 Prediction of the ultimate or failure load of the test specimen

Under **ultimate load $F_{t,u}$** is understood the maximum load these test specimens were able to hold.

Under **failure** is understood either crushing of the concrete underneath the top flange and propagation of the diagonal crack along the top layer of reinforcement or pulling out of the studs without propagation of the diagonal crack. Both these failure modes, for all test specimens, would occur on the falling branch of the load-displacement or load-rotation curve, therefore the ultimate load is, in effect, the failure load, as reaching $F_{t,u}$ and sustaining it by adding displacement to point T in Fig. 7.11 would in time cause failure.

A procedure similar to the one in section 8.5.2.2., was used to find the best theoretical prediction for the different ultimate loads, $F_{t,u}$. Amongst the three theoretical shear failure equations (8.7), (8.9) and (8.12), Bažant's equation gave the best correlation with the experimental results, producing a maximum error of only 12%, excluding test specimen BM2, which failed by pulling out of the studs and not by shear followed by concrete crushing.

All test specimens failed by crushing of the concrete underneath the steel flange due to large displacements of point T, except BM2 which failed by pulling out of the studs of row T in Fig. 7.18. All these specimens which had failed by crushing, showed wide diagonal cracks which had propagated along the top layer of reinforcement and continued to widen under increasing displacement of point T, except for specimen BM5, where the studs of row T in Fig. 7.21 pulled out while the diagonal crack closed up again. The reason for this discrepancy in behaviour between specimens BM2 and BM5 and the other four could be found by examining the empirical formulae for the pull out strength of these specimens.

According to McMackin *et al.* [47] the pull-out strength of the 19 × 125 mm studs used in the tests is determined by the shear strength of the conical surface of concrete being pulled out by these studs, which are considered to be partially embedded. They found that this 'shear cone' makes an angle of 45° with the horizontal and they derived an empirical expression for the strength, given by the equation (8.18).

$$F_{cu} = A_{co} f_{ce} \tag{8.18}$$

$$\begin{aligned} \text{with } A_{co} &= \pi (d_h + h_{sh})\, h_{sh} \sqrt{2} \\ \text{with } d_h &= \text{the diameter of the stud head} \\ h_{sh} &= \text{the height of the stud shank} \end{aligned}$$

and $f_{ce} = 0.297\sqrt{f_{cu}}$

This strength F_{cu}, can only be developed when the full shear cone is formed, which in turn depends on the boundary conditions i.e. on the distance to the sides of the specimen and the longitudinal spacing s_l, between studs. If these boundary conditions are not met and the full shear cone cannot be formed, then the reduced strength is given by equation (8.19).

$$RF_{cu} = (A_{c0} - A_{rc0})\, f_{ce} \tag{8.19}$$

with A_{c0} and f_{ce} as for eq. (8.18)

and A_{rc0} the area reduction of the cone as given in Ref.[111]

In a pamphlet of TRW Nelson Manufacturers [111] these reduced areas are tabulated as a function of the spacing and cube strength for different studs. If the studs are very closely spaced they act as a group and the pull out strength of the truncated pyramidal shear surface is smaller than the sum of the reduced strengths for the different studs. In Table 8.10 the values of F_{cu} and of the total strength for the different stud configurations embedded in concrete of different strength are given. The concrete strength and the stud configurations are those of the studs in tension in the different tested specimens. Therefore these values are not representative of the pull out forces needed in the tests, since part of the shear cone would fall in the area of concrete in compression. Yet, these values indicate that the strength of an equivalent pull out test on the stud configurations of tests BM2 and BM5, is only two thirds of the strength of an equivalent pull out test on the stud configurations of the other tests. This helps to explain why only the studs in row T of tests BM2 and BM5 pulled out.

According to Nielsen *et al.* [112] the head of the stud embedded in concrete will cause punching shear failure within the concrete. For 19 × 125 mm studs with d_h = 32 mm, the failure surface corresponding to the minimal failure load is given in Fig. 8.9 and the corresponding punching loads are given in the last line of Table 8.10 for the concrete strength of test specimens BM2 and BM5. Since such a failure surface can only be formed at one side of the studs in specimens BM2 and BM5 , the failure load would approximate the load needed to obtain two half punching failure surfaces and is therefore comparable with the total pull out strength. This shows that both pull out theory and punching shear theory obtain similar results.

8.6 Prediction of the elastic transverse flexibility of the connection

8.6.1 Calculation of the elastic transverse flexibility for all tested specimens

By comparing the different moment-rotation curves of the test specimens in Fig. 8.10, it can be seen that the slope M_t/θ_r, and therefore also the transverse flexibility, $f_r = \theta_r/M_t$, varies by more than a factor of 2 between test specimens BM7 and BM5. Even so, for each test specimen, the $M_t - \theta_r$ results can be modelled by a straight line until diagonal cracking first becomes visible.

For each set of results, equation (8.20) gives a least squares fit $f_{r,ls}$ for the transverse elastic flexibility. The straightness can be assessed by the value of the standard error of estimate s_θ, and the coefficient of determination r^2, both defined in [126].

$$\theta_r = f_{r,ls} M_t + \varepsilon \tag{8.20}$$

with ε negligible value indicating the displacement of the straight line from the origin

In Table 8.11 these values of s_θ and r^2 are calculated together with $f_{r,ls}$ for each series of test results. The latter is compared with the values of $f_{r,c1} = \theta_{r,c1}/\ M_{t,c1}$, just before cracking becomes visible, which are read from the experimental $M_t - \theta_r$ curves. These values of $f_{r,ls}$ are also compared with the values $f_{r,20}$, defining the flexibility when $F_t = 20\,\text{kN}$ and with the values $f_{r,m}$, defining the flexibility when $F_t = F_{t,c1}/2$.

The theoretical value of $f_{r,c1}$, as calculated in Appendix V, for a longitudinal stud spacing of 150 mm and a transverse spacing of 270 mm, underestimates the experimental value of $f_{r,c1}$, from test BM4 with similar stud configuration, by a factor of 7.

Replacing the theoretical flexibility of the connection by the experimental one, will change the proportions given in section 6.2.2 for the stiffened girder to:

$$\frac{\delta_1}{\delta_2} = 0.56; \quad \frac{\delta_3}{\delta_2} = 1.06; \quad \frac{\delta_3}{\delta_1} = 1.89$$

These new proportions show that the flange-slab connection provides the high-

est contribution to the total lateral deflection δ, calculated by equation (6.1). According to the current Bridge Code, this increase of δ will increase the effective length l_e, and the slenderness parameter, λ_{LT}, thereby reducing the design value for the hogging bending resistance of the beam above the internal support. In the worked out example of Appendix V, M_D would reduce by 13%.

For design purposes a lower bound to the hogging moment of resistance is relevant, which is obtained by taking an upper bound to the transverse flexibility of the connection and therefore using $f_{r,c1}$ instead of $f_{r,m}$ or $f_{r,ls}$. As the difference between $f_{r,c1}$ and $f_{r,m}$ is not greater than 33% for the tested connections, these values will not be too conservative for cases where M_t is only half $M_{t,c1}$.

Of course it has to be said that the present design rules are considered to be over conservative for inverted U-frames and it might be true that with a more accurate lateral distortional analysis the influence of the flexibility of the connection on the slenderness parameter would be much less. However that is not within the scope of this thesis.

8.6.2 Prediction of the transverse elastic flexibility of the connection using different models

Initially, the aim was to model the steel flange as a plate on elastic foundations and the embedded stud connectors as elastic springs, as shown in Fig. 8.11. Before solving this 3D-problem which would require many assumptions (on k_s, k_c, σ_c and a_c) it was decided to try to simplify it first to a 2D-model.

This was done by replacing the steel flange by an equivalent plate of width a_c, subject only to an upward force, F_{st}, at the position of the stiffener and held down by elastic springs as is shown in Fig. 8.12. From the knowledge of the tensile reaction forces in the different studs (F_{st}^i) and the corresponding moment distribution in the equivalent plate, the vertical displacement Δz_1, at the position of the stiffener could be found.

From the knowledge of the upward force F_{st} and the number of studs in tension, the average elastic elongation of these studs would give an average vertical displacement Δz_2. The global vertical displacement $\Delta z_t = \Delta z_1 + \Delta z_2$ at the position of the stiffener would cause a rotation $\Delta z_t / a_c$, which was within 25% of the measured relative rotations, and this for all tested specimens. Since for this model of plate on elastic supports the tensile reaction forces are only a function of $\alpha = (6 E_a I_{ep} k_s)/s_l$, with s_l = the longitudinal stud spacing, I_{ep} = the stiffness of the plate, and k_s = the elastic spring constant of the support [113], and since

there exists a relationship between α and s_t for the different test specimens, this model seemed to work. Unfortunately, this approach yielded values of α and therefore of k_s which were about 10 to 20 times smaller than the theoretical ones $((A_{sh}E_{sh})/h_{sh})$ and this approach also produced deformations of the plate which do not conform to the experimental evidence of test specimen BM1. Although the model produces correct values of θ_r for given values of $F_{t,c1}$, the equivalent length (a_c), the equivalent plate stiffness (I_{ep}) and the spring constant of the embedded studs (k_s) are all three unknown. Several values can be fitted which will predict the results.

There was a similar problem of too many unknown parameters and too few test results when a 3D-Finite Element analysis was performed with the commercial package FLASH at the Free University of Brussels. This time a value of k_s only 2.5 times smaller than $((A_{sh}E_{sh})/h_{sh})$ was chosen. This proportion was obtained from only a few load-displacement curves of pull out tests on anchor studs $(h_{sh}/d_{sh} > 8)$, done by Nelson [111]. The value a_c was chosen as in Table 8.7 and the spring constant k_c is a function of the contact surface corresponding to the different nodes, as indicated in Fig. 8.13. This figure represents also the chosen grid and the external applied forces. In this analysis a linear stress-strain relationship was assumed for concrete. Since the measurements with the dial gauges at D_4 and D_5 are fairly inaccurate (local deformation of concrete surface due to cracking), only θ_r is known for each load stage, and again different combinations of k_s, k_c, σ_c and a_c can be found to reproduce that result.

8.6.3 Prediction of the transverse flexibility – analogy with the prediction of the M – θ relationship for steel beam-column connections

Since there are too few experimental data available to build up a mechanical model or a Finite Element model, only indications regarding the relationship between s_l and s_t with f_r can be given from this research.

In Fig. 8.14 the flexibilities of all tested specimens at two different load levels are shown, as functions of their longitudinal spacing (s_l) and their shortest distance to the symmetrical vertical stiffener (a_{st}). Since the studs are arranged symmetrically around the vertical stiffener for all tested specimens, both parameters s_l and a_{st} are interchangeable for our tests. It is obvious that a symmetrical configuration leads to the highest flexibility for any particular longitudinal spacing. In other words, if a stud were placed underneath the stiffener, as in Fig.

8.15, although the configuration and longitudinal spacing are the same, the corresponding flexibility would be smaller. Therefore, a_{st} is a more useful parameter than s_l. For test specimens BM2, BM3 and BM5 the values of $M_{t,c1}$ are slightly lower than the values in the graph on Fig. 8.14, therefore a linear extrapolated value of θ_r is used to calculate the corresponding value of f_r. This figure shows that f_r increases with s_l for both load levels and both configurations with different transverse stud spacing. This figure also demonstrates that the amount of increase is nearly independent of the load level. The flexibility increases between 1.7 and 1.4 times when s_l increases from 150 to 300 mm, between 1.9 and 1.6 times when s_l increases from 100 to 150 mm and between 3.1 and 2.2 times when s_l increases from 100 to 300 mm.

In Fig. 8.16 the flexibilities of test specimens BM2, BM3, BM4 and BM5 are shown at the same two load levels as functions of their transverse spacing (s_t) and the shortest distance between the studs and the web (a_w). This figure shows that the transverse spacing has little influence on the flexibility of the connection when the longitudinal spacing and the flange width remain constant. Yet, for both configurations of longitudinal spacing and both load levels, the flexibility tends to decrease with increasing value of s_t, although the flexibility only decreases between 0.92 and 0.87 times when s_t increases from 150 to 270 mm.

The behaviour of the connection with regards to the relationship between s_l and s_t and f_r is similar to the behaviour of a bolted flush end plate steel beam-column connection with regards to the relationship between g and d_b and f_r, as indicated in Fig. 8.17. On this basis, an analogy can be drawn between the flush end plate connection and the steel-concrete connection at the position of the vertical stiffener, with regards to the parameters which influence the flexibilities of these connections.

Since there is no other experimental evidence available on the flexibility of the steel beam-concrete slab connection under transverse load and since there has been a lot of research done [114] on the bolted flush end plate connection, this analogy is extremely useful. It enables one to obtain some indication of how different parameters like stud size, flange width, flange thickness ... change the flexibility, simply by studying the corresponding parameters in the bolted flush end plate connection.

This analogy would be more useful if information were available on steel beam-concrete column connections like the ones presented in Fig. 8.18. Unfortunately, only two papers were found on this subject [115], [116] and both are related to the strength of this connection rather than to its $M_t - \theta_r$ relationship. Therefore, the

results on the bolted flush end plate connections are the most relevant amongst existing researched connections to our tests.

In recent years, different methods have been used to predict the $M - \theta$ relationships of these semi-rigid flush end plate connections. Amongst the most commonly used are:

(i) the purely empirical methods.

These involve the choice of a mathematical expression: either a polynomial (Frye and Morris [117], Sommer [118] and Kennedy [119]), a B-spline (Jones, *et al.* [120]) or an exponential (Chen [121]) all of which represent the rotation as a function of the moment via several constants. These constants are obtained by least squares curve fitting on the available data. Although with these empirical methods virtually any shape of $M - \theta$ curve can be fitted, they cannot be applied outside the range of calibration data [122].

(ii) the simplified analytical methods

These involve close observation of the test behaviour to identify the major source of deformation of the connection. Having found the key components of the connection, the shape of the $M - \theta$ curve can be determined as a function of characteristic values obtained from a simplified analysis of their behaviour. This curve still requires empirical curve fitting and is therefore again a function of the calibration data.

(iii) the mechanical methods.

These involve the identification of different components as rigid and deformable 'elemental parts' of the connection. Provided the experimental load-deformation curves of these 'parts' are known, as well as the way in which they interact with each other, a mechanical model can be built. At present, such models are only available for connections with simple physical behaviour.

(iv) the Finite Element methods.

In principle the most suitable tool available for conducting extensive parametric studies. Yet, the level of refinement is not yet attained to model unilateral contact between two surfaces or bolt action. Experimental data are therefore still used in determining the stress distribution over the contact surface or the load-deformation relationship of the bolts. Also, developing a prediction equation using these numerical data would still only be valid within the calibration data [123].

Regardless of what some researchers claim, Benterkia [124] found that all these methods provide models based on several experimental results which are only valid within the range of the calibration data. This makes it clear why it is pointless trying to find any model with only the six results available here.

As far as the analogy between the flexibility of the flush end plate and the stiffened steel – concrete connection at the position of the vertical stiffener is concerned, Table 8.12 gives the way in which the main parameters affect the increment of flexibility for both these types of connections, as shown in Figs. 8.17 and 8.19 respectively. These parameters are:

t_p, t_f: the flush end plate thickness and the corresponding top flange thickness

d_b, b_f: the depth of the beam; the corresponding width of the top flange

g, s_l: the distance between the bolts and the web of the beam; the corresponding longitudinal spacing between studs

d_t, s_t: the vertical distance between the rows of bolts; the corresponding transverse spacing between studs

ϕ_b, h_{st}: the diameter of the bolts; the height of the embedded stud connector

8.7 Scope of the test results: behaviour of a real bridge girder

8.7.1 Validity of $F_{t,c0}$, $F_{t,c1}$ and $F_{t,u}$ for a real structure

Although it is clear from the test results, that after diagonal cracking commenced in the area of the two studs nearest to the web stiffener, the test specimen still sustained their load and the loading path after cracking could be regained after reloading, it can be argued that under repeated loading, this initial reduction of stiffness could be accelerated. To treat this initial crack as 'failure' would be rather onerous, as the flexibility hardly changes, which is both visible from the moment – rotation relationships for the different connections, as well as from the comparison between the values $f_{r,m}$ and $f_{r,c1}$ in Table 8.11. More research is obviously needed to determine whether this initial shear crack could deteriorate the connection.

In absence of this research, the behaviour of the tested connections under statically increasing loads shows that the flexibility remained quasi constant until

the diagonal shear crack reached the sides of the test specimen at load $F_{t,c1}$. Only at this point do the measured moment-rotation curves no longer represent the behaviour of the connection in an inverted U-frame of a real bridge girder.

In a real structure, the rest of the girder and slab would resist the widening of the diagonal crack and the propagation in the transverse direction, although the crack might propagate longitudinally under loads higher than $F_{t,c1}$ or under repeated loading. Therefore neither $F_{t,c1}$ nor $F_{t,u}$ have any physical meaning in a real structure, although $F_{t,u}$ could probably be regarded as a lower bound to the real failure load, causing the concrete to crush under the top flange or the studs to pull out. A comparison between these measured values of $F_{t,u}$ and the calculated value of 23.9 kN for the ultimate applied transverse force F_t from the worked out example of Appendix V — which is known to be very conservative, shows that most measured values are by more than 30% higher than this calculated value, except for specimen BM2. Yet, large longitudinal spacings ($s_l > 300$ mm) between pairs of studs are excluded from the scope of these investigations, whereby the premature failure load of BM2 can be disregarded, since in real bridge structures such spacings would seldom occur.

Although forces higher than $F_{t,u}$ will cause visible failure of a real structure, lower transverse forces might cause excessive rotation of the connection due to the propagation of the diagonal shear crack and therefore the connection might no longer provide sufficient restraint against buckling of the bottom flange. Further research is obviously needed to examine the flexibility and the crack propagation for wider specimens.

8.7.2 Scope of the flexibility of the connection

Although no model can be presented to predict the flexibility as a function of the geometrical and mechanical properties of the connection, the flexibilities corresponding to the applied moments $M_{t,c1}$ in test specimens BM5 and BM3 are close to an upper bound for bridge girders with similar longitudinal spacings between studs. This deduction can be made by studying the variables which affect the value of f_r. Both the width (b_f) and the thickness (t_f) of the top flange are near the bottom value in the range of values used for bridge girders with spans larger than 20 m. Also, studs smaller than 19 × 125 mm (h_{st}) are not commonly used for these types of bridges.

Using the analogy between the flexibility of flush end plate connection and the steel concrete connection as in Fig. 8.19, Table 8.12 shows that the choice of

the three variables b_f, t_f and h_{st} in the test specimen generates a large flexibility of the connection, since the chosen values of b_f and t_f produce a top flange with a low torsional stiffness, which in turn enhances a rapidly diminishing tensile force distribution in the studs placed further away from the stiffener.

In order to obtain an indicative and safe value for the flexibility of a connection with a symmetrical stiffener, an expression is constructed for the flexibility near cracking, which forms an upper bound to the elastic values of f_r. Using the average values of $f_{r,c1}$ from Table 8.11 for s_l = 300 mm and s_l = 150 mm, equation (8.21) is obtained as a safe estimate for the flexibility.

$$f_r = 0.26\, s_l + 0.052\ mrad/kNm \tag{8.21}$$

with s_l in m, and f_r in mrad/kNm

8.7.3 Global behaviour of the connection in a real bridge

In sections 8.3 and 8.5.2.2 it has been suggested that under increasing transverse load F_t, the diagonal crack in the slab first forms in the middle around the symmetrical stiffener over a width $b' \simeq 2s_l$ at a load level $F_{t,c0}$ and later spreads to the sides which happen to be a width of $b \simeq 4s_l$ for specimens BM4, BM3 and BM6. The corresponding $M_t - \theta_r$ curves for these test specimens are bilinear up to $M_{t,c1}$ and the slope changes only slightly at the load level $F_{t,c0}$.

This would indicate that under increasing load F_t, the inner studs resist most of the upward force and their load deflection curve is linear in that region, until the shear crack conditions are met in the concrete surrounding these studs and a crack forms over a width $\approx 2s_l$. It could be assumed that at this point, load sheds onto the stud connectors further away from the stiffener and that under still increasing F_t these studs resist more load until the shear cracking conditions are met in the concrete surrounding them and the diagonal crack propagates and stretches over a width $\approx 4s_l$. This process is represented qualitatively in Fig. 8.20 where both the stud configuration on the top flange and the corresponding moment-rotation curve are given for a bridge girder. In this figure the moment-rotation curve is represented by a multilinear curve where the slope (β_1, β_2, β_3, ...) remains constant in between crack propagations at different load levels (M_c^1, M_c^2, M_c^3, ...) over different widths (b_1, b_2, b_3, ...). Only by changing the torsional stiffness of the top flange and the embedement of the connectors can the tensile forces in the studs be shared more equally closer to the stiffener, whereby the initial flexibility of the connection will reduce.

Table 8.1: Absolute (AER) and percent relative (PER) error for the values of F_t.

F_t (kN)	ΔF_t^{cal} (kN)	ΔF_t^{res} (kN)	ΔF_t^{rep} (kN)	ΔF_t^{tot} (kN)	$\frac{\Delta F_t^{tot} \times 100}{\Delta F_t^{tot}}$ (%)
4	0.08	0.125	0.008	0.21	5.3
8	0.16	0.125	0.016	0.30	3.8
12	0.12	0.125	0.024	0.27	2.3
16	0.16	0.125	0.032	0.32	2.0
20	0.20	0.125	0.040	0.37	2.0
24	0.24	0.125	0.048	0.41	1.7
28	0.28	0.125	0.056	0.46	1.5
32	0.32	0.125	0.064	0.51	1.5
36	0.36	0.125	0.072	0.56	1.5

Table 8.2: Derivatives of main parameters to F_t for BM3.

F_t (kN)	$\frac{\Delta\bar{\varepsilon}^{2,3}_{gh}}{\Delta F_t}$ $\left(\frac{\times 10^{-6}}{kN}\right)$	$\frac{\Delta\bar{\varepsilon}^{1,4}_{gh}}{\Delta F_t}$ $\left(\frac{\times 10^{-6}}{kN}\right)$	$\frac{\Delta\theta^i_c}{\Delta F_t}$ $\left(\frac{mrad}{kN}\right)$	$\frac{\Delta\theta^i_g}{\Delta F_t}$ $\left(\frac{mrad}{kN}\right)$	$\frac{\Delta y_T}{\Delta F_t}$ $\left(\frac{mm}{kN}\right)$	COMMENT
0						
	14.5	1.6	0.028	0.093	0.44	
2.5						
	26.7	19.7	0.036	0.116	0.52	
5.0						
	6.2	29.7	0.052	0.130	0.59	
7.5						
	12.7	18.5	0.018	0.130	0.73	sudden change
10.0						$F_t = F_{t,c0} = 10kN$
	26.1	20.3	0.049	0.161	0.63	
12.5						
	34.5	22.7	0.050	0.171	0.67	
15.0						
	39.9	26.7	0.054	0.206	0.59	
16.5						
	27.7	21.5	0.053	0.256	0.71	
18.0						
	31.3	24.4	0.143	0.371	0.84	sudden change
19.5						$F_t = F_{t,c1} = 19.6kN$
	40.0	37.5	0.118	0.217	0.75	
20.5						
	−40.0	57.5	0.566	3.367	2.79	
21.5						

Table 8.3: Derivatives of main parameters to F_t for BM4.

F_t (kN)	$\frac{\Delta\bar{\varepsilon}_{sh}^{2,3}}{\Delta F_t}$ $\left(\frac{\times 10^{-6}}{kN}\right)$	$\frac{\Delta\bar{\varepsilon}_{sh}^{1,4}}{\Delta F_t}$ $\left(\frac{\times 10^{-6}}{kN}\right)$	$\frac{\Delta\theta_c^i}{\Delta F_t}$ $\left(\frac{mrad}{kN}\right)$	$\frac{\Delta\theta_g^i}{\Delta F_t}$ $\left(\frac{mrad}{kN}\right)$	$\frac{\Delta y_T}{\Delta F_t}$ $\left(\frac{mm}{kN}\right)$	COMMENT
0						
	17.2	1.1	0.029	0.122	0.48	
2						
	37.9	2.2	0.042	0.108	0.49	
4						
	33.5	−2.2	0.047	0.122	0.44	
6						
	43.6	−1.3	0.037	0.111	0.53	
8						
	19.4	9.0	0.025	0.155	0.52	sudden change
10						$F_t = F_{t,c0} = 9.5kN$
	26.8	16.1	0.048	0.206	0.59	
12						
	34.7	19.3	0.085	0.206	0.61	
14						
	51.8	36.3	0.118	0.285	0.82	
16						
	43.9	27.1	0.067	0.224	0.61	
18						
	54.7	13.1	0.099	0.267	0.79	
20						
	55.6	15.9	0.113	0.312	0.89	
22						
	32.8	20.4	0.154	0.316	0.83	
24						
	40.1	232.1	0.685	2.078	3.40	sudden change
26						$F_t = F_{t,c1} = 23.5kN$
	−41.5	−66.3	−0.565	−1.40	−1.93	
28						

Table 8.4: Derivatives of main parameters to F_t for BM6.

F_t (kN)	$\frac{\Delta\bar{\varepsilon}_{4,6}}{\Delta F_t}$ $\left(\frac{\times 10^{-6}}{kN}\right)$	$\frac{\Delta\bar{\varepsilon}_{1,7}}{\Delta F_t}$ $\left(\frac{\times 10^{-6}}{kN}\right)$	$\frac{\Delta\theta_c^i}{\Delta F_t}$ $\left(\frac{mrad}{kN}\right)$	$\frac{\Delta\theta_s^i}{\Delta F_t}$ $\left(\frac{mrad}{kN}\right)$	$\frac{\Delta y_T}{\Delta F_t}$ $\left(\frac{mm}{kN}\right)$	COMMENT
0						
	0.00	−2.50	0.060	0.100	0.45	
2						
	5.00	1.25	0.047	0.108	0.48	
4						
	4.85	1.21	0.048	0.129	0.50	
6						
	6.45	0.00	0.065	0.130	0.54	
8						
	10.0	0.00	0.059	0.141	0.72	
10						
	13.8	5.00	0.073	0.175	0.58	sudden change
12						$F_t = F_{t,c0} = 11kN$
	17.4	12.0	0.100	0.223	0.68	
14						
	24.7	14.1	0.124	0.235	0.70	
16						
	17.5	11.3	0.132	0.283	0.71	
18						
	11.3	15.4	0.151	0.350	0.97	
20						
	−10.0	65.0	0.534	0.900	1.08	sudden change
22						$F_t = F_{t,c1} = 19.75kN$

Table 8.5: Derivatives of main parameters to F_t for BM7.

F_t (kN)	$\frac{\Delta\bar{\varepsilon}_{3,4}}{\Delta F_t}$ $\left(\frac{\times 10^{-6}}{kN}\right)$	$\frac{\Delta\bar{\varepsilon}_{2,5}}{\Delta F_t}$ $\left(\frac{\times 10^{-6}}{kN}\right)$	$\frac{\Delta\theta_c^i}{\Delta F_t}$ $\left(\frac{mrad}{kN}\right)$	$\frac{\Delta\theta_d^i}{\Delta F_t}$ $\left(\frac{mrad}{kN}\right)$	$\frac{\Delta y_T}{\Delta F_t}$ $\left(\frac{mm}{kN}\right)$	COMMENT
0						
	8.75	0.00	0.059	0.092	0.47	
2						
	12.5	1.25	0.049	0.100	0.47	
4						
	21.3	2.50	0.057	0.108	0.52	
6						
	16.3	2.50	0.049	0.100	0.52	
8						
	10.0	15.0	0.055	0.183	0.56	sudden change
10						$F_t = F_{t,c0} = 9kN$
	20.0	23.8	0.057	0.142	0.63	
12						
	31.3	27.5	0.092	0.167	0.65	
14						
	38.8	1.25	0.069	0.167	0.62	
16						
	50.0	0.00	0.085	0.192	0.68	
18						
	61.3	1.25	0.128	0.233	0.72	
20						
	45.0	5.00	0.120	0.242	0.77	
22						
	45.0	22.5	0.184	0.300	0.81	
24						
	47.5	62.5	0.212	2.10	4.18	sudden change
26						$F_t = F_{t,c1} = 24kN$

Table 8.6: Cracking and failure loads of the different test specimens.

		Test specimens					
		BM2	*BM3*	*BM4*	*BM5*	*BM6*	*BM7*
Curve type corresponding with Fig. 8.2		*I*	*III*	*III*	*II*	*III*	*III*
$F_{t,c0}$	(kN)	–	10.0	9.5	–	11.0	9.0
$F_{t,c1}$	(kN)	19.75	19.60	23.50	23.50	19.75	24.00
$F_{t,c2}$	(kN)	–	24.13	28.00	28.13	27.00	29.00
$F_{t,u}$	(kN)	24.71	33.38	37.50	33.00	33.00	36.00[a]
$F_{t,u}/F_{t,c1}$		1.23	1.70	1.59	1.42	1.67	1.50[a]

[a] After repositioning of the test specimen, it was not loaded to complete failure.

Table 8.7: Lever arm between resultant tensile force in the studs F_{st}, and resultant compressive reaction of the slab RF_{st}.

Test Specimen	Load cycle & Load level before (b) & after (a) cracking	F_t^{ave} (kN)	F_{st} (kN)	a_c (mm)	$\frac{a_c}{b_f}$
$BM2$	$I-b$	19.76	108.8	261	0.79
	$II-b$	19.92	104.4	274	0.83
	$II-a$	20.69	120.8	246	0.74
	$II-a$	19.61	115.5	244	0.74
$BM3$	$IV-b$	19.58	107.2	234	0.71
	$IV-b$	20.61	113.2	234	0.71
	$IV-a$	20.63	116.7	211	0.64
	$IV-a$	21.28	115.5	227	0.69
$BM4$	$II-b$	21.72	127.1	245	0.74
	$II-b$	23.56	143.7	235	0.71
	$II-a$	24.31	159.5	219	0.66
	$III-a$	25.36	165.6	220	0.67
$BM5$	$III-b$	23.74	142.4	224	0.68
	$III-b$	24.27	148.0	222	0.67
	$III-a$	26.74	174.4	215	0.65
	$III-a$	25.31	170.6	211	0.64
$BM6$	$III-b$	17.93	98.0	165	0.50
	$III-b$	19.78	111.0	165	0.50
	$III-a$	19.44	118.6	158	0.48
	$III-a$	21.53	129.1	157	0.47
$BM7$	$II-b$	21.94	113.9	276	0.84
	$II-b$	23.75	136.1	250	0.76
	$II-a$	24.50	168.1	209	0.63
	$II-a$	26.56	189.7	201	0.61

Table 8.8: Prediction of applied transverse diagonal cracking load, using Zsutty's [108] shear cracking eq.(8.8), and of the ultimate load, using Bažant's eq.(8.11).

Test specimen	a_c (mm)	$\frac{a_c}{d}$ $(-)$	V_{cr}^{th} (kN)	$F_{t,cr}^{th}$ (kN)	$F_{t,cr}^{exp}$ (kN)	$\frac{F_{t,cr}^{exp}-F_{t,cr}^{th}}{F_{t,cr}^{exp}} \times 100$ (%)	a_c (mm)	V_u^{th} (kN)	$F_{t,u}^{th}$ (kN)	$F_{t,u}^{exp}$ (kN)	$\frac{F_{t,u}^{exp}-F_{t,u}^{th}}{F_{t,u}^{exp}} \times 100$ (%)
$BM2$	261	1.56	122.4	24.65	24.00	−3	245	168.6	31.69	24.71[1]	−28
$BM3$	234	1.40	121.6	24.59	22.75	−8	211	208.9	33.63	33.38	−7
$BM4$	240	1.44	127.2	23.46	26.00	10	220	197.7	33.04	37.50	+12
$BM5$	223	1.34	136.1	25.05	25.50	2	213	215.9	35.54	33.00	−8
$BM6$	165	0.98	103.4	20.39	21.06	3	158	*n.a.*	*n.a.*	33.00	*n.a*
$BM7$	263	1.58	127.2	25.95	26.00	0.2	205	228.6	35.39	36.00	2

[1] pull-out failure precedes shear failure

Table 8.9: Prediction of applied load at initial internal diagonal cracking, using Zsutty's [108] shear cracking eq.(8.8).

Test specimen	a_c (mm)	b' (mm)	V_{c0}^{th} (kN)	$F_{t,c0}^{th}$ (kN)	$F_{t,c0}^{exp}$ (kN)
$BM3$	234	300	60.8	12.3	10.0
$BM4$	240	300	63.6	11.7	9.5
$BM6$	165	300	51.7	10.2	11.0
$BM7$	263	200	42.4	8.57	9.0

Table 8.10: Theoretical Pull-out strength of the groups of studs in tension in the different test specimens.

		Test specimen					
		$BM2$	$BM3$	$BM4$	$BM5$	$BM6$	$BM7$
f_{cu}	(N/mm^2)	43.11	37.81	41.44	50.83	16.24	48.93
spacing*	(mm)	181	189	181	181	267	181
F_{cu}*	(kN)	111	104	109	120	68	118
RF_{cu}*	(kN)	221	322	337	240	320	386
F_{cu}**	(kN)	172	–	–	176	–	–

* See [111]
** See [112]

Table 8.11: Different values for the transverse flexibility of all tested specimen, within the elastic range.

Test specimen	N	r^2	s_θ	f_{rls}	f_{r20}	f_{rc1}	f_{rm}	$\frac{f_{rc1}-f_{rm}}{f_{rc1}} \times 100$
	$(-)$	$(-)$	$(mrad)$	$(mrad/kNm)$	$(mrad/kNm)$	$(mrad/kNm)$	$(mrad/kNm)$	$(\%)$
$BM2$	4	0.976	0.153	0.1124	0.1220	0.1234	0.1095	11
$BM3$	8	0.942	0.196	0.0773	0.0941	0.0945	0.0713	25
$BM4$	11	0.947	0.207	0.0773	0.0850	0.0909	0.0664	27
$BM5$	11	0.992	0.116	0.1270	0.1286	0.1396	0.1220	13
$BM6$	9	0.943	0.132	0.0547	0.0697	0.0669	0.0444	33
$BM7$	11	0.949	0.142	0.0516	0.0547	0.0613	0.0475	23

Table 8.12: Correlation between parameters effecting the flexibility in a flush-end plate connection and in the steel beam – concrete slab connection.

	$f_r \uparrow$				
Fig 8.17	$t_p \downarrow$	$d_b \downarrow$	$g \uparrow$	$d_t \downarrow$	$\phi_b \downarrow$
Fig 8.19	$t_f \downarrow$	$b_f \downarrow$	$s_l \uparrow$	$s_t \downarrow$	$h_{st} \downarrow$

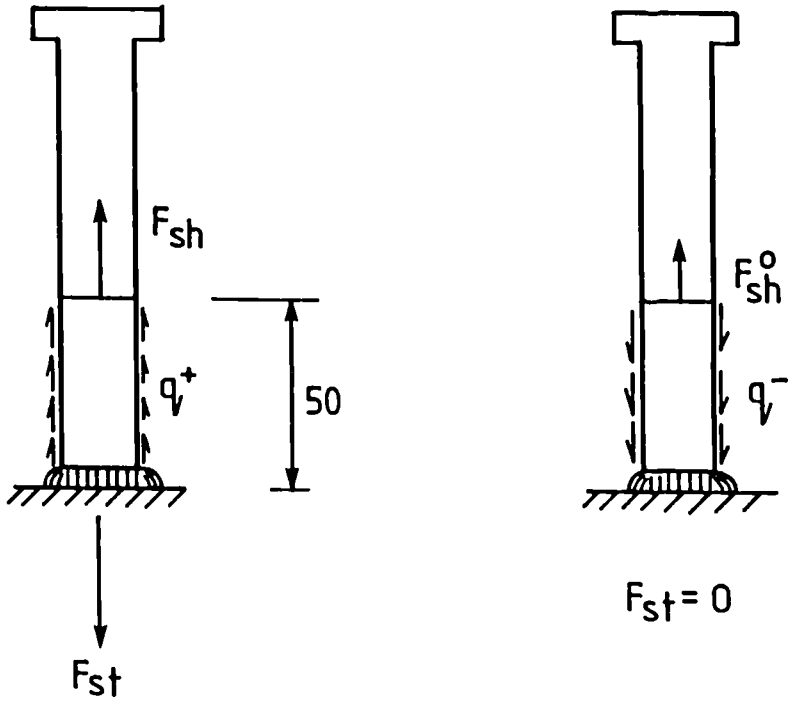

Figure 8.1: The difference between the applied forces to the studs F_{st}, and the calculated forces F_{sh} from the strain measurements in the shanks of the studs.

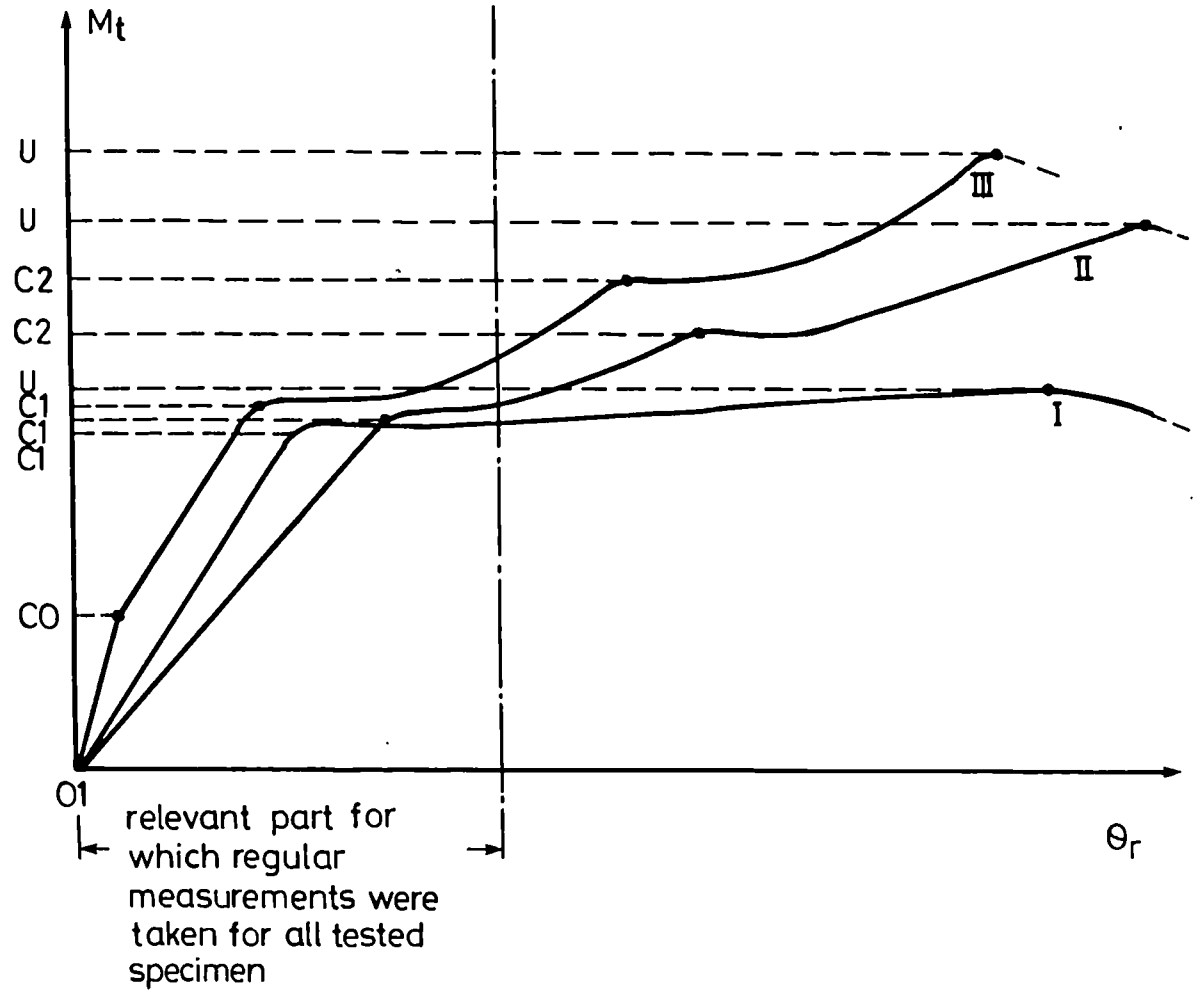

Figure 8.2: Three qualitative curves representing the relationship between the transverse moment and the relative rotation of the connection.

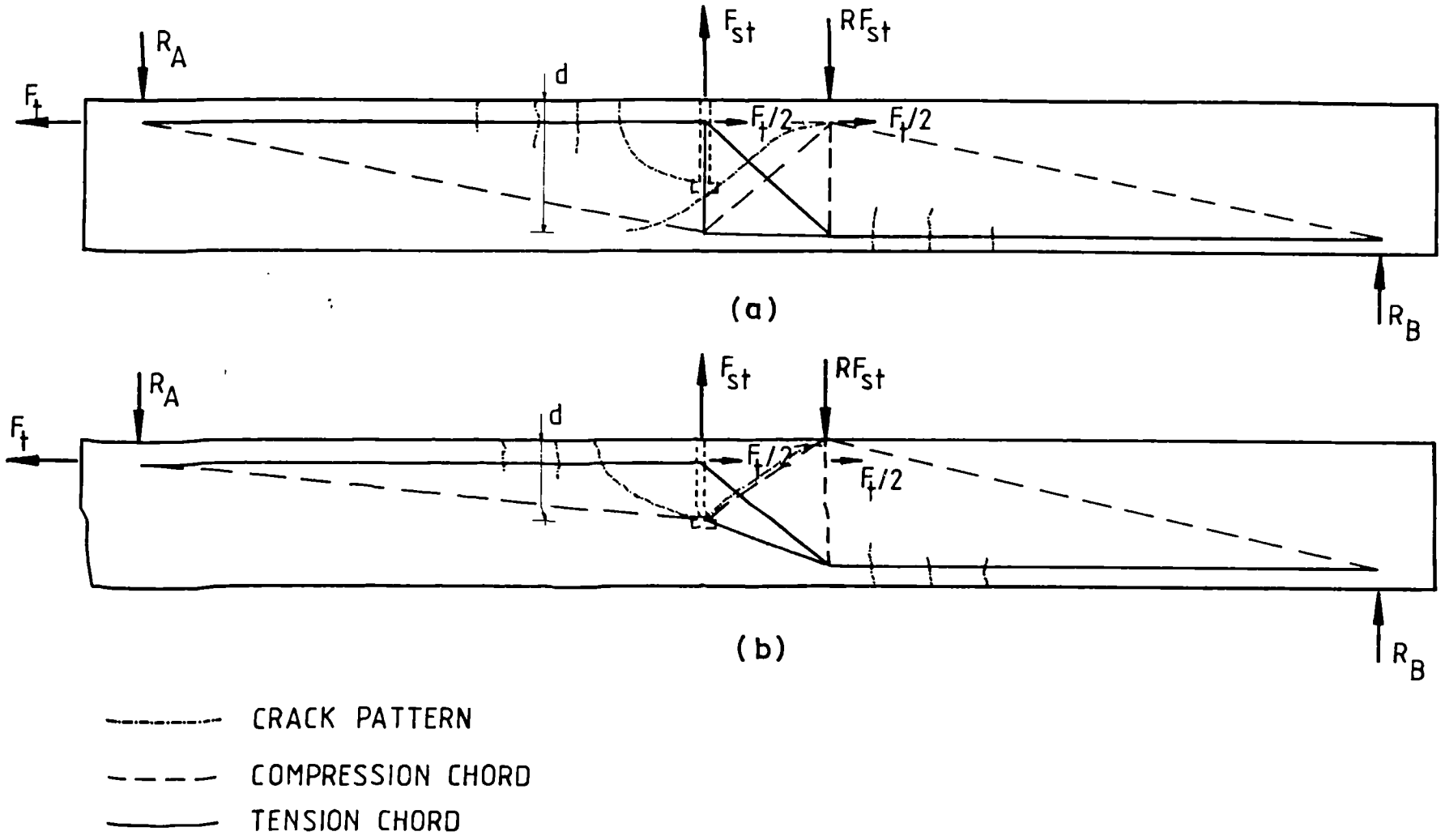

Figure 8.3: Truss analogy of the internal force distribution within the test specimens under a transverse force and moment.

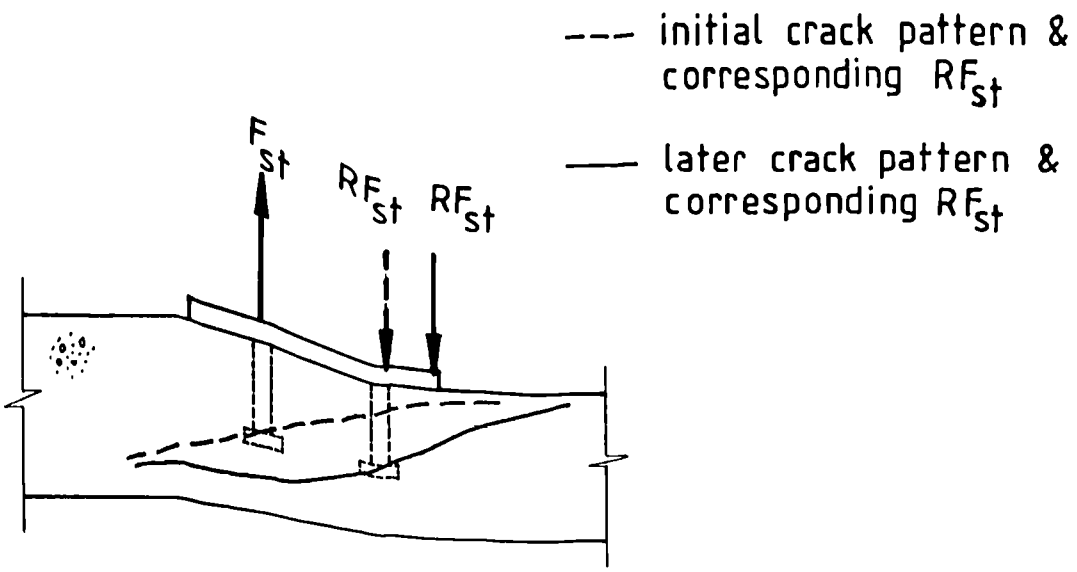

Figure 8.4: The action (F_{st}) and reaction (RF_{st}) forces on the connection, due to the transverse force F_t.

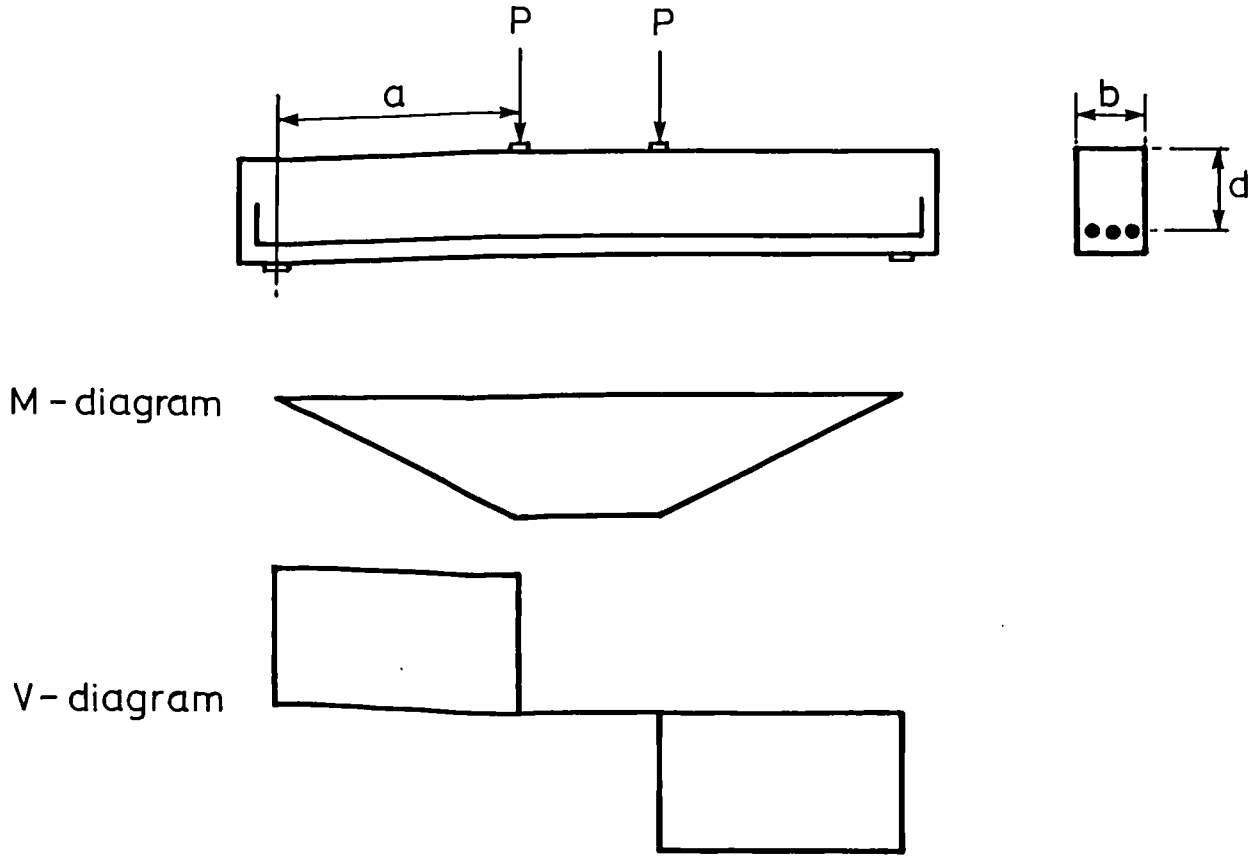

Figure 8.5: Moment and shear force distributions in the concrete slabs, tested for their shear resistance.

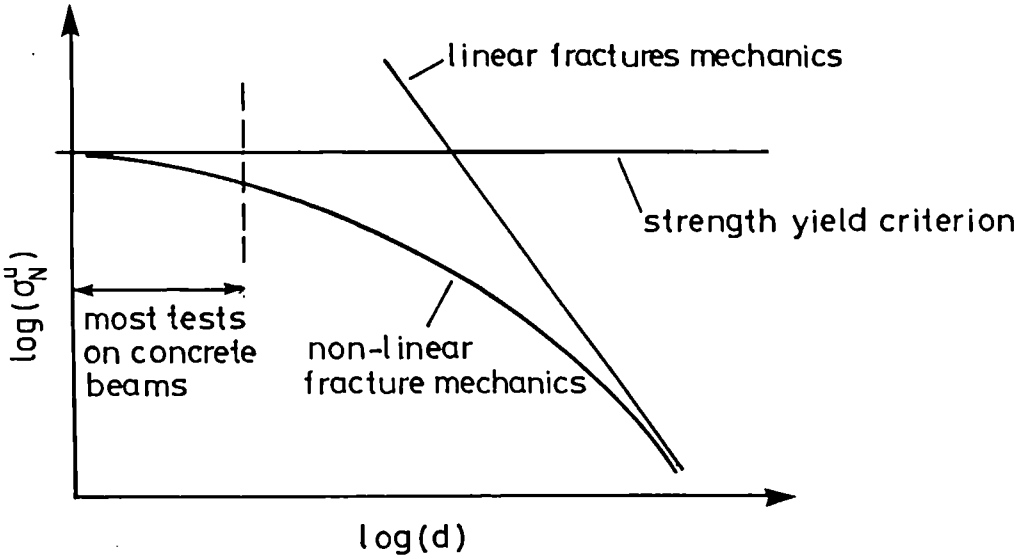

Figure 8.6: Size effect on the nominal shear strength of concrete at failure, as presented in Ref. [99].

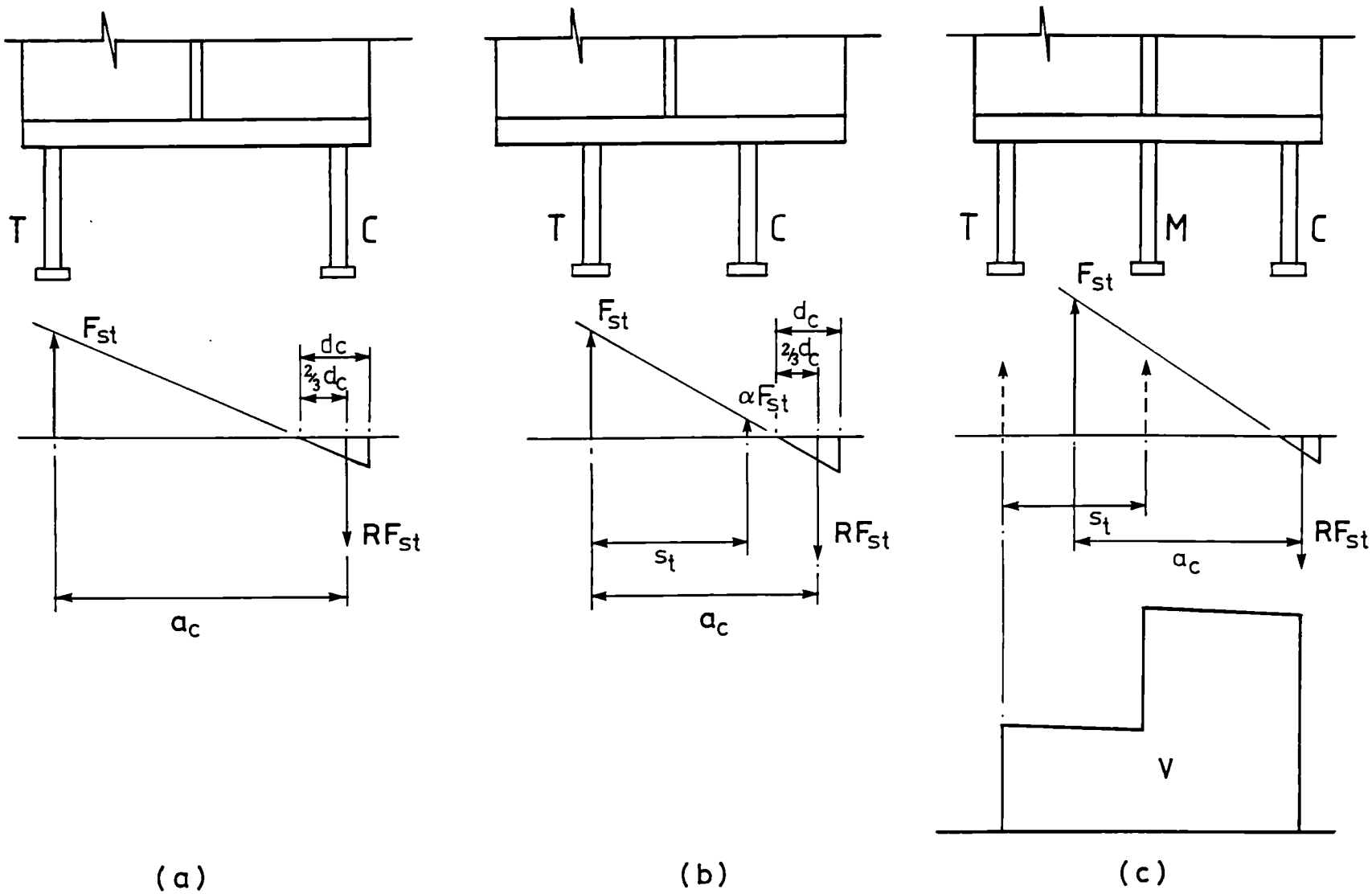

Figure 8.7: Different transverse spacings of the studs, and corresponding stress distributions over the steel-concrete interface.

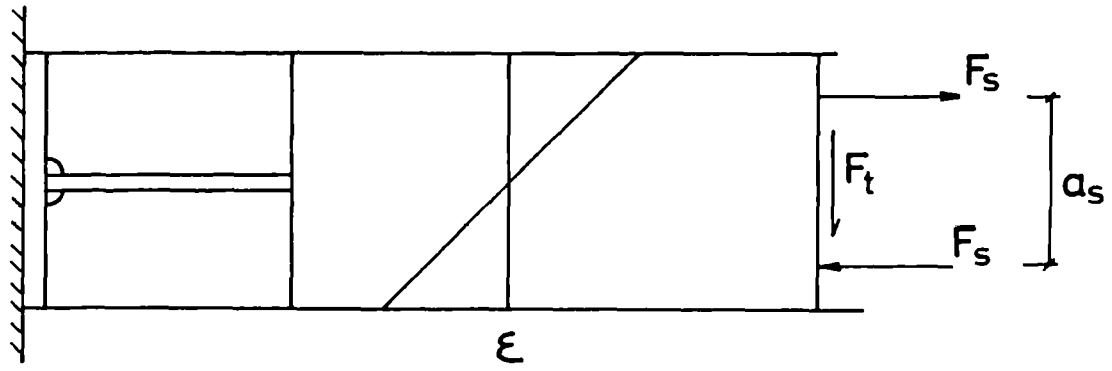

Figure 8.8: Lever arm between the resultant forces in the effective stiffener.

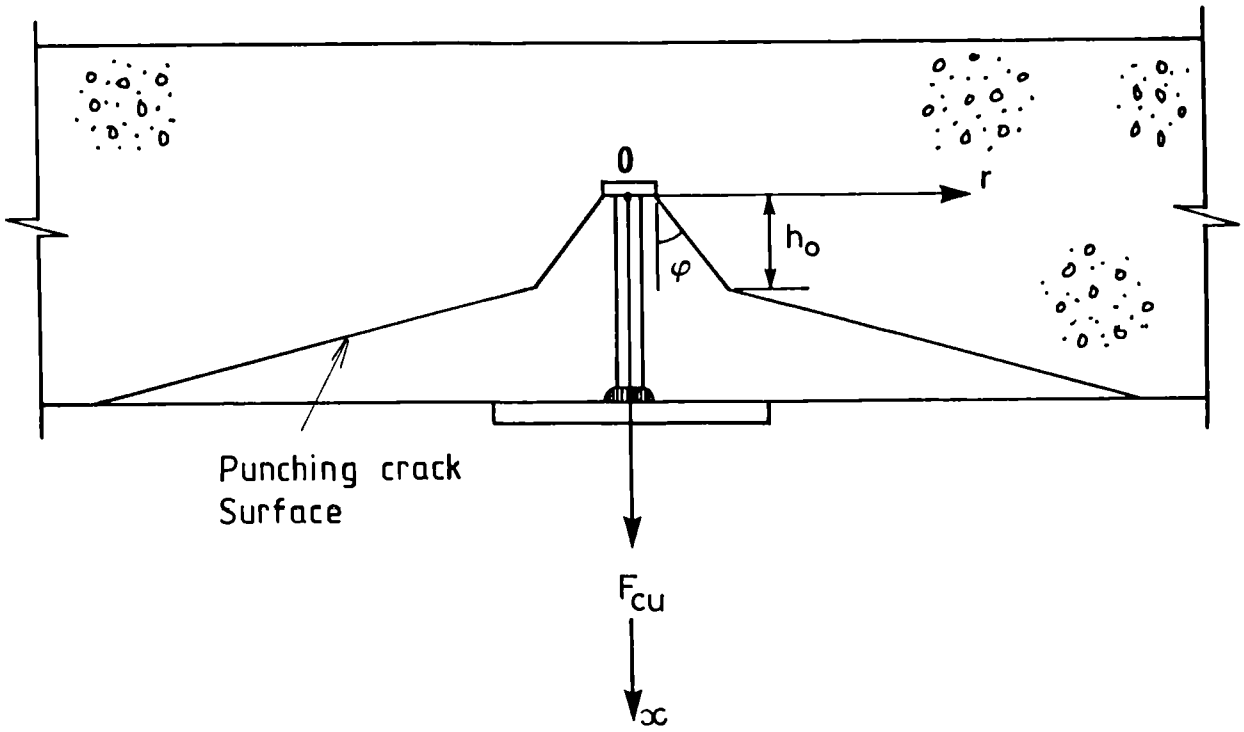

Figure 8.9: Punching shear failure surface underneath a stud head of a stud in tension, according to Ref. [112].

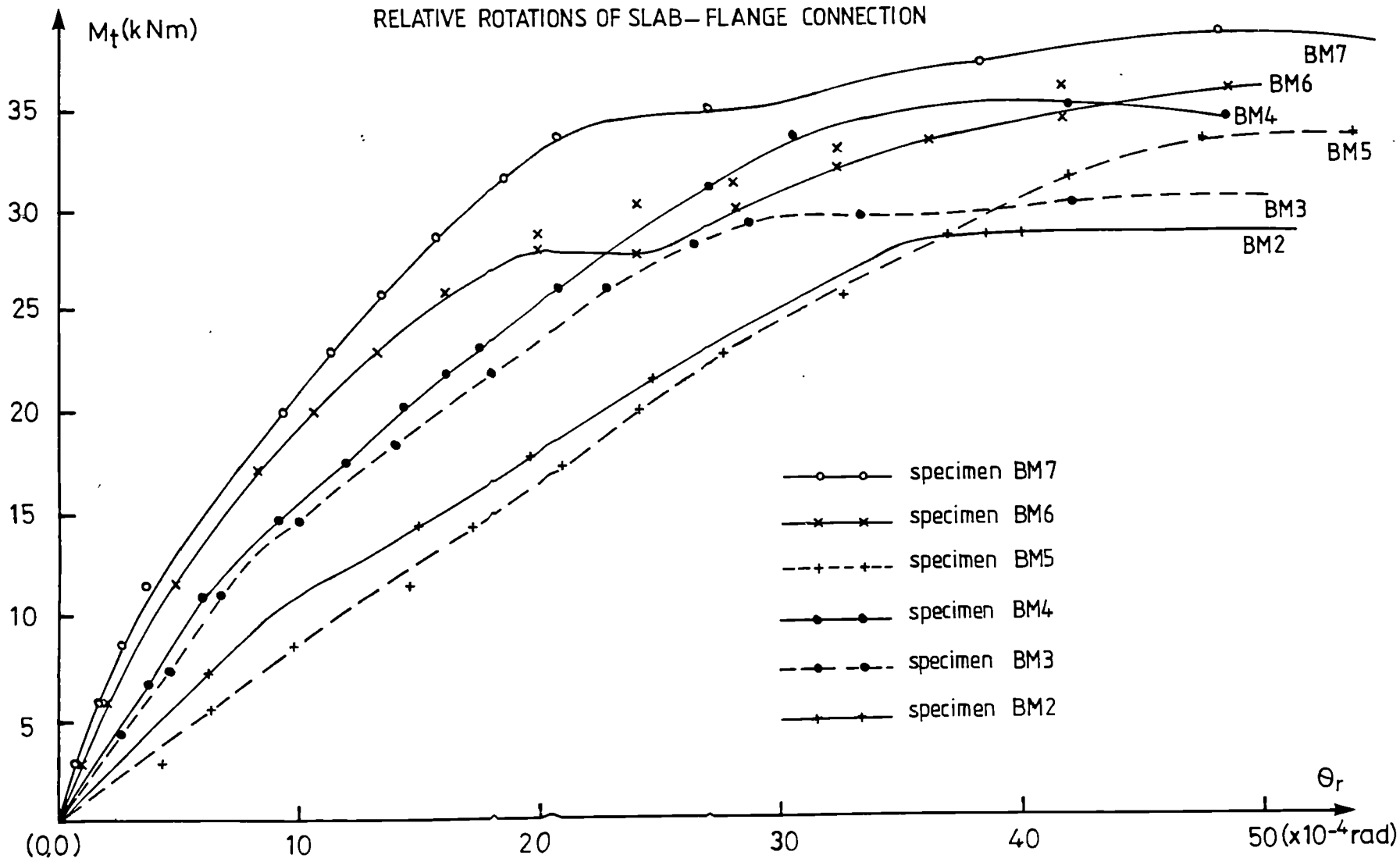

Figure 8.10: Transverse moment – relative rotation curves upto first visible shear cracking for all six test specimens.

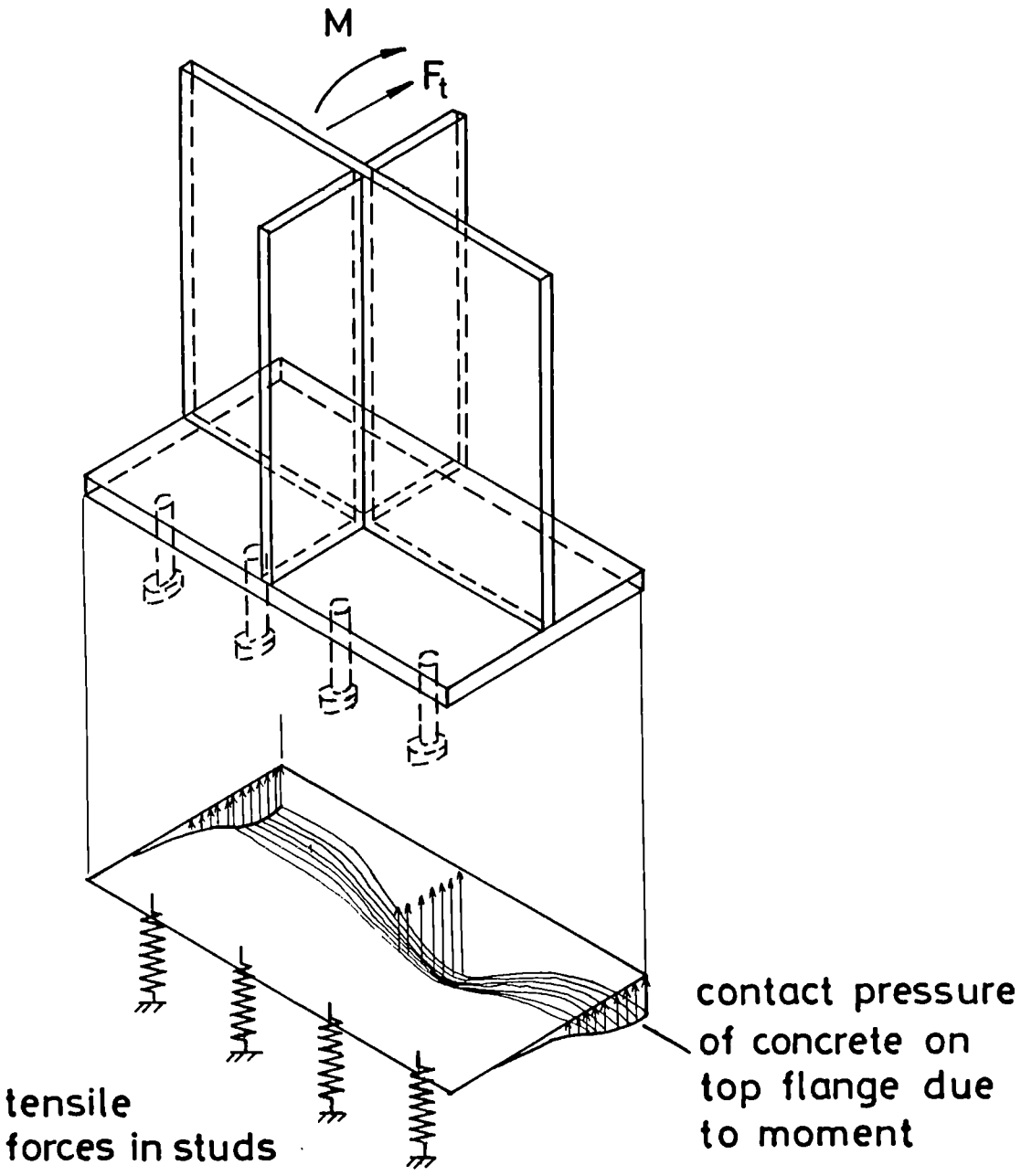

Figure 8.11: Three dimensional representation of the interaction between slab and top flange, modelling the studs as springs and the contact pressure as a higher order curve.

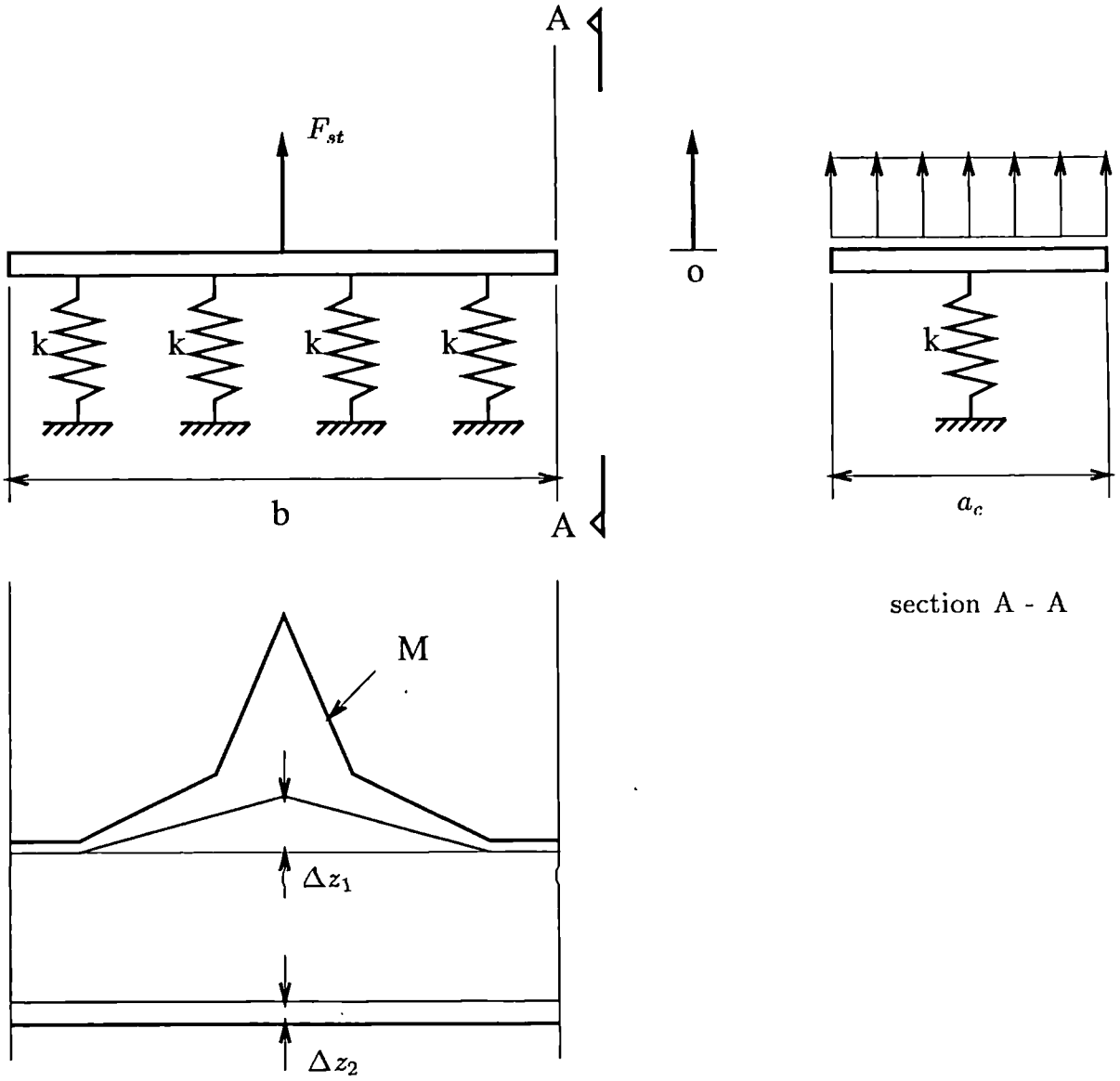

Figure 8.12: Two dimensional model of the interaction between slab and top flange as an equivalent plate on elastic foundations.

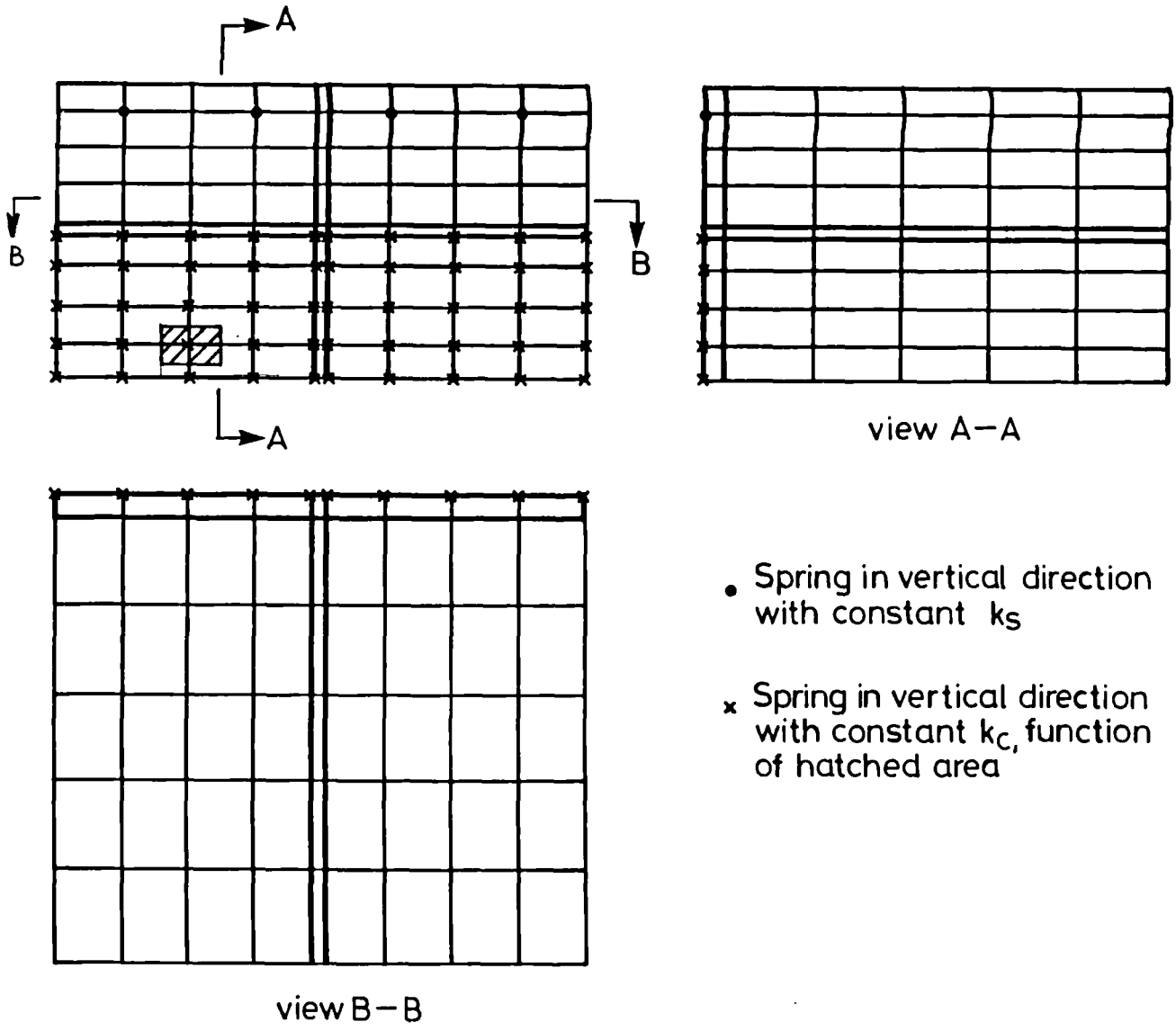

Figure 8.13: Finite Element mesh of the connection of the test specimen.

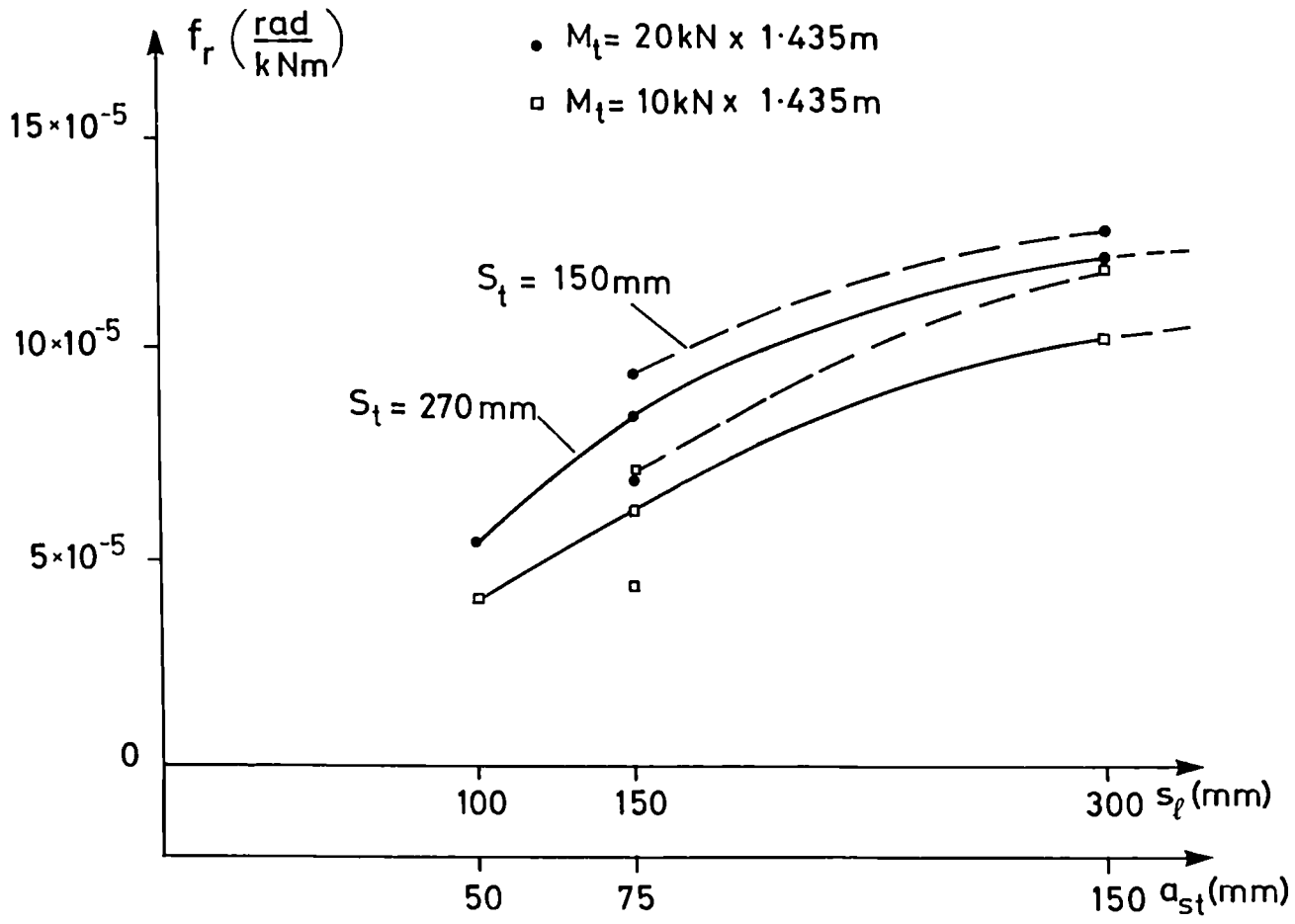

Figure 8.14: Variation of the transverse flexibility of the connection at the position of the vertical web stiffener with the longitudinal stud spacing at two different load levels.

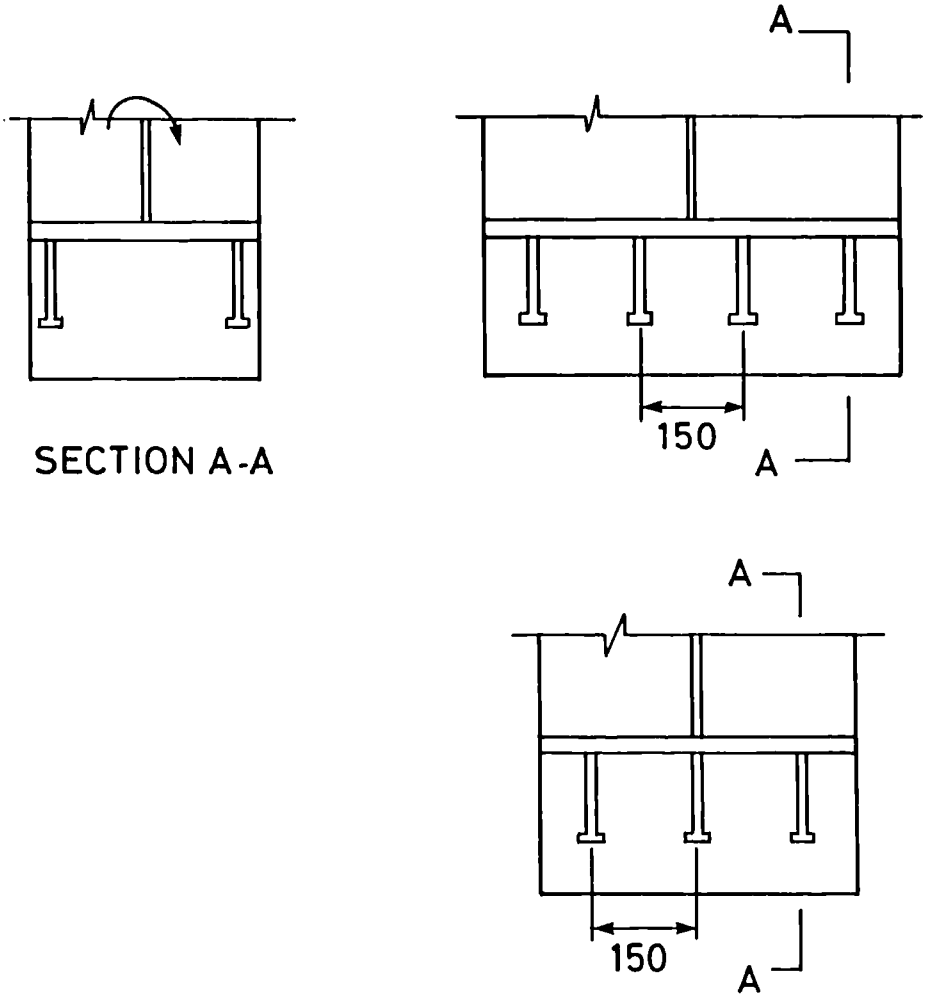

Figure 8.15: Influence of the relative position of the studs to the vertical web stiffener on the transverse flexibility.

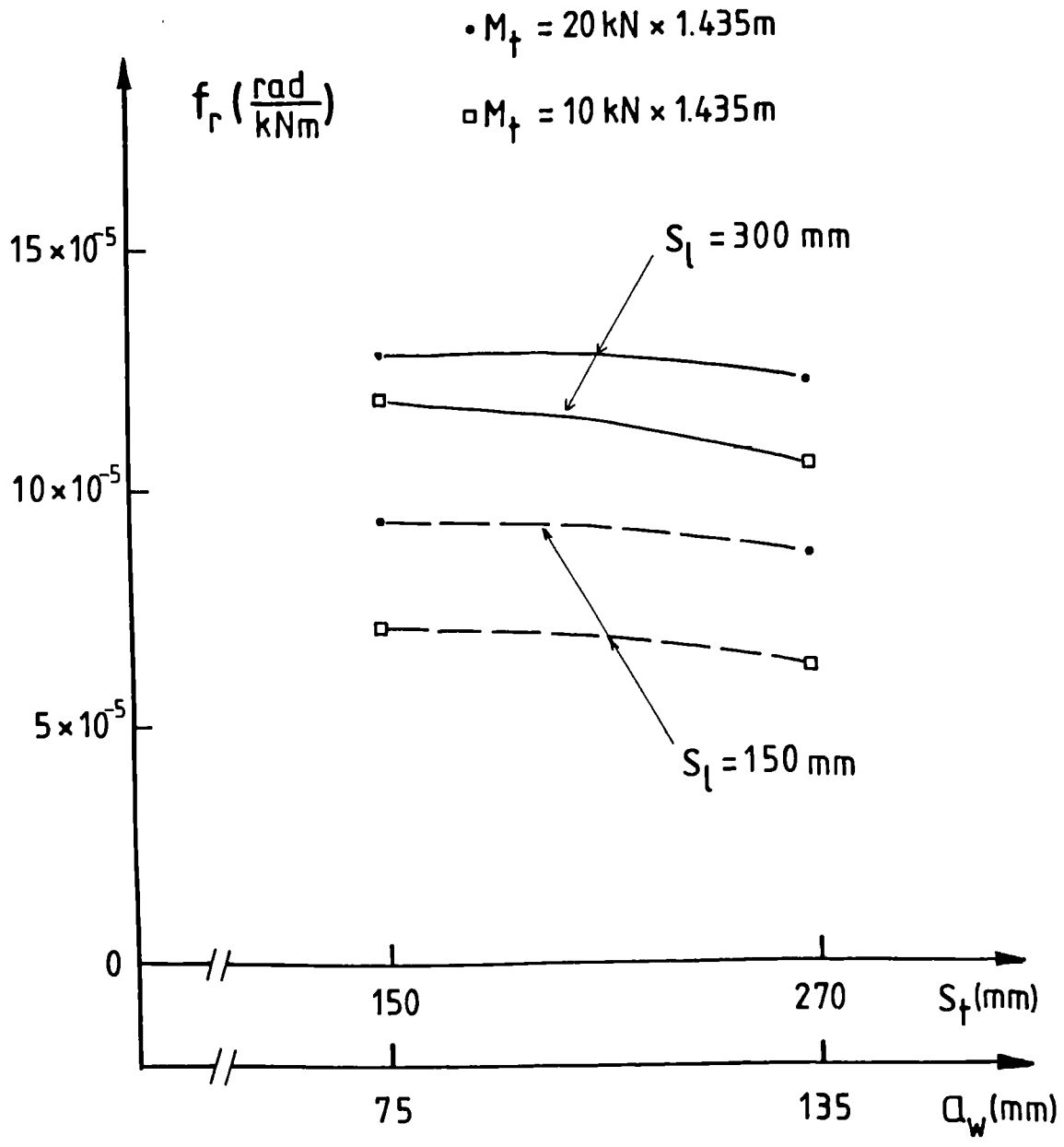

Figure 8.16: Variation of the transverse flexibility of the connection at the position of the vertical web stiffener with the transverse stud spacing either side of the web at two different load levels.

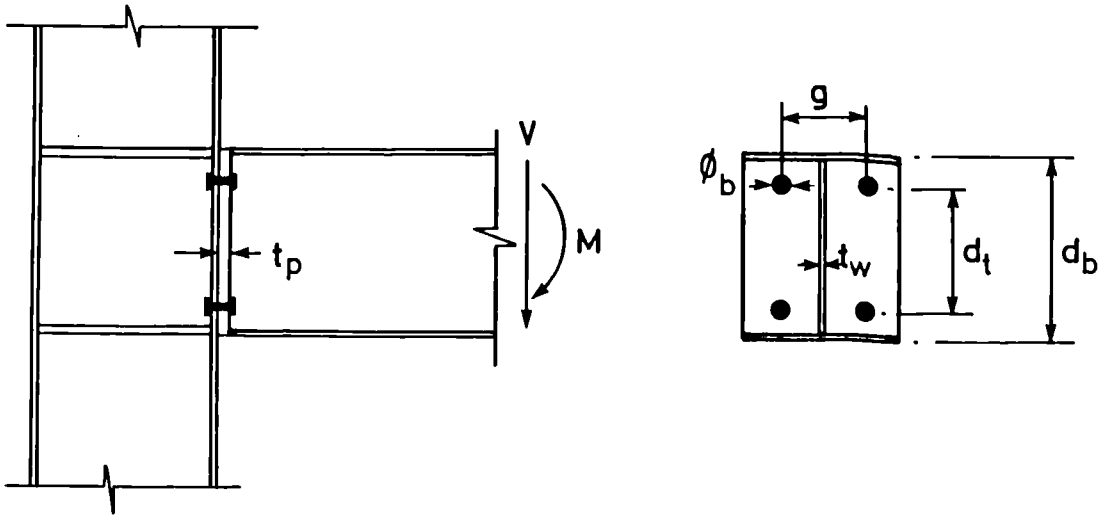

Figure 8.17: Relevant parameters for the flexibility of a bolted beam – column flush end plate steel connection.

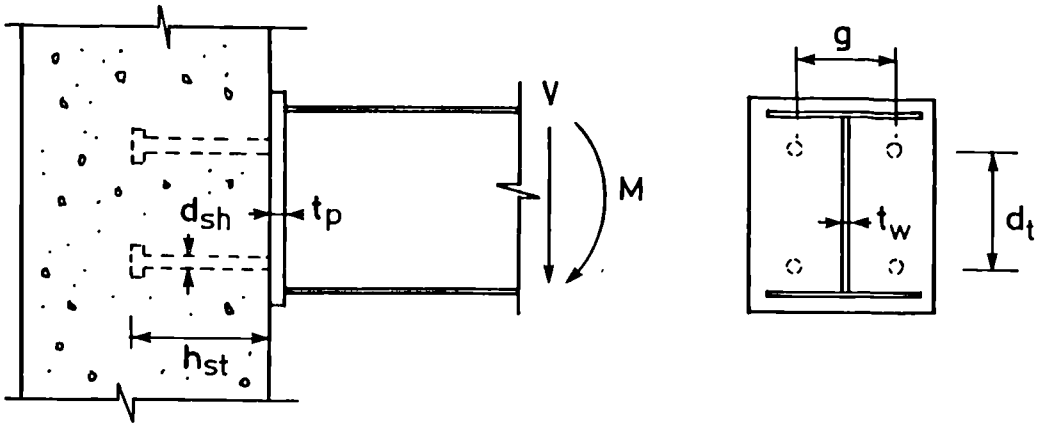

Figure 8.18: Relevant parameters for the flexibility of a steel beam – concrete column embedded stud anchor connection.

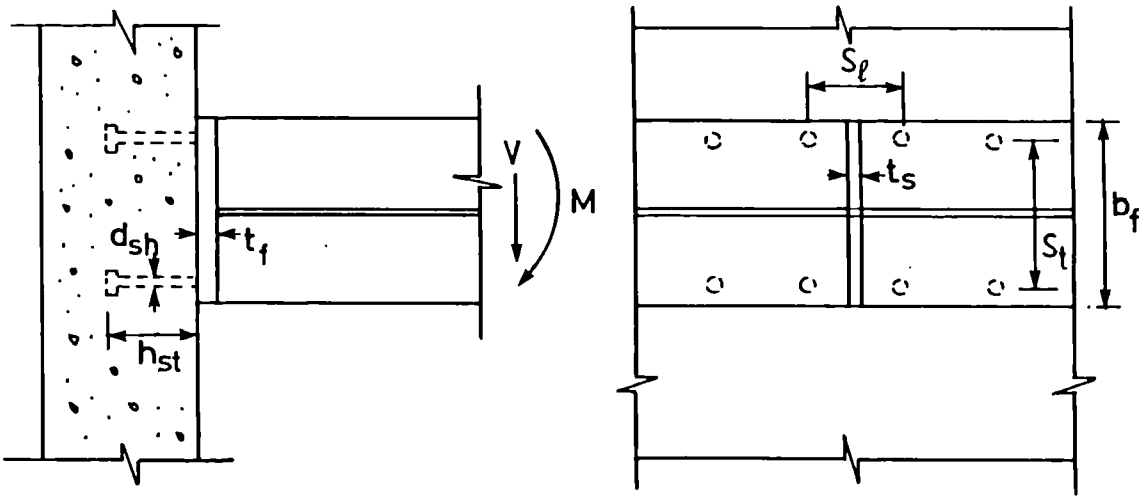

Figure 8.19: Steel beam – concrete slab connection of the tested specimens.

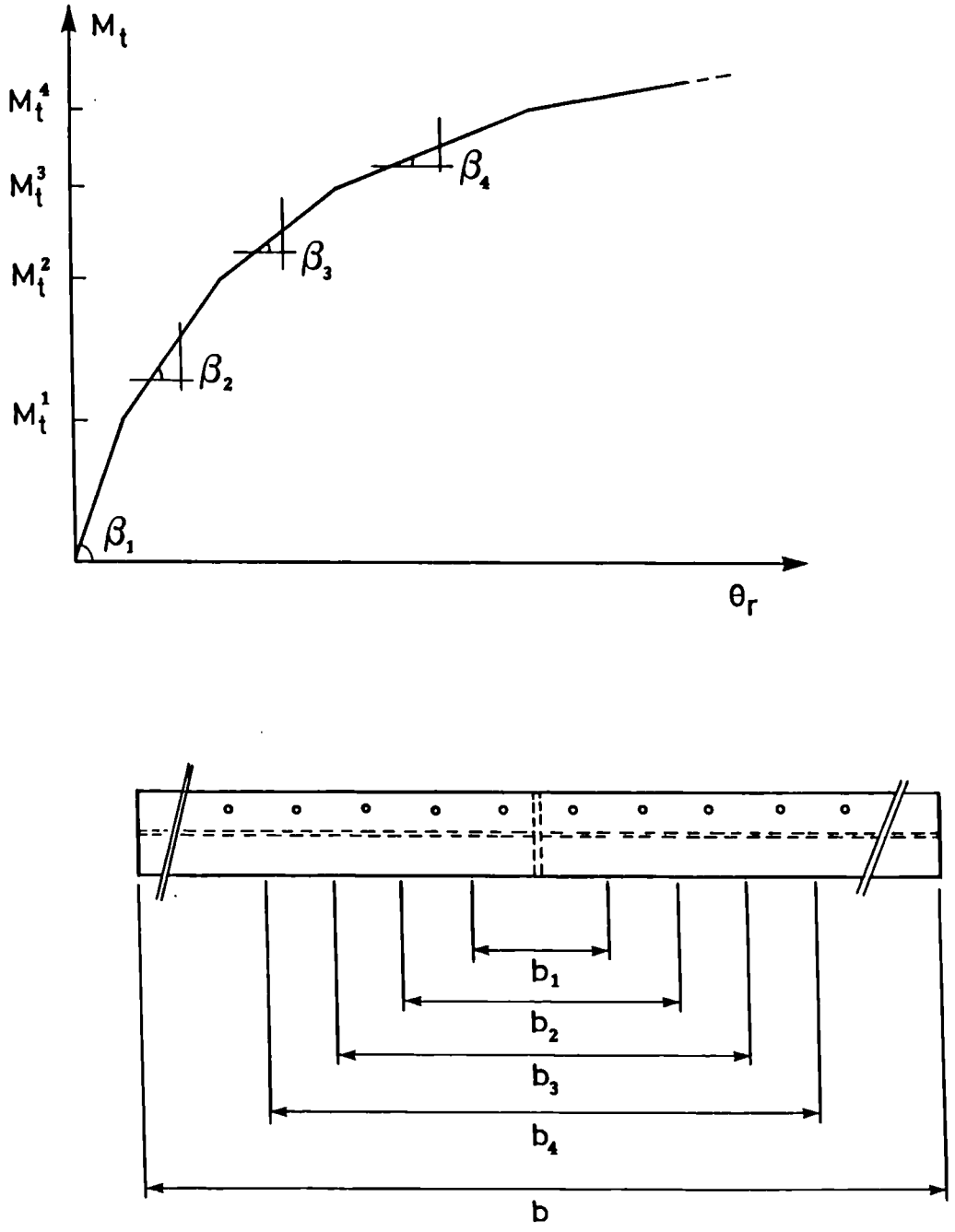

Figure 8.20: Qualitative representation of the progressive increase of the transverse flexibility of the connection with the widening of the diagonal shear crack.

Chapter 9

Conclusions on the transverse flexibility of steel – concrete stud connection in inverted U-frames

9.1 Improvements needed on the different design aspects of inverted U-frames

In order to obtain a less conservative and a more realistic method for the design of inverted U-frames, both strength and stiffness requirements for these frames need to be reviewed.

Although the **strength** requirement is outside the scope of this thesis, in section 6.3 it has been shown that for an average composite plate girder with inverted U-frame action ($l/h \approx 25$ and $\phi \leq 1.5$) where the critical inverted U-frame is at a distance of approximately 0.08 l away from the internal support, the moment will reduce by more than 30%, while the transverse force F_t, will reduce no doubt to less than half of its peak value at the support. These values of F_t are obtained by using a matrix method [85] which takes only account of the moment distribution and the transverse flexibility of the U-frames, assuming rigid joints. This shows that the equation (6.5), which produces the peak value of F_t, over-estimates the transverse force at the position of the critical inverted U-frame by more than 50%, without taking account of the flexibility of the connection. Since the calculated value of F_t is proportional to the factor $l_e/667\delta$, which in turn is proportional to $\delta^{-0.75}$, this peak value obtained by the present Code for inverted U-frames is also over-estimated as long as no account is taken of the transverse flexibility of the steel-concrete connection.

The stiffness of the U-frame does not only affect the strength, but also the maximum allowable limiting buckling stress in the compression flange and therefore the internal support moment. So far, the Bridge Code does not provide any guidelines on the calculation of the transverse flexibility of the connection and therefore the stiffness of inverted U-frames, as calculated in accordance with the Bridge Code, may be over-estimated.

From our limited number of test results, it was found that this flexibility cannot be ignored, as its value is between 1.2 and 2.7 times larger than the flexibilitiy of the most flexible of the range of structural steel connections, for which data are given in BS5400:Pt.3, thereby increasing considerably the values of δ and l_e for the corresponding inverted U-frame.

Finite Element models have demonstrated that for continuous inverted U-frames, where the flexibility of the connection is negligible, σ_{cr} and λ_{LT} are no longer functions of l_e, but of h_w/t_w. It is possible that for discrete inverted U-frames, where the flexibility of the connection becomes larger, similar changes in the derivation of σ_{cr} will be found. However, the increased flexibility of the steel-concrete stud connection will provide less lateral restraint to the bottom flange and will therefore have a negative effect on the effective torsional buckling length, l_e.

Further research efforts ought to be put into examining the incorporation of these experimentally measured transverse flexibilities with models for elastic lateral distortional buckling of composite plate girders with discrete inverted U-frames.

9.2 Improvement suggested for the current stiffness calculation of inverted U-frames in the Bridge Code

In the abscence of any of the above stated global changes to the design formulae for inverted U-frames, it is still possible to provide some improvement within the present Code on the calculation of the transverse stiffness of an inverted U-frame.

Presently, the Bridge Code only provides values for the transverse flexibility of typical standardised bolted connections, which are incorporated in the calculation of the total transverse stiffness of U-frames, as is shown in eq. (6.1) and Fig. 6.2.

Similarly, values could be obtained for the transverse flexibility of different steel-concrete connections. This transverse flexibility is not strictly speaking a constant for each connection, for it increases with the load level. Yet, the steel concrete stud connections tested in the laboratory, were shown to have a fairly constant elastic flexibility, until diagonal shear cracking progressed over the full width of the test specimen, at a load level $F_{t,cl}$. Although the flexibility is known to be a function of the torsional stiffness of the top flange and therefore of t_f and b_f, the spacing of the connectors s_l, and the embedment depth of the studs h_{st}, only s_l changes in the performed test series.

The choice of values for the other parameters of the test specimens will produce conservative values of f_r. Yet, to obtain an upper bound for the flexibility of each specimen, these flexibilities are calculated at a load level of 95% of $F_{t,cl}$. In Fig. 9.1 a curve is fitted through these upper bounds and a straight line marks the upper bound for all values of s_t .

This straight line is given by eq. (9.1) and represents the transverse flexibility of a stud connection, with N $\leq$ 12, at the position of a two sided vertical web stiffener, where the studs are symmetrically placed at either side of the stiffener.

$$f_r = 0.275\, s_l + 0.05\ mrad/kNm \tag{9.1}$$

with $s_l =$ longitudinal stud spacing, in metres

This equation could be incorporated in clause 9.6.5 of the BS5400:Part 3 for the transverse flexibility of steel concrete stud connections of symmetrical inverted U-frames. If the plate girder from Appendix V were to have the same stud configurations as those tested, then the lowest ratio of the transverse connection stiffness to any other transverse stiffness of the U-frame, would still be larger than 0.7. In Table 9.1 these ratios are calculated for the different stud configurations. They show that the flexibility of the connection is of the same order of magnitude as the other flexibilities and therefore should not be ignored for discrete inverted U-frames.

Table 9.1: Ratios of the calculated transverse flexibilities of the tested connections to the calculated flexibilities of the stiffened web and the slab of the plate girder in Appendix V.

		Test Specimen					
		$BM2$	$BM3$	$BM4$	$BM5$	$BM6$	$BM7$
δ_3	(mm/kN)	0.249	0.183	0.181	0.274	0.132	0.122
δ_3/δ_1	$(-)$	2.610	1.920	1.890	2.870	1.380	1.280
δ_3/δ_2	$(-)$	1.460	1.070	1.060	1.600	0.770	0.710

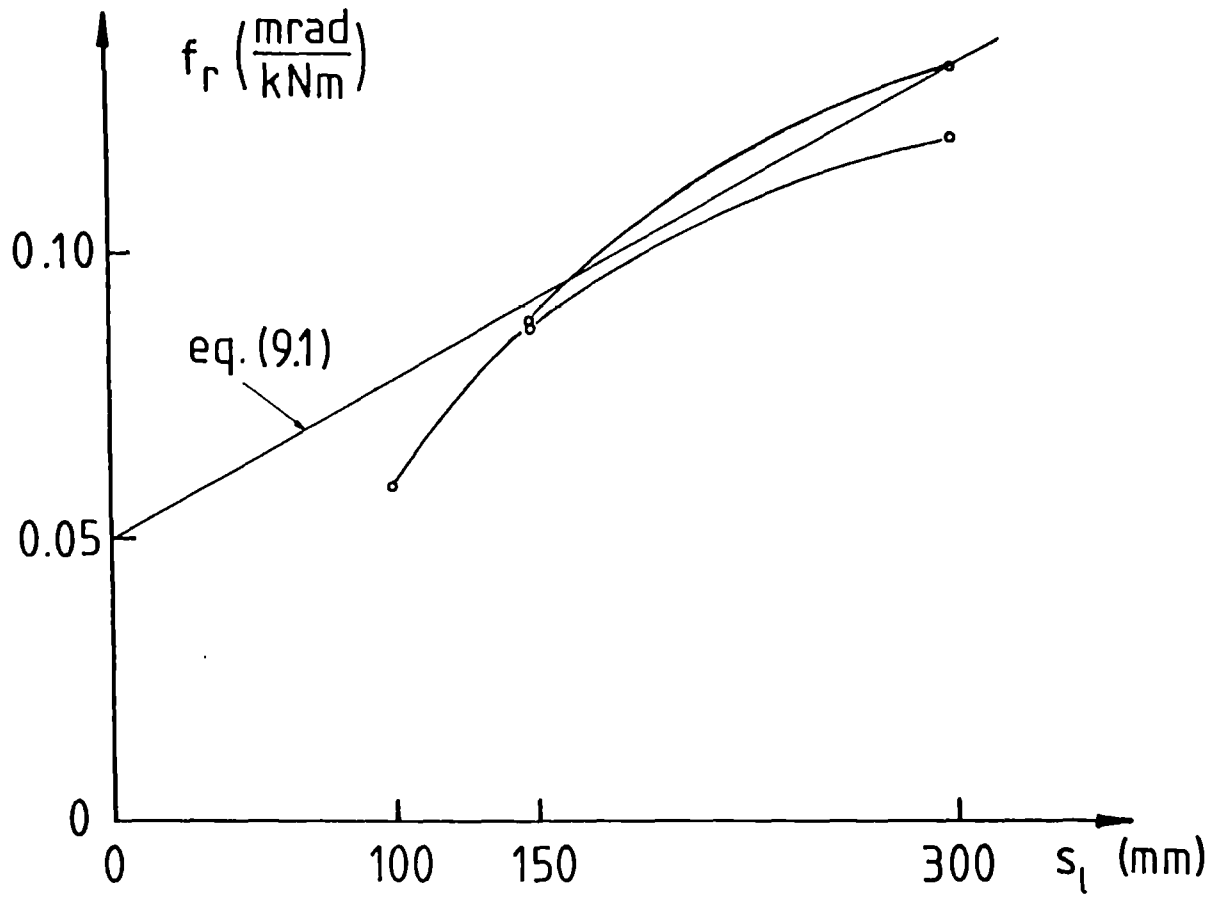

Figure 9.1: Variation of the transverse flexibility of a stud connection, with $N \leq 12$, at the position of a two sided vertical web stiffener with the longitudinal spacing of the studs.

Bibliography

[1] CP 117:Pt.1:1965, 'Composite construction in structural steel and concrete: Supply supported beams in buildings' British Standard Institution.

[2] BS 449:Pt.3, 'The use of structural steel in buildings: Composite construction', British Standard Institution (Draft only issued Aug. 1976).

[3] Eurocode N° 4, 'Common unified rules for Composite steel and concrete structures', Commission of the European Communities, draft, 1985.

[4] BS 5950, 'The structural use of steelwork in buildings', Part 3, 'Design in composite construction', Section 3.1, 'Code of practice for design of composite beams', Draft for Public Comment, issue 8, British Standards Institution, London, Nov. 1988.

[5] Eurocode N° 3, 'Common unified rules of practice for Steel Structures', Commission of European Communities, 2nd draft, 1989.

[6] BS 153, 'Specification for steel girder bridges', British Standard Institution, London, 1958.

[7] BS 5400, 'Steel, concrete and composite bridges', Part 3,'Code of practice for design of steel bridges', British Standard Institution, London, AMD 4051, 1982, 120 pp.

[8] BS 5400, 'Steel, concrete and composite bridges', Part 4, 'Code of practice for design of concrete bridges', British Standard Institution, London, 1984, 68 pp.

[9] Hark A.J., 'Continue staal-betonliggers met stiftdeuvel verbindingen', De Ingenieur, Vol 79, N°. 26, juni 1967.

[10] Stark J.W.B., 'Beproeving van een samengestelde ligger over drie steunpunten', IBBC Rapport B-66-1358/13054, Rijswijk, juni 1966.

[11] Chapman J.C. and Balakrishnan S., 'Experiments on composite beams', Struct. Engr., 1964, Vol. 42, N° 11, pp. 369-383.

[12] Yam L.C.P. and Chapman J.C., 'The inelastic behaviour of simply supported beams of steel and concrete', Proceedings, Instn. Civ. Engrs, 1968, Vol. 41, Dec., pp. 651-683.

[13] Yam L.C.P. and Chapman J.C., 'The inelastic behaviour of continuous composite beams of steel and concrete', Proceedings, Instn. Civ. Engrs, Part 2, 1972,Vol. 53 ,Dec., pp. 487-501.

[14] McGarraugh J.B. and Baldwin J.W., 'Lightweight concrete-on-steel composite beams', AISC Engineering Journal, American Institute of Steel Construction, 1971, Vol. 8, July, pp. 90-98.

[15] Brassinga H.E. and Stark J.W.B., 'Beproeving van liggers op verkleinde schaal', IBBC-Rapport B1-71-52, TNO Instituut voor Bouwmaterialer & Bouwconstructie, Delft, Nov., 1972.

[16] Johnson, R.P and May I.M., 'Partial interaction design of composite beams', Struct. Engr., 1975, Vol. 53, N° 8, pp. 305-311.

[17] Woolsey J., 'A study of composite beams with lightweight concrete slabs', MSc. Thesis, University of Missouri, Columbia, June, 1970.

[18] Vogel G., 'Shear connection behaviour from beam tests', MSc. Thesis, University of Missouri, Columbia, Jan., 1971.

[19] Frodin J.G., Taylor R. and Stark J.W.B., 'A comparison of deflections in composite beams having full and partial shear connection', Proceedings, Instn. Civ. Engrs., Part 2, 1978, Vol. 65, June, pp. 307-322.

[20] Stark J.W.B., 'Statisch bepaalde staal-beton liggers', Rapport N°. 1 van CUR en SG, uitg. Waltman, september, 1974.

[21] Johnson, R.P. and Hope-Gill M.C., 'Applicability of simple plastic theory to continuous composite beams', Proceedings, Instn. Civ. Engrs., Part 2, 1976, Vol. 61, March, pp. 127-143.

[22] Slutter R.G. and Driscoll G.C., 'Flexural strength of steel-concrete composite beams',Journal of the Stuctural Division, A.S.C.E., 1965, Vol. 91, N° ST2, April, pp. 71-99.

[23] Daniels J.H. and Fisher J.W., 'Static behaviour of composite beams with variable load positions', Fritz Engineering Laboratory Report N°. 324.3, Lehigh University, Bethlehem, Pa., March, 1967.

[24] Aribert J.M. and Labib A.G., 'Étude numérique et experimentale de l'influence d'une connection partielle sur le comportement de poutres mixtes', Journées 15-16, 69-89, Association Française des Pont et Charpentes, Mars, 1983.

[25] Grant J.H., 'High strength steel composite beams with formed metal deck and low partial shear connection', MSc. Thesis, Lehigh University, Bethlehem, Pa., Oct., 1973.

[26] Evans H.R., Wright H.D. and Harding P.W., 'Full-scale load tests on super Holorib steel-deck composite beams with TRW Nelson thru-deck welded stud connectors', Report UCC/Nelson/RL, 1984, Feb., pp.21 (unpublished).

[27] Johnson R.P., 'Limitations of the use of partial shear connection in composite beams', Research Report CE21, University of Warwick, Aug., 1986.

[28] Oehlers D.J. and Coughlan C.G., 'The shear stiffness of stud connectors in composite beams', Journal of Constructional Steel Research, 1986, Oct., pp. 273-284.

[29] Roïk K. and Hanswille G., 'Beitrag zur Bestimmung der Tragfähigkeit von Kopfbolzendübeln', Der Stahlbau, 1983, Vol. 10, pp. 301-308.

[30] Skinner T. 'Shear connector behaviour from beam tests, Phase II', MSc. Thesis, University of Missouri, Columbia, June, 1970.

[31] Newmark N.M., Siess C.P. and Viest I.M., 'Tests and analysis of composite beams with incomplete interaction', Society for Experimental Stress Analysis, 1951, Vol. 9, N° 1, pp. 75-92.

[32] Dai K.H. and Siess C.P., 'Analytical study of composite beams with inelastic shear connection', Structural Research Series N°. 267, University of Illinois, Urbana, June, 1963.

[33] Horne D.R. and Plum M.R., 'The analysis of continuous composite beams with partial interaction', Proceedings, Instn. Civ. Engrs., Part 2, 1975, Vol. 59, Dec., pp. 625-643.

[34] Burkhardt P., 'Le comportement élastique et plastique des poutres mixtes', Thèse N°. 264, École Polytechnique Fédérale de Lausanne, 1977.

[35] Arizumi Y. Hamada S. and Kajita T., 'Elastic-plastic analysis of composite beams with incomplete interaction by finite element method', Computers and Structures, 1981, Vol. 14, N° 5-6, pp. 453-462.

[36] Ansourian P. and Roderick J.W., 'Analysis of composite beams', Journal of the Structural Division, A.S.C.E., 1978, Vol. 104, N° ST10, Oct., pp.

[37] Roberts T.M., 'Finite difference analysis of composite beams with partial interaction', Computers and Structures, 1985, Vol. 21, N°. 3, pp. 469-473.

[38] Kŕístek V. and Studnička J., 'Analysis of composite girders with deformable connectors.', Proceedings, Instn. Civ. Engrs., Part 2, 1982, Vol. 73, Dec., pp. 699-712.

[39] Kŕístek V., Vitek J.L. and Wright H.D., 'The effect of connector stiffness on composite beam design',in Proceedings International Symposium **Composite Steel Concrete Structures, Vol. 2**, ed. Dom Techniky CSVTS Bratislava, 1987, pp. 65-69.

[40] Aribert J.M., 'Étude critique par voie numérique de la méthode proposée dans l'EUROCODE 4 pour le dimensionnement des poutres mixtes acier-béton à connection partielle', Construction Métallique, 1988, N°. 1, Mars, pp. 3-26.

[41] Aribert J.M. and Aziz A.K., 'Calcul des poutres mixtes jusqu'à l'état ultime avec un effet de soulèvement à l'interface acier-béton.', Construction Métallique, 1985, N°. 4, pp. 3-36.

[42] Aribert J.M. and Aziz A.K., 'Modèle général pour le calcul des poutres mixtes hyperstatiques jusqu'à la ruine.', Construction Métallique, 1986, N°. 4, pp. 3-41.

[43] Aribert J.M. and Labib A.G., 'Modèle de calcul élastoplastique de poutres mixtes à connection partielle', Construction Métallique, 1982, N°. 4, pp. 3-51.

[44] Lebet J., 'Comportement des ponts mixtes acier-béton avec interaction partielle de la connection et fissuration du béton.', Thèse N°. 661, École Polytechnique Fédérale de Lausanne, 1987.

[45] Robinson H. and Naraine K.S., 'Slip and uplift effects in composite beams', in **Composite construction in steel and concrete**, eds. Buckner C.D. and Viest I.M., A.S.C.E., 1988, pp. 487-497.

[46] Millard S.G. and Johnson R.P., 'Shear transfer across cracks in reinforced concrete due to aggregate interlock and to dowel action', Magazine Concrete Research, 1984, Vol. 36, N° 126, March, pp. 9-22.

[47] McMackin P.J., Slutter R.G. and Fisher J.W., 'Headed steel anchors under combined loading', AISC Engineering Journal, American Institute of Steel Construction, 1973, 2nd Quarter, April, pp. 43-52.

[48] Basu A.K. and Somerville W., 'Derivation of formulae for the design of rectangular composite columns', Proceedings, Instn. Civ. Engrs., 1969, Supplementary Volume, Dec.

[49] Barnard P.R. and Johnson R.P., 'Ultimate strength of composite beams', Proceedings, Instn. Civ. Engrs., 1965, Vol. 32, Nov., pp. 161-179.

[50] Kabaila A, Discussion of 'Equation for stress-strain curve of concrete', by Desayi D. and Krishnan S., A.C.I. Journal, Proceedings, 1964, Vol. 61, N° 9, Sept., pp. 1227-1229.

[51] Smith G.M. and Young L.E., 'Ultimate theory in flexure by exponential function', A.C.I. Journal, Proceedings, 1955, Vol. 52, N° 3, Nov., pp. 349-360.

[52] Rüsch H., 'Versuche zur Festigkeit der Biegedurchzone Deutscher Ausschuss für Stahlbeton', N° 20.

[53] Wang P.T., Shah S.P. and Naaman A.E., 'Stress strain curves in normal and lightweight concrete in compression', A.C.I. Journal, Proceedings, 1978, Vol. 75, N° 11, Nov., pp. 603-611.

[54] Saenz L.P., Discussion of 'Equation for stress-strain curve of concrete', by Desayi D. and Krishnan S., A.C.I. Journal, Proceedings, 1964, Vol. 61, N° 9, Sept., pp. 1229-1236.

[55] Desayi D. and Krishnan S., 'Equation for stress-strain curve of concrete', A.C.I. Journal, Proceedings, 1964, Vol. 61, N° 3, March, pp. 345-350.

[56] Yam L.C.P., 'Ultimate-load behaviour of composite T-beams having inelastic shear connection', PhD. Thesis, Imperial College of Science and Technology, 1966.

[118] Sommer W.H., 'Behaviour of welded header plate connections', MSc. Thesis, University of Toronto, Ontario, Canada, 1969.

[119] Kennedy D.J.L., 'Moment rotation characteristics of shear connections', AISC Engineering Journal, American Institute of Steel Construction, 1969, Oct., pp. 105-115.

[120] Jones S.W., Kirby P.A. and Nethercot D.A., 'Modelling of semi-rigid connection behaviour and its influence on steel column behaviour', in **Joints in Structural Steelwork**, eds. Howlett J.H., Jenkins W.N. and Stainsky R., 1981, Pentech. Press, London, pp. 5.73-5.87.

[121] Yee K.L. and Melchers R.E., 'Moment-rotation curves for bolted connections', Journal of the Structural Division, A.S.C.E., 1986, Vol. 112, N° 3, March, pp. 615-635.

[122] Nethercot D.A. and Zandonini R., 'Methods of prediction of joint behaviour - beam to column connections', in **Connections in Steel Structures: Structural Connection Stability and Strength**, ed. by Narayanan, Elsevier Applied Science Publishers, London, 1989, pp. 23-62.

[123] Kukreti A.R., Murray T.M. and Ablomaali A., 'End-plate connection moment-rotation relationship', Journal of Constructional Steel Research, Vol. 8, 1987, Special issue of Joint flexibility in Steel Frames, pp. 137-157.

[124] Benterkia Z, ' End-Plate Connections and Analysis of Semi-Rigid Steel Frames', PhD Thesis, University of Warwick, 1990 (in preparation).

[125] Abramowitz M. and Stegun I.A., 'Handbook of Mathematical functions', Dover Publications, New York, 1965.

[126] Chapra S.C. and Canale R.P., 'Numerical methods for Engineers', McGraw-Hill, 1985, 570 pp.

[127] Younger M.S., 'A Handbook for linear regression', Duxbury Press, 1979, 569 pp.

[57] CEB-FIP, 'Model code for concrete structures', English Edition, Cement and Concrete Association, 1978, London , 348 pp.

[58] Johnson R.P., 'Composite structures of steel and concrete, volume 1: Beams, Columns, Frames and Applications in Buildings.', Granada, 1975, 210 pp.

[59] Johnson R.P., 'Loss of interaction in short span composite beams and plates', Journal of Constructional Steelwork Research, 1981, Vol. 1, N° 2, Jan., pp. 11-16.

[60] Johnson R.P. and Oehlers D.J., 'Analysis and design for longitudinal shear in composite T-beams', Proceedings, Instn. Civ. Engrs., Part 2, 1981, Vol. 71, Dec., pp. 989-1021.

[61] Grant J.A., Fisher J.W. and Slutter R.G., 'Composite beams with formed steel deck', AISC Engineering Journal, American Institute of Steel Construction, 1977, N° 1, Jan., pp. 24-43.

[62] Mottram J.T. and Johnson R.P., 'Push tests on studs welded through profiled steel sheeting', Research Report CE27, Dept. of Engineering, University of Warwick, Sept., 1989.

[63] Oehlers D.J., 'Stud shear connection for composite beams', PhD. Thesis, University of Warwick, March, 1980.

[64] Rayleigh J.G., 'Axial loads in stud shear connections in composite beams', MSc. Thesis, National University of Ireland, 1984.

[65] Oehlers D.J. and Johnson R.P., 'The strength of stud shear connections in composite beams', Struct. Engr., 1987, Vol. 65B, June, pp. 44-48.

[66] Ollgaard J., Slutter R.G. and Fisher J.W., 'The strength of stud connectors in lightweight and normal weight concrete', AISC Engineering Journal, American Institute of Steel Construction, 1971, Vol 8, N° 2, April, pp. 55-64.

[67] Johnson R.P., Greenwood R.D. and Van Dalen K., 'Stud shear connectors in hogging moment regions of composite beams', Struct. Engr., 1969, Vol. 47, N° 9, Sept., pp. 345-350.

[68] Dallam L.N., 'Push-out tests of stud and channel shear connectors in normal and lightweight concrete slabs', Engineering Experiment Station Bulletin 1968, Series N°. 66, University of Missouri, Columbia, April, 1968.

[69] Menzies J.B., 'CP117 and shear connectors in steel-concrete composite beams', Struct. Engr., 1971, Vol. 49, N° 3, March, pp. 137-153.

[70] Buttry K.E., 'Behaviour of stud shear connectors in lightweight and normal weight concrete', MSc. Thesis, University of Missouri, Columbia, 1965.

[71] Hawkins N.M. and Mitchell D., ' Seismic response of composite shear connections', Journal of Structural Engineering, A.S.C.E., 1986, Vol. 110, N° 9, Sept., pp. 2120-2136.

[72] Robinson H., 'Tests on composite beams with cellular deck', Journal of the Structural Division, A.S.C.E., 1967, Vol. 93, N°. ST4, Aug., pp. 139-164

[73] Fisher J.W., 'Design of composite beams with formed metal deck', AISC Engineering Journal, American Institute of Steel Construction, 1970, Vol. 7, N° 2, July, pp. 88-96.

[74] Jayas B.S. and Hosain M.V., 'Composite beams with perpendicular ribbed metal deck', in **Composite construction in steel and concrete**, eds. Buckner C.D. and Viest I.M., A.S.C.E. 1988, pp. 551-527.

[75] Johnson R.P. and Price T., 'Tests on composite beams with large web openings', Private communication, 1990.

[76] Lungershausen H., 'Zur Schubtragfähigheit von Kopfbolzendúbeln', Doktorarbeit, Ruhr-Universitat Bochum, 1988.

[77] Johnson R.P., 'Continuous composite beams for buildings', IABSE-ECCS Symposium, Luxembourg, IABSE Reports, 1985, Vol. 48, pp. 195-202.

[78] Johnson R.P. and Molenstra N., 'Interim report on a study of partial shear connection in continuous composite beams', Research Report CE23, University of Warwick, 1987.

[79] Chien E.Y.L. and Ritchie J.K., 'Design and construction of composite floor systems', Canadian Institute of Steel Construction, 1984.

[80] Molenstra N. and Johnson R.P., 'Final report on a study of partial shear connections in composite beams', University of Warwick, 1987.

[81] Nethercot D.A., 'Design of beams and plate girders — treatment of overall and local flange buckling', in **The Design of Steel Bridges**, eds. Rockey K.C. and Evans H.R., Granada, 1981, pp. 243-263.

[82] Timoshenko P., 'Theory of Elastic Stability', McGraw-Hill, New-York, 1936, 518 pp.

[83] Johnson R.P. and Buckby R.J., 'Composite Structures of Steel and Concrete, Volume 2: Bridges', 2nd ed., Collins, 1986, 420 pp.

[84] Allen H.G. and Bulson P.S., 'Background to Buckling', McGraw-Hill, Great-Britain, 1980, 582 pp.

[85] Chwalla E., 'Die neuen Hifstafeln zur Berechnung von Spannungsproblemen der Theorie zweiter Ordnung und von Knickproblemen', Der Bauingenieur, 1959, Hefte 4, 6 und 8.

[86] Van de Pitte D., 'Berekeningen van Constructies: deel II', uitg. Story, Gent, 1980, 709 pp.

[87] Winter G., 'Lateral buckling of columns and beams', Journal of the Structural Division, A.S.C.E., 1958, Vol. 84, N° ST2, March, pp. 1561-1 - 1561-22

[88] Longbottom E. and Heyman J., 'Experimental verification of the strength of plate girders designed in accordance with the revised BS 153', Proceedings, Instn. Civ. Engrs., Part III, 1956, Vol.5, N° 2, Aug., pp. 462-486.

[89] Hayward A., 'Cheaper Composite Bridges', in **Composite construction in steel and concrete**, eds. Buckner C.D. and Viest I.M., A.S.C.E. 1988, pp. 194-206.

[90] Johnson R.P. and Bradford M.A.,'Distortional lateral buckling of continuous composite bridge girders', Proceedings Conference **Instability and Plastic Collapse of Steel Structures**',ed. Morris L.J., Granada, 1983, pp. 569-580.

[91] Fukumoto Y. and Kubo M.,'A survey of tests on lateral buckling strength of beams', 2nd International Colloquium, **Stability of Steel structures**, Liege, Preliminary Report, ECCS and IABSE, 1977, pp. 233-240.

[92] Climenhaga J.J., 'Local buckling in composite beams.', Ph.D. Thesis, University of Cambridge, 1970.

[93] Bradford M.A. and Johnson R.P.,'Inelastic buckling of composite bridge girders near internal support', Proceedings, Instn. Civ. Engrs., 1987, Part 2, Vol.83, March, pp. 143-159.

[94] Weston G. and Nethercot D.A., 'Continuous composite bridge beams — Stability of the steel compression flange in hogging bending', in **Stability of Plate and Shell Structures**, ed. Dubas P. and Van de Pitte D., European Convention for Constructional Steelwork, 1987, pp. 47-52.

[95] O'Conner C., 'Design of Steel Bridge Superstructures', Wiley-interscience, 1971, 463 pp.

[96] Badoux J.C., 'Conception des Structures Métalliques: dimensionnement des ponts', Institut de la Construction Métallique, Mai, 1975.

[97] Mörsch E., 'Der Eisenbeton. Seine Theorie und Anwendung', Wittwer, Stuttgart, 1908.

[98] Reinhardt H.W., 'Similitude of brittle fracture of structural concrete', in **Advanced Mechanics of Reinforced Concrete**, IABSE Colloquium, Delft, 1981, pp. 201-220.

[99] Bažant Z.P. and Kim Jin-Keun, 'Size effect in shear of Longitudinally Reinforced beams', A.C.I. Journal, Proceedings, 1984, Vol. 81, N° 5, Sept.-Oct., pp. 456-468.

[100] Regan P.E., 'Shear in reinforced concrete beams', Magazine of Concrete Research, 1969, Vol. 21, N° 66, March, pp. 31-42.

[101] Placas A. and Regan P.E., 'Shear failure of reinforced concrete beams', ACI Journal, Proceedings, 1971, Vol. 68, N° 10, Oct., pp. 763-773.

[102] Regan P.E., 'Behaviour of reinforced and prestressed concrete subjected to shear force', Proceedings, Instn. Civ. Engrs., Paper 74415, 1971 (Supplement XVII), pp. 337-364.

[103] Kennedy R.P., 'A statistical analysis of the shear strength of reinforced concrete beams', Technical Report N°. 78, Department of Civil Engineering, Stanford University, April, 1967.

[104] Kani G.N.J., 'Basic facts concerning shear failure', A.C.I. Journal, Proceedings, 1966, Vol. 63, N° 6, June, pp. 675-692.

[105] Kani G.N.J., 'How safe are our large reinforced concrete beams?', A.C.I. Journal, Proceedings, 1967, Vol. 64, N° 3, March, pp. 128-141.

[106] Leonhardt F.,'Reducing the Shear Reinforcement in Reinforced Conrete Beams and Slabs', Magazine of Concrete Research, 1965, Vol. 17, N° 53, Dec., pp. 187-198.

[107] Taylor H.P.J., 'Shear strength of large beams', Journal of the Structural Division, A.S.C.E., 1972, Vol. 98, N° ST11, Nov., pp. 2473-2490.

[108] Zsutty T.C., 'Beam shear strength prediction by analysis of existing data', A.C.I. Journal, Proceedings, 1968, Vol. 65, N° 11, Nov., pp. 943-951.

[109] Zsutty T.C.,'Shear strength prediction for separate categories of simple beam tests', A.C.I. Journal, Proceedings, 1971, Vol. 68, N° 2, Feb., pp. 138-143.

[110] Elzanaty A.H., Nilson A.H. and Slate F.O., 'Shear capacity of reinforced concrete beams using high-strength concrete', A.C.I. Journal, Proceedings, 1968, Vol. 83, N° 2, March-April, pp. 290-305.

[111] TRW Nelson,'Embedment properties of headed studs', 1977, 47 pp. (unpublished).

[112] Nielsen M.P., Braestrup M.W., Jensen B.C. and Bach F.,'Concrete Plasticity. Beam shear – shear in joints – punching shear', Copenhagen, Technical university of Denmark, 1978, Danish Society for Structural Science and Engineering Special Publication, Oct., 129 pp.

[113] Van de Pitte D., 'Berekeningen van Constructies : deel I', uitg. Story, Gent, 1979, 614 pp.

[114] Nethercot D.A., 'Steel beam to column connections - a review of test data and their applicability to the evaluation of the joint behaviour of the performance of Steel frames', CIRIA Project Record, RP 338, 1985.

[115] Hawkins N.M., Mitchell D. and Roeder C.W., 'Moment resisting connections for mixed construction', A.I.S.C. Engineering Journal, American Institute of Steel Construction, First Quarter, 1980, pp. 1-10.

[116] Roeder C.W. and Hawkins N.M., 'Connections between steel frames and concrete walls', AISC Engineering Journal, American Institute of Steel Construction, First Quarter, 1981, pp. 22-29.

[117] Frye M.J. and Morris G.A., 'Analysis of flexible connected steel frames', Canadian Journal of Civil Engineering, 1975, Vol. 2, pp. 280-291.

[118] Sommer W.H., 'Behaviour of welded header plate connections', MSc. Thesis, University of Toronto, Ontario, Canada, 1969.

[119] Kennedy D.J.L., 'Moment rotation characteristics of shear connections', AISC Engineering Journal, American Institute of Steel Construction, 1969, Oct., pp. 105-115.

[120] Jones S.W., Kirby P.A. and Nethercot D.A., 'Modelling of semi-rigid connection behaviour and its influence on steel column behaviour', in **Joints in Structural Steelwork**, eds. Howlett J.H., Jenkins W.N. and Stainsky R., 1981, Pentech. Press, London, pp. 5.73-5.87.

[121] Yee K.L. and Melchers R.E., 'Moment-rotation curves for bolted connections', Journal of the Structural Division, A.S.C.E., 1986, Vol. 112, N° 3, March, pp. 615-635.

[122] Nethercot D.A. and Zandonini R., 'Methods of prediction of joint behaviour - beam to column connections', in **Connections in Steel Structures: Structural Connection Stability and Strength**, ed. by Narayanan, Elsevier Applied Science Publishers, London, 1989, pp. 23-62.

[123] Kukreti A.R., Murray T.M. and Ablomaali A., 'End-plate connection moment-rotation relationship', Journal of Constructional Steel Research, Vol. 8, 1987, Special issue of Joint flexibility in Steel Frames, pp. 137-157.

[124] Benterkia Z, ' End-Plate Connections and Analysis of Semi-Rigid Steel Frames', PhD Thesis, University of Warwick, 1990 (in preparation).

[125] Abramowitz M. and Stegun I.A., 'Handbook of Mathematical functions', Dover Publications, New York, 1965.

[126] Chapra S.C. and Canale R.P., 'Numerical methods for Engineers', McGraw-Hill, 1985, 570 pp.

[127] Younger M.S., 'A Handbook for linear regression', Duxbury Press, 1979, 569 pp.

Appendix I

Partial shear interaction in both Eurocode 4 and BS 5950:Pt.3

In clause 6.3.2.2 of the draft Eurocode 4 [3] two different methods of analysis are given for partial interaction of composite beams, using both stiff and flexible connectors.

The first method, called here the **interpolation method**, is based on a linear interpolation between the plastic collapse load w_p, of the beam with full shear connection, ($N = N_f$), and the plastic collapse load w_{pa}, of the steel beam only ($N = 0$). The safe load carried by a beam with N ductile connectors, where $0.5N_f \leq N \leq N_f$ is given by eq. (I.1):

$$w_{pp}^{i} = w_{pa} + \frac{N}{N_f}(w_p - w_{pa}) \tag{I.1}$$

The second method, called here the **equilibrium method**, gives the theoretical reduced collapse load of a beam with partial shear connection, obtained from equilibrium under the assumption that the stud connectors have a perfect plastic load-slip behaviour as in Fig. I.1.

For ductile connectors both methods are presented in a qualitative graph in Fig. I.2, just as in clause 6.2.3.2 of Eurocode 4.

In clauses 4.4.5.5 and 4.5.2 and Appendix B of the draft 5950:Pt.3 [4], both the **interpolation method** and the **equilibrium method** are given, to determine the minimal number of connectors between points of maximum and zero moment along the beam. The minimal connector ratio is limited to 0.4 for spans up to 10 m, regardless of the method used to calculate the corresponding ultimate load, w_{pp}. This ratio varies linearly from 0.4 to 1.0 for spans between 10 m and 16 m.

For sagging bending, only two expressions for the plastic moment capacity of composite simply supported beams with partial shear connection characterise the entire range of stress diagrams, depending on the position of the plastic neutral axes (P.N.A.) in the steel profile.
For the P.N.A. in the top flange as in Fig. I.3(a):

$$M_{pp}^{e} = F_{pp}\left(t_c + t_h + y_a - \frac{y_c}{2}\right) + 2b_1 y_a f_{ad}\left(y_a - \frac{y_a}{2}\right) \tag{I.2}$$

$$\begin{aligned} \text{with } F_{pp} &= NQ_d; \\ y_c &= \frac{F_{pp}}{f_{cd} b_e}; \\ \text{and } y_a &= \frac{A_a f_{ad} - F_{pp}}{2b_1 f_{ad}} \end{aligned}$$

For the P.N.A. in the steel as in Fig. I.3(b):

$$M_{pp}^{e} = F_{pp}\left(t_c + t_h - \frac{y_c}{2}\right) + 2b_1 t_1 f_{ad}\left(y_a - \frac{t_1}{2}\right) + b_2 f_{ad}\left(y_a - t_1\right)\left(2y_a - y_a - t_1\right) \tag{I.3}$$

$$\begin{aligned} \text{with } F_{pp} &= A_a f_{ad} - 2b_1 t_1 f_{ad} - 2b_2\left(y_a - t_1\right) f_{ad}; \\ y_c &= \frac{F_{pp}}{f_{cd} b_e}; \\ \text{and } y_a &= \frac{f_{ad}\left(A_a + 2t_1 b_2 - 2b_1 t_1\right) - F_{pp}}{2b_2 f_{ad}} \end{aligned}$$

Similarly, two expressions exist for the plastic moment capacity of class 1 or 2 beams in hogging depending on the moment of slip between the concrete slab and the steel beam, as shown in Figs. I.4(a) and (b).
For the P.N.A. of the slab outside the slab as in Fig. I.4(a):

$$M_{pp}^{e\prime} = F_{pp}\left(y_r + y_a\right) + M_{pa} - \frac{d_a^2 b_2 f_{rd}}{4} \tag{I.4}$$

$$\begin{aligned} \text{with } F_{pp} &= A_r f_{rd} \\ d_a &= \frac{F_{pp}}{b_2 f_{ad}} \end{aligned}$$

For the P.N.A. of the slab inside the slab as in Fig. I.4(b):

$$M_{pp}^{e\prime} = F_{pp}\,(y_r + y_a) + M_{pa} - \frac{d_a^2 b_2 f_{ad}}{4} + (A_r f_{rd} - F_{pp})\left(y_r - t_h - \frac{d_c}{2}\right) \qquad \text{(I.5)}$$

$$\begin{aligned} \text{with } F_{pp} &= NQ_d \\ d_a &= \frac{F_{pp}}{b_2 f_{ad}} \\ d_c &= \frac{A_r f_{rd} - F_{pp}}{b_e f_{cd}} \end{aligned}$$

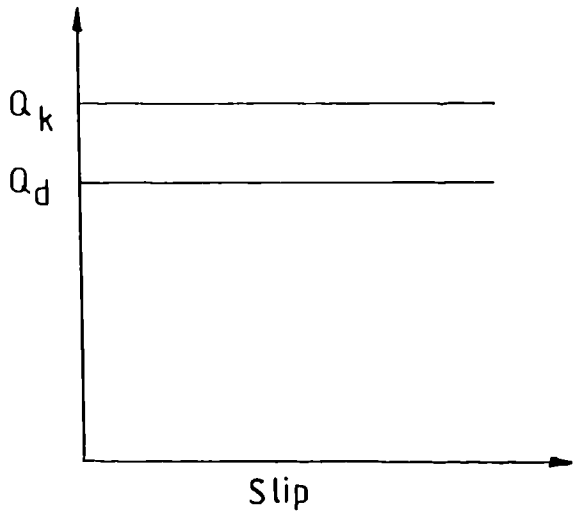

Figure I.1: Ideal plastic load – slip behaviour of the stud connectors.

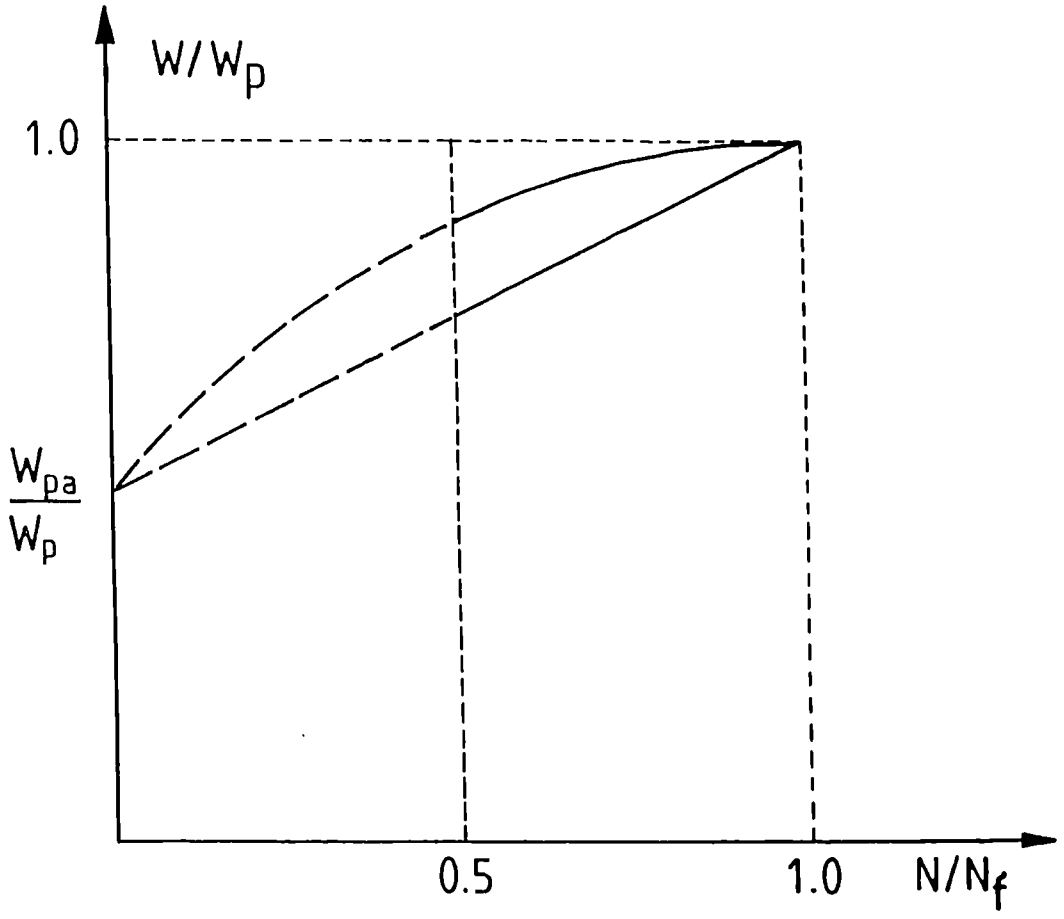

Figure I.2: Qualitative graph of the relationship between the load ratio and the connector ratio for both interpolation and equilibrium methods.

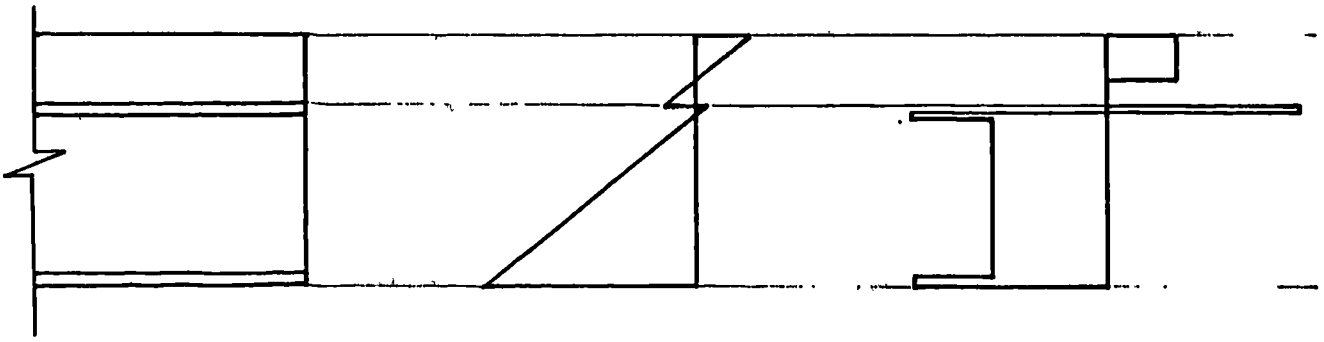

Figure I.3(a): Strain and stress diagram of composite cross-section with partial interaction in sagging bending with the plastic neutral axis in the top steel flange.

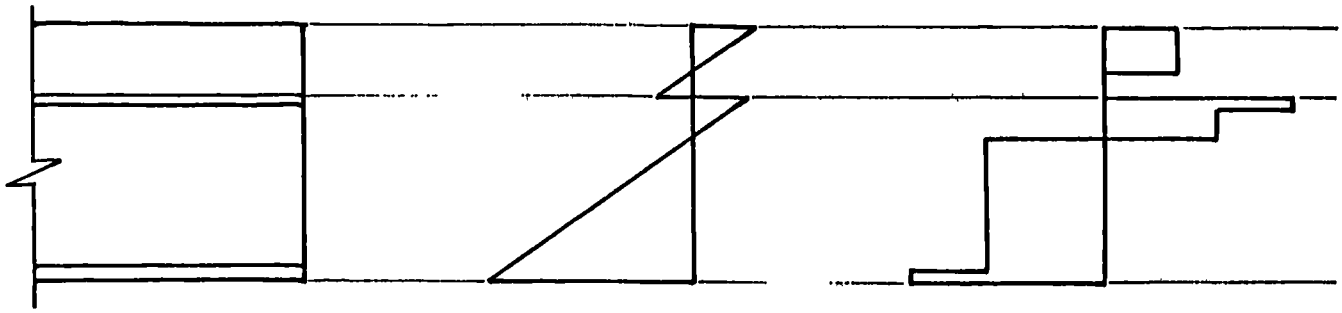

Figure I.3(b): Strain and stress diagram of composite cross-section with partial interaction in sagging bending with the plastic neutral axis in the web of the steel profile.

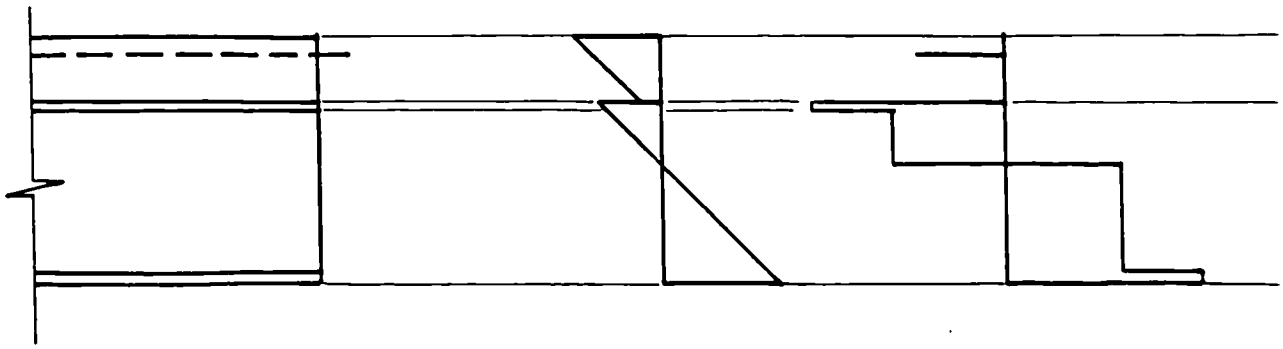

Figure I.4(a): Strain and stress diagram of composite cross-section with partial interaction in hogging bending with the plastic neutral axis outside the concrete slab.

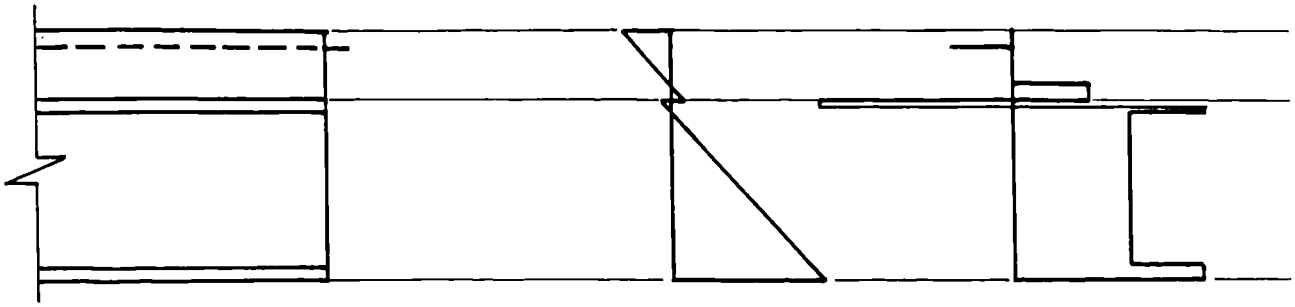

Figure I.4(b): Strain and stress diagram of composite cross-section with partial interaction in hogging bending with the plastic neutral axis in the concrete slab.

Appendix II

Manual for the usage of programme EPPIB

VARIABLES MENTIONED IN THE MANUAL

EPA(I,L)	strain at the centroid of the steelprofile at node I of the beam, under load/interaction cycle L
EPAU	failure strain of the structural steel
EPAB	strain in bottom steel fibre
EPAT	strain in top steel fibre
EPC(I,L)	strain at the centroid of the slab, at node I of the beam, under load/interaction cycle L
EPCT	strain in top concrete fibre
EPCU	crushing strain of concrete, i.e. -0.0035
F(I,L)	longitudinal interface shear force at node I of the beam, under load/interaction cycle L
FA(I,L)	resultant force in steel profile at node I, under cycle L
FC(I,L)	resultant force in concrete slab at node I, under cycle L
GMA(I,L)	slip at node I, under load/interaction cycle L
GMAX	relative displacement between conncrete slab and steel beam, which corresponds with stud shear failure, for the type of slab and stud used.
MA(I,L)	moment in steel profile at node I, under cycle L
MC(I,L)	moment in concrete slab at node I, under cycle L
ME(I,L)	external applied moment at node I, under cycle L
PH(I,L)	curvature at node I, under cycle L
SST(I,L)	slip strain at node I
WD	dead load of the beam (N/m)
WP	plastic collapse load of the beam (N/m)
WL	live load of the beam (N/m)
WS1	design value of live load on the beam (N/m)
WSS1	maximum allowed value of live load (N/m
WU1	u.d. failure load of the beam of span 1
WU2	u.d. failure load of the beam of span 2
WUM	maximum design load =1.6*WS1+1.4*WD
ZK(N)	coordinates of the steel profile in a local coordinate system, with N = 6
ZR(N)	coordinates of the reinforcement in a local coordinate system, with N = 0,1 or 2

INTRODUCTION

EPPIB is an Elasto-plastic program simulating Partial interaction of Composite Beams, written in Fortran 77. Both Simply Supported Beams (S.S.Beams) and Continuous Beam (C.Beams) of class 1 and 2 (as defined in the 1985 draft of Eurocode 4) can be analysed in order to find their failure load and mode.

Roughly speaking, the program can be split up in a numerical and an analytical part. The analytical part will deduce from a mimimum of information (DATA-FILE) all design values needed in order to design the beam in accordance with the draft Eurocode 4 [3] or with the draft BS5950:Pt.3 [4], and to prepare the beam sample for the numerical part, which consists of a mathematical simulation of the behaviour of the beam.

II.1. ANALYTICAL PART

For a given geometry of beam and beam cross section and known material properties, the elastic section characteristics (GEOM) and a number of section constants (SAPO) are calculated, together with the plastic moment of resistance and corresponding longitudinal force of the sections (PLCS).

For a given degree of partial interaction, the corresponding design failure load of the beam can now be found in accordance with the draft Eurocode 4 or with the draft BS5950:Pt.3 (FALD).
The live load, corresponding with the failure load, is checked against a maximum value (WL<WSl) (DIMCHK) and the maximum deflection and stresses under Servicability Limit State are checked (DEFLCT) in accordance with the draft Codes.
These last two subroutines only warn the user of taking an unrealistic beam to analyse, but they will not discontinue the process.

For given stud geometry and material characteristics, the number and the spacing of studs is calculated in accordance with Eurocode 4 or with BS5950:Pt.3 (CONNUM).

At this point in the program the analysis is finished, and if no warnings appeared, the beam is realistically designed in accordance with the either of the two draft Codes.

II.2. NUMERICAL PART

The behaviour of the beam is simulated mathematically assuming:

- -the Bernouilli hypothesis for every cross-section
- -the curvature of the slab and the steel profile are the same in one cross-section
- -the behaviour of studs is the same in sagging or hogging bending
- -the shear force is negligible in the calculation of yield strength
- -the longitudinal interface shear force is transferred continuously along the beam.

The beam is divided into a number of elements (IN-1) and each element is defined by the beam characteristics in the two nodes on either side of the element. For a continuous beam, the mid-support section is also the division between two elements and has node number IP.

The numerical part of the program has 3 loops, 2 of which are active for S.S.Beams and one of which is only used for C.Beams.

The outer iterative loop will either change the degree of partial interaction of the beam, while the load factor remains 1, or it will decrease the load factor, while the degree of interaction remains constant until failure of the beam is met. Failure can occur either by crushing of the concrete at mid span (EPCT > EPCU) or by excessive yielding of the structural steel (EPAT or EPAB > EPA2) or by stud shear failure of the connectors (GMA(I,L) > GMAX).

In the inner loop, starting with the boundary condition F(1,L)=0 the shooting method is used to find the slip, GMA(1,L) at the left hand support which makes the longitudinal force, F(IN,L) at the right hand support tend to zero (smaller than A4). In each node, both equilibrium and compatibility of the deformation at the concrete-steel interface, have to be fulfilled before going to the next node. The former is done by a 3 dimensional Newton Raphson method (NERAP3) which finds from the force, F(I,L), and the external moment, ME(I,L), the values for the strains at the centroids of the steel girder, EPA(I,L), and the slab, EPC(I,L), and the value of the curvature, PH(I,L), in the same node. The latter is done by consequently expressing the slip strains, SST(I,L), in the different nodes.
A numerical integration method is used to express equilibrium in the steel profile, while an analytical expression is used for the concrete slab. For concrete the longitudinal force and moment due to the reinforcement is added afterwards in FCMC. For the steel-profile a transformed trapezoidal rule is used in FAMA, which uses 6 nodes.

For a C.Beam a second loop is needed. In order to express compatibility of the deformation at the internal support (U(IP,L) < A6) a moment redistribution takes place. In most cases the elastic moment is shed from the internal support to the mid-span to allow for plasticity and partial interaction.

II.3. THE SUBROUTINES

In Fig 3.5 a flow-chart of the main steps in the program is drawn. The subroutines appearing on this flow-chart and their main function are listed underneath

GEOM calculates the elastic neutral axes of the critical cross sections, the area and second moment of inertia of different sections and the lever arm (Z) between the longitudinal forces in a section. For a rolled section (N=1) a transformation of the flanges and web is performed without a change of area.

SAPO calculates a number of constants, used in the other subroutines; like the tensile strength of concrete, the coordinates of the flanges and the reinforcement in a local coordinate system (see Fig. 3.12).

PLCS calculates the moments of resistance, the longitudinal force and the plastic neutral axes in hogging and sagging bending -in accordance with Eurocode 4 or BS5950:Pt.3 - of every critical cross section, together with the class of the beam.

SLIP calculates the exponents of the theoretical load-slip curve of a stud connector, from two points on the experimental curve and the asymptotic value for the shear of this curve.

DIMCHK calls first subroutine FALD, which calculates the design failure load. Then checks whether this failure load is realistic for that beam by comparing the corresponding imposed load (WL = (WP-1.4WD)/1.6) with a maximum value (WS1), depending on the type of floor. If WL>WS1, then the width of the slab of the beam is increased. Finally, subroutine DEFLCT is called, which checks the deflection and the stresses under S.L.S. Warnings are given if the live load exceeds the given limit WS1 or when the deflection or stresses become excessive.

FALD calculates the design failure load of the beam in accordance with the `Interpolation method'of draft Eurocode 4, using either a plastic mechanism for the beam (class 1 & 2 beam) (NEC4=0) or using an elastic moment distribution with 30% redistribution (class 2 beam) (NEC4=1). The choice is upto the designer, although the latter method is only valid for class 2 beams. For C.Beams and S.S.Beams a combination of udl and one point load or only a udl can be applied.

```
For  NEC4 = 0
  W1(L) = WU1              ;     P1(L) = PC1*WU1*EL1
 For NDSN = 0
   W2(L) = WUM
 For NDSN = 1              ;     P2(L) = PC2*WU2*EL2
   W2(L) = PD2*WU2
```

```
For NEC4 = 1
  W1(L) = PD1*WUE          ;    P1(L) = PC1*W1(L)*EL1
  W2(L) = PD2*WUE          ;    P2(L) = PC2*W2(L)*EL2
```

FALD also calculates the design ultimate load in accordance with the `Equilibrium method' of Eurocode 4 or BS5950:Pt.3 for simply supported beams with a udl only.

DEFLCT calculates the maximum deflection and stress under S.L.S

CONNUM calculates the number and the spacing of the stud connectors, in accordance with Eurocode 4 or BS5950:Pt3.

NERAP Is the main subroutine of the program. For each moment distribution a longitudinal force and a slip distribution can be found, using the Predictor-Corrector method on F(I,L) and GMA(I,L) and expressing equilibrium and compatibility in every node. Afterwards, a false-position method is used on GMA(1,L) and F(IN,L) to find a solution which fits the boundary condition. For C.Beams, compatibility of the deflection needs to be fulfilled by allowing for a moment redistribution. Afterwards, an interpolation method on ME(IP,L) and U(IP,L) is used in order to find a compatible solution.

NERAP3 A 3 dimensional Newton-Raphson system is solved (equations (3.8(a) to 3.8(c))) numerically by finding in every section the values of EPA(I,L), EPC(I,L) and PH(I,L). FAMA and FCMC are called in order to calculate FA(I,L) & MA(I,L) and FC(I,L) & MC(I,L) for every EPA(I,L), PH(I,L) and EPC(I,L), PH(I,L) combination, which are needed in the matrix (3.18).

INVERS calculates the deflection of the beam from the curvature in every node, solving a system of simultaneous linear equations, each one expressing a first order differentiation.

SLINEQ calculates the error in the 3 dimensional Newton-Raphson method by solving a system of 3 linear equations.

FAMA the values of FA(I,L) and MA(I,L) are calculated, using a stress-strain curve with strain hardening and with or without a yield platform.

FCMC the values of FC(I,L) and MC(I,L) are calculated, using either a parabolic-rectangular or a 4th order stress-strain curve. In both cases with or without tensile strength of concrete. In the latter case analytical expressions for FC and MC are programmed.

II.4. DATA-FILE (N m units throughout)

The variables read into the input file EPPIB are explained underneath. The number between brackets in front of them indicates the start of a new line number.

(1) NAME the name and date of the run can be specified with less than 30 characters.

(2) AE(M) the modular ratios of concrete for short time and long time loading are required.

(3)	EA	the Young's modulus of structural steel in the elastic range
	EP	the Young's modulus of structural steel in the plastic range
	EPAE	the yield strain of the reinforcing bars
	EPAM	the yield strain of the structural steel
	PEPN	ratio of the yield strain at the end of the yield platform to the yield strain at the beginning of the yield platform (value 1.0 means no yield platform).
	EPA1	the strain for which failure of the beam, due to excessive yielding is accepted (recommended value = 0.04)
	EPA2	fixed value which keeps the strain within certain boundaries with the shooting method (recommended value = 0.1)
(4)	NSTC	= 0 4th order stress-strain curve for concrete = 1 parabolic-rectangular stress-strain curve for concrete
	EPR1	limiting value of strain in the reinforcement for which failure is accepted (recommended value = 0.04)
	EPR2	fixed value in order to keep the strain within certain boundaries with the shooting method (recommended value = 1.0)
	CM	fraction of EPCM, corresponding to the maximum tensile stress (recommended value = 0.055)
	CX	fraction of EPCM from which value onwards the tensile stress in concrete is zero (recommended value is 0.06)
	IXP	counter for initialisation of certain variables.
(5)	EPCN	crushing strain of uniaxial compressed concrete
	EPC2	fixed value for compressive strain in order to keep it within boundaries for the shooting method (recommended value = -0.08)
	EPCM	value of compressive strain, where the concrete reaches its maximum strength (recommended value = -0.002)
	EPCU	maximum strain where 4th order curve is used (recommended value = - 0.008)
	SGMU	characteristic cylinder strength of concrete
	ESH	free shrinkage strain of concrete
(6)	LWG	= 0 light weight concrete = 1 normal weight concrete
	WCON	density of concrete (N/m3)
	WGHS	weight of steelprofile (N/m)
	WPPR	weight of partitions (N/m2)
	WIIX	weight of fixings (N/m2)
(7)	PSA	partial safety factor on structural steel strength
	PSCU	partial safety factor on concrete strength
	PSRU	partial safety factor on strength of reinforcement
(8)	LAY	number of layers of reinforcement (0,1 or 2)

(9)	LSH	geometry of slab cross section (see Fig.II.1) = 1 without metal decking or haunch = 2 with haunch = 3 with metal decking transverse to the beam
	BC	width of the slab (m)
	TC	thickness of the slab (m)
	BH	width of haunch or metal decking in transverse direction
	HH	height of haunch or metal decking
	PWG	weight of haunch or layer of metal decking as a % of the weight of the slab
	ART	area of the top layer of reinforcement (m2)
	YRT	distance of the top layer of reinforcement from the top concrete fibre (m)
	ARB	area of the bottom layer of reinforcement (m2)
	YRB	distance of the bottom layer of reinforcement from the top concrete fibre (m)
	NRS	= 1 for rolled sections = 0 for welded sections
	N	number of plates on a steel profile (3 or 4)
(10)	B(J),H(J)	width and height of flanges, web and plates of a steel-profile
(11)	LSE	number of spans of the beam
	NCLD	= 0 in the outer loop the degree of partial interaction is changed = 1 in the outer loop the load factor is changed
(12)	EL1	length of the first span (m) (see Fig.II.2)
	PEL	proportion of the length of the second span to the first span
	PELM	maximum value of PEL according to Eurocode 4
	IN	total number of nodes
	IP	node number of the mid support section
(13)	ELP1	distance from left hand support to first point load
	ELP2	distance from left hand support to second point load.
	PC1	percentage of failure load as point load on first span
	PC2	percentage of failure load as point load on second span
	PD1	percentage of u.d.failure load as u.d.l. on first span
	PD2	percentage of u.d.failure load as u.d.l. on second span
	PRD	percentage of moment redistribution for global elastic analyses according to Eurocode 4.
	WSS1	maximum allowed live load on the beam (N/m2)
(14)	NLD	minimum number of outer loops, even when failure occurs in the first one
	LF	maximum number of outer loops
(15)	NEC4	= 0 a plastic collapse mechanism is used to find the ultimate design load in accordance with the `Interpolation method'of Eurocode 4.

= 1 an elastic momentdistribution with 30% redistribution is used in order to find the design load for class 2 beams.
= 2 the `Equilibrium method' is used in accordance with BS5950:Pt.3.
= 4 the `Equilibrium method' is used in accordance with Eurocode 4.

NDSN = 0 the load on the second span is restricted to the maximum design load WUM
= 1 the load on the second span is not restricted.

(16)LPR = 0 unpropped construction
= 1 propped construction

(17)JL,KN,IJ different number of maximum number of iterations, allowed for in different calculations

(18)CNS percentual increments of EPA(I,L), EPC(I,L) and PH(I,L) in
CNT order to calculate numerically the derivatives of
CNU longitudinal force and moment in function of these independant variables

A1,..A5 tolerances
A7 recommended values A1 = 1E-4
IUM A2 = 1E-5
A9 A3 = 10000.
A4 = 1000.
A5 = 5E-6
A7 = 1E-12
IUM= 25
A9 = .30

with A4 tolerance on the boundary condition F(IN,L)=0
and IUM tolerance on the boundary condition U(IP,L)=0, as a fraction of the maximum deflection with full interaction.

(19)NQ = 0 the ultimate shear strength of the stud equals the design value according to Eurocode 4.
= 1 the ultimate shear strength of the stud equals a value QM given later

HS height of the stud (m)
DS diameter of the stud (m)
XCM maximum spacing of connectors (m)
ECM tangens modulus of concrete (N/m2)
FU tensile strength of the stud shank (N/m2)
LSL type of theoretical load-slip curve
= 1 exponential curve with one exponent
= 2 tri-linear curve with falling branch
= 3 exponential curve with 2 exponents
PCS elasto-platic shear strength as a proportion of the ultimate shear strength
QU ultimate shear strength of stud (N)

QA elastic shear strength of stud (N)

GB slip corresponding to elasto-platic shear strength (m)
GMAX maximum slip for which failure occurs (m)
GA slip correspondimg to the elastic strength of the stud (m)

(20)NSL defines point where tri-linear load-slip curve for the studs changes slope.
NSLP similar as NSL.
NCK = 0 calculate the spacing by dividing a critical length by the number of connectors over that length
= 1 calculate the spacing by dividing a critical length by the real value obtained by dividing the longitudinal shear over that length by the design strength of the connector.
DPIP increment of the degree of interaction in consecutive iterations of the outer loop

PIP(1) partial interaction percentage for first run.
(21)RDT reduction factor on the elastic slip in order to use it as a starting value in the inner loop.
RED,..,RED4 reduction factors for various iterative loops;
recommended values : RED = 0.10
RED1 = 0.20
RED2 = 0.05
RED3 = 0.025
RED4 = 0.80

REM reduction factor (rec. value = 0.01)
(22)QM the maximum shear strength of the studs used as well in determining N, as in the numerical simulation
QBS the design shear strength of the studs according to

BS 5950:Pt.3, read automatically when NEC4 = 2

II.5. OUTPUT (N m units throughout)

There are two forms of output.
The first form is a listed output of the data-echo, the design values and the registration of convergence for every inner loop and in case of a C.Beam, the consecutive moment distributions, together with the percentage of redistribution for each load case. The failure mode for each load level or partial interaction level is stated before proceeding to the next level. The output file is called EPOUT.

The second form is a listed output of the values of

- moment;
- longitudinal force;
- slip;
- deflection;
- strain in top and bottom steel and concrete fibre;
- curvature and
- slip strain

in every 25 nodes along the beam. This output is called GRAPH and is used as input for the graphics program graf, which in turn produces formatted information for the package MATLAB.

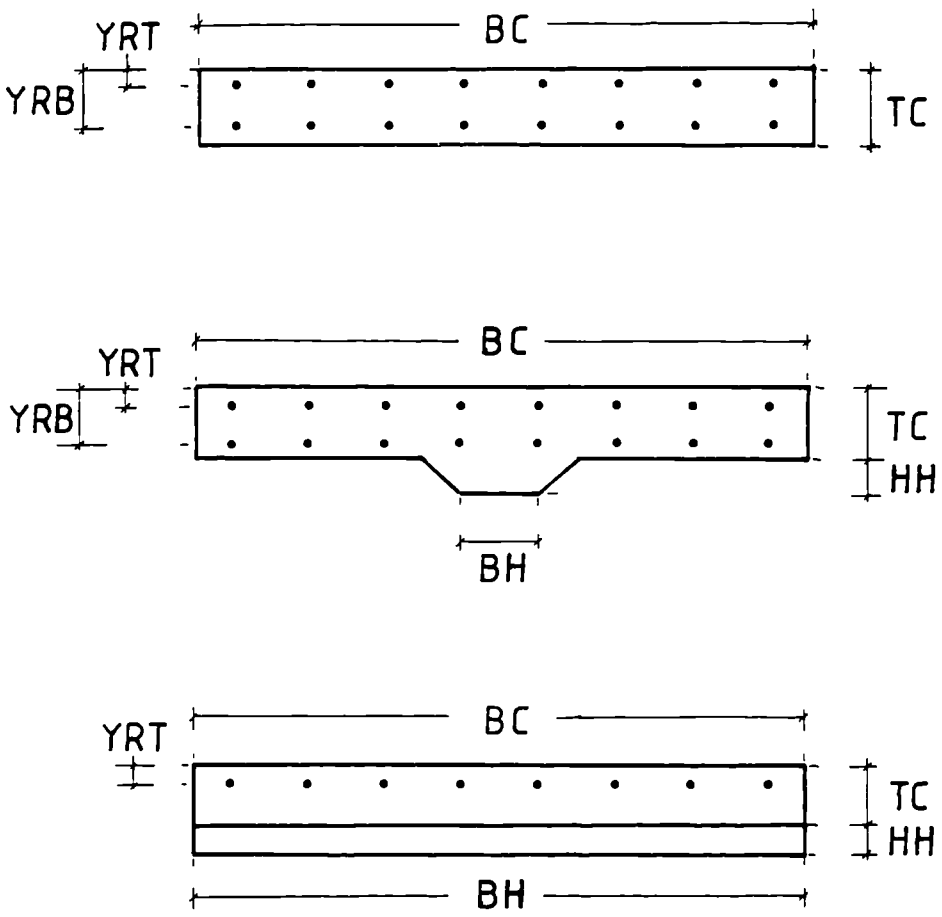

Figure II.1: Different slab geometries as defined by EPPIB.

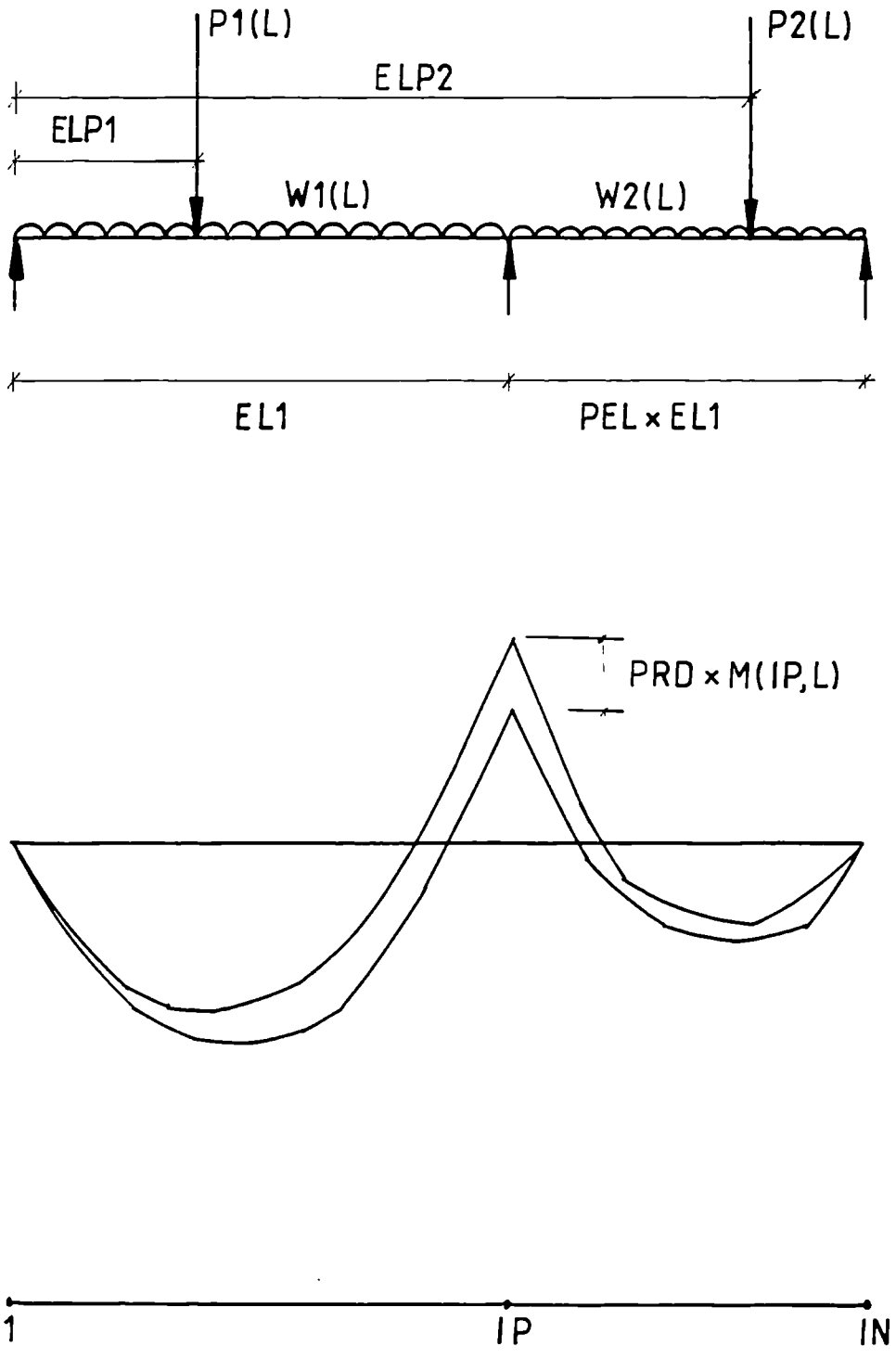

Figure II.2: Geometry and loading as defined by EPPIB.

Appendix III

Simplified deflection calculations

The deflection of a simply supported beam is given by eq. (III.1), where M_1 and V_1 represent the moment and the vertical shear force diagrams under unit load at a point b along the beam.

$$v_b = v_M + v_V$$

$$v_b = \int_l \frac{M M_1}{E_a I_c} dx + \int_l \frac{V V_1}{kG\Omega} dx \qquad \text{(III.1)}$$

If the vertical shear is assumed to be resisted only by the web of the steel beam, then $\Omega = h_a t_2$ and $k = 5/6$. When the point b is chosen in the middle of the beam, then the deflection in b under a vertical point load in b is given by eq. (III.2), while the deflection in b under a uniform distributed load is given by eq. (III.3).

$$v_b = \frac{Pl^3}{48 E_a I_c} + \frac{6(1+\nu)}{10 E_a \Omega} Pl \qquad \text{(III.2)}$$

$$v_b = \frac{5wl^4}{384 E_a I_c} + \frac{12(1+\nu)}{40 E_a \Omega} wl^2 \qquad \text{(III.3)}$$

The deflection calculation in the programme does not take account of the second term in these equations (III.1) to (III.3). An estimate of the error thus made in the assessment of the elastic deflection of three different beams from Table 3.5 is given in the table below:

beam spec.	v_b (mm)	v_M (mm)	$\frac{v_M - v_b}{v_M} \times 100$ (%)
P_1	11.45	9.42	−22
P_3	10.29	8.44	−22
A_6	19.17	16.56	−19

This simplification explains partly why the elastic deflections generated by the programme underestimate systematically the measured deflections.

Appendix IV

Tables with numerical results of values for the maximum slip along simply supported beams

In this appendix, numerical results of 3 different beam categories are given. The samples in the categories are represented by 3 letters and a number. The three letters characterise the category, while the number only indicates the sample number within that category. These letters stand for:

SRF = Simply supported beam **R**olled section **F**ull solid slab

SRM = Simply supported beam **R**olled section **M**etal decking slab

SPF = Simply supported beam **P**lated section **F**ull solid slab

Table IV.1(a): Maximum slip along composite beams with solid concrete slabs and rolled steel profiles, for different degrees of shear connection.

	SRF-1	*SRF*-2	*SRF*-3	*SRF*-4	*SRF*-5	*SRF*-6	*SRF*-7	*SRF*-8	*SRF*-9
l (m)	5.00	5.00	5.00	7.50	7.50	7.50	7.50	7.50	10.00
t_c (m)	0.125	0.125	0.125	0.125	0.125	0.125	0.125	0.125	0.150
b_c (m)	4.000	4.000	4.000	3.500	3.500	3.500	3.500	3.500	3.000
b_e (m)	1.250	1.250	1.250	1.875	1.875	1.875	1.875	1.875	2.500
rolled sections	IPE 220	IPE 220	IPE 220	IPE 270	IPE 270	IPE 270	IPE 270	IPE 270	457 × 191 UB98
f_{ck} (N/mm^2)	25.0	30.0	35.00	20.00	25.00	30.00	35.00	40.00	30.00
f_{ay} (N/mm^2)	355.	355.	355.	355.	355.	355.	355.	355.	355.
$d_{sh} \times h_{st}$ (mm)	19 × 95	19 × 95	19 × 95	19 × 95	19 × 95	19 × 95	19 × 95	19 × 95	19 × 95
w_p (kN/m)	77.19	79.45	80.96	51.93	53.79	55.03	55.93	56.61	119.0
w_{pa} (kN/m)	32.86	32.86	32.86	24.78	24.78	24.78	24.78	24.78	64.18
$\gamma_m(50)$ (mm)	3.18	3.40	3.79	3.24	3.75	3.85	3.87	3.94	4.00
$\gamma_m(60)$ (mm)	2.56	2.77	3.42	2.76	3.22	3.43	3.46	3.54	3.36
$\gamma_m(70)$ (mm)	–	–	2.95	2.45	2.96	3.14	3.18	3.29	2.91
$\gamma_m(80)$ (mm)	–	–	–	2.12	2.81	–	3.00	3.16	2.43
$\gamma_m(90)$ (mm)	–	–	–	–	–	–	–	3.12	–
$\gamma_m(100)$ (mm)	–	–	–	–	–	–	–	–	–
y_p (mm)	67.99	56.66	48.56	78.02	62.42	52.02	44.58	39.01	104.66
F_p (kN)	1204	1204	1204	1658	1658	1658	1658	1658	4448
h_t (mm)	345	345	345	395	395	395	395	395	617.4
N_f $(-)$	16	15	14	26	22	20	19	19	53

Table IV.1(b): (continued ...)

	SRF-10	*SRF*-11	*SRF*-12	*SRF*-13	*SRF*-14	*SRF*-15	*SRF*-16	*SRF*-17	*SRF*-18
l (m)	10.0	10.0	10.0	10.0	10.0	10.0	10.0	12.5	12.5
t_c (m)	0.140	0.140	0.150	0.135	0.135	0.140	0.135	0.165	0.150
b_c (m)	3.000	3.000	3.000	3.000	3.000	3.500	3.000	3.500	3.000
b_e (m)	2.500	2.500	2.500	2.500	2.500	2.500	2.500	3.125	3.000
rolled sections	406 × 178 UB67	356 × 171 UB67	356 × 127 UB39	356 × 127 UB39	356 × 127 UB39	*HEA* 300	356 × 127 UB33	533 × 210 UB122	533 × 210 UB122
f_{ck} (N/mm^2)	35.00	35.00	35.00	30.00	25.00	30.00	30.00	30.00	30.00
f_{ay} (N/mm^2)	355.	355.	355.	355.	355.	355.	355.	355.	355.
$d_{sh} \times h_{st}$ (mm)	19 × 95	19 × 95	19 × 95	19 × 95	19 × 95	19 × 95	19 × 95	19 × 95	19 × 95
w_p (kN/m)	77.24	71.58	42.93	40.43	39.85	76.85	35.05	110.1	105.8
w_{pa} (kN/m)	38.74	34.88	18.39	18.39	18.39	39.92	15.33	58.84	58.84
$\gamma_m(50)$ (mm)	4.54	4.76	6.09	5.26	5.03	4.17	5.83	5.07	4.62
$\gamma_m(60)$ (mm)	4.20	4.44	5.74	4.83	4.57	3.52	5.14	3.99	3.62
$\gamma_m(70)$ (mm)	3.55	3.66	5.60	4.56	4.26	3.06	4.64	3.46	3.08
$\gamma_m(80)$ (mm)	2.85	3.33	–	4.43	4.09	2.66	3.93	2.89	2.56
$\gamma_m(90)$ (mm)	–	3.15	–	–	–	2.45	–	–	–
$\gamma_m(100)$ (mm)	–	–	–	–	–	1.68	–	–	–
y_p (mm)	61.22	50.96	35.37	41.27	49.52	95.28	35.04	104.11	108.45
F_p (kN)	3035	3032	1754	1754	1754	4049	1489	5531	5531
h_t (mm)	549.4	504.0	502.8	487.8	487.8	430	483.5	709.6	694.6
N_f $(-)$	35	35	20	21	24	48	18	66	66

Table IV.1(c): (continued ...)

	SRF-19	*SRF*-20	*SRF*-21	*SRF*-22	*SRF*-23	*SRF*-24	*SRF*-25	*SRF*-26	*SRF*-27
l (m)	12.50	12.50	12.50	12.50	12.50	15.00	15.00	15.00	15.00
t_c (m)	0.140	0.170	0.150	0.150	0.135	0.165	0.150	0.150	0.180
b_c (m)	3.000	4.000	3.000	3.000	3.000	3.500	3.000	4.000	4.000
b_e (m)	3.000	3.125	3.000	3.000	3.000	3.500	3.000	3.750	3.750
rolled sections	457 × 152 UB74	406 × 178 UB60	406 × 178 UB60	356 × 171 UB51	356 × 171 UB67	686 × 254 UB170	IPE 600	IPE 600	533 × 210 UB109
f_{ck} (N/mm^2)	30.00	30.00	20.00	35.00	30.00	25.00	30.00	40.00	30.00
f_{ay} (N/mm^2)	355.	355.	355.	355.	355.	355.	360.	360.	355.
$d_{sh} \times h_{st}$ (mm)	19 × 95	19 × 95	19 × 95	19 × 95	19 × 95	19 × 95	19 × 95	19 × 95	19 × 95
w_p (kN/m)	58.29	47.59	42.89	36.30	44.60	119.8	77.64	81.57	71.22
w_{pa} (kN/m)	29.48	21.46	21.46	16.27	22.02	71.81	44.31	44.31	35.24
$\gamma_m(50)$ (mm)	5.24	7.17	5.50	6.42	5.61	4.41	5.17	5.53	7.22
$\gamma_m(60)$ (mm)	4.36	6.49	4.79	6.15	5.13	3.36	3.90	4.80	6.04
$\gamma_m(70)$ (mm)	4.28	6.06	4.05	5.99	4.19	2.80	3.35	4.16	5.32
$\gamma_m(80)$ (mm)	3.76	5.91	3.73	5.86	4.06	–	2.84	3.45	4.66
$\gamma_m(90)$ (mm)	–	–	–	–	–	–	–	–	–
$\gamma_m(100)$ (mm)	–	–	–	–	–	–	–	–	–
y_p (mm)	66.16	50.78	79.35	38.54	59.45	146.4	110.1	66.06	76.35
F_p (kN)	3374	2698	2698	2293	3032	7259	5615	5615	4920
h_t (mm)	601.3	576.4	556.4	505.6	499.0	857.9	750.0	750.0	719.5
N_f $(-)$	40	32	41	27	36	97	67	64	58

Table IV.1(d): (continued ...)

	SRF-28	*SRF*-29	*SRF*-30	*SRF*-31	*SRF*-32	*SRF*-33	*SRF*-34	*SRF*-35	*SRF*-36
l (m)	15.00	15.00	15.00	15.00	17.50	17.50	17.50	17.50	17.50
t_c (m)	0.170	0.135	0.140	0.135	0.135	0.150	0.150	0.150	0.135
b_c (m)	4.000	2.750	3.000	2.500	5.000	5.000	5.000	5.000	4.500
b_e (m)	3.750	2.750	3.000	2.500	4.375	4.375	4.375	4.375	4.375
rolled sections	533 × 210 UB109	533 × 210 UB82	457 × 191 UB74	457 × 191 UB74	762 × 267 UB147	686 × 254 UB152	686 × 254 UB152	686 × 254 UB170	686 × 254 UB140
f_{ck} (N/mm^2)	30.00	30.00	35.00	35.00	30.00	40.00	35.00	35.00	30.00
f_{ay} (N/mm^2)	355.	355.	355.	355.	355.	360.	360.	360.	355.
$d_{sh} \times h_{st}$ (mm)	19 × 95	19 × 95	19 × 95	19 × 95	19 × 95	19 × 95	19 × 95	19 × 95	19 × 95
w_p (kN/m)	69.49	46.14	40.79	39.50	82.46	83.57	82.65	91.94	72.78
w_{pa} (kN/m)	35.24	24.95	20.90	20.90	48.66	46.94	46.94	57.88	42.91
$\gamma_m(50)$ (mm)	6.83	5.47	6.27	5.63	5.20	6.15	5.95	5.62	5.43
$\gamma_m(60)$ (mm)	5.71	4.50	5.11	4.53	4.51	5.07	4.89	4.51	4.52
$\gamma_m(70)$ (mm)	4.87	3.78	4.89	4.21	3.63	3.89	3.70	3.45	3.60
$\gamma_m(80)$ (mm)	4.43	3.27	4.24	3.84	2.88	3.31	3.12	2.87	2.98
$\gamma_m(90)$ (mm)	–	–	3.79	–	–	2.90	2.71	2.59	–
$\gamma_m(100)$ (mm)	–	–	–	–	–	2.62	2.42	2.29	–
y_p (mm)	76.35	79.27	56.68	68.03	89.79	70.35	80.40	89.85	85.44
F_p (kN)	4920	3706	3373	3373	6678	6977	6977	7798	6355
h_t (mm)	709.5	663.3	597.2	592.2	888.9	837.6	837.6	842.9	818.5
N_f $(-)$	58	44	39	39	79	80	80	89	75

Table IV.1(e): (continued ...)

		SRF-37	*SRF*-38	*SRF*-39	*SRF*-40	*SRF*-41	*SRF*-42	*SRF*-43	*SRF*-44	*SRF*-45
l	(m)	17.50	17.50	17.50	20.00	20.00	20.00	20.00	20.00	20.00
t_c	(m)	0.170	0.175	0.135	0.140	0.150	0.150	0.175	0.150	0.150
b_c	(m)	4.000	4.000	2.750	5.000	5.500	5.000	4.000	3.000	3.000
b_e	(m)	4.000	4.000	2.750	5.000	5.000	5.000	4.000	3.000	3.000
rolled sections		610 × 229 UB140	610 × 229 UB125	533 × 210 UB82	914 × 305 UB224	838 × 292 UB194	762 × 267 UB147	610 × 229 UB140	686 × 254 UB140	610 × 229 UB125
f_{ck}	(N/mm^2)	35.00	35.00	30.00	30.00	30.00	35.00	35.00	35.00	35.00
f_{ay}	(N/mm^2)	360.	355.	345.	355.	360.	355.	355.	355.	355.
$d_{sh} \times h_{st}$	(mm)	19 × 95	19 × 95	19 × 95	19 × 95	19 × 95	19 × 95	19 × 95	19 × 95	19 × 95
w_p	(kN/m)	73.46	65.87	33.90	109.8	92.15	65.79	56.16	55.55	46.26
w_{pa}	(kN/m)	38.99	34.66	18.33	68.53	55.11	36.67	29.43	32.39	26.14
$\gamma_m(50)$	(mm)	6.35	6.89	6.29	5.19	5.93	6.95	8.44	5.92	6.49
$\gamma_m(60)$	(mm)	5.13	6.27	5.12	4.10	4.75	5.61	6.92	4.57	5.06
$\gamma_m(70)$	(mm)	4.25	5.27	4.24	3.05	3.42	4.56	5.73	3.83	4.37
$\gamma_m(80)$	(mm)	3.76	4.56	3.60	2.43	2.76	3.78	4.87	3.17	3.58
$\gamma_m(90)$	(mm)	3.46	4.09	–	–	–	–	4.29	–	–
$\gamma_m(100)$	(mm)	–	–	–	–	–	–	3.66	–	–
y_p	(mm)	80.95	71.41	77.00	118.68	104.68	67.50	79.80	106.52	95.22
F_p	(kN)	6422	5666	3598	10120	8898	6694	6352	6358	5666
h_t	(mm)	787.0	786.9	663.3	1050.3	990.7	903.9	792.0	833.5	761.9
N_f	$(-)$	73	65	43	120	105	77	73	73	65

Table IV.2(a): Maximum slip along composite beams with rolled steel profiles and composite slabs, spanning perpendicular to the beam, for different degrees of shear connection.

		SRM-1	*SRM*-2	*SRM*-3	*SRM*-4	*SRM*-5	*SRM*-6	*SRM*-7	*SRM*-8	*SRM*-9	*SRM*-10
l	(m)	5.00	7.50	10.00	10.00	10.00	10.00	10.00	12.50	12.50	12.50
t_c	(m)	0.090	0.125	0.125	0.125	0.125	0.120	0.110	0.125	0.100	0.084
t_h	(m)	0.050	0.035	0.030	0.040	0.040	0.040	0.030	0.040	0.060	0.046
b_e	(m)	1.250	1.875	2.500	2.500	2.500	2.500	2.500	3.125	3.000	2.500
rolled sections		203 × 133 UB25	IPE 270	406 × 140 UB46	356 × 171 UB51	356 × 171 UB51	305 × 165 UB46	305 × 127 UB48	406 × 140 UB46	356 × 171 UB51	356 × 171 UB57
f_{ck}	(N/mm^2)	40.00	40.00	35.00	25.00	40.00	25.00	20.00	30.00	40.00	30.00
f_{ay}	(N/mm^2)	355.	355.	355.	355.	355.	355.	355.	355.	355.	355.
$d_{sh} \times h_{st}$	(mm)	13 × 75	19 × 95	19 × 95	13 × 75	19 × 95	13 × 75	19 × 95	19 × 95	19 × 95	19 × 95
w_p	(kN/m)	85.80	64.83	56.15	57.38	59.69	48.11	44.89	37.15	37.68	36.63
w_{pa}	(kN/m)	29.54	24.78	25.25	25.42	25.42	20.83	20.05	16.17	16.27	18.33
$\gamma_m(50)$	(mm)	5.27	5.92	5.90	5.89	6.29	6.30	4.69	8.02	7.65	5.40
$\gamma_m(60)$	(mm)	5.06	4.89	5.49	5.22	5.95	5.76	4.15	7.35	7.12	3.89
$\gamma_m(70)$	(mm)	5.51	4.78	4.85	5.09	5.72	5.45	3.79	6.71	7.84	–
$\gamma_m(80)$	(mm)	–	4.89	4.84	4.84	5.39	5.36	3.56	7.13	8.76	–
$\gamma_m(90)$	(mm)	–	5.22	–	–	–	–	–	–	–	–
$\gamma_m(100)$	(mm)	–	–	–	–	–	–	–	–	–	–
y_p	(mm)	16.86	38.82	42.24	64.75	40.46	59.04	76.18	39.43	33.73	60.31
F_p	(kN)	1147	1658	2095	2293	2293	2091	2158	2095	2293	2563
h_t	(mm)	343	430	557	521	521	467	450	567	516	489
N_f	$(-)$	35	24	30	69	33	63	33	30	33	36

Table IV.2(b): (continued ...)

	SRM-11	*SRM*-12	*SRM*-13	*SRM*-14	*SRM*-15	*SRM*-16	*SRM*-17	*SRM*-18	*SRM*-19	*SRM*-20
l (m)	15.00	15.00	15.00	15.00	15.00	15.00	15.00	17.50	17.50	17.50
t_c (m)	0.125	0.135	0.125	0.080	0.125	0.080	0.084	0.125	0.125	0.120
t_h (m)	0.040	0.040	0.040	0.055	0.030	0.055	0.046	0.040	0.040	0.040
b_e (m)	3.750	3.750	3.750	3.500	3.500	3.500	3.000	4.000	4.000	4.000
rolled sections	610 × 229 UB140	610 × 229 UB113	533 × 210 UB109	533 × 210 UB92	457 × 191 UB74	457 × 152 UB74	406 × 178 UB60	686 × 254 UB140	610 × 229 UB140	610 × 229 UB125
f_{ck} (N/mm^2)	35.00	40.00	35.00	30.00	35.00	35.00	30.00	40.00	35.00	25.00
f_{ay} (N/mm^2)	355.	355.	355.	355.	355.	355.	355.	355.	355.	355.
$d_{sh} \times h_{st}$ (mm)	19 × 95	19 × 95	19 × 95	19 × 95	19 × 95	19 × 95	19 × 95	19 × 95	19 × 95	19 × 95
w_p (kN/m)	97.01	80.98	69.57	55.78	43.80	40.93	29.43	73.55	71.72	62.32
w_{pa} (kN/m)	52.38	41.53	35.59	29.85	20.95	20.45	15.02	42.29	38.48	34.13
$\gamma_m(50)$ (mm)	5.79	7.26	6.88	6.73	7.15	7.14	6.93	7.00	6.71	6.43
$\gamma_m(60)$ (mm)	4.85	6.58	5.64	5.85	6.27	6.25	5.24	5.88	5.55	4.91
$\gamma_m(70)$ (mm)	3.87	5.87	5.16	5.29	5.93	6.01	4.72	4.89	4.68	4.02
$\gamma_m(80)$ (mm)	3.41	5.39	4.46	4.80	5.77	5.79	4.42	4.33	4.28	3.28
$\gamma_m(90)$ (mm)	3.12	5.02	–	–	–	5.48	–	–	–	2.73
$\gamma_m(100)$ (mm)	–	–	–	–	–	–	–	–	–	–
y_p (mm)	84.96	60.14	66.35	52.71	48.58	48.58	52.90	70.09	79.65	100.23
F_p (kN)	6319	5112	4935	4189	3373	3373	2698	6355	6319	5680
h_t (mm)	782	782	705	668	612.2	591	536	849	782	772
N_f $(-)$	89	72	70	59	48	48	38	90	89	80

Table IV.2(c): (continued ...)

	SRM-21	*SRM*-22	*SRM*-23	*SRM*-24	*SRM*-25	*SRM*-26	*SRM*-27	*SRM*-28	*SRM*-29	*SRM*-30
l (m)	17.50	17.50	20.00	20.00	20.00	20.00	20.00	20.00	20.00	20.00
t_c (m)	0.100	0.084	0.125	0.125	0.125	0.125	0.084	0.100	0.075	0.085
t_h (m)	0.050	0.046	0.040	0.040	0.040	0.040	0.046	0.060	0.060	0.060
b_e (m)	3.500	3.000	4.000	4.000	4.000	4.000	2.500	2.750	3.000	3.000
rolled sections	533 × 210 UB104	533 × 210 UB92	762 × 267 UB147	686 × 254 UB140	610 × 229 UB140	610 × 229 UB125	610 × 229 UB113	IPE 600	762 × 267 UB147	762 × 267 UB147
f_{ck} (N/mm^2)	35.00	30.00	35.00	35.00	35.00	35.00	30.00	35.00	25.00	40.00
f_{ay} (N/mm^2)	355.	355.	355.	355.	355.	355.	355.	355.	355.	355.
$d_{sh} \times h_{st}$ (mm)	19 × 95	19 × 95	19 × 95	19 × 95	19 × 95	13 × 75	19 × 95	19 × 95	19 × 95	19 × 95
w_p (kN/m)	49.38	38.84	67.45	60.18	54.91	49.30	37.18	45.33	55.90	62.15
w_{pa} (kN/m)	26.15	21.94	36.71	32.38	29.47	26.13	23.36	24.96	36.75	36.75
$\gamma_m(50)$ (mm)	6.80	6.00	7.26	7.58	7.68	8.02	9.45	6.71	12.42	7.65
$\gamma_m(60)$ (mm)	5.58	4.72	5.89	6.24	6.25	6.86	8.52	5.34	11.90	6.17
$\gamma_m(70)$ (mm)	4.83	3.81	4.75	5.20	5.20	5.52	7.68	4.42	10.90	4.99
$\gamma_m(80)$ (mm)	3.97	3.19	4.44	4.45	4.45	4.68	6.76	3.67	10.55	4.13
$\gamma_m(90)$ (mm)	3.51	–	3.86	3.29	–	4.09	5.80	3.12	–	–
$\gamma_m(100)$ (mm)	–	–	–	–	–	–	–	–	–	–
y_p (mm)	71.09	82.14	84.13	80.10	79.65	71.60	139.52	160.24	163.93	149.77
F_p (kN)	4935	4189	6674	6355	6319	5680	3570	5501	3187	5780
h_t (mm)	690	663	918	849	782	777	737	760	889	899
N_f $(-)$	70	59	94	89	89	170	50	78	45	81

Table IV.3(a): Maximum slip along composite beams with solid concrete slabs and welded steel profiles, for different degrees of shear connection.

		SPF-1	*SPF*-2	*SPF*-3	*SPF*-4	*SPF*-5	*SPF*-6	*SPF*-7	*SPF*-8	*SPF*-9	*SPF*-10
l	(m)	5.00	5.00	7.50	7.50	7.50	7.50	10.00	10.00	10.00	10.00
t_c	(m)	0.140	0.145	0.135	0.135	0.140	0.140	0.170	0.140	0.140	0.135
b_c	(m)	3.500	3.500	3.500	3.500	3.500	3.500	4.000	5.000	5.000	3.000
b_e	(m)	1.250	1.250	1.875	1.875	1.875	1.875	2.500	2.500	2.500	2.500
$b_1 - t_1$	(mm)	$100 - 5.5$	$100 - 7.5$	$125 - 8.5$	$125 - 8.5$	$125 - 8.5$	$100 - 10$	$200 - 14$	$220 - 13$	$220 - 13$	$120 - 13$
$b_2 - t_2$	(mm)	$3.6 - 250$	$5.5 - 175$	$5.5 - 300$	$5.5 - 300$	$7 - 225$	$8 - 200$	$8 - 300$	$8 - 300$	$8 - 300$	$6.5 - 280$
$b_3 - t_3$	(mm)	$100 - 6.0$	$100 - 7.5$	$125 - 9$	$125 - 9$	$150 - 9$	$150 - 3$	$250 - 15$	$250 - 15$	$250 - 15$	$180 - 17$
f_{ck}	(N/mm^2)	25.00	40.00	20.00	30.00	25.00	30.00	25.00	30.00	35.00	30.00
f_{ay}	(N/mm^2)	355.	355.	355.	355.	355.	355.	352.	355.	355.	355.
$d_{sh} \times h_{st}$	(mm)	19×95	19×95	19×95	19×95	13×75	13×75	13×75	19×95	19×95	19×95
w_p	(kN/m)	59.65	63.71	51.13	53.86	48.45	56.81	77.04	72.66	74.26	54.17
w_{pa}	(kN/m)	23.35	20.57	23.28	23.28	18.41	18.95	33.61	34.65	34.65	21.75
$\gamma_m(50)$	(mm)	4.31	3.47	3.69	3.94	4.90	6.74	5.64	5.05	4.97	6.77
$\gamma_m(60)$	(mm)	3.85	3.48	3.35	3.62	4.65	5.99	5.01	4.25	4.32	5.99
$\gamma_m(70)$	(mm)	4.05	3.58	3.13	3.59	4.54	5.02	4.60	3.67	3.83	5.46
$\gamma_m(80)$	(mm)	–	3.77	–	4.26	4.59	4.01	4.17	3.87	3.44	5.47
$\gamma_m(90)$	(mm)	–	4.04	–	4.71	–	–	4.10	–	3.19	–
$\gamma_m(100)$	(mm)	–	–	–	–	–	–	–	–	3.51	–
y_p	(mm)	41.09	30.85	64.11	42.74	53.29	50.68	88.74	75.26	64.51	53.79
F_p	(kN)	727.8	874.2	1362.3	1362.3	1415.5	1615.3	3151	3198.5	31.98.5	2286.2
h_t	(mm)	401.5	335.0	452.5	452.5	382.5	363.0	499.0	468.0	468.0	445.0
N_f	$(-)$	10	10	21	17	43	22	95	38	37	27

Table IV.3(b): (continued ...)

		SPF-11	*SPF*-12	*SPF*-13	*SPF*-14	*SPF*-15	*SPF*-16	*SPF*-17	*SPF*-18	*SPF*-19	*SPF*-20
l	(m)	10.00	12.50	12.50	12.50	12.50	12.50	15.00	15.00	15.00	15.00
t_c	(m)	0.135	0.150	0.140	0.135	0.135	0.140	0.165	0.165	0.140	0.170
b_c	(m)	2.500	4.500	4.500	3.000	3.000	4.000	3.500	3.500	5.000	4.000
b_e	(m)	2.500	3.125	3.125	3.000	3.000	3.125	3.500	3.500	3.750	3.750
$b_1 - t_1$	(mm)	$120-13$	$250-15$	$175-15$	$120-13$	$180-13$	$180-13$	$250-15$	$250-15$	$250-15$	$200-14$
$b_2 - t_2$	(mm)	$6-250$	$12-500$	$11-500$	$7-350$	$7-340$	$8-300$	$13-700$	$13-675$	$13-600$	$10-475$
$b_3 - t_3$	$(mm$	$175-14$	$300-25$	$250-15$	$250-20$	$230-20$	$250-15$	$300-20$	$300-25$	$300-20$	$300-20$
f_{ck}	(N/mm^2)	30.00	35.00	30.00	35.00	30.00	30.00	30.00	30.00	25.00	30.00
f_{ay}	(N/mm^2)	352.	355.	355.	355.	355.	355.	355.	355.	355.	355.
$d_{sh} \times h_{st}$	(mm)	19×95	19×95	19×95	19×95	19×95	19×95	19×95	19×95	19×95	13×75
w_p	(kN/m)	42.51	131.5	66.71	60.18	54.80	46.47	124.3	133.9	97.69	74.99
w_{pa}	(kN/m)	17.21	63.05	31.69	22.05	20.69	20.09	64.09	66.49	52.52	32.21
$\gamma_m(50)$	(mm)	5.67	5.67	5.93	8.58	8.18	7.31	5.93	6.44	5.97	8.56
$\gamma_m(60)$	(mm)	5.27	4.69	4.83	8.24	7.65	6.07	4.77	4.93	4.62	7.40
$\gamma_m(70)$	(mm)	5.08	3.97	4.43	7.23	6.42	5.91	3.91	3.25	3.74	6.57
$\gamma_m(80)$	(mm)	5.09	3.46	3.79	6.46	6.24	5.22	3.24	–	2.92	5.83
$\gamma_m(90)$	(mm)	–	2.98	3.70	5.72	5.93	4.69	–	–	–	5.57
$\gamma_m(100)$	(mm)	–	–	3.40	–	–	5.18	–	–	–	5.63
y_p	(mm)	46.02	97.74	72.00	53.6	59.45	56.73	112.47	119.5	118.91	74.64
F_p	(kN)	1956.0	6075	3825	3200	3032	3033	6692	7109	6317	4773
h_t	(mm)	412.0	690	570	518	508.0	468.0	900.0	880.0	775	679
N_f	$(-)$	24	70	46	37	36	36	79	84	84	120

Table IV.3(c): (continued ...)

		SPF-21	*SPF*-22	*SPF*-23	*SPF*-24	*SPF*-25	*SPF*-26	*SPF*-27	*SPF*-28	*SPF*-29	*SPF*-30
l	(m)	15.00	17.50	17.50	17.50	17.50	17.50	17.50	20.00	20.00	20.00
t_c	(m)	0.140	0.150	0.158	0.150	0.150	0.175	0.170	0.150	0.175	0.150
b_c	(m)	4.000	5.000	3.250	5.000	5.000	4.000	4.000	5.000	4.000	4.000
b_e	(m)	3.750	4.375	3.250	4.375	4.375	4.000	4.000	5.000	4.000	4.000
$b_1 - t_1$	(mm)	$150-13$	$250-15$	$250-15$	$250-15$	$250-15$	$175-15$	$200-14$	$250-15$	$200-15$	$175-13$
$b_2 - t_2$	(mm)	$8-375$	$13-750$	$13-675$	$13-675$	$13-675$	$11-600$	$10-575$	$14-500$	$12-675$	$11-650$
$b_3 - t_3$	(mm)	$200-15$	$300-20$	$300-25$	$300-25$	$300-25$	$300-20$	$300-20$	$300-20$	$300-25$	$275-20$
f_{ck}	(N/mm^2)	30.00	30.00	25.00	30.00	35.00	30.00	30.00	30.00	30.00	30.00
f_{ay}	(N/mm^2)	355.	355.	355.	355.	355.	355.	355.	355.	355.	355.
$d_{sh} \times h_{st}$	(mm)	19×95	19×95	19×95	19×95	19×95	19×95	19×95	19×95	19×95	19×95
w_p	(kN/m)	34.57	98.34	93.62	97.78	99.30	72.59	66.72	98.61	73.78	55.08
w_{pa}	(kN/m)	15.43	51.57	48.85	48.85	48.85	31.89	29.98	51.97	33.22	25.43
$\gamma_m(50)$	(mm)	8.32	7.21	6.47	6.97	7.04	9.21	9.20	7.45	9.99	9.64
$\gamma_m(60)$	(mm)	6.73	5.50	5.23	5.76	5.95	8.15	7.89	5.80	8.35	8.34
$\gamma_m(70)$	(mm)	6.36	4.66	4.17	4.88	5.01	6.90	6.71	4.88	7.11	7.33
$\gamma_m(80)$	(mm)	6.26	3.88	3.43	4.29	4.37	6.43	6.03	4.05	6.21	6.44
$\gamma_m(90)$	(mm)	–	3.36	–	3.83	3.92	6.04	5.62	3.45	6.29	5.73
$\gamma_m(100)$	(mm)	–	3.00	–	3.55	3.43	5.78	5.21	3.09	6.03	5.57
y_p	(mm)	44.27	93.08	154.4	95.58	81.93	78.62	75.14	93.34	97.10	62.33
F_p	(kN)	2833	6922.5	7108.8	7108.8	7108.8	5373	5125	7934	6603	5313
h_t	(mm)	543	935.0	873.0	865	865	810	774	1085	890.0	833
N_f	$(-)$	34	82	94	84	81	64	61	94	78	63

Appendix V

Design of 3 span continuous composite plate girder with discrete inverted U–frame action

V.1 **General arrangement of the bridge geometry and design criteria**

spans: three spans, 40m-40m-40m,

cross-sections: continuous as shown in Figure V.1, the deck carries a dual carriageway of 11.25m width. Services are carried in 0.6m wide footways on both sides of the carriageway.

nominal loadings: dead load: steel = 78 kN/m^3
concrete = 23 kN/m^3

superimposed dead load: asphalt = 22 kN/m^3

live loading
(i) HA loading according to BS 5400: Pt. 2
(ii) HA loading according to BS 5400: Pt. 2

wind loading:
as specified in BS 5400: Pt.2 for a sea site near Cardiff, 50m above sea level for a design life of 120 years.

materials and strength:
concrete: Grade 35, f_{cu} = 35 N/mm^2
reinforcement: Grade 460, to BS 4449 f_{ry} = 460 N/mm^2
structural steel: Grade 50C, to BS 4360 f_{ay} = 355 N/mm^2, E_a = 205 MPa

V.2 **Preliminary longitudinal design moments and shear force**

The composite section is assumed to be uncracked and unreinforced throughout its length. Bending moments are calculated by moment distribution of a beam of uniform section. The steel beam alone is assumed to carry the wet concrete slab during and just after casting.

(i) dead load:

steelwork: 4.25 kN/m

deck slab: 0.20m x 2.58m x 23 $\frac{kN}{m^3}$ = 11.87 kN/m

design values:

W_{dead} = 1.05 x 4.25 $\frac{kN}{m}$ + 1.15 x 11.87 $\frac{kN}{m}$ = 18.11 $\frac{kN}{m}$

M'_{dead} = - 0.1 x W_{dead} x 1^2 = - 2898 kNm

V'_{dead} = 0.6 x W_{dead} x 1 = 435 kN

(ii) superimposed dead load:

asphalt and waterproofing:

$(0.045+0.005)\text{m} \times 2.58\text{m} \times 22 \frac{\text{kN}}{\text{m}^3} = 2.84 \frac{\text{kN}}{\text{m}}$

design values:

$W_{s.dead} = 1.75 \times 2.84 \frac{\text{kN}}{\text{m}} = 4.97 \frac{\text{kN}}{\text{m}}$

$M'_{s.dead} = -0.1 \times W_{s.dead} \times 1^2 = -795 \text{ kNm}$

$V'_{s.dead} = 0.6 \times W_{s.dead} \times 1 = 119 \text{ kN}$

BS 5400 Part 2 Cl.3.2.9.3.1

(iii) H.A. loading:

width of the notional lanes = $\frac{\text{carriageway width}}{\text{no. of notional lanes}}$

therefore : width = 3.75m

Cl.6.2.1

loading intensity of HAU loading varies with the loaded length.

For maximum hogging moment over an internal support HAU becomes over the adjacent spans:

$$18.84 \times \frac{2.58}{3.75} = 12.96 \text{ kN/m}$$

Cl.6.2.2

HAK becomes near the middle of the outer span:

$$120 \text{ kN} \times \frac{2.58}{3.75} = 82.56 \text{ kN}$$

For the maximum shear at the internal support HAU becomes over the mid span:

$$26.18 \frac{\text{kN}}{\text{m}} \times \frac{2.58}{3.75} = 18.01 \frac{\text{kN}}{\text{m}}$$

HAK becomes at the internal support : 82.56 kN

design values:

$$M'_{live} = -0.117 \times (1.5 \times 12.96 \frac{kN}{m}) \times (40m)^2 - 0.100 \times (1.5 \times 82.56\ kN) \times 40m$$

Therefore: $M'_{live} = -4135$ kNm

$$V'_{live} = 0.50 \times (1.5 \times 18.01 \frac{kN}{m}) \times 40m + 1.5 \times 82.56\ kN$$

Therefore: $V'_{live} = 664$ kN

(iv) HB loading

Cl.6.3.1 The most severe transverse position of the HB vehicle for the load on the inner girder is as shown in Figure V.2. The axle load, obtained from equilibrium, is $2.449 \times (45 \times \frac{10}{4}\ kN) = 275.58$ kN.

To obtain the maximum hogging moment over the internal support, the load configuration is as shown in Figure V.3-a where

HAU becomes 12.07 kN/m and 0.89 kN/m

and HB has $W_a = 275.58$ kN

To obtain the maximum shear force at the internal support, the load configuration is as shown in Figure V3-b where

HAU becomes 0.89 kN/m

and HB has $W_a = 275.58$ kN

design values:

Using moment distribution to find the elastic moments at the supports

Cl.6.3.4 $M'_{live} = 1.3 \times M'_B = 1.3 \times (-5022.6\ kNm)$

Therefore: $M'_{live} = -6529$ kNm

Cl.6.3.4 $V'_{live} = 1.3 \times V'_E = 1.3 \times (1039\ kN)$

Therefore: $V'_{live} = 1351$ kN

Total Design Moment and Shear Force

$M'_d{}^{tot} = M'_{dead} + M'_{s.dead} + M'_{live}$

$= -2898 \text{ kNm} - 795 \text{ kNm} - 6529 \text{ kNm}$

$= -10222 \text{ kNm}$

Part 5 Cl.6.1.4.2 Due to concrete cracking above the internal support 10% moment redistribution is allowed for:

$M'_d{}^{tot} = -9200 \text{ kNm}$

$V'_d{}^{tot} = V'_{dead} + V'_{s.dead} + V'_{live}$

$= 435 \text{ kN} = 119 \text{ kN} = 1351 \text{ kN}$

$= 1905 \text{ kN}$

V.3 **Preliminary Dimensioning of the Composite Girder's Cross Section**

Assume initially a span:depth ratio of 24 for the composite section. Its overall depth is then 1.666m with a slab of thickness 200mm, the depth of the steel section is 1466mm.

Ref 96 If the top flange thickness is taken as 25mm and the bottom flange thickness as 55mm (both values are within the practical ranges) then the webis only 1385mm deep.

The area of the top flange is principally determined by the dead load carried by the steel section alone.

The required area, $A_{tf}{}^{req}$ is:

$$A^{req}_{tf} = \frac{M'_{dead}}{(h_w + \frac{t_{tf} + t_{bf}}{2}) \times \frac{(f_{ay})}{\gamma_m \times \gamma_{f3}}} = 6617mm^2$$

If a 330 x 25mm top flange is provided, then this flange can also resist part of the moment carried by the composite section, M'_{tf}, given by

$$M'_{tf} = -(A_{tf} - A^{req}_{tf}) \times \frac{f_{ay}}{\gamma_m \gamma_{f3}} \times (h_w + \frac{t_{tf} + t_{bf}}{2})$$

$= -715 \text{ kNm}$

This means that the total moment to be resisted by the longitudinal reinforcement becomes:

$$M'_{rf} = M'^{tot}_{d} - M'_{dead} - M'_{tf} = -5587 \text{ kNm}$$

With a lever arm for the cracked composite section of approximately 1.535m, the required area of reinforcement is calculated by:

$$A^{req}_{rf} = \frac{M'_{rf}}{1.535\text{m} \times 0.87 \times 460 \times \gamma_{f3}} = 8268 \text{ mm}^2$$

This can be provided by T 20 @ 150mm in top and bottom over a width of 2.58m.

Initially the area of the bottom flange is calculated by assuming that the total design moment is carried by the steel section alone, but the lever arm is 1.425m. It is also assumed that $\sigma_{1i} = 0.85\ \sigma_{yc}$ and $\sigma_{fc} = \sigma_u$ so that

$$A^{req}_{bf} = \frac{M'^{tot}_{d}}{1.425\text{m} \times \frac{0.85 \times 355}{\gamma_m \times \gamma_{f3}}} = 28242 \text{ mm}^2$$

Part 3 Cl.9.3.7.3.1

Therefore a bottom flange of 550 x 55 will be sufficient ($A_{bf} = 30250 \text{ mm}^2$).

The amount of transverse reinforcement is usually controlled by crack width limitations at S.L.S. for the bottom and by local wheel loads at U.L.S. for the top.

Avoiding these extensive calculations top and bottom transverse reinforcement were chosen to fulfill only clauses 6.3.3.2 and 6.3.3.4 of Part 5 and therefore taken as T 16 @ 150mm.

V.4 **Preliminary Design of Inner Girder for Bending And Shear**

An aspect ratio of 1.5 has been chosen for the positioning of vertical web stiffeners, which will also act as part of a U-frame against lateral distortional buckling of the bottom flange near the internal support.

Cl.9.9.2.2

For a 12mm web the slenderness ratio = 116 and the value $m_{fw} = 0.00339$, the corresponding limiting shear stress τ_1 equals $0.67\ Z_y$.

The design shear resistance, V_D, of the web is

$$V_D = 0.67 \times \frac{355}{\sqrt{3}} \times \frac{12 \times 1385}{1.05 \times 1.1} = 1993 \text{ kN}$$

And, for the value mfw = 0.0, the corresponding shear resistance, V_R is 1773 kN.

Although the margin between V_D and V'_d is small, the design value of the resistance is conservative as it doesn't take account of the slab. Furthermore, the moment that exists with V'_d will be less than $M'_{d\,tot}$ so that interaction is possible.

Cl9.12.2.2
Cl.9.13.3

Where vertical stiffeners form part of a U-frame, their dimensions will be governed by the strength of the U-frame rather than the loading on the stiffener. As this strength is not yet known, a flat two sided stiffener was chosen, symmetrical about the centre line of the web, in accordance with the shape limitations and the loading on the transverse stiffener. the former determines the thickness: width ratio. If the width on each side is equal to the top flange outstands i.e. 159mm then the thickness is 16mm minimum.

Cl.9.3.4.1.2
Cl.9.13.3

Cl.9.6.5
Cl.9.7.2

The calculation of the effective length of the bottom flange near the internal support is needed to determine the slenderness of the girder.

$$l_e = 2.5 \times k_3 \times (E_a\ I_c\ l_u)^{0.25} = 7677\text{mm}$$

$k_3 = 1.0$ as the compression flange is not restrained against in plan rotation

$$E_a = 205 \times 10^3 \text{ N/mm}^2$$

$$l_u = \phi\ h_w = 1.5 \times 1385\text{mm} \approx 2100\text{mm}$$

$$I_c = \frac{b_{bf}^3 \times t_{bf}}{12} = 7.826 \times 10^8 \text{ mm}^4$$

$$\delta = \frac{d_1^3}{3E_aI_1} + u\,\frac{Bd_2^2}{E_cI_2}$$

$$= 9.55 \times 10^{-5} \frac{\text{mm}}{\text{N}} + 171 \times 10^{-4} \frac{\text{mm}}{\text{N}} = 2.668 \times 10^{-4} \frac{\text{mm}}{\text{N}}$$

where:

d_1 = 1412.5mm

I_1 = transverse stiffness of the effective section of the transverse web stiffener

= 4.797×10^7 mm^4

u = 0.33 (inner girder)

B = 2580 mm

$I_2 = \frac{t_c^3 \times B/4}{12} = 4.30 \times 10^8$ mm^4

$E_c = E_a/7.5$ (short time loading)

d_2 = 1537.5 mm

The deflection due to the flexibility of the connection between steel and concrete is considered below:

If one were to take account of this flexibility, the effective length, le, and the slenderness, λ_{LT}, would increase, while the design moment, M_D, would decrease according to the present Code.

It is known (Part 3: Cl.9.6.5) that in calculating the flexibility of the slab, under unit lateral load at the intersection of the vertical stiffener and the compression flange, an effective slab width of B/8 equal to 323 mm is taken on either side of the U-frame. It is also stated (Part 3: Cl.9.12.2.2) that in calculating the strength of the connection, only those connectors within half the effective width of the slab, acting as cross member, should be assumed to transmit the load. Therefore use 161 mm either side of the stiffener. As no guidelines are given concerning an effective length along the main girder for the calculation of the flexibility of the connection under unit lateral load, a combination of the above stated effective widths for stiffness and strength is taken.

In the calculation of 'f' for that part of the shear connection which forms the joint of the discrete U-frame a number of assumptions are made.

In order to avoid an accurate but long calculation of the shear force at S.L.S, assume that 125 x 19 mm studs are placed in pairs at 150mm spacing near the internal support.

(i) It is assumed that transverse flexibility of the joint at the corner of the U-frame is provided by the number of connectors within a length of 243 mm at each side of the U-frame. This length is the mean value of B/8 and 161 mm and the equivalent joint counts 4 stud connectors within its total length.

(ii) It is assumed that only the left hand connectors in Fig. V.5 are active in resisting the moment M_t.

(iii) It is also assumed that only the elastic elongation of the shank of the stud connector will cause any relative rotation between slab and top flange and that the tensile strain is uniform over each shank cross section.

The tensile force in each stud connector in tension:

$$F_{stud} = M_t/(2 \times 280 \text{ mm}) = 2.567 \text{ N}$$

The stress and strain in the shank and the elongation of the shank:

$$\sigma_{sh} = F_{stud}/A_{sh} = 9.04 \times 10^{-3} \text{ N/mm}^2$$

$$\epsilon_{sh} = \sigma_{sh}/E_a = 4.41 \times 10^{-8}$$

$$l_{sh} = \epsilon_{sh} \times h_{sh} = 5.12 \times 10^{-6} \text{ mm}$$

The flexibility of the connection

$$f = l_{sh}/(1437.5 \times 280) = 1.27 \times 10^{-11} \frac{\text{rad}}{\text{N mm}}$$

This value is between 5 and 15 times smaller than the values obtained from the tests.

The corrected lateral deflection is

$$\delta = 2.668 \times 10^{-4} + 2.63 \times 10^{-5} \frac{\text{mm}}{\text{N}}$$

Therefore: $\delta = 2.930 \times 10^{-4} \frac{\text{mm}}{\text{N}}$

The value of 'f' obtained by these assumptions gives a lower bound to the real value, as all three assumptions are unconservative. Especially this last assumption , (iii) is known to be incorrect, as it ignores completely the deformation of the concrete in which the heads of the studs are embedded but instead assumes the heads of the studs to be fixed under increasing loads on the shank.

$$\lambda_{LT} = \frac{le}{ry} \; k_4 \eta v = 50.5$$

Where $k_4 = 1.0$
$\eta = 1.0$ for beams restrained by U-frames

$$r_y = \sqrt{\frac{I_y}{A}} = 322\text{mm}$$

$$I_y = 6.833 \times 10^9 \text{mm}^4$$

$$A = 65928 \text{ mm}^2$$

Ref. 83

$$v \approx \frac{1}{\sqrt{2}i} = 2.12$$

$$i = \frac{Ic}{Ic + It} \approx \frac{Ic}{Iy} = 0.1116$$

Fig. 10

$$\sigma_{1i} = 0.95 \, \sigma_{yc}$$

Cl.9.3.7.2.1 Although it is unlikely that the web will be compact and therefore make this section a compact section it has to be checked by determining the elastic neutral axis, y_e and the corresponding depth of the web in compression, shown in Fig. V.4.

$y_e = 1025$ mm
$d = 585$ mm 28×12 mm $= 336$ mm

Cl.9.8.3 The limiting compressive stress for this non-compact section is equal to $D\sigma_{1i}/2y_t$. With $D = 1615$ mm and $y_t = 975$ mm, $\sigma_{1c} = 0.828 \; \sigma_{1i} = 279$ N/mm^2

Cl.9.9.1.3 The bending resistance, M_D, is governed by the stress in the compression flange.

$$M_D = \frac{Z_{xc} \sigma_{1c}}{1.2 \times 1.1} = 9599 \text{ kNm}$$

Cl.9.9.3.1 Knowing the design values of the action effects on the girder and of the resistances for bending and shear, interaction has to be checked.

(a) $V'_d{}^{tot} = 1905 \text{ kN} \leq V_D = 1993 \text{ kN}$

(b) $M'_d{}^{tot} = 9200 \text{ kNm} \geq M_D = 9599 \text{ kNm}$

(c) $M'_d{}^{tot} = 9200 \text{ kNm} \leq M_R = 9602 \text{ kNm}$

(d) $V'_d{}^{tot} = 1905 \text{ kN} \geq V_R = 1773 \text{ kN}$

and the condition is not fulfilled by 5% difference.

As the most severe combinations of bending and shear do not occur under the same loading, this is good enough for the present exercise.

V.5 **Restraint to the Compression Flange**

Part 2 Cl.5.3.2.3 Cl.5.3.3 Part 3 Cl.9.12.2.2 When intermediate inverted U-frames are used to provide lateral restraint to the compression flange, these frames and their connections should be designed to resist both wind loads and the horizontal transverse load F_t at the centroid of the compression flange.

Cl.9.12.2.2 $$F_t = \frac{\sigma_{fc}}{\sigma_{ci} - \sigma_{fc}} \times \frac{le}{667\,\delta} = 23.94 \text{ kN}$$

With $$\sigma_{fc} = \frac{\sigma_{lc}}{\gamma_m} = 232.5 \text{ N/mm}^2$$

$$\sigma ci = \frac{\pi^2 E_a (D/2y_t)}{\lambda_{LT}^2} = 647 \text{ N/mm}^2$$

Cl.5.3.2.3 Because of the location of the bridge v_c = 35 m/s

Cl.5.3.3 The nominal transverse wind load, P_t, is obtained from

$$P_t = qA_1C_D = 8.67 \text{ kN}$$

with $q = 750.9 \text{ N/m}^2$
$A_1 = 8.75 \text{ m}^2$
$C_D = 1.32$

and applied 0.418m above the deck surface, therefore not affecting the slab-top flange connection. The part of this load which works onto the girder alone has the same affect on the connection as adding a force of 1.68 kN to F_t.

It is clear from the value of F_t that a single stiffener of 165 x 16mm or a double stiffener of 220 x 12 will not fail, but it might not be stiff enough to mobilise enough connectors to work as a 'joint' under transverse moment.

V.6 Preliminary Study of Transverse Shear in the Slab

Global transverse bending moments and shear forces are not known until a grillage analysis has been completed. Yet without such an analysis an approximate value can be obtained by assuming the slab to be continuously supported over the longitudinal steel girders.

In Fig. V.6 the transverse load combination, which produces maximum shear in the slab near the middle girder is represented. The contract pressure for the nominal wheel load is 1.1 N/mm^2 at the carriageway surface, giving a contact surface at deck slab level of 370 x 370 mm^2. Assuming that the load disperses horizontally under an angle of 45° with the main girder, the wheel load is carried by approximately 1 metre longitudinal steel girder. Therefore, a transverse strip of deck slab of 1m width is considered to span continuous over the main girders.

In Fig. V.7 the transverse shear force distribution is drawn from the load combination in Fig. V.6.

Since a complete study would be too cumbersome and is not relevant to the problem of transverse flexibility of the connection it is sufficient to state that from comparison with other bridge designs, the size of the slab is found to be adequate.

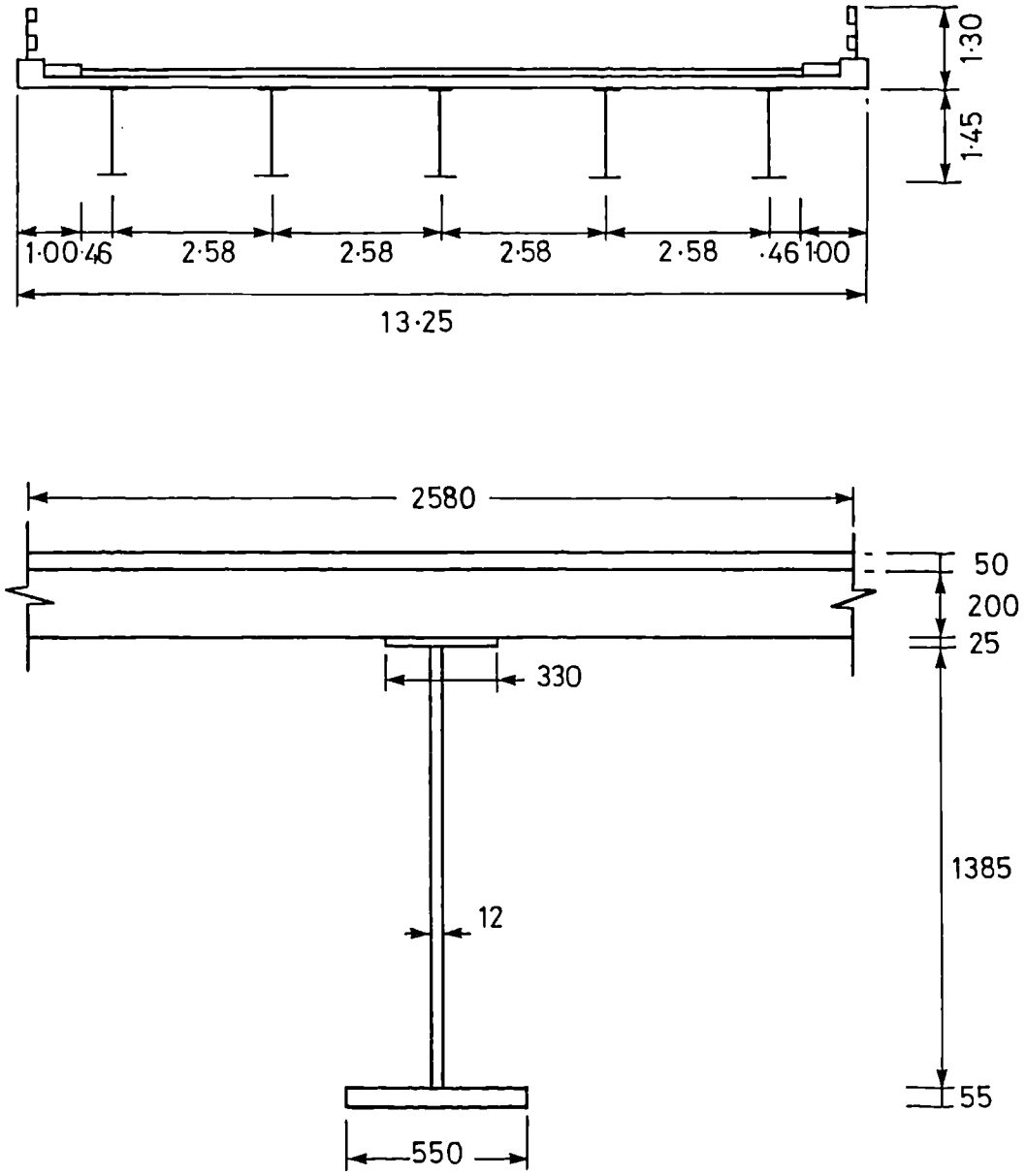

Figure V.1: Cross-section through a three span composite plate girder bridge with inverted U-frame action.

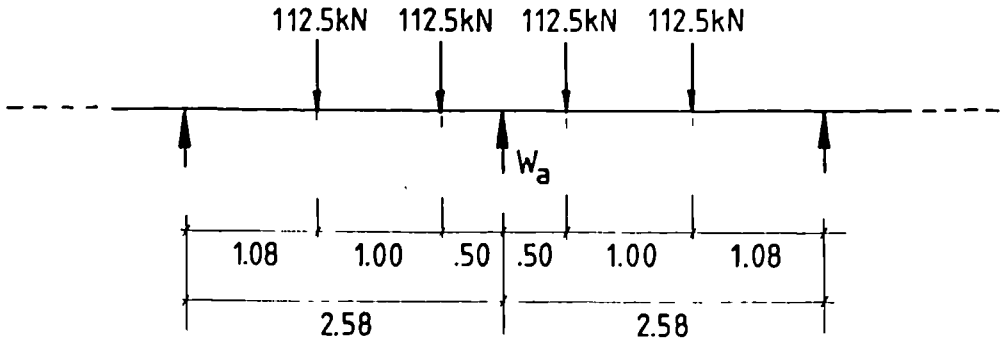

Figure V.2: Most severe transverse position of HB-vehicle load for maximum loading on the inner girder.

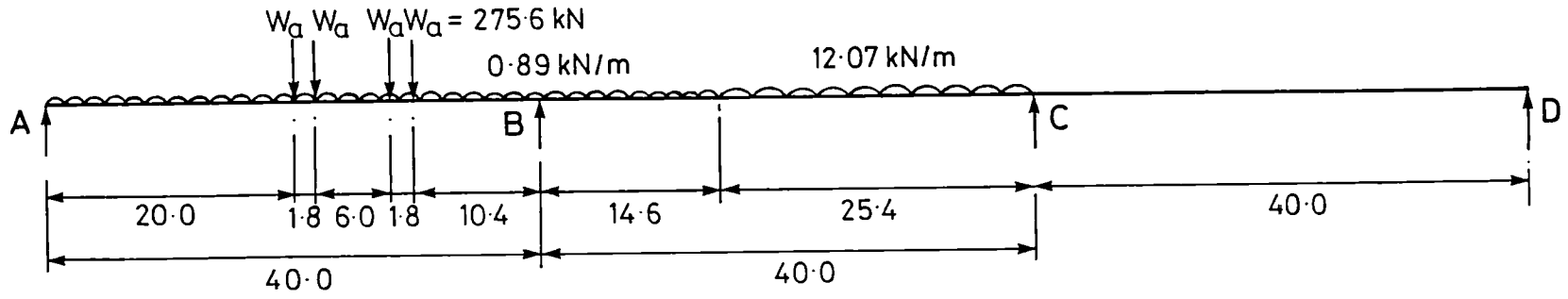

Figure V.3(a): Load configuration for maximum bending over the internal support.

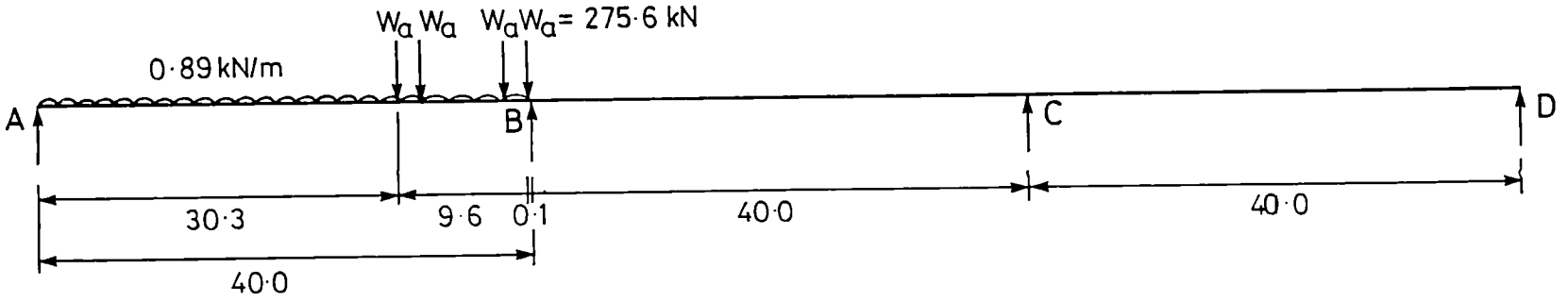

Figure V.3(b): Load configuration for maximum shear force at the internal support.

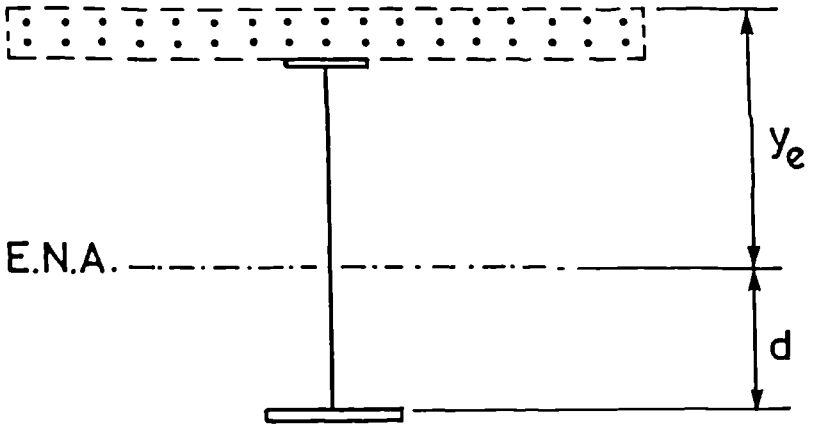

Figure V.4: Cross-section of an unstiffened girder in the hogging bending region with indication of the elastic neutral axis.

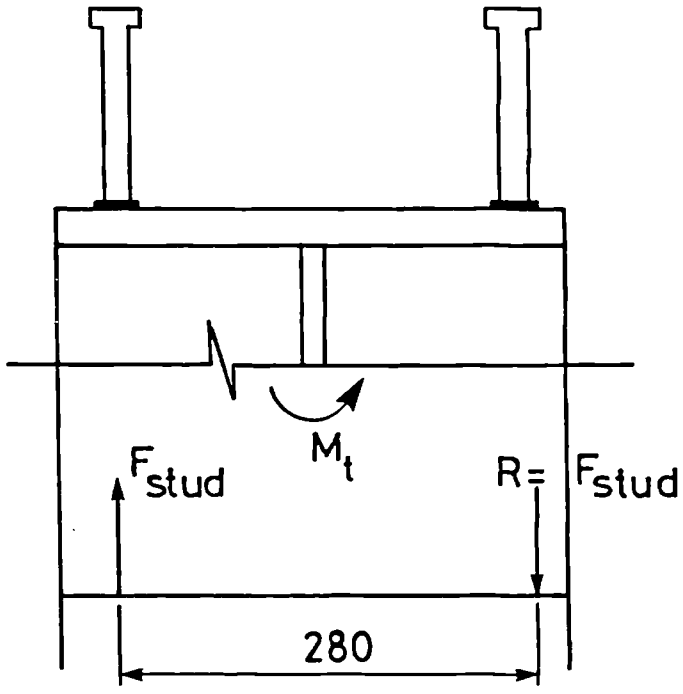

Figure V.5: Theoretical model of resultant force distribution over the top flange of the plate girder.

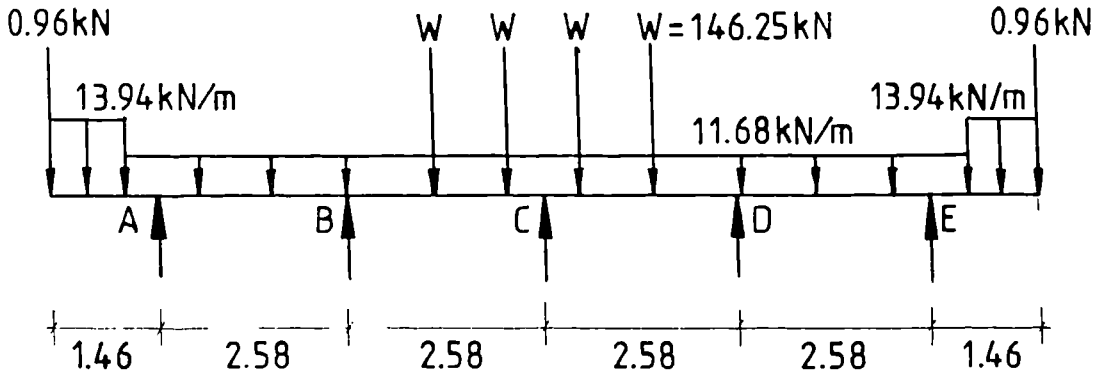

Figure V.6: Transverse load configuration which produces maximum shear in the slab near the central girder.

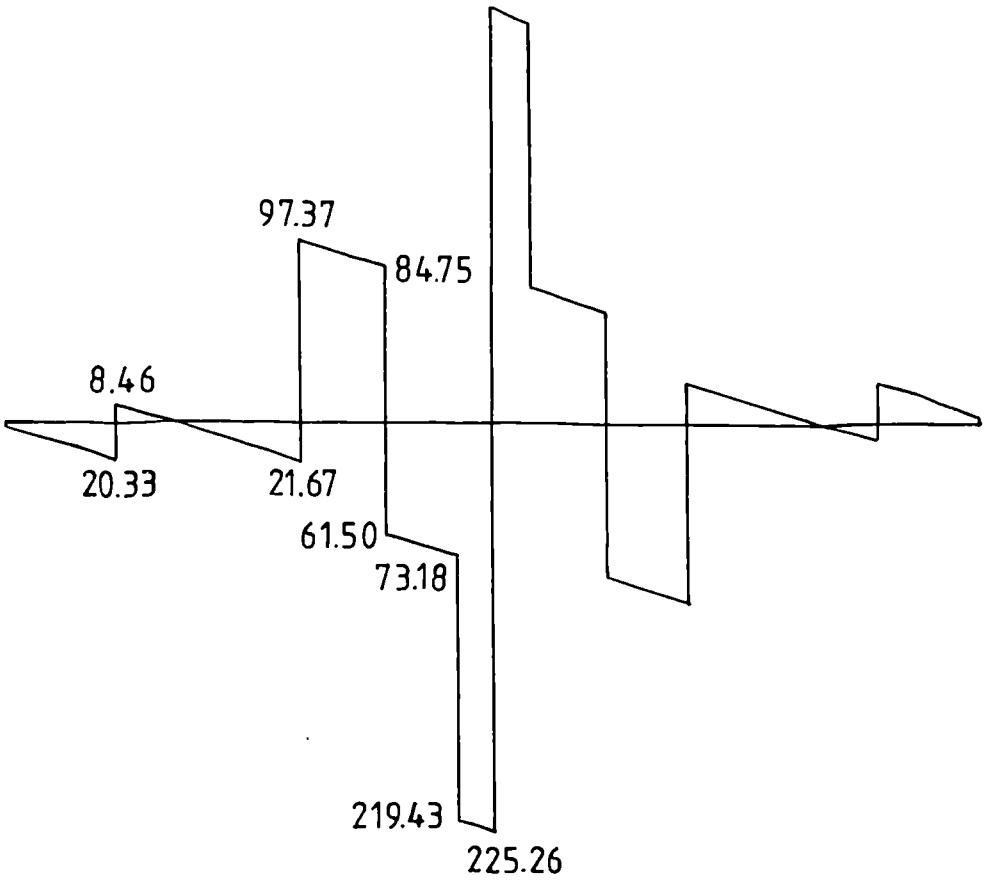

Figure V.7: Transverse shear force distribution of the load configuration in Fig. V.6.

Appendix VI

Tables with experimental results of test specimens BM2 to BM7

Table VI.1: Calculated relative rotations of the connection from inclinometer and dial gauge readings for test specimen BM2.

Load cycle	F_t^{max} (kN)	F_t^{min} (kN)	θ_c^i $(mrad)$	$\Delta\theta_c^i$ $(mrad)$	θ_s^i $(mrad)$	$\Delta\theta_s^i$ $(mrad)$	θ_r^i $(mrad)$	$\Delta\theta_r^i$ $(mrad)$	δh_r (mm)	θ_r^d $(mrad)$	$\Delta\theta_r^d$ $(mrad)$
I	0.0	0.0	0.000	0.002	0.000	0.033	0.000	0.035	0.00	0.000	0.103
	5.0	4.8	0.267	0.014	0.883	0.033	0.616	0.047	0.23	0.590	0.110
	10.0	9.6	0.489	0.011	1.983	0.067	1.495	0.078	0.56	1.436	0.121
	12.5	12.1	0.575	0.025	2.567	0.083	1.992	0.108	0.76	1.949	0.128
	15.1	14.6	0.735	0.022	3.233	0.083	2.498	0.105	0.97	2.487	0.135
	20.1	19.5	1.467	0.020	5.317	1.000	3.850	0.120	1.53	3.923	0.153
	10.5	10.5	0.850	0.017	3.717	0.083	2.867	0.101	1.15	2.949	0.140
II	0.0	0.0	0.217	0.019	1.483	0.067	1.261	0.085	0.51	1.308	0.119
	5.1	5.1	0.566	0.011	2.667	0.033	2.101	0.044	0.80	2.051	0.129
	10.1	10.0	0.800	0.014	3.700	0.067	2.901	0.081	1.05	2.692	0.137
	15.1	14.9	1.134	0.017	4.683	0.067	3.549	0.084	1.31	3.359	0.146
	20.1	19.7	1.550	0.014	5.550	0.117	4.000	0.131	1.60	4.103	0.155
	24.7	20.7	3.032	0.033	12.883	0.233	9.852	0.266	3.25	8.333	0.209
	–	19.6	3.456	0.050	16.517	0.367	13.061	0.417	4.10	10.513	0.237

Table VI.2(a): Calculated relative rotations of the connection from inclinometer and dial gauge readings for test specimen BM3.

Load cycle	F_t^{max} (kN)	F_t^{min} (kN)	θ_c^i $(mrad)$	$\Delta\theta_c^i$ $(mrad)$	θ_s^i $(mrad)$	$\Delta\theta_s^i$ $(mrad)$	θ_τ^i $(mrad)$	$\Delta\theta_\tau^i$ $(mrad)$	δh_τ (mm)	θ_τ^d $(mrad)$	$\Delta\theta_\tau^d$ $(mrad)$
I	0.0	0.0	0.000	0.002	0.000	0.033	0.000	0.035	0.00	0.000	0.103
	3.1	3.0	0.086	0.008	0.283	0.017	0.197	0.025	0.08	0.204	0.108
	5.3	5.1	0.134	0.009	0.500	0.033	0.367	0.043	0.09	0.237	0.108
	7.7	7.6	0.195	0.009	0.783	0.033	0.589	0.043	0.12	0.316	0.109
		7.2	–	–	–	–	–	–	–	–	–
II	0.0	0.0	0.035	0.006	0.267	0.033	0.232	0.040	–	–	–
	2.8	2.8	0.101	0.009	0.533	0.017	0.433	0.026	0.07	0.184	0.108
	5.3	5.2	0.145	0.009	0.733	0.033	0.589	0.043	0.09	0.237	0.108
	7.7	7.6	0.214	0.011	0.981	0.033	0.768	0.044	0.12	0.316	0.109
	10.3	10.1	0.302	0.009	1.233	0.067	0.932	0.076	0.25	0.645	0.114
	12.8	12.6	0.432	0.013	1.600	0.050	1.168	0.063	0.41	1.079	0.120
	15.4	15.1	0.534	0.014	2.067	0.067	1.533	0.081	0.57	1.500	0.125
	12.6	12.6	0.489	0.013	1.833	0.050	1.345	0.063	0.51	1.342	0.123
	10.1	10.1	0.465	0.011	1.600	0.050	1.135	0.061	0.50	1.316	0.123
III	0.0	0.0	0.126	0.016	0.633	0.050	0.508	0.066	0.14	0.368	0.110
	2.7	2.7	0.195	0.008	0.900	0.033	0.705	0.041	0.19	0.500	0.112
	5.2	5.1	0.251	0.011	1.133	0.033	0.882	0.044	0.23	0.605	0.113
	7.8	7.6	0.319	0.014	1.400	0.067	1.081	0.081	0.30	0.790	0.116
	10.3	10.1	0.441	0.013	1.681	0.067	1.240	0.079	0.41	1.079	0.120
	12.8	12.6	0.511	0.014	1.933	0.083	1.423	0.097	0.51	1.342	0.123
	15.3	15.2	0.610	0.017	2.233	0.083	1.624	0.101	0.61	1.605	0.126
	16.7	16.5	0.682	0.020	2.467	0.067	1.785	0.087	0.66	1.737	0.128
	18.3	17.9	0.793	0.024	2.933	0.083	2.140	0.107	0.80	2.105	0.133
	19.8	19.4	0.924	0.028	3.367	0.100	2.443	0.128	0.94	2.474	0.138

Table VI.2(b): Calculated relative rotations of the connection from inclinometer and dial gauge readings for test specimen BM3.

Load cycle	F_t^{max} (kN)	F_t^{min} (kN)	θ_c^i $(mrad)$	$\Delta\theta_c^i$ $(mrad)$	θ_s^i $(mrad)$	$\Delta\theta_s^i$ $(mrad)$	θ_r^i $(mrad)$	$\Delta\theta_r^i$ $(mrad)$	δh_r (mm)	θ_r^d $(mrad)$	$\Delta\theta_r^d$ $(mrad)$
IV	0.0	0.0	0.311	0.019	1.267	0.050	0.956	0.069	0.12	0.316	0.109
	7.7	7.5	0.456	0.014	2.233	0.033	1.778	0.047	0.28	0.737	0.115
	10.3	10.1	0.531	0.013	2.483	0.067	1.952	0.079	0.40	1.040	0.119
	12.7	12.4	0.622	0.011	2.733	0.067	2.111	0.078	0.52	1.368	0.123
	15.2	15.1	0.735	0.016	2.967	0.083	2.232	0.099	0.63	1.658	0.127
	16.6	16.5	0.825	0.019	3.133	0.083	2.309	0.102	0.72	1.895	0.130
	18.3	18.0	0.916	0.024	3.333	0.100	2.418	0.124	0.80	2.105	0.133
	19.8	19.4	1.002	0.033	3.550	0.117	2.548	0.150	0.89	2.329	0.136
	20.8	20.5	1.068	0.042	3.933	0.100	2.865	0.142	1.03	2.697	0.141
	21.7	20.6	1.288	0.050	4.650	0.117	3.362	0.167	1.23	3.224	0.148
	22.5	21.2	1.445	0.057	5.567	0.150	4.088	0.207	1.52	3.987	0.158
	22.8	21.3	1.759	0.058	7.200	0.200	5.441	0.258	1.94	5.092	0.172
	–	19.1	1.778	0.071	7.200	0.200	5.422	0.271	1.95	5.132	0.173
	22.6	22.0	1.894	0.060	7.933	0.233	6.039	0.293	2.11	5.553	0.178
	23.3	22.4	2.097	0.064	8.800	0.250	6.703	0.314	2.45	6.434	0.190
	24.1	23.0	2.215	0.082	10.400	0.282	8.185	0.363	2.77	7.290	0.201
	24.9	23.5	2.364	0.071	11.350	0.300	8.986	0.371	3.07	8.079	0.212
	25.9	24.4	2.653	0.079	12.433	0.367	9.780	0.445	–	–	–

Table VI.3(a): Calculated relative rotations of the connection from inclinometer and dial gauge readings for test specimen BM4.

Load cycle	F_t^{max} (kN)	F_t^{min} (kN)	θ_c^i $(mrad)$	$\Delta\theta_c^i$ $(mrad)$	θ_s^i $(mrad)$	$\Delta\theta_s^i$ $(mrad)$	θ_r^i $(mrad)$	$\Delta\theta_r^i$ $(mrad)$	δh_r (mm)	θ_r^d $(mrad)$	$\Delta\theta_r^d$ $(mrad)$
I	0.0	0.0	0.000	0.002	0.000	0.033	0.000	0.035	0.00	0.000	0.103
	2.3	2.3	0.067	0.004	0.283	0.017	0.217	0.021	0.05	0.135	0.110
	4.6	4.5	0.160	0.003	0.533	0.033	0.373	0.036	0.10	0.270	0.112
	–	4.2	0.251	0.028	0.567	0.000	0.316	0.028	0.10	0.270	0.112
	6.5	6.4	0.339	0.019	0.850	0.017	0.511	0.036	0.13	0.351	0.113
	8.5	8.3	0.413	0.025	1.067	0.033	0.654	0.058	0.16	0.432	0.114
	10.5	10.3	0.463	0.056	1.367	0.033	0.904	0.089	0.24	0.649	0.117
	12.4	12.1	0.552	0.042	1.750	0.050	1.198	0.092	0.29	0.784	0.119
	14.3	14.1	0.717	0.057	2.150	0.083	1.433	0.140	0.36	0.973	0.121
	16.3	16.0	0.946	0.053	2.700	0.067	1.754	0.120	0.44	1.189	0.124
	18.3	18.1	1.083	0.055	3.133	0.067	2.050	0.122	0.51	1.378	0.127
	12.2	12.2	0.891	0.055	2.617	0.083	1.726	0.138	0.48	1.297	0.126
	–	2.6	0.415	0.058	1.350	0.050	0.935	0.108	0.32	0.865	0.120
II	0.5	0.5	0.265	0.073	0.883	0.017	0.619	0.090	0.23	0.622	0.117
	4.6	4.5	0.452	0.014	1.450	0.017	0.999	0.031	0.32	0.865	0.120
	8.5	8.3	0.648	0.016	1.967	0.033	1.319	0.049	0.40	1.081	0.123
	12.4	12.3	0.820	0.020	2.450	0.050	1.630	0.070	0.46	1.243	0.125
		14.3	0.978	0.024	2.783	0.017	1.806	0.040	0.51	1.378	0.127
	18.3	18.1	1.160	0.022	3.300	0.033	2.140	0.055	0.58	1.568	0.129
	20.4	20.0	1.357	0.021	3.800	0.033	2.443	0.054	0.66	1.784	0.132
	22.0	21.4	1.527	0.012	4.250	0.050	2.723	0.062	0.72	1.946	0.134
	24.0	23.1	1.836	0.036	4.900	0.033	3.065	0.069	0.81	2.189	0.138
	26.0	24.3	2.392	0.012	6.583	0.150	4.191	0.162	0.98	2.649	0.144
	20.0	20.0	2.233	0.035	5.950	0.017	3.717	0.052	–	–	–
		14.3	1.861	0.018	5.067	0.067	3.205	0.084	–	–	–

Table VI.3(b): Calculated relative rotations of the connection from inclinometer and dial gauge readings for test specimen BM4.

Load cycle	F_t^{max} (kN)	F_t^{min} (kN)	θ_c^i $(mrad)$	$\Delta\theta_c^i$ $(mrad)$	θ_s^i $(mrad)$	$\Delta\theta_s^i$ $(mrad)$	θ_r^i $(mrad)$	$\Delta\theta_r^i$ $(mrad)$	δh_r (mm)	θ_r^d $(mrad)$	$\Delta\theta_r^d$ $(mrad)$
III	0.3	0.5	0.645	0.024	2.067	0.033	1.422	0.057	0.38	1.027	0.122
	6.5	6.4	0.998	0.007	3.150	0.033	2.152	0.040	0.59	1.595	0.130
	12.3	12.2	1.425	0.003	4.250	0.033	2.825	0.036	0.69	1.865	0.133
	18.3	18.1	1.876	0.009	5.367	0.017	3.490	0.025	0.87	2.351	0.140
	22.0	21.6	2.174	0.000	6.050	0.000	3.876	0.000	0.95	2.568	0.143
	24.0	23.7	2.367	0.017	6.533	0.017	4.166	0.034	1.00	2.703	0.145
	26.0	25.4	2.586	0.009	7.267	0.017	4.681	0.026	1.08	2.919	0.148
	27.0	26.2	2.789	0.026	7.933	0.017	5.144	0.043	1.16	3.135	0.151
	28.0	25.2	2.869	0.030	9.350	0.000	6.481	0.030	1.30	3.514	0.156

Table VI.4(a): Calculated relative rotations of the connection from inclinometer and dial gauge readings for test specimen BM5.

Load cycle	F_t^{max} (kN)	F_t^{min} (kN)	θ_c^i $(mrad)$	$\Delta\theta_c^i$ $(mrad)$	θ_s^i $(mrad)$	$\Delta\theta_s^i$ $(mrad)$	θ_τ^i $(mrad)$	$\Delta\theta_\tau^i$ $(mrad)$	δh_τ (mm)	θ_τ^d $(mrad)$	$\Delta\theta_\tau^d$ $(mrad)$
I	0.0	0.0	0.000	0.002	0.000	0.033	0.000	0.035	0.00	0.000	0.103
	2.0	1.9	0.126	0.008	0.567	0.033	0.441	0.041	0.14	0.378	0.113
	3.9	3.8	0.330	0.024	0.967	0.067	0.637	0.090	0.22	0.595	0.116
	6.0	5.8	0.487	0.024	1.483	0.083	0.996	0.107	0.32	0.865	0.120
	8.0	7.9	0.650	0.016	2.117	0.083	1.466	0.099	0.44	1.189	0.124
	4.0	4.0	0.418	0.003	1.433	0.067	1.016	0.070	0.34	0.919	0.121
II	0.0	0.0	0.028	0.012	0.400	0.000	0.374	0.012	0.15	0.405	0.114
	3.9	3.9	0.311	0.068	1.267	0.067	0.956	0.134	0.30	0.811	0.119
	6.0	5.9	0.475	0.072	1.667	0.067	1.191	0.138	0.38	1.027	0.122
	8.0	7.9	0.632	0.100	2.083	0.117	1.451	0.216	0.46	1.243	0.125
	10.0	9.9	0.802	0.078	2.517	0.183	1.715	0.261	0.56	1.514	0.129
	12.0	11.9	0.966	0.079	3.067	0.233	2.101	0.312	0.67	1.811	0.133
	14.0	13.8	1.177	0.094	3.600	0.267	2.423	0.360	0.71	1.919	0.134
	10.0	10.0	1.027	0.072	3.150	0.183	2.123	0.256	–	–	–

Table VI.4(b): Calculated relative rotations of the connection from inclinometer and dial gauge readings for test specimen BM5.

Load cycle	F_t^{max} (kN)	F_t^{min} (kN)	θ_c^i $(mrad)$	$\Delta\theta_c^i$ $(mrad)$	θ_s^i $(mrad)$	$\Delta\theta_s^i$ $(mrad)$	θ_r^i $(mrad)$	$\Delta\theta_r^i$ $(mrad)$	δh_r (mm)	θ_r^d $(mrad)$	$\Delta\theta_r^d$ $(mrad)$
III	0.0	0.0	0.136	0.050	0.833	0.067	0.698	0.116	0.21	0.568	0.116
	2.0	1.9	0.287	0.002	1.317	0.017	1.030	0.018	0.33	0.892	0.120
	3.9	3.9	0.478	0.012	1.717	0.050	1.239	0.062	0.42	1.135	0.123
	6.0	6.0	0.639	0.024	2.167	0.067	1.528	0.090	0.50	1.351	0.126
	8.0	8.0	0.807	0.004	2.550	0.117	1.743	0.121	0.58	1.568	0.129
	10.0	9.9	0.972	0.020	2.950	0.150	1.978	0.170	0.65	1.757	0.132
	12.0	11.9	1.118	0.000	3.350	0.150	2.232	0.150	0.73	1.973	0.135
	14.0	13.9	1.267	0.024	3.717	0.150	2.450	0.174	0.81	2.189	0.138
	16.0	16.0	1.479	0.000	4.250	0.250	2.771	0.250	0.91	2.460	0.141
	18.0	17.9	1.822	0.020	5.100	0.267	3.278	0.286	1.06	2.865	0.147
	20.0	19.8	2.123	0.000	5.817	0.350	3.694	0.350	1.21	3.270	0.152
	22.0	21.8	2.394	0.012	6.600	0.367	4.206	0.379	1.37	3.703	0.158
	24.0	23.5	2.710	0.002	7.467	0.400	4.756	0.402	1.54	4.162	0.164
	25.0	23.6	3.030	0.035	8.417	0.417	5.387	0.452	1.73	4.676	0.171
	26.0	25.1	3.428	0.032	9.517	0.417	6.089	0.449	1.94	5.243	0.180
	27.0	26.5	3.717	0.039	10.300	0.633	6.583	0.673	2.32	6.270	0.193
	27.4	25.3	3.959	0.196	10.883	1.117	6.924	1.313	2.51	6.784	0.200
	27.8	26.3	4.372	0.145	12.733	1.050	8.362	1.195	2.66	7.189	0.205

Table VI.5(a): Calculated relative rotations of the connection from inclinometer and dial gauge readings for test specimen BM6.

Load cycle	F_t^{max} (kN)	F_t^{min} (kN)	θ_c^i $(mrad)$	$\Delta\theta_c^i$ $(mrad)$	θ_s^i $(mrad)$	$\Delta\theta_s^i$ $(mrad)$	θ_r^i $(mrad)$	$\Delta\theta_r^i$ $(mrad)$	δh_r (mm)	θ_r^d $(mrad)$	$\Delta\theta_r^d$ $(mrad)$
I	0.0	0.0	0.000	0.002	0.000	0.033	0.000	0.035	0.00	0.000	0.103
	2.0	2.0	0.119	0.006	0.200	0.033	0.081	0.040	0.02	0.054	0.109
	4.0	4.0	0.214	0.006	0.417	0.017	0.203	0.023	0.06	0.162	0.110
	6.1	5.9	0.312	0.013	0.683	0.017	0.372	0.030	0.12	0.324	0.113
	8.0	7.9	0.438	0.029	0.933	0.033	0.496	0.062	0.16	0.432	0.114
	4.0	4.0	0.229	0.057	0.617	0.017	0.387	0.073	0.10	0.270	0.112
II	0.0	0.0	0.053	0.037	0.117	0.017	0.064	0.054	0.02	0.054	0.109
	2.0	1.9	0.147	0.016	0.350	0.017	0.203	0.032	0.06	0.162	0.110
	4.0	3.9	0.198	0.004	0.533	0.000	0.335	0.004	0.10	0.270	0.112
	6.0	5.9	0.355	0.012	0.750	0.050	0.395	0.062	0.14	0.378	0.113
	8.1	8.0	0.457	0.020	1.000	0.033	0.543	0.503	0.18	0.487	0.115

Table VI.5(b): Calculated relative rotations of the connection from inclinometer and dial gauge readings for test specimen BM6.

Load cycle	F_t^{max} (kN)	F_t^{min} (kN)	θ_c^i $(mrad)$	$\Delta\theta_c^i$ $(mrad)$	θ_s^i $(mrad)$	$\Delta\theta_s^i$ $(mrad)$	θ_r^i $(mrad)$	$\Delta\theta_r^i$ $(mrad)$	δh_r (mm)	θ_r^d $(mrad)$	$\Delta\theta_r^d$ $(mrad)$
III	0.0	0.0	0.049	0.025	0.083	0.017	0.035	0.041	0.02	0.054	0.109
	4.0	4.0	0.237	0.016	0.533	0.033	0.296	0.049	0.08	0.216	0.111
	7.0	7.0	0.418	0.008	0.867	0.607	0.449	0.075	0.15	0.405	0.114
	8.1	8.0	0.465	0.008	0.967	0.067	0.502	0.075	0.18	0.487	0.115
	10.0	9.9	0.583	0.000	1.217	0.117	0.634	0.117	0.22	0.595	0.116
	12.0	11.9	0.728	0.004	1.567	0.100	0.839	0.104	0.27	0.730	0.118
	13.9	13.7	0.917	0.012	1.983	0.083	1.067	0.095	0.33	0.892	0.120
	16.0	15.7	1.180	0.016	2.483	0.117	1.337	0.132	0.41	1.108	0.123
	18.0	17.8	1.443	0.012	3.050	0.117	1.607	0.128	0.50	1.351	0.126
	20.0	19.6	1.745	0.016	3.750	0.117	2.005	0.132	0.60	1.622	0.130
	21.0	19.4	2.236	0.059	4.650	0.117	2.414	0.176	0.73	1.973	0.135
	22.0	21.1	2.825	0.043	5.650	0.117	2.825	0.160	0.87	2.351	0.140
	23.0	22.5	3.190	0.047	6.433	0.133	3.243	0.181	1.00	2.703	0.145
	24.0	23.3	3.571	0.043	7.200	0.133	3.629	0.177	1.18	3.189	0.151
	25.0	24.1	3.980	0.043	8.150	0.150	4.170	0.193	1.35	3.649	0.157
	26.0	25.1	4.518	0.024	9.383	0.150	4.866	0.174	1.51	4.081	0.163
	27.0	25.6	4.895	0.021	10.350	0.117	5.455	0.138	1.78	4.811	0.173
	28.0	27.2	5.272	0.015	11.333	0.117	6.062	0.132	1.93	5.324	0.182
	29.0	28.3	5.704	0.025	12.300	0.167	6.596	0.192	2.16	5.838	0.187
	30.0	28.8	6.615	0.027	13.450	0.133	6.835	0.160	2.31	6.243	0.193
	31.0		7.777	0.030	19.883	0.150	12.155	0.180	–	–	–

Table VI.6: Calculated relative rotations of the connection from inclinometer and dial gauge readings for test specimen BM7.

Load cycle	F_t^{max} (kN)	F_t^{min} (kN)	θ_c^i $(mrad)$	$\Delta\theta_c^i$ $(mrad)$	θ_s^i $(mrad)$	$\Delta\theta_s^i$ $(mrad)$	θ_r^i $(mrad)$	$\Delta\theta_r^i$ $(mrad)$	δh_r (mm)	θ_r^d $(mrad)$	$\Delta\theta_r^d$ $(mrad)$
I	2.0	2.0	0.185	0.028	0.333	0.033	0.149	0.061	–	–	–
	4.0	3.8	0.389	0.043	0.633	0.067	0.245	0.110	–	–	–
	6.0	6.0	0.770	0.031	1.150	0.050	0.380	0.081	–	–	–
	8.0	8.0	1.233	0.071	1.800	0.067	0.567	0.137	–	–	–
II	2.0	2.0	0.118	0.008	0.183	0.050	0.066	0.058	0.01	0.027	0.109
	4.0	3.8	0.216	0.012	0.383	0.017	0.167	0.028	0.03	0.081	0.109
	6.0	6.0	0.330	0.000	0.600	0.033	0.270	0.033	0.06	0.162	0.110
	8.0	7.8	0.428	0.012	0.800	0.033	0.372	0.045	0.10	0.270	0.112
	10.0	9.8	0.538	0.012	1.167	0.033	0.629	0.045	0.14	0.378	0.113
	12.1	11.8	0.636	0.031	1.450	0.050	0.814	0.081	0.22	0.595	0.116
	14.1	13.8	0.836	0.020	1.783	0.050	0.947	0.070	0.29	0.784	0.119
	16.1	15.9	0.974	0.016	2.117	0.050	1.143	0.066	0.35	0.946	0.121
	18.1	17.8	1.143	0.020	2.500	0.067	1.357	0.086	0.40	1.081	0.123
	20.1	19.8	1.398	0.031	2.967	0.067	1.569	0.098	0.45	1.216	0.125
	22.1	21.8	1.638	0.043	3.483	0.050	1.846	0.093	0.52	1.405	0.127
	24.0	23.5	1.995	0.047	4.083	0.050	2.088	0.097	0.59	1.595	0.130
	26.0	24.5	2.419	0.024	5.133	0.033	2.714	0.057	0.69	1.865	0.133
	27.0	26.1	2.827	0.024	6.650	0.083	3.823	0.107	0.92	2.487	0.142
	28.0	27.1	3.098	0.012	7.933	0.067	4.835	0.078	1.25	3.378	0.154
	29.0	26.4	3.020	0.067	10.833	0.033	7.780	0.100	1.64	4.432	0.168

Table VI.7: Measured strains and corresponding calculated forces in the shanks of the studs in tension of test specimen BM2

Load cycle	F_t^{max} (kN)	F_t^{min} (kN)	ε_{sh}^1 $(\times 10^{-6})$	ε_{sh}^2 $(\times 10^{-6})$	F_{sh}^1 (kN)	F_{sh}^2 (kN)	$\sum_{i=1}^{2} F_{sh}^i$ (kN)	Crack pattern Fig. 7.24
I	5.0	4.8	160	190	10.2	12.1	22.2	
	10.0	9.6	365	395	23.2	25.1	48.2	
	12.5	12.1	495	520	31.4	33.0	64.4	
	15.1	14.6	620	630	39.3	40.0	79.3	
	20.1	19.5	885	830	56.1	52.7	108.8	
	10.5	10.5	550	525	34.9	33.3	68.2	
II	0.0	0.0	0	0	0.0	0.0	0.0	
	5.1	5.1	225	225	14.3	14.3	28.6	
	10.1	10.0	440	420	27.9	26.6	54.6	
	15.1	14.9	650	520	41.2	33.0	74.2	
	20.1	19.7	860	785	54.6	49.8	104.4	
	24.7	20.7	1035	870	65.7	55.2	120.8	
		19.6	940	880	59.6	55.8	115.5	
III	0.0	0.0	25	45	1.6	2.9	4.4	
	20.6	19.8	860	920	54.6	58.4	112.9	5
	20.8	19.4	830	935	52.7	59.3	112.0	6
		19.1	720	845	45.7	53.6	99.3	7
		16.0	565	465	35.8	29.5	65.3	8

Table VI.8: Measured strains and corresponding calculated forces in the shanks of the studs in tension of test specimen BM3

Load cycle	F_t^{max}	F_t^{min}	ε_{sh}^1	ε_{sh}^2	ε_{sh}^3	ε_{sh}^4	F_{sh}^1	F_{sh}^2	F_{sh}^3	F_{sh}^4	$\sum_{i=1}^{4} F_{sh}^i$	Crack pattern
	(kN)	(kN)	$(\times 10^{-6})$	$(\times 10^{-6})$	$(\times 10^{-6})$	$(\times 10^{-6})$	(kN)	(kN)	(kN)	(kN)	(kN)	Fig. 7.25
IV	10.3	10.1	160	295	175	180	10.2	18.7	11.1	11.4	51.4	
	12.7	12.4	200	375	255	225	12.7	23.8	16.2	14.3	66.9	
	15.2	15.1	240	450	325	260	15.2	28.6	20.6	16.5	80.9	
	18.3	18.0	290	545	425	310	18.4	34.6	27.0	19.7	99.6	
	19.8	19.4	315	585	460	330	20.0	37.1	29.2	20.9	107.2	3.20
	20.8	20.5	340	610	485	350	21.6	38.7	30.8	22.2	113.2	
	21.7	20.6	375	610	490	365	23.8	38.7	31.1	23.2	116.7	
	22.5	21.2	415	610	495	375	26.3	38.7	31.4	23.8	120.2	
	22.8	21.3	435	555	460	370	27.6	35.2	29.2	23.5	115.5	
	23.3	22.4	480	550	430	355	30.5	34.9	27.3	22.5	115.1	
	24.1	23.1	505	585	450	365	32.0	37.1	28.6	23.2	120.8	3.90
	24.9	23.5	510	600	460	365	32.4	38.1	29.2	23.2	122.7	4.03
	25.9	24.4	535	640	490	385	33.9	40.6	31.1	24.4	130.0	
	27.0	26.6	555	695	535	400	35.2	44.1	33.9	25.4	138.6	
	28.0	27.4	585	725	570	420	37.1	46.0	36.2	26.6	145.9	
	29.3	28.2	630	770	630	450	40.0	48.8	40.0	28.6	157.3	
	30.1	28.6	695	835	720	510	44.1	53.0	45.7	32.3	175.1	
	–	29.4	770	905	825	575	48.8	57.4	52.3	36.5	195.1	4.84 + 3mm
	31.2	30.7	905	1020	1015	710	57.4	64.7	64.4	45.0	231.5	5.01[1]
	32.1	30.8	1130	1165	1245	930	71.7	73.9	79.0	59.0	283.6	5.17[1]
	33.4	32.0	1320	1325	1440	1120	83.7	84.1	91.3	71.1	330.2	5.35
	33.6	31.8	1455	1430	1605	1335	92.3	90.7	101.8	84.7	369.5	
	36.6		2365	2540	3270	2710	–	–	–	–	–	5.55

[1] Start of crushing of concrete under edge of top flange.

Table VI.9: Measured strains and corresponding calculated forces in the shanks of the studs in tension of test specimen BM4

Load cycle	F_t^{max}	F_t^{min}	ε_{sh}^1	ε_{sh}^2	ε_{sh}^3	ε_{sh}^4	F_{sh}^1	F_{sh}^2	F_{sh}^3	F_{sh}^4	$\sum_{i=1}^{4} F_{sh}^i$	Crack pattern
	(kN)	(kN)	$(\times 10^{-6})$	$(\times 10^{-6})$	$(\times 10^{-6})$	$(\times 10^{-6})$	(kN)	(kN)	(kN)	(kN)	(kN)	Fig. 7.26
II	4.6	4.5	5	80	95	−5	0.3	5.1	6.0	−0.3	11.1	
	8.5	8.3	15	230	250	20	1.0	14.6	15.9	1.3	32.7	
	12.4	12.3	85	320	350	90	5.4	20.3	22.2	5.7	53.6	
	14.3		130	410	440	135	8.3	26.0	27.9	8.6	70.7	
	18.3	18.1	195	560	580	210	12.4	35.5	36.8	13.3	98.0	
	20.4	20.0	235	635	660	250	14.9	40.3	41.9	15.9	112.9	II20
	22.0	21.4	276	709	733	285	17.5	45.0	46.5	18.1	127.1	
	24.0	23.1	325	795	815	330	20.6	50.4	51.7	20.9	143.7	II24[1]
	26.0	24.3	405	835	865	410	25.7	53.0	54.9	26.0	159.5	II26
III	0.0	0.0	175	30	70	180	11.1	1.9	4.4	11.4	28.9	
	18.4	18.2	270	630	655	255	17.1	40.0	41.6	16.2	114.8	
	22.0	21.6	320	755	690	310	20.3	47.9	43.8	19.7	131.6	
	24.0	23.8	355	825	855	345	22.5	52.3	54.2	21.9	151.0	
	26.0	25.4	410	880	920	400	26.0	55.8	58.4	25.4	165.6	26
	27.0	26.3	465	915	950	445	29.5	58.0	60.3	28.2	176.0	
	28.0	25.0	575	880	900	470	36.5	55.8	57.1	29.8	179.2	28
	27.3	26.1	660	900	900	525	41.9	57.1	57.1	33.3	189.4	
	37.0		–	–	–	–	–	–	–	–	–	

[1] Start of crushing of concrete under edge of top flange.

Table VI.10: Measured strains and corresponding calculated forces in the shanks of the studs in tension of test specimen BM5

Load cycle	F_t^{max} (kN)	F_t^{min} (kN)	ε_{sh}^1 $(\times 10^{-6})$	ε_{sh}^2 $(\times 10^{-6})$	F_{sh}^1 (kN)	F_{sh}^2 (kN)	$\sum_{i=1}^{2} F_{sh}^i$ (kN)	Crack pattern Fig. 7.27
III	6.0	6.0	190	150	12.1	9.5	21.6	
	10.0	9.9	385	355	24.4	22.5	46.9	
	14.0	13.9	560	540	35.5	34.3	69.8	
	16.0	16.0	670	655	42.5	41.6	84.1	
	18.0	17.9	790	775	50.1	49.2	99.3	18
	20.0	19.8	905	890	57.4	56.5	113.9	20
	22.0	21.8	1025	1015	65.0	64.4	129.4	22
	24.0	23.5	1135	1110	72.0	70.4	142.4	24
	25.0	23.6	1225	1115	77.3	70.5	148.0	25
	26.0	25.1	1330	1215	84.4	77.1	161.4	26
	27.0	26.5	1430	1320	90.7	83.7	174.4	27
	27.4	25.3	1415	1275	89.8	80.9	170.6	27
	27.8	26.3	1415	1275	89.8	80.9	170.6	
	28.1	27.0	1530	1445	97.1	91.7	188.7	28
	28.9	27.1	1705	1645	108.2	104.4	212.5	
	29.3	27.7	1880	1790	119.3	113.6	232.8	δ_1^1
	33.0	31.2	3860	3225	Yield	Yield	Yield	δ_4
	31.6	29.5	4250	3575	Yield	Yield	Yield	δ_6
	30.6	28.2	4367	3240	Yield	Yield	Yield	δ_7

[1] Start of crushing of concrete under edge of top flange.

Table VI.11: Measured strains and corresponding calculated forces in the shanks of the studs in tension of test specimen BM6

Load cycle	F_t^{max}	F_t^{min}	F_{sh}^1	F_{sh}^2	F_{sh}^3	F_{sh}^4	F_{sh}^5	F_{sh}^6	F_{sh}^7	F_{sh}^8	$\sum_{i=1}^{odd} F_{sh}^i$	$\sum_{i=2}^{even} F_{sh}^i$	Crack pattern
	(kN)	(kN)	(kN)	(kN)	(kN)	(kN)	(kN)	(kN)	(kN)	(kN)	(kN)	(kN)	Fig. 7.28
III	7.0	7.0	0.0	0.6	6.3	5.1	5.1	1.3	0.0	0.6	11.4	7.6	
	10.0	9.9	0.3	1.6	9.8	7.0	7.9	2.5	0.3	1.9	18.4	13.0	
	16.0	15.7	4.4	7.0	20.6	13.6	14.6	10.2	4.1	6.7	43.8	37.4	
	18.0	17.8	5.4	9.5	23.5	15.5	16.5	12.7	6.0	8.9	51.4	46.6	
	20.0	19.6	6.3	11.1	26.0	17.1	17.8	14.0	8.3	10.5	58.4	52.7	
	21.0	19.4	10.2	12.1	29.2	16.8	20.9	13.0	6.3	10.2	66.6	52.0	
	22.0	21.1	13.0	11.4	31.1	17.4	22.8	13.6	9.8	9.8	76.8	52.3	
	23.0	22.5	15.2	11.7	33.0	18.7	24.7	14.9	12.1	10.2	85.0	55.5	
	24.0	23.3	18.1	11.7	33.3	20.6	25.7	19.0	14.3	10.5	91.3	61.9	
	25.0	24.1	21.6	12.4	33.3	24.7	26.0	18.1	16.5	11.7	97.4	66.9	
	27.0	25.6	27.9	14.6	36.2	30.1	27.6	20.0	21.6	16.5	113.2	81.2	
	28.0	27.2	30.1	15.9	37.7	32.0	28.6	28.9	23.8	18.4	120.2	95.2	
	29.0	28.3	32.0	17.1	39.3	33.6	29.2	31.1	24.7	20.9	125.3	102.8	
	30.0	29.1	33.0	18.4	40.6	35.2	30.1	33.9	26.0	23.2	129.7	110.7	
	31.0	30.1	33.9	18.1	42.4	37.9	31.7	38.1	27.5	25.7	135.6	119.8	
	33.0	30.8	36.2	13.6	46.0	33.6	34.9	36.2	29.8	25.4	146.9	108.8	
	32.8	30.6	–	–	–	–	–	–	–	–	–	–	$\delta 1$[1]
	32.1	29.8	–	–	–	–	–	–	–	–	–	–	$\delta 2$
	31.8	29.8	crushing of concrete under edge of top flange										$\delta 3$
	30.6	38.4	–	–	–	–	–	–	–	–	–	–	$\delta 4$
	28.4	26.1	–	–	–	–	–	–	–	–	–	–	$\delta 5$
	28.1	25.8	–	–	–	–	–	–	–	–	–	–	$\delta 6$

[1] Start of crushing of concrete under edge of top flange.

Table VI.12: Measured strains and corresponding calculated forces in the shanks of the studs in tension of test specimen BM7

Load cycle	F_t^{max}	F_t^{min}	F_{sh}^1	F_{sh}^2	F_{sh}^3	F_{sh}^4	F_{sh}^5	F_{sh}^6	$\sum_{i=1}^{6} F_{sh}^i$	Crack pattern
	(kN)	(kN)	(kN)	(kN)	(kN)	(kN)	(kN)	(kN)	(kN)	Fig. 7.29
II	6.0	6.0	0.3	0.3	6.3	4.4	0.6	0.3	12.4	
	10.0	9.8	0.6	2.5	9.8	7.6	2.9	1.0	24.4	
	16.1	15.9	3.2	8.9	20.6	19.7	9.8	2.2	64.4	
	18.1	17.8	4.4	8.9	26.6	26.3	9.8	3.2	79.3	
	20.1	19.8	4.4	8.9	33.6	34.9	10.2	5.4	97.4	
	22.1	21.8	5.4	9.5	38.4	41.6	10.8	8.3	113.9	
	24.0	23.5	7.9	11.7	43.8	47.6	14.3	10.8	136.1	
	26.0	24.5	15.5	14.3	47.3	50.1	19.7	21.3	168.1	26
	27.0	26.1	19.7	17.1	50.1	52.7	23.8	26.3	189.7	27
	28.0	27.3	22.2	18.7	50.8	53.3	26.0	29.2	200.1	28
	29.0	26.6	27.9	23.5	46.6	58.4	31.1	34.3	221.7	29
	30.0	27.3	31.7	26.0	50.1	60.9	33.0	36.5	238.2	
	36.0	–	–	–	–	–	–	–	–	

Appendix VII

Truss model for internal forces in slab of test specimen

In Fig. VII.1 a general shape of the truss model is given. Assuming the direction of the forces in the chords as indicated on the figure, the values of the internal forces obtained from equilibrium are:

$$
\begin{aligned}
N_{AC} &= N_{CA} = \frac{-R_A}{\sin \alpha_A} \\
N_{AD} &= N_{DA} = R_A \cot \alpha_A + H \\
N_{CD} &= N_{DC} = N_{CA} \frac{\sin (\alpha_A + \alpha_{cr})}{\sin (\alpha_{cr} - \alpha_c)} \\
N_{CE} &= N_{EC} = -N_{CA} \frac{\sin (\alpha_A + \alpha_{cr})}{\sin (\alpha_{cr} - \alpha_c)} \\
N_{DF} &= N_{FD} = \frac{(F_{st} - N_{DC} \sin \alpha_c)}{\sin \alpha_F} \\
N_{EF} &= N_{FE} = \frac{-N_{DF} \sin \alpha_F}{\sin \alpha_E} \\
N_{BF} &= N_{FB} = R_B \cot \alpha_B \\
N_{BE} &= N_{EB} = \frac{-R_B}{\sin \alpha_B}
\end{aligned}
$$

For test specimen BM3, the first diagonal crack is formed when $F_t = 22.5$ kN and the crack forms an angle $\alpha_{cr} = 30°$ with the horizontal.

For the model in Fig. 8.3(a):

$l_1 = 1215$ mm $\qquad$ $l_4 = 220$ mm;
$l_2 = 0$ mm $\qquad$ $l_5 = 0$ mm;
$l_3 = 220$ mm $\qquad$ $l_6 = 1145$ mm

For the model in Fig. 8.3(b):

$l_1 = 1225$ mm $\qquad l_4 = 213$ mm;
$l_2 = 0$ mm $\qquad l_5 = 0$ mm;
$l_3 = 213$ mm $\qquad l_6 = 1142$ mm

so that the forces in the different chords are given by the values in Table VII.1.

	N_{AC} (kN)	N_{AD} (kN)	N_{CD} (kN)	N_{CE} (kN)	N_{DF} (kN)	N_{EF} (kN)	N_{BF} (kN)	N_{BE} (kN)
Fig. 8.3(a)	−123	145	86	−143	124	−61	116	−116
Fig. 8.3(b)	−209	231	133	−241	29	−14	86	−87

For test specimen BM7, the first diagonal crack is formed when $F_t = 26$ kN and the crack forms an angle $\alpha_{cr} = 33°$ with the horizontal.

For the model in Fig. 8.3(a):

$l_1 = 1155$ mm $\qquad l_4 = 191$ mm;
$l_2 = 0$ mm $\qquad l_5 = 0$ mm;
$l_3 = 191$ mm $\qquad l_6 = 1234$ mm

For the model in Fig. 8.3(b):

$l_1 = 1155$ mm $\qquad l_4 = 180$ mm;
$l_2 = 0$ mm $\qquad l_5 = 0$ mm;
$l_3 = 180$ mm $\qquad l_6 = 1245$ mm

so that the forces in the different chords are given by the values in Table VII.2.

	N_{AC} (kN)	N_{AD} (kN)	N_{CD} (kN)	N_{CE} (kN)	N_{DF} (kN)	N_{EF} (kN)	N_{BF} (kN)	N_{BE} (kN)
Fig. 8.3(a)	−136	161	102	−161	172	−94	144	−145
Fig. 8.3(b)	−227	252	162	−270	80	−45	108	−109

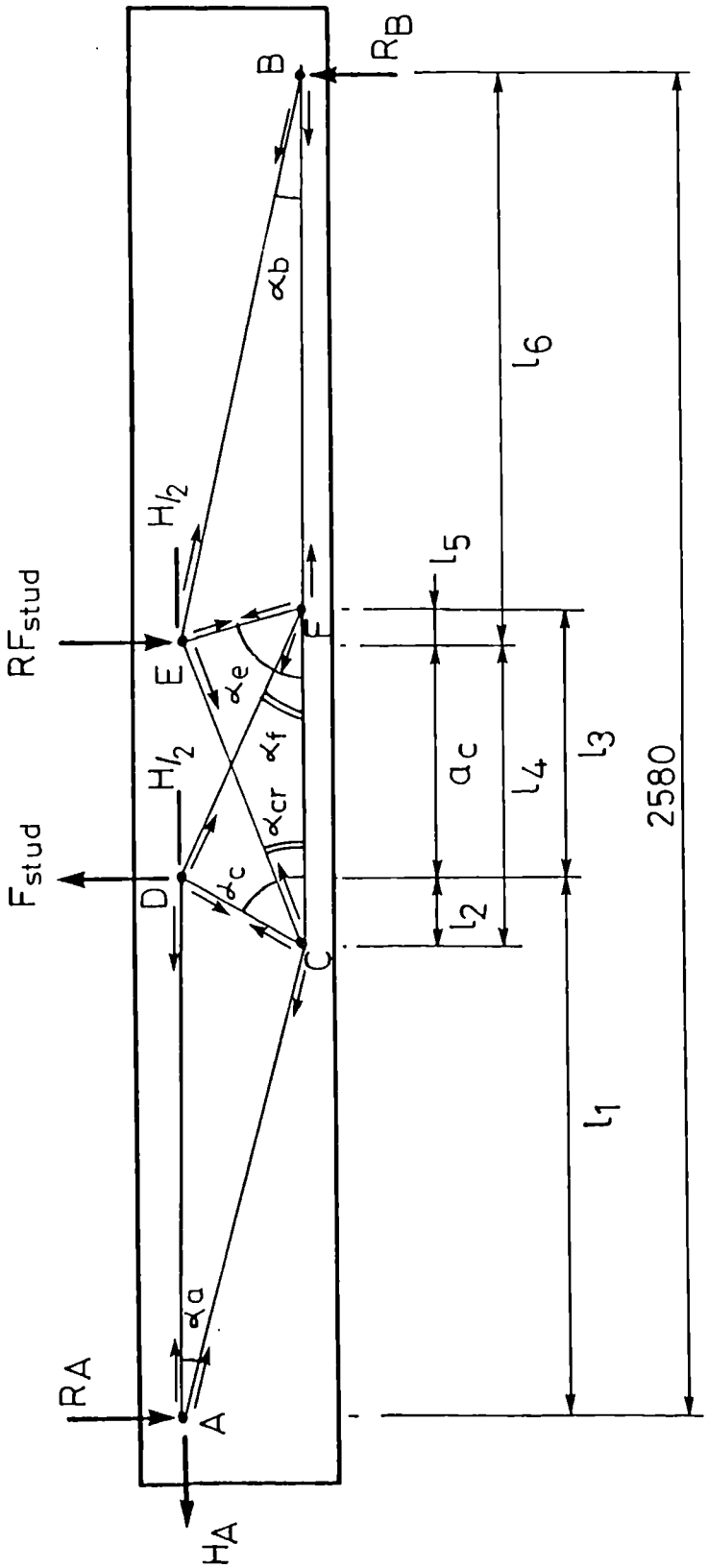

Figure VII.1: General shape of truss model.